



Pulse-shape studies with coplanar grid CdZnTe detectors and searches for rare nuclear decays with the COBRA experiment

DISSERTATION

zur Erlangung des akademischen Grades

Doctor rerum naturalium
(Dr. rer. nat.)

vorgelegt der
Fakultät Physik
der Technischen Universität Dresden

von
Dipl.-Phys. Stefan Zatschler
geboren am 19.06.1989 in Dresden

Gutachter: Prof. Dr. Kai Zuber
Prof. Dr. Kevin Kröninger

Abgabe: 29. Juni 2020
Disputation: 23. September 2020

“The universe is not only queerer than we suppose, but queerer than we can suppose.”
– J.B.S. Haldane in *Possible Worlds*.

Abstract

The inference of massive neutrino states through the observation of flavor oscillations boosted the importance of direct and indirect mass searches, including the search for the hypothesized neutrinoless double beta decay ($0\nu\beta\beta$ -decay). Nowadays, the search for this ultra-rare nuclear transition is one of the most active research fields at the intersection of nuclear, particle and astroparticle physics. Its main and evident feature is the explicit violation of the total lepton number, which is an accidentally conserved quantity in the Standard Model of particle physics, and would prove the Majorana nature of neutrinos. This, in turn, would support the theoretical explanation of the origin of the observed baryon asymmetry in the universe through the process of leptogenesis and could shed light on the role of neutrinos in the early universe's structure formation.

For the theoretical description of the $0\nu\beta\beta$ -decay, nuclear structure effects play an important role as they may affect considerably the decay rate. These nuclear effects are summarized as the nuclear matrix elements (NMEs), containing information about the initial and final states of the involved atomic nuclei and the decay mechanism. Under the assumption of light Majorana neutrino exchange, the inverse half-life is proportional to the effective Majorana neutrino mass, a kinematic phase-space factor, the involved NMEs and the fourth power of the weak axial-vector coupling g_A . The search for the $0\nu\beta\beta$ -decay is driven by experiments and an accurate description of the nuclear structure effects is essential to estimate the required sensitivity to cover a certain mass range. In order to match theoretical calculations and the results of β -decay and $\beta\beta$ -decay studies, there is a scientific discussion regarding quenching effects of g_A in nuclear media.

Different methods are being investigated to determine an effective g_A at the energy scale of nuclear transitions. One of those recently proposed methods exploits the dependency of the spectrum-shape of highly forbidden β -decays on g_A . An ideal candidate for such an investigation is the fourfold forbidden non-unique β -decay of ^{113}Cd , which is the most prominent signal in the current stage of the COBRA experiment searching for $0\nu\beta\beta$ -decays with cadmium zinc telluride (CZT) solid state detectors. The detector material CZT acts as a semiconductor at room temperature and contains intrinsically several candidates for rare nuclear transitions. The experiment is located at the LNGS underground facility in Italy, which is shielded against cosmic rays by a mean rock coverage of about 1400 m. In the present demonstrator phase, it consists of 64 coplanar grid (CPG) detectors that are arranged in four layers of 4×4 crystals.

In the scope of this thesis, conventional and novel prototype CPG-CZT detectors, which are the basis for an anticipated large-scale experiment, are characterized by evaluating homogeneous and localized γ -ray irradiation measurements. Moreover, a novel pulse-shape discrimination (PSD) technique is established, optimized and applied in the analysis of the physics data obtained with the demonstrator array. The PSD optimization is complemented by dedicated laboratory measurements with the aim to create a pulse-shape library of signal-like single-site events and high-energy cosmic muon interactions for which an analytic reconstruction model has been developed.

For the first time, the COBRA demonstrator's full exposure from Sept.'11 to Nov.'19 is analyzed, including a detailed background characterization as well as an automatized data partitioning to identify periods with increased backgrounds. The main subject is the study of the ^{113}Cd β -decay's spectrum-shape to address the quenching of g_A in low-momentum exchange nuclear processes. The analysis of the experimental data is carried out in the context of three nuclear frameworks and confirms the idea of a significantly quenched g_A . Furthermore, the data are analyzed with respect to the $2\nu\beta\beta$ -decay of ^{116}Cd and the long-lived α -decay of ^{190}Pt as a localized contaminant in the CZT detectors' electrode metalization. Finally, the prospects of a search for excited state transitions of the $\beta\beta$ -nuclides ^{116}Cd and ^{130}Te are studied with elaborate Monte-Carlo simulations. The analysis section is concluded with an estimate of the achievable $0\nu\beta\beta$ -decay half-life sensitivity for multiple $\beta\beta$ -nuclides given the full exposure of the COBRA demonstrator and the recently achieved upgrade to the COBRA eXtended DEMonstrator (XDEM).

Kurzdarstellung

Der Beweis der Existenz von massiven Neutrinos durch die Beobachtung von Flavour-Oszillationen bestätigt die Wichtigkeit direkter und indirekter Massen-Studien, wie der Suche nach dem bisher unbeobachteten neutrinolosen Doppelbetazerfall ($0\nu\beta\beta$ -Zerfall). Die Beobachtung dieses Prozesses hat weitreichende Folgen und bedingt die Verletzung der Leptonzahl, welche im Standardmodell der Teilchenphysik eine zufällige Erhaltungsgröße ist. Des Weiteren würde der Nachweis bestätigen, dass es sich bei Neutrinos um Majorana-Fermionen handelt. Dies wiederum stützt die These zur Erläuterung des Materie-Antimaterie-Ungleichgewichts im Universum durch den Prozess der Leptogenese und die Bedeutung von Neutrinos bezüglich der Strukturbildung im frühen Universum.

In der theoretischen Beschreibung des $0\nu\beta\beta$ -Zerfalls spielen Kernstruktureffekte eine wesentliche Rolle. Diese werden in Form von Kernmatrixelementen, welche Informationen über die Ausgangs- und Endzustände der involvierten Atomkerne beinhalten, zusammengefasst. Unter der Annahme des Austauschs von leichten Majorana-Neutrinos, ist die invertierte Halbwertszeit proportional zur effektiven Majorana-Neutrinomasse, einem kinematischen Phasenraumfaktor, den involvierten Kernmatrixelementen sowie zur vierten Potenz der axialen Vektorkopplungsstärke g_A . Um experimentelle Ergebnisse von β - und $\beta\beta$ -Zerfallstudien in Einklang mit theoretischen Modellrechnungen zu bringen, besteht eine wissenschaftliche Diskussion bezüglich sogenannter Quenching-Effekte und dem damit verbundenen effektiven Wert von g_A in kernphysikalischen Prozessen.

Hierbei werden verschiedene Methoden untersucht, um einen effektiven Wert von g_A zu bestimmen. Eine der kürzlich vorgeschlagenen Methoden basiert auf der g_A -Abhängigkeit der spektralen Form von speziellen β -Zerfällen. Ein idealer Kandidat für eine derartige Untersuchung ist der vierfach verbotene β -Zerfall von ^{113}Cd . Dieser Zerfall dominiert den niederenergetischen Teil des Energiespektrums der aktuellen Ausführung des COBRA Experimentes, welches sich mit der Suche nach $0\nu\beta\beta$ -Zerfällen basierend auf Cadmium-Zink-Tellurid (CZT) Detektoren befasst. Hierfür befindet sich das Experiment im italienischen Untergrundlabor LNGS, wo es durch eine mittlere Gesteinüberdeckung von etwa 1400 m vor kosmischer Strahlung abgeschirmt wird. Das verwendete Detektormaterial agiert als Halbleiter bei Raumtemperatur und beinhaltet mehrere Kandidaten für seltene Kernumwandlungen entsprechend der natürlichen Isotopenzusammensetzung von CZT. In der aktuellen Demonstrator-Phase umfasst es 64 CPG-CZT Detektoren, welche in vier Lagen von jeweils 4×4 Kristallen angeordnet sind.

Im Rahmen der vorliegenden Arbeit werden konventionelle, sowie neuartige Prototypen von CPG-CZT Detektoren, welche der Grundstein für ein zukünftiges Großexperiment sind, in umfassenden Gammabestrahlungsreihen charakterisiert. Des Weiteren wird eine neuartige Form der Pulsformanalyse etabliert, optimiert und in der Datenanalyse des COBRA Demonstrators angewendet. Um tiefere Einblicke in die Möglichkeiten zur Unterscheidung zwischen signal- und untergrundartigen Pulsformen zu gewinnen, werden dedizierte Labormessungen durchgeführt. Das Ziel dieser Messungen ist, eine Pulsform-Bibliothek von signalartigen Einzelwechselwirkungen mit Hilfe von koinzidenter Comptonstreuung, sowie von hochenergetischen Myon-Interaktionen anzulegen, wodurch die Formulierung eines analytischen Modells der Ereignisrekonstruktion möglich wird.

Weiterhin erfolgt erstmalig eine Analyse des kompletten Datensatzes des COBRA Demonstrators, inklusive einer genauen Charakterisierung des Untergrundes. Dabei liegt das Hauptaugenmerk auf der Untersuchung der spektralen Form des ^{113}Cd β -Zerfalls und der damit einhergehenden g_A -Abhängigkeit. Zudem beschäftigt sich die Arbeit mit der Datenanalyse hinsichtlich des $2\nu\beta\beta$ -Zerfalls von ^{116}Cd , sowie des langlebigen α -Zerfalls von ^{190}Pt als einer der prominentesten Untergrundbeiträge. Schließlich werden die Perspektiven der Suche nach Kernübergängen in angeregte Zustände für die vielversprechendsten Kandidaten ^{116}Cd und ^{130}Te mit Hilfe von detaillierten Monte-Carlo Simulationen untersucht. Den Abschluss des Analysekapitels bildet eine Abschätzung der erreichbaren Halbwertszeit-Sensitivität bezüglich verschiedener $0\nu\beta\beta$ -Zerfälle in Anbetracht des vollständigen Datensatzes des COBRA Demonstrators und dem jüngst erfolgten Upgrade des Experimentes zum erweiterten Demonstrator COBRA XDEM.

Contents

1	Introduction	1
1.1	The Standard Model of particle physics	2
1.1.1	Lagrange formalism in QED	2
1.1.2	General aspects of QFTs and the SM	4
1.1.3	Particle content and classifications	6
1.2	Radioactivity and masses of atomic nuclei	8
1.2.1	Droplet model of atomic nuclei	8
1.2.2	α -decay	11
1.2.3	β -decay	11
1.2.4	De-excitation via γ -ray emission	13
1.3	Interaction between particles and matter	13
1.3.1	γ -ray interactions	13
1.3.2	Charged particles	15
2	Neutrino physics	19
2.1	Neutrino discovery and characteristics	20
2.1.1	Theoretical prediction and experimental discovery	20
2.1.2	Verification of neutrino properties	21
2.1.3	Flavor mixing and neutrino oscillation	23
2.1.4	Pending questions in the neutrino sector	26
2.2	Neutrino mass generation	27
2.2.1	Origin of neutrino masses	27
2.2.2	Dirac versus Majorana mass terms	28
2.2.3	Overview of seesaw mechanisms	31
2.3	Neutrino mass searches	32
2.3.1	Direct kinematic approaches	32
2.3.2	Cosmological surveys	33
2.3.3	Neutrinoless double beta decay	33
2.3.4	Interplay of neutrino mass observables	34
3	Double beta decay	35
3.1	Classification of double beta decays	36
3.1.1	Double beta decay modes	36
3.1.2	Experimental signature	37
3.2	Theoretical description	38
3.2.1	Connection to droplet model	38

3.2.2	Schechter-Valle theorem	39
3.2.3	Half-life prediction	40
3.2.4	Overview of nuclear models	43
3.2.5	Quenching of g_A in nuclear β -decay	44
3.3	Experimental aspects	45
3.3.1	Sensitivity approximation	45
3.3.2	Experimental techniques	46
3.3.3	Overview of recent results	48
4	The COBRA experiment	49
4.1	CZT as semiconductor material	50
4.1.1	Material properties	50
4.1.2	Crystal fabrication and detector technologies	53
4.1.3	Coplanar grid approach	55
4.1.4	Shockley-Ramo theorem	56
4.2	CZT as source material for rare decays	59
4.3	The COBRA demonstrator at LNGS	60
4.3.1	Overview of the LNGS underground laboratory	60
4.3.2	Design of detector array	62
4.3.3	DAQ and electronics	64
4.3.4	Upgrade to COBRA XDEM	66
4.3.5	Proposal for large-scale experiment	67
5	Data processing and Monte-Carlo simulation tools	69
5.1	Basics of signal processing	70
5.1.1	Weighting potentials in CPG-CZT detectors	70
5.1.2	Weighting factor optimization and gain-balancing	71
5.1.3	Processing tools	73
5.2	Event reconstruction	75
5.2.1	Pulse-height determination	76
5.2.2	Energy calibration	76
5.2.3	Trapping correction of interaction depth	77
5.2.4	Threshold definition	79
5.3	Monte-Carlo simulation tools	80
5.3.1	VENOM	80
5.3.2	DECAY0 event generator	81
5.3.3	COBRA GDML	82
5.3.4	COMSOL multiphysics	83
6	Characterization of CPG-CZT detectors	85
6.1	Overview of COBRA's detector technology	86
6.1.1	Conventional CPG-CZT detectors	87
6.1.2	Prototype qCPG-CZT detectors	88
6.1.3	Instrumentation of guard-ring electrode	89
6.2	Homogeneous γ -ray measurements	89
6.2.1	Working point determination	89
6.2.2	Absolute full-energy efficiency	93
6.2.3	Additional laboratory studies	94
6.3	Localized γ -ray measurements	95
6.3.1	Review of COBRA demonstrator data	96

6.3.2	Localized characterization of qCPG-CZT detectors	97
6.3.3	Validation of depth reconstruction	99
7	Pulse-shape discrimination	101
7.1	Event classification via PSD	102
7.1.1	Data-cleaning and noise rejection	102
7.1.2	Near anode and cathode events	105
7.1.3	Lateral surface events	108
7.1.4	Single-site and multi-site events	109
7.1.5	Coincident events	110
7.2	Identification of multi-site events	111
7.2.1	Peak-search algorithm	111
7.2.2	A/E criterion	113
7.2.3	Optimization procedure	114
7.2.4	A/E calibration	121
7.3	Pulse-shape library via coincident Compton scattering	124
7.3.1	Experimental setup	124
7.3.2	Data-taking and pre-selection	127
7.3.3	Coincident energy spectra	129
7.3.4	Single-site event selection	130
7.3.5	Single-site pulse-shape library	131
7.3.6	Summary and outlook	133
7.4	Characterization of muon-induced interactions	134
7.4.1	Background contribution of cosmic muons	134
7.4.2	Analytic model of event reconstruction	137
7.4.3	Evaluation of laboratory measurements	141
7.4.4	Analysis of muon-induced events	147
8	Rare nuclear decay searches with the COBRA demonstrator	153
8.1	LNGS data management	154
8.1.1	Raw data	154
8.1.2	Calibration parameters	155
8.1.3	COBRA CouchDB	158
8.1.4	Overview of physics data-taking	159
8.2	Background characterization	161
8.2.1	Performance of PSD cuts	164
8.2.2	Low-energy features	165
8.2.3	Prominent γ -lines	166
8.2.4	Identified α -decay contaminants	169
8.2.5	Muon-induced background	171
8.3	Quenching of g_A deduced from the ^{113}Cd β -decay	174
8.3.1	The spectrum-shape method	174
8.3.2	Previous studies on ^{113}Cd	177
8.3.3	Threshold study and optimization	181
8.3.4	Detector calibration	186
8.3.5	Selection of detector pool	188
8.3.6	Event selection	192
8.3.7	Low-energy background model	193
8.3.8	Preparation of templates	202
8.3.9	Spectrum-shape analysis	207

8.3.10 Discussion of results	212
8.3.11 Systematic uncertainties	217
8.3.12 Preliminary results under the CVC hypothesis	219
8.3.13 Half-life determination via the SSM	226
8.4 Conventional double beta decay of ^{116}Cd	230
8.4.1 Previous experiments	230
8.4.2 Data partitioning and event selection	232
8.4.3 Comparison of LNGS data and MC simulation	237
8.4.4 Concluding remarks	238
8.5 Long-lived α -decay of ^{190}Pt	240
8.5.1 Motivation and introduction	240
8.5.2 Pre-characterization of platinum layer	241
8.5.3 Monte-Carlo simulation of ^{190}Pt α -decay	243
8.5.4 Analysis of COBRA's LNGS data	245
8.6 Double beta decays into excited states	252
8.6.1 Motivation and recent experimental results	252
8.6.2 COBRA's isotopes of interest	254
8.6.3 Monte-Carlo simulation of excited state transitions	256
8.6.4 Event selection based on M2 spectra	266
8.6.5 Determination of signal selection efficiency	270
8.6.6 Prospects of detector pair optimization	273
8.6.7 Conclusion and outlook	280
8.7 Update on COBRA's $0\nu\beta\beta$ -decay modes	283
8.7.1 Determination of intrinsic efficiency	283
8.7.2 Half-life sensitivity estimate	284
8.7.3 Outlook and future projection	286
9 Conclusions	289
Appendices	291
A Impressions of LNGS setup	291
A.1 COBRA demonstrator setup	291
A.2 Installation of XDEM upgrade	292
A.3 Detector arrangement	293
B Experimental equipment at TUD	294
B.1 Localized crystal characterization	294
B.2 Long-term background measurements	294
B.3 Compton scattering experiment	295
C Statistics and limits	296
C.1 Basic equations	296
C.2 Coverage factor for sensitivity and limit setting	297
C.3 Bayes' theorem and Bayesian statistics	298
D Supplementary material	299
D.1 Pulse-shape discrimination	299
D.1.1 Lateral surface events	299
D.1.2 A/E criterion	300
D.1.3 Muon-induced events	301

D.2	LNGS data evaluation	302
D.2.1	Natural decay chains	302
D.2.2	Failure of nitrogen flushing at LNGS	303
D.2.3	Overview of the demonstrator's LNGS calibrations	304
D.3	Characterization of qCPG-CZT prototype detector	306
D.4	^{113}Cd spectrum-shape analysis	308
D.4.1	Run method example	308
D.4.2	Single detector spectra	309
D.4.3	Interaction depth distribution for ^{113}Cd	312
D.4.4	Analytic low-energy background model	313
D.4.5	Prediction under the CVC hypothesis	314
D.5	Double beta decays into excited states	315
D.5.1	Detector pair distributions	315
D.5.2	Normalized Monte-Carlo spectra	317
D.5.3	Detector pair optimization	319
E	Characterization of LNGS detectors	320
List of Figures		325
List of Tables		332
List of Acronyms		335
List of co-supervised theses		339
Bibliography		341
Acknowledgments		367

Chapter 1

Introduction

The first chapter of this thesis is a brief introduction into the key concepts of modern particle and nuclear physics. This includes a summary of the theoretical aspects of the so-called Standard Model of elementary particle physics as well as the classification of its particle content according to the properties of those particles with respect to the underlying fundamental interactions. Moreover, the phenomenon of radioactive decays of atomic nuclei and their modeling in nuclear physics will be discussed. Finally, the most common interaction processes between elementary particles and matter will be summarized in the last section of the introduction, focusing on the description of the energy regime of nuclear decays.

1.1 The Standard Model of particle physics

The development of the theory known today as the Standard Model (SM) of elementary particle physics is driven by many theoretical and experimental physicists since more than 60 years. Its modern formulation is based on the original works of S. Glashow [Gla61], S. Weinberg [Wei67] and A. Salam [Sal68], who were jointly awarded with the Nobel Prize in Physics in 1979 [Nob79]. In their honor, the electroweak SM is also referred to as the GWS model. The complete SM makes it possible to describe three of the four known fundamental forces in nature within a general framework based on local gauge theories. This includes the electromagnetic, weak and strong interaction, while only gravity remains unexplained. Moreover, it allows for a classification of all known elementary particles given their quantum numbers and predicts their interactions with each other.

The following section will introduce the fundamental concept of the SM – relying on quantum mechanics, special relativity and local gauge invariance – based on the Lagrangian of quantum electrodynamics (QED) [Fey85]. Furthermore, the general aspects of a quantum field theory will be addressed briefly. In the end, an overview of the SM’s particle content and its connection to the fundamental interactions will be given.

1.1.1 Lagrange formalism in QED

QED refers to the relativistic quantum field theory (QFT) of electrodynamics. It is the first theory achieving a full agreement between quantum mechanics and special relativity, which are two of the three fundamental concepts used for the formulation of the SM. Moreover, it served as the template for all subsequent QFTs including the description of the weak interaction (quantum flavor dynamics, QFD) and the strong interaction (quantum chromodynamics, QCD). For their works in this area the Nobel Prize of Physics was awarded jointly to S. Tomonaga, J. Schwinger and R. Feynman in 1965 [Nob65]. The essence of QED will be summarized in the following based on the introduction of [Zat14].

In conventional one-particle quantum mechanics, the location x of a quantum state has to be treated as an operator while, on the other hand, the time t is usually treated as a parameter. This does not conform with the concept of special relativity as time and space are treated equally in relativistic theories. One solution to combine both concepts is to interpret x as a parameter as well, which leads to *local observables* expressed as $\mathcal{O}(t, x)$. Such objects can be treated in classical field theories using Lagrangian mechanics based on generalized coordinates in mathematical functions called the *Lagrangian* $\mathcal{L}(t, x)$. The quantization of such fields results in so-called *Feynman rules* which can be used to construct all possible scalar kinematic and interaction terms of the related QFT. In the lowest order of QED there is only one interaction vertex as can be seen in Fig. 1.1 in form of a *Feynman diagram*.

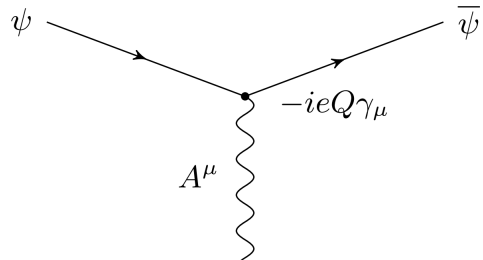


Figure 1.1: Fundamental vertex in lowest order QED (adapted from [Zat14]). The vector field A^μ represents the photon which couples to an incident fermion field ψ with a coupling strength given by the vertex factor. The outgoing fermion field is labeled as $\bar{\psi}$. By combining this fundamental vertex with additional propagators and vertices, all possible Lagrangian terms can be produced to calculate e.g. cross sections for QED interactions.

The photon as mediator of the electromagnetic interaction is represented by the vector field A^μ and interacts with massive fermions represented as so-called *spinor fields* ψ . With the help of the Feynman rules depicted in Fig. 1.2, it is possible to derive all terms of the QED Lagrangian with respect to the Feynman diagrams.

outer lines = wave functions	inner lines = propagators
incoming fermion ψ	
outgoing fermion $\bar{\psi}$	
	fermion
	photon

Figure 1.2: Feynman rules of the QED (taken from [Zat14]). Outer fermion lines are replaced with wave functions $u(p)$. Inner lines connecting two vertices are referred to as *propagators* and get replaced by the corresponding terms. All QED interactions can be expressed in the form of such Feynman diagrams by combining inner and outer fermion lines with the fundamental vertex shown in Fig. 1.1.

The Lagrangian terms associated with a Feynman diagram are obtained by multiplying all the contributions according to the Feynman rules against the direction of the arrows for all outer fermion lines. The full QED Lagrangian can then be written as

$$\mathcal{L}_{\text{QED}} = \bar{\psi}(i\cancel{\partial} - m)\psi - \frac{1}{4}F^{\mu\nu}F_{\mu\nu} - eQA^\mu\psi\gamma_\mu\bar{\psi} \quad (1.1)$$

with $F^{\mu\nu}$ representing the electromagnetic field strength tensor. Moreover, the commonly used short notation $\cancel{\partial} = \gamma_\mu\partial^\mu$ is applied. The first term in Eqn. (1.1) corresponds to the gauge invariant equation of motion for fermions of mass m and is referred to as the free *Dirac equation* [Dir28]. The last term represents the interaction of the massive fermions with the photon field coupled by their electric charge Q . Demanding invariance of the free Dirac equation under the following local gauge transformations

$$\psi(x) \longrightarrow e^{iQ\Theta(x)}\psi(x), \quad \Theta(x) \in \mathbb{R} \quad (\text{hom. transf.}) \quad (1.2)$$

$$A^\mu(x) \longrightarrow A^\mu(x) - \frac{1}{e}\partial^\mu\Theta(x) \quad (\text{inhom. transf.}) \quad (1.3)$$

requires to adjust the covariant derivative such as shown in Eqn. (1.4)–(1.5).

$$\partial^\mu \longrightarrow \partial^\mu + ieQA^\mu \quad (1.4)$$

$$\Rightarrow D^\mu \equiv \partial^\mu + ieQA^\mu. \quad (1.5)$$

The demand for local gauge invariance directly leads to the existence of a so-called *gauge field*, which can be identified as the vector field A^μ representing the photon in QED. Because of the structure of Eqn. (1.5), connecting the original covariant derivative ∂_μ with the electric charge Q , the procedure is also referred to as *minimal coupling*. The respective gauge transformation of the kinematic term $D^\mu\psi(x)$ can be expressed as

$$D^\mu\psi(x) \longrightarrow e^{iQ\Theta(x)}D^\mu\psi(x), \quad (1.6)$$

leading to the absorption of the additional term introduced by the inhomogeneous transformation shown in Eqn. (1.3). Moreover, with the gauge invariant formulation of the covariant derivative, the electromagnetic field strength tensor can be expressed via the following commutator relation

$$[D^\mu, D^\nu] = [\partial^\mu + ieQA^\mu, \partial^\nu + ieQA^\nu] \quad (1.7)$$

$$= ieQ(\partial^\mu A^\nu - \partial^\nu A^\mu) \quad (1.8)$$

$$= ieQF^{\mu\nu}. \quad (1.9)$$

All together, the QED Lagrangian can be expressed with purely covariant terms representing the immanent gauge invariance.

$$\mathcal{L}_{\text{QED}} = \bar{\psi} (iD^\mu - m) \psi - \frac{1}{4} F^{\mu\nu} F_{\mu\nu} \quad (1.10)$$

Note that the structure of all QED interactions was solely fixed by the demand for gauge invariance, which is an arbitrary choice, but proven to be very effective in the theoretical description of fundamental processes on the basis of quantum field theories.

The unification of the electromagnetic and the weak interaction was firstly demonstrated by S. Glashow in 1961 [Gla61]. Shortly afterwards the so-called *Brout-Englert-Higgs mechanism* (see e.g. [EB64], [Hig64]) was added to the unified interaction by S. Weinberg [Wei67] and A. Salam [Sal68], completing the GWS model of electroweak interaction. This mechanism, often simply referred to as the *Higgs mechanism*, makes it possible to introduce gauge invariant mass terms in the description of the electroweak interaction for the involved particles. A more detailed summary of the Standard Model's interactions and its particle content is given in section 1.1.3. Before that, the concept of gauge invariance will be addressed in a more general sense in the following section with the aim to highlight the similarities of nature's fundamental interactions and mathematical description in the framework of the SM.

1.1.2 General aspects of QFTs and the SM

The concept of the SM relies on the interplay of several ingredients as illustrated in Fig. 1.3. Its fundamental principle is based on symmetry groups that determine the overall structure of the Lagrangians by demanding gauge invariance as demonstrated in the previous section. Moreover, the interplay is based on the famous theorem of E. Noether (see [Noe71], originally published in 1918), which states essentially that any continuous symmetry of a physical system leads to a conserved quantity, respectively. According to this statement, there are fundamental conservation laws (besides energy, momentum and spin conservation) due to the construction of QFTs based on symmetry groups. Those conservation laws involve scalar quantities that are invariant under Lorentz transformation, which are usually referred to as *charges*. By demanding gauge invariance, gauge bosons as mediators of the interaction between the fermions are introduced into the theory via the minimal coupling concept.

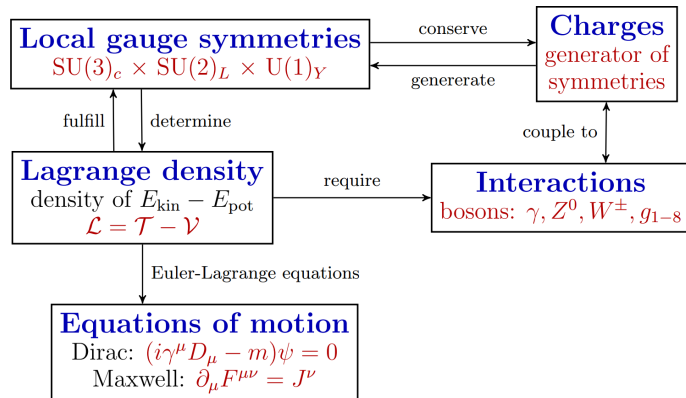


Figure 1.3: Concept of the Standard Model of particle physics (inspired by the “*Nuclear and particle physics*” lecture, IKTP, TU Dresden). The central element is the SM symmetry group representing the structure of the strong and electroweak interactions. Based on this, gauge invariant Lagrangian terms can be constructed, leading to the usual equations of motions. Moreover, the concept of gauge invariance leads to conserved quantities, referred to as charges, and the existence of gauge bosons acting as mediators of the interactions.

Finally, the usual equations of motions can be derived from the full Lagrangian of the QFT via the generalized Euler-Lagrange equations as known from classical mechanics. The full Lagrangian can be derived by following the steps outlined in the next paragraph.

The starting point is usually a Lagrangian describing the kinematics of a massive fermion field ψ based on the fundamental Dirac notation

$$\mathcal{L}_{\text{Dirac}} = \bar{\psi} (i\gamma^\mu \partial_\mu - m) \psi. \quad (1.11)$$

The demand for gauge invariance requires a transformation of the covariant derivative following the minimal coupling concept

$$\partial_\mu \longrightarrow D_\mu = \partial_\mu + igT_a W_\mu^a. \quad (1.12)$$

This way, a connection between the generalized gauge fields W_μ^a and the so-called *generators* T_a is introduced. Moreover, the coupling ig determines the coupling strength of the bosons to the matter particles. The structure of the interaction is determined by the so-called *structure constant* f_{abc} , fulfilling the following algebraic commutator relation

$$[T_a, T_b] = if_{abc} T_c \quad (1.13)$$

of the generators T_a . Finally, the field strength tensor can be defined as

$$iqW^{\mu\nu} \equiv [D^\mu, D^\nu] = D^\mu D^\nu - D^\nu D^\mu. \quad (1.14)$$

In the case of the weak interaction, associated with the symmetry group $SU(2)_L$, the generators are given by the three Pauli 2×2 spin matrices $\sigma_1 - \sigma_3$ fulfilling

$$[\sigma_i, \sigma_j] = 2i \sum_{k=1}^3 \varepsilon_{ijk} \sigma_k \quad (1.15)$$

with f_{abc} corresponding to the Levi-Civita symbol ε_{ijk} . The mediators of the electroweak interaction result as superpositions of the vector fields W_μ^a . In the low-energy limit of the SM those superpositions form the electrically neutral and massless photon, denoted as γ , as well as the heavy gauge bosons Z^0 and W^\pm . All of them acquire their mass through the electroweak symmetry breaking introduced by the Higgs mechanism.

For the strong interaction, which is associated with the symmetry group $SU(3)_c$, the structure constant is much more complicated and related to eight complex 3×3 Gell-Mann matrices as the respective generators. The $SU(3)_c$ symmetry group results in a multiplet structure in three dimensions with eight mediator vector bosons known as *gluons*. Moreover, according to the Noether theorem a new conserved, additive quantity results from the fundamental symmetry referred to as *color charge*. Because of this association, the quantum field theory is known as quantum chromodynamics (QCD) using the Greek expression for color. For non-abelian gauge theories, such as QCD, there is also a self-interaction of the involved gauge bosons as some of them are charged under the respective interaction.

Regarding the previously discussed QED, which is an example of an abelian gauge theory, the corresponding symmetry group is $U(1)_Q$, with the index referring to the electric charge Q as the associated conserved quantity. Similarly, a new conserved charge Y^w is found for the unified electroweak interaction described by the non-abelian $SU(2)_L \times U(1)_Y$ symmetry group. As electroweak interactions are flavor changing, the corresponding quantum field theory is known as quantum flavor dynamics. The so-called *weak hypercharge* Y^w is a linear combination of the electric charge Q and the third component of the weak isospin I_3^w , which will be discussed in the next section. Its definition can be expressed as

$$Y^w = 2(Q - I_3^w). \quad (1.16)$$

Moreover, the isospin singlet and doublet character of the $SU(2)_L \times U(1)_Y$ symmetry group determines the general structure of the SM (see e.g. Tab. 1.1).

1.1.3 Particle content and classifications

The SM includes several classes of elementary particles as depicted in Fig. 1.4, which can be distinguished according to their quantum numbers. The first classification can be done based on the fundamental behavior in a many-body system. According to the spin-statistics theorem (see e.g. [TD35]), fermions respect the Pauli exclusion principle [Pau80] and obey the Fermi-Dirac statistics. While they carry per definition a half-integer spin s , all elementary fermions of the SM can be described with $s = \frac{1}{2}$. On the other hand, bosons carry an integer spin and obey the Bose-Einstein statistics. They act as the mediators of the fundamental interactions. The previously introduced vector bosons are characterized by $s = 1$ and consist of the photon as the mediator of the electromagnetism, the weak gauge bosons Z^0 and W^\pm and the gluons mediating the strong interaction.

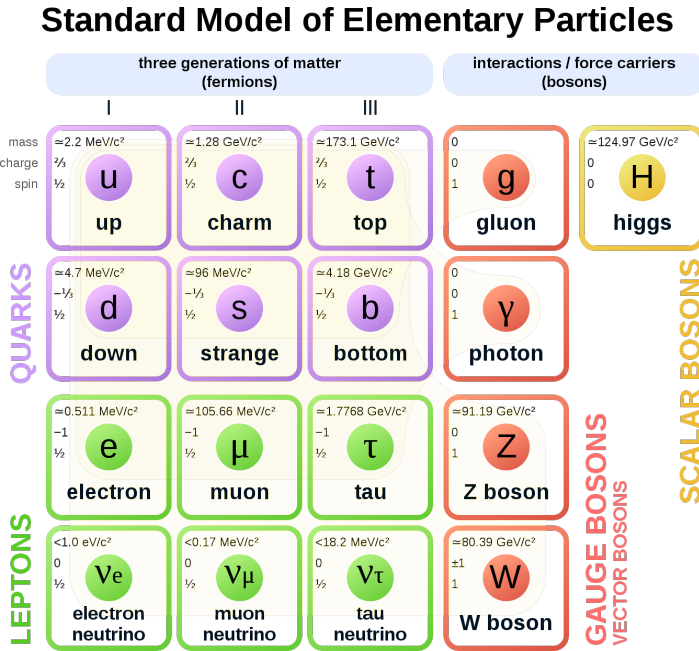


Figure 1.4: Overview of the particle content of the Standard Model [Wika]. Firstly, the elementary particles are divided according to the spin-statistics theorem into fermions and bosons. Each generation of the fermions is divided into pairs of particles that exhibit a similar physical behavior. Moreover, they are classified as leptons and quarks depending on the charges they carry. The gauge bosons act as mediators of the fundamental interactions, whereas the Higgs boson is related to the standard mass generation mechanism.

The Higgs boson is a scalar particle with $s = 0$, highlighting its unique role in the SM. It is related to the standard mass generation process, which is introduced via the Higgs mechanism. In 2012, the LHC experiments ATLAS and CMS at CERN announced independently the discovery of a SM-like Higgs boson, which was subsequently confirmed to match the expected properties within the SM over the following years. Shortly afterwards, the Nobel Prize of Physics was awarded to F. Englert and P. Higgs in 2013 [Nob13] for their theoretical work and the prediction of this new type of boson. In particular, the Higgs boson explains why the photon has no mass, while the W^\pm and Z^0 bosons are very heavy. Moreover, it connects several SM parameters that allow for a precise prediction of those masses in a self-consistent way. However, the generation of fermion masses can only be described by so-called *Yukawa couplings*, whereas the coupling strengths and thus the masses remain essentially as free parameters. This leaves room for potential *new physics* phenomena.

The class of fermions can be divided into *quarks* and *leptons* according to the charges that they carry. Each fermion has a corresponding antiparticle of the same mass but with opposite

charges. An overview of the fundamental charges with respect to the unified electroweak interaction is given in Tab. 1.1.

Table 1.1: Summary of the particle content of the SM with respect to the fundamental $SU(2)_L \times U(1)_Y$ symmetry group of the unified electroweak interaction. Apart from the spin s , the electric charge Q , and the weak isospin I_3^w (only third component), the weak hypercharge Y^w according to Eqn. (1.16) is conserved in all Standard Model interactions. Regarding the gauge bosons, only the electrically charged W^\pm bosons and the Higgs boson carry a non-zero isospin: $I_3^w(W^\pm) = \pm 1$, $I_3^w(h) = -\frac{1}{2}$. The weak hypercharge of those bosons results in $Y^w(W^\pm) = 0$ and $Y^w(h) = +1$.

fermions ($s = \frac{1}{2}$)	$Q \cdot e$	I_3^w	Y^w	gauge bosons ($s = 1$)
leptons				
$\begin{pmatrix} \nu_e \\ e^- \end{pmatrix}_L$	$\begin{pmatrix} \nu_\mu \\ \mu^- \end{pmatrix}_L$	$\begin{pmatrix} \nu_\tau \\ \tau^- \end{pmatrix}_L$	0 -1 -1	$+\frac{1}{2}$ $-\frac{1}{2}$ 0
e_R^-	μ_R^-	τ_R^-	-1	-1 -2
quarks				
$\begin{pmatrix} u \\ d' \end{pmatrix}_L$	$\begin{pmatrix} c \\ s' \end{pmatrix}_L$	$\begin{pmatrix} t \\ b' \end{pmatrix}_L$	$+\frac{2}{3}$ $-\frac{1}{3}$ $+\frac{2}{3}$	$+\frac{1}{2}$ $-\frac{1}{2}$ 0
u_R	c_R	t_R	$+\frac{1}{3}$	$+\frac{1}{3}$ $+\frac{4}{3}$
d_R	s_R	b_R	$-\frac{1}{3}$	0 $-\frac{2}{3}$
				γ, W^\pm, Z^0 γ, W^\pm, Z^0 γ, Z^0, g γ, Z^0, g

Both quarks and leptons exist in three generations that exhibit a similar physical behavior, whereas only the first generation is able to form stable bound states. This is why all ordinary (so-called *baryonic*) matter is made of those first generation particles. Specifically, all atoms consist of electrons orbiting around atomic nuclei, ultimately constituted of up and down quarks. On the other hand, second- and third-generation electrically charged particles decay with very short half-lives and are observed only in very high-energy environments.

The defining property of quarks is their color charge, while they come in six different so-called *flavors*: up, down, charm, strange, top, bottom. Because of the phenomenon of *color confinement* in the strong interaction, quarks are bound very strongly to one another, forming color-neutral composite particles called *hadrons*. Hadrons can be further characterized according to their particle content: *baryons* are formed by three quarks, while a quark and an antiquark form a *meson*. The lightest baryons are the proton and the neutron, which contain quarks of the first generation, and form atomic nuclei for their part.

The remaining fermions that do not carry a color charge are called leptons. Thus, the electrically charged leptons referred to as the electron, muon and tau interact with other fermions via electromagnetism and the weak interaction. The neutral leptons, referred to as *neutrinos* only interact via the weak interaction, which makes them notoriously difficult to detect. Furthermore, the early experimental data and its theoretical interpretation seemed to suggest that neutrinos, unlike the other fermions, were massless. Because of this, the original founders of the SM did not include right-handed neutrino states, which prevents the formulation of valid neutrino mass terms within the SM. However, the observation of flavor oscillations in the neutrino sector proves the existence of non-vanishing neutrino masses. Its discovery was awarded with the Nobel Prize in Physics in 2015 [Nob15]. Neutrinos of all generations are assumed to be stable, hence, do not decay and pervade the universe, while rarely interacting with baryonic matter. This makes them challenging to detect as will be further elaborated in chapter 2 dedicated to the subject of neutrino physics.

The structure within a fermion generation is determined by the electroweak interaction and its isospin algebra that couples the weak gauge bosons to left-handed doublets and

right-handed singlet states. It is related to the conservation of the third component of the weak isospin I_3^w by all interactions described in the SM. This structure is also referred to as $V - A$ (vector – axial-vector) and was first proposed by R. Feynman and M. Gell-Mann [FGM58] to explain the observed parity violation in weak interactions. Furthermore, the unified electroweak interaction leads to the conservation of the weak hypercharge Y^w which relates I_3^w and the electric charge Q via Eqn. (1.16).

Fermions with a negative chirality are called *left-handed* and can be grouped into doublets with $I_3^w = \pm \frac{1}{2}$ (see Tab. 1.1). This way, the conversion of an up-type quark (u, c, t) into a down-type quark (d', s', b') is accompanied by the exchange of W^\pm bosons. The same applies to the lepton sector for the conversion of a charged lepton into a corresponding neutrino and vice versa. On the other hand, right-handed fermions with a positive chirality, form singlets with $I_3^w = 0$. The W^\pm bosons only couple to the isospin doublets, while Z^0 couples to both singlet and doublet states, but with different coupling strengths.

In the standard picture of neutrinos in the SM, remaining exactly massless, there would be no participation of right-handed neutrinos in the weak interaction. This leaves them as potentially *sterile fields* without any known interaction in the SM.

The focus of the present thesis is on phenomena of the weak interaction, especially on rare nuclear decays as will be briefly introduced in the next section. The investigation of such nuclear transitions could help to gain knowledge about the role of neutrinos in the early universe and general aspects of the weak interaction in the context of low-momentum exchange processes and rare radioactive decays.

1.2 Radioactivity and masses of atomic nuclei

Radioactivity describes the phenomenon of the spontaneous disintegration of an atomic nucleus and was already discovered in 1896 by H. Becquerel. Further research by M. and P. Curie coined the term *radioactivity* and provided the basis for modern nuclear physics. All three were jointly awarded with the Nobel Prize in Physics in 1903 [Nob03].

The statistical aspect of radioactivity can be expressed as the universal decay law

$$N(t) = N_0 \cdot e^{-\lambda t} \quad (1.17)$$

connecting the number of active nuclei $N(t)$ with the initial amount $N_0 = N(t=0)$ and the decay constant λ . The latter parameter is related to the half-life via $T_{1/2} = \frac{\ln 2}{\lambda}$. While the majority of the elementary particles discussed in the previous section only exist for a tiny fraction of a second after their creation in high-energy reactions, the half-lives of radioactive atomic nuclei feature a huge range from nearly instantaneous decay to far longer than the age of the universe. This section introduces the basic concepts of nuclear physics following Ref. [PRSZ97] and [Roh94] with an emphasis on the description of radioactive decays. The starting point is the so-called droplet model of atomic nuclei, followed by a short discussion of the three most common types of radioactive decays.

1.2.1 Droplet model of atomic nuclei

The characterization of the structure of an atomic nucleus in analogy to a liquid droplet was first proposed by G. Gamow in 1930 [Gam30]. The corresponding droplet model of atomic nuclei was further elaborated by the works of N. Bohr and J. A. Wheeler by incorporating quantum mechanical effects (see e.g. Ref. [PRSZ97]). It relies on the attraction of nucleons, referring to protons and neutrons that form the nucleus, through the residual effect of the strong interaction binding the quarks to hadrons. Because of the short range of the strong

interaction, the attraction is effectively limited to neighboring nucleons, which is similar to the hydrogen bounds in almost spherical water droplets. However, the density of an atomic nucleus, while treated as an incompressible fluid, is about 10^{14} times higher than for water.

Following this rather simple model, C. F. v. Weizsäcker developed a semi-empirical formula to estimate the mass of an atom $M(A, Z)$ based on its number of protons, electrons and neutrons [Wei35]. The original formula was further improved by H. Bethe in 1936 [BB36], which is why it is often referred to as the *Bethe-Weizsäcker mass formula*. Essentially, it relates the single proton, neutron and electron masses with the respective number of those particles in an atom and its binding energy $E_B(A, Z)$ according to Eqn. (1.18).

$$M(A, Z) = (A - Z) \cdot m_n + Z \cdot (m_p + m_e) - E_B(A, Z), \quad (1.18)$$

$$E_B(A, Z) = a_V A - a_S A^{2/3} - a_C \frac{Z(Z-1)}{A^{1/3}} - a_A \frac{(A-2Z)^2}{A} - \frac{\delta}{A^{1/2}}. \quad (1.19)$$

An illustration of the five terms contributing to the binding energy in Eqn. (1.19) is depicted in Fig. 1.5. The origin and motivation of the terms with respect to the droplet model is outlined in Tab. 1.2.

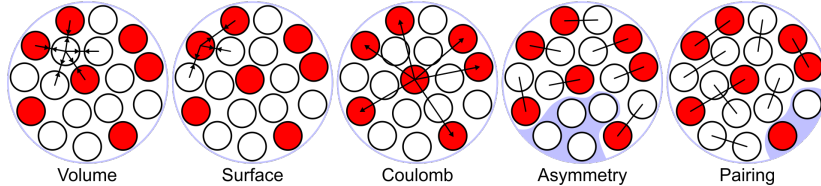


Figure 1.5: Illustration of the connection between the Bethe-Weizsäcker mass formula and the droplet model of atomic nuclei. The nucleus is made of protons (red) and neutrons (white) which are attracted by the residuum of the strong interaction. Its short range only attracts next neighbors, whereas the binding energy scales with the number of nuclei, thus, the atomic mass number A . Because there are less neighboring nucleons close to the surface, the binding energy gets reduced. The same results from the Coulomb repulsion of the positively charged protons. Lastly, quantum mechanical effects lead to a reduction of the binding energy for an asymmetry of the number of protons and neutrons as well as unpaired nucleons.

The empirical motivation of the terms in the approximation of the nuclear binding energy based on the droplet model of atomic nuclei is complemented by the determination of the corresponding parameters based on experimental surveys. This is why the mass formula is referred to as *semi-empirically*. Fig. 1.6 illustrates the binding energy per nucleon with respect to a schematic representation of the chart of nuclei. While the area of experimentally observed nuclei is in good agreement with the predictions according to the semi-empirical mass formula, deviations occur far away from the line of stable nuclei. Moreover, it fails to explain the existence of observed lines of greater binding energy at certain numbers of protons and neutrons. These numbers, known as *magic numbers* (e.g. 2, 8, 20, 28, 50, 82 and 126), are the foundation of more elaborate nuclear models such as the *nuclear shell model*. Nuclei whose proton and neutron numbers are found to be equal to one of the magic numbers are especially stable against radioactive decay. Furthermore, if both Z and N match with a magic number, such as for ${}^4_2\text{He}$ and ${}^{56}_{28}\text{Ni}$, the nuclide is referred to as *doubly magic*.

The probability for the occurrence of a radioactive decay is given by the Q -value of a nuclear reaction which is defined as the mass defect between an initial and final state. If the Q -value is negative, the corresponding reaction is endothermic and indicates a threshold energy that needs to be provided in order to accomplish the reaction. On the other hand, nuclear reactions with a positive Q -value can occur spontaneously, whereas radioactive decays are characterized by their half-life and the universal decay law according to Eqn. (1.17). Usually, there are empiric relations between the Q -value and the half-life with respect to the

Table 1.2: Explanation of the terms contained in the semi-empirical Bethe-Weizsäcker mass formula and their origin in the droplet model of atomic nuclei. By assuming an almost spherical shape and a universal nuclear density, the radius of a nucleus can be approximated as $r \approx r_0 \cdot A^{1/3}$ with $r_0 = 1.25 \text{ fm}$. This motivates the overall dependency of the binding energy on the atomic mass number A . The values of the parameters in Eqn. (1.19) are taken from Ref. [Roh94] and results from experimental surveys.

parameter	value	description
a_V	15.75 MeV	volume term: under the assumptions of the droplet model, the volume of a nucleus is proportional to the atomic mass number.
a_S	17.80 MeV	surface term: fewer neighboring nucleons at the surface lead to a reduction of the binding energy proportional to the surface.
a_C	0.711 MeV	Coulomb term: the electrostatic repulsion of protons reduces the binding energy proportional to the radius of the assumed sphere.
a_A	23.70 MeV	asymmetry term: takes into account a quantum mechanical effect that reduces E_B for unequal numbers of protons and neutrons.
δ	$\begin{cases} -11.18 \text{ MeV} & \text{for even-even} \\ 0 & \text{for even-odd/odd-even} \\ +11.18 \text{ MeV} & \text{for odd-odd} \end{cases}$	pairing term: as protons and neutrons obey the Pauli principle, an even number of both results in the most stable configuration.

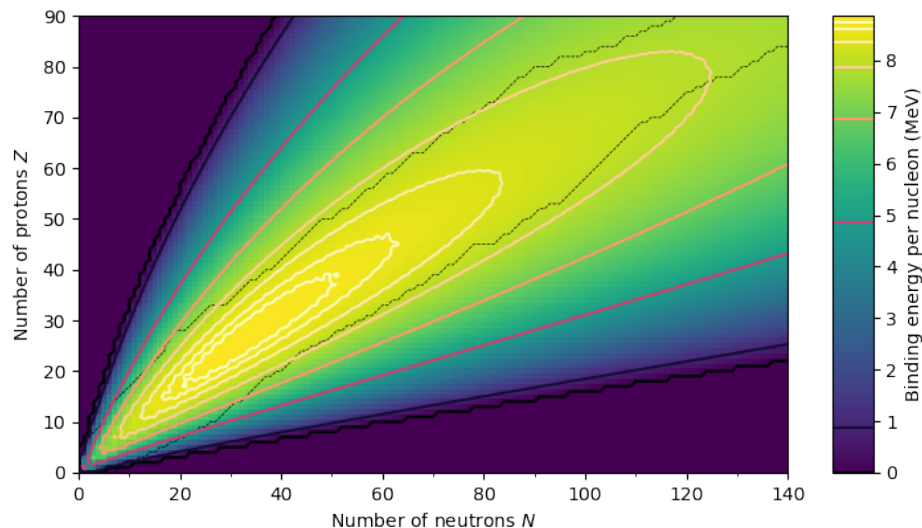


Figure 1.6: Illustration of the binding energy per nucleon for a schematic representation of the chart of nuclei [Wikc]. The illustration makes use of the expression in Eqn. (1.19) and the parameters listed in Tab. 1.2. The dashed lines indicate the area of experimentally observed nuclei. While the maximum of the approximated binding energy agrees well with the observed area of stable nuclei, more elaborate features such as the magic numbers indicating especially stable nuclei cannot be described by the simple droplet model.

decay mode. However, as the Q -value is equal to the mass defect of the mother and daughter nuclei, its exact value depends also on the actual nuclear transition. For the most common decay modes as discussed in the following sections, the mass defect is tabulated in nuclear databases such as provided by the atomic mass evaluation (AME) [AME17].

1.2.2 α -decay

The process of α -decay was first described in the investigation of radioactivity by E. Rutherford by the end of the 19th century. Its physical explanation was formulated by G. Gamow in 1928, making use of the newly discovered principles of quantum mechanics (see e.g. Ref. [Stu86]). While the α -particle is trapped in a potential well of the nucleus, there is a tiny but non-zero probability for tunneling through the Coulomb barrier. Moreover, by solving a model potential for the nucleus analytically, the previously found empirical relation between $T_{1/2}$ and the Q_α -value, known as the *Geiger-Nuttal law* [GN11], could be derived from first principles by G. Gamow.

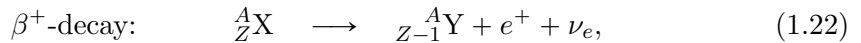
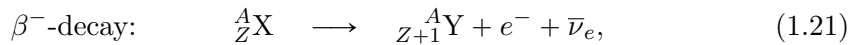
An α -decay is characterized by the emission of a doubly magic ${}^4_2\text{He}$ nucleus, which is referred to as the α -particle. At the same time, the original nucleus loses four atomic mass units and gets transformed into another nucleus according to



Because of the simple kinematics, the emitted α -particle is mono-energetic, while the actually carried kinetic energy E_α is usually a few keV below Q_α due to the nuclear recoil in order to fulfill the momentum conservation. An exemplary half-life analysis involving the long-lived α -decay of ${}^{190}\text{Pt}$ will be presented in section 8.5 of the present thesis.

1.2.3 β -decay

The process of β -decay is triggered by the weak interaction and involves three common decay modes such as shown in Eqn. (1.21) – (1.23).



The first two processes involve the emission of leptons of the first generation, namely an electron or positron accompanied by the respective neutrinos in order to conserve the so-called *lepton number*. As the respective final states involve three constituents, whereas the daughter nuclei are usually immobile, the Q -value is shared between the emitted leptons. While the charged leptons can be easily observed with suitable radiation detectors, the neutrino usually escapes unnoticed because of their tiny interaction probability. Historically, the continuous spectrum of the e^-/e^+ momentum distribution resulted in the postulation of the neutrino as an additionally released particle to ensure the energy and angular momentum conservation in nuclear β -decays. This subject will be further elaborated in chapter 2.

In general, the β^+ -decay competes with the electron capture (EC) from electron orbitals near the atomic nucleus as both processes result in the same nuclear final state. While the Q -value of the EC is usually larger, the decay rate depends also on the probability to capture an electron from the atomic shell. In case of the β^+ -decay mode, two times the electron rest mass $m_e = 511 \text{ keV}$ needs to be provided by the respective Q -value of the transition.

On the level of Feynman diagrams involving the elementary particles, the processes Eqn. (1.21) – (1.23) can be depicted as illustrated in Fig. 1.7. The explanation for a β^- -decay is the conversion of a down quark into an up quark, causing the conversion of a bound neutron into a proton, through the emission of a W^- boson that decays into an e^- and electron-antineutrino $\bar{\nu}_e$. Similarly the other β -decay modes can be explained.

In contrast to the previously discussed α -decay, which does not carry any angular momentum, a wide variety of potential nuclear spin states can be accessed directly via β -decay

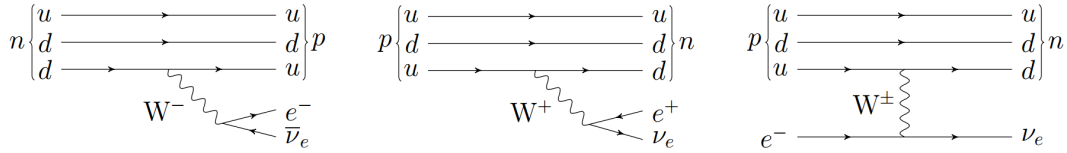


Figure 1.7: Feynman diagrams illustrating the three common forms of nuclear β -decay (taken from [Zat14]). *Left:* β^- -decay with an electron and electron-antineutrino in the final state. *Middle:* β^+ -decay with a positron and an electron-neutrino in the final state. *Right:* EC with a mono-energetic electron-neutrino in the final state. Typically, the latter two decay modes compete with each other.

transitions. According to the coupled spin S of the emitted leptons, β -decay transitions are either classified as *Fermi transitions* with $S = 0$ or, respectively, as *Gamow-Teller transitions* involving a coupling to $S = 1$. Moreover, the internal structure of atomic nuclei results in a total angular momentum J , which is a conserved quantity and determines the combined angular momentum L of the emitted particles. Furthermore, the classification of β -decay transitions involves the angular momentum change ΔJ between the initial and final nuclear state. While Fermi transitions result in $\Delta J = 0$, Gamow-Teller transitions are possible for $\Delta J \in [0, \pm 1]$ (under the assumption of a so-called *allowed transition*).

If the leptons carry no angular momentum, indicated by $L = 0$, the respective β -decay is referred to as *allowed*, while it is otherwise called *forbidden*. More explicitly, $L > 0$ corresponds to a suppression of the decay rate as a result of the involved quantum mechanics. The degree of suppression can be expressed with the help of the following nuclear selection rules based on the total angular momentum change ΔJ and the change of parity $\Delta\pi$.

$$\Delta J = \begin{cases} L - 1 \\ L \\ L + 1 \end{cases}, \quad \Delta\pi = (-1)^L \quad (1.24)$$

A change of parity is indicated by $\Delta\pi = -1$, which is referred to as a *unique* transition. On the other hand, so-called *non-unique* transitions conserve the parity indicated by $\Delta\pi = +1$ between the initial and final state. An overview of the corresponding classification is given in Tab. 1.3. The typical β -decay half-life increases with each order of forbiddenness, whereas allowed and super-allowed transitions proceed very quickly and highly forbidden transitions can involve half-lives that surpass the age of the universe of about 13.8 billion years [Pla19].

Table 1.3: Classification of nuclear β -decays with respect to the involved change of the angular momentum ΔJ and parity $\Delta\pi$ between the initial and final states. The examples are taken from [ESZ19] and [NDS20].

classification	ΔJ	$\Delta\pi$	example transitions (J^π)
super-allowed (Fermi)	0	+	${}^3\text{H}\left(\frac{1}{2}^+\right) \rightarrow {}^3\text{He}\left(\frac{1}{2}^+\right)$
allowed (Gamow-Teller)	0, 1	+	${}^{14}\text{C}\left(0^+\right) \rightarrow {}^{14}\text{N}\left(1^+\right)$
1 st -forbidden, unique	0, 1, 2	-	${}^{210}\text{Bi}\left(1^-\right) \rightarrow {}^{210}\text{Po}\left(0^+\right)$
2 nd -forbidden, non-unique	1, 2, 3	+	${}^{99}\text{Tc}\left(\frac{9}{2}^+\right) \rightarrow {}^{99}\text{Ru}\left(\frac{5}{2}^+\right)$
3 rd -forbidden, unique	2, 3, 4	-	${}^{87}\text{Rb}\left(\frac{3}{2}^-\right) \rightarrow {}^{87}\text{Sr}\left(\frac{9}{2}^+\right)$
4 th -forbidden, non-unique	3, 4, 5	+	${}^{113}\text{Cd}\left(\frac{1}{2}^+\right) \rightarrow {}^{113}\text{In}\left(\frac{9}{2}^+\right)$

One of the main topics in the analysis section of the present thesis is the study of the electron momentum distribution, usually referred to as the β -spectrum, of the highly forbidden β -decay of ${}^{113}\text{Cd}$. This subject will be discussed in section 8.3.

1.2.4 De-excitation via γ -ray emission

As the daughter nucleus of a preceding radioactive decay usually remains in an excited state, a fraction of the originally released energy is not directly transferred to the emitted α - and β -radiation. In fact, α -radiation is characterized as $J^\pi(\alpha) = 0^+$, thus cannot alter the nuclear angular momentum between the initial and final state. Instead, the daughter nucleus needs to undergo internal transitions to reach its ground-state. This can proceed by releasing characteristic electromagnetic γ -rays or by transferring the energy of the excited state to a shell electron. This way, so-called mono-energetic *conversion electrons* and x-rays are produced (see e.g. [PRSZ97]). The labeling of the previously discussed radiation types is based on their typical penetration power, which increases accordingly from α over β to γ for the same energy regime as has been studied by E. Rutherford and others.

Because of the internal nuclear structure, the characteristic γ -rays released in a radioactive decay carry rather unique energies for each nuclide and allow for very precise analytical methods such as γ -spectroscopy. Moreover, artificially produced radionuclides of known γ -ray energies E_γ and intensities can be used in the calibration of radiation detectors as demonstrated in section 8.1.2 and related sections.

The typical interaction processes between the most frequently encountered particles in the course of this thesis, while focusing on the typical energy region of radioactive decays, will be briefly discussed in the next section.

1.3 Interaction between particles and matter

The observation and study of elementary particles requires substantial knowledge of the possible interaction mechanisms between those particles and matter. Moreover, the respective detector concept needs to be optimized by a suitable material selection and by considering the expected energy regime as most interaction processes feature a non-trivial energy dependence. The first part of the following section is dedicated to the interactions of γ -rays, focusing on the energy region covered by typical nuclear reactions. In the second part, the interaction of charged particles, which differs fundamentally from the neutral electromagnetic γ -ray interactions, will be discussed.

1.3.1 γ -ray interactions

The term γ -rays refers to the characteristic de-excitation radiation of atomic nuclei, which usually originates in the aftermath of a nuclear transition. As the excitation energies are specific for each isotope, the observation of characteristic γ -rays can be used for the identification of radioactive nuclides. Furthermore, highly energetic particles, such as cosmic muons produced in primary cosmic ray interactions in the upper atmosphere of the Earth, or neutrons originating from e.g. (α, n) reactions can generate γ -rays with energies up to several MeV via inelastic scattering processes. The most common types of γ -ray interactions in this energy regime will be covered in the following.

In general, the probability for an interaction can be expressed with the so-called *cross section* σ as a measure for the effective area taking part in the interaction. Because particle physics involves interactions on very short length scales at the order of only a few femtometer ($1 \text{ fm} = 10^{-15} \text{ m}$), a suitable cross section unit is referred to as *barn* with $1 \text{ barn} = 10^{-28} \text{ m}^2$.

The main processes contributing to the total γ -ray cross section are photoelectric absorption (PA), Compton scattering (CS) and electromagnetic $e^- - e^+$ pair creation. Thus, the total interaction cross section can be expressed as the sum of the single contributions such

as shown in Eqn. (1.25).

$$\sigma_{\text{tot}} = \sigma_{\text{PA}} + \sigma_{\text{CS}} + \sigma_{\text{pair}} \quad (1.25)$$

The single processes dependent strongly on the energy of the involved γ -rays as illustrated in Fig. 1.8 for the γ -ray attenuation within the semiconductor material cadmium zinc telluride (CZT), which is the basis of the radiation detectors investigated by the COBRA experiment for the search for the neutrinoless double beta decay (see e.g. chapter 3 and 4).

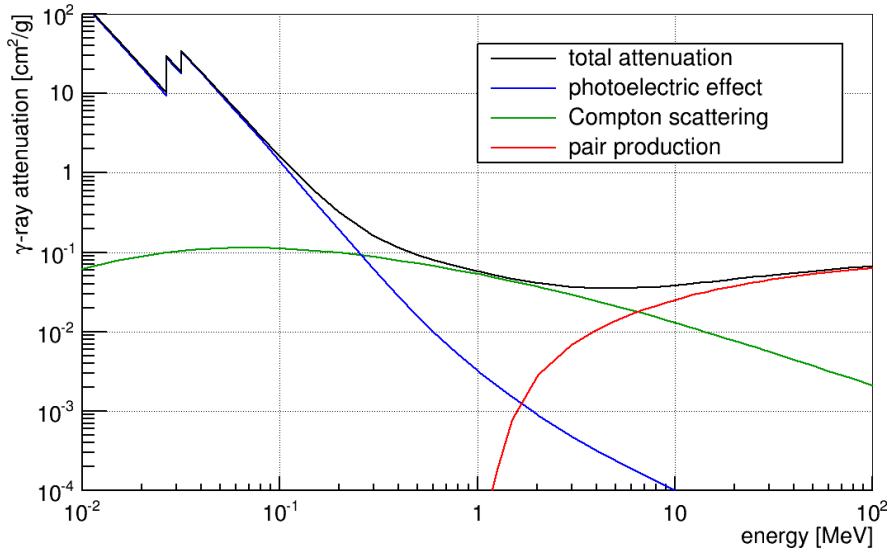


Figure 1.8: Attenuation of γ -rays in CZT based on the NIST database for photon cross sections [BHS⁺10] (taken from [Zat14]). CZT is treated as a compound of cadmium (45%), zinc (5%) and tellurium (50%). The low energy region is dominated by photoelectric absorption whereas the characteristic discontinuities indicate prominent absorption edges. For higher γ -ray energies, the process of Compton scattering and electromagnetic pair creation get more and more dominant.

The excitation of an atom by the absorption of a photon is referred to as the photoelectric effect, which is the dominant interaction process of γ -rays at low energies. Its explanation based on the quantized character of electromagnetic radiation was formulated by A. Einstein in 1905 [Ein05] and marked one of the most remarkable discoveries leading to the development of the concept of quantum mechanics as one of the basic principles of the SM.

The related γ -ray cross section (see e.g. Ref. [PRSZ97]) can be expressed in dependence on the nuclear charge Z of the target material and the incident energy E_γ according

$$\sigma_{\text{PA}} \sim \frac{Z^5}{E_\gamma^{7/2}} \quad \text{for } E_\gamma < m_e, \quad (1.26)$$

$$\sigma_{\text{PA}} \sim \frac{Z^n}{E_\gamma} \quad \text{for } E_\gamma \gg m_e, \text{ with } n = 3.0 - 3.6. \quad (1.27)$$

Regarding the example depicted in Fig. 1.8, the σ_{PA} cross section features prominent discontinuities as a consequence of the characteristic thresholds for atomic ionization in CZT.

For increasing γ -ray energies, the contribution of the incoherent scattering on loosely bound shell electrons, which is usually referred to as Compton scattering [Com23], becomes more dominant as the probability of PA decreases (see Fig. 1.8). As the binding energy of the outer electrons of an atom is small compared to γ -ray energies on the order of $m_e = 511 \text{ keV}$, the Compton scattering process can be described as an elastic collision with a resting electron. The kinematics can be expressed depending on the scattering angle ϑ between the initial and

outgoing γ -rays such as shown in Eqn. (1.28) – (1.29) using the relativistic energy-momentum-relation and the four-momentum conservation.

$$E'_\gamma = \frac{E_\gamma}{\frac{E_\gamma}{m_e}(1 - \cos \vartheta) + 1}, \quad (1.28)$$

$$E_e = E_\gamma - E'_\gamma. \quad (1.29)$$

The energy of the scattered γ -ray is labeled as E'_γ and makes it possible to calculate the energy transfer to the electron as the difference of the initial energy E_γ and E'_γ . In the lowest order of quantum electrodynamics as discussed in section 1.1.1, the differential cross section of the Compton scattering process can be expressed according to the *Klein-Nishina formula*

$$\left(\frac{d\sigma}{d\Omega} \right)_{\text{KN}} = \frac{r_e^2}{2} \left(\frac{E'_\gamma}{E_\gamma} \right)^2 \left(\frac{E_\gamma}{E'_\gamma} + \frac{E'_\gamma}{E_\gamma} + \mu^2 - 1 \right) \quad (1.30)$$

with $\mu = \cos \vartheta$ being the direction cosine and $r_e \approx 2.818 \text{ fm}$ the classical electron radius. An illustration of the energy dependency of the Compton kinematics and the Klein-Nishina cross section is exemplarily shown in Fig. 7.22 of section 7.3.2. Using the differential cross section Eqn. (1.30) makes it possible to estimate the contribution of Compton scattering to the total photon cross section for energies $E_\gamma > m_e$, which leads to

$$\sigma_{\text{CS}} \sim \frac{Z}{E_\gamma}. \quad (1.31)$$

Finally, the high-energy region above 10 MeV for the example depicted in Fig. 1.8 is dominated by the γ -ray induced electromagnetic pair creation. This process requires at least an energy of $E_\gamma > 2m_e$ in order to produce an electron-positron pair at rest. Furthermore, the conversion can only appear in the vicinity of an interaction partner, such as provided by the Coulomb potential of a nucleus, to ensure momentum conservation. This requirement leads to an approximately quadratic dependence of the pair production cross section regarding the nuclear charge of the target material, while the energy dependence follows a logarithm as shown in Eqn. (1.32).

$$\sigma_{\text{pair}} \sim Z^2 \ln E_\gamma \quad (1.32)$$

Alternative processes such as coherent γ -ray scattering, which is also referred to as *Rayleigh scattering*, are usually negligible at the typical energy scales of interest in nuclear physics applications.

1.3.2 Charged particles

The dominant interaction processes of charged particles passing through matter can be described by two phenomena of the electromagnetic interaction – ionization loss and radiative processes such as bremsstrahlung [PRS97]. Typically, the energy loss is referred to as the average energy loss per path length, denoted as dE/dx and depends on the actual particle species as well as the target material.

Incident particles of charge z and rest mass m_0 , which are more massive than electrons with $m_e = 511 \text{ keV}$, are usually referred to as *heavy particles*. While this specification applies essentially to all elementary particles of the SM, it separates the first generation of charged leptons including electrons and positrons. This categorization is motivated by the analytic treatment of the energy loss via ionization using approximations that are not valid for electrons and positrons. In fact, the description of electron interactions requires to account

for spin-spin correlations and the identical mass of the projectiles and the target electrons. Moreover, additional corrections are needed to account for $e^+ - e^-$ interactions and the annihilation process at sufficiently low energies. An overview of the different contributions for the energy loss of e^- and e^+ in lead with a nuclear charge of $Z = 82$ is depicted in Fig. 1.9.

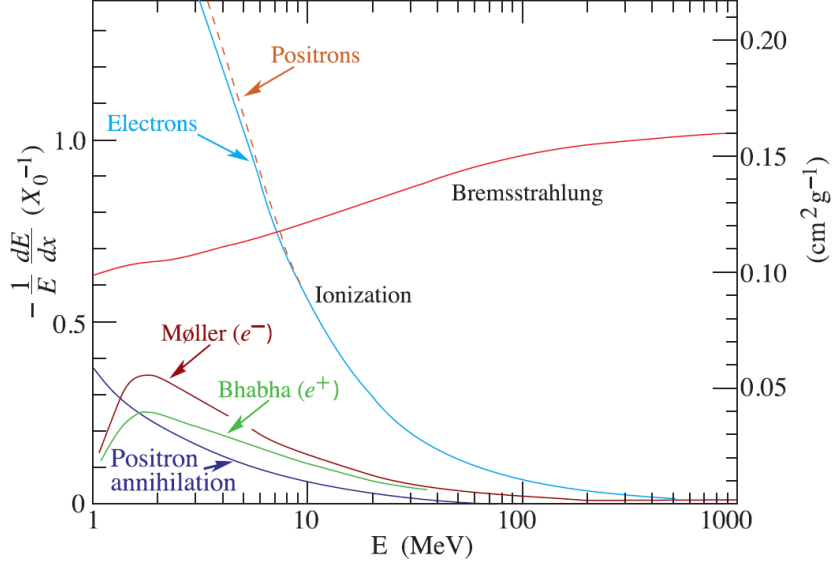


Figure 1.9: Illustration of the energy loss of electrons and positrons in lead with $Z = 82$ (adapted from [PDG18]). The low-energy regime is dominated by the ionization loss and differs only slightly for e^+ and e^- . The differences are mainly caused by the underlying scattering processes such as Bhabha ($e^+ - e^-$) and Møller scattering ($e^- - e^-$). For increasing particle energies, the energy loss due to bremsstrahlung increases and surpasses the continuously decreasing contribution of the ionization loss at a critical energy of about 7 MeV.

By using the common particle physics notation of *natural units* with

$$\hbar = c = k_B = 1, \quad (1.33)$$

the momentum p of a relativistic particle can be expressed in terms of the *Lorentz boost* $\beta = v/c$, referring to the particle's velocity in units of the speed of light c , and the so-called *Lorentz factor* denoted as γ .

$$p = mv = \gamma m_0 \beta, \quad \gamma = \frac{1}{\sqrt{1 - \beta^2}} \quad (1.34)$$

$$\Rightarrow \beta\gamma = p/m_0. \quad (1.35)$$

With this notation, the material specific mean energy loss of moderately relativistic heavy charged particles can be well-described with the *Bethe-Bloch formula* (see e.g. [PRSZ97]) as shown in Eqn. (1.36).

$$-\frac{1}{\varrho} \left\langle \frac{dE}{dx} \right\rangle = K z^2 \frac{Z}{A} \frac{1}{\beta^2} \left[\frac{1}{2} \ln \left(\frac{2m_e \beta^2 \gamma^2 T_{\max}}{I^2} \right) - \beta^2 - \frac{\delta(\beta\gamma)}{2} \right] \quad (1.36)$$

Besides the kinematic variables β and γ , the energy loss according to Eqn. (1.36) depends on the material properties of the target medium such as the nuclear charge Z and the atomic mass A , as well as the mean excitation energy I in units of eV. Moreover, there is a dependence on the characteristics of the incident particle including its charge z in units of the elementary charge e and a maximum kinetic energy transfer T_{\max} , which is the momentum transfer that can be transferred to a target electron in a single collision. The value of T_{\max} can be

calculated from the underlying kinematics according to Eqn. (1.37) using the mass m_0 of the incident particle.

$$T_{\max} = \frac{2m_e\beta^2\gamma^2}{1 + 2\gamma m_e/m_0 + (m_e/m_0)^2} \quad (1.37)$$

The constant K in Eqn. (1.36) can be expressed as

$$K = 4\pi N_A r_e^2 m_e \approx 0.3071 \text{ MeV mol}^{-1} \text{ cm}^2 \quad (1.38)$$

and depends on the Avogadro number $N_A = 6.022 \times 10^{23} \text{ mol}^{-1}$, the classical electron radius r_e and the electron rest mass m_e .

The last term in the Bethe-Bloch formula incorporates a correction of density effects labeled as $\delta(\beta\gamma)$. As the particle energy increases, the electric field is deformed due to relativistic effects and flattens progressively. This leads to an increase of the mean energy loss per path length, which is roughly proportional to $\ln(\beta\gamma)$. At even higher energy scales, radiative processes become dominant for all charged particles. Because of this, it is convenient to express the energy loss of e.g. atmospheric muons as produced by cosmic ray interactions in the following form

$$-\frac{1}{\varrho} \left\langle \frac{dE}{dx} \right\rangle = a(E) + b(E)E. \quad (1.39)$$

In the present case $a(E)$, denotes the ionization according to the Bethe-Bloch approximation and $b(E)$ comprises the sum of high-energy effects including $e^- - e^+$ pair production, bremsstrahlung and photonuclear reactions. Exemplarily, the energy loss of muons as prototypes for heavy charged particle is shown in Fig. 1.10 as a function of the momentum expressed in units of $\beta\gamma$. A more detailed discussion of the approximation for the low and high energy range can be found in Ref. [PDG18].

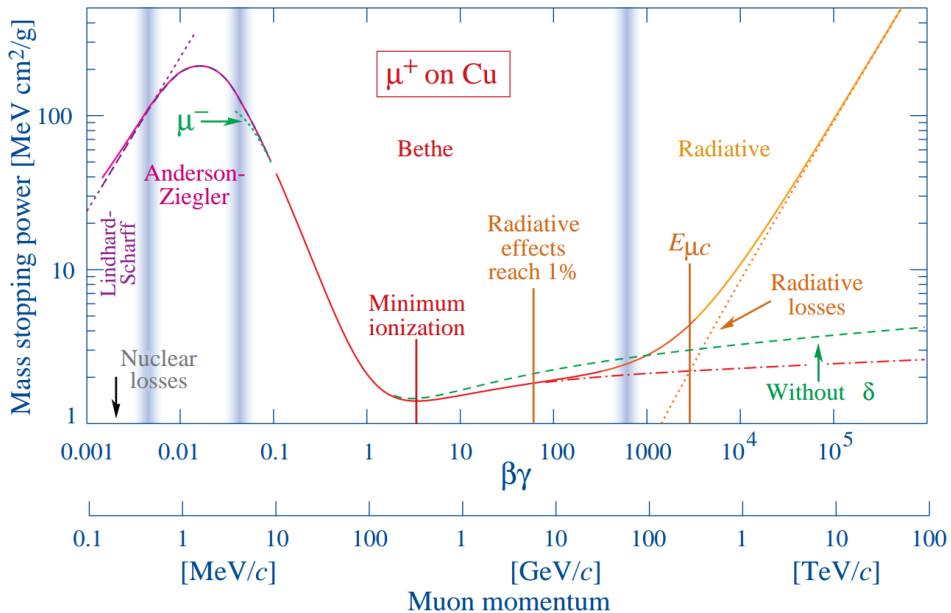


Figure 1.10: Illustration of the muon stopping power in copper with $Z = 29$ as a function of the momentum in units of $\beta\gamma$ (taken from [PDG18]). A wide range of the depicted nine order of magnitudes of the muon momentum can be approximated with the Bethe-Bloch formula according to Eqn. (1.36). Muons with $\beta\gamma \approx 3 - 4$ are referred to as *minimum-ionizing* because of the associated global minimum in the stopping power.

Chapter 2

Neutrino physics

Neutrinos are elementary particles in the family of leptons and play an important role in many research fields of modern particle, astroparticle and nuclear physics. As they carry no electric charge and only interact via the weak interaction, they are able to traverse large quantity of matter like the Sun or the Earth without interacting. Moreover, neutrinos are produced in vast amounts in a variety of processes such as radioactive decays in the Earth's crust and mantle, nuclear reactors (about 10^{20} per second) or cosmic ray interactions and the fusion processes in the core of the Sun. The latter produces about $2 \cdot 10^{38}$ electron-neutrinos ν_e per second, corresponding to a solar neutrino flux of about $65 \cdot 10^9 \text{ cm}^{-2}\text{s}^{-1}$ on Earth. However, one of the main sources of neutrinos is the universe itself as the relic density of neutrinos from the *Big Bang* is about 330 per cm^3 , which makes neutrinos after photons the second most abundant particles in the known universe.

The study of neutrino properties, from the discovery over the determination of its helicity to the long-awaited proof of flavor oscillations, had an important impact on the development of the particle theory resulting in the SM. In 2015, the Nobel Prize in Physics was awarded to T. Kajita and A. McDonald “for the discovery of neutrino oscillations, which shows that neutrinos have mass” [Nob15]. Moreover, “new discoveries about the deepest neutrino secrets are expected to change our current understanding of the history, structure and future fate of the universe” [Nob15], which shows the central role of neutrinos in elementary physics.

While the discovery of neutrino oscillations established that neutrinos are massive, they were introduced as massless particles in the SM due to the absence of any direct indication for their mass available at the time. Moreover, it is not possible to construct a gauge invariant, renormalizable neutrino mass term without adding additional particle states to the theory. This is also why there is neither a flavor mixing nor so-called *CP-violation* (charge conjugation parity violation) in the lepton sector of the conventional formulation of the SM. Therefore, the observation of neutrino oscillations and the required non-zero masses imply the first known departure from the SM of particle physics.

The present chapter introduces the key aspects of neutrino physics, starting with a brief summary of the neutrino’s history and discovery. A more complete overview of the subject of neutrino physics can be found in several dedicated textbooks such as [Sch97], [Zub11] and [OO19], as well as in recent review articles involving [MAB⁺07] (theory of neutrinos), [GLZ18] (in-depth review of the PMNS mixing matrix), [SGM⁺18] (review of neutrino oscillation) and [EGGHG⁺19] (latest NuFIT results).

In the course of a conference on the “*History of the Neutrino*”, a very informative website was created [IN220], which is dedicated to the historical development of the field of neutrino physics and the elusive role of the neutrino over the past 90 years since its postulation.

2.1 Neutrino discovery and characteristics

The history of the neutrino is closely connected to the description of nuclear β -decays as will be discussed in the first part of this section. Moreover, the discovery that neutrinos can oscillate between different flavors (ν_e , ν_μ , ν_τ) marked a turning point in the understanding of particle physics and represents the first hard evidence for the existence of *new physics* beyond the well-established SM. An overview of the flavor mixing and the neutrino oscillation phenomenon is given in section 2.1.3. Finally, open questions related to the neutrino sector will be summarized in the last paragraph of the present section.

2.1.1 Theoretical prediction and experimental discovery

The existence of a new neutral particle was first postulated by W. Pauli in 1930 [Pau30] in order to explain how the fundamental conservation laws of energy, momentum and angular momentum can be fulfilled in nuclear β -decays. Alternative explanations suggested by N. Bohr and others involved the proposal of a statistical version of the conservation laws, whereas Pauli hypothesized an undetected particle referred to as a “neutron”. First spectroscopic studies of β -decays were already performed by J. Chadwick and H. Geiger in 1913. They were able to confirm a systematic deviation of the detected energy release from the expected mass difference between the initial and final nuclear states. In contrast to the previously known phenomena of α -decay and the observation of characteristic de-excitation radiation in form of γ -rays, resulting in a narrow energy distribution, the momentum distribution of the emitted β -particles was found to be continuous (see e.g. Ref. [EW27]).

By assuming that an additional particle is emitted from an atomic nucleus together with the β -particle (e^- or e^+), all conservation laws under question could be fulfilled. Moreover, it was found that the newly proposed particle must obey the Fermi-Dirac statistics, thus, carry an half-integer spin. The spin concept was introduced in 1928 by P. Dirac [Dir28] as a direct consequence of the unification of quantum mechanics and special relativity in an attempt to find a universal description of massive fermions.

The term *neutrino* appeared firstly in the scientific discussion of a new theory of weak interactions proposed by E. Fermi in 1934 [Fer34]. After J. Chadwick discovered a much more massive neutral nuclear particle in 1932 [Cha32], which was also referred to as neutron in analogy to the already known proton, the Italian term for “little neutron” was proposed for Pauli’s neutral particle. Fermi’s theory of the weak interaction unified Pauli’s neutrino and Chadwick’s neutron together with the idea of antiparticles postulated by P. Dirac and the newly developed model of the atomic nucleus consisting of nucleons (see e.g. [FGM58] and [Wil68]). According to this model, the β^- -decay could be interpreted as the conversion of a neutron into a proton with the emission of an electron and an electron-antineutrino

$$n \longrightarrow p + e^- + \bar{\nu}_e. \quad (2.1)$$

Although Fermi’s model provided a solid basis for future experiments, it took more than twenty years until the neutrino could be discovered. An important milestone is marked by the calculations of B. Pontecorvo, who suggested in 1946 that nuclear reactors and the Sun are copious sources of neutrinos. A decade later, C. Cowan and F. Reines established the neutrino’s existence by performing a reactor neutrino experiment following Pontecorvo’s proposal of a radiochemical detection method based on an *inverse β -decay* process [CRH⁺56]. Because of the neutron excess in heavy nuclei, the majority of the radioactive fission products in nuclear reactors undergo β^- -decays according to Eqn. (2.1) and provide an enormous flux of $\bar{\nu}_e$. The typical neutrino release is on the order of 10^{20} per second and makes it possible to

counter the low interaction cross sections. The discovery experiment consisted of a water tank surrounded by two scintillator detectors and took advantage of the inverse β -decay reaction



producing a positron and neutron in the final state. The signature of such a neutrino interaction consists of a prompt and a delayed signal due to the reactions of the positron and neutron with the target material. At first, the positron annihilates with an electron of the surrounding water producing two monoenergetic γ -rays with $E_\gamma = 511\text{ keV}$. Secondly, the neutron is moderated down to thermal energies within a few microseconds and ultimately captured in a (n, γ) -reaction. The capture cross section was increased by dissolving cadmium in the water tank in form of CdCl_2 . Natural cadmium contains about 12.2% of the isotope ^{113}Cd which is known for a very high cross section for thermal neutron capture reactions such as $^{113}\text{Cd}(n, \gamma)^{114}\text{Cd}$ with $\sigma \approx 20\text{ kbarn}$. The excited ^{113}Cd nucleus relaxes under γ -rays emission, thus, provides a delayed signal. The detection of two γ -ray signals, separated in time by a few microseconds, is a distinct signature of the inverse beta decay reaction in Eqn. (2.2) and confirmed the existence of neutrinos by observing the reactor $\bar{\nu}_e$ flux [CRH⁺56].

Soon after its discovery, the search for astrophysical neutrinos began. The early experiments aimed to observe the solar neutrino flux by applying once again the radiochemical methods as originally suggested by Pontecorvo. The first ambitious experiment was performed by R. Davis and collaborators in 1968 [DHH68] in the Homestake mine. However, the reported flux turned out to be significantly smaller than predicted by the most sophisticated solar models provided by J. Bahcall (see e.g. [Bah64] and the review [BP92]). The solution to this famous “*solar-neutrino puzzle*” could eventually be explained in terms of so-called *neutrino oscillations* as originally proposed by B. Pontecorvo (see e.g. Ref. [Pon58] and [Pon60]). Inspired by the discovery of the muon-neutrino ν_μ in 1962 [DGG⁺62], the Japanese theoretical physicists Z. Maki, M. Nakagawa and S. Sakata predicted that there exists mixing between flavor and massive neutrino states within the same year [MNS62]. The idea was applied to solar neutrinos in 1968 by B. Pontecorvo [Pon68].

An overview of the standard neutrino oscillation mechanism based on three neutrino flavors as observed in the SM will be given in section 2.1.3. The following section is dedicated to a brief summary of the experimental innovations that lead to the confirmation of the three flavor picture of neutrinos within the SM.

2.1.2 Verification of neutrino properties

Soon after the discovery of the neutrino by Cowan and Reines based on the $\bar{\nu}_e$ flux from a nuclear reactor, accelerator based experiments started their search for neutrino interactions. This is how the second neutrino flavor ν_μ , which is associated to muon interactions, was found in 1962 at the *Brookhaven National Laboratory* [DGG⁺62]. A summary of further experimental milestones that ultimately confirmed the three flavor neutrino picture in the SM is given in Tab. 2.1.

After the first observation of weak neutral currents in the elastic scattering of ν_μ on e^- interactions in the Gargamelle experiment at CERN, proving the existence of the Z^0 boson as predicted by the GWS model (see e.g. section 1.1), the number of active neutrino flavors could be determined in e^+e^- collisions for the resonance production of Z^0 with a center-of-mass energy of $\sqrt{s} \approx M_Z = 91.2\text{ GeV}$ [PDG18]. This measurement relies on the so-called *invisible partial width*, denoted as Γ_{inv} , which is the residuum after subtracting the measured visible widths corresponding to Z^0 decays into quarks and charged leptons from the total width Γ_Z [PDG18]. The invisible width is assumed to be due to the universal coupling of N_ν light neutrino species, whereas each contributes the partial width Γ_ν as given by the

Table 2.1: Timeline of important experimental milestones with respect to the role of neutrinos within the SM (inspired by [IN220]). Since the discovery of the neutrino with the help of nuclear reactors, the three flavor picture could be proven in a wide range of astroparticle and accelerator based experiments. Most of those breakthroughs were awarded with the prestigious Nobel Prize in Physics.

year	subject	experiment and reference	Nobel Prize
1956	first experimental evidence for neutrinos (reactor $\bar{\nu}_e$)	C. Cowan and F. Reines [CRH ⁺ 56]	1995
1962	discovery of ν_μ flavor	L. Lederman, M. Schwartz and J. Steinberger [DGG ⁺ 62]	1988
1968	first radiochemical observation of solar neutrinos (ν_e)	R. Davis [DHH68]	2002
1973	discovery of leptonic and hadronic neutral currents	Gargamelle at CERN [Gar73a], [Gar73b]	
1975	discovery of τ lepton implying existence of ν_τ flavor	M. Perl at SLAC [PAB ⁺ 75], [PFA ⁺ 77]	1995
1987	observation of the neutrinos from the supernova SN1987A	Kamiokande [Kam87], IMB [IMB87], Baksan [Bak88]	(2002)
1989	proof for only three neutrino generations	LEP at CERN [ALE89], [OPA89], [DEL89]	
1998	discovery of atmospheric neutrino oscillations	Super-Kamiokande [Sup98]	2015
2001	observation of ν_τ interactions	DONUT [DON01]	
2001	discovery of solar neutrino oscillations and MSW effect	SNO [SNO01]	2015
2013	first observation of high-energy astrophysical neutrinos	IceCube [Ice13]	

SM. Furthermore, in order to reduce the model dependency, the ratio of the neutrino to the charged leptonic partial widths is compared between the experimental data and the SM prediction. This leads to the following expression

$$N_\nu = \frac{\Gamma_{\text{inv}}}{\Gamma_l} \left(\frac{\Gamma_l}{\Gamma_\nu} \right)_{\text{SM}} \quad (2.3)$$

with the first ratio arising from the experimental observation. The combined analysis of the four LEP experiments (ALEPH, DELPHI, L3 and OPAL) resulted in $N_\nu = 2.984 \pm 0.008$ [ALE06] and confirmed the three flavor neutrino picture of the SM, even before the direct observation of the ν_τ neutrino in 2001 [DON01] (see also Tab. 2.1).

Finally, after about 30 years of experimental innovation, the momentous discovery of atmospheric neutrino oscillations was announced by the Super-Kamiokande collaboration in 1998 [Sup98]. The experiment could show that ν_μ , induced by cosmic ray interactions in the upper atmosphere, disappear as a function of the distance traveled. Moreover, only a few years later, the SNO experiment confirmed that solar neutrinos can transform from ν_e into ν_μ and ν_τ by measurements of the total solar-neutrino flux [SNO01]. These two milestones were awarded with the Nobel Prize in Physics in 2015 [Nob15]. The key aspects of neutrino oscillations will be summarized in the subsequent section.

2.1.3 Flavor mixing and neutrino oscillation

The phenomenon of neutrino oscillation refers to the transformation of a neutrino from one flavor into another as it propagates. It is a fundamentally quantum-mechanical process arising from a misalignment of the *flavor states* (ν_e , ν_μ , ν_τ) which take part in weak interaction processes, compared to the so-called *mass eigenstates* (ν_1 , ν_2 , ν_3). At the source, a neutrino of a well-defined flavor is produced as the coherent superposition of the three mass eigenstates, which propagate with different phases due to their different masses. While weak interactions are described in the flavor eigenstates, the propagation through space is described in the mass eigenstates. As neutrinos travel, the shift in phase results in a change of the flavor composition, depending on the distance between the source and their detection, as well as on the neutrino's energy. The existence of neutrino oscillations necessarily requires neutrinos to be massive fermions and to mix in a defined way. Both effects are beyond the prediction of the SM in its original formulation. This is why it is widely believed that neutrino oscillations are the first and so far only hard evidence for *new physics* beyond the SM [Sil16].

The concept of neutrino mixing is a natural outcome of gauge theories with massive neutrinos (see e.g. [Sch97] and [GLZ18]) and can be characterized by a unitary transformation relating the flavor and mass eigenbasis according to

$$|\nu_\alpha\rangle = \sum_i U_{\alpha i}^* |\nu_i\rangle \quad \text{or} \quad |\nu_i\rangle = \sum_\alpha U_{\alpha i} |\nu_\alpha\rangle. \quad (2.4)$$

The term $U_{\alpha i}$ and its complex conjugate represents the neutrino mixing matrix. Following e.g. Ref. [Sch97], the evolution of the mass eigenstates $|\nu_i\rangle$ and their propagation can be described by plane wave functions of the form

$$|\nu_i(t)\rangle = e^{-i(E_i t - \vec{p}_i \cdot \vec{x})} |\nu_i(0)\rangle, \quad (2.5)$$

where E_i is the energy of $|\nu_i\rangle$ that can be approximated in the relativistic limit to

$$E_i = \sqrt{p_i^2 + m_i^2} \simeq p_i + \frac{m_i^2}{2p_i} \stackrel{m_i \ll p_i}{\approx} E + \frac{m_i^2}{2E} \quad (2.6)$$

with E being the total energy of the neutrino. By using the equity of time and space under the choice of *natural units* referring to Eqn. (1.33), Eqn. (2.5) results in

$$|\nu_i(L)\rangle = e^{-i\frac{m_i^2 L}{2E}} |\nu_i(0)\rangle, \quad (2.7)$$

neglecting the additional phase factor introduced by the first term in Eqn. (2.6). In this form, it gets obvious that eigenstates of different masses m_i propagate with different frequencies, whereas heavier ones oscillate faster than lighter states over the traveled distance L . As the mass eigenstates are a superposition of the flavor eigenstates according to Eqn. (2.4), the frequency differences cause interference between the corresponding flavor components. The probability that the original neutrino flavor state $|\nu_\alpha\rangle$ will be observed as $|\nu_\beta\rangle$ in dependence on L can be expressed as

$$P_{\alpha \rightarrow \beta} = |\langle \nu_\beta(L) | \nu_\alpha \rangle|^2 = \left| \sum_i U_{\alpha i}^* U_{\beta i} e^{-i\frac{m_i^2 L}{2E}} \right|^2. \quad (2.8)$$

Eqn. (2.8) can be written in the more convenient form of

$$P_{\alpha \rightarrow \beta} = \delta_{\alpha \beta} - 4 \sum_{i > j} \operatorname{Re} (U_{\alpha i}^* U_{\beta i} U_{\alpha j} U_{\beta j}^*) \sin^2 \left(\frac{\Delta m_{ij}^2 L}{4E} \right) \quad (2.9)$$

$$+ 2 \sum_{i > j} \operatorname{Im} (U_{\alpha i}^* U_{\beta i} U_{\alpha j} U_{\beta j}^*) \sin \left(\frac{\Delta m_{ij}^2 L}{2E} \right), \quad (2.10)$$

following Ref. [Sch97]. The phase factor in Eqn. (2.10), which is responsible for the actual occurrence of the flavor oscillation, is often expressed as

$$\frac{\Delta m_{ij}^2 L}{4E} \approx 1.27 \frac{\Delta m_{ij}^2}{[\text{eV}^2]} \frac{L}{[\text{km}]} \frac{[\text{GeV}]}{E} \quad (2.11)$$

using the *natural unit* convention according to Eqn. (1.33). The term $\Delta m_{ij}^2 = m_i^2 - m_j^2$ describes the squared mass difference of two mass eigenstates. For the conventional three flavor neutrino picture as highlighted in the previous section, the mixing is given by the so-called Pontecorvo-Maki-Nakagawa-Sakata (PMNS) matrix, denoted as U_{PMNS} . This complex unitary 3×3 matrix connects the flavor and mass eigenstates via the following expression.

$$\begin{pmatrix} \nu_e \\ \nu_\mu \\ \nu_\tau \end{pmatrix} = \underbrace{\begin{pmatrix} U_{e1} & U_{e2} & U_{e3} \\ U_{\mu 1} & U_{\mu 2} & U_{\mu 3} \\ U_{\tau 1} & U_{\tau 2} & U_{\tau 3} \end{pmatrix}}_{U_{\text{PMNS}}} \begin{pmatrix} \nu_1 \\ \nu_2 \\ \nu_3 \end{pmatrix} \quad (2.12)$$

The PMNS matrix is the analogue of the CKM matrix describing the mixing of quarks and can be parametrized by three Euler angles ($\theta_{12}, \theta_{23}, \theta_{13}$) and one CP-violating phase δ_{CP} (see e.g. [PDG18] and [GLZ18]). However, its numerical structure is very different from the almost diagonal form of the CKM matrix and implies much stronger mixing in the neutrino sector. By using the short notation of $s_{ij} \equiv \sin \theta_{ij}$, $c_{ij} \equiv \cos \theta_{ij}$ and $\delta \equiv \delta_{\text{CP}}$, it can be expressed as shown in Eqn. (2.13)–(2.14).

$$U_{\text{PMNS}} = \begin{pmatrix} c_{12}c_{23} & s_{12}c_{13} & s_{13}e^{-i\delta} \\ -s_{12}c_{23} - c_{12}s_{23}s_{13}e^{i\delta} & (c_{12}c_{23} - s_{12}s_{23}s_{13}e^{i\delta})e^{i\alpha_1} & s_{23}c_{13} \\ s_{12}s_{23} - c_{12}c_{23}s_{13}e^{i\delta} & -c_{12}s_{23} - s_{12}c_{23}s_{13}e^{i\delta} & c_{23}c_{13}e^{i\alpha_2} \end{pmatrix} \quad (2.13)$$

$$= \underbrace{\begin{pmatrix} 1 & 0 & 0 \\ 0 & c_{23} & s_{23} \\ 0 & -s_{23} & c_{23} \end{pmatrix}}_{\text{atmospheric}} \underbrace{\begin{pmatrix} c_{13} & 0 & s_{13}e^{-i\delta} \\ 0 & 1 & 0 \\ -s_{13}e^{i\delta} & 0 & c_{13} \end{pmatrix}}_{\text{reactor}} \underbrace{\begin{pmatrix} c_{12} & s_{12} & 0 \\ -s_{12} & c_{12} & 0 \\ 0 & 0 & 1 \end{pmatrix}}_{\text{solar}} \underbrace{\begin{pmatrix} 1 & 0 & 0 \\ 0 & e^{i\alpha_1} & 0 \\ 0 & 0 & e^{i\alpha_2} \end{pmatrix}}_{\text{Majorana}} \quad (2.14)$$

The first part of Eqn. (2.14) can be studied with atmospheric neutrino experiments involving a typical energy scale of $E_\nu \sim 1 \text{ GeV}$. The corresponding parameters are the mixing angle $\theta_{\text{atm}} \equiv \theta_{23}$ and the atmospheric mass splitting $\Delta m_{\text{atm}}^2 \equiv |\Delta m_{32}^2| \approx |\Delta m_{31}^2|$, whereas the sign of Δm_{atm}^2 is currently unknown. On the contrary, the sign of $\Delta m_{\text{sol}}^2 \equiv \Delta m_{21}^2$ is known due to the imprints of matter effects inside the Sun for the high energy regime ($E_\nu > 2 \text{ MeV}$) of solar neutrino oscillations. This effect is referred to as the Mikheyev-Smirnov-Wolfenstein (MSW) effect and was first described in [Wol78] and [MS86]. Furthermore, the solar mixing is described by the mixing angle $\theta_{\text{sol}} \equiv \theta_{12}$. Finally, reactor neutrino experiments are sensitive to the third mixing angle θ_{13} and the CP-violating phase δ_{CP} .

The last part of Eqn. (2.14), containing the additional phase factors $\alpha_{1,2}$, is only relevant if neutrinos are so-called *Majorana fermions* – meaning that one cannot distinguish between the particle and the corresponding antiparticle state – and does not affect the actual oscillation phenomena regardless of the underlying nature of neutrinos. A more detailed discussion of Majorana particles and their implication will be covered in the following sections (see e.g. section 2.2.1). However, if experiments should show that U_{PMNS} is not unitary, an additional *sterile neutrino* or some other new physics would be required. In this case, the matrix would be extended to 4×4 and higher, introducing new mixing angles and parameters.

Because of the unknown sign of the atmospheric mass splitting Δm_{atm}^2 , there are two possible neutrino mass orderings referred to as the *normal ordering* with $m_1 < m_2 \ll m_3$ and the *inverted ordering* indicated by $m_3 \ll m_1 < m_2$. This way, the mass eigenstate ν_3 could be associated with the heaviest or lightest mass, whereas the lightest neutrino mass could be exactly zero, without contradicting the experimental observations. An illustration of the two possible neutrino mass orderings is depicted in Fig. 2.1.

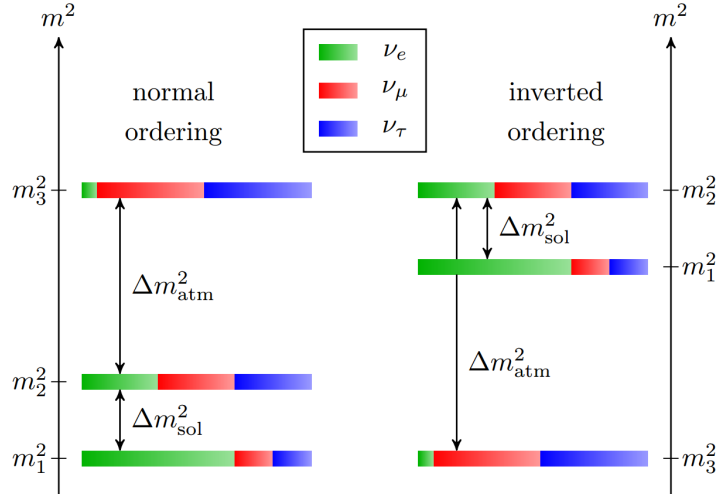


Figure 2.1: Illustration of the two possible neutrino mass orderings resulting from the three flavor PMNS parametrization. The two scenarios depend on the mass eigenstate ν_3 being associated to either the lightest or heaviest neutrino. Moreover, while each of the three mass eigenstates can be expressed as a superposition of the flavor eigenstates according to Eqn. (2.4), the quantum mechanical interference could result in a neutrino state with exactly zero mass.

The current knowledge about the PMNS parameters is summarized in Tab. 2.2 based on the most recent global data analysis by the NuFIT initiative [NuF20]. The global analysis includes the experimental data of reactor, solar, atmospheric and astrophysical neutrino experiments worldwide [EGGHC⁺19].

Table 2.2: Summary of the PMNS parameters as determined in a global analysis of the available neutrino oscillation data (see e.g. Ref. [EGGHC⁺19]). The latest status is referred to as *NuFIT 4.1 (2019)* and provided by an online database [NuF20]. The present best-fit values were obtained without the inclusion of the tabulated χ^2 data on atmospheric neutrinos provided by the Super-Kamiokande collaboration. The assigned uncertainties correspond to $\pm 1\sigma$ (68% C.L.).

parameter	osc. process	normal ordering	inverted ordering
θ_{23} / $^\circ$	atmospheric	$48.3^{+1.1}_{-1.9}$	$48.6^{+1.1}_{-1.5}$
θ_{13} / $^\circ$	reactor	$8.61^{+0.13}_{-0.13}$	$8.65^{+0.13}_{-0.12}$
θ_{12} / $^\circ$	solar	$33.82^{+0.78}_{-0.76}$	$33.82^{+0.78}_{-0.76}$
δ_{CP} / $^\circ$	several	222^{+38}_{-28}	285^{+24}_{-26}
Δm_{21}^2 / 10^{-5} eV 2	solar	$7.39^{+0.21}_{-0.20}$	$7.39^{+0.21}_{-0.20}$
Δm_{3l}^2 / 10^{-3} eV 2	atmospheric	$+2.523^{+0.032}_{-0.030}$	$-2.509^{+0.032}_{-0.030}$

Although the understanding of the neutrino flavor mixing has tremendously improved over the last years, reaching almost sub-percent precision on all mixing angles (see e.g. Ref. [EGGHC⁺19]), fundamental questions need still to be answered by the current and future generation of experiments. A short overview will be given in the next section.

2.1.4 Pending questions in the neutrino sector

Despite the precision reached by the current generation of neutrino experiments, still many neutrino properties remain unknown (see e.g. Ref. [Sil16]). This leads to a couple of fundamental pending questions including:

- What is the nature of neutrinos? (*Dirac* versus *Majorana* fermion)
- Which mass ordering is realized in nature? (*normal* versus *inverted* ordering)
- What is the absolute mass scale of neutrinos?
- Why are neutrinos so much lighter than the charged leptons?
- Could there be additional sterile neutrinos?
- Is there CP-violation in the neutrino sector?

The answer to those open questions requires input of future laboratory, accelerator and reactor experiments as well as astrophysical probes and cosmological surveys. A positive signal in any of those searches would reinforce the evidence for physics beyond the SM. The simplest SM extension comprises the adding of sterile neutrinos, which do not take part in the SM interactions. The corresponding sterile neutrino mass could take any value, from the very small up to the scale of so-called Grand Unified Theories (GUT) with $M_{\text{GUT}} \sim 10^{16}$ GeV (see e.g. [Lee80]). A large fraction of the model space could be probed in e.g. short-baseline neutrino oscillation experiments.

Moreover, direct mass searches could identify the absolute mass scale and help to determine the respective mass ordering. An overview of the interplay and complementary of the searches for different neutrino mass observables will be summarized in section 2.3. The mass ordering and scale directly affects the prediction of the oscillation patterns as it modifies the way in which neutrinos propagate over long distances in media such as the Earth. Because of the MSW effect, which describes the matter effect via weak interactions of neutrinos with electrons and nucleons, neutrinos acquire an effective mass that modifies their energy and the mixing. In the case of the normal ordering, the neutrino flavor oscillations are enhanced, while they are suppressed for the inverted ordering. The opposite effect would be observed for the case of antineutrinos.

Furthermore, the neutrino mass ordering determines the rate of the hypothesized neutrinoless double beta decay ($0\nu\beta\beta$ -decay), which is an ultra-rare nuclear transition that has not yet been observed experimentally. Nonetheless, it provides a unique tool to probe the Majorana character of neutrinos as will be discussed in chapter 3.

However, even knowing the neutrino mass ordering still leaves open the question of the overall neutrino mass scale (see section 2.3). The absolute mass scale affects the structure formation in the early universe, whereas heavier neutrinos would result in the suppression of the growth of large-scale structures. This is why cosmological surveys are sensitive to the overall sum of all neutrino mass eigenstates.

Within the next decade, it is expected that proposed and upcoming large-scale neutrino experiments such as DUNE (U.S.) [DUN20], Hyper-Kamiokande (Japan) [Hyp18] and JUNO (China) [JUN15], as well as the upgrades of the neutrino telescopes KM3NeT [KM316] in the Mediterranean Sea and IceCube/PINGU [Ice17] at the south pole will resolve the issue of the mass ordering.

2.2 Neutrino mass generation

As pointed out in the previous section, neutrinos have always played the role of an elusive particle. Based on the interpretation of the early experiments' data, it was suggested that neutrinos, unlike other fermions, were massless. This conclusion was supported by the measurement of the neutrino's helicity in the famous *Goldhaber experiment* in 1958, which confirmed that neutrinos are always left-handed [GGS58], and the formerly performed *Wu experiment* providing proof for parity violation in weak interactions [LY56]. Because of this, the founders of the SM (see section 1.1) did not include right-handed neutrinos in their theory of the electroweak interaction, which is why neutrinos remained massless.

By proving the existence of flavor oscillations in the neutrino sector, corresponding to at least two non-zero mass eigenstates, one of the most important question about neutrinos concerns the type of masses they have. So far, all of the fundamental fermions of the SM are referred to as *Dirac particles*, with particles and antiparticles being distinguished by opposite charges. The associated Dirac masses arise from the coupling to the SM Higgs field. This general model could apply to neutrinos as well, but as they are electrically neutral, it is possible that they acquire their mass via a different mechanism. Indeed, neutrinos and antineutrinos might be fundamentally indistinguishable, constituting what is called a *Majorana particle* as proposed by E. Majorana already in 1937 [Maj37]. Unlike Dirac fields, which have four components, Majorana fields are characterized by only two degrees of freedom. Moreover, Majorana particles cannot possess any charge, not even a lepton number, which is why their existence is usually associated with sterile neutrinos.

As the origin of neutrino masses is still unresolved, an extension of the SM is required. In its minimal formulation, it has various global symmetries, including the conservation of the baryon number B and the lepton number L , which are referred to as *accidental symmetries* (see e.g. Ref. [DMVV16]). However, those accidental symmetries are only an artifact of the specific particle content of the SM and the hypothesis of the renormalizability of the theory. On the other hand, some combinations such as the " $B - L$ symmetry" are conserved also non-perturbatively. While this forbids i.e. the existence of the hypothesized $0\nu\beta\beta$ -decay, which violates the lepton number conservation by $\Delta L = 2$ (see chapter 3), an evidence for such a transition would directly imply physics beyond the SM. At the same time, the minimal formulation of the SM prevents the construction of gauge invariant neutrino mass terms in contradiction to the experimental observation of flavor oscillations. Therefore, the question of how to modify the SM arises, particularly concerning the underlying nature of neutrinos and the related mass generating mechanism.

2.2.1 Origin of neutrino masses

The simplest extension of the SM assumes the existence of right-handed neutrinos, which behave as singlets with respect to the gauge group of the electroweak interaction (see section 1.1.3). This way, Yukawa couplings with the left-handed lepton doublets and the Higgs field will be allowed, while the lepton number is preserved. This allows for the construction of gauge invariant Dirac mass terms as for all the other fundamental SM fermions. However, this mechanism provides no insight into why neutrino masses are so small. Regarding the Yukawa coupling, it would need to be more than five orders of magnitude smaller than for the electron as the lightest of the charged leptons.

On the one hand, one could simply accept such an extreme fine-tuning, while it is deeply unsatisfactory, as a fundamental aspect of nature. On the contrary, by following this simplest implementation of neutrino masses, one could naively expect a similar flavor mixing as

observed in the quark sector, leading to a strong hierarchy in the respective mass ordering, whereas neither of which is observed.

One well-motivated alternative option is that neutrinos are Majorana particles. The idea was first proposed by E. Majorana [Maj37] as shortly addressed in the previous section. In contrast to the case of Dirac fermions, Majorana neutrinos will have a mass term in the Lagrangian that breaks lepton number conservation. Although such a mass term is forbidden by the gauge group of the SM, it could arise as the low-energy realization of a more fundamental theory. Several of such GUTs were developed in the 1970s by G. Glashow and others (see e.g. Ref. [Gla80]). In this case, the SM would be supplemented by additional interaction terms related to *higher-dimensional operators*, which are suppressed by powers of an energy scale Λ , that is characteristic for the scope of the applied framework.

One prominent example is the so-called *Weinberg operator* as introduced by S. Weinberg in 1979 [Wei79]. This operator involves two lepton and two Higgs doublets and breaks the lepton number conservation, while it generates Majorana neutrino masses according to $M_\nu \sim M_W^2/\Lambda$. By assuming a Majorana neutrino mass on the order of 50 meV in combination with the mass of the W^\pm bosons $M_W = 80.4$ GeV [PDG18] in the SM, the characteristic energy scale results in $\Lambda \sim 1.3 \cdot 10^{14}$ GeV, which is close to the previously quoted GUT scale $M_{\text{GUT}} \sim 10^{16}$ GeV.

Similarly, GUTs based on the SO(10) gauge group were found to be able to explain light neutrino masses compatible with the SM, while they predict at the same time heavy Majorana neutrino states (see e.g. [GMRS79], [Gla80] and [MS80]). The coupling of the heavy Majorana neutrinos to the lepton and Higgs fields induces the Weinberg operator via the so-called *seesaw mechanism* (see e.g. [Min77] and [Yan80]). An overview of different seesaw implementations will be discussed in section 2.2.3. The key aspect of this mechanism is that the heavy neutrino states are typically found a few orders of magnitude below the GUT scale, causing the SM neutrino masses to appear in the sub-eV range. In this way, the existence of heavy Majorana neutrinos can be viewed as a prediction of the seesaw mechanism and, more generally, of GUTs with the SM being a low-energy limit.

Unfortunately, it is very challenging to confirm this appealing model for the generation of neutrino masses experimentally. A first necessary – but not sufficient – step would be to prove the nature of neutrinos, which could be done by observing the $0\nu\beta\beta$ -decay as an unambiguous indication for the Majorana character. Moreover, it should be noted that the observation of other processes like the proton decay, which is assumed to be absolutely stable in the SM, would strongly support the GUT hypothesis (see e.g. [GG74] and [CEG77]). While the GUTs' typical reunification scales predict a proton lifetime on the order of $\tau_p \sim 10^{34}$ yr, experiments such as Super-Kamiokande can already exclude a wide range of $9.2 \times 10^{33} - 3.4 \times 10^{34}$ yr at 90% C.L. depending on the assumed final state [Sup20].

Finally, the ultimate theory behind neutrino masses must also explain the observed structure of the flavor mixing, containing large mixing angles with respect to the quark section, as well as the potential presence of CP-violation. Many approaches have been proposed in the past, e.g. the use of continuous or discrete flavor symmetries, but no unique underlying principle has yet been identified (see Ref. [MAB⁺07]). This is why there is a strong experimental effort involving the search for the $0\nu\beta\beta$ -decay in a variety of experiments or the search for charged-lepton flavor-violating processes involving muon transitions (see e.g. [BGK⁺18]).

2.2.2 Dirac versus Majorana mass terms

The fact that neutrinos carry no U(1) charge endow them with certain properties that are not shared by the charged fermions of the SM. Regarding a generic approach to construct Lorentz invariant mass terms, it is possible to introduce both Dirac and Majorana mass terms for the neutrino, whereas for the charged fermions, the conservation of the electric charge

allows only Dirac-type mass terms. In the usual four component spinor notation as used for the QED expression in section 1.1.1, the Dirac mass term has the form $m\bar{\psi}\psi$, whereas the sign with respect to the Dirac equation will be neglected in the following. The combination of the outgoing $\bar{\psi}$ and incoming fermion spinor ψ is Hermitian and Lorentz invariant, hence, the mass m cannot be complex to ensure the scalar character of the Lagrangian. Furthermore, the fermion field can be separated into its chiral components by using the projection operators $P_{L,R}$ as defined in Eqn. (2.15).

$$P_L = \frac{1}{2}(\mathbb{1} - \gamma^5), \quad P_R = \frac{1}{2}(\mathbb{1} + \gamma^5). \quad (2.15)$$

The chiral partitioning reveals the underlying $V - A$ structure of weak interactions as it leads to terms proportional to γ_μ (vector) and $\gamma^5\gamma_\mu$ (axial-vector). The definitions in Eqn. (2.15) make use of the Dirac representation of the γ -matrices according to

$$\gamma^5 \equiv i\gamma^0\gamma^1\gamma^2\gamma^3 = \begin{pmatrix} 0 & \mathbb{1} \\ \mathbb{1} & 0 \end{pmatrix}, \quad (2.16)$$

$$(\gamma^5)^2 = \mathbb{1}, \quad \{\gamma^5; \gamma^i\} = 0. \quad (2.17)$$

In this way, a generic fermion field can be expressed as

$$\psi = \psi_L + \psi_R, \quad \text{with } \psi_{L,R} = P_{L,R}\psi. \quad (2.18)$$

Consequently, the respective Dirac mass term associated with the mass m_D results in

$$\mathcal{L}_{\text{Dirac}} = m_D\bar{\psi}\psi \quad (2.19)$$

$$= m_D(\bar{\psi}_L + \bar{\psi}_R)(\psi_L + \psi_R) \quad (2.20)$$

$$= m_D(\underbrace{\bar{\psi}_L\psi_L}_{=0} + \underbrace{\bar{\psi}_L\psi_R}_{=0} + \underbrace{\bar{\psi}_R\psi_L}_{=0} + \underbrace{\bar{\psi}_R\psi_R}_{=0}) \quad (2.21)$$

$$= m_D\bar{\psi}_L\psi_R + \text{h.c.}, \quad (2.22)$$

with h.c. referring to the Hermitian conjugate of the written term. The zero-identity in Eqn. (2.21) results from the definition of the algebra according to Eqn. (2.17) leading to

$$\bar{\psi}_L\psi_L = \psi^\dagger P_L \gamma^0 P_L \psi = \psi^\dagger \underbrace{\gamma^0 P_R P_L}_{=0} \psi = 0, \quad (2.23)$$

and vice versa for the combination $\bar{\psi}_R\psi_R$. The general Dirac notation makes use of four fermion states, involving left- and right-handed particle states $\psi_{L,R}$ and the corresponding antiparticle states $\psi_{L,R}^c$ using the charge conjugation of the fermion field. As the mass term Eqn. (2.22) connects fields of opposite chirality, while right-handed neutrinos ν_R (respectively left-handed antineutrinos ν_L^c) are not part of the minimal formulation of the SM, the corresponding Dirac mass of neutrinos has to be zero to ensure the Lorentz invariance of the Lagrangian. Moreover, in the case of $m_D = 0$ only two of the four possible Dirac states, indicating left-handed neutrinos ν_L and right-handed antineutrinos ν_R^c , participate in weak interactions while the others remain as sterile neutrinos.

By considering that the neutrino is a Majorana particle, the four Dirac spinors get reduced to two Majorana spinors combining the states of the same chirality

$$\nu = \nu_m \equiv \frac{\nu_L + \nu_L^c}{\sqrt{2}} \quad \text{and} \quad N = N_m \equiv \frac{\nu_R + \nu_R^c}{\sqrt{2}}. \quad (2.24)$$

Because Majorana fermions do not carry a U(1) charge, it is usually claimed that they are identical to their antiparticle state. The respective Lagrangian can be constructed from four Lorentz invariant combinations such as

$$\mathcal{L}_{\text{Majorana}} = m_\nu \bar{\nu} \nu^c + m_\nu^* \bar{\nu}^c \nu + m_N \bar{N} N^c + m_N^* \bar{N}^c N \quad (2.25)$$

$$= m_\nu \bar{\nu} \nu^c + m_N \bar{N} N^c + \text{h.c.} \quad (2.26)$$

By using the partition into chiral components according to the definitions of the Majorana spinors given in Eqn. (2.24), the Lagrangian in Eqn. (2.26) can be expressed as

$$\mathcal{L}_{\text{Majorana}} = \frac{1}{2} m_\nu \bar{\nu}_L \nu_R^c + \frac{1}{2} m_N \bar{\nu}^c_L \nu_R + \text{h.c.} \quad (2.27)$$

Finally, the Dirac mass term Eqn. (2.22) and the Majorana mass term Eqn. (2.27) can be combined, yielding the most general Lagrangian with respect to the gauge invariant expression of neutrino masses. The combination results in

$$\mathcal{L}_\nu = \mathcal{L}_{\text{Dirac}} + \mathcal{L}_{\text{Majorana}} \quad (2.28)$$

$$= \frac{1}{2} m_D (\bar{\nu}_L \nu_R + \bar{\nu}^c_L \bar{\nu}^c_R) + \frac{1}{2} m_\nu \bar{\nu}_L \nu_R^c + \frac{1}{2} m_N \bar{\nu}^c_L \nu_R + \text{h.c.} \quad (2.29)$$

$$= \frac{1}{2} (\bar{\nu}_L, \bar{\nu}^c_L) \mathcal{M} \begin{pmatrix} \nu_R^c \\ \nu_R \end{pmatrix} + \text{h.c.} \quad \text{with} \quad \mathcal{M} = \begin{pmatrix} m_\nu & m_D \\ m_D & m_N \end{pmatrix}. \quad (2.30)$$

The corresponding effective neutrino mass for an active, dominantly left-handed neutrino, as well as for a sterile, dominantly right-handed neutrino can be expressed as the eigenvalues of the mass matrix \mathcal{M} in Eqn. (2.30). These eigenvalues are referred to as $m_{L,R}$ and can be evaluated by further assumptions involving the *seesaw mechanism*. One of the most common approaches is to assume that one of the Majorana fields is very massive, while the other features only a small mass. This way, both light and heavy Majorana neutrinos are predicted by the seesaw mechanism. Moreover, the Dirac mass involved in neutrino oscillation remains unaffected by the generalized procedure outlined above. By assuming $m_\nu \approx 0$ and $m_N \gg m_D$, the eigenvalues of \mathcal{M} can be derived analytically as

$$m_L = \frac{m_D^2}{m_N} \ll m_D, \quad m_R = m_N \left(1 + \frac{m_D^2}{m_N^2} \right) \approx m_N. \quad (2.31)$$

In this way, the left-handed neutrino mass gets the smaller, the higher the mass of the right-handed neutrino turns out to be, which is the essential feature of the seesaw mechanism. An overview of alternative seesaw realizations will be addressed in the next section.

In conclusion, Majorana neutrino masses can appear on the sub-eV scale up to M_{GUT} . Both heavy and light Majorana neutrinos are linked to the Weinberg operator as one of the simplest non-trivial extensions of the SM Lagrangian, which makes them strongly motivated from the theoretical and phenomenological point of view. For charged fermions, such as the electron, muon and tau leptons, Majorana mass terms are forbidden by the U(1) invariance of the SM. Hence, all electrically charged fermions are Dirac particles. On the other hand, a Lagrangian with both Majorana and Dirac masses describes, necessarily, a pair of Majorana fermions, irrespective of how small the Majorana mass might be. Because of this, Majorana mass terms are only forbidden if there is an additional global symmetry under which the respective particle species has a non-zero charge. Consequently, it seems only *natural* to predict that neutrinos are Majorana fermions, meaning that the Majorana case relies on fewer assumptions than a pure Dirac scenario. The proof of its Majorana nature could potentially shed light on the connection between particle physics and cosmological observations explained

by the presence of dark matter. Heavy right-handed neutrinos are possible candidates for cold dark matter and could explain simultaneously the baryon asymmetry of the universe as discussed e.g. in Ref. [AS05]. Finally, the presence of Majorana neutrinos would not contradict with the experimental observation of neutrino oscillation, but could provide a natural explanation for the smallness of neutrino masses by means of the seesaw mechanism.

2.2.3 Overview of seesaw mechanisms

As mentioned in the previous section, the seesaw mechanism can be implemented based on different approaches such as summarized in Ref. [CHLR18]. The simplest and most studied extension beyond the SM regarding neutrino masses is referred to as the *seesaw type-I mechanism*. Essentially, this implementation has been addressed in the previous section and produces a light neutrino for each of the three known neutrino flavors, accompanied by a corresponding very heavy neutrino, which has yet to be observed. Because right-handed neutrinos are completely neutral with respect to the SM gauge symmetries, they could be much heavier than the other fundamental fermions. The Lagrangian associated with the type-I seesaw contains both a Yukawa coupling with the Higgs boson, as for the quarks and charged leptons, as well as a Majorana neutrino mass term for the right-handed neutrinos with $m_R \approx m_N$. By the process of electroweak symmetry breaking, the neutral Higgs boson gets a vacuum expectation value, generating a left-handed light neutrino mass m_L which is proportional to the square of the respective Yukawa coupling. By assuming the Yukawa coupling to be of order $\mathcal{O}(1)$ and $m_N \sim 10^{14}$ GeV, a sub-eV neutrino mass scale can be ensured in compliance with the oscillation data and the observed mass splittings.

However, this is, by no means, the only way to provide an explanation for the origin of neutrino masses. First of all, since there are no restrictions on the right-handed neutrino masses, they can take any value. In fact, there are seesaw models that extend m_N even below the electroweak scale, allowing some of them to be tested at the LHC. Typical final state signatures are same-sign dileptons with no missing energy, indicating a violation of the lepton number, as well as flavor-violating multi-lepton events. Even though several searches have been conducted by the LHC's ATLAS and CMS collaborations (see e.g. Ref. [ATL15] and [CMS17]), so far no positive hint has been found [Sil16]. Furthermore, the heavy fermion state triggering the seesaw mechanism could also be inferred from a different perspective involving e.g. a fermion triplet (*seesaw type-III*) or a scalar triplet (*seesaw type-II*) [CHLR18]. Finally, some models providing heavy Majorana particles, such as radiative and R-parity violating supersymmetric models (see Ref. [Moh15] for an overview), do not invoke the seesaw mechanism at all.

With so many possibilities for the theoretical description of the origin of neutrino masses and their phenomenology, one needs to hunt for other beyond-SM signatures to try to identify the dominant mass mechanism. One of those is referred to as *leptogenesis* in physical cosmology (see e.g. [PR81]) and offers a way to generate dynamically a baryon asymmetry in the early universe. In several theoretical works (see e.g. [FY86]) it could be shown that the three so-called *Sakharov conditions* (see e.g. [Sak91]) – lepton or baryon number violation, C- and CP-violation, and an out-of-equilibrium state (e.g. by the expansion of the universe) – can be satisfied by the seesaw mechanism. The key concept is based on the freeze-out of right-handed neutrino states as the temperature of the expanding universe drops below their mass. Because of the heavy neutrinos being potentially unstable, decays into leptons and Higgs bosons could proceed, producing a net lepton asymmetry given a sufficiently strong CP-violation. This asymmetry in the lepton sector could then be converted into a baryon asymmetry by non-perturbative SM effects.

Future neutrino oscillation experiments might be able to shed light on the CP-violation in the lepton sector, while the search for the $0\nu\beta\beta$ -decay could ultimately confirm the non-conservation of the total lepton number. Moreover, as both search strategies are strongly complementary, any positive signature would already be a strong hint that leptogenesis is at the origin of the baryon asymmetry of the universe.

An overview of the research field dedicated to direct and indirect neutrino mass searches is given in the next section.

2.3 Neutrino mass searches

As neutrino masses and their unknown origin provide a window to address physics beyond the SM, there is a large variety of research activity in this field. This includes laboratory experiments aiming to investigate the endpoint of β -decay transitions with unprecedented precision, the search for the hypothesized $0\nu\beta\beta$ -decay, as well as cosmological surveys and astroparticle experiments observing the neutrino outburst in supernova explosions. The first and last approach make use of the pure kinematics of the interactions to probe the absolute neutrino mass in a rather model independent way. An overview of such direct mass searches will be given in the first part of this section. Following this, the sensitivity of cosmological surveys and the search for the $0\nu\beta\beta$ -decay will be discussed. Finally, a summary and comparison of the different mass observables will be presented in the concluding section. More information can be found in recent review articles such as [SGM⁺18] and [DMVV16].

2.3.1 Direct kinematic approaches

Historically, the observation of the neutrino outburst of the supernova SN1987A provided the first direct information on neutrino masses. By analyzing the observed time and energy distribution of the diffuse neutrino flux on Earth, an upper limit of about 6 eV could be set on the electron-antineutrino mass (see Ref. [LL02] and [PRTV10]). Nowadays, the perspectives of future observations are connected to improved detector systems that are organized in the Supernovae Early Warning System (SNEWS) [AFF⁺04]. The current list of SNEWS participants consists of Borexino [Bor19], Daya Bay [Day19], KamLAND [Kam16a], HALO [HAL08], IceCube [Ice13], LVD [LVD15], and Super-Kamiokande [Sup98].

Furthermore, a model-independent, direct method for probing the neutrino mass scale is provided by kinematic studies of weak-interaction processes such as the β -decay of tritium ^3H or the EC on the holmium isotope ^{163}Ho . The tritium β -decay is under investigation by the KATRIN experiment [KAT19] using a large-scale spectrometer based on the magnetic adiabatic collimation with an electrostatic (MAC-E) filter approach. Alternatively, the same decay can be probed by using the cyclotron radiation emission spectroscopy (CRES) technique as investigated in the course of *Project 8* [Pro17]. Similarly, the EC on ^{163}Ho is sensitive to the same mass observable and currently studied by the ECHo collaboration [ECH17].

All these experiments search for the small, characteristic shape distortions close to the endpoint of the respective β -spectra caused by a non-zero neutrino mass. However, the sensitivity is typically limited to the *quasi-degenerated regime*, where the mass eigenvalues m_i are about the same (see also Fig. 2.2 in section 2.3.4). The actual mass observable is the incoherent sum of the squared mass eigenvalues and the absolute square of the electron-flavor matrix elements given by Eqn. (2.32).

$$m_\beta^2 = \sum_{i=1}^3 |U_{ei}|^2 m_i^2, \quad \text{with } m_i \lesssim 0.2 \text{ eV.} \quad (2.32)$$

In the quasi-degenerated regime, the measured neutrino mass is usually associated as $m_\beta \approx m_i$. While the experimental advances have steadily increased over the last decades, the most strictest limit has been set by the first four-week science run by the KATRIN experiment [KAT19]. The reported upper limit of $m_\beta < 1.1$ eV at 90% C.L. coincides with the current experimental sensitivity, whereas the collaboration is confident to reach an ultimate sensitivity on the order of 0.2 eV in five years of operation. Moreover, searches for physics beyond the SM involving sterile neutrino admixtures with masses from the eV to the keV scale are part of KATRIN's science program.

2.3.2 Cosmological surveys

Because of the unique role of primordial neutrinos in the formation of large-scale structures in the universe, observations of matter clustering in different epochs of the universe allow one to probe the sum of the neutrino mass eigenstates according to

$$M_\nu = \sum_{i=1}^3 m_i < 0.12 \text{ eV} \quad [\text{Pla19}]. \quad (2.33)$$

While the indications for neutrino masses from cosmology has kept changing for the last two decades (see e.g. Ref. [LMMP13] for a comprehensive review), the latest data release of the Planck collaboration includes new tight limits on M_ν as shown in Eqn. (2.33). However, those cosmological bounds depend on the selection of the data included in the analyses and are only valid within the Λ CDM concordance model (see e.g. Ref. [LCA⁺19] and [Pla19]).

2.3.3 Neutrinoless double beta decay

Finally, the observation of the hypothesized $0\nu\beta\beta$ -decay would not only proof the Majorana nature of neutrinos, but allow for the determination of the so-called *effective Majorana mass*, denoted as $m_{\beta\beta}$, by measuring its half-life. Details on the conversion will be discussed in chapter 3. The accessible mass observable in $0\nu\beta\beta$ -decay searches is the coherent sum

$$m_{\beta\beta}^2 = \left| \sum_{i=1}^3 U_{ei}^2 m_i \right|^2, \quad (2.34)$$

where the index i runs over the three neutrino mass eigenstates. In contrast to the observable m_β in Eqn. (2.32), which can be accessed in single β -decay experiments, Eqn. (2.34) might lead to cancellation effects depending on the neutrino mass ordering (see also Fig. 2.2). While in the extreme this could lead to $m_{\beta\beta} \rightarrow 0$, it also provides some sensitivity to fix the mass ordering by observing the decay in multiple nuclides within a matching neutrino mass range. Furthermore, even though both m_β and $m_{\beta\beta}$ contain only the electron-flavor matrix elements, connecting the mass observables with the electron flavor, they have a different physical interpretation. However, both can be seen as the respective *electron-type neutrino mass* that rules the nuclear transition, accordingly.

Regarding the seesaw mechanisms discussed in section 2.2.3, it should be noted that the approximation $m_\nu \approx 0$ for the light Majorana neutrino mass term in Eqn. (2.30) and the general mass matrix \mathcal{M} does not necessarily lead to $m_{\beta\beta} \approx 0$. In fact, in type-I seesaw models, the left-handed neutrino mass can be expressed as $m_L = m_D^2/m_N$ as shown in Eqn. (2.31). This well-known result can be converted into

$$m_{\beta\beta} = m_L \left(1 + \frac{\langle q^2 \rangle}{m_N^2} \right) \quad (2.35)$$

as discussed in Ref. [MSV12] and [DMVV16]. The quantity $\langle q^2 \rangle$ in the second part depends on the actual nuclear structure of an atomic nuclei and is on the order of $(100 \text{ MeV})^2$. Moreover, the heavy neutrino mass m_N enters Eqn. (2.35) and suppresses the term in compliance with the seesaw mechanism. In this way, Eqn. (2.35) is valid for $m_L \ll 100 \text{ MeV} \ll m_R \approx m_N$. More information can be found in various review articles on this subject such as e.g. [DMVV16].

2.3.4 Interplay of neutrino mass observables

A summary of the mass observables discussed in the previous section is given in Tab. 2.3. Cosmological surveys as well as the precise study of β -decay endpoints have the potential to place strong bounds on the lightest neutrino mass eigenstate. The interplay and complementarity of those approaches with respect to the effective Majorana neutrino mass that could be assessed via the observation of the hypothesized $0\nu\beta\beta$ -decay is depicted in Fig. 2.2.

Table 2.3: Comparison of the neutrino mass observables in cosmology, β -decay investigations and the search for the hypothesized $0\nu\beta\beta$ -decay. All three approaches have the potential to improve the current experimental upper limits by about one order of magnitude in future iterations (see e.g. [LCA⁺19] and [DMVV16]).

	cosmology	β -decay (+ EC)	$0\nu\beta\beta$ -decay
observable	$M_\nu = \sum_i m_i$	$m_\beta^2 = \sum_i U_{ei} ^2 m_i^2$	$m_{\beta\beta}^2 = \sum_i U_{ei}^2 m_i ^2$
present limit	$M_\nu < 0.12 - 1.0 \text{ eV}$	$m_\beta < 1.1 \text{ eV}$	$m_{\beta\beta} < 0.2 - 0.4 \text{ eV}$
potential	$M_\nu \sim 15 - 50 \text{ meV}$	$m_\beta \sim 200 \text{ meV}$	$m_{\beta\beta} \sim 15 - 50 \text{ meV}$
characteristics	multi-parameter cosmological models	only kinematics, no cancellations in incoherent sum	Majorana neutrinos, LNV, uncertainty of nuclear effects

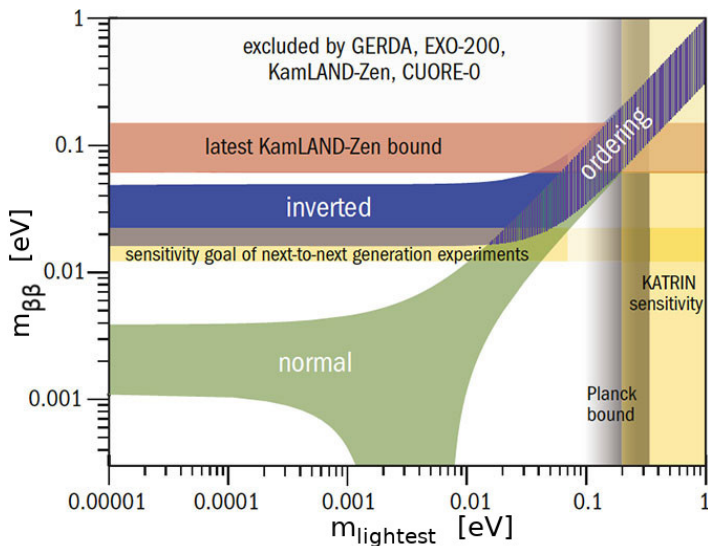


Figure 2.2: Interplay of different neutrino mass observables (adapted from [Sil16]). The direct mass searches as performed by KATRIN and the cosmological bound on the sum of the neutrino mass eigenstate exclude the parameter space of the lightest neutrino mass from the righthand side. While the search for the $0\nu\beta\beta$ -decay depends critically on the ordering of the neutrino masses, the current generation of experiments is about to touch the top of the band indicating the parameter space of the inverted mass ordering. Future experiments are expected to reach sensitivities that allow to probe the full band, while it will be rather challenging to reach the predicted mass regime of the normal ordering.

Chapter 3

Double beta decay

The discovery of neutrino masses through the observation of flavor oscillations boosted the importance of direct and indirect mass searches including the search for the hypothesized neutrinoless double beta decay ($0\nu\beta\beta$ -decay). Nowadays, the search for this ultra-rare nuclear transition is one of the most active research field at the intersection of nuclear, particle and astroparticle physics. Its main and evident feature is the explicit violation of the total lepton number, which is an accidentally conserved quantity in the SM. Furthermore, its observation would demonstrate that the lepton number is not protected by a fundamental symmetry of nature, while neutrinos would be identified as Majorana fermions. This, in turn, would support the exciting theoretical explanation of the origin of the observed baryon asymmetry in the universe through the process of leptogenesis and, potentially, the role of neutrinos in the early universe's structure formation. For these reasons, besides being an outmost interesting nuclear process, $0\nu\beta\beta$ -decay provides a key tool for studying neutrinos, probing their fundamental nature, and could shed light on their unknown mass scale and ordering.

The possibility of a second order weak nuclear $\beta\beta$ -transition with two neutrinos in the final state was already discussed in 1935 by M. Goeppert-Mayer [GM35]. After E. Majorana proposed a novel model to describe fermions in a relativistic quantum field theory in 1937 [Maj37], W. Furry studied this scenario in the context of the formerly discussed $\beta\beta$ -transitions [Fur39] and proposed the existence of a process with a rather simple form such as

$$(A, Z) \longrightarrow (A, Z + 2) + 2e^- . \quad (3.1)$$

This process is referred to as $0\nu\beta\beta$ -decay due to the absence of any neutrinos. The conventional double beta decay is analogously referred to as $2\nu\beta\beta$ -decay. An overview of the different $\beta\beta$ -decay modes will be given in the first section of this chapter.

It took more than 50 years of experimental advance until the ordinary $2\nu\beta\beta$ -decay could be observed in a direct counting experiment by M. Moe and colleagues in 1987 [EHM87]. This group could not only confirm the existence of this process but determined the corresponding half-life of ^{82}Se to $T_{1/2}^{2\nu} \sim 10^{20}$ yr. On the contrary, several false-positive results of previously performed geochemical and radiometric experiments could not be confirmed by later experiments. Since then, the ordinary $2\nu\beta\beta$ -decay was observed in a total of eleven different nuclides [Bar19a]. However, none of those experiments found an indication for the neutrinoless process, raising the half-life lower bound to approximately $T_{1/2}^{0\nu} > 10^{25}$ years.

This chapter covers both the theoretical as well as the experimental aspects of the search for the $0\nu\beta\beta$ -decay. Even though the half-life predictions still suffer from numerous uncertainties, great progress in assessing the expectations for this process has been made, which will be briefly addressed in the course of the following sections.

3.1 Classification of double beta decays

At first, the classification of double beta decay transitions with respect to the nuclear and leptonic final states will be discussed. The underlying procedure is closely related to the single β -decay of radioactive atomic nuclei as discussed before in section 1.2.3.

3.1.1 Double beta decay modes

The conventional $2\nu\beta\beta$ -decay with two neutrinos in the final state involves the following processes summarized in Eqn. (3.2)–(3.5).

$$2\nu\beta^-\beta^- : \quad {}_Z^AX \longrightarrow {}_{Z+2}^AY + 2e^- + 2\bar{\nu}_e, \quad (3.2)$$

$$2\nu\beta^+\beta^+ : \quad {}_Z^AX \longrightarrow {}_{Z-2}^AY + 2e^+ + 2\nu_e, \quad (3.3)$$

$$2\nu\beta^+EC : \quad {}_Z^AX + e^- \longrightarrow {}_{Z-2}^AY + e^+ + 2\nu_e, \quad (3.4)$$

$$2\nuECEC : \quad {}_Z^AX + 2e^- \longrightarrow {}_{Z-2}^AY + 2\nu_e. \quad (3.5)$$

In all of those processes, two nucleons of the atomic nuclei undergo simultaneously a single β -decay transition. This is why most of the characteristics as discussed for the single β -decay modes apply also for the case of $\beta\beta$ -decays. In particular, there is a competition between the $\beta^+\beta^+$ modes due to the equity of the nuclear final state, which results in three possibilities – $\beta^+\beta^+$, β^+EC and $ECEC$. Again, the Q -value of those transitions depends on the number of involved positrons and gets reduced by two times the electron mass for each involved positron, yielding the highest Q -value for the $2\nuECEC$ process.

By combining the single β -decay processes depicted in the Feynman diagrams shown in Fig. 1.7, the corresponding diagrams for the double beta decay modes can be constructed. Exemplarily, Fig. 3.1 illustrates the conventional and neutrinoless $\beta^-\beta^-$ transition on the nucleon level. The latter case involves the exchange of a Majorana neutrino ν_m , which is the default scenario leading to the sensitivity to the mass observable $m_{\beta\beta}$ as defined in Eqn. (2.34). However, this is by no means the only way to provide an explanation for the existence of $0\nu\beta\beta$ -decay in nature as will be further elaborated in section 3.2.2. The experimental signatures of both decay modes will be discussed in the subsequent section.

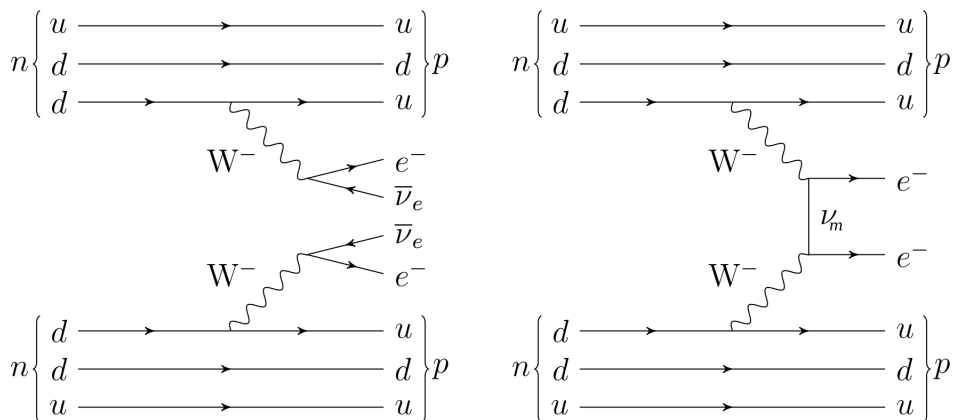


Figure 3.1: Feynman diagrams of double beta transitions with two electrons in the final state (adapted from [Zat14]). *Left:* $2\nu\beta\beta$ -decay. *Right:* $0\nu\beta\beta$ -decay. While the ordinary double beta decay with two electron-antineutrinos $\bar{\nu}_e$ in the final state is an allowed, second order weak process in the SM, the neutrinoless version violates the lepton number conservation by $\Delta L = 2$. Moreover, the exchange of the Majorana neutrino ν_m requires a flip of the neutrino's helicity, which can only be explained if the neutrino is its own antiparticle.

3.1.2 Experimental signature

An illustration of the expected double beta decay signatures, as observed by a suitable detector system, is depicted in Fig. 3.2. The example is based on the $\beta^- \beta^-$ decay of ^{116}Cd with $Q_{\beta\beta} = 2.8 \text{ MeV}$. In the case of the $2\nu\beta\beta$ -decay, a continuous spectrum of the sum energy of the two electrons, similar to the momentum distribution of the β -electrons resulting from a conventional single β^- -decay, is expected. As the emitted neutrinos carry away a fraction of the released energy, the electrons will only very rarely carry the full Q -value, while the maximum rate is found at approximately one third of the Q -value. On the contrary, the spectrum of the $0\nu\beta\beta$ -decay would result in a sharp peak at $Q_{\beta\beta}$ because of the two electrons carrying the full transition energy.

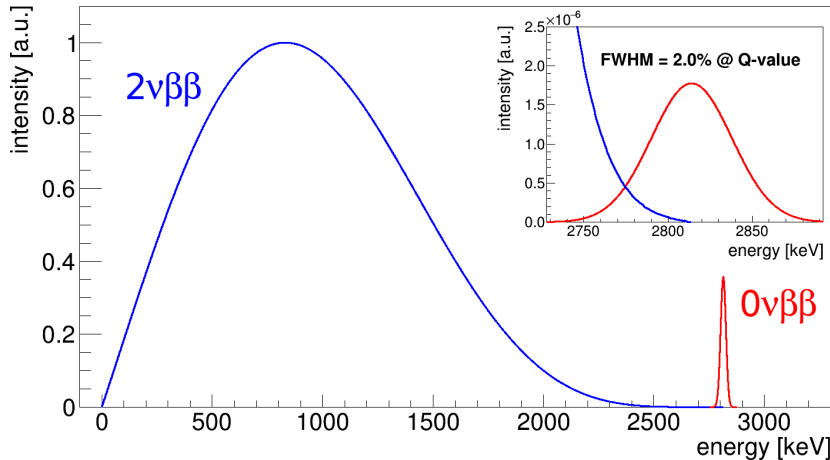


Figure 3.2: Expected experimental signatures of the double beta decay modes of ^{116}Cd (adapted from [Zat14]). The modeling of the continuous $2\nu\beta\beta$ -spectrum (blue) is based on the analytic expressions presented in Ref. [TZ95]. The intensity of the $0\nu\beta\beta$ -peak (red) in the main frame is increased by about 10^5 times for a better visibility. The inset shows a realistic ratio between the two decay modes, assuming an effective Majorana mass of 50 meV and an energy resolution of 2.0% FWHM at $Q_{\beta\beta} = 2.8 \text{ MeV}$.

One of the crucial experimental parameters is the energy resolution in terms of the full-width at half-maximum (FWHM) for a given discrete energy. The depicted example applies a Gaussian energy resolution of 2.0% relative FWHM at $Q_{\beta\beta}$, which is sufficient to discriminate the high-energy tail of the $2\nu\beta\beta$ -spectrum from the $0\nu\beta\beta$ -peak region. The worse the energy resolution, the stronger the overlap will become, providing an intrinsic, irreducible background in the search for the $0\nu\beta\beta$ -peak feature. While the intensity of the expected $0\nu\beta\beta$ -peak has been enhanced by about a factor of 10^5 in the main frame of Fig. 3.2, the inset shows a realistic scaling of the two decay modes. The respective scaling makes use of an effective Majorana neutrino mass of $m_{\beta\beta} = 50 \text{ meV}$, which corresponds to the top of the inverted ordering (see Fig. 2.2), and the known $2\nu\beta\beta$ -decay half-life (see section 8.4).

An overview of different experimental techniques that are used for the search for the $0\nu\beta\beta$ -decay will be given in section 3.3.2. However, one prerequisite for the potential observation is that a single nuclear β -decay of the $\beta\beta$ -nuclide of interest needs to be energetically forbidden or otherwise strongly suppressed by e.g. angular momentum conservation. If this is not the case, the sought signal is likely to be hidden by the much more frequent single β -decay. This statement applies to both the neutrino-accompanied as well as the neutrinoless decay mode and is the reason why double beta decays can only be observed for a couple of known nuclides in nature. The theoretical description of the decay mechanism and its connection to the previously discussed model of atomic nuclei as well as to the involved particle physics will be discussed in the next section.

3.2 Theoretical description

Even though the observation of the $0\nu\beta\beta$ -decay would prove the Majorana nature of neutrinos as stated by the *Schechter-Valle theorem* (see section 3.2.2), the extraction of the associated effective Majorana mass, assuming the default case of light Majorana neutrino exchange as the dominant decay mechanism, is highly non-trivial. Since the process occurs in atomic nuclei, nuclear structure effects play an important role and may affect the decay rate considerably. Those nuclear effects are summarized as the nuclear matrix elements (NMEs) and contain information about the initial and final states of the involved nuclei and the dynamic of the transition. Moreover, due to the complexity of the nuclear physics in combination with the unknown properties of the neutrino, such as the mass ordering, it is not possible to disentangle the effects experimentally. Thus, the evaluation of the NMEs needs to be assessed with the help of numerical methods based on nuclear theory frameworks that are suitable for the nuclei under consideration. The successively increasing sensitivity of double beta decay experiments is driving the nuclear structure calculations towards better performance. Nowadays, various nuclear models have been proposed, whereas none of which has proven to be superior yet. A brief overview based on Ref. [EM17] is presented in section 3.2.4.

Before turning to the nuclear structure theory, the connection between the previously presented droplet model of atomic nuclei (see section 1.2.1) and the origin of $\beta\beta$ -decays will be presented. Following this, the interplay of the nuclear physics and the new physics parameter, e.g. the effective Majorana neutrino mass, are discussed. Both are needed to interpret an experiment's result in terms of an eventually determined $0\nu\beta\beta$ -decay half-life. Furthermore, there is the long-standing question of potential *quenching effects* that alter the coupling strength of the weak interaction in nuclear processes as briefly reviewed in section 3.2.5. On the other hand, the theoretical prediction of the sought $0\nu\beta\beta$ -decay's half-life range is required for the planning of future experiments as will be addressed in section 3.3.

3.2.1 Connection to droplet model

The occurrence of $\beta\beta$ -transitions can be explained in the simple droplet model of atomic nuclei as introduced in section 1.2.1. According to the Bethe-Weizsäcker mass formula presented in Eqn. (1.18) and (1.19), the dependency of $M(A, Z)$ on the nuclear charge Z results in a parabola, assuming a fixed mass A . Moreover, for *even-even* and *odd-odd* nuclei, there is a separation of the mass parabolas due to the pairing term (see Tab. 1.2). As a fundamental principle of nature, atomic nuclei undergo radioactive decays in order to reach the state of maximum binding energy, which is found near the minimum of the respective mass parabola.

In principle, all nuclei that gain binding energy in the process can undergo $\beta\beta$ -transitions. However, if the same nuclide could decay by single β -decay, the branching ratio of the corresponding double beta transitions would be too difficult to be observed due to the overwhelming background rate from the more frequent single decay mode. As a matter of fact, experimentally observable $\beta\beta$ -transitions need to coincide with a transition to the minimum along the even-even parabola, whereas the intermediate transition involving the odd-odd parabola needs to be strongly suppressed. This situation is illustrated in Fig. 3.3 for the case of $A = 116$ involving the $\beta^- \beta^-$ transition of ^{116}Cd , which is one of the main $\beta\beta$ -nuclides of interest for the COBRA experiment (see chapter 4). It is worthwhile to point out that, since $\beta\beta$ -candidates are even-even nuclei, it follows immediately that their angular momentum is always zero, thus, their ground-state can be expressed as $J^\pi = 0^+$.

In total, 69 of all known nuclides in nature are expected to provide a kind of $\beta\beta$ -decay signature (see Ref. [Bar19a] for a complete review). Regarding the decay modes with electrons in the final state, 35 nuclides have been identified, whereas the $2\nu\beta^- \beta^-$ decay has been

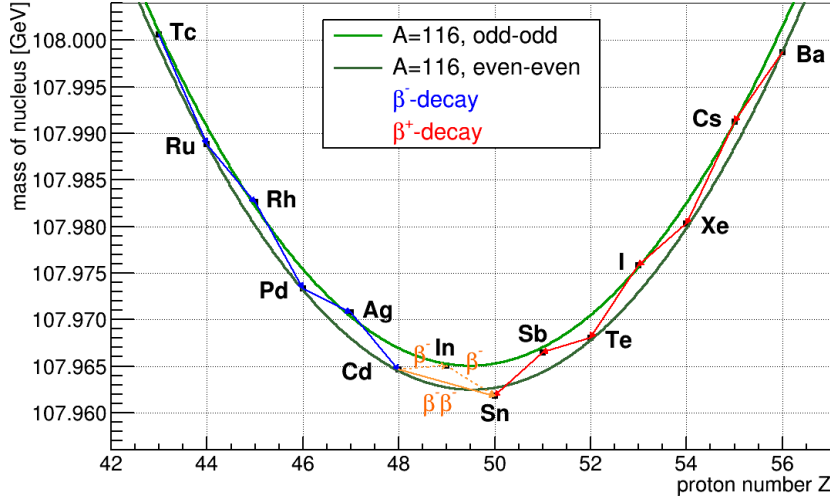


Figure 3.3: Illustration of the mass parabolas according to the Bethe-Weizsäcker mass formula for atomic nuclei with $A = 116$ (taken from [Zat14]). The upper parabola corresponds to nuclei with an odd number of protons and neutrons and the lower, respectively, to the cases of even numbers. As the parabolas are calculated with the semi-empirical formula given in Eqn. (1.19) and the parameters listed in Tab. 1.2, while the actual masses of the atomic nuclei are taken from [AME17], some small discrepancies occur in the plot. All nuclei undergo radioactive decays to reach the minimum of the parabolas, whereas β -decay transitions result in an alternating change between them. As a single β -decay is energetically forbidden for ^{116}Cd , it can only convert to the minimum state corresponding to ^{116}Sn via a $\beta^- \beta^-$ transition.

confirmed in only nine nuclides with a direct counting approach: ^{48}Ca , ^{76}Ge , ^{82}Se , ^{96}Zr , ^{100}Mo , ^{116}Cd , ^{130}Te , ^{136}Xe and ^{150}Nd . Additionally, there have been indirect observations of this decay mode in ^{128}Te and ^{238}U using geochemical and radiochemical methods.

The remaining 34 out of 69 $\beta\beta$ -candidates are expected to undergo $\beta^+ \beta^+$, $\beta^+ \text{EC}$ or ECEC transitions, whereas only the $2\nu\text{ECEC}$ has been observed experimentally in three nuclides. This involves one geochemical measurement for ^{130}Ba and two direct measurements for ^{78}Kr and ^{124}Xe , respectively. The latter finding was only published very recently by the XENON1T collaboration [XEN19b] using a dual-phase liquid xenon TPC, while the actual research field of this experiment is the search for dark matter interactions.

3.2.2 Schechter-Valle theorem

In 1982, J. Schechter and J. Valle postulated what is today known as the *black box* or *Schechter-Valle theorem* [SV82]. It states, essentially, that the observation of $0\nu\beta\beta$ -decay confirms the Majorana nature of neutrinos, while generating Majorana neutrino masses radiatively at the four-loop level. However, the corresponding *black box operator* could also result from other lepton number violating *new physics*, which are not directly connected to neutrino masses. Moreover, although the black box operator guarantees finite Majorana neutrino masses, a quantitatively evaluation of the theorem revealed that the smallness of its contribution implies that additional neutrino mass terms (Dirac or Majorana) must exist [DLM11]. If other beyond SM processes would dominate the $0\nu\beta\beta$ -decay, neutrinos might also be predominantly Dirac fermions, while the principal statement of the Schechter-Valle theorem would still remain valid.

An illustration of the black box operator that contributes to the Majorana neutrino mass is depicted in the Feynman diagram in Fig. 3.4. At its core, the process of neutrinoless double beta decay can be treated as a $\bar{\nu}_e$ -to- ν_e transition that involves two $u\bar{d}$ pairs and two electrons, independently of the underlying mechanism that triggers the decay. This statement holds

under the assumption that the weak interaction can be described by a local gauge theory (see section 1.1.2) and the validity of the imposed *crossing symmetries* [DLM11]. Further information can be found in the original article [SV82] and following works such as [Tak84] and [DLM11] or the review on $0\nu\beta\beta$ -decay published in [DMVV16].

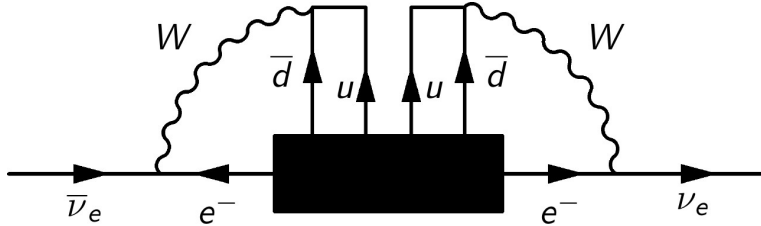


Figure 3.4: Illustration of the Schechter-Valle theorem in form of a *black box* Feynman diagram (see [SV82] and [DLM11]). The corresponding black box operator arises from some underlying *new physics* that violates lepton number conservation and induces a generic $\bar{\nu}_e$ -to- ν_e transition.

3.2.3 Half-life prediction

By assuming the exchange of light Majorana neutrinos as the dominant mechanism triggering the process of $0\nu\beta\beta$ -decay, the inverse half-life can be predicted via

$$\left(T_{1/2}^{0\nu}\right)^{-1} = (g_A)^4 \cdot \mathcal{G}^{0\nu}(Q_{\beta\beta}, Z) \cdot |\mathcal{M}^{0\nu}(A, Z)|^2 \cdot \left|\frac{m_{\beta\beta}}{m_e}\right|^2. \quad (3.6)$$

This factorization involves the weak axial-vector coupling g_A , the kinematic phase-space factor $\mathcal{G}^{0\nu}(Q_{\beta\beta}, Z)$, the nuclear matrix element $\mathcal{M}^{0\nu}(A, Z)$ as well as the effective Majorana neutrino mass $m_{\beta\beta}$ as defined in Eqn. (2.34). While $\mathcal{G}^{0\nu}(Q_{\beta\beta}, Z)$ is given in units of yr^{-1} , $\mathcal{M}^{0\nu}(A, Z)$ is a dimensionless quantity on the order of 1–10. The last term is usually scaled by the electron mass m_e to express the *new physics* parameter in a dimensionless way as well. For alternative $0\nu\beta\beta$ -decay mechanisms, the term would be replaced by a generic dimensionless function $f(m_i, U_{ei})$ containing the particle physics beyond the SM, while depending on the neutrino masses m_i and the mixing matrix elements U_{ei} (see e.g. Ref. [DMVV16]).

A similar factorization into an atomic and a nuclear part can be done to predict the inverse half-life for $2\nu\beta\beta$ -decays resulting in

$$\left(T_{1/2}^{2\nu}\right)^{-1} = (g_A)^4 \cdot \mathcal{G}^{2\nu}(Q_{\beta\beta}, Z) \cdot |\mathcal{M}^{2\nu}(A, Z)|^2, \quad (3.7)$$

whereas the term indicating new physics remains left out. It should be noted that the phase-space factors and nuclear matrix elements in Eqn. (3.6) and Eqn. (3.7) are numerically different, but rely usually on similar model assumptions.

Nowadays, there is a scientific discussion regarding quenching effects that lead to significantly smaller values of g_A in low-momentum exchange nuclear processes, involving single and double beta transitions, compared to free nucleon interactions (see section 8.3). Because of the strong g_A dependency in Eqn. (3.6), already a small change of g_A by about 20% would result in a deviation of more than a factor of two with respect to the corresponding half-life. As large-scale experiments aim to reach a certain half-life sensitivity in order to probe the corresponding neutrino mass range (see e.g. Fig. 2.2), the potential quenching of g_A needs to be addressed both theoretically and experimentally. More on this subject will be discussed in section 3.2.5. Before getting to this, some details about the atomic and nuclear physics input parameters will be discussed in the following.

Phase-space factors

The first calculations of phase-space factors (PSFs) were performed in the late 1950s using simplified expressions of the involved leptonic wave functions and potentials. Since then, more accurate descriptions and numerical evaluation methods became available which made it possible to calculate PSFs very accurately for both single and double beta decays. A detailed review can be found in Ref. [SM19].

The key ingredients of the evaluation of the PSFs are the lepton wave functions and the modeling of the nuclear potential. This is why $\mathcal{G}(Q_{\beta\beta}, Z)$ depends on the Q -value of the transition, predetermining the kinematics of the involved leptons and the decay rate, as well as on the nuclear charge Z . The dependence of the decay rate on the Q -value is different for the neutrino accompanied and the neutrinoless decay mode and can be expressed as

$$\mathcal{G}^{2\nu}(Q_{\beta\beta}, Z) \sim Q_{\beta\beta}^{7..11}, \quad \mathcal{G}^{0\nu}(Q_{\beta\beta}, Z) \sim Q_{\beta\beta}^5 \quad [\text{SM19}]. \quad (3.8)$$

Recent PSF calculations for $\beta\beta$ -transitions can be found in Ref. [KI12] and [SM13], with an update in [MPS14]. The results obtained in these references are quite similar, although the numerical methods are not exactly the same. However, this can be seen as a good consensus. In contrast to previous approaches, the present calculations include relativistic corrections for the Dirac wave functions and account for the finite size of the nucleus (modification of $r \approx r_0 \cdot A^{1/3}$, see section 1.2.1), as well as the effect of the atomic screening regarding the emitted charged leptons and a realistic model of the Coulomb potential of the nucleus.

Nuclear matrix elements

As mentioned before, the nuclear matrix elements (NMEs) refer to the nuclear structure of the involved initial and final states as well as the dynamic of the transition. Compared to the PSFs, an analytic evaluation is not as straight forward due to the complex, usually not well-known structure of open-shell nuclei. Although the initial state is always an even-even nuclei with $J^\pi = 0^+$ (see section 3.2.1), the combinations of intermediate, ground and excited states of the daughter nuclei are rather unique for each transition. While this makes the calculation of the corresponding NMEs a difficult task, the challenge is faced by using different approaches, whereas especially in the last few years, the reliability of the calculations improved a lot (see e.g. Ref. [DMVV16]). An impression of the NME results for different theory frameworks is shown in Fig. 3.5. In section 3.2.4, a brief overview of the respective nuclear models will be presented.

One particular difference in the description of the $2\nu\beta\beta$ -decay and its neutrinoless counterpart is related to the particle physics contribution in the latter case. Because of the required short-range interplay between the two simultaneously decaying nucleons on the femtometer scale, assuming the exchange of e.g. a Majorana neutrino (see Fig. 3.1), the momentum transfer in $0\nu\beta\beta$ -decay turns out to be on the order of ~ 100 MeV. This energy scale results from a simple numerical estimate based on the *Heisenberg uncertainty principle* of quantum mechanics. This is why all intermediate and final states up to this energy scale have to be considered in the calculation of the respective NMEs. Moreover, the actual matrix element $\mathcal{M}^{0\nu}(A, Z)$ is a combination of Gamow-Teller (GT) contributions (spin-spin interactions), Fermi contributions (spin independent interaction) and a tensor operator matrix element, while in case of the $2\nu\beta\beta$ -decay only transitions of GT type up to $Q_{\beta\beta}$ have to be considered (see also the classification of β -decays in section 1.2.3).

A convenient parametrization of the NME related to the $0\nu\beta\beta$ -decay (see e.g. [SM19]) is

$$\mathcal{M}^{0\nu} = \mathcal{M}_{\text{GT}}^{0\nu} - \left(\frac{g_V}{g_A} \right)^2 \cdot \mathcal{M}_{\text{F}}^{0\nu} - \mathcal{M}_{\text{T}}^{0\nu}, \quad (3.9)$$

where g_V and g_A are the vector and axial-vector couplings. The form of Eqn. (3.9) emphasizes the role of g_A and reveals that the matrix element $\mathcal{M}^{0\nu}$ itself depends on the ratio of g_V and g_A . However, if the same quenching for g_V and g_A would be assumed, the dependency vanishes. An overview of this subject is presented in section 3.2.5.

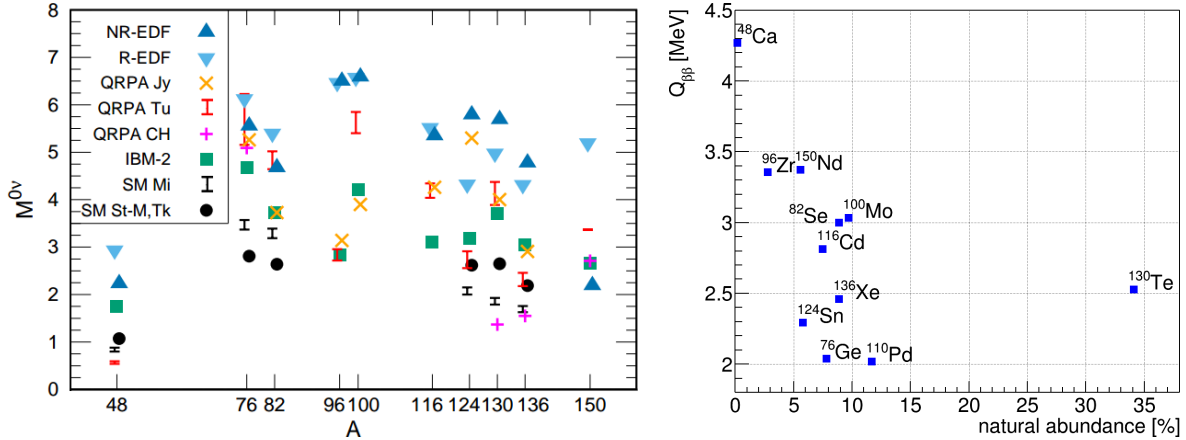


Figure 3.5: Comparison of nuclear matrix elements, Q -values and natural isotopic abundance for the most promising $0\nu\beta\beta$ -decay candidates. *Left:* NMEs as calculated in different theory frameworks (adapted from [EM17]). The spread of the NMEs for the same atomic mass and different nuclear models is an indication for the uncertainty arising from the modeling of the nuclear structure effects. All results are obtained by assuming that g_A is unquenched, highlighting the plain spread of the NMEs. An overview of the respective nuclear models is given in section 3.2.4. *Right:* $Q_{\beta\beta}$ versus natural abundance (values taken from [AME17] and [IUP16]). Both a large Q -value and isotopic abundance are beneficial with respect to the experimental half-life sensitivity as discussed in section 3.3. Because there is no clearly superior nuclide, a large variety of different experimental techniques is applied in the search for $0\nu\beta\beta$ -decay.

By comparing the NME results of different nuclear model frameworks for the most promising $\beta\beta$ -candidates (see Fig. 3.5), no clearly superior nuclide can be identified. The same applies, essentially, to the other characteristics such as the Q -value and the natural abundance of the isotope of interest. From an experimental point of view, nuclides with $Q_{\beta\beta} > 2.0$ MeV provide an advanced signal-to-background ratio, while benefiting from the large phase-space. Moreover, the isotopic abundance affects the experimental sensitivity in a linear way, which will be further elaborated in section 3.3.

The list of the most promising $\beta\beta$ -candidates coincides largely with those nuclides for which the $2\nu\beta\beta$ -decay has already been confirmed experimentally (see section 3.2.1). However, this is only due to the applied selection of nuclides with large Q -values, resulting in comparably low $T_{1/2}^{2\nu}$ half-lives. In order to gain deeper insights into the relevant nuclear physics, the investigation of multiple double beta decay processes, especially for isotopes of the same element, are requested from the theory community. Those measurements could help to resolve discrepancies between the models and to improve the theory frameworks. This is why the search for $2\nu\beta\beta$ -decays via excited state transitions gained more attention in the last few years. An overview is presented in the course of section 8.6. Moreover, the pending question of g_A quenching needs to be addressed experimentally. One way, as will be pointed out in section 3.2.5, is to investigate strongly forbidden β -decays. This subject is one of the main topics of the present thesis and discussed in section 8.3 of the analysis section.

Apart from treating the PSFs and NMEs separately, there are also first attempts to determine them in combination using a general framework such as discussed in Ref. [Sto19].

3.2.4 Overview of nuclear models

The following brief overview of the main theoretical models for the description of double beta decay processes is based on the review articles [DMVV16] and [EM17]. For each of the nuclear models, only some of the relevant features will be addressed, while further information can be found in the highlighted references.

Interacting shell model

The interacting shell model (ISM) (also simply referred to as *nuclear shell model*) is a well-established many-body method in the description of $\beta\beta$ -decays (see e.g. [CMPN⁺05] and [MPCN09]). Moreover, the ISM is applied successfully in a broad range of nuclear physics applications. It is based on the idea that the nucleons near the Fermi level dominate the low-energy nuclear properties, while all correlations between these nucleons are considered important. This motivates that instead of solving the Schrödinger equation for the full nuclear interaction in the complete many-body Hilbert space, it is possible to restrict the dynamics to a limited so-called *configuration space* (also denoted as *valence space*). This configuration space comprises usually only a relatively small number of *active nucleons* outside a core of nucleons that are frozen in the lowest-energy orbitals. Furthermore, the active nucleons can occupy only a limited set of single-particle levels around the Fermi surface, which are referred to as *orbitals* or *shells*. Referring to the resulting NMEs as shown in Fig. 3.5, the ISM results (labeled as SM) are usually smaller than the other nuclear model predictions.

Quasiparticle random phase approximation

The second major theoretical framework that has been developed over the last 30 years is referred to as the quasiparticle random phase approximation (QRPA) (see [ŠRFV13] and [HS15]). It is a generalization of the ordinary random phase approximation and has several variants (see Fig. 3.5). In contrast to the ISM, the QRPA uses a large valence space without an inert core, but at the price of a restricted set of correlations. Moreover, it takes into account proton-proton and neutron-neutron pairing similar to the BCS theory of superconductivity in solid state physics [BCS57]. The original nucleon-nucleon interaction is typically modeled as a realistic potential, which is then adapted to the QRPA configuration space through many-body perturbation theory. However, the interaction is modified more severely than in the ISM, which results in several variations of this model depending on the applied renormalization procedure. With respect to the $0\nu\beta\beta$ -decay NMEs, the QRPA results are almost uniformly larger than the ISM values, whether or not a renormalized QRPA calculation is used.

Interacting boson model

In the interacting boson model (IBM) [BKI15], the low-lying states of the nucleus are modeled in terms of bosons. The bosons interact through one- and two-body forces giving rise to bosonic wave functions. The IBM aims to share the strength of the ISM, being able to include all correlations around the Fermi surface, while describing electromagnetic transitions up to heavy nuclei. It leverages the algebra of boson creation and annihilation operators to provide simple Hamiltonians that provide a more phenomenological approach to the description of the nuclear structure and more abstract degrees of freedom than nucleons. In this way, the bosons represent on the one hand nucleon pairs and on the other quadrupole phonons. The NMEs produced by the IBM are close to the QRPA values for several isotopes and are generally larger than the ISM results (see Fig. 3.5).

Projected Hartree-Fock Bogoliubov method

The projected Hartree-Fock Bogoliubov (PHFB) method [RCC⁺13] makes use of projected wave functions in a valence space of between one and two shells. Those PHFB wave functions are eigenvectors of four different parametrizations of a Hamilton involving a schematic pairing and multipolar effective two-body interactions. The resulting $0\nu\beta\beta$ -decay NMEs are usually larger than the results obtained by the ISM.

Energy density functional method

The energy density functional (EDF) method [RMP10] is considered to be an improvement with respect to the PHFB approach. Essentially, it refers to the process of minimizing an energy functional with respect to local densities such as the number density, the spin density or the current density. The functional represents the minimum possible value for the expectation value of the Hamiltonian under certain constraints placed on the local densities. Once the functional is found, its minimization with respect to its arguments provides the exact ground-state energy level and density values. This minimization can be expressed in a way that is similar to a mean-field theory with only one-body potentials and orbitals. However, compared to the well-established ISM and QRPA approaches, the applications of the EDF method in the context of $0\nu\beta\beta$ -decay have been relatively few. The resulting NMEs are generally larger than the ISM results and usually also larger than the QRPA values.

3.2.5 Quenching of g_A in nuclear β -decay

The potential quenching of the weak axial-vector coupling strength g_A in nuclei is of general interest, e.g. in nuclear astrophysics, the understanding of rare single β -decays as well as the search for $\beta\beta$ -decays. The predicted rate for the $0\nu\beta\beta$ -decay, in particular in the case of light Majorana neutrino exchange, depends strongly on the numerical value of g_A through the leading Gamow-Teller part of the $\mathcal{M}^{0\nu}$ matrix element (see section 3.2.3). This statement applies as well to the case of $2\nu\beta\beta$ -decays and GT-dominated single β -decays. A wide set of nuclear theory frameworks has been adopted to calculate the corresponding NMEs as discussed in the previous section (see in particular the review articles [EM17] and [ESZ19]), but the associated quenching of g_A is usually not addressed quantitatively.

However, it is somewhat disconcerting to find that the predicted half-lives for these processes are almost always shorter than determined experimentally. As the PSFs can nowadays be calculated very precisely (see section 3.2.3), the mismatch is found to be caused by the treatment of the NMEs. Moreover, the PSFs are quantities which do not depend on g_A , while the NMEs feature a direct dependency through the g_V/g_A ratio of the GT part (see e.g. [SM19]). In fact, the single- β Gamow-Teller and $2\nu\beta\beta$ -decay matrix elements are routinely found to be too large to reproduce the experimental half-life results. This issue is usually “cured” by reducing the strength of the spin-isospin GT transition operator artificially. One of the common approaches is to introduce an effective value of g_A that multiplies this operator in place of the free value of $g_A^{\text{free}} = 1.276(4)$ [UCN10]. This phenomenological modification is usually referred to as the *quenching* or *renormalization* of the axial-vector coupling g_A . Recently, systematic studies of the g_A quenching were addressed in low-momentum exchange processes such as single β - and $2\nu\beta\beta$ -decays (see e.g. [Suh17]).

However, as the $0\nu\beta\beta$ -decay is a high-momentum exchange process involving states up to ~ 100 MeV, it is not clear how the results obtained for the quenching of g_A in the low-momentum exchange processes can be translated to this case. This is why it is important to study the quenching of g_A in as many ways as possible, even in low-energy processes,

like single β -decays. The quenching of g_A at low energies has several different sources: non-nucleonic degrees of freedom (e.g. delta resonances) and giant multipole resonances (like the GT giant resonance) removing transition strength from low excitation energies. Further sources of quenching (or sometimes also enhancement, see Ref. [KS18]) are nuclear processes beyond the impulse approximation (in-medium meson-exchange or two-body weak currents) and deficiencies in the handling of the nuclear many-body problem (too small single-particle valence spaces, lacking many-body configurations, omission of three-body nucleon-nucleon interactions, etc.). Different methods have been introduced to quantify the quenching effect in decay processes of low momentum exchange (see the review in [Suh17]).

One method recently proposed exploits the dependence of the β -spectrum shape of highly-forbidden non-unique decays on g_A . The experimental verification of g_A quenching in the context of strongly forbidden β -decays is one of the main topics of the present thesis and is extensively discussed in section 8.3 of the analysis part.

3.3 Experimental aspects

This section is dedicated to the experimental aspects of the search for double beta decay transitions. The first part introduces the half-life sensitivity of an experiment and its dependency on characteristic parameters. Following this, a brief overview of the most promising experimental techniques is given in section 3.3.2. In the end, recent results obtained by the world-leading $0\nu\beta\beta$ -decay experiments will be summarized in section 3.3.3.

3.3.1 Sensitivity approximation

One of the central quantities in the search for rare nuclear decays is the achievable half-life sensitivity of the corresponding experiment. Depending on the statistical interpretation and scientific questioning, the term *sensitivity* refers either to the discovery potential or the median ability to put a limit on the sought decay mode in case of the absence of a statistically significant signal at a certain confidence level.

In general, the experimental half-life sensitivity scales with the exposure gained by an experiment, which is usually quoted as the product of the sensitive detector mass M and the live-time t in units of kg yr or similar units. For the case of a quasi background-free experiment, the scaling of the sensitivity with the accumulated exposure would be linear. However, $0\nu\beta\beta$ -decay experiments are often dominated by the presence of background in the region of interest (ROI) around $Q_{\beta\beta}$, which is why the sensitivity only scales with the square root of the exposure to take into account the Poisson variation of the background counts. The background B is usually quoted in form of the so-called background index (BI) in units of cts/(kg keV yr) or similar. Furthermore, the width ΔE of the ROI enters the sensitivity, whereas it is usually associated with the energy resolution in terms of FWHM at $Q_{\beta\beta}$. Finally, the number of available source nuclei N per kg, the abundance of the $\beta\beta$ -nuclide of interest, as well as the total efficiency ε to detect the $0\nu\beta\beta$ -decay as a full-energy event in the experiment need to be considered. This leads to an analytic expression of the following form

$$\tilde{T}_{1/2}^{0\nu} \leq \frac{\ln 2}{k_\alpha} \cdot a \cdot \varepsilon \cdot N \cdot \sqrt{\frac{M \cdot t}{\Delta E \cdot B}}. \quad (3.10)$$

The first term in Eqn. (3.10) results from the statistical interpretation of the sensitivity approximation and contains the coverage factor k_α . This factor refers to the statistical significance that is involved in the limit setting procedure, respectively, of the presumed discovery

potential. More information on the statistical aspects of Eqn. (3.10) and a derivation of the parameter k_α can be found in section C.2 of the appendix.

In order to reach the required half-life sensitivity to explore the Majorana neutrino mass scale close to the top of the inverted mass ordering (see Fig. 2.2), a typical background rate of less than 10^{-3} cts/(kg keV yr) is required, while maintaining a high efficiency and energy resolution. The energy resolution is also of key importance to minimize the irreducible background of the $2\nu\beta\beta$ -decay with respect to the $0\nu\beta\beta$ -peak region (see e.g. Fig. 3.2).

3.3.2 Experimental techniques

During the past 30 years, several promising experimental techniques were developed in order to address the requirements to search for the existence of $0\nu\beta\beta$ -decay with ever increasing detector masses and sensitivities. An overview of the recently applied techniques is given in Tab. 3.1, highlighting the characteristic advantages as well as the typically faced challenges of the most promising experimental approaches. Those characteristics are evaluated with respect to the parameters that enter the approximation formula of the half-life sensitivity given in Eqn. (3.10) of the previous section.

Table 3.1: Overview of recently applied experimental techniques and their associated advantages (+) and challenges (–) regarding the search for the hypothesized $0\nu\beta\beta$ -decay in different nuclides. The characteristics are evaluated with respect to the parameters entering the half-life sensitivity according to Eqn. (3.10).

exp. technique	advantages and challenges	experiment (nuclide)
calorimeters		
solid state	+ excellent resolution (ΔE) + high efficiency (ε) + pulse-shape discrimination (B) – operation at cryogenic temp.	GERDA/LEGEND (^{76}Ge) MAJORANA (^{76}Ge)
bolometer	+ excellent resolution (ΔE) + high efficiency (ε) – operation at cryogenic temp. – surface contaminations (B)	CUORE (^{130}Te)
scintillator	+ high efficiency (ε) + scalability (M) – low resolution (ΔE) – known contaminations (B)	SNO+ (^{130}Te) KamLAND-Zen (^{136}Xe) CANDLES-III (^{48}Ca)
tracking detectors		
tracking-calorimeter	+ excellent background suppression (B) + topological measurements – scalability (M)	NEMO-3/SuperNEMO (several nuclides)
liquid xenon TPC	+ good resolution (ΔE) + high efficiency (ε) + scalability (M) – operation at cryogenic temp. – known contaminations (B)	EXO-200/nEXO (^{136}Xe)

The variety of the applied techniques is partly motivated by the fact that, from several points of view, there is no superior candidate nuclide for the search for the $0\nu\beta\beta$ -decay (see

e.g. section 3.2.3). Most importantly, the magnitude of the expected decay rate is predetermined by the Q -value, rather independently from the actual nuclear physics incorporated by the NMEs (see Fig. 3.5). While ^{48}Ca offers by far the highest Q -value with $Q_{\beta\beta} = 4.3 \text{ MeV}$ [AME17], its natural isotopic abundance is far below one percent. On the contrary, ^{130}Te features a rather high abundance of more than 30% while providing a Q -value of $Q_{\beta\beta} = 2.5 \text{ MeV}$. All the other previously highlighted $\beta\beta$ -candidates with $Q_{\beta\beta} > 2.0 \text{ MeV}$ feature typically a natural abundance of about 5 – 12%. This is why large-scale experiments usually enrich their target material in the nuclide of interest in order to boost the half-life sensitivity according to Eqn. (3.10) proportional to the enrichment factor. Under those considerations, experimental aspects such as the energy resolution, known contaminants as well as the total detection efficiency have to be taken into account.

Based on the fundamental detection technique, $0\nu\beta\beta$ -decay experiments can be classified into calorimetric detector systems, measuring the deposited energy of the charged leptons via e.g. ionization or scintillation light, and tracking detectors, which are able to resolve the two charged leptons spatially. Usually, such a spatial discrimination is not possible in the case of classical calorimeters as they are only sensitive to the total deposited energy. On the other hand, the tracking detector approach infers the energy of the charged leptons from the reconstructed path length and orientation, which usually comes at the cost of a worsened energy resolution compared to e.g. solid state calorimeters. Furthermore, classical tracking detectors apply thin source foils, that are usually enriched in the $\beta\beta$ -nuclide of interest, in between sensitive detector elements. This approach, however, results in a rather poor full-energy detection efficiency on the level of only a few percent.

Calorimetric detector systems, on the contrary, usually apply the *detector equals source* principle, which ensures a high intrinsic detection efficiency (50 – 90%) depending on the detector size. Such calorimeters can be divided into solid state detectors, bolometers and scintillators. Among those, high-purity germanium detectors and bolometers achieve the best energy resolution, while they have to be operated at cryogenic temperatures. This requirement comes with the need for a complex cryogenic infrastructure made of potentially weakly radioactive materials, affecting the achievable background index. However, dedicated techniques have been developed by most of those experiments to discriminate background-like and signal-like events with the help of pulse-shape discrimination (see chapter 7).

Experiments based on liquid scintillators or scintillating crystals feature also a high intrinsic efficiency but achieve usually a worse energy resolution. Especially in the case of liquid scintillators, the scaling of an experiment towards higher masses is rather easy and cost efficient. On the other hand, a large homogeneous volume potentially worsens the granularity, which is in general a very efficient way to suppress coincident events, which are typically induced by external and internal backgrounds.

An excellent background suppression is achieved by tracking calorimeters and liquid noble gas time projection chambers (TPCs). In the latter case, scintillation light is used as a prompt signal, while the charge signal through ionization provides a second, delayed signal. For both tracking approaches, it is possible to perform topological measurements providing a deeper insight into the decay mechanism of double beta transitions. Additional hybrid detector designs that use more than one signal channel (e.g. scintillation light + charge or scintillation light + heat) are currently under development.

The presently running or soon to be finished experiments include GERDA [GER18a] and the MAJORANA demonstrator [MAJ16] (^{76}Ge), NEMO-3 [NEM04, NEM10, NEM15, NEM17a] (^{82}Se , ^{96}Zr , ^{100}Mo , ^{116}Cd), CUORE [CUO19b] (^{130}Te), EXO-200 [EXO18a] and KamLAND-Zen [Kam16c] (^{136}Xe). Future experiments aiming to probe the full range of the inverted neutrino mass ordering or to establish novel techniques are LEGEND [LEG17] (^{76}Ge), SuperNEMO [Sup10], AMoRE [AMo19] and LUMINEU [LUM16] (^{100}Mo), MOON

[MOO10] (^{82}Se , ^{100}Mo), Aurora [Aur18] (^{116}Cd), SNO+ [SNO15] and CUPID [CUP17] (^{130}Te), NEXT-100 [NEX16] as well as nEXO [nEX18] and PandaX-III [Pan17] (^{136}Xe).

The present thesis is related to the COBRA experiment [COB16b] aiming to search for the $0\nu\beta\beta$ -decay in ^{116}Cd and ^{130}Te . The detector concept of COBRA and its experimental infrastructure will be introduced in chapter 4. Before getting to this, an overview of recent experimental results of the world-leading experiments will be presented in the next section.

3.3.3 Overview of recent results

Although there was the claim of a positive $0\nu\beta\beta$ -decay signal by a subgroup of the former Heidelberg-Moscow (HdM) experiment in 2001 [KKDHK01], this claim was strongly doubted by the physics community and could never be confirmed, not even by a reanalysis of the same data set. Follow-up experiments such as GERDA were able to disprove the claim for the same $\beta\beta$ -nuclide ^{76}Ge and placed strong bounds on the associated $T_{1/2}^{0\nu}$ half-life. Tab. 3.2 contains a compilation of the most recent experimental results of the world-leading experiments GERDA, CUORE, EXO-200 and KamLAND-Zen. For completeness, the present limits for the most promising $\beta\beta$ -nuclides that are accessible with the COBRA experiment are listed as well. A complete review of recent double beta decay results can be found in Ref. [Bar19a] ($2\nu\beta\beta$ -decay) and Ref. [Bar19b] ($0\nu\beta\beta$ -decay).

Table 3.2: Compilation of experimental results of the most recent double beta decay surveys. The list of experiments is ordered according to the atomic mass of the respective $\beta\beta$ -nuclides. The originally quoted statistical and systematic uncertainties were added in quadrature, if quoted separately, and the values in the third and fifth columns were rounded to two digits. The conversion of the lower half-life limit on $T_{1/2}^{0\nu}$ at 90% C.L. into an upper limit on the effective Majorana neutrino mass is done via Eqn. (3.6). The spread of the available NMEs for the respective transitions (see e.g. Fig. 3.5) results in the quoted $m_{\beta\beta}$ mass ranges.

nuclide	experiment	$T_{1/2}^{2\nu}$ [yr]	$T_{1/2}^{0\nu}$ [yr] (90% C.L.)	$m_{\beta\beta}$ [eV] (90% C.L.)	reference
^{76}Ge	GERDA	$(1.93 \pm 0.09) \times 10^{21}$	$> 5.3 \times 10^{25}$	$< 0.15 - 0.33$	[GER15b, GER17]
^{116}Cd	NEMO-3	$(2.74 \pm 0.22) \times 10^{19}$	$> 1.0 \times 10^{23}$	$< 1.40 - 2.50$	[NEM17a]
	Aurora	$(2.63 \pm 0.12) \times 10^{19}$	$> 2.2 \times 10^{23}$	$< 1.00 - 1.70$	[Aur18]
^{130}Te	CUORE	$(7.90 \pm 0.22) \times 10^{20}$	$> 1.5 \times 10^{25}$	$< 0.11 - 0.52$	[CUO19b, CUO18]
^{136}Xe	EXO-200	$(2.17 \pm 0.06) \times 10^{21}$	$> 1.1 \times 10^{25}$	$< 0.19 - 0.45$	[EXO14, EXO18a]
	KamLAND-Zen	$(2.21 \pm 0.07) \times 10^{21}$	$> 1.1 \times 10^{26}$	$< 0.06 - 0.17$	[Kam16c]

Nowadays, there is also a scientific discussion regarding the possibility of a so-called *quadruple beta decay*, which would in its neutrinoless version also be possible for the case of Dirac neutrinos (see e.g. Ref. [HR13]), and other more exotic $\beta\beta$ -decay modes involving positron emission. A first experimental search for the quadruple beta decay was performed by the NEMO-3 collaboration based on the most promising candidate nuclide ^{150}Nd [NEM17b]. However, no signal could be reported for any of the expected decay modes.

This is why, in general, novel detector concepts are needed to overcome the present experimental challenges and to reach half-life sensitivities that allow for the probing of the complete Majorana neutrino mass regime of the inverted ordering in the next generation of $0\nu\beta\beta$ -decay experiments.

Chapter 4

The COBRA experiment

The Cadmium Zinc Telluride 0-Neutrino Double Beta Research Apparatus (COBRA) is a next-generation experiment aiming to search for the existence of the $0\nu\beta\beta$ -decay with CZT semiconductor detectors. In the present demonstrator phase, the detectors are of natural isotopic composition and allow for the investigation of several ultra rare nuclear processes of different isotopes of cadmium, zinc and tellurium. In the first part of this chapter, the detector material and its unique properties as a semiconductor will be discussed. Moreover, the typical challenges with respect to the crystal growth of CZT and the detector fabrication will be addressed. Following this, the most common detector technologies will be presented and evaluated according to their suitability to search for $0\nu\beta\beta$ -decays. Finally, the first part is concluded with a brief review of the Shockley-Ramo theorem and its application towards the signal reconstruction and interpretation.

The second part is dedicated to the various nuclear transitions that are accessible with CZT detectors, involving all kinds of double beta decay transitions as presented in the previous chapter, as well as strongly forbidden single β -decay and EC processes.

Finally, the current status of the COBRA experiment at the Italian underground facility LNGS will be discussed, starting with an overview of the underground infrastructure and its variety of hosted experiments in section 4.3.1. Until very recently, the main stage of the COBRA experiment at the LNGS comprised the so-called COBRA demonstrator array consisting of four layers of 4×4 CZT crystals. This chapter contains a detailed description of the design of the demonstrator setup as well as its data acquisition and electronics. In March 2018, an additional layer of 3×3 prototype CZT detectors was added to the existing infrastructure, marking the start of the so-called eXtended DEMonstrator (XDEM) phase. An overview of the XDEM upgrade and some of the contributions related to the present thesis will be given in section 4.3.4. In the end, the current version of a proposal for a potential large-scale COBRA experiment will be presented, including a projection of the achievable half-life sensitivity for the $0\nu\beta\beta$ -decay of ^{116}Cd as the main $\beta\beta$ -nuclide of interest.

4.1 CZT as semiconductor material

The first section of this chapter introduces the detector material CZT (cadmium zinc telluride, CdZnTe) which is a commercially available room temperature semiconductor and investigated by the COBRA collaboration regarding its application in a future large-scale $0\nu\beta\beta$ -decay experiment. Its unique material properties makes CZT a suitable radiation detector in a wide range of applications such as environmental control, γ -ray spectroscopy, medical imaging, security screening and non-destructive testing procedures [Red20].

However, the crystal growth and detector fabrication are complex processes as will be shortly addressed in the following section. Moreover, the charge carrier's properties are very different for electrons and holes, requiring special readout designs in order to overcome this issue. This subject is closely related to the key aspects of the *Shockley-Ramo theorem* of the charge carrier transport in semiconductors and will be further elaborated in section 4.1.4.

4.1.1 Material properties

As discussed in section 3.3, there are several aspects that directly affect the achievable half-life sensitivity of a $0\nu\beta\beta$ -decay experiment. One of the most promising approaches is the use of solid state devices, especially semiconductor detectors, as they feature an excellent energy resolution and full-energy detection efficiency for intrinsically present $\beta\beta$ -nuclides. In contrast to the extensive cooling infrastructure needed for the operation of e.g. high-purity germanium detectors as used for the GERDA and Majorana experiments, CZT allows for the operation at room temperature, reducing the amount of potentially radioactive construction materials and additional shielding. A comparison of characteristic properties of several conventional semiconductor materials with respect to CZT and CdTe can be found in Tab. 4.1.

Table 4.1: Properties of CZT compared to other well known semiconductor materials (adapted from [Köt12] and [Zat14]). Because of its high nuclear charge of $Z \approx 50$ and density, CZT provides very good prospects as radiation detector. In contrast to Ge and Si, CZT and CdTe feature a very high electric resistivity. In fact, radiation detectors made of the latter two materials are operated as resistors and not in the reversed bias mode as e.g. germanium diodes. Moreover, the typical lifetime of the created charge carriers (electrons, holes) is orders of magnitude lower than compared to the conventional semiconductors. While this effect can be compensated in principle by the applied bias voltage, the difference in the mobility-lifetime product for electrons and holes in CZT requires a more complex readout design as discussed in section 4.1.3.

property	Cd _{0.9} Zn _{0.1} Te	CdTe	Ge	Si
nuclear charge Z	48, 30, 52	48, 52	32	14
density ϱ [g/cm ³]	5.78	5.85	5.33	2.33
band gap E_g [eV]	1.57	1.50	0.67	1.12
pair creation energy E_{pair} [eV]	4.64	4.43	2.95	3.63
resistivity R [Ω cm]	3×10^{10}	10^9	50	$< 10^4$
electron mobility μ_e [cm ² /Vs]	1000	1100	3900	1400
electron lifetime τ_e [s]	3×10^{-6}	3×10^{-6}	$> 10^{-3}$	$> 10^{-3}$
hole mobility μ_h [cm ² /Vs]	50 - 80	100	1900	480
hole lifetime τ_h [s]	10^{-6}	2×10^{-6}	10^{-3}	2×10^{-3}
$(\mu\tau)_e$ [cm ² /V]	$(3 - 10) \times 10^{-3}$	3.3×10^{-3}	> 1	> 1
$(\mu\tau)_h$ [cm ² /V]	5×10^{-5}	2×10^{-4}	> 1	≈ 1

One particular challenge of the manufacturing process of CZT is that the three constituents cadmium, zinc and tellurium need to be provided in a liquid phase close to the

boiling point of cadmium at ~ 1040 K. Moreover, the three phases have to be well mixed in order to prevent defects in the crystallization process. One way to meet those requirements is to apply a high pressure as further discussed in section 4.1.2. However, this makes the crystal fabrication quite challenging. Furthermore, the compound elements cadmium and zinc are of the same period in the periodic table, which is why the actual zinc content in the crystal structure of CZT is hard to monitor. In fact, the II-VI semiconductor material is often referred to as $\text{Cd}_{1-x}\text{Zn}_x\text{Te}$ with $x \approx 0.1$ being the usual stoichiometric factor in the structure formula. Nonetheless, it is a well-known phenomenon that there is a zinc gradient along the direction of the crystal growth, causing a significant variation of x across a crystal boule. A very brief summary of the attempts to characterize the potential zinc gradient experimentally is given in the first part of section 8.5.2.

As discussed in section 1.3.1, the probability of γ -ray interactions depends strongly on the nuclear charge of the target material, which is why CdTe and CZT with $Z \approx 50$ and their high densities are very promising radiation detector materials. Compared to germanium, the band gap of CdTe results in a sufficiently high electric resistivity that allows for the operation as semiconductor at room temperature. The band gap energy E_g can be further increased by inserting a small fraction of zinc into the crystal structure, which also improves the mechanical resistance of the raw crystal material. Nonetheless, it has been shown in past studies that a mild cooling to about 10°C leads to a slightly improved detector performance (see e.g. section 8.3.3 and linked references). The disadvantage of the higher band gap is that an increased amount of energy is needed in order to create an electron-hole pair in a particle interaction, which ultimately affects the achievable energy resolution.

From a particle point of view, ionizing radiation excites electrons from the so-called valence band (VB) into the conductive band (CB), causing a positively charged hole in the former state. In solid state physics, materials can be characterized by the Fermi energy E_F , which describes the energy level up to which the quantum states are filled with electrons at the absolute temperature minimum. In the case of semiconductors, E_F lies in between the VB and the CB. The temperature dependency of the likelihood of a state being filled with an electron of energy E is given by the *Fermi-Dirac distribution* shown in equation (4.1)

$$f(E, T) = \frac{1}{1 + \exp\left(\frac{E - E_F}{k_B T}\right)} \quad (4.1)$$

with k_B as the Boltzmann constant of thermodynamics. This way, the underlying Pauli exclusion principle for fermions is taken into account. An entirely filled VB is inert, which means that it does not conduct any current. On the other hand, if electrons are excited into the higher energetic CB, the formerly fully occupied VB is missing a charge. From another point of view one can interpret this as a completely empty band containing only one positively charged particle moving in the same way as an electron – a so-called *hole*.

The typical concentration of electrons in the CB and holes in the VB turns out to be rather dilute, which motivates the treatment of the charge carriers' drift based on the treatment of a classical, ideal gas in thermodynamics. In this context, the charge carriers are assumed to move rather freely without being subject to the Pauli principle in the CB, while they could be manipulated by an outer electric field. With the help of such a model, it is possible to assign the typical properties such as the mobility, lifetime and mobility-lifetime product to the charge carriers (see Tab. 4.1). By comparing those values for the case of CZT, it is found that they differ between electrons and holes by several orders of magnitude. Consequently, holes would be trapped within a very short drift path of far less than 1 mm, independently of the applied bias voltage. Because of this, the expected signal height will depend on the distance between the primary particle's interaction and the electrode collecting the amount

of produced charges. This is why a special signal readout is required to compensate the effect as discussed in section 4.1.3. It is noteworthy to mention that some of those characteristics, such as the electron mobility-lifetime product, can be determined via calibration data in laboratory experiments such as discussed in detail in [Zat14].

For the application of the half-life sensitivity approximation formula given in Eqn. (3.10), the weighted molar mass of CZT based on the known stoichiometry of the crystal structure is needed. The resulting values can be found in Tab. 4.2.

Table 4.2: Molar masses of CZT compound elements and their respective stoichiometry factor s in the II-VI crystal structure. The mass values are based on the isotopic composition of the elements according to [IUP16] and the atomic masses reported in [AME17]. The uncertainty on the last digit is shown in parentheses.

element	s	atomic mass [g/mol]
Cd	0.9	112.414(4)
Zn	0.1	65.38(2)
Te	1.0	127.60(3)
CZT	-	235.31(4)

Regarding the CZT crystal fabrication, there are ever ongoing improvements of various production processes to increase the crystal's quality and size, while continuously raising the fraction of recyclable material in the initial crystal growth process. These developments provide excellent prospects for the construction of a future large-scale experiment based on the results obtained in COBRA's R&D phase (see e.g. section 4.3.5). While an improved crystal quality has a direct impact on the expected half-life sensitivity in terms of energy resolution and full-energy efficiency, which scales with the crystal size, the usage of radiopure base materials minimizes the amount of intrinsic contaminations. Furthermore, the crystal growing involves a form of *self-purification* as only the three compound elements can be grouped into the typical CZT crystal structure. This is why the contaminants are expected to concentrate in the so-called *spent solvent*. The results of a dedicated investigation of the radiopurity of CZT spent solvent material based on a technique referred to as inductively coupled plasma - mass spectrometry (ICP-MS) is presented in Tab. 4.3.

Table 4.3: CZT impurities as reported by Redlen Technologies [Red20] using ICP-MS on material samples from a spent solvent. The unit parts per billion (ppb) refers to a mass fraction of 10^{-9} g per gram sample mass. All contamination levels are below the experimental detection limit of the applied ICP-MS method.

element	concentration in ppb
Pb	< 3.0
Th	< 0.5
U	< 0.5
Pt	< 3.0
Ag	< 6.0
Co	< 2.0
K	< 200

The results confirm the excellent radiopurity of CZT, which is one of the key requirements to construct a low-background experiment with the aim to search for the existence of the $0\nu\beta\beta$ -decay such as COBRA. The unit parts per billion (ppb) refers to a mass fraction of 10^{-9} with respect to a foreign element and the entire sample, meaning that 1 ppb translates

to 10^{-9} g per gram samples mass. Under certain assumptions it is possible to convert the concentration of foreign elements in ppb into a specific activity in units of mBq/kg. This is exemplarily shown in section 8.3.7, where the steps towards a low-energy background model for the COBRA demonstrator are described.

4.1.2 Crystal fabrication and detector technologies

The main difficulties with CZT are related to the complex fabrication process which involves a number of critical steps. The primary step is the growth of defect-free, high-resistivity CZT in form of a boule or ingot. Following steps include typically the slicing and polishing of the device volume, the application of metal contacts (including photolithographic processes), the passivation of the surface in order to limit surface leakage currents, and finally the bonding to external electronics. In the beginning of the COBRA project there was the plan to develop dedicated growth procedures taking into account the experiment's needs such as a high detector yield, especially in the case of isotopic enrichment in future iterations. However, due to the complexity of the process, this undertaking had to be postponed and commercially available crystals with marginally adapted lithography designs were investigated instead. The current aim is to prove the feasibility of the concept in a demonstrator phase.

The crystal growth starts from a melt of the compound elements at about 1000°C. In this phase, a complex mixing reaction of the melted elements takes place which is strongly exothermic. Following this, a number of methods have been successfully employed in the growth of $\text{Cd}_{1-x}\text{Zn}_x\text{Te}$ crystals with quite good control of the zinc-to-cadmium ratio x . Details on the various crystal growing methods can be found in e.g. Ref. [STY⁺01]. Two of the most commonly used procedures will be discussed in the following.

High-pressure Bridgman method

The basic Bridgman method involves the movement of a crucible containing the melt of nearly equal quantities of cadmium and tellurium through a furnace that is designed to provide a suitable temperature profile. There are different approaches to realize a relative movement of the crucible and the either vertically or horizontally orientated furnace (see e.g. Ref. [CCC⁺97]). The horizontal Bridgman technique offers a potential advantage over vertical designs as the crystal growth does not need to overcome the gravitational field along the growth axis. Furthermore, it is also possible that both the furnace and the crucible are stationary, while the temperature profile is altered by a programmable temperature controller. Due to the different vapor pressures of the melt components, with cadmium having the highest, the melt is enriched in tellurium during the crystal growth. The corresponding loss of cadmium can be partly compensated by the advanced high-pressure Bridgman (HPB) method using a melt with a small excess of cadmium (see e.g. Ref. [SCS⁺04]). The excess generates a high vapor pressure which is stabilized with an additional inert gas such as typically argon to maintain a constant overpressure. This way, the loss of volatile components is suppressed. While on the one hand, the HPB procedure requires specialized furnaces that can handle the high pressure, the elevated pressure reduces the loss of cadmium and the risk of crystal defects such as tellurium inclusions. Typically, the CZT crystals grow at a rate of 0.1 – 1.0 mm/h at temperatures on the order of 1100°C. In the post-growth annealing, which helps to resolve crystal defects such as tellurium inclusions, the temperature is kept between 600 – 850°C for about 2 – 3 weeks. In practice, the constituent elements undergo multiple purification steps and are weighed to stoichiometric proportions prior to the melting in the crucibles. Following the growth and annealing phase, the raw crystals are gradually brought to room temperature and ambient pressure.

Traveling heater method

Another approach that has been developed based on the standard Bridgman technique is referred to as the traveling heater method (THM) [CAI⁺08]. Again, the basic principle involves a relative movement between the crucible and the heater, whereas in THM the crucible is stationary. Moreover, chlorine doped crystals are grown from a tellurium solution. The ratio of cadmium to tellurium within the solution determines its melting point. This allows for lower growing temperatures, that are usually adjusted to the range of 650 – 700°C. Although the low growth temperature limits the growth rate to typically a few millimeters per day, it is nowadays the standard method to produce high quality crystals and detectors. One practical issue is also that the failure rate of a furnace is reduced due to the absence of a high overpressure and the reduced growth temperature.

Detector technologies

Over the past 20 years a small number of CZT detector configurations have proven to be of particular interest in nuclear spectroscopy and radiation detection. This includes detector geometries and electrode configurations that function as so-called *electron-only devices* [Luk94], detectors that exploit what has become known as the *small pixel effect* [EBB99], and devices in which the size of the collecting electrode is adjusted for optimal performance for a particular mobility-lifetime product [AL97]. Some generic device configurations as discussed in the review [STY⁺01] are shown schematically in Fig. 4.1.

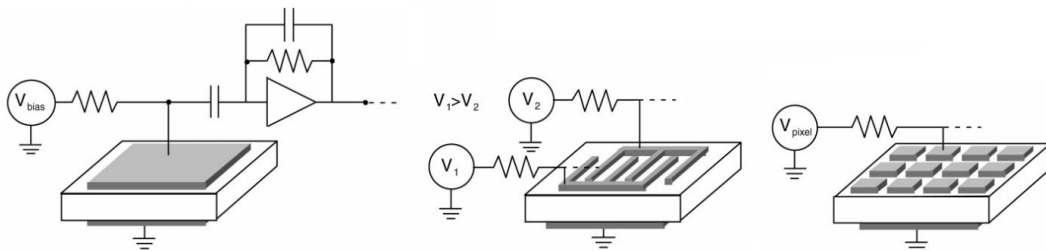


Figure 4.1: Schematic drawing for the three most common CZT detector types (adapted from [STY⁺01]). *Left:* simple planar device. *Middle:* coplanar grid detector (electron-only device). *Right:* pixelated array for imaging applications. Based on the scientific application, different external electronics and lithography masks are used, while the base geometry is typically cuboidal.

In general, each of these CZT detector types is optimized for a specific application. As CZT is a rather fragile and brittle material, the usual base geometry is cuboidal as it involves the least mechanical processing steps while the raw surfaces can be finished via different polishing techniques. The planar detector type is fairly easy to be instrumented and requires only very simple readout electronics to detect e.g. x-rays. More advanced technologies such as the coplanar grid approach offer a better energy resolution while it is also possible to detect γ -rays in the MeV range with high efficiency. Details on this kind of detectors will be discussed in section 4.1.3 as they are the default devices investigated in the course of the COBRA experiment. The typical application of pixelated CZT devices are imaging systems, where the position information is contained in the signals from individual pixels. However, due to the comparably small source mass of such detector systems in combination with the need to place the readout electronics very close to the sensitive volume without the opportunity to apply any shielding in between, pixelated designs are not prioritized for an anticipated large-scale experiment. Nonetheless, some results regarding the application of this technology in $0\nu\beta\beta$ -decay searches can be found in Ref. [GAF⁺15].

In each case, lithographic techniques are employed to define the geometry of the metal electrodes, which are applied to the surface of the semiconductor material. The choice of metal and the control of the deposition method (e.g. sputtering, evaporation, or electroless deposition) can affect the quality of the device. Under operating conditions, a typical bulk voltage on the order of 1000 V/cm is applied to collect the charges created in a particle interaction. The drift of the charges through the detector volume induces a current on the readout electrodes as will be further elaborated in the next sections. This current is typically integrated by external electronics resulting in the total charge which is proportional to the initial energy deposition. By creating a histogram of the pulse-heights recorded in this manner, an energy spectrum can be constructed. Details on COBRA's data acquisition and signal processing will be discussed in section 4.3.3 and 5.1.

4.1.3 Coplanar grid approach

As pointed out in the previous section, CZT detectors require a special readout concept due to the characteristic properties of the charge carriers (see Tab. 4.1). By taking into account the requirements of $0\nu\beta\beta$ -decay experiments, considering the parameters entering the half-life sensitivity according to Eqn. (3.10), the COBRA collaboration identified monolithic crystals as the most promising option. An overview of the detector types investigated by the collaboration is given in section 6.1. In the following, the working principle of the electrode configurations referred to as *simple planar* and *coplanar grid* will be discussed briefly.

In planar detectors, two opposing surfaces act as areal electrodes. Most CZT detectors' electrode metalization consists of a thin layer of platinum in between the CZT surface and a gold layer on the outside. The platinum layer ensures a long-term stability of the metalization and prevents the diffusion of gold atoms into the detector bulk volume. More information on the characterization of those layers based on COBRA data can be found in section 8.5.2. The working principle of planar detectors is demonstrated in Fig. 4.2. An external bias, referred to as bulk voltage (BV), forces a drift of the created charge carriers towards the electrodes. CZT detectors are operated in resistor mode as they provide an electric resistivity on the order of $G\Omega$, in contrast to e.g. conventional HPGe detectors that are usually operated as diodes in the reversed bias mode. The bulk voltage U_{BV} is set to a negative potential on the cathode side, while the anode side is kept at ground potential. This way, electrons (e^-) drift towards the anode side, respectively holes (h^+) to the opposite cathode.

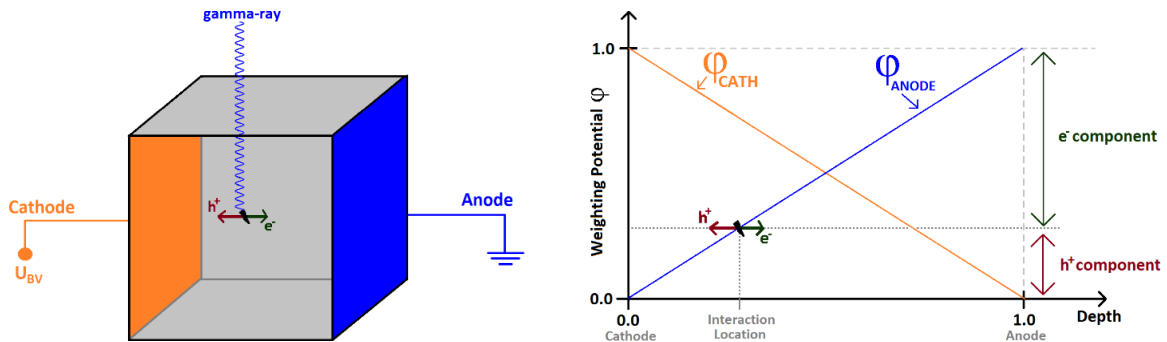


Figure 4.2: Working principle of planar electrode CZT detectors (adapted from [Arl16]). *Left:* schematic drawing of the electrode configuration with a planar cathode at U_{BV} and a grounded planar anode. *Right:* expected relative signal contributions depending on the depth of interaction. As h^+ have a poor mobility in CZT, the depicted signal model is limited to thin detectors where charge trapping can be neglected.

The normalized distance between the anode and cathode surface is referred to as *interaction depth* and is usually orientated along the z -axis with $z = 0$ being the cathode and $z = 1$

the anode surface. The larger the distance between the planar electrodes, the more severe is the effect of charge trapping, especially for the case of holes. If holes get trapped, their signal component is drastically decreased, which introduces a depth dependency of the total signal amplitude. This is why the application of planar CZT detectors is limited to thin devices in practice. The correlation between the charge carrier's drift and the induced current signals will be further elaborated in section 4.1.4 by using the Shockley-Ramo theorem.

In order to overcome the problem of hole trapping, the so-called coplanar grid (CPG) approach was developed by P. Luke [Luk94]. It involves a special anode electrode design consisting of two interleaved, comb-shaped electrodes as depicted in Fig. 4.3. One of those is grounded and acts as the collecting anode (CA) for electrons, while the other is kept at a small negative potential referred to as grid bias (GB). Consequently, the electrode acts as a non-collecting anode (NCA). By using this special configuration, the signal amplitude of the detector relies only on the signal induced by the electrons drifting towards the anode side. During the drift through the detector bulk, they induce the same charge on the CA and NCA. Only in the vicinity of the anode, the electrode at the higher potential is expected to collect the electrons, providing a depth independent information on the initially created amount of charge. A more detailed explanation of the signal formation process in the context of the Shockley-Ramo theorem will be presented in the following section.

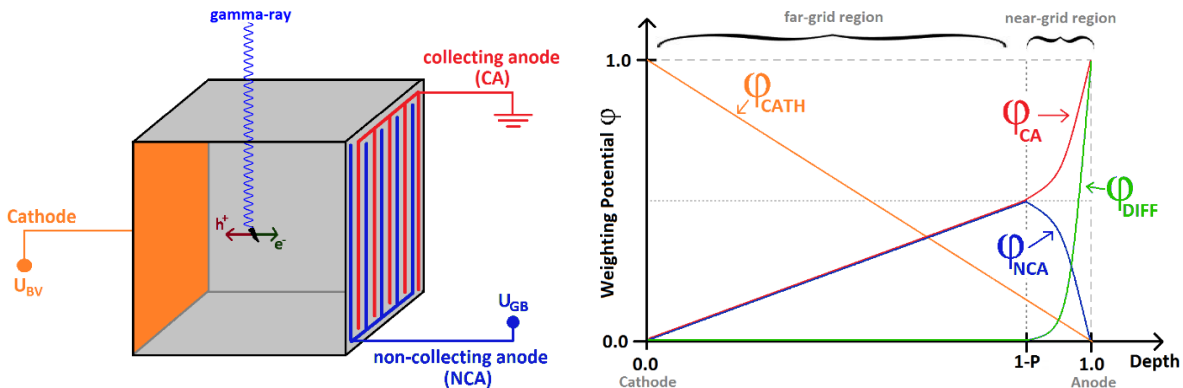


Figure 4.3: Working principle of CPG-CZT detectors (adapted from [Arl16]). *Left:* schematic drawing of the electrode configuration with a planar cathode at U_{BV} , a non-collecting anode at U_{GB} and a grounded collecting anode. *Right:* expected relative signal contributions depending on the depth of interaction. The CPG approach allows to resolve the dependency of the signal strength on the interaction depth by only using the induced signal of the electrons. This way, the difference signal of CA and NCA only depends on the induced current in the near-grid region, while it is flat in the detector bulk.

4.1.4 Shockley-Ramo theorem

The Shockley-Ramo theorem allows for the prediction and explanation of the signal shapes recorded by specific electrode configurations based on classical electrodynamics. While it was firstly formulated by W. Shockley in 1938 [Sho38], it was independently derived and proven shortly afterwards by S. Ramo [Ram39]. A review on the application of the theorem in the context of γ -ray semiconductor detectors can be found in Ref. [He01].

Essentially, it states that the recorded signal on an electrode is the induced charge caused by the drift of charge carriers through the bulk volume in response to an externally applied electric potential. Furthermore, it provides a general concept on how to calculate the induced charge with the help of a so-called *weighting potential* φ_w . Although the weighting potential depends on the electrode configuration, it is only a unitless, mathematical tool rather than

a physical potential. In this sense, it can be interpreted as the normalized potential that represents the charge induced on an electrode caused by the drift of a test charge.

As an example, it can be assumed that a point charge q moves along a velocity vector $\vec{v}(\vec{r})$ inside a generic detector volume that is surrounded by an arbitrary number of electrodes with fixed potentials. According to the Shockley-Ramo theorem, the fact that the charge is moving provides enough information to access the weighting potential, without the need to calculate the electric forces explicitly. In order to assess φ_w , the electric field E_w that appears within the detector for the i -th electrode of interest is set to $\varphi_i = 1$, while all the other n electrodes are kept at ground potential $\varphi_{n \neq i} = 0$. In this way, the induced current on the electrode i caused by the drift of the charge q for each point \vec{r} can be expressed as

$$I_i(\vec{r}) = q \cdot \vec{v}(\vec{r}) \cdot \vec{E}_w(\vec{r}). \quad (4.2)$$

Similarly, the integrated electrode signal s_i , providing a measure of the actual charge q , can be defined by means of an assumed weighting potential φ_w to calculate the net charge building up while q drifts from \vec{r}_1 to \vec{r}_2

$$s_i = q \cdot [\varphi_{w,i}(\vec{r}_2) - \varphi_{w,i}(\vec{r}_1)] \quad (4.3)$$

$$= q \cdot \Delta\varphi_{w,i}. \quad (4.4)$$

The correlation presented in Eqn. (4.4) is the usual compact version of the Shockley-Ramo theorem [He01]. In the following, this form of the theorem will be derived from basic electrodynamics following the procedure outlined in Ref. [Zat14] and [EBB99].

The first step is to calculate the induced charge on the electrode i , whereas all other electrodes are held at ground potential. Because of the presence of the test charge q , a virtual electrostatic potential φ can be defined throughout the detector volume with the constraint that the potential is zero at all electrodes. Furthermore, this potential has to satisfy the Laplace equation in Eqn. (4.5) for the charge-free region between the electrodes.

$$\Delta\varphi = 0, \quad \text{with } \Delta f = \vec{\nabla}^2 f = \sum_{n=1}^3 \frac{\partial^2 f}{\partial x_n^2}. \quad (4.5)$$

Within a small sphere S_q around the test charge q , the potential φ_q is realized. By considering this, the relation between the enclosed charge and the potential can be derived by using Gauss's divergence theorem in two dimensions as shown in Eqn. (4.6).

$$\oint_{S_q} \vec{\nabla}\varphi_q d^2 r = 4\pi \cdot q \quad (4.6)$$

In a second step, the charge q is removed, while the potential of the electrode i is raised to $\varphi_i = 1$. This step indicates the charge collection at this electrode and results in new potentials on the surface of the former sphere, labeled as φ'_q , as well as within the detector of volume V , labeled as φ' . By using Green's theorem, the potentials are connected in the following way

$$\oint_V (\varphi' \Delta\varphi - \varphi \Delta\varphi') d^3 r = - \oint_{S_q} (\varphi' \vec{\nabla}\varphi - \varphi \vec{\nabla}\varphi') d^2 r. \quad (4.7)$$

As both potentials φ and φ' have to fulfill the Laplace equation given in Eqn. (4.5), the left side of Eqn. (4.7) is equal to zero. This leaves only the integration over the right-hand side, which can be separated into the following three parts.

- i) The surface integral over all electrodes except of electrode i . All these terms are zero due to the initial constraints of $\varphi = \varphi' = 0$.
- ii) The surface integral over the electrode i . The boundary conditions given by $\varphi_{n \neq j} = 0$ and $\varphi_i = 1$ result in a non-zero contribution of the surface integral over the sphere S_i surrounding the electrode i according to

$$-\oint_{S_i} \vec{\nabla} \varphi_i d^2 r. \quad (4.8)$$

- iii) The surface integrals over the original sphere S_q around the former test charge q

$$-\varphi'_q \cdot \oint_{S_q} \vec{\nabla} \varphi d^2 r + \varphi_q \cdot \oint_{S_q} \vec{\nabla} \varphi' d^2 r. \quad (4.9)$$

The second term in Eqn. (4.9) turns out to be zero using Gauss's theorem as there is no charge enclosed in this integral. The remaining terms can be evaluated by using Gauss's theorem to reduce the surface integrals according to Eqn. (4.6). This leads to

$$0 = -\oint_{S_i} \vec{\nabla} \varphi_i d^2 r - \varphi'_q \cdot \oint_{S_q} \vec{\nabla} \varphi d^2 r \quad (4.10)$$

$$= 4\pi \cdot Q_i - 4\pi \cdot q \cdot \varphi'_q. \quad (4.11)$$

The first term in Eqn. (4.11) contains the induced charge Q_i on electrode i . Finally, Eqn. (4.11) can be rewritten as $Q_i = q \cdot \varphi'_q$, resulting in the known form of the Shockley-Ramo theorem for a point charge q . For the more general case of a moving charge distribution $\rho(\vec{r})$, the theorem can be expressed as

$$Q_i = \int \rho(\vec{r}) \cdot \varphi_w d^3 r, \quad (4.12)$$

taking into account the respective weighting potential φ_w . The induced current measured on the electrode of interest for the case of the drifting test charge q results from

$$I_i = \frac{dQ_i}{dt} = q \cdot \frac{d\varphi'_q(\vec{r})}{dt} = q \cdot \vec{\nabla} \varphi'_q \cdot \frac{\partial \vec{r}}{\partial t}. \quad (4.13)$$

By defining the *weighting field* E_w corresponding to φ_w as $E_w = \vec{\nabla} \varphi_w$ and the velocity as $\vec{v}(\vec{r}) = \frac{\partial \vec{r}}{\partial t}$, the initial starting point of Eqn. (4.2) can be recovered. For the case that \vec{E}_w and $\vec{v}(\vec{r})$ point into the same direction, the induced current on electrode i can be expressed as

$$I_i = q \cdot v(r) \cdot E_w(r) \quad (4.14)$$

$$= q \cdot \mu \cdot E(r) \cdot E_w(r). \quad (4.15)$$

In the last step, the velocity has been replaced by $v(r) = \mu \cdot E(r)$, introducing the material specific mobility μ of the charge carriers. It is noteworthy to mention that the actual trajectory and velocity of the charge carriers depend on the outer electric field $E(r)$, while the weighting field $E_w(r)$ just depends on the electrode configuration. Moreover, $E_w(r)$ can be seen as the way the charge movement is coupled to the electrodes. This makes it possible to derive the weighting potential φ_w for complex electrode designs, like the previously discussed CPG approach, by using Monte-Carlo methods such as the finite-element technique and commercial software tools like e.g. COMSOL multiphysics (see section 5.1.1 and 5.3.4).

The application of the Shockley-Ramo theorem in the context of COBRA's CPG-CZT event reconstruction will be discussed in section 5.2.

4.2 CZT as source material for rare decays

According to its naturally occurring isotopic composition, CZT contains several particularly interesting isotopes of zinc, cadmium and tellurium that are candidates for rare and exotic nuclear decays. A summary of the nuclides of interest is shown in Tab. 4.4.

Table 4.4: List of nuclides contained in CZT that are known for rare nuclear transitions. The natural abundances are taken from [IUP16] with the respective uncertainties quoted in parentheses. The Q -values are either taken from recent Penning trap mass spectrometer measurements or follow from the mass excess values that are listed in the recent AME database. For the latter case, the uncertainty refers to the combined standard deviations of the involved database entries according to Eqn. (C.3) of the appendix.

isotope	decay mode	nat. abund.	Q -value [keV]
^{64}Zn	$\beta^+\text{EC}$, ECEC	49.17(75)%	1094.9(8) [AME17]
^{70}Zn	$\beta^-\beta^-$	0.61(10)%	997.2(21) [AME17]
^{106}Cd	$\beta^+\beta^+$, $\beta^+\text{EC}$, ECEC	1.245(22)%	2775.01(56) [SBB ⁺ 12]
^{108}Cd	ECEC	0.888(11)%	272.04(55) [SBB ⁺ 12]
^{113}Cd	β^- (4 th -forbidden)	12.227(7)%	323.83(27) [AME17]
^{114}Cd	$\beta^-\beta^-$	28.754(81)%	544.79(28) [AME17]
^{116}Cd	$\beta^-\beta^-$	7.512(54)%	2813.50(13) [REE ⁺ 11]
^{120}Te	$\beta^+\text{EC}$, ECEC	0.09(1)%	1714.81(125) [SCS ⁺ 09]
^{123}Te	EC (2 nd -forbidden)	0.89(3)%	51.91(7) [AME17]
^{128}Te	$\beta^-\beta^-$	31.74(8)%	865.87(131) [SCS ⁺ 09]
^{130}Te	$\beta^-\beta^-$	34.08(62)%	2526.97(23) [REE ⁺ 11]

Among the list of potential double beta emitters are five out of only 35 nuclides in nature, which are capable of double beta decays with two electrons in the final state ($\beta^-\beta^-$). Furthermore, there are four candidates for double beta decays involving double positron emission ($\beta^+\beta^+$), double electron capture (ECEC) and a mixed mode of both ($\beta^+\text{EC}$). An overview of the different decay modes can be found in section 3.1.1. The most promising of the $\beta\beta$ -nuclides listed in Tab 4.4 are ^{116}Cd , ^{130}Te and ^{106}Cd in order of importance.

One of the key parameters is the Q -value of the nuclear transitions as it predetermines not only the expected decay rate, but helps discriminate the sought signal from potential background events. In fact, the cadmium isotopes ^{116}Cd and ^{106}Cd feature Q -values that are well above the highest, prominent γ -line (^{208}Tl , $E_\gamma = 2614.533$ keV) originating from the natural decay chains of uranium and thorium (see also section D.2.1 in the appendix). Although the Q -value of ^{130}Te is below this, it is still favored due to its comparably high natural abundance and the fact that its Q -value lies between the ^{208}Tl γ -line and the expected Compton edge at $E_e(\vartheta = \pi) = 2381.8$ keV according to Eqn. (1.28) – (1.29). Naturally, the γ -ray interaction probability is reduced in the Compton valley as only multiple interactions of the initial high-energy γ -ray, without an photoelectric absorption in the end, or primary Compton scattering outside the detector can deposit enough energy in this region. The latest results obtained with the COBRA demonstrator with respect to the five accessible $\beta^-\beta^-$ decay modes are discussed in [COB16a] and will be shortly addressed in section 8.7.2.

For the more exotic decay modes involving positron emission, ^{106}Cd is the most interesting and promising one. Its high Q -value allows for all three positron modes to exist, but with decreasing probability according to the number of involved positrons (see e.g. section 3.1.1).

Nonetheless, positron annihilation processes provide a unique signature in the detector involving energy depositions in coincidence of several crystals. Such a distinct signature of up to four annihilation γ -rays in coincidence with the initial $\beta^+\beta^+$ decay, is very unlikely to be mimicked by any background. Unfortunately, the natural abundance of ^{106}Cd is very low.

Of particular interest is the ordinary, but highly forbidden, single β -decay of ^{113}Cd . Despite its low Q -value and long half-life of about 8×10^{15} years, the COBRA project is in the unique position to contribute to the decay's investigation without inferring with the aim to search for the hypothesized $0\nu\beta\beta$ -decay at typically higher energy scales. Recently, the investigation of the ^{113}Cd has become one of the most important parts of COBRA's physics program as will be pointed out in section 8.3.

4.3 The COBRA demonstrator at LNGS

The Cadmium Zinc Telluride 0-Neutrino Double Beta Research Apparatus (COBRA) is an experiment aiming to search for the hypothesized $0\nu\beta\beta$ -decay by using CZT detectors. It was proposed by K. Zuber in 2001 [Zub01] and involves several stages until today. After the limitations of surface laboratories with artificial shallow depth overburden were reached, a request to the LNGS scientific committee was made asking for experimental space in the underground laboratory. Shortly afterwards, consecutive R&D setups were deployed at the Italian underground facility starting in 2003 [Mün07]. In 2011, the experiment moved to its current location in the former housing of the Heidelberg-Moscow experiment [Hei01]. Following this, the construction of the so-called COBRA demonstrator started in Sept.'11 and was finalized in Nov.'13 with its full commissioning.

An overview of the LNGS infrastructure will be given in section 4.3.1, followed by a description of the COBRA demonstrator and its hardware, the recent upgrade to the extended demonstrator and possible future steps towards a large-scale experiment.

4.3.1 Overview of the LNGS underground laboratory

The Laboratori Nazionali del Gran Sasso (LNGS) [INF20] is one of the four national laboratories of Italy's Istituto Nazionale di Fisica Nucleare (INFN). The surface structures are located next to the village of Assergi, near the city of L'Aquila, about 120 km to the north-east of Rome in central Italy. Below an average rock overburden of 1400 m, the underground complex is at one side of the 10 km long highway tunnel between L'Aquila and Teramo which crosses the Gran Sasso mountain massif as a part of the Abruzzo region. The access to the underground via the highway is very convenient and a big advantage over the majority of underground laboratories worldwide. A comparison of existing and proposed facilities, which will become available in the next few years, indicating their location, available laboratory volume and natural coverage against cosmic rays, is shown in Fig. 4.4. For further information and a detailed description of a compilation of major underground laboratories see the review articles [Bet12] and [Bet14].

One measure to compare the shielding capabilities against cosmic rays of different underground facilities is the effective depth, which is usually referred to in units of meter of water equivalent (m.w.e.), taking into account the density of the surrounding rock and coverage. The average overburden of the LNGS translates to about 3400 m.w.e. and provides a reduction of the cosmic muon flux by more than one million times. Moreover, the flux of neutrons in the underground is reduced by three orders of magnitude compared to the surface level. This reduction is also due to the very small amount of uranium and thorium of the dolomite calcareous rock of the surrounding mountain.

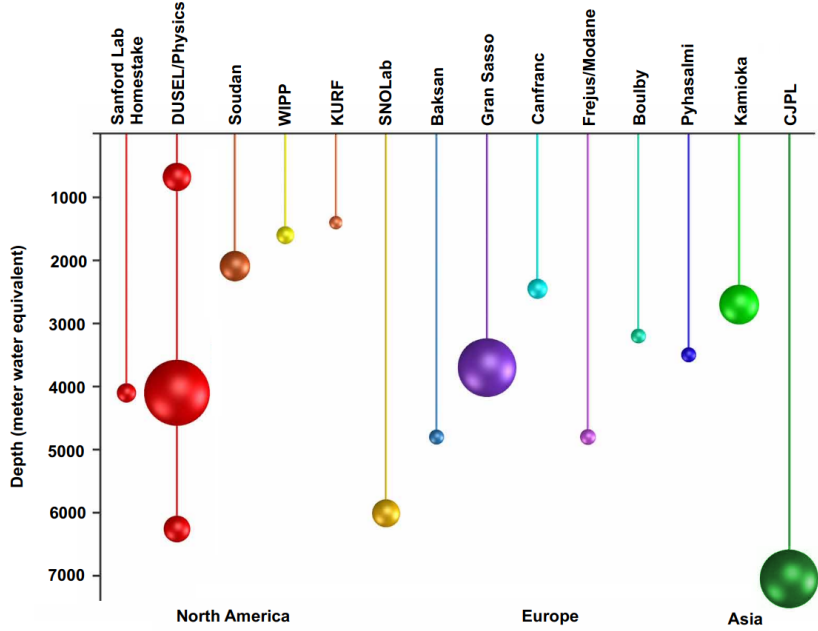


Figure 4.4: Comparison of underground laboratories around the world (adapted from [Les10]). The spheres represent the relative volumes of the laboratories' space and their effective depth. In the near future, proposed facilities like the Deep Underground Science and Engineering Laboratory (DUSEL) [Nat12] in the U.S. and the China JinPing underground Laboratory (CJPL) [CKL⁺17] will surpass the size and depth of the LNGS and provide promising experimental sites to broaden the field of ultra low-background physics.

A schematic map of the LNGS underground complex is shown in Fig. 4.5. The laboratory consists of three huge experimental halls (each 100 m long, 20 m wide and 18 m high) and bypass tunnels resulting in an overall volume of about 180 000 m³. As one of the biggest underground facilities in the world, the LNGS provides a splendidly constructed infrastructure for low-background experiments in a wide range of science.

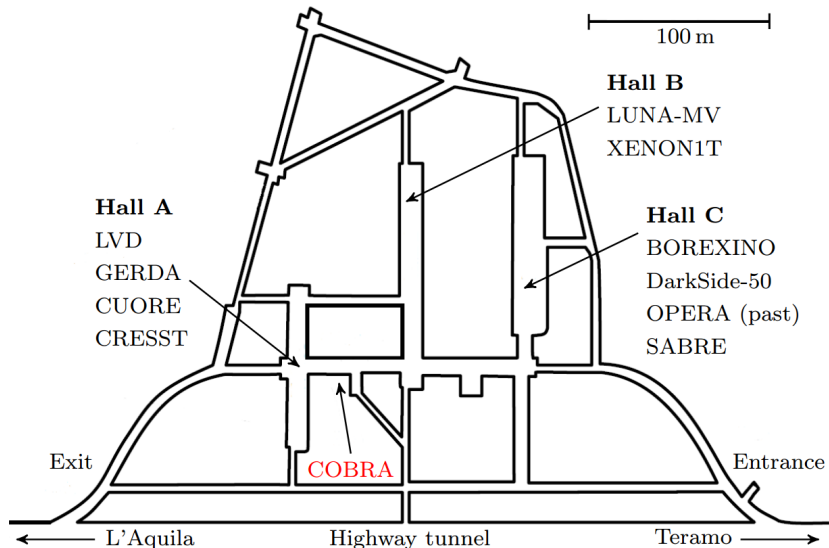


Figure 4.5: Schematic map of the LNGS underground complex (adapted from [HBB¹¹]). A variety of low-background experiments searching for the existence of the $0\nu\beta\beta$ -decay, dark matter or neutrino interactions are located inside the three experimental main halls. Since 2011, the COBRA experiment is located in one of the connecting tunnels between Hall A and B.

The list of projects includes world’s leading experiments searching for the $0\nu\beta\beta$ -decay such as GERDA (^{76}Ge) [GER18a] and CUORE (^{130}Te) [CUO18] as well as their planned successors LEGEND [LEG17] and CUPID (^{82}Se) [CUP15]. Running neutrino experiments are Borexino [Bor19], which is exploring the interior of the Sun by investigating solar neutrinos, and LVD [LVD15], which is dedicated to the observation of the neutrino signal of a core collapse supernova within our galaxy. Both experiments are part of the SNEWS initiative [AFF⁺04]. Additionally, past experiments like OPERA [OPE18] and ICARUS (LAr TPC) [ICA15] studied neutrinos from the former CERN Neutrinos to Gran Sasso (CNGS) beam.

Another strong field of activity at the LNGS is the direct search for dark matter interactions involving the experiments XENON1T (dual-phase xenon TPC) [XEN19a], Darkside (dual-phase argon TPC) [Dar18] and CRESST (CaWO₄ scintillators) [CRE19] as well as a couple of experiments using sodium iodide (NaI) detectors including COSINUS [COS16] and SABRE [SAB19]. The latter NaI based experiments aim to crosscheck the long-standing claim of annual modulations induced by a potential dark matter halo as reported by the DAMA/LIBRA collaboration [DAM18].

As the majority of the nuclear reactions in stars and other astrophysical environments proceed at very low energies, thus, with very low cross sections, their study can only be done with ion beam accelerators underground. One of the world’s leading experiments in the field of nuclear astrophysics is the LUNA project [LUN18]. It is hosted at the LNGS for more than two decades and currently in the upgrade phase to LUNA-MV.

Moreover, the LNGS hosts experiments testing fundamental principles like the GINGER project [GIN17] (terrestrial test of Einstein’s general relativity) or the VIP experiment [VIP17] (Pauli principle). Since a couple of years there is also an increasing activity in environmental studies such as ERMES [ERM13] as well as in low-dose radiobiology experiments in the context of the *Cosmic Silence* initiative [Cos09] and the FLYINGLOW program [MII⁺18].

4.3.2 Design of detector array

The present main stage of the COBRA experiment is referred to as the COBRA demonstrator and consists of an array of 64 CPG-CZT detectors that are arranged in four layers of 4×4 crystals. Each crystal has a cuboidal volume of about 1 cm^3 and a mass of 5.9 g . All of them were produced by *eV Products* (now *Kromek*) [Kro20] and thoroughly characterized prior their installation into the LNGS setup (see e.g. chapter 6). Details on the CPG lithography mask will be discussed in section 6.1. An overview of the experimental infrastructure and the shielding concept is shown in Fig. 4.6. Recently, the setup has been upgraded to the COBRA eXtended DEMonstrator (XDEM) stage as reported in section 4.3.4.

In order to prevent the CZT crystals from degrading, e.g. to prevent an increase of the surface leakage current due to the presence of moisture or dust, they have to be protected with an encapsulation coating. Moreover, the coating improves the mechanical strength. All of the demonstrator’s detectors are coated with a clear encapsulation, referred to as *Glyptal*, which is known to have a good radiopurity (see section 8.3.7). Although the coating is usually only a few tens of micrometers thick, while it covers all sides except the planar cathode, it can contribute significantly to the background level. In previous iterations of the experiment, it was found that the formerly applied encapsulation lacquer contained intrinsic contaminants on the order of 1 Bq/kg for the long-lived radionuclides ^{238}U , ^{232}Th and ^{40}K . The radiopurity of the present encapsulation lacquer has been investigated with ICP-MS at the LNGS. The recent measurements could confirm that the specific activities are much lower, namely on the order of 1 mBq/kg for ^{238}U and ^{232}Th and about 10 mBq/kg for ^{40}K (see section 8.3.7).

The detector layers are framed by polyoxymethylene (POM) holders that are installed in a support structure made of electroformed oxygen-free high-conductivity (OFHC) copper.

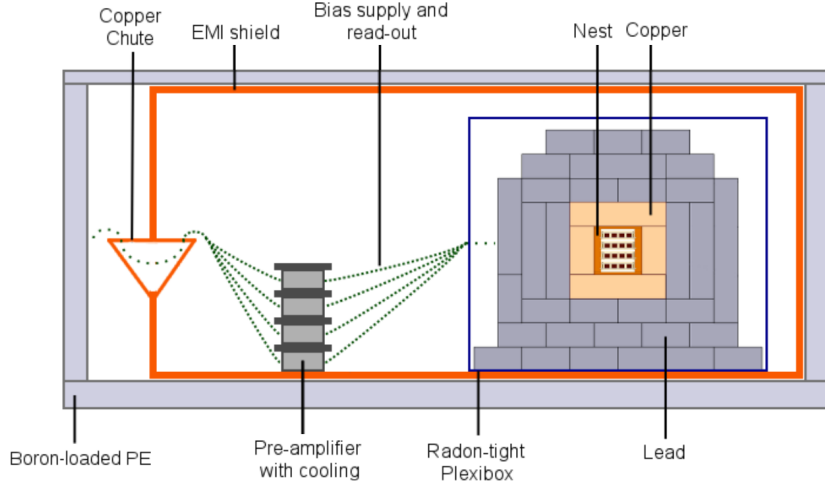


Figure 4.6: Schematic drawing of the COBRA demonstrator setup at the LNGS (taken from [Hei14]). The outer layer of 7 cm thick boron-loaded polyethylene serves as a shield against neutrons, followed by a shield against EMI made of 2 mm thick iron sheets. The inner shield consists of an air-tight acrylic box, which is constantly flushed with evaporated dry nitrogen, and a multi-layered lead castle as a shield against γ -rays. The inner-most layer is made from ULA lead with a specific ^{210}Pb activity of less than 3 Bq/kg. Inside, the four layers of 4×4 CPG-CZT detectors are housed in the so-called nest made from OFHC copper. The EMI shield also contains the first stage of the custom-made electronics used for the signal amplification and transmission to the main electronics that are located outside the shielded detector setup.

POM is a widely used thermoplastic material in industry and also known under the label *Delrin*. Moreover, it is known for its good radiopurity and stability. Nonetheless, the detector layers' design and material budget were improved in the stage-wise construction of the demonstrator array as illustrated in Fig. A.3 of the appendix. An illustration of the general structure of the POM holder and the layer layout is depicted in Fig. 4.7.

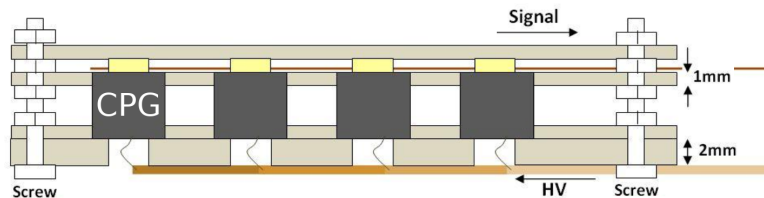


Figure 4.7: Schematic side view of a 4×4 CPG-CZT detector holder (adapted from [Raj10]). The beige-colored parts indicate the four plates that form the POM holder structure. The CPG electrodes are contacted from the top side via manually glued 50 μm thin gold wires using a conductive silver lacquer. Those gold wires are attached to a flexible PCB Kapton cable, which is used for the signal transmission to the pre-amplifier stage. The bottom plate acts also as a low-Z shield against the residual radioactivity of the HV cables, whereas the cable routing and design has been improved over time (see e.g. Fig. A.3 in the appendix). The horizontal spacing between the CZT crystals is about 4 mm and the vertical between the layers is about 12 mm.

The electrical contacting of each detector's CPG electrode is achieved with two 50 μm thin gold wires – one for the CA and one for the NCA – which are fixed to each of the electrode's contact pads with a conductive silver lacquer (referred to as *LS200*). As the conductive lacquer provides only low mechanical strength, an additional fixation using a conventional industrial glue is needed to reduce the gold wires' tension and to ensure the long-term stability of the wire contacting. The anode signals are connected to a flexible Kapton printed circuit board (PCB), which is also used to supply the grid bias for each detector individually. On the opposite side, there is another gold wire contacting the planar

cathode electrode, connecting each detector to its own high voltage (HV) channel. As the demonstrator array has been commissioned in stages, each layer has its own PCB signal readout and routing for the HV cables, which are then connected to the pre-amplifier boxes outside the lead castle and radon shield. The signal transmission from the pre-amplifier stage towards the digitization is described in the next section. More information on the electrode contacting can be found in the PhD thesis of T. Köttig [Köt12].

The inner housing containing the four detector layers is surrounded by 5 cm of electro-formed OFHC copper, followed by 5 cm of ultra low-activity (ULA) lead ($< 3 \text{ Bq/kg}$ of ^{210}Pb) and 15 cm of standard lead. Additionally, the inner part is enclosed in an air-tight sealed acrylic box, which is constantly flushed with evaporated dry nitrogen to suppress radon-induced backgrounds. The complete detector setup, including the first stage of the readout electronics, is enclosed by a construction of iron sheets with a thickness of 2 mm, which acts as a shield against EMI. The last part of the shielding is a layer of 7 cm borated polyethylene with 2.7 wt.-% of boron to effectively suppress the external neutron flux.

Some pictures of the LNGS setup can be found in section A.1 of the appendix. A complete review of COBRA’s data acquisition system and hardware equipment can be found in Ref. [COB16b] and the PhD thesis of J. Tebrügge [Teb16]. In the following, the key aspects of the data acquisition (DAQ) system will be summarized.

4.3.3 DAQ and electronics

An overview of COBRA’s DAQ system is shown in Fig. 4.8. In operating mode, each CPG-CZT detector is supplied with a negative BV on the order of 1 kV and a negative GB of about 40–110 V. The optimal bias voltages have been determined in the crystal characterization as will be summarized in section 6.2.1 of the present thesis. A compilation of the optimal operation settings for the demonstrator array can be found in Tab. E.1–E.4 in the appendix.

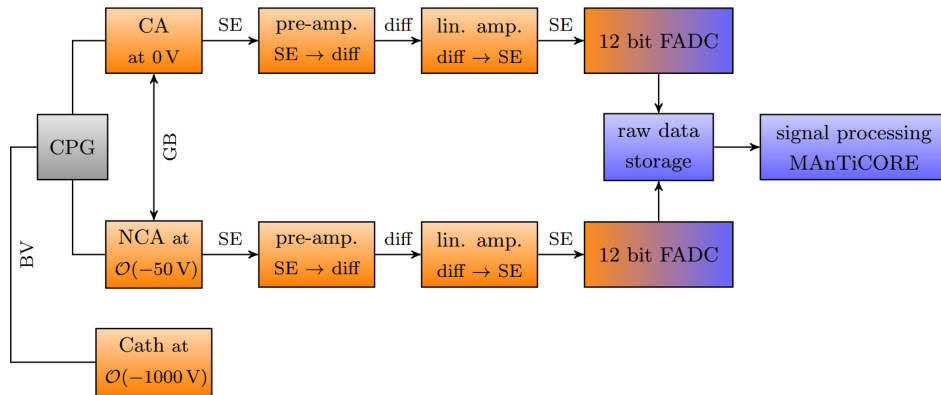


Figure 4.8: Block scheme of COBRA’s DAQ chain (adapted from [Zat14] and [Sch11]). Each detector’s CA and NCA signals are transmitted and amplified in several stages. Finally, both of them are digitized by an FADC device (*Struck SIS3300*) with a sampling frequency of 100 MHz. The raw data are stored in ROOT files and need to be processed to extract information about the recorded events like e.g. the deposited energy. The COBRA processing tool is referred to as MAnTiCORE and will be discussed in section 5.1.3.

Inside the EMI shield, but outside the lead castle and about 50 cm away from the detector array, four custom-made pre-amplifier boxes are located (see Fig. 4.6). Each of those is connected to one of the four detector layers via a flexible PCB readout cable and the respective single channel HV cables. Furthermore, in between the boxes there are cooling plates through which a liquid coolant gets circulated. This way, the waste heat produced by the pre-amplifier stage can be effectively dissipated. Even though the CZT detectors are not cooled directly,

they are in a thermal equilibrium with the shielding. More information on the pre-amplifier cooling and its effect on the detector performance will be discussed in section 8.3.3.

Every pre-amplifier box is equipped with 32 charge-sensitive pre-amplifier modules (*Creemat CR-110*) that integrate the current pulses coming from the 16 connected CPG-CZT detectors. Moreover, the single-ended (SE) detector signals are converted into differential signals in order to minimize the effect of electronic noise during the transmission. The working principle of the differential signaling is depicted in Fig. 4.9.

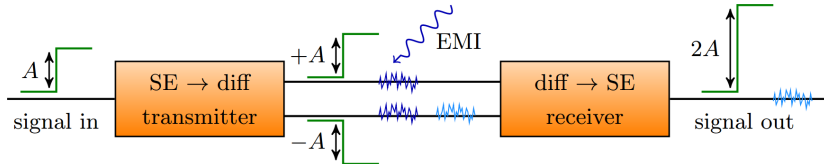


Figure 4.9: Working principle of differential signaling (adapted from [Zat14] and [Teb11]). At first, an incoming SE signal gets duplicated and, secondly, inverted using a differential transmitter. For the transmission towards the differential receiver, preferably twisted wire pairs are used (such as CAT6 Ethernet cables). This way, electromagnetic disturbances affecting the signals during the transmission are most likely very similar for the two differential channels. At the receiver, the two signals are subtracted from each other, resulting again in a SE signal. The advantage is that most of the noise gets very much reduced while the amplitude is doubled. Even in the case that only one of the differential channels would be affected by noise, an effective improvement of the signal-to-background ratio can be achieved by using this technique.

The differential signaling of the 128 pre-amplifier channels via twisted wire pairs requires in total 32 CAT6 Ethernet cables with eight signal channels each. One of those cables transmits the differential CA and NCA signals of two physical detectors. The distance between the pre-amplifiers and the differential receiver, which also acts as an additional linear signal amplifier, is about 10 m. The reason for such a rather unconventional concept is that the COBRA experiment is situated on two floors at the LNGS underground laboratory. While the lower floor hosts the detector setup including the shielding and the corresponding operation infrastructure, the main DAQ electronics are located in a different cabinet on the upper floor. This separation became necessary in the stage-wise construction of the demonstrator array as the waste heat production increased with each installed layer and its required NIM and VME electronics. However, by using the differential signaling there is hardly any disadvantage regarding the successful long-term operation of the demonstrator.

The differential signaling ends at the custom-made linear amplifier NIM modules, which act at the same time as the differential receivers and convert the signals back to single-ended. Each of the 16 modules provides two Ethernet inputs and eight SE outputs, while eight of them are hosted within a NIM crate. The SE outputs are connected one-to-one via standard coaxial RG174 LEMO cables to the input channels of 16 *Struck SIS3300* fast analog-to-digital converters (FADCs) covering all 128 detector signals. The linear signal amplification ensures an optimal usage of the fixed input range of the applied FADCs and can be adapted depending on the physics application (see e.g. the first part of section 7.4.3). Finally, the pulse-shapes are digitized using a sampling frequency of 100 MHz, a sampling length of 10 μ s and a resolution of 12 bit, which is equal to 4096 FADC channels.

The entire data acquisition system can be accessed via COBRA's Data-Acquisition and Control Environment (DAQCorE). This software package is written in *Scala*, which is a general purpose programming language providing support for functional programming, and has been founded by O. Schulz in the course of his PhD thesis [Sch11]. It allows to run executable code on a Java virtual machine, even in interactive sessions, and supports the ROOT software package developed at CERN [BR97]. DAQCorE takes care of the communication and instantiation of different hardware components. Moreover, it controls the data flow of the FADCs

by using a VME server protocol including the writing of the ROOT data structure based on *TTree* objects. Those objects contain general run information such as the DAQ settings, the duration and unix timestamps for each triggered event, as well as the full pulse traces.

In order to validate the functionality of the DAQ chain, a pulse generator (*BNC PB-5*) injects periodically artificial signal into the pre-amplifier stage. This way, the injected pulses undergo the same signal transmission and amplification as real detector signals. This makes it possible to identify potential hardware problems on-the-fly. The artificial signals are flagged by a TTL signal of the pulse generator and provide well-defined synchronization points for an offline synchronization of the single FADCs, which are usually delayed by several ten seconds in the initialization of a physics run (see e.g. section 7.1.5).

The full pulse-shape sampling allows for a complex offline analysis and is one of the key instruments to discriminate signal from background events. More information on the subject of COBRA’s pulse-shape discrimination can be found in chapter 7. One of those methods is the reconstruction of the interaction depth making use of the previously discussed depth dependency of the signal heights due to charge trapping effects. The event reconstruction and data processing will be discussed in chapter 5.1.

4.3.4 Upgrade to COBRA XDEM

In March 2018, the LNGS setup has been upgraded to the COBRA eXtended DEMonstrator (XDEM) by adding an additional layer consisting of 3×3 prototype CZT detectors with an increased volume of 6 cm^3 . An overview of the detector technology is given in section 6.1.

The implementation of the XDEM layer into the existing demonstrator setup required modifications on both the hardware and software level, whereas the Technische Universität Dresden (TUD) group took care of the manufacturing of the additional shielding components and detector housing made of ULA lead and OFHC copper. The conception, characterization and commissioning of the XDEM setup is well-documented in the PhD thesis of R. Temminghoff [Tem19]. In preparation of the installation, the necessary additional shielding components were designed in the Master thesis of L. Bodenstein-Dresler [BD18]. Some illustrations can be found in Fig. 4.10.

All of the depicted parts were manufactured in the workshop of the physics department at TUD. Special care was taken in the material selection and manufacturing process to prevent any contamination (e.g. dry machining, minimum storage time on surface level, removal of all potentially radon-exposed outer surfaces). Moreover, a large sample of the initial 500 kg OFHC copper block was produced to perform a radiopurity measurement of the raw material in the Modane underground laboratory LSM [CNR20] (see section 8.3.7). The raw material has been stored at the *Dresden Felsenkeller* providing a shielding of about 140 m.w.e. for more than five years, which reduced the amount of cosmogenic activation products significantly. Finally, all copper parts were electro-polished providing much cleaner surfaces than available for the construction of the demonstrator setup at that time.

The first step of the preparation towards COBRA XDEM was to transfer the CZT crystal characterization routines as developed at TUD to the new prototype detector geometries. The very first characterization results are reported in the Diploma thesis of K. Rohatsch [Roh16] and will be briefly summarized in the course of chapter 6. Based on the collaboratively developed test procedure, all XDEM detectors were characterized by R. Temminghoff [Tem19] prior to their installation at the LNGS. In all commissioning steps, a more careful detector handling was ensured to avoid the exposure of the crystals’ surfaces to air and radon, which was found to be the dominant background for the COBRA demonstrator (see section 8.2). This included the operation and storage under strict nitrogen atmosphere, starting already at the manufacturer’s side. Moreover, a more reliable contacting scheme was applied to

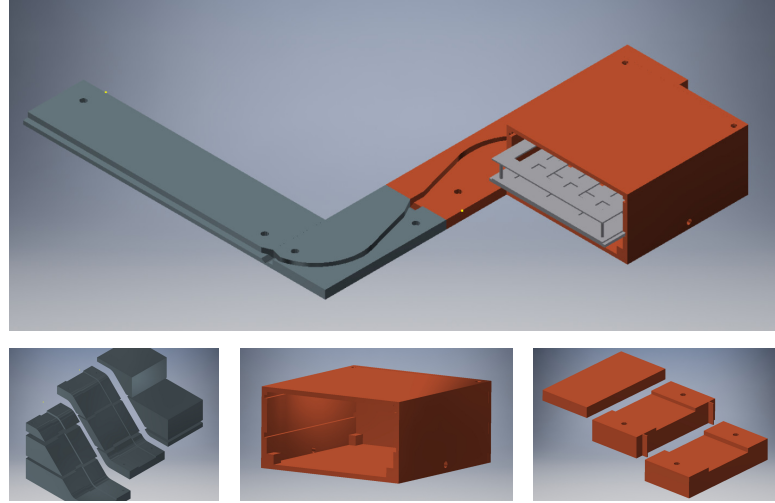


Figure 4.10: Illustration of the XDEM shielding components using *autodesk inventor professional* [Aut20]. *Top*: base assembly of the lead and copper shield highlighting the routing for the calibration tube. The copper housing containing the POM holder with the new prototype detectors is located in the center of the lead castle on top of the existing demonstrator setup. *Bottom*: HV and signal cable feed-through made of lead (*left*) and copper (*right*). The HV and flexible PCB signal cables are separated into a lower and upper signal lane. The middle picture is an inside view of the copper nest, which consists of five separate parts.

connect the detector electrodes to the flexible PCB readout. The former silver lacquer was exchanged with a silver-based epoxy that is well suited for low-background applications (see e.g. [MAJ16]) and referred to as *TRA-DUCT 2902* (Tra-Con Inc.). Its mechanical strength does not require an additional glue as it was the case for the demonstrator’s detectors.

In summary, the overall procedure could be significantly improved by applying a more careful material selection, an improved handling during the crystal characterization and, last but not least, the availability of high-quality CZT detectors with additional veto capabilities (see e.g. section 6.1) and a more reliable contacting scheme. Some impressions of the implementation of the XDEM layer into the LNGS setup can be found in section A.2 of the appendix. In parallel, there have been efforts to develop a large-scale concept as will be briefly summarized in the next section.

4.3.5 Proposal for large-scale experiment

The ultimate goal of the COBRA collaboration is to prove the feasibility of a large-scale experiment based on CZT detectors. According to the relation between the predicted half-life $T_{1/2}^{0\nu}$ and the effective Majorana neutrino mass $m_{\beta\beta}$ in Eqn. (3.6), a sensitivity on the order of $\tilde{T}_{1/2}^{0\nu} \sim 2 \times 10^{26}$ yr is required to explore the top of the inverted mass ordering at $m_{\beta\beta} = 50$ meV using the $0\nu\beta\beta$ -decay of ^{116}Cd . Based on the sensitivity approximation given in Eqn. (3.10), the required source mass, background level and other experimental parameters can be estimated such as shown in Fig. 4.11 for several scenarios.

A design proposal for a potential King-COBRA experiment can be found in Fig. 4.12. The development of a Monte-Carlo based optimized shielding and background estimate can be found in the PhD thesis of N. Heidrich [Hei14]. The proposal makes use of the detector layer concept of the demonstrator array. Each layer of the design consists of eight so-called detector module carriers (DMCs), whereas each DMC consists of eight detector modules (DMs) based on the 3×3 crystal design of the XDEM layer. Because of the large number of required readout channels, an upgrade of the complete DAQ system is necessary. However, a first R&D project

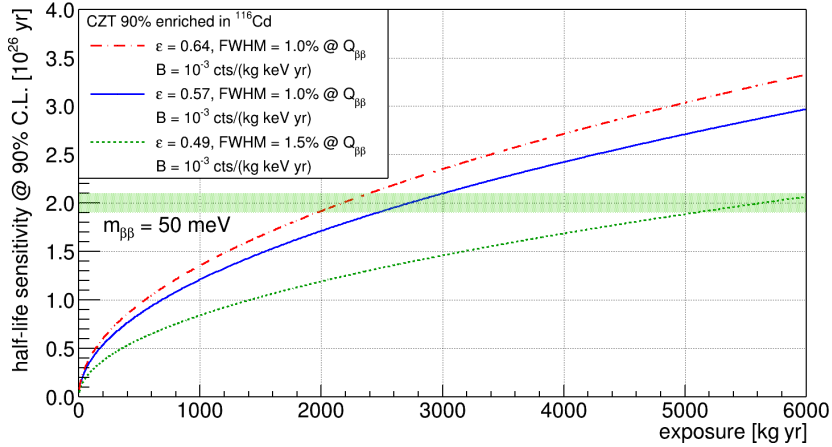


Figure 4.11: Projected half-life sensitivity of a large-scale COBRA experiment. The three studied scenarios are rather independent from the actual design and correspond to an up-scaled version of the demonstrator array (dotted green), the current XDEM approach (solid blue) and the same approach but assuming a more efficient background discrimination (dashed red). In each case, a background index of 10^{-3} cts/(kg keV yr) has been assumed. The efficiency values are derived in section 8.7 of the analysis part of the present thesis.

in the context of the XDEM upgrade had to be postponed because of unresolvable technical issues with the documentation of the already purchased ASIC and FPGA system (see e.g. [Tem19]). Each DMC is connected to an ASIC (application-specific integrated circuit), which would need to provide at least $9 \cdot 9 \cdot 8 = 648$ readout channels to record the data of the 72 detectors per DMC using the currently favored electrode design. The design is referred to as quad coplanar-grid (qCPG) with an instrumented guard-ring electrode and will be discussed in section 6.1. For the proposed design of 20 layers, a total number of 11 520 crystals would be needed. There are a lot of open questions regarding the construction and commissioning of such an experiment that need to be addressed thoroughly in future studies.

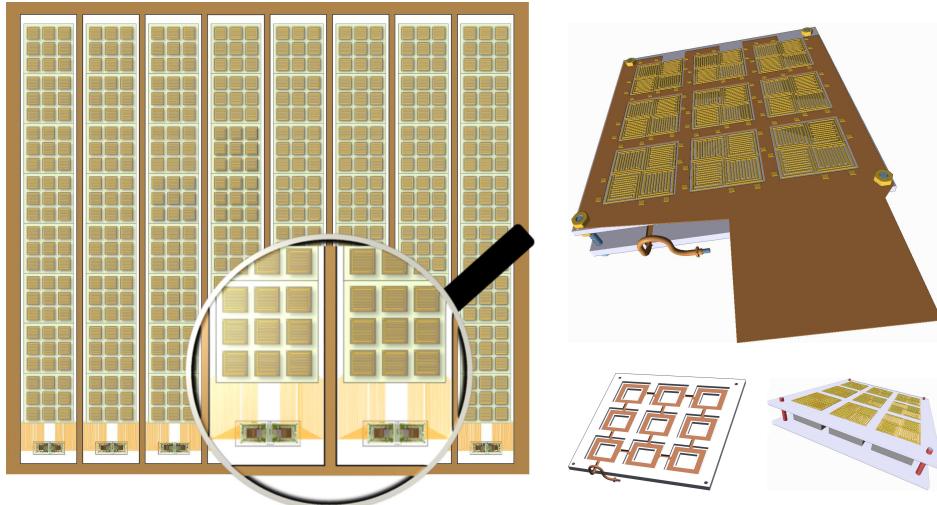


Figure 4.12: Design proposal for a potential King-COBRA large-scale experiment (based on [Raj13] and [Hei14]). *Left:* schematic detector layer consisting of eight DMCs. Each DMC supports eight DMs and is assumed to be readout via an ASIC module. *Right:* concept drawing of a DM based on the XDEM prototype layer. Each DM is equipped with 3×3 qCPG-CZT detectors. In a first iteration, a large-scale array would consist of 20 layers corresponding to 11 520 crystals with a total mass of about 415 kg and a volume of roughly 1 m^3 . By assuming an enrichment of 90% in ^{116}Cd , this corresponds to an isotopic mass of about 180 kg.

Chapter 5

Data processing and Monte-Carlo simulation tools

The evaluation of COBRA's pulse-shape data involves elaborate software tools and processing routines, which will be introduced in the following chapter. As most of the tools are subject to rather frequent changes, introducing new features and improvements for the present routines, the overview given in the course of this chapter should be seen as a snapshot of the current status. The aim of COBRA's software development is to provide multi-purpose tools that allow for the data evaluation of small-scale laboratory setups, involving usually only a single or up to a few detectors, and the full COBRA demonstrator. Recently, the support of the new detector types applied in the XDEM setup at the LNGS has been implemented.

In the first part of this chapter, the basics of the signal processing will be discussed. This includes a review of the Shockley-Ramo theorem in the context of the signal forming process in CPG-CZT detectors as applied in the COBRA demonstrator and the involved weighting potentials. Furthermore, the general concept of the data processing starting at the pulse-shape level and the related software tools will be presented.

The second part is dedicated to the actual reconstruction methods. This part includes a review on the zeroth-order reconstruction of the deposited energy and interaction depth, as well as the incorporation of electron trapping corrections for both of those quantities. This summary is also meant as an introduction for the analytic derivation of a novel approach to assess the trapping effect for holes based on long-term laboratory measurements as will be further elaborated in section 7.4. Finally, an overview of COBRA's Monte-Carlo simulation framework, which is based on GEANT4, and some of the related packages will be given.

5.1 Basics of signal processing

The signal processing refers to the task of evaluating the recorded pulse-shapes and is the very first step of any advanced data analysis. It involves multiple steps as will be summarized in the following. The first part of this section introduces the weighting potentials as derived from the Shockley-Ramo theorem for COBRA’s default coplanar grid electrode design which is used for the 1 cm^3 detectors of the demonstrator array. Following this, the standard procedures of the *weighting factor optimization* and the so-called *gain-balancing correction* will be discussed. Finally, an overview of the data processing procedure itself and the respective software tools developed by the COBRA collaboration is given in section 5.1.3.

5.1.1 Weighting potentials in CPG-CZT detectors

As has been discussed in the general context of the signal forming process based on the Shockley-Ramo theorem in section 4.1.4, the weighting potential φ_w depends only on a given electrode configuration. A schematic drawing of the CPG-CZT detector design applied for the COBRA demonstrator array is depicted in Fig. 5.1. The electrode design consists of a planar cathode at a negative BV on the order of 1 kV and two interleaved anode grids held at slightly different potentials with respect to the ground potential. The distance between the cathode and anode side is referred to as the normalized interaction depth. However, the *reconstructed depth* z defines the cathode side as $z = 1$ and the anode side as $z = 0$, in contrast to the terminology introduced before in section 4.1.3. In the far-grid region, the BV potential forces the charge carriers (e^- and h^+) to drift, while the holes are trapped in less than one millimeter, which introduces a depth dependency of the induced charge signal on the electrodes. In order to overcome this problem, the CPG design was found as discussed previously. It acts as a virtual steering grid for the charge carriers, while the induced charge on the CA and NCA is the same for the charge drift through the bulk of the detector volume. Consequently, the difference signal of CA and NCA is insensitive to the bulk drift. Only in the near-grid region, the effect of the applied GB results in a collection of the electrons at the CA, which leads to a sharp rise of the difference signal as depicted in Fig. 4.3.

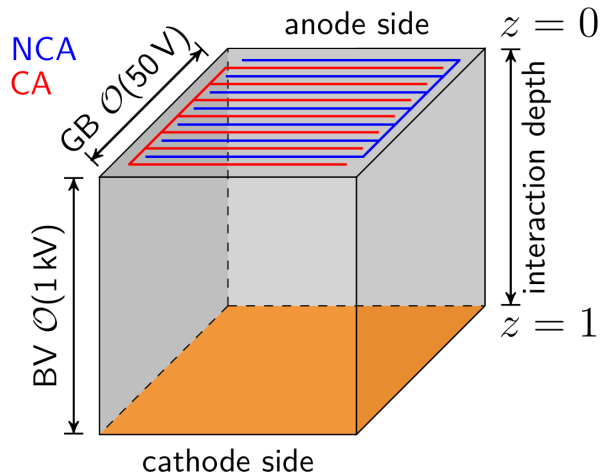


Figure 5.1: Schematic electrode layout of the CPG-CZT detectors deployed in the COBRA demonstrator (adapted from [Zat14]). The anode side at the top is equipped with a CPG electrode consisting of two interleaved grids that are held at slightly different potentials. This way, electrons drifting in the bulk potential between the anode and the planar cathode electrode get collected at the anode held at the higher potential referred to as collecting anode (CA), while the second grid acts as a non-collecting anode (NCA). The normalized distance between the anode and the cathode is referred to as the interaction depth.

While the previous illustration in Fig. 4.3 only includes the projection of $\varphi_w(z)$ for one pair of anode rails, the weighting potential is a complex three-dimensional object that can only be assessed by numerical methods. A more elaborated representation of the weighting potentials is depicted in Fig. 5.2, making use of COBRA's terminology for the orientation of the interaction depth. Those potentials are the results of field line calculations using the commercial *COMSOL multiphysics* package. An overview is given in section 5.3.4. The respective $\varphi_w(y, z)$ in Fig. 5.2 follow as the projection of a plane that is orientated perpendicularly to the grids through the center of a CPG-CZT detector at $x = 0.5$ (see e.g. Fig. 5.1).

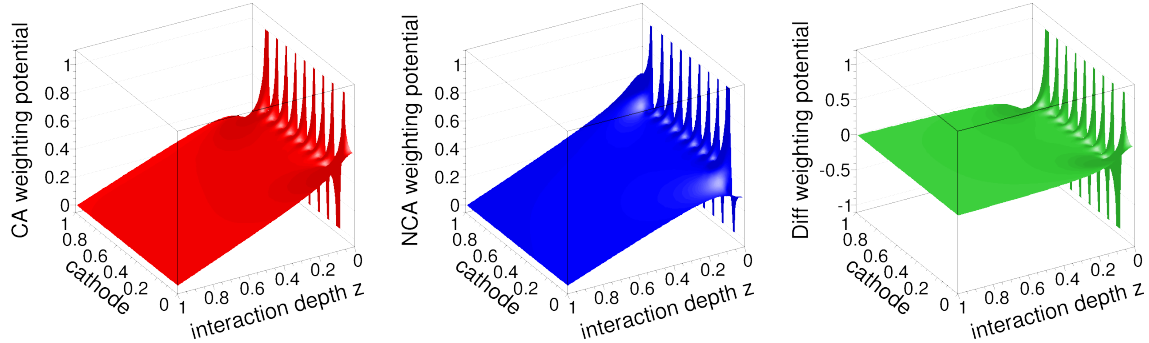


Figure 5.2: Illustration of the projected weighting potentials for the raw signals of the CA (red) and NCA (blue) and the corresponding difference signal (green) in the bulk region of a CPG-CZT detector (updated version of [Zat14]). As the induced charge signal measured by an electrode is proportional to the weighting potential as stated by the Shockley-Ramo theorem in Eqn. (4.4), the amplitudes of the raw signals depend on the origin of the charge cloud with respect to the z coordinate. By subtracting the CA from the NCA potential, a flat uniform difference weighting potential is achieved. In this case, the induced charge is proportional to the amount of created charges in a particle interaction, thus, the actually deposited energy.

The two-dimensional representations of the weighting potentials confirm the general features such as the rising slope of the CA and NCA from $\varphi_w(z = 1) = 0$ to $\varphi_w(z = 0) = 1/2$ and the resulting flat distribution of the difference signal's potential. At most positions in the bulk region of the detector, the weighting potentials of the CA and NCA are nearly equal. According to the prediction of the Shockley-Ramo theorem, they approach $\varphi_w(\text{CA}) = 1$ and $\varphi_w(\text{NCA}) = 0$ at $z = 0$ for the position of a CA rail and vice versa for the position of a NCA rail. The same pattern in the near-grid region is observed for the difference signal, which causes some distortions in the event reconstruction for this region. A detailed discussion of the effect and its implication for the efficiency of the reconstruction is presented in section 7.1.2. Moreover, the imprints of the distortions for interactions close to the surfaces can be used to discriminate surface and central events by means of the respective pulse-shapes. This subject will be covered in section 7.1 summarizing the pulse-shape discrimination techniques developed in the course of the COBRA experiment.

In reality, the weighting potentials are not realized perfectly due to small variations of the applied lithography masks and imperfections of the underlying crystal structure. This includes microscopic defects such as tellurium inclusions, which act as trapping zones for electrons and holes. While holes are trapped anyhow, the trapping of electrons affects the signal reconstruction and the achievable energy resolution significantly. However, it can be compensated by introducing a so-called *weighting factor* as discussed in the following section.

5.1.2 Weighting factor optimization and gain-balancing

The standard procedure to optimize the weighting factor w is documented in [Zat14] and will be briefly reviewed in the following. It is based on the so-called *differential-gain method*

introduced by P. Luke to address the effect of electron trapping and provide a measure to account for it analytically [LE96]. The optimization of the weighting factor belongs to the *pre-processing* of COBRA data and provides important input parameters for the processing tools, which are usually extracted from dedicated calibration measurements.

The idea is to optimized the energy resolution as one of the parameters entering the half-life sensitivity approximation by modifying the simple difference signal to

$$\text{Diff}[i] = \text{CA}[i] - w \cdot \text{NCA}[i] \quad (5.1)$$

for each of the sample indices $i \in [0, 1023]$. However, the optimal value of w needs either to be already known to perform the processing of the raw data or needs to be assumed to find the optimum value in an iterative way. As the iterative processing is rather slow, especially in the light of a full calibration of the COBRA demonstrator with up to 64 detectors, the optimization involves quantities that are already accessible after a single processing run with e.g. default parameters (see also section 5.1.3). Instead of constructing the actual difference signal for every event based on the 1024 samples of the CA and NCA pulses, Eqn. (5.1) can be modified to

$$\text{PH}(\text{Diff}) = \text{PH}(\text{CA}) - w \cdot \text{PH}(\text{NCA}) \quad (5.2)$$

using the pulse-heights (PHs) of the corresponding signals. The determination of the PHs is described in section 5.2.1. This simplification makes it possible to assume different values of w without the need to perform the time consuming processing step for each of those values.

The next step is to construct a histogram of the PHs for the *virtual difference signal* in Eqn. (5.2) for each of the assumed weighting factors. An example of a laboratory measurement with a single CPG-CZT detector using a ^{137}Cs calibration source is shown in Fig. 5.3. The radionuclide ^{137}Cs provides a single prominent de-excitation γ -ray of $E_\gamma = 661.7\text{ keV}$ [NDS20]. In order to assess the energy resolution of the observed γ -line, a modified Gaussian fit as introduced in Eqn. (5.7) of section 5.2.2 is applied. The resulting fit parameters can be used to determine the FWHM of the full-energy peak for each assumed value of w .

Finally, the correlation of FWHM and w can be approximated with an empirical polynomial function. It is found that the correlation can be well described with a parabola, whereas the optimum value of the weighting factor is found at the minimum of the analytic FWHM(w) expression such as shown in Fig. 5.3.

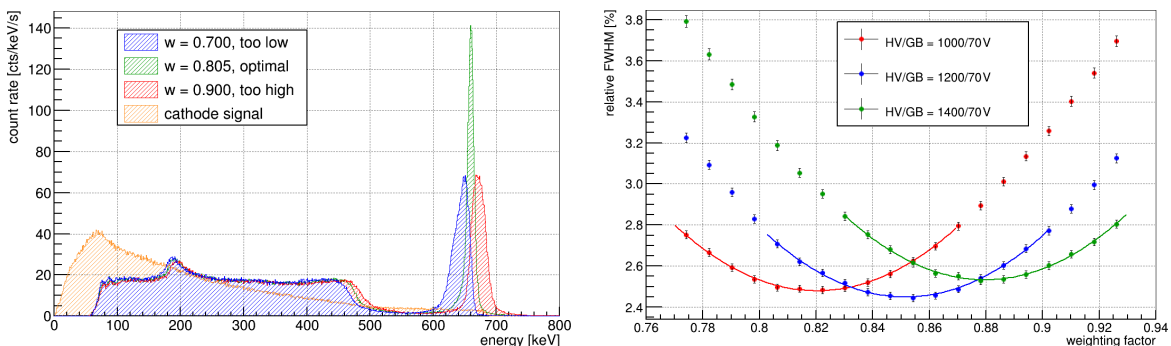


Figure 5.3: Impressions of the weighting factor optimization using laboratory data of a single CPG-CZT detector for a calibration with ^{137}Cs (taken from [Zat14]). *Left:* example energy spectra for different assumed weighting factors. For both too high or too low values of w , the achievable energy resolution in terms of FWHM is worsened significantly. In the present example, the optimized value results in a relative FWHM of 1.9% at 661.7 keV, whereas the other cases lead to about 4.7%. *Right:* Example of the FWHM(w) correlation for different applied bias voltages. The optimal w is determined via a parabola fit around the minimum.

As the weighting factor is expected to depend on the applied bias voltages, especially the BV, the optimum value has to be determined for each detector and bias setting separately. This circumstance is one of the main challenges in the CZT crystal characterization as discussed in section 6.2.1. The higher the applied BV, the less dominant should the electron trapping appear as the electron mobility increases with the bulk voltage as well. This is why the weighting factor is expected to increase towards unity for sufficiently high values of the applied BV. However in practice, the applicable BV is limited by the occurrence of leakage currents, which worsen the energy resolution again (see e.g. section 6.2.1).

The same procedure as outline above is part of the calibration of the LNGS detector array and used to monitor the detectors' stability. More information on this subject can be found in section 8.1.2. At this point it should be mentioned that there are also alternative procedures to perform the weighting factor optimization such as described in the Diploma thesis of T. Wester [Wes12] (step-wise approximation of the CA-versus-NCA full-energy peak) and the PhD thesis of R. Temminghoff [Tem19] (adapted procedure for the working point determination of qCPG-CZT detectors). However, the present method was found to be the most robust for the evaluation of the demonstrator's physics data. Moreover, there are alternative event reconstruction approaches other than the differential-gain method just discussed. For an overview see e.g. the Master thesis of J.-H. Arling [Arl16].

One particular correction to the above procedure is required because of the design of COBRA's DAQ system. While all signals are amplified by essentially the same hardware, the different components are subject to variations, e.g. due to the manufacturing process and the manufacturer's specifications. In case of the energy reconstruction via the differential-gain method, the differences are already absorbed in the weighting factor. However, a potential imbalance of the amplification of the paired CA and NCA signals would affect the reconstruction of the interaction depth (see section 5.2.3). In order to achieve an independent *gain-balancing*, an additional parameter g_b is introduced to correct the NCA's amplification with respect to the CA signal. The currently best option to determine this correction factor is based on the ratio of the initial slopes of the CA and NCA signals (see e.g. Fig. 7.1) under certain selection criteria. Alternatively, there have been efforts to use the periodically injected signals of the pulse generator for this matter. However, there are a couple of challenges that could not be resolved. This includes the rather unknown stability of the pulse generator, the necessary splitting of the initial signal in order to distribute it to all 128 pre-amplifier channels and the different thermal environments regarding the location of the detector array on the lower floor and the pulse generator in the cabinet of the DAQ electronics.

All of the above can be avoided by utilizing the actual detector signals such as described in detail in [Zat14]. Because of the gain-balancing being independent of the optimization of the energy resolution, while g_b appears as an additional parameter in the construction of the difference pulse, the optimized weighting factor in Eqn. (5.1) and (5.2) can be replaced by $w = g_b \cdot w_g$. This way, the gain-balancing correction only alters the value of w to w_g without interfering with the independently optimized energy reconstruction.

5.1.3 Processing tools

The full pulse-shape sampling applied by COBRA allows for a complex offline analysis and reconstruction. However, the raw data need to be processed in order to access the derived quantities such as the interaction depth and deposited energy. For this purpose, there were several software tools developed by the COBRA collaboration. The main project is referred to as the Multiple-Analysis Toolkit for the COBRA Experiment (MAnTiCORE) and acts as the interface between the raw data at the pulse-shape level and the so-called *processed data* containing derived information about the recorded events. MAnTiCORE is based on

the analysis framework ROOT and thus written in C++. Like the DAQ software DAQCorE, it makes use of STL vectors, providing an effective way to organize multi-detector events. Fig. 5.4 illustrates schematically the data flow and processing steps realized by MAnTiCORE.

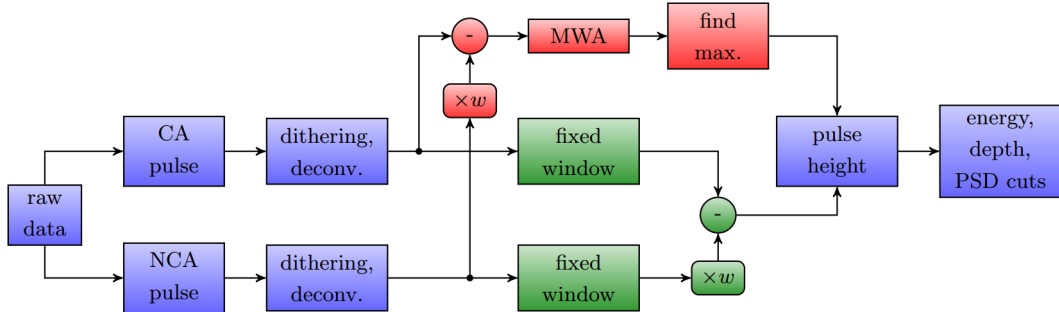


Figure 5.4: Block scheme of the signal processing with MAnTiCORE (adapted from [Zat14] and [Sch11]). After the pre-processing steps dithering (default) and deconvolution (optional), there are two possible ways to obtain the weighted difference signal from the raw CA and NCA signals. The red path applies a moving window average (MWA) to determine the pulse-height of the difference signal directly, but requires the optimized value of the weighting factor w . The pulse-height is taken as the maximum returned by the MWA and found to be robust against noise. The green path is based on a simpler reconstruction using the amplitudes of the CA and NCA signals, but makes it possible to determine the weighting factor as described in section 5.1.2.

The first step in the processing chain is a correction of quantization errors, which is referred to as *dithering* and involves the adding of triangular noise to both signals. In an optional step, a deconvolution of the pulse-shapes can be performed to correct the exponential decay of the charge signal over the RC element of the DAQ. However, the deconvolution requires additional input parameters such as the decay constant, which usually differs between the single channels. Regarding the actual pulse-heights, especially of the weighted difference signal $\text{PH}(\text{Diff})$, there are two different methods implemented into MAnTiCORE. The first makes use of a *fixed window* approach, which is the same method as used for the quantities $\text{PH}(\text{CA})$ and $\text{PH}(\text{NCA})$ appearing in Eqn. (5.2). The second, more advanced method is based on a moving window average (MWA), but requires the optimized weighting factor in order to reach its full potential in terms of achievable energy resolution. Some details of both methods will be discussed in section 5.2.1. An introduction into how to provide MAnTiCORE with the required configuration and calibration parameters to process a set of raw data can be found in [Zat14]. Some of MAnTiCORE's original routines have been outsourced into more general software packages, namely FROASt (Functional ROOT-oriented Analysis and Settings) and SigProCxx (Signal Processing Classes for C++), which are both maintained by a former collaboration member (O. Schulz, MPI Munich, formerly TU Dortmund).

More recently, an additional module has been added to MAnTiCORE with the aim to synchronize the unix timestamps provided by the 16 FADCs and their internal clocks. As the clock speed differs slightly between the single devices, a noticeable drift over time can be observed. More information on this subject can be found in section 7.1.5. The output of MAnTiCORE, especially the number of output variables, can be customized by user commands in order to adapt and limit the output of meta data for certain analysis tasks.

The maintenance and improvement of MAnTiCORE is a collaborative effort and an ever ongoing process. Usually, all software projects of the COBRA collaboration are maintained via the free and open source distributed version control system *git* [Git20a]. The main repositories were hosted centrally at TU Dortmund, but recently the policy has changed and more and more projects are moved to the online platform *Github* [Git20b]. Github provides the functionality to share the source code between the collaborating institutes without the need of local computing accounts of external members. Furthermore, role models such as

administrator, *contributor* or *user* can easily be assigned by granting the according access rights. Moreover, it is possible to define teams for certain tasks and discuss changes directly online before pushing them into the main repository.

In addition to the actual processing programs, there are a couple of specialized tools developed in the course of the present thesis. One of those is a standalone pulse-viewer that allows for the visualization of the raw data in a user-friendly and standardized way (see e.g. Fig. 7.7–7.9 and Fig. 7.25 in chapter 7). Moreover, all necessary processing steps for the evaluation of a LNGS calibration run, requiring the determination of the parameters listed in Tab. 8.1 for each detector, were combined in a collection of several macro routines. In the following, the basics of the event reconstruction will be summarized.

5.2 Event reconstruction

The event reconstruction of CPG-CZT detectors is closely related to the Shockley-Ramo theorem as derived in section 4.1.4. Referring to Fig. 5.2, the subtraction of the raw signals results in a very uniform weighting potential, which is almost independent of the interaction depth. By using the Shockley-Ramo theorem, the final amplitudes of the two anode charge signals caused by the electrons' drift in an ideal model case can be expressed as

$$Q_{\text{CA}} = \frac{1}{2} \cdot q_0 \cdot (z_0 + 1), \quad (5.3)$$

$$Q_{\text{NCA}} = \frac{1}{2} \cdot q_0 \cdot (z_0 - 1). \quad (5.4)$$

The initial amount of charge produced in ionization processes induced by incoming radiation is indicated as q_0 , while z_0 represents the zeroth-order reconstruction of the interaction depth. By subtracting the raw signals in Eqn. (5.3) – Eqn. (5.4) from each other, the induced charge of the difference signal is obtained.

$$Q_{\text{Diff}} = Q_{\text{CA}} - Q_{\text{NCA}} = q_0 \sim E \quad (5.5)$$

It is found that the difference signal yields the initially created amount of charge and therefore, by performing an energy calibration, the deposited energy E . It should be noted that the actual amplitude of the NCA signal is expected to be almost always close to zero or negative as the electrons are forced to drift to the nearest CA rail in the near-grid region, thus, away from the NCA rails. Details about the calibration procedure, involving radionuclides with well-known γ -lines, will be discussed in section 5.2.2 and related sections. Moreover, the achievable energy resolution can be improved by introducing a weighting factor w as discussed before in section 5.1.2.

The zeroth-order interaction depth z_0 can be expressed as the ratio of the amplitude of the reconstructed cathode signal, which scales as $Q_{\text{Cath}} \sim z_0 \cdot E$, and Q_{Diff} . By assuming charge conservation, the cathode signal can be derived as the sum of the CA and NCA signals (see e.g. Fig. 4.3 in section 4.1.3). This leads to the following expression

$$z_0 = \frac{Q_{\text{Cath}}}{Q_{\text{Diff}}} = \frac{Q_{\text{CA}} + Q_{\text{NCA}}}{Q_{\text{CA}} - Q_{\text{NCA}}}. \quad (5.6)$$

In Ref. [FDG⁺13], a subgroup of the COBRA collaboration published an analytic model of the event reconstruction incorporating a correction of electron trapping effects. The impact on the interaction depth will be briefly reviewed in section 5.2.3. In practice, the basis of COBRA's event reconstruction relies on the determination of the pulse-heights of the raw signals using MAnTiCORE as presented in the next section.

5.2.1 Pulse-height determination

As highlighted in Fig. 5.4, there are two options to determine the pulse-height using COBRA’s processing tool. The first method, referred to as the *fixed window* approach, determines a simple sample average for a fixed window size of $n_w = 128$ for the first and last samples of a given pulse. The position of those sample averages are referred to as the pre- and post-baseline with respect to the trigger point, which is usually set to $\text{Diff}[i=640]$, while $i \in [0, 1023]$, in the configuration of DAQCorE (see also the example in Fig. 7.1).

Both baseline regions are also used to determine characteristic properties such as the root mean square (RMS) for the application of COBRA’s data-cleaning cuts (see section 7.1.1). Finally, the corresponding pulse-height follows as the difference of the sample averages of the post- and pre-baseline levels. This method is used to determine the quantities PH(CA) and PH(NCA) in Eqn. (5.2), which are used in the optimization of the weighting factor based on the virtual difference signal’s amplitude.

The second and more advanced approach highlighted in Fig. 5.4 makes use of a moving window average (MWA) using two windows of $n_w = 256$ samples that are separated by a gap comprising the same number of samples. For each sample of the actual difference pulse according to Eqn. (5.1), the difference between both of the MWA windows is calculated, whereas the maximum difference yields the weighted pulse-height PH(Diff). The application of the MWA method improves the achievable energy resolution by about 20%, due to the fact that the respective sample averages are closer to the signal rise than in the previous case. This way, the effect of the exponential signal decay is very much reduced, while the MWA method is found to be also very robust against noise. Moreover, the actual weighted difference signal is expected to be much cleaner than the raw CA and NCA signals due to the cancellation of in-phase baseline fluctuations in the subtraction process.

5.2.2 Energy calibration

The first step of an energy calibration involving COBRA data is the optimization of the weighting factor according to section 5.1.2. This is usually achieved by using suitable radionuclides with prominent γ -lines close to the respective region of interest. In the course of the present thesis, a standardized way to approximate γ -lines for various kind of analyses has been developed and optimized. Its key feature is a universal fit model involving a modified Gaussian function and a polynomial description of the usually present Compton background.

$$f(x) = A \cdot e^{-\frac{1}{2} \left(\frac{x-\mu}{\sigma_{LR}} \right)^2} + a \cdot x + b, \quad \text{with } \sigma_{L,R} = \begin{cases} \sigma_L & \text{for } x < \mu, \\ \sigma_R & \text{for } x > \mu. \end{cases} \quad (5.7)$$

The first term in Eqn. (5.7) describes a two-sided Gaussian including a normalization factor A , the mean of the distribution μ and the standard deviation σ_{LR} with two separate values depending on the mean μ . With this parametrization, a tailing towards lower values can be modeled very accurately without requiring an arbitrary number of additional parameters. The Compton background in the peak region is assumed to be linear, expressed by the fit parameters a and b , which is in most cases a valid approximation. An impression of the linearity between the determined peak positions in FADC units using Eqn. (5.7) and the tabulated γ -ray energies is presented in Fig. 8.1 of section 8.1.2.

Another quantity that can be derived from the Gaussian approximation is the energy resolution, which is usually quoted in terms of

$$\text{FWHM} = 2\sqrt{2 \ln 2} \cdot \sigma \approx 2.3548\sigma, \quad (5.8)$$

using $\sigma = \frac{1}{2}(\sigma_L + \sigma_R)$ as an average of the resulting fit parameters. A typical example for the energy dependence of the resolution $\text{FWHM}(E)$ is depicted in Fig. 8.19 of section 8.3.4.

The usage of the modified two-sided Gaussian was firstly proposed in the Diploma thesis of T. Wester [Wes12]. In Ref. [Zat14], it was successfully implemented into the weighting factor optimization routine as described in section 5.1.2. Based on the observed robustness and reliability of the obtained results, Eqn. (5.7) became the default fit model for most of the data evaluation steps involving γ -ray calibration data of the COBRA demonstrator array. Furthermore, the developed procedure includes an automatized fit range optimization based on the χ^2 of the two-sided Gaussian. It is applied in the energy calibration of all laboratory measurements presented in this thesis, as well as for the regular calibration of the COBRA demonstrator (see section 8.1.2) and the optimization of pulse-shape discrimination techniques (see section 7.2.3). For the latter case, a short summary of alternative fit models, which were investigated in the Master thesis of J. Köttler [Küt19], will be presented.

5.2.3 Trapping correction of interaction depth

As has been mentioned in the introduction to this section, a subgroup of the collaboration developed an analytic model for the CPG-CZT event reconstruction taking into account the effect of electron trapping for both the energy and the interaction depth (see Ref. [FDG⁺13]). While in the case of the energy reconstruction, a linear correction factor could be introduced to account of the trapping and to improve the achievable energy resolution (see section 5.1.2), the electron trapping correction of the interaction depth is more complex.

As a starting point, a mean *trapping length* λ for the electrons' drift through the detector can be introduced. Consequently, the reduced charge q after a drift distance d with respect to the initial charge q_0 can be expressed as

$$q = q_0 \cdot e^{-\frac{\lambda}{d}}. \quad (5.9)$$

Because of the dependence on d , the expected anode signal's amplitudes have to be calculated with an integral form of the Shockley-Ramo theorem. The respective integration can be split into two parts assuming an ideal weighting potential as explained in the following. The first part of the electron drift is through the uniform bulk of the weighting potential with a slope of $\frac{d\varphi_w}{dz} = -\frac{1}{2}$ for CA and NCA (see e.g. Fig. 5.2). The corresponding integral using Eqn. (5.9) results in

$$s_{q_1} = \int_0^{z_0} \frac{1}{2} \cdot q_0 \cdot e^{-(z_0-z)/\lambda} dz \quad (5.10)$$

$$= \frac{1}{2} \cdot q_0 \cdot \lambda \cdot \left(1 - e^{-z_0/\lambda}\right). \quad (5.11)$$

This result is valid for both the CA and NCA. In the second part of the drift, the abrupt change of the ideal potential φ_w at the position of the anodes needs to be taken into account.

$$\Delta\varphi_w(z=0) = \begin{cases} +1/2 & \text{for CA,} \\ -1/2 & \text{for NCA.} \end{cases} \quad (5.12)$$

This leads to the following terms after the integration

$$s_{q_2}(\text{CA}) = +\frac{1}{2} \cdot q_0 \cdot e^{-z_0/\lambda}, \quad (5.13)$$

$$s_{q_2}(\text{NCA}) = -\frac{1}{2} \cdot q_0 \cdot e^{-z_0/\lambda}. \quad (5.14)$$

The combination of both drift parts results in Eqn. (5.15)–(5.16).

$$s_q(\text{CA}) = \frac{1}{2} \cdot q_0 \cdot \left[\lambda \cdot \left(1 - e^{-z_0/\lambda} \right) + e^{-z_0/\lambda} \right] \xrightarrow{\lambda \rightarrow \infty} \frac{1}{2} \cdot q_0 \cdot (z_0 + 1), \quad (5.15)$$

$$s_q(\text{NCA}) = \frac{1}{2} \cdot q_0 \cdot \left[\lambda \cdot \left(1 - e^{-z_0/\lambda} \right) - e^{-z_0/\lambda} \right] \xrightarrow{\lambda \rightarrow \infty} \frac{1}{2} \cdot q_0 \cdot (z_0 - 1). \quad (5.16)$$

In the limit of $\lambda \rightarrow \infty$, indicating the absence of electron trapping, the exponential terms can be approximated in a Taylor series using $e^{-z_0/\lambda} \approx 1 - \frac{z_0}{\lambda}$. This results in the former zeroth-order formulas Eqn. (5.3)–(5.4) as stated in the introduction to section 5.2. As in the zeroth-order case, the position dependency can be removed by a linear combination of the full expressions. In the present case, the exponential terms can be absorbed in a combination of the following form (see Ref. [FDG⁺13])

$$s_q(\text{CA}) - \left(\frac{\lambda - 1}{\lambda + 1} \right) \cdot s_q(\text{NCA}) = \frac{\lambda}{\lambda + 1} \cdot q_0 \sim E. \quad (5.17)$$

The constant factor on the right-hand side of Eqn. (5.17) will be absorbed in the energy calibration. By comparing the previous result for the weighted difference signal given in Eqn. (5.1) with the trapping corrected formula, the following relation between the empirically introduced weighting factor w and the mean trapping length λ can be derived

$$\lambda = \frac{w + 1}{w - 1}. \quad (5.18)$$

Furthermore, the zeroth-order interaction depth according to Eqn. (5.6) can be modified by using the results derived in Eqn. (5.15)–(5.16). This leads to the following expressions for the sum and difference of the anode signals

$$s_q(\text{CA}) + s_q(\text{NCA}) = q_0 \cdot \lambda \cdot \left(1 - e^{-z_0/\lambda} \right), \quad (5.19)$$

$$s_q(\text{CA}) - s_q(\text{NCA}) = q_0 \cdot e^{-z_0/\lambda}. \quad (5.20)$$

Finally, the initial charge q_0 in Eqn. (5.19) can be eliminated by converting Eqn. (5.20) accordingly. Finally, the result can be resolved for the interaction depth leading to

$$z_{\text{tc}} = \lambda \cdot \ln \left(1 + \frac{1}{\lambda} \cdot \frac{Q_{\text{CA}} + Q_{\text{NCA}}}{Q_{\text{CA}} - Q_{\text{NCA}}} \right). \quad (5.21)$$

This is the trapping corrected version of the reconstructed interaction depth, whereas the default depth will be referred to as $z \equiv z_{\text{tc}}$ in all following sections. It should be noted that Eqn. (5.21) follows the original notation with $s_q(\text{CA/NCA}) = Q_{\text{CA/NCA}}$ and that the zeroth-order formula can be derived in the limit of large λ , which would indicate a negligible electron trapping as discussed before. Regarding the event reconstruction with MAnTiCORE, the parameter λ in Eqn. (5.21) can be expressed with the help of Eqn. (5.18) using the same weighting factor as introduced in the context of the energy reconstruction.

Based on the presently discussed procedure to account for electron trapping, a similar approach will be introduced in section 7.4.4 for the trapping of holes. This novel approach makes use of dedicated long-term laboratory measurements and the present cosmic muon flux at sea level. Moreover, the effect will be evaluated for three different CZT detector types that are under investigation by the COBRA collaboration.

5.2.4 Threshold definition

In order to discriminate between physical signals and e.g. thermal noise at low energies, a so-called threshold energy E_{th} needs to be defined. In practice, the value of E_{th} depends on the trigger mode of the DAQ system and the chosen trigger settings. The trigger condition is optimized based on the typical decay rate that is encountered in a certain application and the scientific questioning – e.g. laboratory experiment, calibration measurement or physics data-taking at the LNGS. For the latter case, the trigger rate is optimized based on the intrinsic β -decay of ^{113}Cd , which dominates the low-energy range (see section 8.3).

In the light of the analytic reconstruction model discussed in the previous section, the minimum energy E_{min} that can be recorded by the readout electronics for a fixed trigger setting will depend on the interaction depth. The effect of the depth-dependent trigger is depicted in Fig. 5.5 for the example of a laboratory measurement using a single CPG-CZT detector and the radionuclide ^{137}Cs with $E_{\gamma} = 661.7 \text{ keV}$. In the respective plot, the reconstructed interaction depth versus the corresponding energy of an interaction is shown, with the observed number of counts encoded in color.

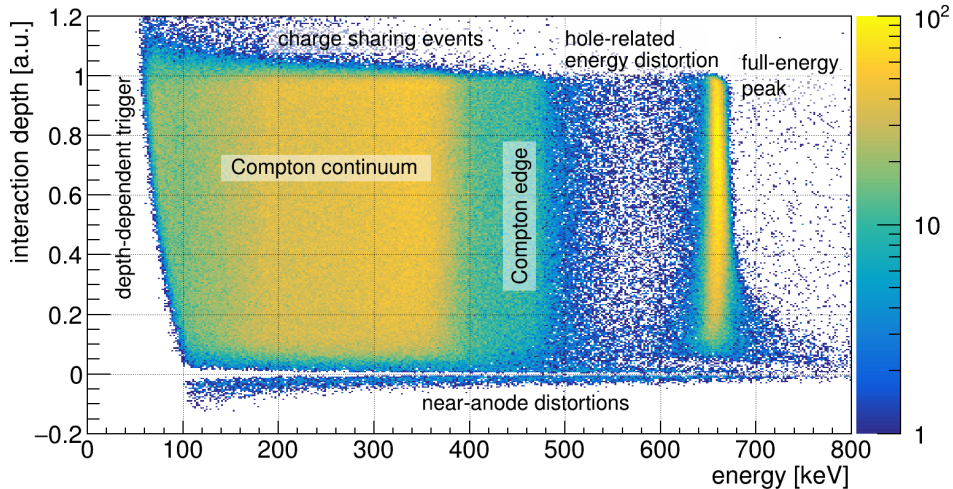


Figure 5.5: Characteristics of the analytic event reconstruction for CPG-CZT detectors. The non-uniformity of the low-energy threshold is an artifact of the applied trigger mode based on the CA signal. Above 100 keV, the Compton continuum of the ^{137}Cs de-excitation γ -line – up to the Compton edge at 477.4 keV – can be seen. As expected for the applied homogeneous irradiation of the detector volume, a uniform depth distribution is achieved in this energy range. While the same can be reported for most of the area covered by the full-energy peak, there are characteristic distortions near the position of the electrodes. For the cathode at $z = 1$, there is a small kink due to the collection of holes. On the opposite side, the distortions of the weighting potentials in the near-grid region result in a worsened energy resolution. Both areas are usually discarded by a cut on the interaction depth as discussed in section 7.1.2. Events that appear at $z > 1$ in the Compton region are typically caused by the *charge-sharing effect*. In those cases, the GB potential is not able to collect all the electrons at the CA, leading to a subdominant collection of electrons at a NCA rail. This leads to an overestimation of the interaction depth caused by an underestimation of the deposited energy.

The depth dependency can be resolved by choosing E_{th} as the minimum energy, for which the full z -range is sensitive. Depending on the actual trigger mode – dual versus single anode trigger – the following definitions are applied in the signal processing

$$E_{\text{th}} = \begin{cases} 1.05 \cdot (c_0 + c_1 \cdot \text{PH(Diff)}) & \text{for CA/NCA trigger,} \\ c_0 + c_1 \cdot (1 + w) \cdot \text{PH(CA)} & \text{for CA-only trigger.} \end{cases} \quad (5.22)$$

The parameters c_0 and c_1 refer to the linear conversion of the pulse-heights from FADC units into the calibrated energy (see e.g. Tab. 8.1 in section 8.1.2). The numerical values

according to Eqn. (5.22) enter the so-called *below-threshold cut*, which ensures a uniform exposure in the physics data-taking. In the course of the present thesis and the operation of the COBRA demonstrator at the LNGS, it was found that the CA-only trigger is more robust against noise compared to the dual electrode trigger (see also the discussion in section 7.4.2 and 8.3.3). Moreover, as the typical NCA trigger settings are usually significantly higher than for the corresponding CA channels, it was found that there is hardly any benefit of applying the dual mode in the physics data-taking. Consequently, the CA-only trigger is chosen as the default trigger mode in most of the COBRA measurements.

A general description of low-energy features close to E_{th} can be found in section 7.1.1 (review of data-cleaning cuts) and 8.2.2 (LNGS data-taking). Moreover, a detailed investigation of the threshold evolution of the COBRA demonstrator and applied measures to optimize the detector performance at low energies for the study of the fourfold forbidden β -decay of ^{113}Cd will be presented in section 8.3.3.

5.3 Monte-Carlo simulation tools

Besides the data processing tools described in section 5.1.3, the COBRA collaboration uses Monte-Carlo (MC) simulations to study the characteristics of rare nuclear decays and the detector response of different kinds of CZT detectors. Usually, important experimental parameters such as the detection efficiency or the expected background contribution cannot be measured directly. Moreover, the analytical treatment of those effects is in most cases not possible due to the complexity of the underlying physics. That is why MC simulation techniques are often the only way to obtain information on these parameters. An overview of the MC tools and methods used by the COBRA collaboration will be given in the following sections, starting with the COBRA GEANT4 simulation toolkit (VENOM).

5.3.1 VENOM

VENOM is a GEANT4 (GEometry ANd Tracking) application designed for the simulation of semiconductor detectors with its focus on different kinds of CZT geometries and their application for the search for intrinsically present double beta decay candidates. The underlying simulation framework GEANT4 [GEA03] has been developed at CERN and provides validated MC models for the passage and transport of particles through matter. It is applied by many high energy particle physics experiments, such as ATLAS and CMS, but also in space-based astroparticle physics (e.g. several ESA projects), in a wide range of nuclear and accelerator physics, as well as in medical and biological research, e.g. radiation dosimetry and ion-beam radiation therapy (see examples in Ref. [GEA16]). Due to its toolkit character, it is possible to simulate a variety of particle interactions with matter at energy scales that differ by several orders of magnitude. This includes the interactions of hadrons such as protons and α -particles, as well as the electromagnetic (EM) interactions of electrons, muons and γ -rays. At high energy scales, it is possible to calculate the cross section of such EM processes analytically. However, at the energy scale of interest for the search for rare nuclear decays or dark matter interactions at a few keV up to several MeV, those analytic calculations become unreliable. That is why there are several low-energy extensions to GEANT4, which consist in most cases of an optimized physics list and dedicated models of the EM physics at low energies such as the *Livermore* model (validation down to about 250 eV).

The physics list applied by VENOM is referred to as the *shielding* list and is recommended especially for low-background experiments in underground environments. For VENOM it is combined with GEANT4's underground physics example, whereby both are part of the

GEANT4 software release since version 9.4. The default version of GEANT4 in use by the COBRA collaboration at the time of this thesis is geant4-10.04.p02.

The development and distribution of VENOM is carried out using the version control system git. By the end of Jan.'20, the main project was moved to GitHub, an online host for git repositories, in order to achieve a more convenient way to distribute and maintain the code. The private GitHub repository is hosted by the collaboration members at TUD.

Like GEANT4, the VENOM source code is written in C++ with a close incorporation of ROOT and its distinct file format. Moreover, due to its close connection to the CERN software, it makes use of a parser for so-called Geometry Description Markup Language (GDML) files. The GDML format has also been developed at CERN and is supported by both GEANT4 and ROOT. It allows for the encoding of the experiment's geometry in a both human and machine readable data format as discussed in section 5.3.3.

Another feature of VENOM is the confining of radioactive decays within parts of the experiment's geometry such as volumes, surfaces or thin coatings. For each of these there is an optimized position generator to ensure uniformly distributed random variables as pointed out in [Köt12]. Furthermore, the generation of a primary vertex is divided into two parts, whereby the position generator is only the second step. At first, the primary particles with their characteristic energies and momenta according to the nuclear decay or physics process have to be generated. This is either done by GEANT4's internal particle gun, VENOM's single isotope (*bkggen*) or decay chain generator (*chaingen*), or by providing the initial kinematics externally. One of the key features of VENOM is its support of the DECAY0 event generator, which will be discussed in the next section. After the generation of the primary particles' kinematics, the positions of the initial vertices within the setup are generated and assigned to the particles. Both random generators can be supplied with their own seed to avoid artifacts by reusing the same initials, especially in parallel computing on multiple cores.

Further information and an in-depth description of VENOM's key features can be found in the PhD theses of T. Köttig [Köt12] and N. Heidrich [Hei14].

5.3.2 DECAY0 event generator

Although written more than 20 years ago, DECAY0 (originally referred to as DECAY4 [PTZ00]) is the most developed event generator available today for the simulation of a variety of double beta decay processes. It was originally written in *FORTRAN*, but nowadays there exist several derivative versions based on C++. A recent overview regarding the key features of DECAY0 is given in [Tre15]. As it was written at a time when GEANT4 and its internal event generators for nuclear decays did not exist, it also contains a number of α - and β -decays that are known backgrounds which might mimic the sought double beta decay signal, or are used as prominent calibration sources. The primary conditions provided by DECAY0 include the initial energies, decay times, directions and the angular distribution of the emitted particles.

In total, 40 out of 69 nuclides that are candidates for the double beta decay modes presented in section 3.1.1, including $\beta^- \beta^-$, ECEC, $\beta^+ \text{EC}$ and $\beta^+ \beta^+$, can be simulated with DECAY0. The user interface makes it possible to choose between several options such as $0\nu\beta\beta$ -decay and $2\nu\beta\beta$ -decay assuming light Majorana neutrino exchange, right-handed currents, different Majoron exchange modes and other decay mechanisms. Moreover, DECAY0 is the only known tool to provide the initial kinematics for excited state transitions involving a few excited 2^+ and 0^+ levels of the respective daughter nuclei.

The theoretical basis for the decays' analytical treatment is documented in Ref. [TZ95] and [TZ02], whereas the latter ones is an update by the same authors.

5.3.3 COBRA GDML

COBRA’s VENOM simulation tool supports the encoding of the experiment’s geometry in form of the GDML data format [CMPS06]. This includes not only the construction of the volumes composing the physical geometry, but also the definition of the applied materials as well as their properties. The syntax of a GDML file follows the XML (extensible markup language) document structure rules and contains five sections.

In the first *define* section it is possible to declare global variables such as constants, position coordinates, rotations and scales. This section is followed by either an internal *material list* or the inclusion of an external *material.xml* file. The material list contains the properties and the structure of all user-specific materials such as their densities or the chemical, respectively isotopic, compositions. This way, it is possible to define e.g. isotopically enriched CZT made from elements of cadmium, zinc and tellurium according to a fixed isotope mix. This is especially important when studying neutron interactions since the cross sections are usually strongly dependent on the isotope. Furthermore, chemical compounds such as the encapsulation lacquer can be defined by quoting the respective elements’ fractions and its known density. The next *solids* section contains a list of the actual geometry parts according to the possible basic definitions following the GDML manual [CER17]. More advanced solids of the same material can be defined by so-called *unions* and *subtraction* blocks. The second to last *structure* section combines the solids and materials to form the nested geometry tree. Usually, the position of a solid is taken as its center. Furthermore, it is possible to construct physical volumes out of several daughter volumes before they are placed into the top geometry. Finally, the *setup* section specifies which volume is the top volume including the nested geometry tree.

One of the advantages of using GDML files for the description of the MC geometry is the easy implementation of new features without having to know the details of the source code of the underlying simulation framework. Moreover, it allows for a very flexible application of the same geometry for different simulation frameworks (e.g. different GEANT4 versions) or user projects. Similarly beneficial is the close connection between the two CERN software projects ROOT and GDML, which allows for an easy and quick visualization of complex detector geometries. However, there are several open source alternatives for the visualization of GDML files such as e.g. FreeWRL. An impression of the MC geometry implementation of the COBRA demonstrator is shown in Fig. 5.6.

The simulations of the COBRA demonstrator in the present thesis are based on an improved version of the GDML implementation developed by T. Quante (formerly TU Dortmund) in the course of COBRA’s latest $0\nu\beta\beta$ -peak search analysis [COB16a]. Following this work, a review of the geometry has been performed to ensure the correct treatment of detector coincidences. Moreover, a model of a generic calibration source as shown in Fig. 5.6 has been added. The source can be placed in any of the five calibration tubes in order to compare simulated and experimental calibration data of different radionuclides that are available at the LNGS. The updated GDML files have been used in the Master thesis of J. Volkmer for the investigation of β^+EC decays of ^{106}Cd . Part of this work were the evaluation of the updated MC geometry and the optimization of the FADC’s synchronization.

In parallel, the GDML description of the XDEM 3×3 layer and its implementation into the existing framework was achieved in the course of the Master thesis of C. Herrmann [Her18]. In a collaborative effort, VENOM’s default material list was updated in 2018. This includes the isotopic composition of the elements following [IUP16], the atomic masses according to [AME17] and the related physical properties using recent material databases.

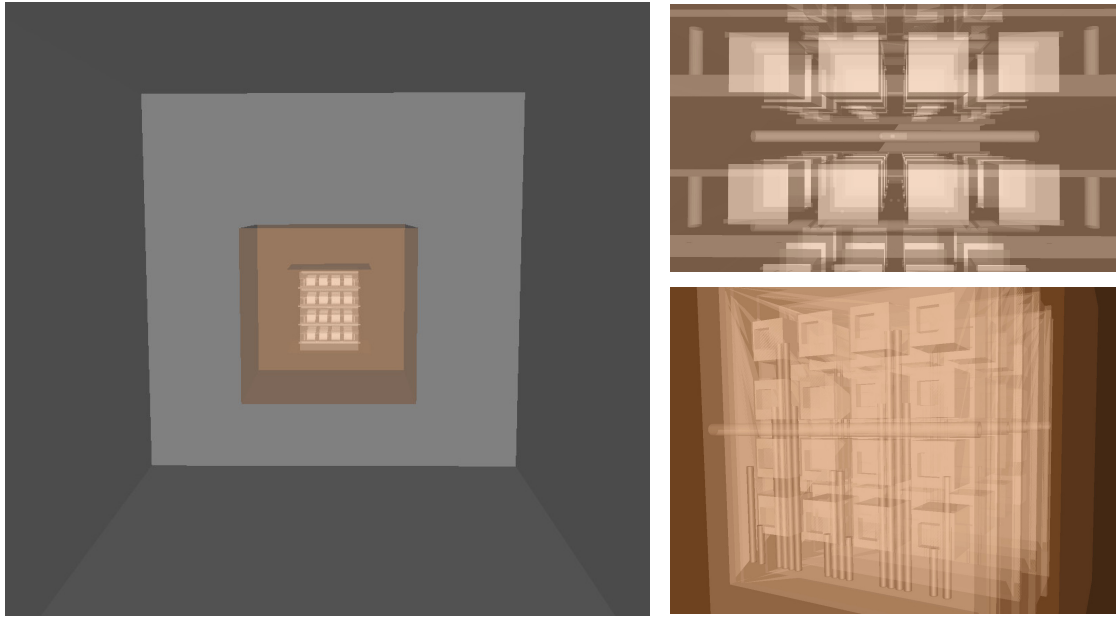


Figure 5.6: Visualization of the GDML implementation of the COBRA demonstrator using the FreeWRL viewer (version 4.3.0). *Left:* overview of the complete detector array within the inner shield made from lead and copper. *Top right:* zoom into the center of the detector array. The scene includes a calibration source, which is placed in the middle of the central calibration tube. *Bottom right:* bottom view of the first detector layer. The current modeling of the demonstrator setup includes the cathode wiring of L1 and L2. The layers installed later feature an improved HV cabling with their routing hidden inside the Delrin frames. Some pictures of the design evolution of the demonstrator layers can be found in section A.1 of the appendix.

5.3.4 COMSOL multiphysics

The COMSOL multiphysics package is a commercial software for the simulation and analysis of complex phenomena in physics [COM19]. Moreover, it is possible to couple different physics phenomena and to define non-standard materials such as CZT. The physics simulation is based on solving differential equations numerically using finite element methods. These methods require to apply a solving mesh on the defined electrode geometry, which can be directly imported from a CAD file or be defined with the internal CAD builder.

The first COMSOL simulations of COBRA’s 1 cm^3 single CPG detector’s weighting potential and electric potential were done by J. Durst in 2011 based on the outcome of his PhD thesis [Dur08]. The results of the simulation were used to develop the analytic model of COBRA’s event reconstruction (see e.g. section 5.2) and have been obtained with version 4.1 of COMSOL using the *AC/DC Module*. In the Master thesis of H. Rebber, those weighting potential calculations were repeated to use the outcome as input for a pulse-shape simulation with the aim to investigate the discrimination of α - and β -interactions [Reb15]. The applied version of COMSOL v5.0 included an additional *Semiconductor Module* to incorporate commonly used electric components of the signal readout and to offer more control over the involved microphysics. Even though COBRA’s CPG design features a guard-ring (GR) electrode, it has never been instrumented in the demonstrator phase. In fact, it remained on a floating potential in all previous simulation and experimental studies. The simulation study of weighting potentials was continued by J.-H. Arling including an instrumentation of the GR electrode for both single CPG detectors as well as for several prototypes of qCPG detectors using COMSOL v5.2 [Arl16]. Both of the more recent studies applied the physics-steered solving mesh using the *extra-fine* configuration. An overview of the investigated electrode configurations can be found in section 6.1.

Chapter 6

Characterization of CPG-CZT detectors

In order to identify and account for the potential presence of microscopic defects in monolithic CZT crystals, an extensive detector characterization procedure has been developed by the COBRA collaboration. Such defects lead to a degradation of the detector performance and cause device-specific variations, which need to be taken into account during the data analysis. The general scope of the crystal characterization is to gain knowledge about the spatial distribution of the defects and to determine the optimal working point settings for each detector in a reliable way, while maintaining a clean and contamination-free handling under laboratory conditions. Furthermore, the laboratory measurements offer the opportunity to determine important input variables as a guideline for the data evaluation and analysis, which might not be directly accessible in the final detector configuration. Moreover, the recorded data allow for a crosscheck of the event reconstruction algorithms and pulse-shape discrimination techniques. Based on the results of the characterization measurements, the best-performing detectors can be identified and selected for the installation at the LNGS.

The development of COBRA's CZT crystal characterization has been strongly driven by the TUD group and was improved continuously in multiple theses in the past. The following chapter contains a summary of the general characterization procedures with an emphasis on the improvements achieved in the course of the present thesis. As has been already pointed out before, the currently favored detector technology is based on the CPG electrode readout. An overview of the available design options is given in the first part of this chapter. Following this, the working point determination procedure and related measurement campaigns will be discussed. Finally, the last section contains a compilation of results obtained by localized γ -ray measurements in order to probe the uniformity of the crystals' quality and to validate the interaction depth reconstruction quantitatively.

6.1 Overview of COBRA’s detector technology

As has been pointed out in section 4.1.2, monolithic CZT detector designs provide the best prospects for the search for the hypothesized $0\nu\beta\beta$ -decay with respect to the experimental parameters that appear in the half-life sensitivity approximation given in Eqn. (3.10). An overview of the design options investigated by the COBRA collaboration is given in Fig. 6.1. One of the main objectives regarding the construction of a large-scale experiment (see section 4.3.5) is to achieve the instrumentation of a sufficiently large source mass, while maintaining a reasonable number of readout channels. An earlier design of the current large-scale proposal comprised about 64 000 crystals with a size of 1 cm^3 as applied in the COBRA demonstrator. However, as larger CZT crystals became available commercially in recent years, the number of crystals could be reduced to 11 520 in the current design, whereas the up-scaled single CPG lithography mask would be beneficial in terms of the required readout channels. Details on the different design options will be discussed in the following sections.

In general, the large volume crystals do not only provide an improved surface-to-volume ratio, which directly reduces the contribution of potential surface contaminants, but feature a higher intrinsic full-energy detection efficiency, which is one of the parameters affecting the achievable half-life sensitivity linearly. A comparison of the intrinsic efficiencies based on MC simulations can be found in section 8.7.1 of the analysis part. Because of those recent developments and the good prospects for eventually even larger crystals in the future, the monolithic crystal technology is clearly favored over pixelated designs.

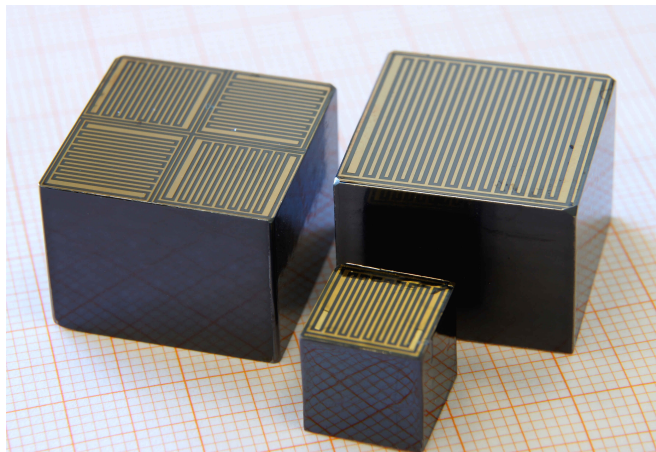


Figure 6.1: Overview of monolithic CPG-CZT detector designs investigated by the COBRA collaboration (adapted from [Geh17]). The size of the crystal in the front is $1.0 \times 1.0 \times 1.0\text{ cm}^3$ and applied in the COBRA demonstrator array. The other two prototype crystals have an increased volume of $2.0 \times 2.0 \times 1.5\text{ cm}^3$. Both the up-scaled version of the single CPG as well as the so-called quad coplanar-grid (qCPG) design have been investigated in the course of the present thesis.

As per supplier information, CZT detectors are usually provided in two different quality categories. Based on the pre-characterization by the manufacturer using standardized operation settings, some key parameters such as the energy resolution in terms of the FWHM at $E_\gamma = 661.7\text{ keV}$ for ^{137}Cs and the leakage currents are evaluated. The devices that achieve a better resolution than 4% FWHM are referred to as *spectrometer grade* detectors, while worse performing detectors with reasonable low leakage currents are simply labeled as *detector grade* quality. The better the reported energy resolution, the higher is the price per detector unit, whereas other parameters such as the full-energy efficiency are usually not monitored on the manufacturer’s side. This is why the COBRA collaboration developed its own testing procedure as will be reported later in this chapter.

6.1.1 Conventional CPG-CZT detectors

The term *conventional CPG-CZT detector* refers to a device with a single coplanar grid electrode consisting of a CA and NCA as discussed previously in section 4.1.3. The design of the COBRA demonstrator detectors is depicted in Fig. 6.2. The outer electrode is referred to as guard-ring (GR) and usually kept at a floating potential. However, it could be shown that the instrumentation of this electrode is beneficial in terms of suppression of surface events as will be briefly addressed in section 6.1.3. Both CA and NCA grids consist of nine anode rails, whereas most of the demonstrator detectors feature a preferred CA/NCA assignment. The determination of which of the grids is kept at the ground potential, indicating the CA electrode, is the first step of the characterization procedure.

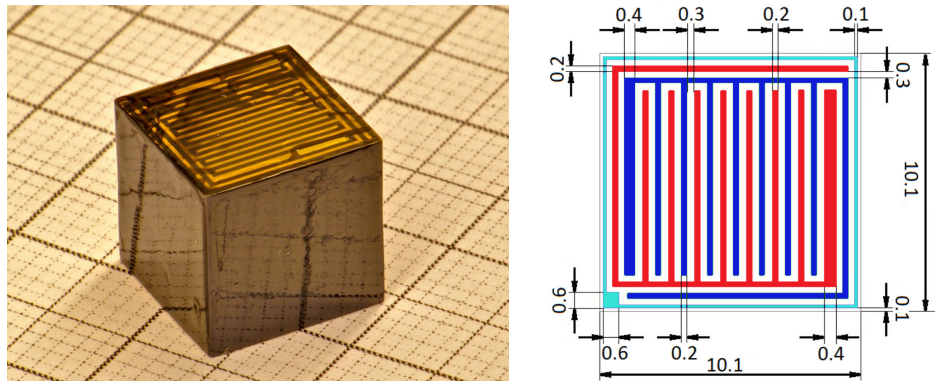


Figure 6.2: Overview of the CPG-CZT detector concept of the COBRA demonstrator. *Left:* picture of a 1 cm³ crystal with the coplanar grid anode on top. *Right:* schematic drawing of the CPG pattern with the CA (red), NCA (dark blue) and the surrounding GR electrode (cyan) (adapted from [Arl16]). The outer wider strips as well as the GR landing pad in the lower left corner are used for the electrodes' contacting. In the demonstrator phase, the GR electrode is left on a floating potential and is not instrumented.

All crystals deployed in the demonstrator array are graded as *detector quality*, which is a compromise between the affordable number of crystals and their individual performance in the early funding phase of the experiment. However, by optimizing the operation settings and the elaborate signal processing involving a correction of electron trapping effects as discussed before, the performance could be improved tremendously and is found to be on the level of spectrometer graded devices (see also section 6.2.1).

One of the limiting factors regarding the performance of a CZT detector is the occurrence of leakage currents. As the leakage currents scale with the instrumented area and the applied bulk voltage, they limit in practice the maximum dimension of the CPG design. In fact, as larger CZT crystals became available through several suppliers, the usage of different up-scaled versions of the conventional CPG design confirmed largely those limitations. This triggered the development of a novel approach referred to as the quad coplanar-grid (qCPG) technology, which will be discussed in section 6.1.2. In the collaborative development process with *Redlen technologies*, several prototype detectors with different lithography masks were produced. Among those unique prototypes were several devices that failed some of the manufacturer's pre-selection criteria, which is why they were labeled as *sample quality*. Nonetheless, one large crystal of sample quality was equipped with an up-scaled version of COBRA's conventional CPG design. This unique prototype device will be denoted as sample-CPG (sCPG) detector in the following. Its up-scaled CPG pattern consists of 14 CA and NCA rails with slightly increased widths and gaps and does not include a surrounding GR electrode. The results of its characterization will be reported in section 6.2.1.

6.1.2 Prototype qCPG-CZT detectors

The design of the qCPG electrode is depicted in Fig. 6.3. It consists of four individual CPG electrodes that are rotated against each other by 90° . This way, it is possible to keep the inner, respectively outer electrodes at the same potential resulting in a rather homogeneous weighting potential in the bulk region. The preferred option is to keep the inner electrodes at the NCA potential, providing a virtual steering grid that minimizes the effect of charge sharing close to the border of two neighboring coplanar grids. The four CPG electrodes are usually referred to as *sectors*. The grid pattern of a sector is similar to the lithography mask of the small CPG-CZT detectors, but involves smaller gaps and wider stripes in the final design. Those adjustments became necessary to make room for the implementation of the surrounding GR electrode. By dividing the anode's instrumentation into four individual sectors, the limiting leakage current problem can be resolved as the currents can be drained more efficiently. Furthermore, it allows for additional veto approaches making it possible to identify multiple-scattered γ -rays between different sectors as background for the search for the point-like energy deposition of intrinsic double beta decays. The first characterization of a qCPG-CZT detector, focusing on its electric properties as well as the spectrometric performance, has been published in [COB16c].

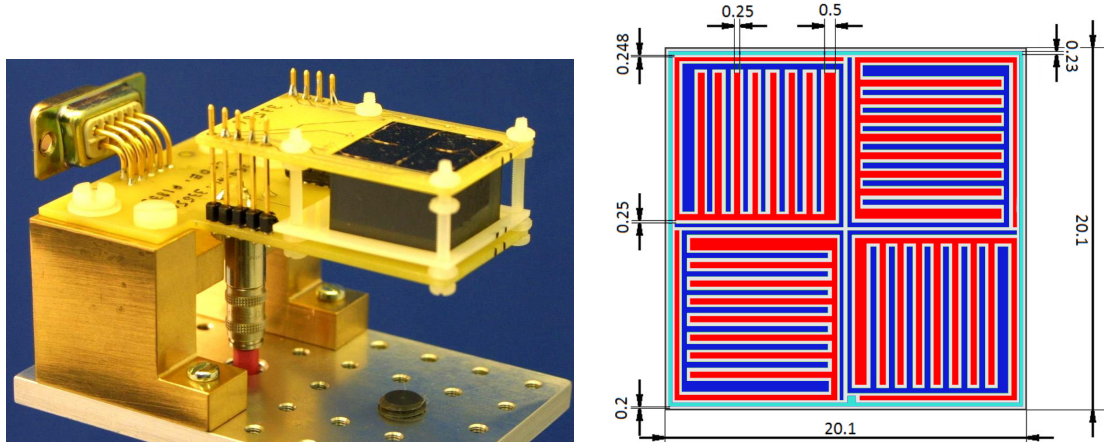


Figure 6.3: Overview of the qCPG-CZT detector concept for the COBRA XDEM upgrade. *Left:* picture of a 6 cm^3 crystal inside a PCB holder used for laboratory measurements (taken from [COB16c]). *Right:* schematic drawing of the qCPG pattern with the CAs (red), NCAs (dark blue) and the surrounding GR electrode (cyan) (adapted from [Arl16]). The outer wider strips as well as the GR landing pad in the lower middle are used for the electrodes' contacting. The GR electrode is connected to the ground potential as done for the CA.

In parallel, the investigation of the GR instrumentation (see section 6.1.3) as well as the transfer of the crystal characterization procedure from the single CPG to the qCPG concept were pushed forward. An overview of the results achieved in the characterization of the first prototype qCPG detectors based on the outcome of the Diploma thesis of K. Rohatsch [Roh16] will be given in the following sections. The collaborative work served well in the planning of the XDEM upgrade and the development of an optimized test procedure. For the actual XDEM upgrade, *spectrometer graded* detectors of two different suppliers were applied (*Redlen technologies, eV Products*). The adapted qCPG-CZT crystal characterization focuses solely on the optimization of the detector performance and was performed at the TU Dortmund. The result are documented in the PhD thesis of R. Temminghoff [Tem19].

6.1.3 Instrumentation of guard-ring electrode

The instrumentation of the GR electrode was found to be a very promising tool to veto surface events appearing in the vicinity of to the so-called lateral detector walls. While the depth reconstruction is sensitive to the distance between the planar cathode and the CPG electrode, there is no sensitivity with respect to the other two spatial dimensions. Although the characteristic distortions of the weighting potential near the detector walls can be used to discriminate between central and lateral surface events by means of the respective pulse-shapes, such as discussed in section 7.1.3, the instrumentation of the GR electrode results in an actual fiducialization of the detector volume.

The effect of the GR instrumentation was both studied with COMSOL multiphysics simulations and suitable charge diffusion models as well as in dedicated laboratory experiments in the Master thesis of J.-H. Arling [Arl16]. It could be confirmed that setting the GR electrode to ground potential, defining it as an additional CA electrode, results in the collection of charge clouds created close to the lateral detector surfaces. Experimentally, those near surface interactions were created with the help of a pre-collimated ^{241}Am α -source ($E_\alpha = 5.5\text{ MeV}$). On the contrary, a ^{232}Th source was used to monitor the overall γ -ray detection efficiency ε_γ for the case of an instrumented and floating GR. It was found that α -particle interactions close to the surfaces can be suppressed by a factor of $S_\alpha = 5300^{+2660}_{-1380}$, while maintaining an acceptance of bulk events induced by the γ -ray interactions of about $\varepsilon_\gamma = 85.3 \pm 0.1\%$. The results have also been published in [COB17].

It should be noted that the GR electrode only needs to be instrumented in the sense that the respective potential needs to be applied, while the readout of the charge signal is not necessary for the veto to work as intended. However, additional information about the vetoed events such as the deposited energy can only be accessed by recording the GR signals. This subject remains as an open topic in the qCPG event reconstruction. For the XDEM setup, the GR are recorded but have not yet been taken into account in the event processing.

6.2 Homogeneous γ -ray measurements

The following section is a brief summary of the CZT crystal characterization procedure developed at TUD in the preparation of the COBRA demonstrator and the XDEM upgrade. The first and mandatory step is the determination of the optimal combination of the applied biases BV and GB, which is referred to as the *working point setting*. In order to achieve a trustworthy and reliable statement for each crystal, independent from local performance variations, a uniform irradiation of the detector volume with a ^{137}Cs γ -ray source is ensured. Following this, dedicated measurements at the working point are performed to access the absolute full-energy detection efficiency. Besides those mandatory measurement campaigns, several specialized laboratory experiments have been performed at TUD, which will be shortly discussed in the last part of the present section.

6.2.1 Working point determination

The aim of the working point determination is to find the optimal combination of the applied bulk voltage (BV) and grid bias (GB). This way, the individual detectors' performance can be improved significantly, whereas the specifications quoted by the manufacturer of the demonstrator crystals have been surpassed for the majority of the investigated devices. The general procedure has been developed in the Diploma theses of A. Sørensen [Sør11] and T. Wester [Wes12]. In the follow-up work reported in [Zat14], the determination of the weighting factor has been revised (see e.g. section 5.1.2). A detailed review of the hardware

aspects of the developed laboratory infrastructure at TUD can be found in the PhD thesis of D. Gehre [Geh17]. In the following, the general experimental procedure will be briefly summarized with an emphasis on the results obtained in the course of the present thesis.

Experimental procedure

As there is an interplay of multiple effects related to the applied BV and GB, the working point needs to be determined experimentally by varying both biases in a given range and step size. For each BV-GB combination, the γ -ray spectrum of a ^{137}Cs source of about 250 kBq activity is taken to determine several detector-specific quantities such as the energy resolution and the charge collection efficiency (CCE). As the procedure is not only time but storage consuming, all experimental parameters such as the bias steps, the energy threshold, the distance between source and crystal and the required irradiation time per bias combination have been thoroughly optimized in previous theses. Details can be found in e.g. [Geh17].

Regarding the data evaluation and processing, the same routines as presented in section 5.1.2 and 5.2 are applied. This includes an optimization of the weighting factor for each bias combination and the use of the standard event selections which will be discussed in section 7.1. Some of the experimental results will be discussed in the following.

Conventional CPG-CZT detectors

The original procedure of the working point determination was developed in the construction phase of the COBRA demonstrator array based on the available CPG-CZT detector pool at that time. In Fig. 6.4, the bias range applied for the characterization of those 1 cm^3 volume crystals and some of the results obtained for a single detector are shown. The BV is usually varied between 900–1500 V in steps of 100 V and the GB between 40–100 V in steps of 10 V. In the beginning, the main quantity considered for the determination of the working point was the energy resolution in terms of FWHM that was achieved for the ^{137}Cs full-energy peak (FEP). Furthermore, the CCE as derived from the position of the FEP and the integral over the peak range were taken as secondary criteria.

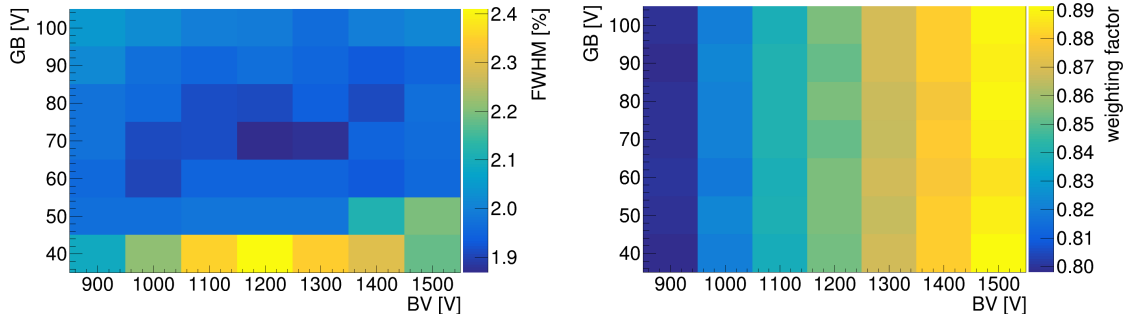


Figure 6.4: Illustration of the working point determination for a CPG-CZT detector (Det102) using ^{137}Cs . *Left:* dependency of the energy resolution in terms of FWHM at 661.7 keV on the applied BV and GB. The optimum performance is found for the combination $\text{BV}/\text{GB} = 1200/70\text{ V}$. *Right:* dependency of the optimal weighting factor. The weighting factor is optimized for each BV-GB separately. The observed distribution confirms the expected dependence on the applied BV, whereas the GB causes only small variations.

With respect to the BV, there are two mainly opposite effects that dominate the detector performance (see e.g. Ref. [AAGI14]). For an increasing BV, the CCE and FWHM are expected to improve as they are affected by the mean drift length which scales linearly with the applied potential. At the same time, a tailing of the FEP towards lower energies is expected to be reduced. The positive effects related to an increase of the applied BV is

highlighted in Fig. 6.4 for the example of the optimal weighting factor and its observed BV dependency. For higher BV, the weighting factor tends to approach the ideal case of $w = 1$. On the other hand, the leakage current between the cathode and the anodes increases with BV as well, although not linearly or in an easily predictable way. In general, a higher leakage current leads to an increase of signal noise, which might worsen the energy resolution such as observed in the example depicted in Fig. 6.4. Because of the interplay of those two effects, the optimal BV has to be determined experimentally.

A similar relationship exists for the GB. It needs to be high enough to provide a sufficient definition of the CA and NCA potentials to avoid a charge sharing between both electrodes, but is usually limited by the occurrence of inter-grid leakage currents. Although charge sharing is expected to only marginally affect the achievable energy resolution, causing a tailing of the FEP towards lower energies, it can alter the full-energy detection efficiency significantly. Moreover, there is a certain interplay between the BV and GB as the strength of the charge sharing depends also on the ratio of both biases. This is why the optimization of the operation settings cannot be done separately but needs to be done for a set of BV-GB combinations. A complete compilation of the working point optimization results for the detectors of the COBRA demonstrator array is given in Tab. E.1 – E.4 in the appendix.

Characterization of prototype detectors

Based on the same procedure, the characterizations of the first prototype 6 cm^3 detectors were performed at TUD. In the course of the Diploma thesis of K. Rohatsch, the original laboratory infrastructure and data processing scheme was upgraded with respect to the requirements for the operation of qCPG-CZT detectors. This work has been carried out in close cooperation with the author of the present thesis. Furthermore, several additional quantities were introduced to complement the working point determination. Exemplarily, some of the combined results for a fully functional prototype detector are shown in Fig. 6.5. The single sector results can be found in Fig. D.10 – D.13 in the appendix.

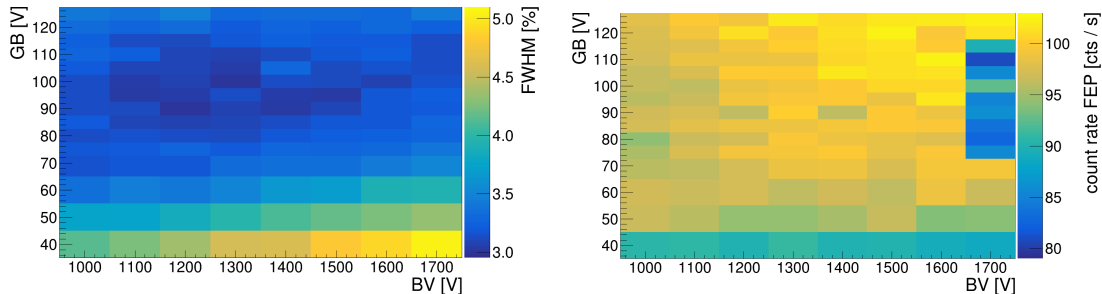


Figure 6.5: Results of the working point determination measurements for a 6 cm^3 prototype qCPG-CZT detector (Redlen-33556). The depicted results are a combination of the single sector results that can be found in Fig. D.10 – D.13 in the appendix. In the present case, the global working point has been determined as $\text{BV}/\text{GB} = 1300/100\text{ V}$ as a good compromise of the individual sectors' preferences.

One of the main objectives of the early studies was to investigate whether all outer electrodes should be operated as either CA or NCA. Essentially, no significant differences could be reported, which is why the preferred option as indicated in Fig. 6.3 was chosen as the default. This requirement was added to the list of mandatory functionality checks that were performed by the manufacturers of the XDEM detectors prior to the shipment of the devices. Furthermore, it was found that the majority of the investigated qCPG-CZT detectors were not benefiting from the opportunity of applying an individual GB to the single sectors, which entered the design planning of the XDEM setup. However, one particular problem

that occurred during the characterization of the first prototype detectors was the limitation of the BV to about 1.6 kV due to the insufficient certification of parts of the DAQ electronics. Consequently, new pre-amplifier boxes and updated HV board designs were developed at the electronics workshop of the TU Dortmund. Moreover, a more robust contacting scheme was developed in the course of [Tem19] at the same institute, which is why the characterization of the final XDEM detector pool has been carried out at the TU Dortmund as well. This way, the contamination risk could be kept at an absolute minimum, while the updated working point procedure served as a guideline for the work reported in [Tem19].

Finally and for the sake of completeness, the characterization of the unique sCPG detector has been performed in the course of the present thesis. The procedure makes use of an even more extended parameter space, while an upgrade of the DAQ electronics allows to extend the BV range to a maximum of 2300 V. However, because of the poor crystal quality, the results are partly inconclusive as reported in Fig. 6.6 and can only be evaluated quantitatively.

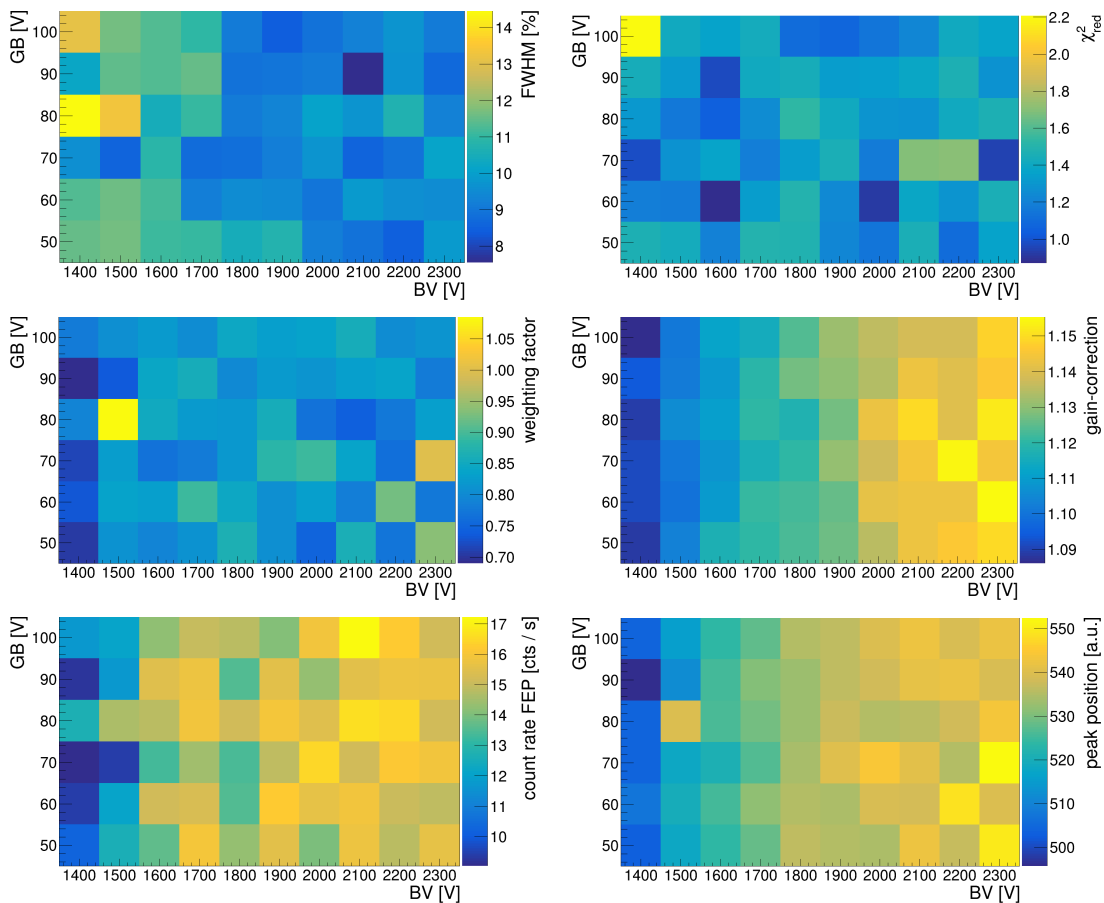


Figure 6.6: Results of the working point determination measurements for the 6 cm³ sCPG-CZT detector. Because of its rather poor performance, the evaluation of the data can only be done quantitatively. The point of best performance is found for BV/GB = 2100/90 V, whereas the actually determined FWHM is likely caused by a fluctuation with respect to the surrounding points in the BV-GB parameter space. However, the distribution of the χ^2_{red} values of the FEP fit is rather flat. The same applies to the distribution of the weighting factor, whereas the usually constant gain-balancing correction seems to depend on the applied BV. The latter two observations contradict with the expectation for a fully functional detector. On the other hand, the distribution of the integral count rate in the FEP and the dependence of the peak position in FADC units as a measure of the charge collection efficiency agrees well with the expected behavior.

Nonetheless, it should be noted that the up-scaled single CPG detector design might still be of interest for a future large-scale COBRA experiment as most of the reconstruction steps

can be directly transferred from the well-understood detector concept of the demonstrator array and the fabrication of high-quality large volume CZT crystals is progressing very fast. Moreover, while the readout of a qCPG-CZT detector requires eight anode channels (neglecting the optional GR readout), the single CPG design only requires a fourth of the readout channels for the same instrumented volume. This can help to keep the number of readout channels reasonably low. Last but not least, there are excellent prospects to transfer the pulse-shape discrimination techniques that were developed for the background suppression in the COBRA demonstrator to larger CPG-CZT detectors, whereas their application for qCPG-CZT detectors needs to be investigated thoroughly in future studies.

6.2.2 Absolute full-energy efficiency

Following the working point measurements, the second step of the detector characterization is the determination of the absolute full-energy efficiency $\varepsilon_{\text{FE}}(^{137}\text{Cs})$. This quantity is a measure for the efficiency to observe a full-energy deposition of the de-excitation γ -ray of $E_\gamma = 661.7 \text{ keV}$ within the detector. Its determination is based on the following relation between the observed FEP entries N_{FEP} , the source activity A and irradiation time t , the relative emission probability of the de-excitation γ -ray I_r , the effectively irradiated area F_{eff} , as well as the distance r between the center of the source and the CPG-CZT detector.

$$N_{\text{FEP}} = \frac{\varepsilon_{\text{FE}} \cdot A \cdot t \cdot I_r \cdot F_{\text{eff}}}{4\pi \cdot r^2} \quad (6.1)$$

The denominator in Eqn. (6.1) denotes the spherical surface that is irradiated by the source in dependence on the distance. The actual source activity is calculated from the initial value for each date of the respective measurements to account for the fading activity over the course of the characterization of all 64 crystals of the demonstrator array. The intensity of the ^{137}Cs γ -line is $I_r = 85.1(2)\%$ [NDS20]. The effective area F_{eff} refers to the side of the crystal that faces the source. It is estimated as 1 cm^2 and corrected by a factor taking into account the known crystal mass and density of CZT. A direct measurement of the crystal dimensions is avoided to prevent the danger of damaging the device. Moreover, the measurable dimension would need to be corrected for the thickness of the encapsulation.

In order to remove events that are affected by the distortions of the weighting potential in the vicinity of the CPG anode and the hole contribution close to the cathode, a cut on the interaction depth is applied before determining the peak entries in the ^{137}Cs FEP. The usual standard- z cut is defined as $0.2 < z \leq 0.97$ and will be motivated in more detail in section 7.1.2. By using the two-sided Gaussian fit as presented in Eqn. (5.7), the number of peak entries can be determined from the integral over a $\pm 3\sigma$ range around the mean of the peak position. This range corresponds to a Gaussian coverage of 99.73% (see section C.2 in the appendix). The peak integral is corrected by a simple background projection over the range of $[-6\sigma, -3\sigma]$ and $[+3\sigma, +6\sigma]$, which finally results in N_{FEP} .

As all parameters in Eqn. (6.1) besides the efficiency ε_{FE} can be determined independently, the value of ε_{FE} can be derived from a $1/r^2$ fit such as illustrated in Fig. 6.7. Usually, each crystal is irradiated for three to five different distances between detector and source, which is sufficient for the simple fit model to converge. A complete compilation of the individual results obtained for the demonstrator's detector pool in the course of the present thesis can be found in Tab. E.1–E.4 of the appendix. The observed variations can be used as prior knowledge in the analysis of the COBRA data such as briefly discussed in section 8.7. The same approach was applied in the latest $0\nu\beta\beta$ -peak search analysis reported in Ref. [COB16a].

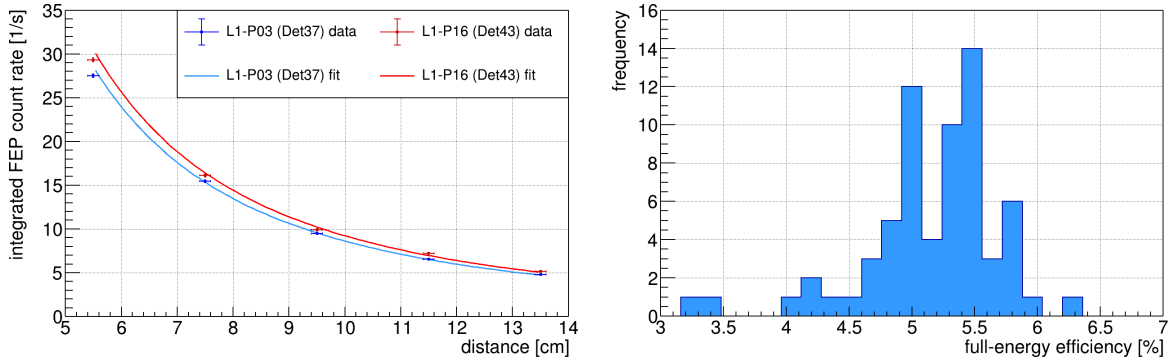


Figure 6.7: Determination of the absolute full-energy efficiency for homogeneous ^{137}Cs irradiation measurements at different distances. *Left:* fit results for two single detector examples. The resulting efficiencies are $\varepsilon_{\text{FE}}(^{137}\text{Cs}) = 5.42 \pm 0.26\%$ for Det37 (L1-P03) and $\varepsilon_{\text{FE}}(^{137}\text{Cs}) = 5.74 \pm 0.29\%$ for Det43 (L1-P16). *Right:* distribution of all single detector results. The mean of the distribution is $\bar{\varepsilon}_{\text{FE}}(^{137}\text{Cs}) = 5.17 \pm 0.03\%$.

6.2.3 Additional laboratory studies

Besides the working point determination, several specialized measurement campaigns were performed for a subset of the available CPG-CZT detector pool during the commissioning of the COBRA demonstrator. The following section is a very brief summary with the focus on laboratory studies performed at TUD. Further investigations have been performed at the University of Hamburg (operation of CZT detectors in liquid scintillator [Old15]) and at the TU Dortmund (localized α -irradiation [Teb16]).

Temperature studies

The temperature behavior and its effect on the working point settings was originally studied in the Bachelor thesis of L. Schröder [Sch12] in 2012. The main focus was set on the detector technology and electronics planned to be used for the demonstrator array. In 2017, a reevaluation of the data was performed in the Bachelor thesis of T. Kreße [Kre17] by using the updated signal processing routines and evaluation steps developed in the course of [Zat14] and the present thesis. A compilation of the results can also be found in [Geh17].

The temperature studies provided valuable input for the investigation of the low-energy β -decay of ^{113}Cd and the optimization of the demonstrator setup towards minimum threshold operation as will be presented in section 8.3 of the analysis chapter.

Discrimination of α - and β -interactions

In order to investigate the discrimination of α - and β -interactions by means of the associated pulse-shapes, several small-scale laboratory experiments were performed in the past. One of those involved the irradiation of a CPG-CZT detector with quasi monoenergetic neutrons that were produced in a D-T generator (deuterium-tritium fusion), while the detector was actively read out. The original motivation was to search for intrinsic (n, α) and (n, p) reactions and to select a statistical sample for those intrinsic events on the pulse-shape level. However, the neutron-induced background turned out to dominate the recorded energy spectra, which prevented the identification of clear shape features. The results of these investigations can be found in the Diploma thesis of F. Kandzia [Kan14].

After the crystal characterization and selection of the best-performing detectors for the demonstrator setup were finished, the existing laboratory infrastructure and remaining CPG-CZT detector pool were used for several special calibration runs. In contrast to the previous

attempt, a simpler experimental approach was chosen. Instead of producing intrinsic α - or β -interactions over the complete crystal volume, only the case of near-cathode events was investigated. This idealization is expected to produce the most severe differences as the created charge clouds need to drift through the entire bulk. The applied radioactive sources were a mixed $^{239}\text{Pu}/^{241}\text{Am}/^{244}\text{Cm}$ α -source and a $^{90}\text{Sr}-^{90}\text{Y}$ β -source of a few kBq activity. The evaluation of the recorded data revealed a rather weak statistical separation between α - and β -interactions as reported in the Master thesis of H. Rebber [Reb15] and in [Geh17].

Lastly, the monitoring of an active nitrogen flushing system to prevent the build-up of radon and its radioactive daughters on the crystal surfaces and its effect on the performance of CPG-CZT detectors has been studied in the Bachelor thesis of A. Hemmetter [Hem16].

Pulse-shape studies

In Ref. [Zat14], an additional laboratory setup was developed to collect a pulse-shape library of interactions that are topologically similar to the expected signatures of double beta decays. An overview of the developed setup and the collected data will be presented in section 7.3. Furthermore, several special calibration runs with a natural ^{232}Th sample were performed in the course of the present thesis that served as guideline in the development of a new pulse-shape discrimination approach (see section 7.2.2). Finally, the existing laboratory infrastructure was used to perform multiple long-term background measurements with three different CZT detector designs with the aim to study the characteristics of interactions induced by cosmic muons. The interpretation of the collected data culminated in an analytic model of the event reconstruction which could also be transferred to the LNGS setup. This subject will be discussed in detail in section 7.4.

6.3 Localized γ -ray measurements

Besides the previously discussed investigations involving a homogeneous irradiation of the CZT detectors, a scanning device with a highly collimated ^{137}Cs γ -ray source of about 100 MBq activity was developed at TUD to probe the uniformity of the detector response. As for the working point measurements, the emitted de-excitation γ -rays can penetrate deeply into the detector bulk, while providing a high probability for photoelectric absorption in CZT. Moreover, it is possible to construct a reasonably sized source container to achieve a good collimation. Some pictures of the laboratory setup and the collimator can be found in section B.1 of the appendix. The collimation allows for a localized irradiation on the scale of 1 mm², while the source container is mounted on a computer-controlled *x-y*-table with two stepper motors with micrometer precision. The CZT detector mount as well as the *x-y*-table can be rotated in multiple ways giving access to four detector sides. Details on the scanning setup can be found in past theses such as [Sör11], [Wes12] and [Geh17].

In the course of the present thesis, a detailed review of the collected scanning data of the COBRA demonstrator detectors was performed. This includes a pre-selection on the raw data level to improve the fraction of full-energy events with respect to the dominating Compton background and the noise induced by the electronics of the stepper motors, as well as the processing of the complete data set with MAnTiCORE. This way, the scanning data is well prepared for future studies that might affect the analysis of the LNGS physics data.

Furthermore, the scanning procedure could be transferred to the novel qCPG-CZT detector approach in [Roh16] and the present work. Some results of the localized investigations will be presented in section 6.3.2. One particular application of the scanning data is the experimental validation of the zeroth-order and trapping corrected depth reconstruction. A brief summary on this subject is given in the final section.

6.3.1 Review of COBRA demonstrator data

For the spatially resolved mapping of the detector response of the demonstrator crystals with a nominal surface area of $10 \times 10 \text{ mm}^2$, a default raster of 12×12 scanning points with a step width of 1 mm is applied. For each scanning point, an irradiation time of 10 min is chosen, resulting in a total acquisition time of about 24 h per side. The raster size and acquisition time ensure a sufficient coverage of the sensitive volume and good statistics of full-energy events. For most of the demonstrator detectors, two scans were performed – one from a lateral side and one from the anode, whereas the detector is operated at the point of best performance as determined in the previous working point measurements. The combined information allows for a three-dimensional projection of the detector response as demonstrated in [Wes12] and [Geh17]. Although the scan from the anode side could already be used for a three-dimensional projection by making use of the depth reconstruction, the additional side scan allows for an independent crosscheck of the linearity of the depth reconstruction for each detector (see also section 6.3.3). For some devices, there exist complete mappings of all four accessible sides, which were used for intense analyses of local performance variations in the past.

The main objective of the localized performance studies is the mapping of the local charge collection efficiency (CCE). This quantity can be derived from an approximation of the ^{137}Cs FEP using the procedure described above in the determination of the optimal working point settings. As most of the derived quantities that are of interest in the localized performance study are related to the FEP, while in practice the recorded data are dominated by a strong Compton background as a result of the applied collimation of the highly active γ -ray source, a pre-selection of the scanning data has been performed in the course of the present thesis. This measure aims to improve the fraction of full-energy events by introducing an increased energy threshold that is based on the analytic threshold definition as discussed in section 5.2.4. It is chosen as $E_{\text{th}} \geq 300 \text{ keV}$ so that the Compton edge at $E_C(^{137}\text{Cs}) = 477.4 \text{ keV}$ (see e.g. Fig. 5.5) is still contained in the pre-selected data. For most of the data sets, this corresponds to an increase of the original threshold by about a factor of two. This way, the energy range that is dominated by the noise originating from the electronics of the stepper motors can be effectively discriminated. For higher signal amplitudes, the noise influence gets reduced by the usage of the robust MWA energy reconstruction (see section 5.2.1). By using the mapping between the processed data and the raw data, it is possible to discard all recorded pulse-shapes that belong to *below-threshold events*. It was found that the pre-selection rejects about half of the originally recorded data without limiting the information content with respect to full-energy events. A summary is presented in Tab. 6.1.

Table 6.1: Summary of the pre-selection results for the entire two-dimensional scanning data recorded in the course of the characterization of the COBRA demonstrator detectors. For most of the installed detectors, there have been scans of at least two sides. By applying the pre-selection with a threshold of $E_{\text{th}} \geq 300 \text{ keV}$ on the pulse-shape level, about half of the original raw data turn out to be *below threshold* and can be excluded from the data processing and evaluation. The differences in the *below threshold fraction* for L1/L2 and L3/L4 are the result of higher initial threshold settings for the latter measurement campaigns.

2d-scans	sides	raw data	pre-selection	below threshold fraction
L1	40	1961 GB	736 GB	62.5%
L2	29	1343 GB	467 GB	65.2%
L3	32	692 GB	526 GB	24.0%
L4	32	490 GB	361 GB	26.3%
additional	11	391 GB	171 GB	56.3%
total	144	4877 GB	2261 GB	53.6%

After finalizing the pre-selection of the raw data, all data sets were processed with the most recent version of MAnTiCORE to provide the basis for future analyses. Exemplarily, some impressions of the updated evaluation of the two-dimensional mapping of the detector response are depicted in Fig. 6.8. The peak position of the FEP is a measure of the CCE. In the present example, the absolute variation of the peak position of about 10 keV is compatible with the mean energy resolution of $\text{FWHM} = 1.87\%$ at the working point (see Fig. 6.4), which corresponds to an absolute FWHM of 12.4 keV. The two-dimensional mapping of the relative FWHM is affected by the noise introduced by the electronics of the stepper motors, but confirms nonetheless the uniformity of the crystal. The same applies to the observed variation of the FEP fraction, referring to the integral over the FEP divided by the total integral, which is also compatible with statistical fluctuations.

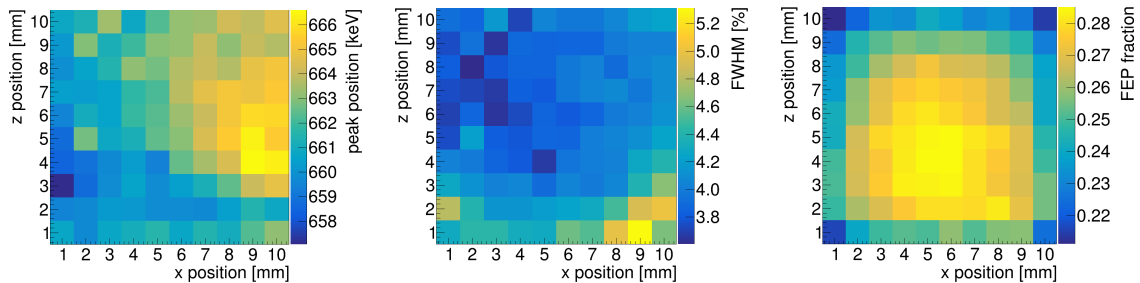


Figure 6.8: Exemplary results of the two-dimensional γ -ray scanning of a side wall of a 1 cm^3 CPG-CZT detector (Det102). *Left:* mapping of the peak position of the ^{137}Cs FEP as a measure of the local CCE. *Middle:* mapping of the relative FWHM. *Right:* mapping of the FEP fraction based on a $\pm 3\sigma$ integral of the peak region. The determination of all parameters is based on the two-sided Gaussian approximation as presented in Eqn. (5.7) and the processed data after the pre-selection step.

6.3.2 Localized characterization of qCPG-CZT detectors

As soon as the working point settings were determined for the first qCPG-CZT detectors, their local detector response was studied extensively. This section is a brief summary of the characterization results obtained in the Diploma thesis of K. Rohatsch [Roh16]. First of all, it should be noted that due to the increased crystal size, the raster of the localized γ -ray scanning had to be increased to 17×22 for a side wall scan and to 22×22 for the anode side. In order to achieve similar statistics per sector as for the previous 1 cm^3 crystals, the same acquisition time of 10 min per scanning point is chosen. However, this increases the total scanning time per side to about 60 – 80 h depending on the actual raster. Moreover, the study of the crosstalk between the different sectors requires to record all anode signals for a single sector trigger, which increases the number of recorded pulse-shapes by at least a factor of four. Because of this, it is not possible to implement a meaningful pre-selection of the raw data as the crosstalk is expected to appear below the typical trigger threshold. This is why in practice a complete two-dimensional scan of a 6 cm^3 crystal requires the long-term storage of several hundred GB of raw data. In the preparation phase of the COBRA XDEM upgrade, most of the available prototype qCPG-CZT detectors were characterized thoroughly, whereas none of the final XDEM detectors has been scanned at TUD to prevent any contamination during the comparably long operation time in the scanning setup. This step might be caught up on as soon as the XDEM phase is completed.

Some impressions of the localized characterization of the previously highlighted prototype labeled as Redlen-33556 (see Fig. 6.5) can be found in Fig. 6.9 and Fig. 6.10. In both cases, the results of a side wall scan are compared for two different processing methods. The first approach is to apply a global weighting factor for each of the four independent sectors as

determined in the global working point measurements. Alternatively, the weighting factor is optimized locally for each scanning point using the same procedure as for the global analysis.

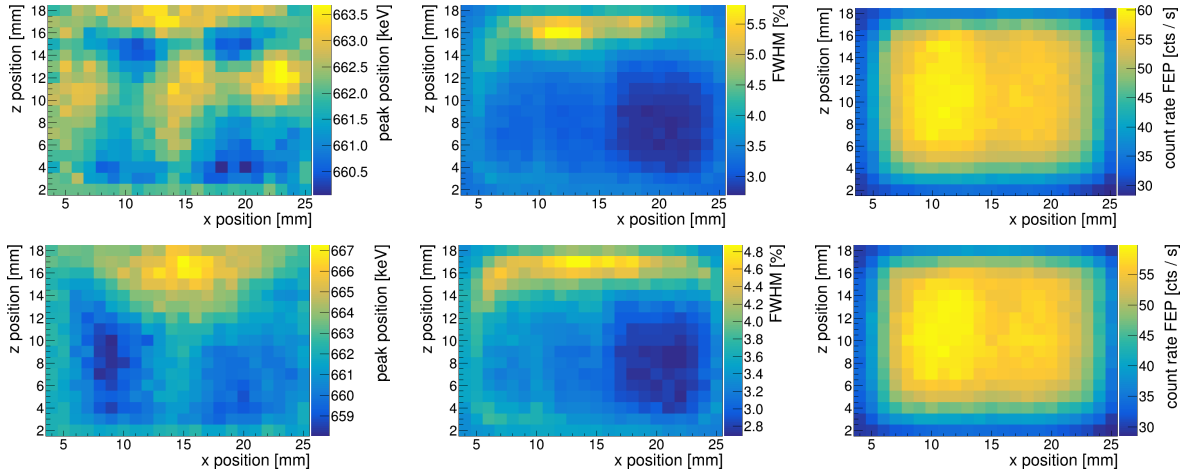


Figure 6.9: Localized ^{137}Cs γ -ray scanning of one side of a qCPG-CZT prototype detector (Redlen-33556). *Top*: characterization results using a global optimized weighting factor for each sector. *Bottom*: characterization results based on a local optimization of the weighting factor for each sector and scanning point. The latter approach results in a slightly more homogeneous distribution of the parameters of interest. However, the observed near-grid features such as a worsened energy resolution remain. On the other hand, the very small variation of the FEP peak position and the uniform distribution of the integral count rate of the FEP indicate a very homogeneous charge collection efficiency, independently of the applied weighting factor optimization.

Independently of the applied weighting factor optimization, a worsening of the energy resolution in the near-grid region is observed. This is a general finding for all investigated prototype detectors and can be interpreted as the limit of the current stage of the event reconstruction based on the combination of the single sector results as presented in [Tem19]. Moreover, the effect seems not to be related to multi-sector events, where the full-energy is shared between multiple sectors such as shown in Fig. 6.10. Instead, the stronger distortions of the weighting potential are expected to be the root cause of it (see e.g. [Arl16]). As the final qCPG layout of the XDEM detectors is slightly different from the investigated prototypes, the effect might not be as severe in this case. Nonetheless, localized performance studies should be performed after the XDEM operation at the LNGS is completed.

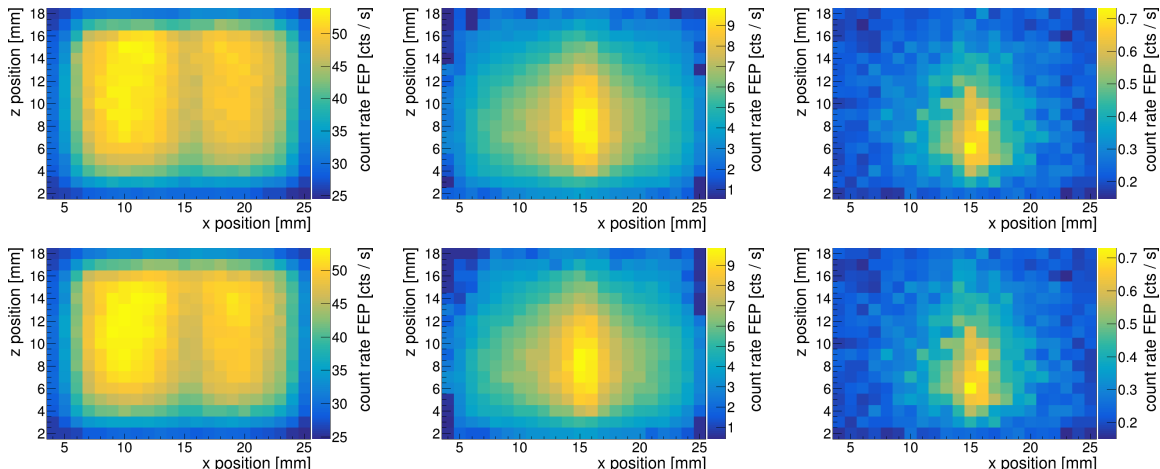


Figure 6.10: Distribution of multi-sector full-energy events for a localized ^{137}Cs γ -ray scanning of one side of a qCPG-CZT prototype detector (Redlen-33556). The plots show from left to right the distribution of *single-sector*, *two-sector* and *three-sector* events for the case of a global (*top*) or local weighting factor (*bottom*).

6.3.3 Validation of depth reconstruction

A particular application of the localized γ -ray scanning data is the quantitative validation of the interaction depth reconstruction for the different kind of CZT detectors that are investigated in the framework of the COBRA experiment. The concept of using collimated γ -ray sources to probe the performance of the interaction depth reconstruction for conventional CPG-CZT detector was already discussed and applied in some of the earliest publications related to the topic of depth-sensing devices (see e.g. [HKW⁺96] and [HKWM97]). Regarding previous studies related to the 1 cm³ CPG-CZT detectors as applied in the COBRA demonstrator, similar studies can be found in [Wes12] and [Teb16]. More recently, a quantitative validation has been performed in [Tem17]. Some of the results are depicted in Fig. 6.11 and will be discussed in the following.

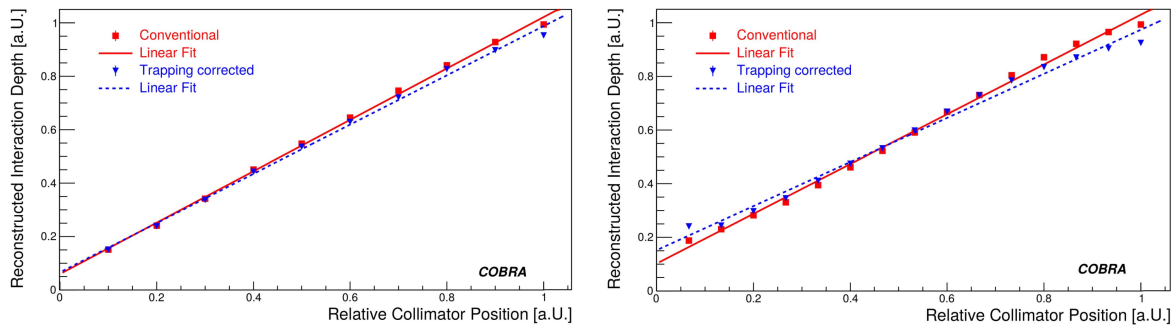


Figure 6.11: Quantitative validation of the depth reconstruction for different kinds of CPG-CZT detectors using the central γ -ray scanning data along the z -axis (taken from [Tem17]). *Left:* conventional 1 cm³ CPG-CZT detector. *Right:* novel 6 cm³ qCPG-CZT detector. For both of the depicted examples, the conventional zeroth-order depth reconstruction (red squares) and the respective trapping-corrected versions (blue triangles) are shown. In all cases, a good linearity between the relative position of the collimator and the reconstructed interaction depth can be observed, which is indicated by a linear approximation. The assigned uncertainties on each data point are too small to be visible due to the high statistics achieved in the scanning measurements.

For the conventional CPG-CZT detectors, the zeroth-order and trapping corrected depth reconstruction formulas have been derived in section 5.2.3. The quantitative validation of those formulas is based on a subset of the two-dimensional scanning data. In the present example, the data were selected as the line corresponding to the central position along the z -axis. However, similar results are obtained for deviating positions from the arbitrarily chosen central position. For each data point, the mean of the reconstructed depth spectrum is approximated with a simple Gaussian plus a polynomial fit to account for a linear background component due an imperfect collimation of the γ -ray beam. Furthermore, only events in a $\pm 3\sigma$ range around the FEP are considered. Following this, the reconstructed mean position is plotted against the relative collimator position along the z -axis. The collimator position has been normalized to the same range of values as obtained for the reconstructed quantity. A linear approximation of the data points confirms a good linearity between the two position parameters for both reconstruction formulas, whereas the trapping corrected version limits the z -range to the physical detector dimensions and significantly improves the achievable depth resolution (see e.g. Ref. [FDG⁺13]). The small deviations observed for the position of the cathode at $z = 1$ are caused by an increasing asymmetry of the z -peak for positions close to the edges. Moreover, the depth resolution gets worse near the anode due to the characteristic distortions of the weighting potential in the near-grid region.

In the case of the qCPG approach, the anode signals of all four sector pairs need to be combined in order to obtain a realistic estimate of the magnitude of the cathode signal. This

modifies the original zeroth-order formula given in Eqn. (5.6) to

$$z_0(\text{qCPG}) = \sum_{i=1}^4 \frac{Q_{\text{CA}}^i + Q_{\text{NCA}}^i}{Q_{\text{CA}}^i - Q_{\text{NCA}}^i}. \quad (6.2)$$

Furthermore, based on the original analytic model for the event reconstruction in COBRA-like CPG detectors as reported in [FDG⁺13], a trapping corrected interaction depth for qCPG-CZT detectors has been derived in [Tem17]. Again, all anode signals need to be taken into account. This leads to the following expression for an interaction related to sector s

$$z_{\text{tc}}(\text{qCPG}) = \lambda_s \cdot \ln \left(1 + \frac{1}{\lambda_s} \cdot \sum_{i=1}^4 \frac{Q_{\text{CA}}^i + Q_{\text{NCA}}^i}{Q_{\text{CA}}^i - Q_{\text{NCA}}^i} \right). \quad (6.3)$$

A comparison of both reconstruction algorithms presented in Eqn. (6.2) and (6.3) is shown in Fig. 6.11 for a scan along the z -axis in front of the third sector. The fitting procedure of the z -peaks is the same as described before, with the additional restriction that the total energy needs to be dominantly contained in a single sector. Although the deviations from a perfectly linear behavior are stronger than for the conventional CPG example, the linearity is still sufficient. Furthermore, the corrections introduced by the incorporation of the electron trapping model have a similar effect on near-cathode events. A more detailed discussion of the deviations can be found in Ref. [Tem17].

Finally, It should be noted that because of the poor performance of the only available large single CPG detector, no localized γ -ray scanning has been performed with this device. However, the depth reconstruction capabilities have been studied with the help of laboratory long-term measurements and the characteristic imprints of muon-induced interactions as will be discussed in section 7.4.

Regarding the characterization of future CZT detector generations, a complete localized mapping might not be needed as the crystal fabrication and quality is continuously progressing. Moreover, the current procedure is not compatible with the requirements of a potential large-scale experiment comprising thousands of crystals. In that case, the best option would be to consolidate the cooperation with the detector manufacturers to perform the crystal characterization on-site on an industrial scale. In the mean time, the collected scanning data sets might help to evaluate the prospects of establishing an x - y -reconstruction for the qCPG-CZT detector approach, which could contribute to the discrimination of backgrounds for the search for the $0\nu\beta\beta$ -decay or allow to perform topological measurements.

Chapter 7

Pulse-shape discrimination

Pulse-shape discrimination (PSD) techniques are well-established and powerful tools to distinguish signal- and background-like events by means of the respective signal traces in rare event searches. Their application relies on the sampling of the full signal traces enabling an offline signal processing and complex reconstruction algorithms. One requirement is a sufficient timing resolution in order to resolve the imprints of particular characteristics that are caused by the drift of charge carriers towards the readout electrodes.

Because of the wide range of detection techniques, different approaches are being followed in nuclear physics applications such as the search for the neutrinoless double beta decay (see e.g. GERDA [GER13a] and EXO-200 [EXO14]). Nowadays, the prospects of deep learning and neural network algorithms are explored in order to further optimize the veto capabilities using PSD (see e.g. Ref. [HHM⁺19] and [EXO18b]). Apart from the double beta decay community, PSD methods are also applied in the field of γ -ray spectroscopy with complex detector systems aiming to reach a full 4π coverage [LRB⁺19].

The first part of the following chapter is an overview of COBRA's event classification using different sets of PSD criteria that were developed during the operation of the COBRA demonstrator. One of the main objectives of the present thesis is the determination of the corresponding signal efficiencies, which are needed in the analysis of the physics data collected with the demonstrator array. Furthermore, an improved PSD concept has been developed with the aim to combine the previously available techniques into a single-parameter-based approach. This concept allows for a calibration of the optimal cut value in order to simplify the physics data analysis substantially.

Moreover, the optimization of the new PSD approach was complemented by the performance of a dedicated laboratory experiment including the analysis of the collected data. By using the Compton coincidence technique and a two-detector-system consisting of a COBRA CPG-CZT detector and a conventional high-purity germanium (HPGe) detector, a pulse-shape library of signal-like events has been collected. The concept of the constructed experiment as well as the data analysis and results will be reported in this chapter.

Finally, several long-term laboratory measurements were performed with different CZT detector types aiming to collect a statistical sample data set of cosmic muon interactions. The outcome of the data evaluation and an analytical model for the reconstruction of muon-induced events will be presented in the last section of this chapter.

7.1 Event classification via PSD

The main objective of pulse-shape discrimination (PSD) is the differentiation of signal-like and background-like events by means of characteristic features in the pulse-shapes. While the exact definition of the term *signal-like* might vary for specific analyses, this signature involves usually a point-like interaction within a single detector. The shape of the resulting charge pulse carries information about the charge carriers' drift through the detector bulk, which can be interpreted with the help of the known weighting potentials (see section 5.1.1). Point-like interactions are referred to as single-site events (SSEs) and provide prototypes for the signatures of rare nuclear decays such as the potential decays of the $\beta\beta$ -nuclides present in CZT or the highly forbidden β -decay of ^{113}Cd (see Tab. 4.4 for an overview).

An example of a signal-like SSE as measured with the readout electronics developed by the COBRA collaboration (see section 4.3.3) and its characteristic features is depicted in Fig. 7.1. The labels CA and NCA refer to the collecting and non-collecting anode signals (see section 4.1.3). The difference of both is referred to as the *difference* or *charge pulse*.

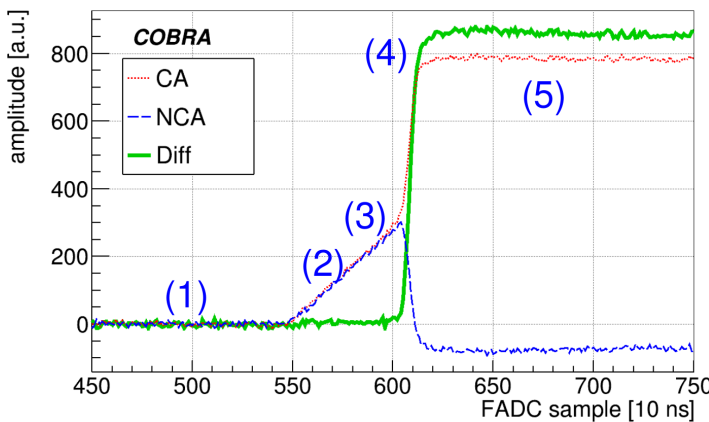


Figure 7.1: Typical pulse-shape of a single-site interaction from a calibration measurement with ^{228}Th of the COBRA demonstrator at the LNGS (taken from [Zat17a]). The energy deposition is reconstructed from the pulse-height of the charge pulse as the difference of the CA and NCA raw signals and results in about 2.2 MeV. The general features are highlighted as: (1) pre-baseline before trigger, (2) common initial rise (drift of charge in bulk potential), (3) splitting point (influence of localized grid potential), (4) charge collection (electrons get collected at CA electrode), (5) Final pulse-height (decreases exponentially).

In the following sections the PSD techniques developed during the operation of the COBRA demonstrator will be summarized. This includes the optimization of the respective cut values as well as performance studies based on LNGS calibration and physics data.

7.1.1 Data-cleaning and noise rejection

The first stage of COBRA's PSD consists of a set of conditions that are meant to reject noise and unphysical pulse traces, which occur dominantly at low energies. A complete list of the recent implementation can be found in Tab. 7.1. Some of the relations are motivated by the correlation of different quantities that are determined during the signal processing via MAnTiCORE and their expected range according to the Shockley-Ramo theorem (see section 4.1.4). The complete set of those conditions is referred to as the data-cleaning cuts (DCCs) and was originally introduced by M. Fritts based on the evaluation of the COBRA demonstrator's L1 and L2 data in the two-layer period from Sept.'11 – Jun.'13 (see e.g. section 8.1.4). An event is flagged by the DCCs, if at least one of the conditions reported in

Tab. 7.1 is fulfilled. The overlap of the selection criteria and the corresponding impact on the DCCs' signal efficiency are discussed in the Bachelor thesis of R. Kantelberg [Kan17].

Table 7.1: Overview of MAnTiCORE's data-cleaning conditions (taken from source code). The criteria used in the definition of the single conditions are mainly based on the minimum/maximum values of the raw signals CA and NCA and the corresponding pulse-heights (PHs) including the difference pulse. Furthermore, there are conditions that contain the RMS of the CA's post-baseline as well as the maximum change (MaxChange) of the usually continuously increasing CA and difference signals. Some criteria are also based on multiple conditions, whereas only one of those has to be fulfilled to veto an event by the DCCs. The constants and factors were optimized based on the demonstrator's L1 and L2 data in the two-layer period.

label		definition	
wrong trace length	N_{samples}	<	1024
CA range high	$\text{Max}(\text{CA}) - \text{Min}(\text{CA})$	>	$\text{PH}(\text{CA}) + 180$
CA change low	$\text{MaxChange}(\text{CA})$	<	$0.25 \cdot \text{PH}(\text{CA})$
CA RMS high	$\text{RMS}(\text{postBL}(\text{CA}))$	>	$10.0 \cdot \text{PH}(\text{CA})$
		>	200
NCA range high	$\text{Max}(\text{NCA}) - \text{Min}(\text{NCA})$	>	$1.03 \cdot \text{PH}(\text{CA}) + 130$
NCA range low	$\text{Max}(\text{NCA}) - \text{Min}(\text{NCA})$	<	$0.25 \cdot \text{PH}(\text{CA}) + 130$
NCA amplitude low	$\text{PH}(\text{NCA})$	<	$-1.05 \cdot \text{PH}(\text{CA})$
NCA amplitude high	$\text{PH}(\text{NCA})$	>	$0.5 \cdot \text{PH}(\text{CA})$
Diff change high	$\text{MaxChange}(\text{Diff})$	>	$4.0 \cdot \text{PH}(\text{Diff})$
Diff simple low	$\frac{\text{PH}(\text{CA}) - \text{PH}(\text{NCA})}{\text{PH}(\text{Diff})}$	<	0.93
		>	$0.815 + 1 \cdot 10^{-3} \cdot \text{PH}(\text{Diff})$
Diff simple high	$\frac{\text{PH}(\text{CA}) - \text{PH}(\text{NCA})}{\text{PH}(\text{Diff})}$	>	1.02
		>	$1.06 - 2 \cdot 10^{-4} \cdot \text{PH}(\text{Diff})$

The key properties used in the construction of the DCCs are the pulse-heights (PHs) of the raw signals recorded by the CA and NCA as well as of the derived difference signal and their absolute minimum and maximum values. The determination of the different pulse-heights is discussed in section 5.2.1

Secondly, there are criteria involving the *maximum change* along a pulse, which is referred to as the maximum absolute value between two samples with a 15-sample-wide gap in between. Another quantity of interest is the RMS of the baselines. The baseline characteristics are usually determined for the first and last 128-sample-average of each pulse trace.

Additionally, the standard data-cleaning procedure applies a cut to remove *below-threshold events* as discussed in section 5.2.4, artificially injected pulses used for the monitoring of the electronics' stability and the synchronization of the FADCs (see section 7.1.5), as well as low- z events, which are affected by distortions of the event reconstruction (see section 7.1.2). Even though the artificially injected pulses can be usually identified by the presence of a TTL flag, there are some periods in the beginning of the experiment for which the flagging was not working perfectly. However, due to the distribution of the same signal amplitude towards all channels, independently from the CA/NCA labeling, the reconstructed energy and interaction depth are expected to be close to zero. Hence, the rejection of low- z events with $z < 0.2$ already takes care of potentially unflagged injected pulses.

In the original implementation of the DCCs, the present constants and factors in the definition of the conditions have been optimized based on the data of the first two detector layers. An in-depth review of the DCCs presented in [Kan17] revealed that some of the criteria tend to flag a much larger event fraction for certain channels and data-taking periods in more recent runs involving also L3 and L4. However, this preliminary impression could

be resolved later on by performing a partitioning of the data as will be presented in the course of section 8.4.2. Moreover, the evaluation of a dedicated low-threshold study of the ^{113}Cd β -decay, which is one of the main parts of the present thesis (see e.g. section 8.3 and following), could be used to perform a qualitative analysis of the DCCs' efficiency.

Part of the mentioned low-threshold study is a special run of about one week with an altered software trigger. Instead of only recording the signals of the channels fulfilling the trigger condition, there is the option to readout all channels of a FADC device for a single-channel trigger. While this option is usually not used in the standard data-taking mode, it provides the opportunity to collect a sample of baseline pulses. By rejecting the triggered events, only the baseline pulses remain. The effect on the reconstructed energy spectrum as the combination of all detectors of the COBRA demonstrator for different steps of the data-cleaning is depicted in Fig. 7.2.

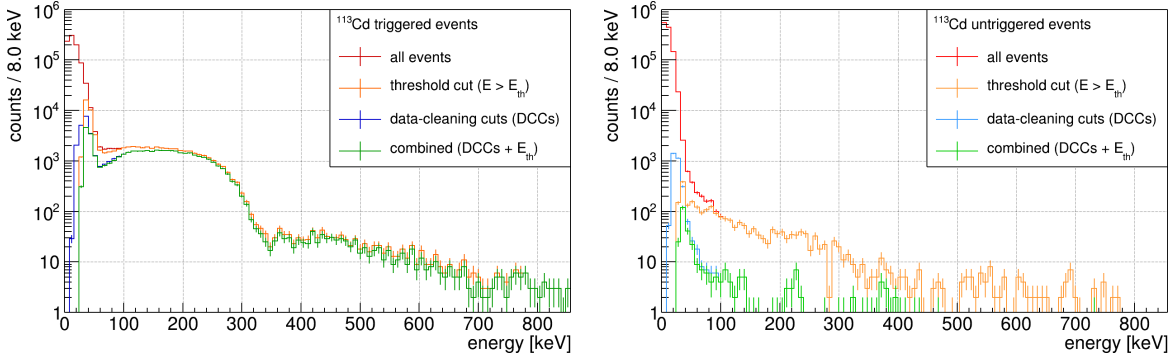


Figure 7.2: Effect of the data-cleaning steps with respect to the combined energy spectrum for a special trigger run of the COBRA demonstrator at the LNGS. *Left:* triggered events. *Right:* untriggered events. While the spectra of the triggered events are clearly dominated by the highly forbidden β -decay of ^{113}Cd with a Q -value of about 320 keV, there is no such feature in the continuously decreasing spectra based of the untriggered events. As intended, the below-threshold cut affects only events near the threshold. In case of the triggered events an acceptance of $\varepsilon_{\text{DCC}}^{\text{sig}} = 87.5 \pm 0.6\%$ is found. At the same time, the removal of the baseline pulses results in $\varepsilon_{\text{DCC}}^{\text{bg}} = 99.8 \pm 0.1\%$ as a measure of the background rejection. The quoted uncertainties are a measure for the observed spread between the single detectors of the demonstrator array.

By treating all events in the spectrum of the triggered events above the average threshold of about 80 keV as signal, an acceptance of $\varepsilon_{\text{DCC}}^{\text{sig}} = 87.5 \pm 0.6\%$ is found for the DCCs over the ^{113}Cd energy range. Furthermore, the identification of the baseline pulses taken as proxy for noise-only events results in a background rejection of $\varepsilon_{\text{DCC}}^{\text{bg}} = 99.8 \pm 0.1\%$. However, this is only a qualitative analysis as both the signal and background partitions contain contaminations of the other category. Because of the unknown composition of the partitions, the uncertainties on the efficiencies have been estimated conservatively as the observed spread of the investigated detector pool (see also section 8.3.5).

The results obtained with the ^{113}Cd physics data could be confirmed by the evaluation of LNGS calibration data. The combination of several calibration runs with the radionuclide ^{228}Th and the effect of the DCCs is presented in Fig. 7.3. The energy and intensity of the γ -lines involved in the decay series of ^{228}Th can be found in Tab. 8.6 of section 8.3.4.

Additionally, the variation of the signal acceptance has been checked with the low-energy γ -lines of ^{152}Eu (121.8 keV, 344.3 keV). The variation across the ^{113}Cd energy range was found to be compatible with the assigned uncertainties, hence, can be assumed to be constant. However, for higher γ -line energies the signal acceptance increases and yields $97.5 \pm 0.3\%$ at 583.2 keV, $99.9 \pm 0.1\%$ at 1592.5 keV and the same value for the full-energy peak at 2614.5 keV.

Besides of those data-driven approaches to characterize the efficiency of the DCCs, there have been dedicated studies regarding the shielding concept of the COBRA experiment with

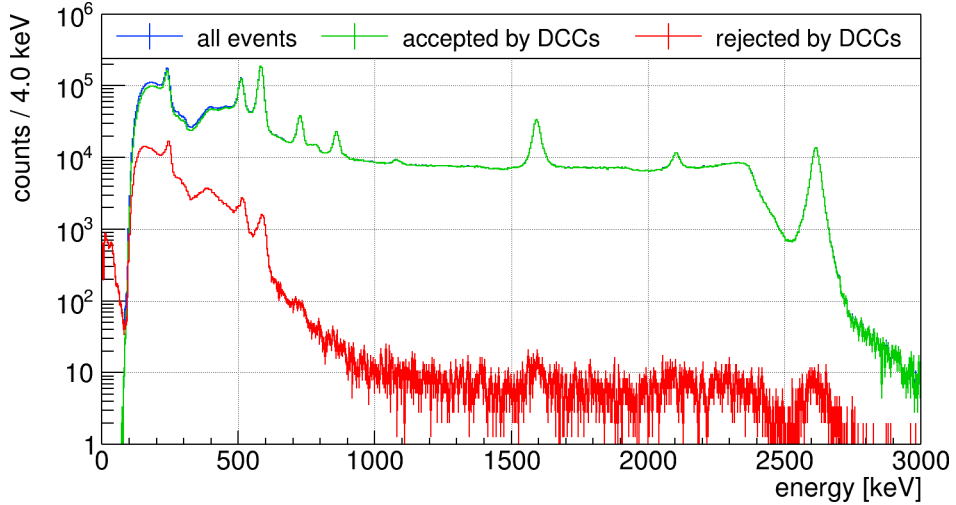


Figure 7.3: Crosscheck of the data-cleaning cuts based on the combination of several calibration runs of the COBRA demonstrator using the radionuclide ^{228}Th . Due to the splitting of the calibration runs in high- and low-threshold data there is an artificial step above the lowest energetic γ -line at $E_\gamma = 238.6\text{ keV}$ resulting from the combination. The survival fraction for this line is found to be $89.3 \pm 0.7\%$, which is on the same order as the result obtained for the ^{113}Cd average presented in Fig. 7.2.

respect to the reduction of electromagnetic disturbances in general. Exemplarily, a qualitative investigation of COBRA’s EMI shielding concept, as presented in section 4.3.3, is documented in the Bachelor thesis of Y. Bernau [Ber13]. It was found that the applied concept provides excellent shielding properties, which is an indication for the origin of the residual noise to be caused internally. A more detailed discussion of this subject can be found in section 8.2.2 and related sections.

7.1.2 Near anode and cathode events

The reconstruction of the interaction depth (see section 5.2.3) is a powerful tool to identify surface events, which are typically caused by external α -decays due to their limited penetration power. However, the depth information covers only one dimension of the cuboidal CZT detectors, which is why only near-anode ($z = 0$) and near-cathode ($z = 1$) contaminations can be suppressed efficiently with this method. Moreover, the z -reconstruction allows for a detailed characterization of prominent background components such as discussed in section 8.2. The analysis of the demonstrator’s physics data reveals that especially the cathode electrode features long-lived α -contaminations, which originate from the decay of radon and its daughter nuclei. Because of the applied negative bulk voltage of about 1 kV, ionized daughter atoms get attracted and stick to the cathode surface. A more detailed discussion of the identified nuclides contributing to the near-cathode background is given in section 8.2.4.

As already mentioned in the previous section, the near-anode region is affected by reconstruction artifacts due to the presence of the weighting potentials’ inhomogeneities in the vicinity of the CPG electrode (see section 5.1.1). While it is in both cases – near-cathode and near-anode – rather easily possible to identify the affected depth regions via a suitable display of the data, the calculation of the corresponding efficiencies is much more challenging. The determination of those efficiencies, regarding the actual selected sensitive CZT volume, will be addressed in the following.

Fig. 7.4 illustrates the combined physics data of the COBRA demonstrator in form of a depth spectra for events above the ^{113}Cd energy region. A two-dimensional illustration

representing a z -versus- E plot of the same data is shown in Fig. 8.4 of section 8.2. Because of the overwhelming dominance of the ^{113}Cd β -decay, it is necessary to restrict the energy range to $E > 350\text{ keV}$ in order to investigate the imprints of backgrounds at higher energies with respect to the interaction depth.

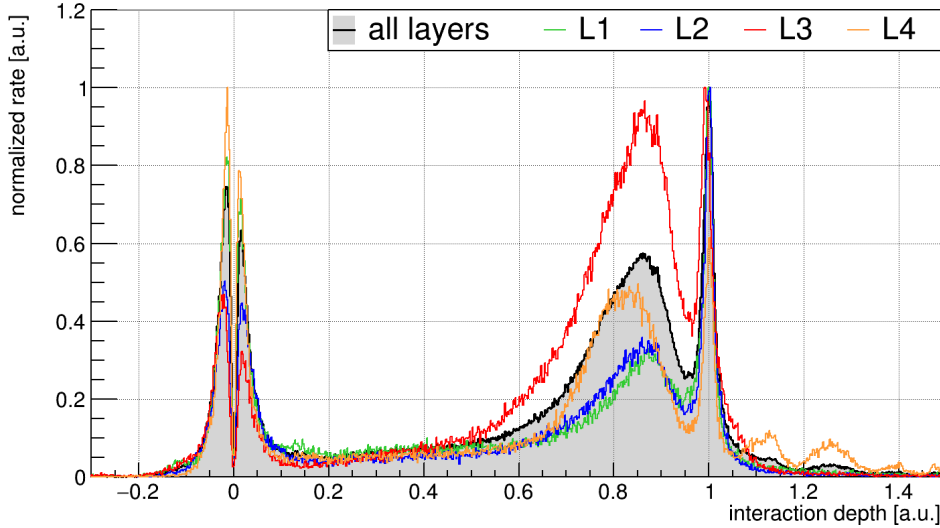


Figure 7.4: Distribution of the interaction depth above the ^{113}Cd energy region for the total exposure of the COBRA demonstrator. Besides the energy restriction, the DCCs are applied. The maximum of each spectrum has been scaled to unity. It is found that each of the detector layers (L1–L4) share common features such as the rather symmetric double peak distribution close to the anode at $z = 0$, which originates mainly from the weighting potential distortions, and the increasing count rate towards the cathode at $z = 1$. The characterization of the so-called z -hump for $z \sim 0.6 – 0.9$ will be discussed in section 8.2. The actual near-cathode contaminations are found in the sharp peak around $z = 1$.

The differences in the depth spectra of the four layers are mainly caused by the presence of the so-called z -hump. An explanation of this feature and its distribution across the detector array is given in section 8.2. The focus of the present section is on the near-surface regions in the combined spectrum. The peak at the cathode side is caused by α -contaminants. It can be characterized by a two-sided Gaussian fit according to Eqn. (5.7) around $z = 1$. The fit results in $\mu_z = 1.0009 \pm 0.0002$ and $\sigma_z = 0.0095 \pm 0.0003$. This corresponds to an average depth resolution of $\text{FWHM}_z = 2.22\%$ at $z = 1$, independently from the energy deposition. It can be assumed that the depth resolution is almost constant for the bulk of the detector, but gets worse in the near-anode region due to the weighting potential distortions. Based on the Gaussian fit results a conservative z -cut results in an exclusion of $z > 0.97$ at $\pm 3\sigma$, whereas an upper bound of the physical detector dimension is found for $z \leq 1.03$. The Gaussian coverage of the cathode's z -peak selection corresponds to a 99.87% one-sided confidence interval (see e.g. appendix C.2 for more information on the coverage).

Regarding the near-anode region, a cut of $z \gtrsim 0.1$ seems to be sufficient to exclude the distorted depth region. However, the analytic description cannot be done with a single Gaussian and the real extent cannot be assessed with the known to be localized features discussed so far. Instead, a homogeneously distributed signal would be more suitable and representative for the complete depth range. Such a signal is provided by the intrinsic β -decay of ^{113}Cd , which is the main analysis subject in the present thesis. The utilization of the ^{113}Cd β -decay is also advantageous with respect to other potential measures.

Previous attempts to determine the depth selection efficiency involved γ -ray characterization measurements such as discussed in section 6.3. While the linearity of the z -reconstruction has been verified with the spatially resolved γ -ray measurements along the z -dimension, the

efficiency determination is corrupted by the typical depth resolution of the CZT detectors, the collimation of the initial ^{137}Cs γ -ray beam and the thickness-dependent absorption of it. Because of the superposition of those effects, which leads to a broadening of the z -peak in the corresponding depth spectrum, it is hardly possible to make a statement about the actually irradiated detector volume to crosscheck the depth selection efficiency. The same applies to an external α - or β -irradiation of a CZT detector. Because of the typical penetration depths, it would only be possible to create events close to the surface, while the detector bulk could not be probed in a reliable way (see also section 8.2.4).

Even though the ^{113}Cd β -decay provides only a low-energetic signal, which is limited by the Q -value of about 320 keV, leaving the problem to deal with threshold effects, it is the best option to determine the depth selection efficiency. The depth spectrum of the ^{113}Cd energy range is depicted in Fig. 7.5 and includes the combined data of the dedicated ^{113}Cd run as well as a single detector example.

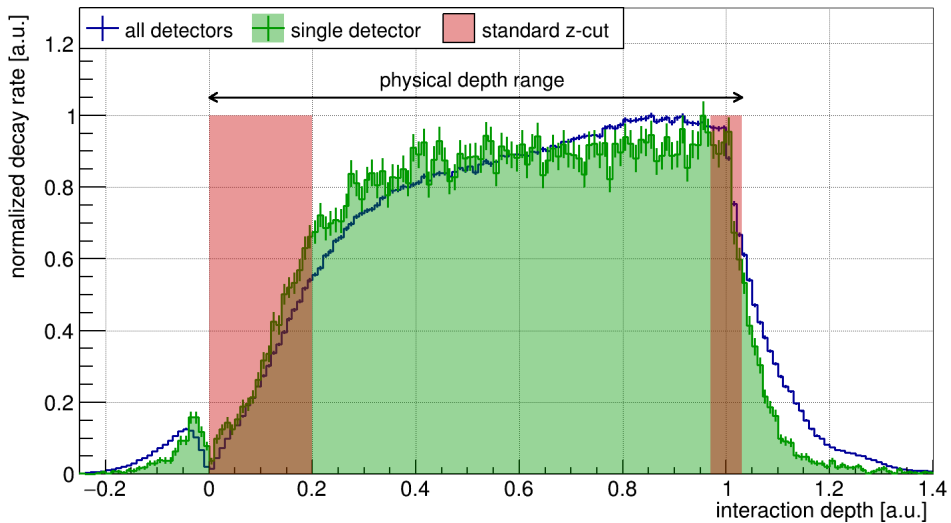


Figure 7.5: Distribution of the interaction depth in the ^{113}Cd energy range based on the data of the COBRA demonstrator. The maximum of the two example spectra for the combination of all detectors (blue) and Det50 (L4-P02) as a single detector reference (green) is set to unity. The highlighted physical depth range is defined as $0 < z \leq 1.03$ and limited by the standard z -cut according to $0.2 < z \leq 0.97$. The exclusion of the low- z range is motivated by the increase of the decay rate towards the rather flat plateau, indicating the expected uniform distribution of the ^{113}Cd source nuclei. The high- z range has been motivated before by the exclusion of cathode contaminations (see also Fig. 7.4).

The ^{113}Cd depth distribution allows to determine the actual selected physical volume fraction given a certain z -restriction. In case of the near-anode region, the previous suggested cut of $z > 0.1$ is increased to $z > 0.2$ in order to cover the rising edge of the depth spectrum towards the expected plateau for the bulk of the detector volume. The slight slope towards the cathode is assumed to be caused by the hole contribution to the signal amplitudes, which is not taken into account in the trapping correction of the z -reconstruction (see section 5.2.3). An elaborate discussion of the hole contribution can be found in the second part of section 7.4.4. The combined standard z -cut of $0.2 < z \leq 0.97$ is found to be optimal for most of the detectors (see also the discussion in section 8.3.5 and Fig. D.20 in the appendix).

Moreover, by comparing the selected areas of the z -cuts to the total integral of the depth distribution, it is possible to deduce the actually selected volume fractions which are taken as the signal efficiency of the depth selections. The applied *cut and counting* approach is independent of an analytic description of the ^{113}Cd depth distribution, but requires a dedicated iteration for each potential z -cut combination. The resulting efficiencies of the

depth selections applied in the course of this thesis are summarized in Tab. 7.2.

Table 7.2: Deduced efficiencies of the physical volume selection via different z -cut definitions based on the intrinsic ^{113}Cd β -decay. The quoted uncertainties follow from the Poisson statistics of the selected number of events. While the low- z cut removes less than half of the naively expected range, the high- z selection matches well with the expectation regarding the actual physical volume (see also Fig. 7.5).

label	definition	depth selection efficiency [%]	
		Det50 (L4-P02)	combined ^{113}Cd data
low- z	$z < 0.2$	9.12 ± 0.13	7.73 ± 0.02
high- z	$z > 0.97$	6.35 ± 0.11	6.72 ± 0.02
standard- z	$0.2 < z \leq 0.97$	86.57 ± 0.41	87.52 ± 0.07
strict- z	$0.2 < z \leq 0.60$	43.79 ± 0.29	41.70 ± 0.05

A compilation of each detector’s $\varepsilon_z(^{113}\text{Cd})$ for the standard- z selection can be found in Tab. E.1 – E.4 of the appendix. The strict- z selection also covers the z -hump present in the depth distributions above the ^{113}Cd energy range (see Fig. 7.4). Although it reduces the effective volume by more than 50%, it allows for an ultra-low background for the search for double beta decays. The application of this cut is demonstrated explicitly in the search for the $2\nu\beta\beta$ -decay of ^{116}Cd in section 8.4.

7.1.3 Lateral surface events

Because of the limitations of the depth reconstruction, there is the need for complementary techniques to cover background events appearing close to the remaining detector surfaces. Such interactions are referred to as lateral surface events (LSEs). The development of the techniques to identify LSEs marked the starting point of COBRA’s pulse-shape discrimination. Details can be found in [COB14]. The LSE identification makes use of the distortions of the weighting potential close to the lateral walls. An illustration of the weighting potential corresponding to the difference pulse of the raw signals CA and NCA is shown in Fig. 7.6.

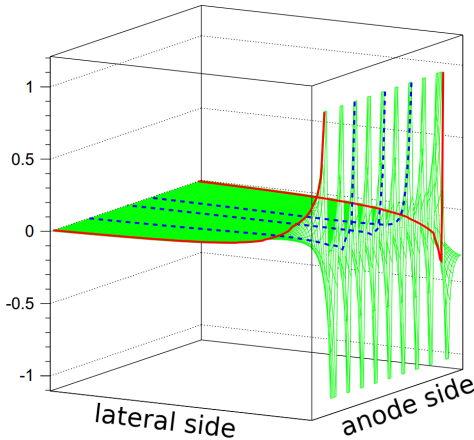


Figure 7.6: Illustration of the difference signal’s weighting potential (adapted from [COB14]). The projection of the weighting potential follows the procedure discussed before in section 5.1.1. Highlighted are the paths of test charges, which are generated by a simple model assuming propagation directly towards the anode plane through the detector bulk, followed by a straight path to the nearest CA strip of the CPG electrode. While the variations for the depicted bulk paths (dashed blue) are only marginal, there are clear deviations for the paths close to the lateral sides (solid red). Those features are used in the construction of the LSE cuts.

Two examples for LSEs are depicted in Fig. 7.7, highlighting the differences in the pulse-shapes for events of approximately the same energy deposition of about 2.5–3.5 MeV. The definitions of the LSE selection criteria and their parameter distributions for calibration data of the demonstrator array can be found in Fig. D.1 and Fig. D.2 of the appendix.

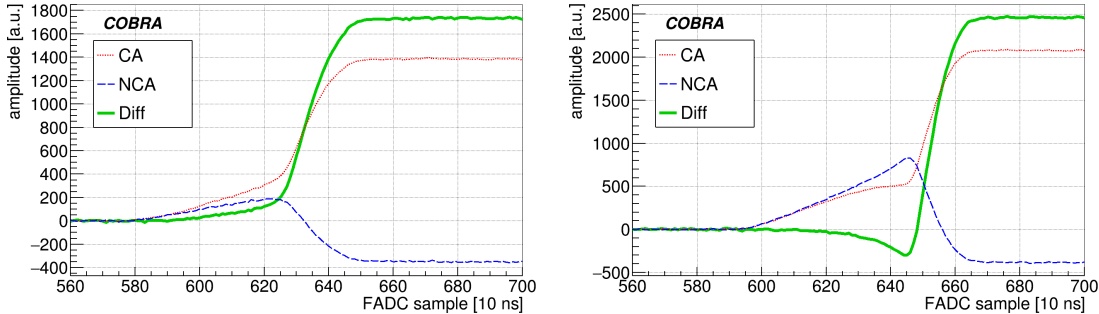


Figure 7.7: Typical example pulse-shapes for lateral surface events as found in calibration measurements of the COBRA demonstrator (taken from [Zat17b]). The imprints of the weighting potential’s distortions near the lateral detector sides are enhanced for the difference pulse. *Left:* CA-side event leading to an early-rise of the difference signal. *Right:* NCA-side event featuring a prominent dip below the baseline.

The signal acceptance of the two selection criteria can be tuned independently to about 90% by pre-selecting signal-like events from calibration measurements as discussed in section 7.2.3. However, due to their disjunctive definitions and characteristics, the combined efficiency is expected to be only about 80%. In fact, the signal efficiency has been determined to $\varepsilon_{\text{LSE}}^{\text{sig}} = (76 \pm 2)\%$ in COBRA’s latest $0\nu\beta\beta$ -decay peak search analysis [COB16a]. As the combined signal efficiency enters the half-life sensitivity according to Eqn. (3.10) linearly, any improvement regarding the signal acceptance, while maintaining the background suppression level, would have a direct impact on the experiment. Moreover, it was found that the optimal cut values leading to an individual signal acceptance of 90% differ between several evaluated calibration measurements, even for the same detector. While the usage of average cut values, as done for the analysis presented in [COB16a], can be expected to even out, it introduces a significant systematic uncertainty. Furthermore, the optimization of the early rise time criterion (see Fig. D.1 in the appendix) can only be done in rather rough steps as the quantity relies on integer values. This is why more robust and efficient techniques have been explored as will be summarized in the following sections.

7.1.4 Single-site and multi-site events

All of the previous PSD methods have in common that they are supposed to reject near-surface events. However, γ -rays can penetrate deeply into the sensitive volume unlike α - and β -radiation. Although the natural γ -ray background of the primordial decay chains turns out to be of minor concern for the ROI of the $0\nu\beta\beta$ -decay of ^{116}Cd because of its high Q -value (see Tab. 4.4) and is further suppressed by a careful material selection and the multi-layered shielding against external radiation (see section 4.3.3), several processes can produce highly energetic photons in the vicinity of the detector array.

While the rock overburden of the LNGS reduces the flux of relativistic muons by more than six orders of magnitude compared to the surface, the remaining muons are able to trigger nuclear reactions in the vicinity of the experiment. Besides those muon-induced reactions, there are e.g. (α, n) reactions in the surrounding rock producing high-energetic neutrons. The produced secondary particles typically scatter inelastically with any material creating highly energetic γ -rays with energies up to several MeV. Those γ -ray interactions can mimic

the $0\nu\beta\beta$ -decay by depositing energy in the region of interest. However, the chance of a full energy deposition inside a 1 cm^3 CZT crystal is relatively low. More often Compton scattering or pair creation will happen, depending on the initial energy of the γ -ray (see e.g. Fig. 1.8 in section 1.3.1). A single Compton scatter event causes a single-site interaction, as there is only one energy deposition. On the other hand, multiple Compton scattering within the same crystal result typically in so-called multi-site events (MSEs) due to the localized energy depositions in different spots. If the single energy depositions are spatially well-separated, the collection of the disjunctive charge clouds provides a distinct signature on the pulse-shape level. This way, there is the chance to identify MSE bulk interactions, potentially depositing the same energy as expected from double beta decays, by means of the respective pulse-shapes. A typical example is depicted in Fig. 7.8.

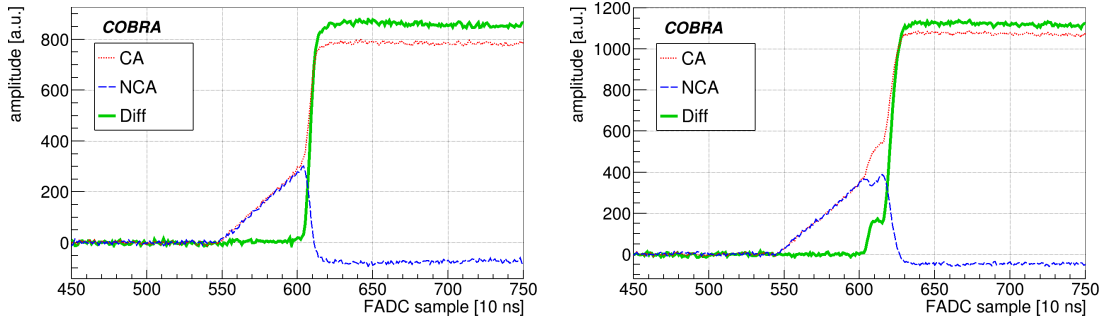


Figure 7.8: Typical example pulse-shapes for single-site (*left*) and multi-site interactions (*right*) as found in calibration measurements of the COBRA demonstrator (taken from [Zat17b]). In the present MSE example the plateau feature in the difference pulse is caused by the delayed collection of two separate charge clouds. The delay is caused by the spatial separation of the charge clouds' origins and their presumably constant drift velocity. Thus, the imprints of MSEs only appear if the energy depositions are separated well enough with respect to the interaction depth dimension of the CZT detectors.

The likelihood of observing a SSE or MSE in a γ -ray interaction depends on the initial energy, affecting the cross section of the possible interaction mechanisms as discussed in section 1.3.1, as well as on the size of the CZT crystals. As the COBRA collaboration is currently upgrading to larger crystals with a volume of 6 cm^3 (see e.g. section 4.3.4), the chance for a second γ -ray interaction inside a single crystal is expected to increase, whereas the sought double beta decay signals will dominantly appear as single-site events. Hence, to be able to distinguish between both event categories is essential for an envisaged large-scale experiment. An overview of the developed PSD techniques is given in section 7.2.

7.1.5 Coincident events

In the light of the presence of γ -ray induced background and the expected single-site signature of potential $\beta\beta$ -decays, another rather natural choice of background suppression is to reject coincident events between multiple detectors. Even for an intended large-scale experiment as envisioned in section 4.3.5, the rate of random coincidences due to $\beta\beta$ -decays taking place in different detectors within a certain coincidence time window is negligibly small. On the contrary, γ -ray scattering is expected to deposit energy in multiple crystals, whereas the event signature – SSE or MSE – is only secondary. This is why granular detector designs as summarized in section 3.3.2 provide intrinsically an efficient way to reject γ -ray coincidences.

Moreover, there are search strategies that make explicitly use of detector coincidences such as expected from $\beta\beta$ -decays involving excited state transitions or from the more exotic $\beta^+\beta^+$ modes. A feasibility study based on the COBRA demonstrator regarding the search for excited state transitions of ^{116}Cd and ^{130}Te will be discussed in section 8.6.

However, the identification of detector coincidences turns out to be non-trivial in the current stage of the experiment and its electronics (see also section 4.3.3). This is mainly due to the FADCs, which digitize the pulse-shapes of triggered events and assign the corresponding unix timestamps. Each of the applied STRUCK SIS3300 modules has its own clock providing the default sample frequency of 100 MHz. It is found that there is an intrinsic spread of the clocks' speed causing a drift of the assigned timestamps over the typical run duration of the experiment. As the drift is mainly linear, it can be corrected in an offline procedure as part of the data processing with MAnTiCORE. The procedure makes use of artificially injected pulses from a generator that provide a timestamp reference for all FADC devices every 10 min. More information can be found in section 4.3.3 and 8.1.1.

The synchronization tool was originally designed by O. Reinecke in 2012. Since its initial implementation into MAnTiCORE it has been adapted by the COBRA analysis team several times, e.g. M. Fritts (Oct.'13), S. Zatschler (Apr.'15, Nov.'15, Jan.'17) and J. Volkmer (Sept.'18), in order to maintain its compatibility with the frequently changing data format requirements. The first applications are documented in the Master thesis of M. Kleineberg [Kle16] and the PhD thesis of J. Timm [Tim15]. The latter study aimed to estimate the intrinsic contamination level of the COBRA demonstrator detectors based on delayed coincidences of the natural decay series (see Fig. D.8 in the appendix and Tab. 8.4 in section 8.2.4).

The recent status of the FADC synchronization tool and its application towards the search for the EC/ β^+ decays of the nuclides contained in CZT (see e.g. Tab. 4.4) is presented in the Master thesis of J. Volkmer [Vol18]. The linear drift of the FADCs' clocks is found to be 0.1 – 1.0 s, depending on which FADC channels are compared to each other, for the standard run duration of 4 h (see section 8.1.1). Furthermore, the accuracy of the offline synchronization could be determined to about 0.1 ms, which is about ten times the sampling length of 10 μ s of a complete pulse trace. The limitations of the synchronization are non-linear effects that cannot be addressed analytically at the moment.

In the present thesis only a weaker version of the full coincidence cut is available for most of the data, as the synchronization has not yet been applied to the complete data set. Nonetheless, as all detector channels that are connected to the same FADC unit receive their timestamps from the same clock, they are perfectly synchronized on the raw data level. Consequently, coincidences between up to four detectors of the same FADC (see section 4.3.3) can be rejected without the need of the clock synchronization. The full coincidence cut is applied in the course of the ^{113}Cd β -decay analysis as explained in section 8.3.6.

7.2 Identification of multi-site events

As it has been motivated in section 7.1.4, the identification of MSEs provides a key instrument to reduce the γ -ray background in the $\beta\beta$ -decay region of interest of the COBRA experiment. An overview of the most promising approaches is given in the following sections. More information can also be found in the previous works presented in [Zat14] and [Küt19].

7.2.1 Peak-search algorithm

The typical characteristic of a multi-site event is a plateau feature in the difference pulse, whereas SSEs can be described by a single step function (compare the examples in Fig. 7.8). Based on this feature, a software algorithm has been developed in [Zat14] to distinguish between both event types. The key idea is to search for peaks above an empiric threshold in a particularly constructed derivative of the difference pulse. As the difference pulse represents the charge signal, its derivative is referred to as the *current signal*.

The definition of the applied derivative makes use of a moving window to calculate the pulse-height difference along the full trace using a 5-sample-wide gap. Details can be found in [Zat14]. The resulting current pulse is then checked for peak structures that exceed a threshold level as indicated in the example shown in Fig. 7.9. This is done by a specialized peak-search algorithm (PSA), which is why the procedure is referred to as the PSA method.

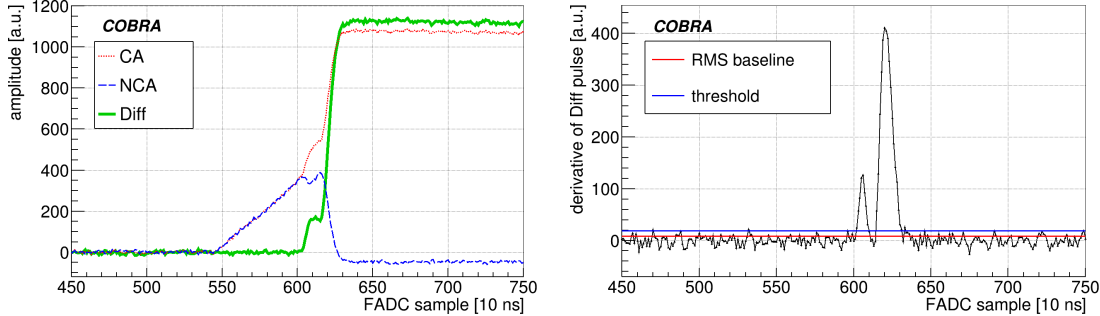


Figure 7.9: Example of the derivative definition applied in the PSA method to identify multi-site interactions (taken from [Zat17a]). *Left:* MSE pulse-shape. *Right:* corresponding derivative of the difference pulse. The threshold of the peak-search is based on the RMS of the baseline and calculated on an event-by-event basis.

If the number of peaks that exceed the threshold is greater than one, the event is flagged as a MSE. The determination of the threshold is based on a robust approach, using the RMS of the pre-baseline of the current pulse. The baseline statistics are calculated for a 256-sample-wide window on an event-by-event basis. In the end, the resulting RMS is multiplied by an optimized constant factor, referred to as x_{rms} . This constant is the only free parameter in the optimization of the peak-search algorithm. The general optimization procedure is described in section 7.2.3.

The application of the PSA towards the physics data of the COBRA demonstrator could confirm that the main background is dominated by surface α -contaminants, while there are only a few clearly identified γ -lines in the $\beta\beta$ -decay region of interest (see section 8.2.3). However, the combination with the LSE criteria revealed that there is a strong overlap between the PSA and the early rise time (ERT) criterion. Due to the definition of the latter quantity (see Fig. D.1 in the appendix), a rather high fraction of MSEs is also flagged by the ERT criterion. This is a problem when it comes to the signal efficiency calculation. Furthermore, by assuming no correlation between the combined selection, a signal acceptance of only about 72% would be expected by combining the LSE cut with the PSA method.

Although the PSA method's optimization was found to be very robust in laboratory measurements, its application towards the demonstrator array revealed severe performance issues. The definition of the optimized single threshold parameter intrinsically assumes a certain baseline behavior, which is not necessarily fulfilled by each of the LNGS detectors in all physics runs. Moreover, the constant multiplication factor x_{rms} needs to be fixed before the processing with MAnTiCORE and can only be optimized via multiple processing iterations. This makes the optimization very time consuming, especially in the light of an intended detector-wise procedure as part of the standard detector calibration routines. While such an attempt was never performed for the LSE cuts, it would have been possible after a single processing step due to the LSE parameters being stored for each event. This allows to investigate their distributions in a second analysis step (see also Fig. D.2 in the appendix). In contrast to this, the PSA method provides a boolean decision whether an event is a MSE according to the algorithm. Unfortunately, it turned out that this generic concept is not suitable in case of the LNGS setup given the observed deviations in the demonstrator's detector performances. Consequently, the outcome of the previous work [Zat14] triggered

the development of a completely new pulse-shape discrimination method for the COBRA experiment and its CZT-CPG detectors.

7.2.2 A/E criterion

An alternative method to discriminate single-site and multi-site events has been developed and applied successfully in the GERDA experiment searching for the $0\nu\beta\beta$ -decay in ^{76}Ge with HPGe detectors. The approach is based on a single quantity described by the A/E parameter [GER13a]. It relies on the maximum amplitude of the current pulse, denoted as A , and a scaling by the energy-equivalent pulse-height of the charge pulse, referred to as E . An illustration of the common A/E definition can be found in Fig. D.3 of the appendix.

The application and optimization of the A/E approach towards COBRA's detector technology has been developed in cooperation with J. Küttler. The aim was to combine the background suppression of the well-established LSE criteria and the previous MSE algorithm within a similar single parameter method. Furthermore, such an option offers the potential to calibrate the respective method on the single detector level, making it possible to explore the full potential of the COBRA demonstrator. Another benefit of a calibration would be the convergence of the individual detectors' optimal cut values to keep a certain level of the signal acceptance. In the optimal case, a unique cut value could be used for all detectors, while the signal efficiency would be the same for all channels at a predefined level.

After achieving promising first results with the help of dedicated laboratory measurements as reported in section 7.3, a complete systematic study was performed in the Master thesis of J. Küttler [Küt19] in order to identify the optimal combination of the parameters entering the A/E criterion. In total six combinations of different current amplitudes A (with and without weighting factor) and energy-equivalent amplitudes E of the charge pulse (with and without weighting factor and optional energy calibration) were tested. The most robust results, according to the optimization procedure discussed in section 7.2.3, were obtained with the simplest version based on the plain charge pulse's definition without using the weighting factor (see section 5.1.2) and the actual energy calibration parameters (see section 8.1.2) [Küt19]. A comparison of the A/E parameter distributions for the most promising options is shown in Fig. D.4 of the appendix.

However, in the beginning of the A/E study it was found that the previous derivative definition used for the PSA approach is not serving well in the case of A/E . In fact, the special PSA derivative is optimized in the sense that the expected features should appear well-distinguishable from the flat baseline and, even more importantly, allow for the resolution of MSEs, where the derivative peaks are close to each other. Instead of smoothing the derivative by averaging over a certain sample window, the applied 5-sample-gap emphasizes the peak features. On the other hand, it was found that the maximum amplitude of such a derivative is not a reliable indication to discriminate SSEs and MSEs.

Based on the original approach presented in [GER13b], a simple smoothing algorithm was introduced in the course of [Küt19]. The final definition of the current pulse as the derivative of the difference signal for each sample i of the pulse traces is shown in Eqn. (7.1).

$$\text{Deriv}[i] = \sum_{j=i-n_{\text{sm}}}^{i+n_{\text{sm}}-1} \frac{\text{Diff}[j - n_{\text{sm}}] - \text{Diff}[j + n_{\text{sm}}]}{2 \cdot n_{\text{sm}}} \quad (7.1)$$

The smoothing window size n_{sm} is one of the parameters that needs to be optimized in the following section.

7.2.3 Optimization procedure

The general optimization procedure for the MSE identification algorithms was developed in the course of [Zat14]. Following the previous work, the concept could be refined and applied to the A/E approach as well. Preliminary results for the PSA method using laboratory data were presented in [Zat17a]. The first results of the automated A/E optimization routines developed for the COBRA demonstrator can be found in [Küt19].

Concept and requirements

One of the key requirements regarding the optimization is an intended universal feasibility. Even though dedicated laboratory measurements such as presented in section 7.3 could provide valuable input in the development process, it is not possible to provide those data for all detectors of the COBRA demonstrator or in future stages of the experiment. However, in order to probe and optimize the efficiency of the developed PSD techniques, a pure sample of signal-like events is needed. The main quantity of interest is the signal acceptance or signal survival fraction, which contributes to the combined signal efficiency that enters linearly into the half-life sensitivity according to Eqn. (3.10). Moreover, in the optimal case, also a sample of background-like events would be present, which could be used to address the background suppression of a selection. Both type of events can be created in calibration measurements using a radionuclide with a sufficiently high γ -ray energy and intensity.

Pair production via γ -ray interactions

For highly energetic γ -rays with $E_\gamma > 2m_e$ there is the chance to produce electron-positron (e^-e^+) pairs in interactions with the CZT detectors. At this energy scale it is very unlikely that γ -rays deposit their full energy via photoelectric absorption. According to the γ -ray cross sections, Compton scattering is the dominant process (see Fig. 1.8 in section 1.3.1). However, the full energy deposition of γ -rays at the MeV scale is typically a combination of multiple processes, whereas the pair production inside the CZT detectors is accompanied by particularly interesting kinematics (see Fig. 7.10).

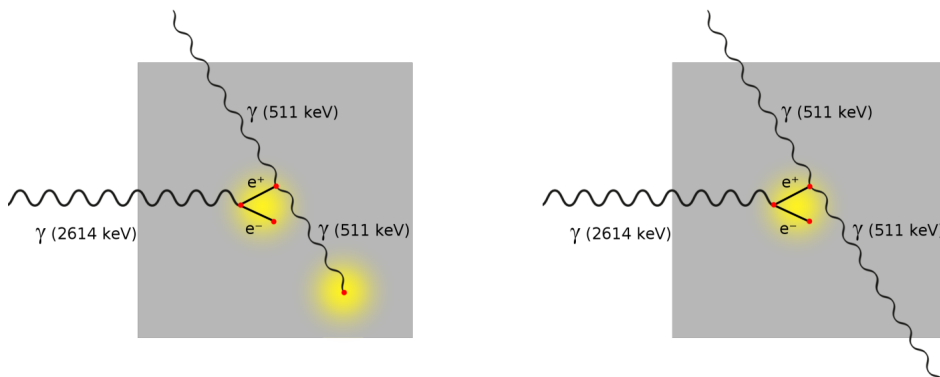


Figure 7.10: Illustration of the kinematics involving pair production via γ -ray interactions inside CZT (taken from [Küt19]). Initially, a highly energetic γ -ray such as from the de-excitation of ^{208}Tl can create an e^-e^+ pair. Both of the leptons cause a localized energy deposition via ionization, which is indicated with the yellow spot. The positron annihilates with an electron of the detector material and converts into two back-to-back annihilation γ -rays with $E_\gamma = m_e$ each. If one of those γ -rays is absorbed within the initial CZT detector (indicated with the yellow spot), while the other escapes undetected, the total energy deposition results in an entry in the single-escape peak (SEP). SEP events are proxies for multi-site interactions (*left*). On the contrary, if both γ -rays escape, leading to entries in the double-escape peak (DEP), the underlying kinematics provide prototypes for $\beta\beta$ -decays, thus, single-site interactions (*right*).

A suitable γ -ray energy being able to perform pair production in CZT is provided by the de-excitation of ^{208}Tl ($E_\gamma = 2.6 \text{ MeV}$), which is part of the natural ^{232}Th decay chain (see Fig. D.8 in the appendix). The same γ -line is produced in the decay series of ^{228}Th , which is used as one of the standard radionuclides in the regularly performed energy calibrations of the demonstrator array at the LNGS (see section 8.1.2).

The initial energy deposition of the e^-e^+ pair is similar to the energy release of a $\beta\beta$ -decay, thus, results in prototype single-site events. Ultimately, the positron will annihilate with a shell electron of the surrounding detector material after both particles slowed down due to the energy loss via ionization. In the annihilation process two back-to-back γ -rays with $E_\gamma = m_e = 511 \text{ keV}$ are created inside the CZT crystal, leading to three interesting scenarios with respect to the energy deposition of the annihilation radiation. The first option is that both annihilation γ -rays deposit their total energy in the initial crystal. This case would contribute to the full-energy peak (FEP) at $E_\gamma = 2.6 \text{ MeV}$. Secondly, one or both γ -rays could escape the initial crystal without an additional interaction. This causes the so-called single-escape peak (SEP) at $E_\gamma - m_e$ and the double-escape peak (DEP) at $E_\gamma - 2m_e$. In the latter case, the primary energy deposition is only due to the initial e^-e^+ pair, thus, provides a population of SSEs. On the other hand, a large fraction of events in the SEP can be expected to show multi-site character due to the photoelectric absorption of one of the annihilation γ -rays in a spot that is very likely separated from its origin. An overview of the kinematics leading to the DEP and SEP is given in Fig. 7.10.

In the following, the optimization of the MSE identification algorithms will be discussed. The procedure makes use of the expected SSE population for entries in the DEP and, respectively, the MSEs expected for SEP entries.

Optimal A/E definition

As briefly discussed in section 7.2.2, there are several options to derive the A/E parameter. While the simplest version based on the plain difference pulse without further corrections produces the most promising results in the pre-characterization and fixes the general method, the smoothing window size n_{sm} remains a free parameter. For the laboratory data, which was originally collected during the development of the PSA method, an optimal value of $n_{\text{sm}} = 6$ has been found for the first implementation of the A/E parameter. By applying the same optimization routine to calibration data of the COBRA demonstrator at the LNGS in [Küt19], it was found that a slightly larger value of $n_{\text{sm}} = 8$ provides the highest sensitivity. However, with respect to the intended calibration of the A/E parameter, a much wider window of $n_{\text{sm}} = 32$ seems to be necessary. The reason is that for some channels the A/E distributions could not be described well with the set of investigated fit functions. Fortunately, the average sensitivity loss turns out to be acceptable and is not expected to limit the A/E approach after its calibration as discussed in section 7.2.4. An example of the dependency of the A/E distribution on the n_{sm} parameter is shown in Fig. D.4 of the appendix.

Sensitivity and efficiency optimization

The optimization of both MSE identification algorithms makes use of the DEP and SEP associated with the ^{208}Tl γ -line at 2.6 MeV. Moreover, the FEP is used as a control region consisting of both SSE and MSE. Each of the corresponding region of interests (ROIs) is defined as $E_\gamma \pm \text{FWHM}(E_\gamma)$ using the full-width at half-maximum (FWHM) at the respective γ -line energy. The resolution curve $\text{FWHM}(E)$ is one of the parameters that is extracted individually for each detector and each calibration run (see also section 8.1.2 and 8.3.4). Fig. 7.11 illustrates the ROIs for the example of a laboratory measurement with a natural

^{232}Th sample. In comparison to the spectrum of the artificial ^{228}Th calibration source at the LNGS (see e.g. Fig. 8.2), there are some additional γ -lines originating from the extended decay sequence (e.g. from ^{228}Ac at 969 keV and 911 keV [NDS20]).

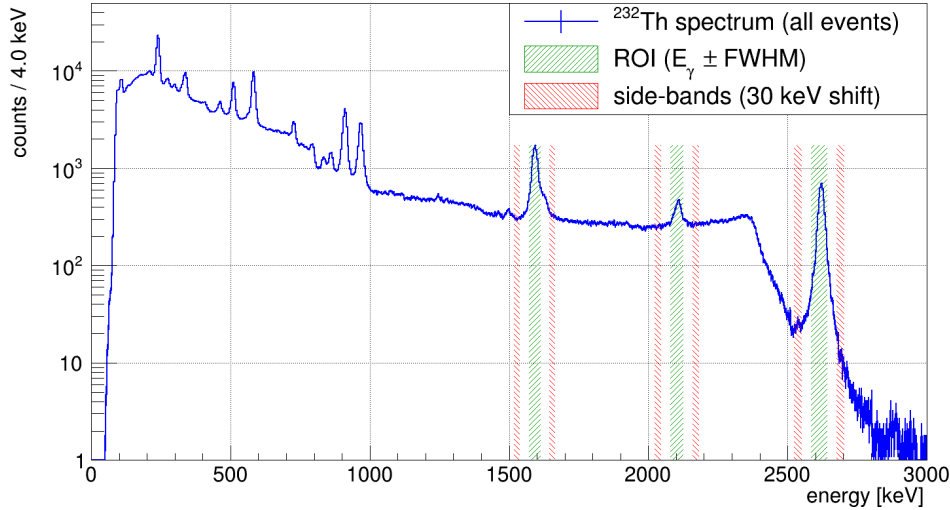


Figure 7.11: Laboratory measurement of the energy spectrum of a natural ^{232}Th sample by a CPG-CZT detector. The spectrum includes the DCCs discussed in section 7.1.1 and the standard z -cut motivated in section 7.1.2. The ROIs and SBs highlight the DEP at 1.6 MeV, the SEP at 2.1 MeV and the FEP at 2.6 MeV. The gap between a ROI and its SBs is found to be optimal for 30 keV. Each ROI covers a range of $E_\gamma \pm \text{FWHM}(E_\gamma)$ corresponding to a Gaussian peak coverage of 98.15% (see section C.2 in the appendix).

The primarily developed optimization routine is based on a sensitivity maximization using the number of peak entries N_{ROI} for different assumed cut values. The range and step size of the cut values' iterations were optimized for each method separately. In the course of the optimization, the calibration data is split into two classes of spectra according to the cut selection, which results in a signal-like spectrum and a background-like spectrum. All events surviving a certain cut are treated as signal, while the rest is treated as background in the iterative process. The aim is to maximize the sensitivity for DEP events in the signal spectrum and for SEP events in the background spectrum.

Because of the presence of the underlying Compton continuum, especially for the DEP and SEP regions, and its unknown composition regarding the SSE/MSE fraction, there is a certain contamination of the previously discussed DEP and SEP event populations. This is why the number of peak entries is corrected by an estimate of the Compton background using so-called side-band (SB) regions. They are placed symmetrically around each ROI and cover in combination the same area. An optimized offset ensures that there is no double counting of events. The SB shift was varied between 2–100 keV and found to be optimal for 30 keV. Another advantage of the SB approach is that the methods provides a robust tool against single detector effects such as a varying resolution or shape of the Compton continuum due to the position of the detector of interest in the demonstrator array. With the number of counts in the ROI and the SBs, the sensitivity can be defined as the following figure of merit

$$s = \frac{N_{\text{ROI}} - N_{\text{SB}}}{\sqrt{N_{\text{SB}}}}. \quad (7.2)$$

Eqn. (7.2) is used for the evaluation of the signal and background spectra corresponding to the assumed cut values in order to determine the optimum values $x_{\text{rms}}^{\text{opt}}$ (in case of the PSA approach) and $(A/E)_{\text{opt}}$. The scaling by the square root of the SB counts is motivated by the Poisson fluctuations of the Compton background.

The results of the sensitivity optimization of the PSA method are depicted in Fig. 7.12. Two optimum values of $x_{\text{rms}}^{\text{opt}}(\text{SSE}) = 2.4$ and $x_{\text{rms}}^{\text{opt}}(\text{MSE}) = 4.6$ are found. The sensitivity curves suggest that sacrificing part of the signal acceptance could result in a higher background rejection. However, the optimization of both quantities at the same time requires a different analysis scheme. Moreover, the application of the PSA optimization approach towards the COBRA demonstrator revealed severe performance issues as mentioned before. This is why an additional figure of merit has been explored in the optimization of the A/E parameter, keeping in mind the use of A/E as the main PSD method in future analyses and its potential calibration.

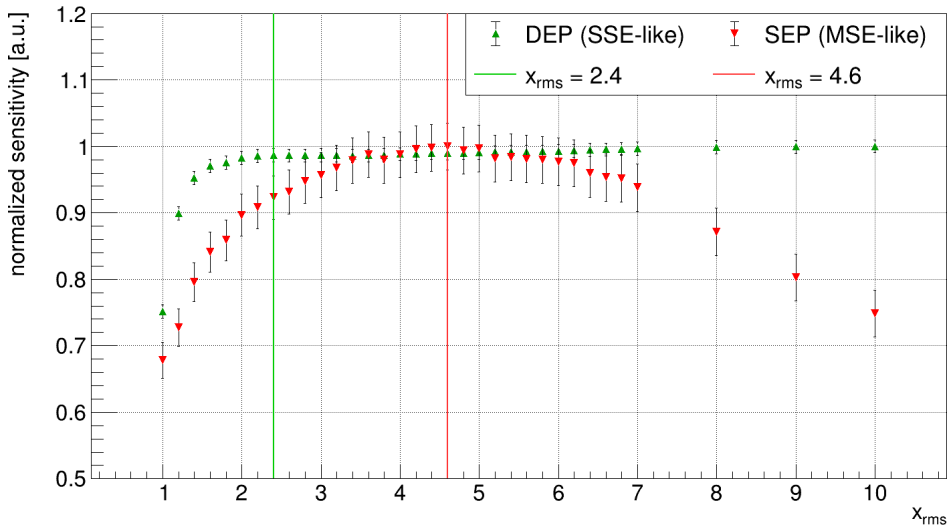


Figure 7.12: Results of the sensitivity optimization for the PSA method. The maximum of the sensitivity with respect to the signal acceptance of the DEP is found for $x_{\text{rms}}^{\text{opt}} = 2.4$. As the sensitivity for the MSE identification in the SEP region is still increasing at that point, it is feasible to combine both quantities in order to search for a compromise between signal acceptance and background rejection.

The alternative optimization procedure makes directly use of the signal acceptance $\varepsilon_{\text{acc}}^{\text{sig}}$ and the background rejection $\varepsilon_{\text{rej}}^{\text{bg}}$. Both are derived from the entries in the signal spectrum's DEP and the background spectrum's SEP, but are set into relation to the corresponding peak entries of the initial spectrum. As the entries without applying an A/E cut are taken as reference, there is no need to estimate the Compton background for each ROI. The $(A/E)_{\text{opt}}$ cut value is found for the maximum of the product of both efficiencies.

An exemplary comparison of the sensitivity optimization and the approach based on the efficiencies is depicted in Fig. 7.13. The latter option has the advantage that the signal acceptance could also be fixed to a certain level, which simplifies the efficiency treatment in later physics analyses of the LNGS data. In fact, this is what will be done in the calibration of the A/E parameter described in section 7.2.4. It should be noted that the results presented in Fig. 7.13 are based on the final definition of the current pulse using a smoothing window of $n_{\text{sm}} = 32$ in order to determine the A/E quantity.

In general there is a good agreement between the two optimization approaches, whereas the previous sensitivity optimization serves as a crosscheck. It was found that the efficiency method proves more reliable when applied to the calibration data of single detectors instead of using a combination as depicted in Fig. 7.13. A particular problem of the sensitivity is its drop in the SEP background channel. For each ROI the optimum A/E , denoted as $(A/E)_{\text{opt}}$, as well as the value corresponding to a signal acceptance of at least 90%, indicated by $(A/E)_{90\%}$, has been highlighted. It is found that the $(A/E)_{90\%}$ value is close to the

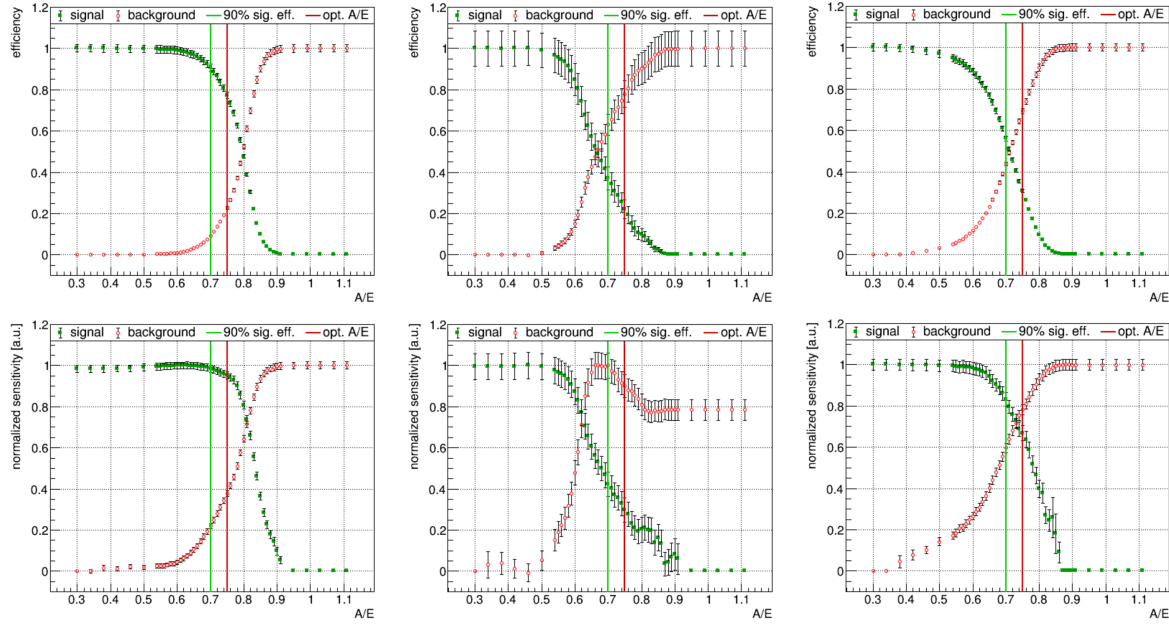


Figure 7.13: Results of the A/E optimization based on the combined data of a single ^{228}Th calibration measurement of the COBRA demonstrator (adapted from [Küt19]). *Top:* default optimization via efficiencies. *Bottom:* crosscheck optimization via sensitivities. The results of the two optimization approaches agree well with each other for all three selected ROIs: DEP (*left*), SEP (*middle*), FEP (*right*). The vertical lines indicate the $(A/E)_{\text{opt}}$ parameter (red) corresponding to the maximum of the product $\varepsilon_{\text{acc}}^{\text{sig}} \cdot \varepsilon_{\text{rej}}^{\text{bg}}$ and the $(A/E)_{90\%}$ value (green), which ensures a signal acceptance of at least 90%.

sensitivity maximum for the DEP's signal spectrum and the SEP's background spectrum. Furthermore, there is a smoother transition of the efficiency curves towards the low and high A/E values compared to the ones obtained by the sensitivity approach.

Determination of optimal efficiencies

Even though there are some flaws in the optimization of the PSA method using the sensitivity as a figure of merit in combination with LNGS calibration data, it is still possible to compare it to the A/E approach in terms of the achieved efficiencies. The achieved signal acceptance and background rejection is summarized in Tab. 7.3.

Table 7.3: Summary of the PSA and the A/E optimization results with respect to the achieved signal acceptance $\varepsilon_{\text{acc}}^{\text{sig}}$ and background rejection $\varepsilon_{\text{rej}}^{\text{bg}}$. The PSA results are based on the laboratory data reported in [Zat17a]. The A/E optimization results involve the combined data of a single calibration run of the demonstrator array and are taken from [Küt19]. Both MSE identification algorithms show a similar performance with respect to the determined efficiencies based on the ^{208}Tl single- and double escape peak.

method	PSA				A/E criterion				
	$x_{\text{rms}}^{\text{opt}} = 2.4$	$\varepsilon_{\text{acc}}^{\text{sig}} [\%]$	$\varepsilon_{\text{rej}}^{\text{bg}} [\%]$		$(A/E)_{\text{opt}} = 0.75$	$\varepsilon_{\text{acc}}^{\text{sig}} [\%]$	$\varepsilon_{\text{rej}}^{\text{bg}} [\%]$	$(A/E)_{90\%} = 0.70$	$\varepsilon_{\text{acc}}^{\text{sig}} [\%]$
DEP	94.8 ± 1.6	5.2 ± 0.6			77.3 ± 1.4	22.7 ± 0.7	90.7 ± 1.6	9.3 ± 0.5	
SEP	37.6 ± 1.9	62.4 ± 2.4			22.0 ± 4.5	78.0 ± 6.4	37.0 ± 5.4	63.0 ± 5.0	

By using the optimized PSA method with $x_{\text{rms}}^{\text{opt}} = 2.4$ it is possible to investigate the energy dependency of the MSE fraction. This is done by calculating the MSE fraction for each energy bin of the input spectrum such as shown in Fig. 7.14.

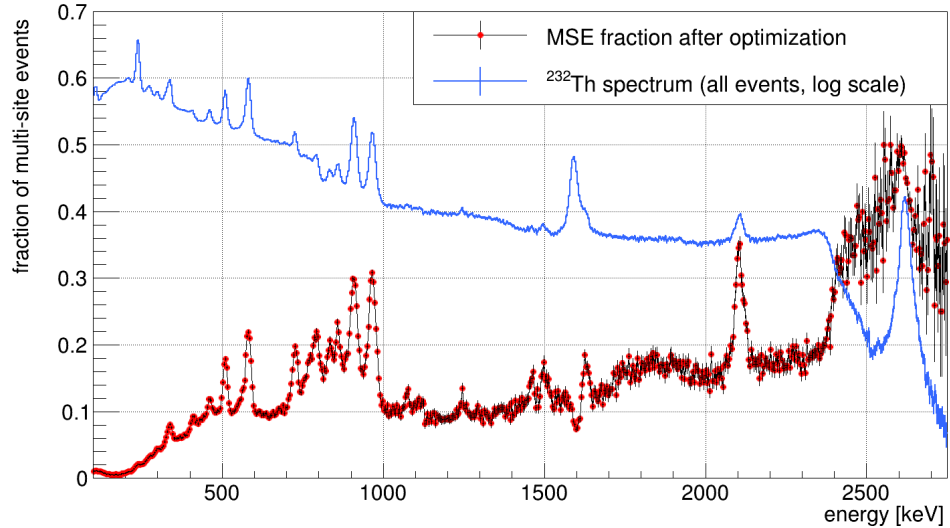


Figure 7.14: Energy dependency of the MSE fraction based on the optimized PSA approach and a single detector laboratory measurement using a natural ^{232}Th sample (updated version of [Zat17a]). For comparison, the ^{232}Th energy spectrum is shown in a logarithmic scale. The graph of the MSE fraction reveals a clear dip for the DEP at 1.6 MeV and a prominent increase at the position of the SEP at 2.1 MeV. Moreover, the MSE fraction is increased for the position of a γ -line, which perfectly agrees with the expectation of the underlying kinematics. The initial γ -ray interaction is very likely a Compton scattering, reducing the energy of the initial γ -ray, which increases the likelihood of a second interaction via photoelectric absorption in the same crystal according to the cross section's energy dependency. Furthermore, the MSE fraction is rather low along the Compton continuum between 1.0–2.3 MeV, which is also in agreement with the expectation from the underlying kinematics and cross sections.

In agreement with the energy dependence of the γ -ray interaction cross sections there is a very low fraction of MSEs below 200 keV (see Fig. 1.8 in section 1.3.1). This is due to the fact that the low-energy range is dominated by the photoelectric absorption, featuring SSE-like interactions. Furthermore, it is found that the MSE fraction increases for the position of the γ -lines emitted in the decay series of ^{232}Th . This behavior can be explained by the underlying kinematics. The primary interaction is very likely a Compton scattering, because it is the dominating process at those energies. However, by loosing energy in the scattering process, the chance for a second interaction via photoelectric absorption within in the same CZT crystal increases. On the contrary, the Compton continuum between 1.0–2.3 MeV features a rather low MSE fraction with a small increase towards higher energies. For the single-escape peak at 2.1 MeV there is a prominent increase of the MSE fraction, while the double-escape peak features a clear dip below the level of the Compton background.

The energy dependence of the MSE fraction based on the A/E criterion is very similar to the example depicted in Fig. 7.14 for the PSA method and needs no further discussion. An application of both PSD algorithms in the analysis of the LNGS physics data is discussed in section 8.2.3. Furthermore, the effect of the optimized $(A/E)_{\text{opt}}$ and $(A/E)_{90\%}$ cut value will be discussed in the course of the search for the $2\nu\beta\beta$ -decay of ^{116}Cd in section 8.4.

Finally, in preparation of the intended calibration of the A/E parameter, the interplay of the PSA and the A/E approach will be briefly discussed in the next section.

Interplay of PSA and A/E

The interplay of the MSE identification algorithms can be studied by taking a look at the distribution of A/E values. This is done by using the laboratory data obtained with the natural ^{232}Th sample as depicted in Fig. 7.15. It should be noted that the data presented in

the following is based on the optimization results obtained for the laboratory setup, including a smoothing window of $n_{sm} = 6$ in the construction of the current pulse. Because of the modified signal amplification of the COBRA demonstrator setup at the LNGS, the scale of the optimum A/E values deviates with respect to the laboratory results. Furthermore, an abnormal A/E distribution has been observed for some channels as reported in a previous thesis [Küt19], which is why the smoothing window was increased to $n_{sm} = 32$ for all LNGS data. In the end, only the absolute scale of the A/E parameter is affected by a change of n_{sm} (see e.g. Fig. D.4 in the appendix) while the overall shape is preserved.

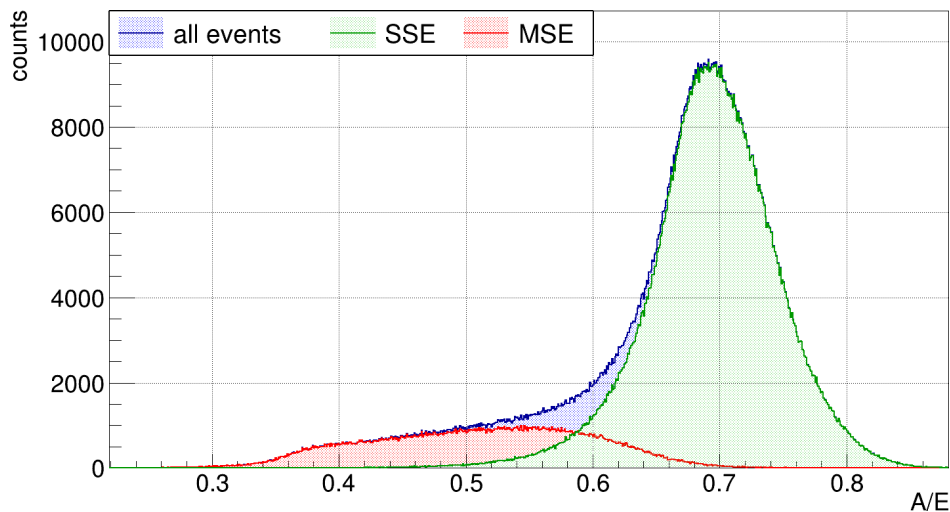


Figure 7.15: Distribution of the A/E criterion for a single detector laboratory measurement using a natural ^{232}Th sample. The distribution includes the DCCs and the standard z -cut, but no restriction of the energy range. The A/E distribution of all events (blue) is crosschecked with the optimized PSA cut by dividing the data into SSE-like (green) and MSE-like events (red). The shape of the SSE fraction is found to be approximately Gaussian while the MSEs are dominantly found in the tail towards lower A/E values.

The crosscheck confirms that MSEs result in lower A/E values compared to SSEs. Moreover, the distribution of the SSE fraction is approximately Gaussian, which is an important finding regarding the calibration of the A/E criterion with the help of the DEP as presented in section 7.2.4. Before discussing the actual calibration procedure and the reasoning behind this measure, some comments regarding the application of the MSE identification besides the background suppression will be made in the final passage of this section.

Application of MSE identification

Primarily, the MSE identification is meant as a tool for the background suppression of γ -ray induced events. However, besides its original application it is possible to apply the developed algorithms in the background characterization with the aim to shed light on its composition. Furthermore, they can help to identify present radionuclides by increasing the sensitivity towards interactions leading to a full-energy deposition within a single CZT crystal. This can be achieved by inverting the original cut, meaning that single-site events are rejected as background. This way an effective reduction of the continuous Compton background is reached, which enhances the intensity of potentially present weak γ -lines. An example as a proof of concept is presented in Fig. 7.16 using the PSA approach and the laboratory measurement with a natural ^{232}Th sample.

The same approach is applied in the characterization of the γ -ray background of the COBRA demonstrator (see section 8.2.3). It is found that in this specific scenario the PSA

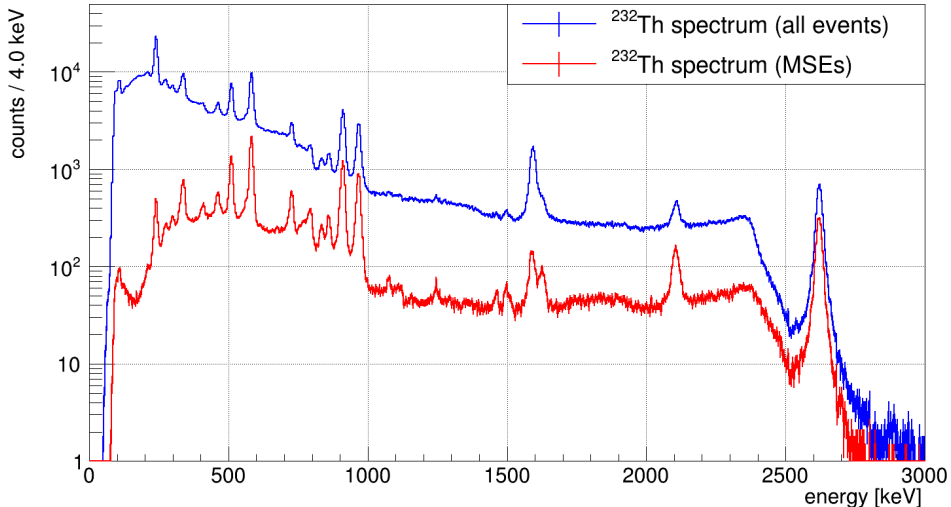


Figure 7.16: Application of the inverted PSA method to enhance the intensity of weak γ -lines in a single detector laboratory measurement using a natural ^{232}Th sample (adapted from [Zat17a]). As the Compton continuum contains dominantly events with single-site character (see e.g. Fig. 7.14), the rejection of SSEs results in an enhancement of the actual full-energy peaks. With this method it is possible to identify weak γ -lines that were previously hidden by the Compton background. In particular, the presence of a subdominant γ -line from ^{212}Bi as part of the ^{232}Th decay chain could be verified. The ^{212}Bi γ -line at $E_\gamma = 1620.5\text{ keV}$ [NDS20] is in the immediate vicinity of the DEP at 1.6 MeV and contributes to the MSE contamination of the SSE-like signal region. In the spectrum including all events, it is not possible to resolve both γ -lines.

method is superior to the A/E approach, as the A/E parameter is by definition also sensitive to LSEs, while the inverted PSA cut selects primarily MSEs. In case of the A/E parameter, the γ -line enhancement turns out to be weaker. A comparison of the effect is exemplarily shown in Fig. 8.8 of section 8.2.3 for the full exposure of the COBRA demonstrator. The enhancement of low-intensity γ -lines offers a wide range of potential applications not only in nuclear physics, but also in medical imaging and environmental control where the signature of weak radioactive nuclides is hidden under a strong Compton continuum or β -decay spectrum.

7.2.4 A/E calibration

The calibration of the A/E parameter has the aim to unify the optimum A/E cut values with respect to the optimization of the selection efficiency of the demonstrator's detectors. The procedure was primarily developed in the course of the Master thesis of J. Kütter [Küt19] and will be briefly summarized in the following.

In the previous section it was shown that the interplay of the PSA method and the A/E criterion reveals an approximately Gaussian shape of the SSE-like part of the A/E distribution using laboratory measurements with a natural ^{232}Th sample. Because of this finding it can be expected that the A/E distribution of DEP entries, which are taken as proxies for single-site interactions, should also feature a Gaussian shape. Furthermore, it could be confirmed with the same pre-characterization that the contamination of the SSE-like DEP population due to MSE-like interactions in the Compton continuum and the present ^{212}Bi γ -line is only a minor effect (see e.g. Fig. 7.14 and Fig. 7.16). The same applies to the energy dependence of the optimal A/E parameter, which is shown in Fig. 7.15.

As expected from the behavior of the MSE fraction depicted in Fig. 7.14, there is a clear spread of the A/E parameter towards lower values for the energies corresponding to the location of a γ -line. This is due to the increased probability of depositing the full γ -ray energy via a multi-site interaction. Moreover, a rather flat A/E band is found for the

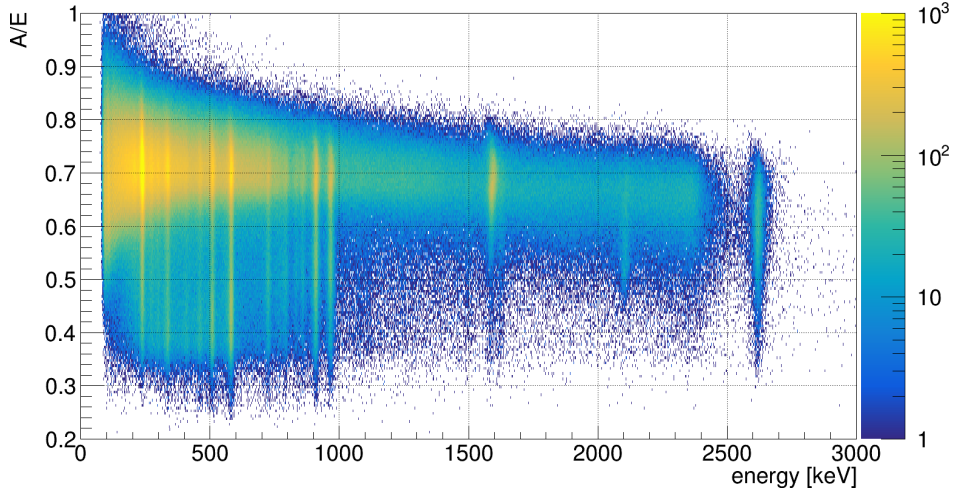


Figure 7.17: Illustration of the energy dependence of the A/E parameter based on a single detector laboratory measurement using a natural ^{232}Th sample. The data selection consists of the DCCs (see section 7.1.1) and the standard z -cut according to section 7.1.2. For the γ -line energies a spread towards lower A/E values is found, which is caused by an increased MSE fraction. On the contrary, the Compton continuum between 1 MeV – 2.3 MeV results in a rather flat band. This applies also to the location of the DEP at 1.6 MeV.

Compton continuum dominating the energy range between 1 MeV – 2.3 MeV. The position of the DEP as proxy for SSE-like interactions is only slightly shifted towards higher A/E values with respect to the surrounding Compton band. The A/E variation across the Compton region is about 5.9% per MeV. Compared to its width and the extension of the DEP region it can be concluded that the energy dependence of the A/E parameter is only a secondary effect, which might be further elaborated in a future iteration of COBRA’s PSD.

The A/E calibration procedure developed in [Küt19] makes exclusively use of the A/E distribution of DEP events. The aim is to find an analytic description of the approximately Gaussian A/E distribution in order to determine its mean $\mu_{A/E}$ and width in terms of $\sigma_{A/E}$. By using these two parameters it is possible to construct a calibrated A/E via fixing the Gaussian parameters to $\mu = 1.0$ and $\sigma = 0.1$ according to Eqn. (7.3) [Küt19].

$$(A/E)_{\text{cal}} = \frac{\sigma}{\sigma_{A/E}} \cdot ((A/E) - \mu_{A/E}) + \mu \quad (7.3)$$

This way, a universal cut value based on the Gaussian coverage can be chosen which corresponds by definition to a certain level of the signal acceptance and can be calculated analytically. Exemplarily, the one-sided 90% quantile $k_\alpha = 1.282$ of a Gaussian A/E distribution with $\mu = 1.0$ and $\sigma = 0.1$, which would correspond to a DEP signal acceptance of 90%, is achieved for $(A/E)_{90\%} = 0.872$ (see details given in section C.2 of the appendix).

For the analytic approximation of the DEP’s A/E distribution, several fit models were considered in [Küt19]. The first approach was based on the original A/E publication by the GERDA collaboration [GER13a] suggesting a tailed Gaussian to address the tailing towards lower A/E values. However, the fit results were accompanied by a poor convergence and description of the A/E distribution for same channels of the COBRA demonstrator. Thus, alternative fit models were tested including an exponentially modified Gaussian (EMG), the sum of a conventional Gaussian and an EMG, as well as the sum of two EMGs. While some of the more elaborate models could describe most of the A/E distributions sufficiently, there was only a poor match between the extracted width based on the fit parameters and the plain observation. The observed discrepancy is caused by the superposition of several

analytic expressions, which result in a sufficient convergence, but come at the cost that e.g. the peak width cannot be derived directly from a single component of the combined fit.

In the end, the matching of the individual detectors' A/E distributions could be improved by increasing the smoothing window in the construction of the current signal as discussed in section 7.2.3. Furthermore, an adequate description of the updated A/E distributions could be achieved with the two-sided Gaussian according to Eqn. (5.7) including a linear background component for the tailing. The usage of this fit model has the advantage that it is already well-established in the standard calibration procedure of the COBRA demonstrator and features a custom optimization routine of the fit range.

An impression of the initial A/E calibration performed in [Küt19] is shown in Fig. 7.18 for one example calibration run of the demonstrator array. The same procedure was applied to 38 calibration runs performed between Sept.'11 and Sept.'16 in the same reference. In the course of the present thesis, the original procedure was revised and finally implemented into COBRA's standard calibration procedure. Due to some minor changes of the procedure, it was necessary to perform a re-evaluation of all 56 calibration runs performed during the operation of the COBRA demonstrator (see also section 8.1.2)

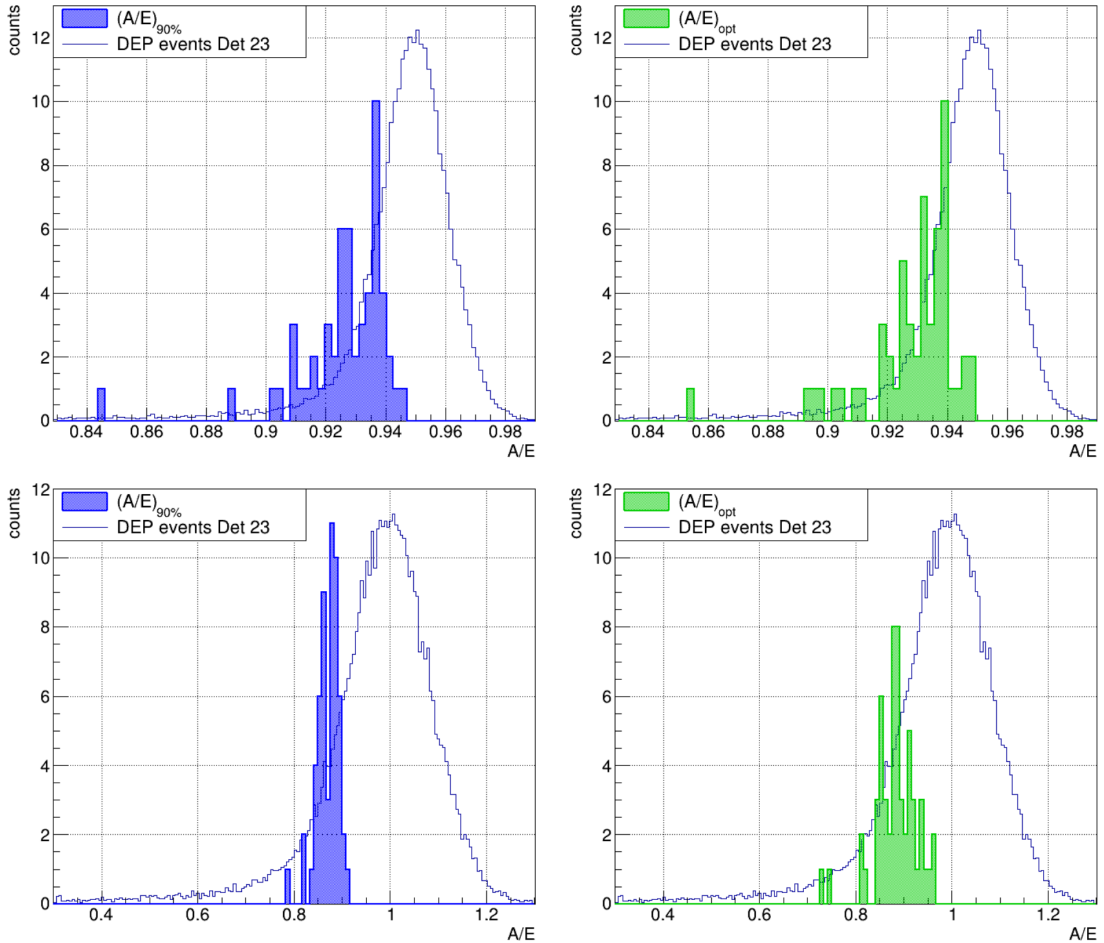


Figure 7.18: Comparison of the optimized $(A/E)_{90\%}$ (left) and $(A/E)_{\text{opt}}$ cut values (right) before and after a calibration of the A/E parameter based on DEP events. *Top:* before calibration. *Bottom:* after calibration. Although the results are based on a single calibration run, they are representative for the optimization and calibration of A/E on the individual detector level. For comparison, the DEP A/E distribution of Det 23 (L2-P07) is shown. After its calibration there is a sharp distribution of the single detectors' $(A/E)_{90\%}$ cut value around the analytically expected one-sided Gaussian 90% quantile corresponding to $(A/E)_{90\%} = 0.872$.

For the example presented in Fig. 7.18 an average of $\overline{(A/E)}_{90\%} = 0.872$ is found which coincides perfectly with the one-sided 90% quantile of the Gaussian model quoted before. This is an impressive confirmation of the feasibility of the A/E calibration and allows for the usage of an universal A/E parameter for all detectors. For the analysis projects presented in the course of the present thesis a value of $(A/E)_{90\%} = 0.872$ will be applied.

Using this $(A/E)_{90\%}$ cut criterion an averaged signal acceptance of $\varepsilon_{\text{acc}}^{\text{sig}} = 90.0 \pm 1.5\%$ is found for the data reported in Fig. 7.18 while a background suppression of about 65% is achieved for events in the SEP (see also Tab. 7.3 in section 7.2.3). The latter value is found to deviate up to 30% as a consequence of the varying intensity of the SEP in the respective calibration spectra of the single detectors. The presence of the SEP depends on the position of a detector in the demonstrator array with respect to the source position during the calibration. For detectors that are farther away from the source, the rate of primary γ -ray interactions is reduced, while the fraction of secondary interactions due to backscattering from the surrounding shielding is significantly higher. The non-uniform distribution of full-energy interactions across the detector array is also addressed in section 8.1.2 regarding the effect on the overall calibration procedure.

7.3 Pulse-shape library via coincident Compton scattering

The development of the MSE identification algorithms has been accompanied by the construction and commissioning of a laboratory experiment at TU Dresden with the aim to create a pulse-shape library of single-site interactions. The construction of this setup and a preliminary analysis of the data obtained in the commissioning process is documented in [Zat14]. In the course of the present thesis, the data-taking was continued and further optimized. In the end, about ten times more data could be collected compared to the original work. An update on the experimental progress and the data evaluation was presented at the *2016 IEEE NSS/MIC/RTSD* conference and has been published in the respective conference proceedings [Zat17a]. A summary of the experimental results and an impression of the pulse-shape library will be given in the following.

7.3.1 Experimental setup

The key idea of the dedicated laboratory experiment is based on the so-called Compton coincidence technique (CCT), which is commonly used in a wide range of nuclear physics applications such as high-precision γ -ray spectroscopy with nearly full 4π coverage (see e.g. the AGATA and GRETA projects [KL19]) or the characterization of scintillator materials (see e.g. [RPH⁺09]). The present approach makes use of a two-detector-system consisting of a single 1 cm^3 CPG-CZT detector as applied for the COBRA demonstrator and a conventional high-purity germanium (HPGe) detector. The CZT detector acts as a scatter device for a preferably mono-energetic γ -ray source, while the second detector is used to detect scattered γ -rays in a certain solid angle. The solid angle acceptance is limited by several passive absorbers, the optimized distance between the pre-collimated γ -ray source and the scatter detector, as well as the positioning of the secondary HPGe detector.

If both detector systems detect an interaction within a certain coincidence time window, while the sum of the energy depositions matches the initially emitted γ -ray's energy, it can be concluded from the underlying kinematics that a single Compton scattering took place inside the CZT detector. Moreover, the scattered γ -ray was fully absorbed in the HPGe detector. A single Compton scattering provides a SSE-like signature, which was already proven experimentally in the previous section in the characterization of the A/E parameter. By limiting the solid angle acceptance to a certain mean scattering angle, it is possible to

calculate the expected energy depositions of both detectors analytically. In the present case, the general expressions in Eqn. (1.28)–(1.29) given in section 1.3.1 result in

$$E_{\text{HPGe}} = \frac{E_\gamma}{\frac{m_e}{m_e}(1 - \cos \vartheta) + 1}, \quad (7.4)$$

$$E_{\text{CZT}} = E_\gamma - E_{\text{HPGe}}. \quad (7.5)$$

The energy deposits E_{CZT} and E_{HPGe} depend on the scattering angle ϑ between the incoming and outgoing γ -ray as well as its initial energy E_γ and the electron rest mass $m_e = 511 \text{ keV}$. The expected mean energies according to Eqn. (7.4)–(7.5) allow for an even more restrictive selection as will be discussed in section 7.3.4. Its application reduces the contribution of random coincidences depositing E_γ in sum of both detector interactions.

An overview of the experimental setup is depicted in Fig. 7.19. Its construction, characterization and commissioning is described in [Zat14]. The well-shielded source container is placed on rails connected to a goniometer device with the CZT detector at the pivot position as shown in Fig. 7.20. This allows to adjust the distance between the scatter detector and the source container, as well as the manipulation of the scattering angle ϑ . The pre-collimation of the γ -ray source leads to a homogeneous irradiation of the CZT crystal. Furthermore, the design of the setup ensures that both detector centers and the center of the γ -ray source share the same elevation. For the accomplishment of the experiment one of the best-performing CPG-CZT detectors from the L3/L4 batch was chosen. It is labeled as Det102 according to TUD's internal naming scheme. Because of its long-term operation in the Compton scattering experiment and its usage for other laboratory projects (see e.g. section 7.4.2), it was not installed at the LNGS after finishing the measurement campaigns.

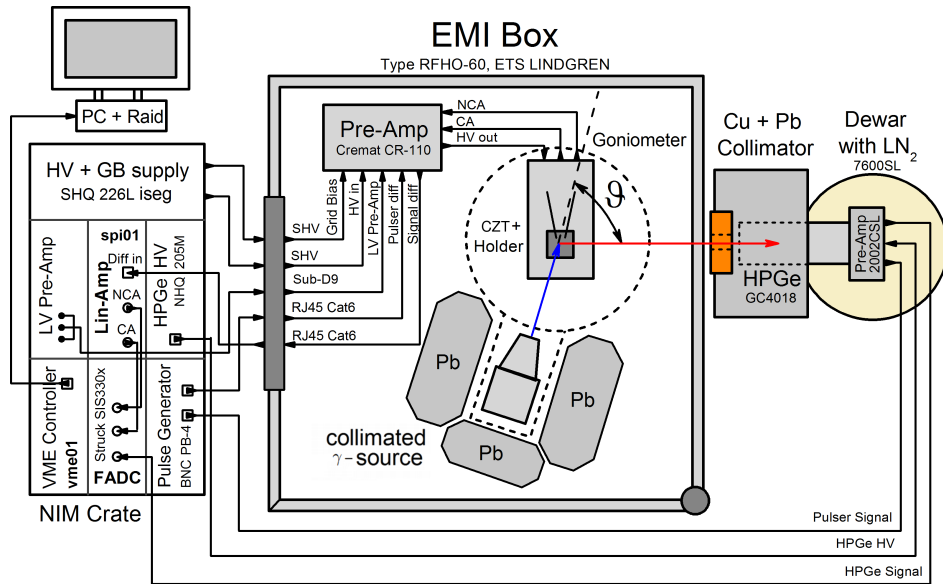


Figure 7.19: Schematic drawing of the Compton scattering setup developed at TUD (adapted from [Zat14]). Details about the DAQ system and the detector characterizations can be found in Ref. [Zat14]. The key concept of the experiment is based on coincident detector interactions as highlighted in the picture. The initially emitted γ -ray (blue) is able to undergo a single Compton scattering at the CZT detector located at the pivot position of the goniometer device. Consequently, the scattered γ -ray (red) could be absorbed by the HPGe detector outside the EMI box housing the scatter experiment. If both energy depositions match with the expectation from the underlying Compton kinematics according to Eqn. (7.4)–(7.5), the primary interaction recorded by the CZT detector features a single-site character.

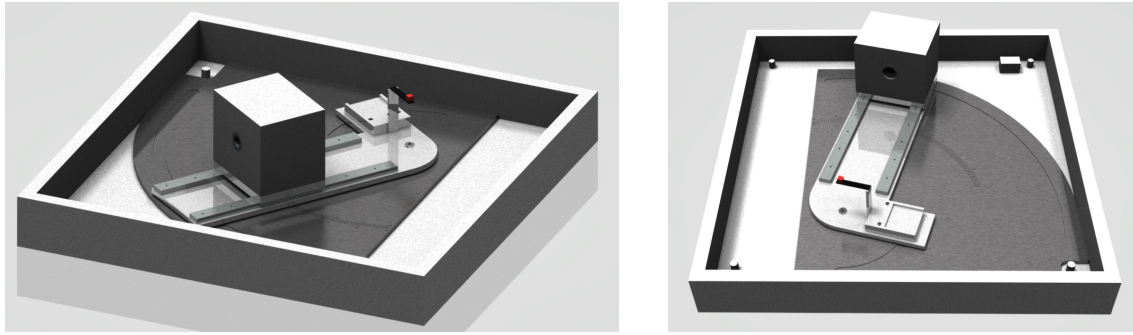


Figure 7.20: Illustration of the goniometer device developed for the Compton scattering setup at TUD (taken from [Zat14]). Both pictures are computer renderings of the CAD project sketch created via the program *autodesk inventor professional* [Aut20]. The L-shaped structure holds the source container, which can be moved along rails to adjust the distance between the pre-collimated γ -ray source and the CZT detector at the pivot position. The complete part can be rotated along a teflon-coated indentation of the ground plate in order to adjust the scattering angle. Details can be found in the appendix of [Zat14].

The CZT detector setup and part of the required readout electronics are placed inside a light-tight steel box acting as a shield against electromagnetic interference (EMI). Outside the EMI box, a multi-layer passive shield made of copper and lead limits the solid angle acceptance of the HPGe detector to about $\pm 10^\circ$ with respect to its sensitive volume of about 185 cm^3 [Zat14]. Pictures of the setup can be found in section B.3 of the appendix.

The original concept of the experiment foresees the usage of a LAA type ^{137}Cs source of 2.8 MBq activity, providing a monoenergetic prominent γ -line of $E_\gamma = 661.7 \text{ keV}$. The distance between the source container acting as a pre-collimator and the CZT scatter detector was found to be optimal at about 20 cm. As the maximum scattering angle is limited to $\vartheta = 90^\circ$ (see e.g. Fig. 7.19), only the energy range up to $E_{\text{CZT}}(\vartheta = 90^\circ) = 373.4 \text{ keV}$ can be probed (see also Fig. 7.22). After the concept of the Compton scattering experiment could be successfully proven in [Zat14], a survey of alternative γ -ray sources was performed in order to access a higher energy scale for the investigation of single-site events. However, the list of suitable candidates is rather short as the respective radionuclides are either short-lived or feature complex γ -ray cascades. Such cascades would make it very challenging to discriminate true coincidences fulfilling the Compton scattering conditions according to Eqn. (7.4) – (7.5) from random coincidences caused by unrelated γ -ray interactions. Moreover, the energy dependence of the Compton scattering process has to be taken into account. While it dominates in the 0.5 – 3.0 MeV region, indicating the double beta decay region of interest, pair production becomes dominant around 10 MeV , which would be the ultimate upper limit.

Out of the available γ -ray calibration sources at TUD, a suitable ^{60}Co source with an activity of about 5.0 MBq could be used for an extension of the Compton scattering experiment. Its geometric LAA type is the same as for the originally deployed ^{137}Cs source, hence, it fits perfectly into the same source container. Furthermore, the activity is found to be of the same order. However, due to its increased γ -ray energies, which exceeds the ^{137}Cs γ -line by about two times, additional shielding material is required in order to maintain the angular acceptance of the previous setup and to prevent random detector coincidences.

The decay scheme of the ^{60}Co β -decay is depicted in Fig. 7.21. It involves a strongly correlated cascade of two γ -rays of similar energies from the first two excited states of ^{60}Ni . The angular correlation function of the involved γ -rays can be expressed as

$$W(\vartheta) = 1 + \frac{1}{8} \cos^2 \vartheta + \frac{1}{24} \cos^4 \vartheta, \quad (7.6)$$

assuming a sequential $4^+ \rightarrow 2^+ \rightarrow 0^+$ quadrupole-quadrupole transition. A comparison

between the theoretical description of the angular distribution according to Eqn. (7.6) and a dedicated experiment is shown in Fig. 7.21.

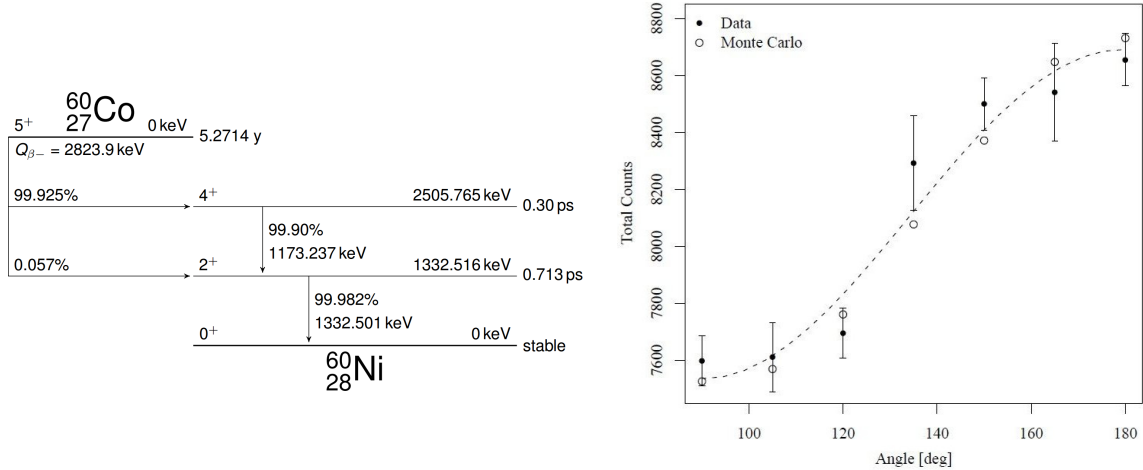


Figure 7.21: Characteristics of the ^{60}Co β -decay via the first excited states of ^{60}Ni and the involved de-excitation γ -rays. *Left:* decay scheme with values from [NDS20] (adapted from [Zat14]). The intermediate $J^\pi = 2^+$ state in ^{60}Ni has a very short lifetime, which is why the emission of the two de-excitation γ -rays is practically in coincidence. *Right:* angular distribution of the γ -ray cascade involving the first two excited states of ^{60}Ni (adapted from [Muh08]). The corresponding angular correlation function can be described by a sequential $4^+ \rightarrow 2^+ \rightarrow 0^+$ quadrupole-quadrupole transition according to Eqn. (7.6).

Even though the ^{60}Co decay scheme involves a γ -ray cascade, there is a high probability for a back-to-back correlation of the two γ -rays due to the spin states of the intermediate levels in ^{60}Ni . Consequently, an effective suppression of random coincidences can be achieved for a sufficiently large distance between the pre-collimated γ -ray source and the two-detector-system. This is why the source container was moved to the maximum distance of about 35 cm. The positioning of the CZT scatter detector and the HPGe was improved as well. Moreover, an additional layer of lead has been placed on the side between the source and the HPGe detector in order to reduce the rate of direct hits (see also Fig. 7.19). Lastly, the software trigger condition was changed so that only the secondary HPGe detector triggers the readout of both detector systems. All of those measures aim to ensure that the same analysis strategy as developed for the ^{137}Cs measurements can be applied for the ^{60}Co data, assuming that the γ -ray cascade is virtually decoupled and can be treated as two separate decay branches. A summary of the data-taking is reported in the next section.

7.3.2 Data-taking and pre-selection

In the course of the Compton scattering experiment two γ -ray sources were deployed into the setup. The first campaign was performed using the radionuclide ^{137}Cs with $E_\gamma = 661.7\text{ keV}$. Its single γ -ray emission allows for an optimization of the measuring time based solely on the angular dependency of the Compton kinematics without the need to consider multiple γ -ray energies. Fig. 7.22 illustrates the angular dependency of the expected energy transfer to the electron (detected by the CZT scatter detector) and the scattered γ -ray (absorbed by the HPGe detector) for the case of ^{137}Cs . Furthermore, the differential cross section according to the Klein-Nishina formula given in Eqn. (1.30) of section 1.3.1 is shown.

While the largest possible scattering angle of $\vartheta = 90^\circ$ provides the highest energy deposition within the CZT detector, it features the minimal cross section. This is why the irradiation time needs to be adjusted for each scattering angle in order to achieve sufficient

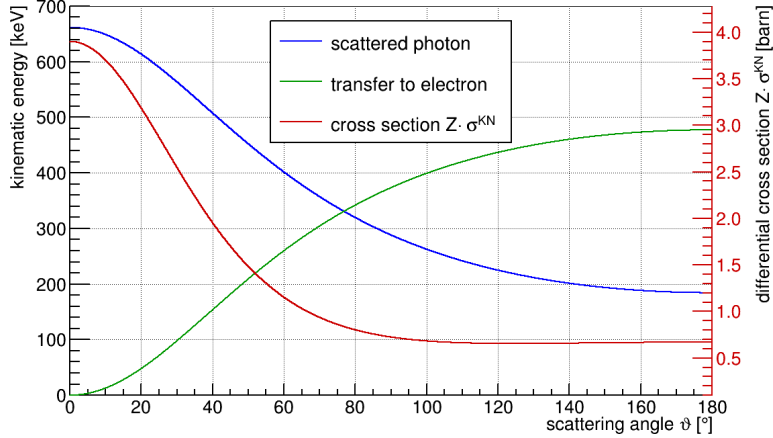


Figure 7.22: Illustration of the angular dependency of the Compton kinematics and the differential cross section for the example of $E_\gamma(^{137}\text{Cs}) = 661.7\text{ keV}$ (taken from [Zat14]). The differential cross section (red) follows the Klein-Nishina formula given in Eqn. (1.30). The energy transfer to the electron (green) is expected to remain in the CZT detector acting as the scatter device, while the scattered γ -ray (blue) needs to be fully absorbed by the HPGe detector in order to fulfill the required coincidence condition. The maximum energy deposit in the CZT detector is achieved for a scattering angle of $\vartheta = 90^\circ$, which is accompanied by the minimum of the cross section. For smaller scattering angles, a higher cross section is found, which allows for an estimate of the measuring time to reach comparable statistics for each investigated scattering angle.

statistics. The aim of the experiment is to collect a minimum of 10 000 SSE-like pulse-shapes representing the energy range that is predetermined by the choice of the scattering angle. Independently from the chosen scattering angle, the angular acceptance of the two-detector-system is found to be about $\pm 10^\circ$. Based on this finding, an angular step width of $\Delta\vartheta = 10^\circ$ is applied for most of the measurements. Moreover, there is a limitation of the minimum scattering angle due to various experimental aspects. This includes the typical threshold of the CZT detector setup, the maximum trigger rate that can be handled by the DAQ system and the increasing chance of direct hits regarding the HPGe detector for decreasing ϑ . Because of those experimental boundaries, a minimum scattering angle of $\vartheta = 45^\circ$ has been chosen. An overview of the complete data-taking is given in Tab. 7.4.

Table 7.4: Summary of the data-taking with the Compton scattering experiment at TUD. As the Compton scattering cross section (see Fig. 7.22) depends on the scattering angle ϑ , the irradiation time needs to be adapted for each applied ϑ . The minimum cross section is found for $\vartheta = 90^\circ$, which is why the largest amount of raw data has been recorded for this setting. In order to reduce the data amount, a pre-selection based on the amplitudes of the raw pulses was performed. This measure reduces the initial data by about one third. The final selection takes into account the coincidence conditions according to Eqn. (7.4) – (7.5), as well as the angular acceptance of the two-detector-system. The true coincidences matching the single Compton scattering hypothesis make up for about 0.3% of the total raw data.

data set	irradiation time	raw data	pre-selection	final selection
$^{137}\text{Cs}, \vartheta = 45^\circ$	4 days	83 GB	58 GB	0.5 GB
$^{137}\text{Cs}, \vartheta = 50^\circ$	5 days	113 GB	78 GB	0.6 GB
$^{137}\text{Cs}, \vartheta = 60^\circ$	7 days	239 GB	166 GB	0.9 GB
$^{137}\text{Cs}, \vartheta = 70^\circ$	12 days	323 GB	227 GB	0.9 GB
$^{137}\text{Cs}, \vartheta = 80^\circ$	16 days	396 GB	275 GB	0.8 GB
$^{137}\text{Cs}, \vartheta = 90^\circ$	41 days	1658 GB	1398 GB	2.6 GB
$^{60}\text{Co}, \vartheta = 60^\circ$	11 days	559 GB	245 GB	2.9 GB
$^{60}\text{Co}, \vartheta = 90^\circ$	31 days	824 GB	407 GB	3.0 GB
total	127 days	4295 GB	2854 GB	12.2 GB

As the default trigger of COBRA's DAQ software is not able to explicitly trigger on coincidences, the selection of two-detector-hits is only possible in an offline analysis. In order to reduce the amount of raw data, which contains the full pulse traces of both detectors, a pre-selection has been performed. For the ^{137}Cs runs both detectors could trigger the readout of the two-detector-system while in the case of ^{60}Co only the HPGe was chosen as the trigger. The true coincidences can be selected by requiring a minimum amount of deposited energy in both detectors, similarly to the method applied for the pre-selection of the two-dimensional γ -scans (see Tab. 6.1). As the pre-selection is performed on the raw data level, without processing the entire data with MAnTiCORE, only the raw pulses' amplitudes in FADC units are available. In the present case, a threshold of 20 units is chosen, which translates to about 30 keV for the CPG-CZT detector and to about 75 keV in case of the HPGe detector. Both of those values are far below the expected energy depositions for the coincident Compton scattering processes in the respective detectors, which ensures that none of the interesting data is thrown out in the pre-selection. The achieved reduction is about one third with respect to the initial amount of raw data. Compared to the final selection using the Compton coincidence conditions formulated in Eqn. (7.4) – (7.5), revealing a fraction of only about 0.3%, it can be confirmed that the pre-selection is a conservative measure. The resulting coincident energy spectra for the measurement campaigns reported in Tab. 7.4 will be presented in the following section.

7.3.3 Coincident energy spectra

The spectra of the pre-selected, coincident ^{137}Cs events are depicted in Fig. 7.23. Each entry in one of the spectra of the CZT detector has a counter part in the corresponding spectrum of the HPGe detector. As the scattered γ -rays do not necessarily deposit their full energy in the HPGe detector, the total count rate in the CZT detector's scatter peaks is higher with respect to the absorption peaks in the HPGe spectra. However, the integrals over the spectra corresponding to the same scattering angle match each other.

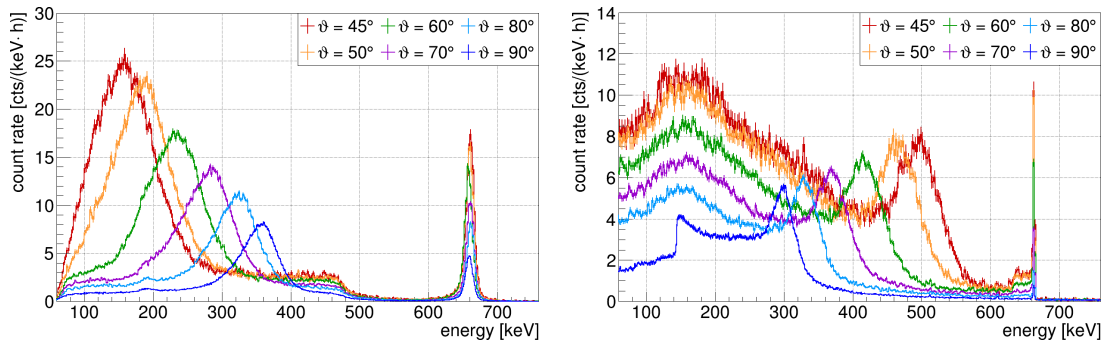


Figure 7.23: Coincident energy spectra of the CPG-CZT detector (*left*) and the HPGe detector (*right*) for various scattering angles ϑ using the Compton scatter setup with a pre-collimated ^{137}Cs γ -ray source. The count rate is normalized to the experimental live-time and the energy binning of 2 keV. Because of the pre-selection there is a threshold of 30 keV in case of the CZT detector and a threshold of 75 keV for the HPGe detector. The widths of the prominent scatter and absorption peaks indicate a constant angular acceptance of about $\pm 10^\circ$. The presence of the ^{137}Cs full-energy peak at $E_\gamma = 661.7$ keV is a measure for the occurrence of random coincidences. The probability of random coincidences increases with smaller scattering angles, which is perfectly in agreement with the expectation from the design of the experiment.

As expected from the underlying kinematics depicted in Fig. 7.22, the positions of the scatter peaks are shifted towards higher energies for increasing scattering angles, while the count rate decreases due to the angular dependence of the Compton scattering cross section. The same trend of the count rate can be observed for the spectra of the HPGe detector,

whereas the absorption peaks get shifted to lower energies for increasing values of ϑ . The position of the peaks is consistent with the expectations following Eqn. (7.4)–(7.5).

Furthermore, the presence of the ^{137}Cs full-energy peak at $E_\gamma = 661.7\text{ keV}$, which is due to random coincidences, depends on the choice of ϑ . For the applied thresholds in the pre-selection process, it is found to be the more prominent, the lower the scattering angle. Moreover, it provides a measure of the typical energy resolution of the two detector systems, which is much better than indicated by the prominent scatter and absorption peaks.

The evaluation of the widths of the prominent scatter and absorption peaks confirms an approximately constant angular acceptance of about $\pm 10^\circ$ for the complete range of the investigated scattering angles $\vartheta \in [45^\circ, 90^\circ]$. Consequently, the angular acceptance is used to estimate the expected energy ranges for the selection of single-site events based on the Compton coincidence conditions Eqn. (7.4)–(7.5). The corresponding energy ranges are summarized in Tab. 7.5. For the ^{60}Co runs, the angular acceptance was reduced to $\pm 5^\circ$ in order to lessen the overlap of the ROIs. The complete set of SSE selection criteria will be discussed in the next section.

Table 7.5: List of the expected energy depositions corresponding to an applied scattering angle ϑ and its angular acceptance of the two-detector-system. The expected mean energy depositions E_{CZT} and E_{HPGe} , as well as their assigned asymmetric energy ranges follow from Eqn. (7.4)–(7.5). For the ^{137}Cs runs there is a good agreement of the assigned energy ranges and the widths of the scatter peaks illustrated in Fig. 7.23. In the case of the ^{60}Co irradiation there are two γ -rays released as a cascade (see Fig. 7.21). Although the two γ -lines can be well distinguished given the energy resolution of both detectors, the Compton kinematics lead to a strong overlap of the expected energy ranges, especially for the E_{HPGe} values. In order to lessen the effect, the angular acceptance has been reduced artificially to $\pm 5^\circ$.

radionuclide	scattering angle ϑ [$^\circ$]	E_{CZT} [keV]	E_{HPGe} [keV]
^{137}Cs $(E_\gamma = 661.7\text{ keV})$	45 ± 10	182^{+53}_{-56}	480^{+56}_{-53}
	50 ± 10	209^{+51}_{-55}	452^{+55}_{-51}
	60 ± 10	260^{+44}_{-51}	402^{+51}_{-44}
	70 ± 10	304^{+38}_{-44}	357^{+44}_{-38}
	80 ± 10	342^{+31}_{-38}	320^{+38}_{-31}
	90 ± 10	373^{+26}_{-31}	288^{+31}_{-26}
^{60}Co $(E_\gamma = 1173.2\text{ keV})$	60 ± 5	627^{+42}_{-47}	546^{+47}_{-42}
	90 ± 5	817^{+20}_{-23}	356^{+23}_{-20}
^{60}Co $(E_\gamma = 1332.5\text{ keV})$	60 ± 5	754^{+47}_{-53}	578^{+53}_{-47}
	90 ± 5	963^{+22}_{-25}	369^{+25}_{-22}

7.3.4 Single-site event selection

The selection of single-site events makes use of several criteria. The first category only concerns the CZT detector and consists of the standard DCCs (see section 7.1.1) and a restriction of the interaction depth according to $0.1 < z \leq 1.03$. Secondly, the time correlation between the two detectors is used to reduce the amount of random coincidences. In the original work [Zat14] the time delay was determined to $\tau_{\text{delay}} = 65 \pm 10\text{ ns}$ with an external pulse generator. As the trigger position of the CZT detector's raw signals depends also on the interaction depth (see e.g. Fig. 7.1), the position of the point, where the difference pulse's amplitude reaches 50% of its final pulse-height is used as a reference (see e.g. the definition of the ERT criterion in Fig. D.1 of the appendix).

Finally, the energy restrictions according to the angular acceptance as reported in Tab. 7.5 of the previous section are applied. The signatures of the coincident Compton scattering

processes with respect to the energy depositions in the two-detector-system are depicted in Fig. 7.24. The energy spectra presented before in Fig. 7.23 would correspond to the projections of the two-dimensional representations. The chosen examples illustrate the ^{137}Cs and ^{60}Co irradiation for $\vartheta = 90^\circ$ under the selection criteria summarized above.

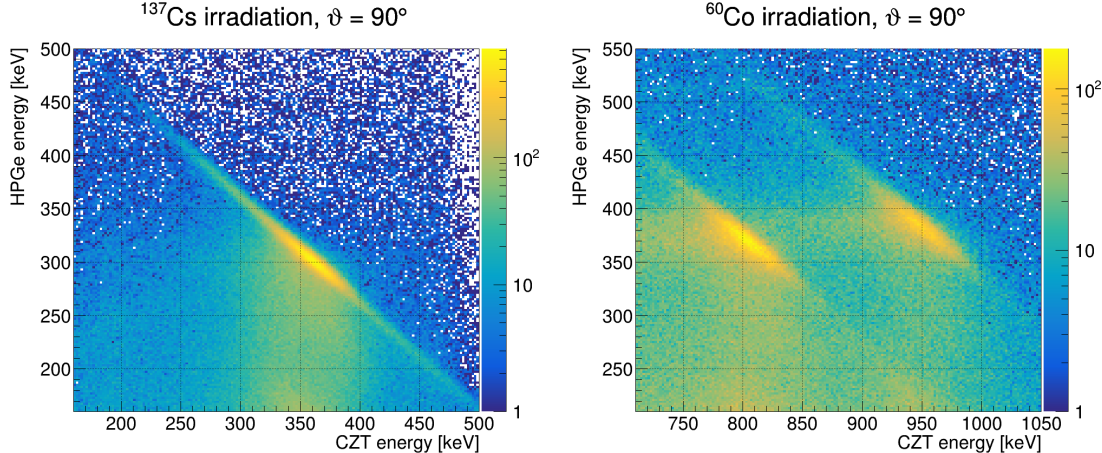


Figure 7.24: Examples of the two-dimensional representation of the coincident energy spectra obtained by the Compton scattering experiment. *Left:* spectrum of the ^{137}Cs irradiation for $\vartheta = 90^\circ$. *Right:* spectrum of the ^{60}Co irradiation for $\vartheta = 90^\circ$. Each axis features a binning of 2 keV with E_{CZT} along the x -axis and E_{HPGe} along the y -axis, respectively. The areas of the highest intensity correspond to the coincident Compton scattering events and indicate the region of interests (see also Tab. 7.5). For the case of the ^{60}Co irradiation, the two ROIs are well separated from each other, even though there would be a strong overlap in the projected HPGe spectrum. The triangular region above the signal ROI is assumed to be dominated by random coincidences of unrelated γ -ray interactions.

In both cases the coincident Compton events are found to be very prominent with respect to the appearance of random coincidences. However, in case of the ^{60}Co irradiation the signal regions are much more smeared out, which is mainly caused by the increased γ -ray energies. As the original setup and its shielding concept was designed explicitly for $E_\gamma(^{137}\text{Cs}) = 661.7$ keV, additional passive shielding and a change of the trigger mode were necessary to perform the experiment with ^{60}Co . The limiting factor was identified as the maximum trigger rate that could be managed by the backplane of the VME-based DAQ system. Nonetheless, it is easily possible to distinguish the signatures of the two ^{60}Co γ -rays by using the energy restrictions as reported in Tab. 7.5, despite featuring an overlap of the expected E_{HPGe} ranges.

7.3.5 Single-site pulse-shape library

The data evaluation and selection criteria discussed in the previous section allow to identify true coincident events in an efficient way. Moreover, the coincident energy spectra illustrated in Fig. 7.24 reveal that the data obtained by the Compton experiment are clearly dominated by such true coincidences and that, hence, a library of single-site events can be build up using the selected CZT detector's pulse traces. An impression of the SSE pulse-shape library is given in Fig. 7.25 for a subset of the total data. For all performed γ -ray irradiation measurements and applied scattering angles more than 10 000 SSE-like pulse-shapes were recorded, which was the declared goal of the Compton scattering experiment.

The illustration makes use of a density profile highlighting the most probable pulse-shapes for the raw signals CA and NCA, and the derived difference signal of both. The latter signal is the basis for COBRA's past and current PSD techniques (see section 7.1.3 and 7.1.4).

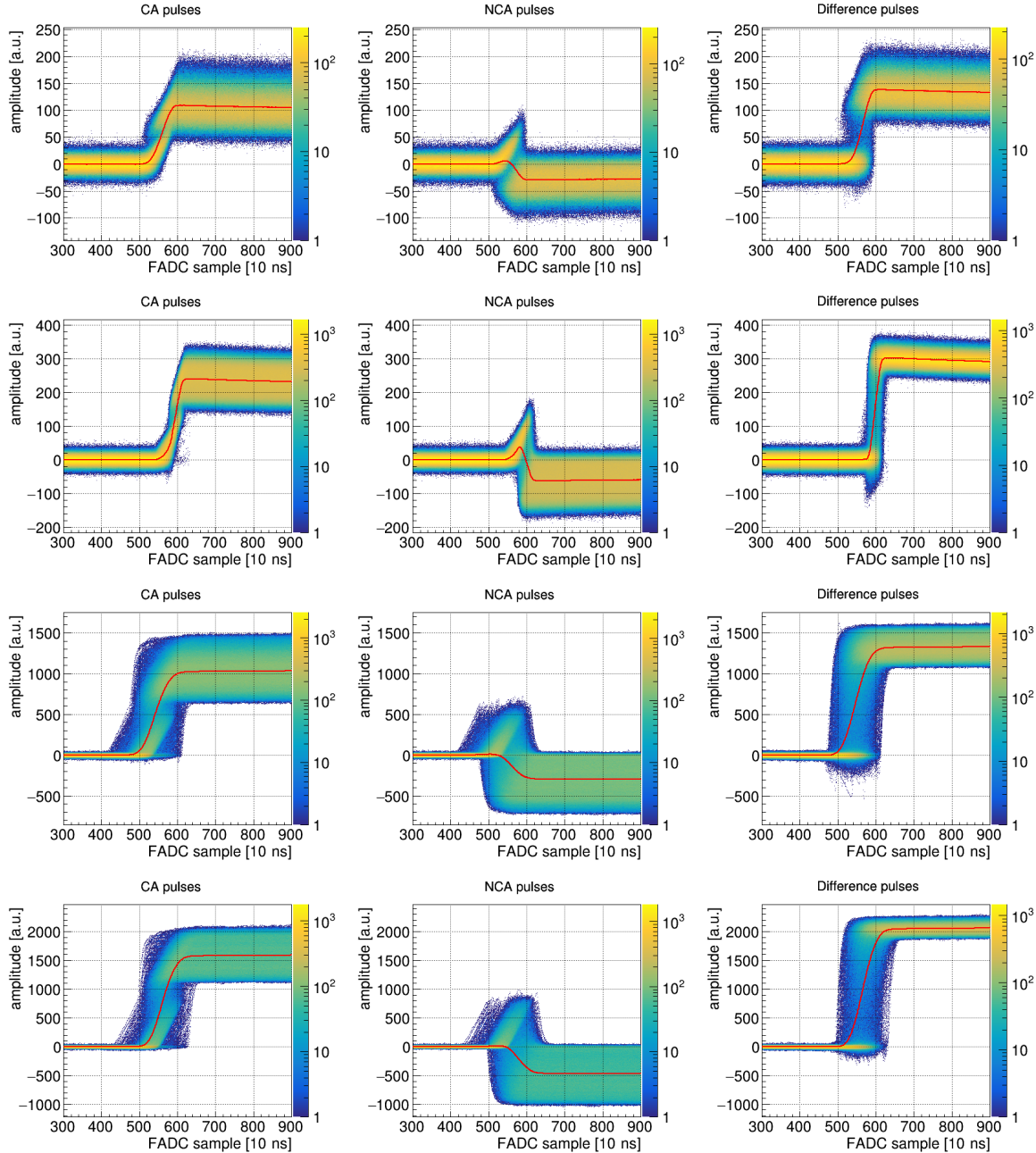


Figure 7.25: Illustration of some examples of the created SSE pulse-shape library based on the Compton coincidence technique. The mean deposited energy in the CZT detector increases from top to bottom for the depicted examples (see Tab. 7.5). Each row contains a density plot for the raw signals CA and NCA, as well as for the corresponding difference pulse. For comparison, the mean pulse-shape as the average of all the selected pulses is shown as a red graph for each kind of signal. *First row:* ^{137}Cs , $\vartheta = 45^\circ$, $E_{\text{CZT}} = 182 \text{ keV}$, 12570 events. *Second row:* ^{137}Cs , $\vartheta = 90^\circ$, $E_{\text{CZT}} = 373 \text{ keV}$, 58838 events. *Third row:* ^{60}Co , $\vartheta = 60^\circ$, $E_{\text{CZT}} = 627 \text{ keV}$, 26609 events. *Fourth row:* ^{60}Co , $\vartheta = 90^\circ$, $E_{\text{CZT}} = 963 \text{ keV}$, 13145 events.

Furthermore, each density profile is complemented by the average of all selected pulse-shapes, which is indicated by an overlay graph. While the observed widths of the pre-baselines before the signal rise are dominated by random fluctuations, the post-baselines feature an additional component due to the range of the energy restrictions.

For the case of the ^{137}Cs examples, the average pulses agree very well with the expected

shape of single-site interactions (see e.g. Fig. 7.1) and recover the typical characteristics such as the common initial slope of the raw signals. On the contrary, the examples of the ^{60}Co irradiation do not show those features. Moreover, the spread observed for the position of the prominent step in the difference pulse is much larger. It should be noted that the ^{60}Co data has been obtained with an alternative pre-amplifier module, which was one of the measures aiming to handle higher trigger rates. This is also the reason for the different scales between the pulse heights, which are not corrected for the intrinsic signal amplification. However, the pre-amplifier module is expected to only affect the overall amplification and the intrinsic width of the baselines, but not the position of the signal rise. A potential explanation could be the altered trigger mode regarding the read-out of the two-detector-system, using solely the HPGe detector as trigger. An optimization of the coincidence time window and the application of more restrictive energy cuts using fixed energy windows between 5–60 keV could not resolve this issue. Nonetheless, despite the non-optimal trigger time alignment, also the ^{60}Co data provides a valuable set of SSE examples.

The combination of the ^{137}Cs and the ^{60}Co data sets allows for the investigation of SSEs for an energy range of a few hundred keV up to 1 MeV. Moreover, due to the achieved statistics it is possible to split the energy partitions into several depth slices to investigate a potential z -dependency of the single-site characteristics. A preliminary survey is part of the original work presented in [Zat14]. Compared to the previous study, about ten times more data has been collected in the course of the present thesis. A short summary and outlook regarding the usage of the available SSE library will be given in the concluding section of this chapter.

7.3.6 Summary and outlook

The outcome of the Compton scattering experiment proves that single-site interactions can be created under laboratory conditions using the Compton coincidence technique. However, the accessible energy range of the current approach is limited to about 1 MeV and covers only about one third of the $\beta\beta$ -decay region of interest. The access to higher energy scales would require the realization of larger scattering angles and, more importantly, the usage of radioactive sources providing γ -rays of higher energies. As no suitable candidate nuclide could be identified, considering also the required activity of the order of several MBq and the pre-collimation of the γ -ray source, the higher energy range might remain inaccessible.

An immediate application of the SSE library could be a cross check of the energy dependence of the A/E parameter as discussed in section 7.2.4. Its current calibration relies solely on the ^{208}Tl DEP at 1.6 MeV, which is the only reliable origin for a SSE-like event population for the LNGS setup. However, it was already discussed that the laboratory results cannot be transferred directly to the LNGS setup due to different settings of the DAQ readout. Moreover, it is not clear how a single detector laboratory measurement would compare to the demonstrator array, consisting of detectors of varying quality.

Nonetheless, the created pulse-shape library could serve well in future studies aiming to improve the pulse-shape discrimination capabilities of COBRA's detector approach for the demonstrator array. Of special interest might be deep learning algorithms and neural network applications such as already investigated for germanium detectors [HHM⁺19] or in the framework of the EXO-200 experiment [EXO18b]. One common feature of those machine learning techniques is the need for testing data, which could be provided by the collected SSE library. The extraction of the single-site events could be improved by an optimization of the two-dimensional ROI selection of the true coincidences. Possible options include a two-dimensional Gaussian approximation of the signal region or a non-rectangular cut selection.

With respect to the recently upgraded detector technology for the COBRA XDEM setup it would be advisable to repeat at least part of the measurements with one of the avail-

able qCPG prototype detectors. Especially the efficiency of the data-cleaning cuts and the interplay of the four assumed to be independent sectors could be studied with a follow-up experiment. The required changes are only marginal as the homogeneous irradiation of a 6 cm^3 CZT detector can already be achieved with the available equipment and optimization of the distance between detector and source container. One potential issue could be the increased absorption probability due the larger crystal volume and the related γ -ray interaction rate. However, it could be shown in the present work that a sufficient triggering of the two-detector-system can be achieved by the secondary HPGe alone.

7.4 Characterization of muon-induced interactions

Besides the natural decay chains of the primordial isotopes of uranium and thorium, one of the most common background contributions for surface laboratories originates from cosmic ray interactions in the upper atmosphere producing a constant flux of high-energy muons. While performing the CZT detector characterizations as discussed in the previous sections, it was found that the laboratory background at high energies is dominated by the interaction of minimum-ionizing muons. The origin of the cosmic muon flux will be briefly described in the first part of this section.

Because of the typical rates achieved in the artificial irradiation of CZT detectors under laboratory conditions, the natural background contributions of both categories – radio-nuclides and cosmic rays – are usually negligible. On the other hand, a statistical sample of muon-induced interactions at the surface level could provide valuable insights with respect to the operation of the COBRA experiment in an ultra low-background environment such as the LNGS in Italy. Although the LNGS provides a shielding against cosmic rays of about 3400 m.w.e. (see section 4.3.1), reducing the cosmic muon flux by more than one million times, there is still a measurable residual flux which contributes to the overall background. In the extreme case, muon-induced interactions could mimic the energy signature expected from the sought $0\nu\beta\beta$ -decay. As the current design of the COBRA demonstrator does not include an active muon veto, the study of muon-induced interactions could help to develop veto criteria for the search for double beta decays. Moreover, cosmic muons are usually highly energetic and expected to interact as minimum-ionizing particles (see e.g. section 1.3.2). The typical energy loss via ionization along their path through a detector creates distinct signatures that are very different from the already discussed cases of particle interactions involving external or internal α - and β -decays as well as accompanying γ -rays.

Based on an elaborate background characterization of the laboratory setups at TUD and the observed high-energy features, an analytical model of the event reconstruction of minimum-ionizing muon interactions for CPG-CZT detectors could be established in [Zat14]. The basis of the model relies on the general event reconstruction developed for such detectors in the framework of the COBRA experiment [FDG⁺13]. The analytic muon reconstruction model was found in cooperation with M. Fritts and will be introduced in the following. Moreover, an update on the model's experimental verification based on dedicated laboratory measurements will be presented. This includes the application of the reconstruction model to all three CZT detector types investigated by the collaboration during the last years.

7.4.1 Background contribution of cosmic muons

Highly energetic muons are created as the product of primary cosmic ray interactions in the upper atmosphere of the Earth. Because of their origin, they are usually referred to as *cosmic* or *atmospheric muons*. Primary cosmic rays originate mostly from outside the solar system and consist primarily of protons and α -particles ($\sim 99\%$), as well as a small fraction of heavier

nuclei ($\sim 1\%$) and an extremely minute amount of positrons and antiprotons [PDG18]. The primary particles, with primary high-energy protons p_p being the dominant species, create secondary particles in deep inelastic scattering processes such as

$$\begin{aligned} p_p + p &\longrightarrow p_p + n + \pi^+, \\ p_p + n &\longrightarrow p_p + p + \pi^-. \end{aligned}$$

The typical product of those interactions are light mesons such as charged and neutral pions (π^\pm, π^0), as well as other secondary hadrons including protons and neutrons. Pions are the lightest mesons ($m_\pi = 140$ MeV [PDG18]), thus, provide the largest phase-space and are created in vast amounts. On the level of Feynman diagrams the example processes above can be illustrated as shown in Fig. 7.26.

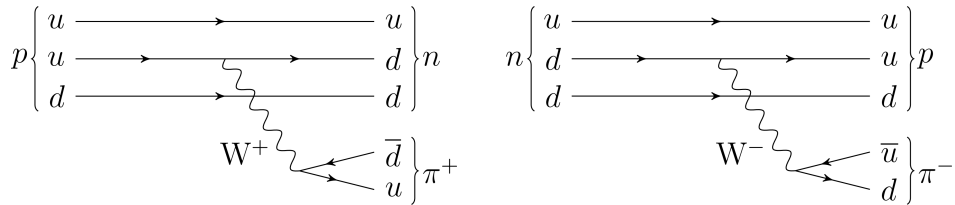


Figure 7.26: Feynman diagrams of the production of charged pions π^\pm in deep inelastic proton interactions induced by primary cosmic rays (taken from [Zat14]). *Left:* pp -reaction creating a neutron and a positively charged pion π^+ in the final state. *Right:* pn -reaction converting a neutron into a proton and a negatively charged pion π^- . Beside the depicted weak processes, light mesons are also produced in strong interactions with a large variety of the hadronic final states.

Alternatively, light mesons can be produced by the strong interaction or in electromagnetic pair production processes in the vicinity of a nucleus creating $q\bar{q}$ pairs that form hadrons via hadronisation. However, most of those secondary particles decay before they can reach the Earth's surface. The decay chains of charged mesons typically create muons and neutrinos, while electrons and photons originate from the decay of neutral mesons such as π^0 .

$$\begin{aligned} \pi^0 &\longrightarrow \gamma + \gamma, \\ \pi^+ &\longrightarrow \mu^+ + \nu_\mu, \\ \pi^- &\longrightarrow \mu^- + \bar{\nu}_\mu. \end{aligned}$$

For the latter examples of the charged pions, which only have a mean lifetime of $\tau_\pi = 2.6 \times 10^{-8}$ s, the dominant decay channel involves the conversion into muons and neutrinos [PDG18]. Because of their comparably long lifetime of $\tau_\mu = 2.2 \times 10^{-6}$ s and mean energy of $E_\mu \approx 4$ GeV at ground level, atmospheric muons are relativistic particles and can have a decay length on the order of several 10 km. Moreover, muons are found to be the most numerous charged particles at sea level with an expected flux of about $100 - 150 \text{ m}^{-2}\text{s}^{-1}$ [PDG18]. Their energy and angular distribution reflect a convolution of the primary cosmic ray spectrum, the energy loss in the atmosphere and other materials, and the exponential decay law. The energy spectrum is found to be almost flat below 1 GeV and steepens gradually in the 10–100 GeV range [PDG18]. Finally, muons decay into the lightest charged leptons and the corresponding neutrinos through the processes illustrated in Fig. 7.27.

Given their mean energy of $E_\mu \approx 4$ GeV at sea level, muons from cosmic rays can be treated as minimum-ionizing particles. This makes it possible to calculate their average expected energy deposition by ionization according to the Bethe-Bloch formula given in Eqn. (1.36) of section 1.3.2. For minimum-ionizing particles and a given material the av-

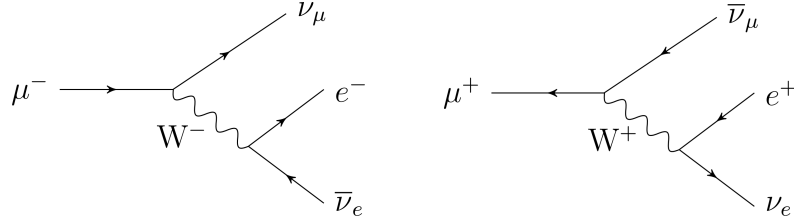


Figure 7.27: Feynman diagrams of the weak decay of muons into the lightest charged leptons and the corresponding neutrinos (taken from [Zat14]). For the case of the μ^- decay (*left*), the muon converts into a muon-neutrino ν_μ while emitting a charged W^- boson, which produces an electron e^- and an electron-antineutrino $\bar{\nu}_e$. The decay of μ^+ (*right*) can be explained analogously using the corresponding antiparticles.

verage energy loss per path length can be expressed as

$$\frac{1}{\varrho} \left\langle \frac{dE}{dx} \right\rangle_{\min} = \sum_i w_i \left\langle \frac{dE}{dx} \right\rangle_{\min,i} \quad (7.7)$$

using the material density ϱ and the tabulated specific energy losses as reported in Tab. 7.6 following from Ref. [GMS01]. A compound material such as CZT is treated as sequence of thin layers of the individual constituent elements with a weighting w_i according to the atomic mass fraction. In the present case, the detector material is referred to as $\text{Cd}_{1-x}\text{Zn}_x\text{Te}$ with $x \approx 0.1$ given by the manufacturer. However, due to the complex production process and slow crystal growing, there is a variation of the zinc concentration which was determined to about 20% by external measurements supervised by the COBRA collaboration (see e.g. section 8.5.2). The resulting mean zinc mass fraction could be determined to 5.6% [Zat14], which converts to $x \approx 0.11$ for the further analysis in this thesis.

Table 7.6: Estimate of the expected mean energy loss of minimum-ionizing muons in CZT based on the Bethe-Bloch formula (adapted from [Zat14]). The detector material CZT is treated as a compound consisting of thin layers made of cadmium, zinc and tellurium with a weighting w_i according to the respective mass fraction of the elements. The specific energy losses are taken from Ref. [GMS01]. The tellurium value has been approximated as the mean of the tabulated data for $Z = 51$ and $Z = 53$.

element	symbol	Z	$\langle dE/dx \rangle_{\min,i}$	w_i
zinc	Zn	30	1.411 MeV · cm ² /g	0.056
cadmium	Cd	48	1.277 MeV · cm ² /g	0.444
tellurium	Te	52	≈ 1.260 MeV · cm ² /g	0.500
CZT		≈ 49	1.276 MeV · cm ² /g	-

By combining the information summarized in Tab. 7.6 with the density of $\varrho = 5.78 \frac{\text{g}}{\text{cm}^3}$ for CZT (see Tab. 4.1) and Eqn. (7.7), an average energy loss via ionization of

$$\langle dE/dx \rangle_{\min} = 7.375 \text{ MeV/cm} \quad (7.8)$$

is expected for minimum-ionizing muons. The absolute value of the energy deposit depends on the path length traveled by the muon in CZT, which is one of the key features used in the formalism of the analytic reconstruction model presented in the next section.

7.4.2 Analytic model of event reconstruction

The original motivation leading to the reconstruction model for muon-like interactions for CPG-CZT detectors was to find an explanation for specific high-energy features observed in laboratory background measurements that were performed and analyzed in [Zat14]. It was found that some of the underlying pulses lead to a saturation of the FADC's dynamic range. Usually, the usage of the available dynamic FADC range is optimized based on the typical energy scale of an application and the involved radionuclides. By adjusting the linear signal amplification of the COBRA DAQ (see section 4.3.3), it is possible to increase the number of available FADC channels for a certain energy range in order to achieve an optimal resolution. On the other hand, the total number of channels is limited by the resolution of 12 bit corresponding to 4096 channels. This way, a lowering of the amplification leads to an effective increase of the number of channels at lower energies, but also limits the maximum amplitudes that can be recorded without running into the saturation of the electronics. Hence, the choice of the amplification is a compromise between the resolution in terms of available channels for a certain energy range and the maximum pulse-height that can be digitized.

It should be noted that the maximum energy is usually limited by the FADC saturation and not by a saturation of the pre-amplifiers or COBRA's CZT detectors. Although it is possible that the capacity of the pre-amplifiers could be reached, the saturation limit is found at much higher amplitudes compared to the usual DAQ settings applied for the linear amplification and the FADCs. In fact, it is possible to record amplitudes corresponding to energy depositions up to several 10 MeV with the appropriate settings of COBRA's DAQ.

Moreover, the initial 12-bit-resolution is increased by shifting the raw signals CA and NCA with respect to the baseline. As the CA signal is expected to continuously increase up to its full amplitude, while the final pulse-height of the NCA signal is usually below its initial baseline level, an optimal coverage of the FADC range is achieved by applying a negative offset for the CA channels and a positive offset for NCA channels. This leads to an effective increase of the dynamic energy range while maintaining an optimal resolution. The FADC saturation and its effect on the signal reconstruction can be expressed analytically as will be discussed in the following.

Effect of FADC saturation

The effect of the FADC saturation can be derived in a quite simple model assuming a zeroth-order event reconstruction without a correction of electron trapping or the contribution of holes as charge carriers (see e.g. section 4.1.4 and 5.2). The zeroth-order energy and interaction depth reconstruction can be expressed as

$$E = \text{PH(CA)} - \text{PH(NCA)}, \quad (7.9)$$

$$z = \frac{\text{PH(CA)} + \text{PH(NCA)}}{\text{PH(CA)} - \text{PH(NCA)}}, \quad (7.10)$$

using the pulse-heights (PHs) of the raw signals recorded by the CA and NCA. If the CA amplitude reaches the maximum possible value M , which indicates a generic upper FADC saturation limit, Eqn. (7.9) – (7.10) lead to the following distorted expressions.

$$E' = M - \text{PH(NCA)}, \quad (7.11)$$

$$z' = \frac{M + \text{PH(NCA)}}{M - \text{PH(NCA)}} = \frac{2M - E'}{E'} = \frac{2M}{E'} - 1. \quad (7.12)$$

In that case, the distorted depth z' in Eqn. (7.12) follows a hyperbola with $E \leq 2M$ being the maximum reconstructed energy for $z = 1$ events. For lower depths, even higher energies

can be properly reconstructed as shown in Fig. 7.28. By taking into account a minimum possible NCA amplitude $N < 0$, now expressing a saturation of the lower FADC range, the zeroth-order reconstruction leads to

$$E' = \text{PH(CA)} - N, \quad (7.13)$$

$$z' = \frac{\text{PH(CA)} + N}{\text{PH(CA)} - N} = \frac{2N + E'}{E'} = \frac{2N}{E'} + 1. \quad (7.14)$$

According to Eqn. (7.13) – (7.14) a properly reconstructed energy is found for $E \leq -2N$ independently from the interaction depth. Because of the hyperbolical z -dependency, higher energies can only be reconstructed for higher depths.

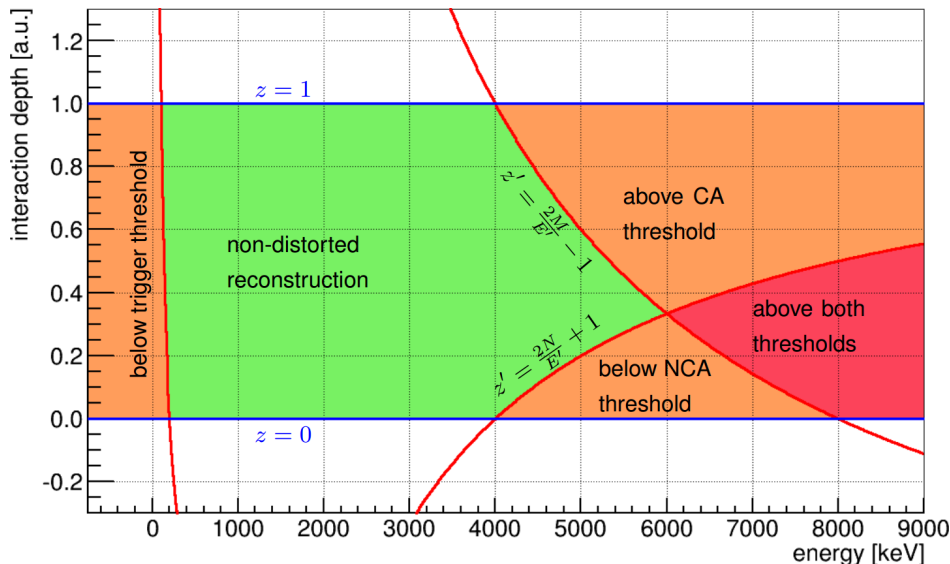


Figure 7.28: Effect of the FADC saturation of the raw CPG detector signals CA and NCA with respect to the reconstruction of the energy and interaction depth (taken from [Zat14]). If one of the signals reaches its saturation threshold, the event reconstruction is expected to follow the hyperbolic saturation curves (indicated in red). For events reaching the CA and NCA maximum amplitudes simultaneously, the reconstruction of z and E results in unique values indicating the intersection of both saturation curves. This is why a prominent saturation peak would appear in the projection of the energy spectrum. The z -position of the intersection depends on the baseline offset of the CA and NCA signals. The same applies to the asymmetry observed for the single CA and NCA saturation curves. At low energies, the typical z -dependency due to the energy threshold condition used for the readout trigger can be seen. The depicted example is based on typical values for the maximum values M and N , which are motivated by laboratory measurements.

The combination of both thresholds M and N results in an area with a non-distorted event reconstruction as indicated in Fig. 7.28. If one of the raw signals gets saturated, the event reconstruction is affected by the typical saturation limit meaning that all events with $E \geq 2M$ and $E \geq -2N$ will be found along the distorted z' hyperbola according to Eqn. (7.12) and (7.14). Moreover, if both signals reach the saturation threshold, all respective events fall on a single spot which causes a prominent event population at the intersection of the saturation curves. The shift of the curves with respect to the detector's center at $z = 0.5$ is caused by the FADC baseline offsets of the CA and NCA signals as mentioned before. This is also the root cause for the observed asymmetry close to the point of saturation.

In the same way, the depth dependent energy threshold introduced by the trigger condition can be explained. As the NCA signal amplitude is usually negative or close to the baseline, the falling edge trigger is found to be more strongly affected by noise than the rising edge trigger used for the continuously increasing CA signal. Physical events are expected to almost

always trigger the CA channel, whereas NCA-only triggers appear solely in extreme cases at low energies. This is why most of the COBRA data is taken with only a CA trigger (see also the discussion in section 8.3.3). The resulting z -dependent threshold curve indicates the proper event reconstruction at low energies. In order to remove the z -dependency with respect to the exposure gained in this energy regime, the *below-threshold cut* as introduced in 5.2.4 is applied as part of the standard data-cleaning.

Classification of muon interactions

A classification of muon-induced interactions can be done by considering geometrical aspects such as illustrated in Fig. 7.29. As minimum-ionizing atmospheric muons feature a decay length on the order of 10 km, it is very likely that they just pass through a laboratory setup and its potential shielding without being absorbed. Moreover, the CZT detectors currently investigated by the COBRA collaboration are rather small in size. In fact, the absorption probability turns out to be negligibly small for the available crystal geometries of $1.0 \times 1.0 \times 1.0 \text{ cm}^3$ and $2.0 \times 2.0 \times 1.5 \text{ cm}^3$ (see e.g. section 6.1).

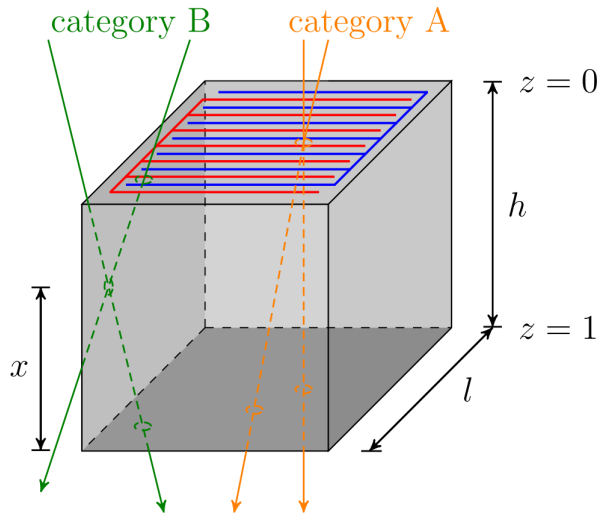


Figure 7.29: Illustration of the classification of expected muon-induced interactions for the example of a single CPG-CZT detector as used for the COBRA demonstrator array (taken from [Zat14]). The cuboidal geometry features an approximate height and length of $h = l = 1 \text{ cm}$ resulting in a volume of about 1 cm^3 . Muons of *category A* feature a nearly vertical incident angle and traverse the entire z -range between the anode at $z = 0$ (top) and the cathode at $z = 1$ (bottom) along their paths. On the contrary, muons with a highly non-vertical incident angle, labeled as *category B* streak only a part of the detector bulk, hence, cover only a fraction x of the overall z -range. In all cases the path length can be used to estimate the deposited energy via the expected energy loss according to Eqn. (7.7) based on the Bethe-Bloch formula.

For nearly vertically incoming muons, labeled as *category A*, the corresponding muon paths traverse the entire detector bulk covering the complete z -range from the anode at $z = 0$ to the cathode at $z = 1$. As the reconstructed interaction depth corresponds to the mean of the charge cloud created by the continuous ionization along the muon's path, it is expected to yield $z_\mu \approx 0.5$. Moreover, the expected energy deposition can be estimated based on the path length and the specific energy loss in CZT according to Eqn. (7.8) as the result of the modified Bethe-Bloch formula given in Eqn. (7.7).

Apart from muon interactions of *category A*, traversing the complete z -range from top to bottom, it is also possible that non-vertically incoming muons, denoted as *category B*, streak only part of the detector volume. In that case, the muon paths cover only a fraction x of the complete crystal height h . Consequently, the reconstructed interaction depth will

be correlated with the fraction of the traversed volume. Furthermore, the energy depositions corresponding to muon-induced interactions of *category B* are expected to be significantly lower as the resulting path length in CZT is likely shorter.

By combining the geometrical aspects with the analytic description of the previously discussed saturation effects, it is possible to construct an analytic model for the appearance of muon-induced interactions with respect to their expected energy and interaction depth ranges. Details will be given in the following paragraph.

Expected muon ranges

The mean energy depositions for muon-induced interaction can be estimated with the help of Eqn. (7.8) and an expression of the muon path length. For muon interactions fulfilling the *category A* definition, the energy range is limited by the vertical path length (VPL) given by the CZT crystal's height h and the maximum path length (MPL) as the connection between two corners on the diagonal opposite sides of the cuboidal crystal geometry. The MPL can be expressed as the cube diagonal $d_c = \sqrt{h^2 + d_s^2} = \sqrt{h^2 + 2l^2}$ using the side wall diagonal of $d_s = \sqrt{l^2 + l^2} = \sqrt{2}l$. By those definitions the path length can be expressed for any of the available CZT crystal geometries discussed in section 6.1. Moreover, it is possible to tune the model with respect to each crystal's individual height and xy -dimensions. For a 1 cm^3 crystal as depicted in Fig. 7.29, nearly vertically incoming muons would result in $\langle E_\mu^{\min} \rangle = 7.4\text{ MeV}$ for the VPL and $\langle E_\mu^{\max} \rangle = 12.8\text{ MeV}$ for the MPL.

In the alternative case of only partly streaking muons, leading to *category B* interactions, the energy loss inside the CZT crystal will only be a fraction of those values according to

$$\langle E_\mu \rangle = x \cdot \langle dE/dx \rangle_{\min} \quad \Rightarrow \quad x = \frac{\langle E_\mu \rangle}{\langle dE/dx \rangle_{\min}}. \quad (7.15)$$

The fraction x is related to the intersected volume and the expected energy loss according to Eqn. (7.8). As the reconstructed interaction depth is the weighted average of a muon's continuous energy loss along its path with respect to the z -dimension, it can be expressed in dependence on x leading to

$$z_\mu(x) = \begin{cases} 1/2 & \text{full } z\text{-range} \rightarrow \text{category A}, \\ x/2 & \text{bottom-streaking} \rightarrow \text{category B}, \\ 1 - x/2 & \text{top-streaking} \rightarrow \text{category B}. \end{cases} \quad (7.16)$$

Note that the reconstructed z_μ refers to the normalized interaction depth, which is why it does not explicitly depend on the actual detector dimensions. However, by replacing x in Eqn. (7.16) with the expression derived in Eqn. (7.15) an energy dependency is introduced, whereas $\langle E_\mu \rangle$ depends on the traveled path length, thus, the actual detector dimensions. The corresponding energy ranges can be expressed as

$$\begin{aligned} \text{full } z\text{-range:} \quad & h \cdot \langle E_\mu \rangle \leq E \leq \sqrt{h^2 + 2l^2} \cdot \langle E_\mu \rangle, \\ \text{bottom-streaking:} \quad & x \cdot \langle E_\mu \rangle \leq E \leq \sqrt{h^2 + 2l^2} \cdot \langle E_\mu \rangle, \\ \text{top-streaking:} \quad & x \cdot \langle E_\mu \rangle \leq E \leq \sqrt{h^2 + 2l^2} \cdot \langle E_\mu \rangle. \end{aligned} \quad (7.17)$$

By taking into account the expected energy ranges according to Eqn. (7.17) and the actual detector dimensions h and l , the general expression of the reconstructed $z_\mu(x)$ in Eqn. (7.16)

can be adjusted for highly non-vertically incoming muons leading to

$$z_\mu(E) = \begin{cases} 1/2 & \text{full } z\text{-range,} \\ \frac{1}{2}\sqrt{\left(\frac{E}{h\langle E_\mu \rangle}\right)^2 - 2l^2/h^2} & \text{bottom-streaking,} \\ 1 - \frac{1}{2}\sqrt{\left(\frac{E}{h\langle E_\mu \rangle}\right)^2 - 2l^2/h^2} & \text{top-streaking.} \end{cases} \quad (7.18)$$

Finally, the combination of the energy ranges according to Eqn. (7.17) and the restrictions on the reconstructed $z_\mu(E)$ according to Eqn. (7.18) lead to the following expressions, which take into account both categories of muon interactions.

$$\begin{aligned} \text{full } z\text{-range:} \quad & z_\mu(E) = 1/2, \\ \text{bottom-streaking:} \quad & \frac{E}{2h\langle E_\mu \rangle} \leq z_\mu(E) \leq \frac{1}{2}\sqrt{\left(\frac{E}{h\langle E_\mu \rangle}\right)^2 - 2l^2/h^2}, \\ \text{top-streaking:} \quad & 1 - \frac{E}{2h\langle E_\mu \rangle} \leq z_\mu(E) \leq 1 - \frac{1}{2}\sqrt{\left(\frac{E}{h\langle E_\mu \rangle}\right)^2 - 2l^2/h^2}. \end{aligned} \quad (7.19)$$

The derived analytic expressions for the appearance of minimum-ionizing muon interactions with respect to the expected energy and interaction depth ranges could explain the observed high-energy features in the energy spectra of the laboratory background measurements performed in [Zat14]. Nonetheless, it should be noted that the model is only based on a zeroth-order reconstruction, thus, relies on certain assumptions and simplifications. In its current form the finite energy and depth resolution, as well as electron trapping effects or a potential signal contribution from holes as charge carriers are not considered. This is why additional laboratory measurements need to be performed to crosscheck the original results and to investigate the limits of the analytic description.

7.4.3 Evaluation of laboratory measurements

In order to extend the muon reconstruction model and to confirm the previous results, dedicated long-term background measurements were performed in the course of the present thesis. An overview of the measurements involving three different CZT detector types will be given in the first part of this section. The following evaluation of the collected background data includes an estimate of the cosmic muon flux at the surface level. By comparing the observed flux with the expected muon rate from past experiments, an internal consistency check can be performed. Furthermore, the agreement of the muon reconstruction model and the obtained data for the three different CZT detector types will be investigated.

Overview of experimental data

Compared to the original work presented in [Zat14], an improved shielding concept was developed in the present work. While the previous background measurements were performed with only a slightly modified version of the Compton coincidence experiment (see section 7.3), the follow-up campaigns make use of several improvements. First of all a complete lead castle surrounds the actual detector setup, providing a shielding in every direction with at least 5 cm of standard lead bricks. Moreover, the inner volume of the lead castle was sealed into an almost air-tight acrylic box, which is constantly flushed with evaporated nitrogen. The nitrogen originates as the natural boil-off from the dewar vessel of the HPGe detector system next to the CZT detector setup. The installation of the nitrogen flushing has been done in cooperation with A. Hemmetter in the course of his Bachelor thesis [Hem16]. Some pictures of the setup can be found in section B.2 of the appendix.

With those measures an effective suppression of external backgrounds arising from natural decay products such as ^{222}Rn and other radionuclides of the natural decay chains could be achieved (see e.g. section 8.2 and section D.2.1 in the appendix). An overview of the performed long-term background measurements is given in Tab. 7.7.

Table 7.7: Overview of long-term laboratory background measurements performed with different CPG-CZT detectors to study muon-induced interactions. The 1 cm^3 detectors are from the L3/L4 crystal batch, while the 6 cm^3 versions are prototype detectors that were developed in cooperation with *Redlen Technologies* [Red20]. The table contains the DAQ settings including the optimal working point biases, the linear amplification (LA) setting and the energy threshold E_{th} . Furthermore, the accumulated detector live-time and the expected energy range for nearly vertically incoming muons, corresponding to the VPL and MPL, are listed.

label	det. type	DAQ settings			live-time [days]	$\langle E_{\mu}^{\text{min}} \rangle - \langle E_{\mu}^{\text{max}} \rangle$ [MeV]
		BV/GB [V]	LA	E_{th} [keV]		
Det65	1 cm^3 , CPG	1500/90	BB	55	20.3	7.4–12.8
		1500/90	99	110	5.9	7.4–12.8
Det102	1 cm^3 , CPG	1200/70	77	220	40.9	7.4–12.8
Redlen	6 cm^3 , sCPG	2100/90	77	220	37.4	11.1–23.6
Redlen	6 cm^3 , qCPG	1300/100	77	220	46.2	11.1–23.6

Both of the small 1 cm^3 detectors, labeled as Det65 and Det102 following the TUD’s internal naming scheme, were characterized extensively in [Zat14] in preparation of the co-incident Compton scattering experiment (see section 7.3). In the end, only Det102 was used for the actual experiment while Det65 was added to the demonstrator array as Det53 (L3-P05). However, Det65 was used for a first background characterization applying a linear amplification, which was optimized for the intended Compton scattering experiment using the radionuclide ^{137}Cs with $E_{\gamma} = 661.7\text{ keV}$.

The linear amplification (LA) factor of COBRA’s custom-made LA modules can be adjusted manually in 16 steps of 3 dB each according to Eqn. (7.20).

$$\text{LA}(b) = 0.5 \cdot 10^{\frac{3 \cdot b}{20}} \quad \text{with } b \in [0, 15]. \quad (7.20)$$

The parameter b is treated as a hexadecimal numeral with alphanumerical values from 0–F representing the 16 steps. According to its definition given in Eqn. (7.20), the lowest setting would result in an effective signal attenuation of $\text{LA}(b=0) = 0.5$ and the highest setting in an amplification by $\text{LA}(b=15) \approx 89$. This system leads to a doubling of the signal amplification every two steps. As the amplification should be the same for a pair of CA and NCA signals, the LA setting is usually referred to as ‘00’–‘FF’ (see e.g. Tab. 7.7).

In the original work reported in [Zat14], only a lowering of the amplification by a factor of two was applied to study the effect on the FADC saturation as discussed in section 7.4.2. The final setting of ‘99’ is the same as used for the operation of the COBRA demonstrator at the LNGS. For the measurements performed in the present thesis, the LA setting was reduced by another factor of two, which increases the maximum energy that could be reconstructed without encountering the FADC saturation limits as depicted in Fig. 7.28.

The same LA setting as used for the long-term background measurement with Det102 was applied in two follow-up campaigns using the very first prototype detectors with a volume of 6 cm^3 . Both CZT detectors were provided by *Redlen technologies* [Red20] with two different designs of the anode electrode – one with an up-scaled version of the conventional CPG and a second one with the first iteration of the so-called quad coplanar-grid (qCPG) technology. However, as pointed out in section 6.1, the prospects of the up-scaled single CPG approach were expected to be limited by the occurrence of leakage currents. This is why the unique

prototype, labeled as sCPG was produced by using a base crystal of the lowest quality standard offered by the manufacturer (referred to as *sample* quality). Its characterization was briefly discussed in section 6. The second 6 cm³ prototype (official ID: Redlen-33556) with a qCPG electrode has been studied extensively in [Roh16]. Some of the results have been summarized in section 6 as well.

For each of the three long-term background measurements a respective live-time of about 40 days was achieved, surpassing the original laboratory background data obtained with Det65 by more than five times. Furthermore, each detector has been calibrated before and after the background data-taking using the radionuclides ¹³⁷Cs and ¹⁵²Eu (see e.g. Tab. 8.6 in section 8.3.4). The processing of the raw data is done with averaged calibration parameters following the procedure described in section 8.1.2 for the regular calibration of the demonstrator array. The results of the data evaluation will be summarized in the following sections starting with an estimate of the cosmic muon flux at the surface level.

Estimate of cosmic muon flux

The estimate of the cosmic muon flux makes use of the standard event selection including the DCCs and a restriction of the interaction depth in order to exclude the z -range that is affected by distortions of the weighting potentials. In the present case the interaction depth is restricted to $0.1 < z \leq 0.9$, which reduces the effective sensitive volume by about 15% (see e.g. section 7.1.2). This volume reduction is considered in the extraction of the final flux. Regarding the DCCs, it should be noted that none of the criteria was optimized for the applied signal amplification and that the usage for both 6 cm³ detector types has not yet been validated. On the other hand, based on the results discussed in section 7.1.1 it can be expected that the signal loss at the MeV scale should be negligibly small. Moreover, the reconstruction algorithms applied in the signal processing of the qCPG detector data are still preliminary. They are based on the laboratory characterization measurements performed in [Roh16] and the analysis results that were partly published in [Tem17]. The same reconstruction is used in the PhD thesis of R. Temminghoff [Tem19]. A systematic study of the event reconstruction for qCPG-CZT detectors is expected to appear in the PhD thesis of Y. Chu.

Finally, events in the lower energy range should be excluded from the cosmic muon flux estimate as the region below 2.6 MeV is dominated by γ -lines of naturally present radionuclides (see e.g. the discussion of the γ -ray background of the demonstrator array in section 8.2.3). However, muon interactions could also appear at such low energies if the incoming particles only streak part of the sensitive volume. This is why the muon flux is determined in dependence on a lower energy threshold in steps of 0.2 MeV. The determined number of counts for a certain selection gets normalized by the live-time and the surface area of the different detectors, which is why the extracted muon flux is only an estimate of its actual value. The assumption of an effective area of about 1 cm² for the small CZT detectors and 4 cm² for the larger crystals is a simplification as the actual effective area depends also on the incident angle. Nonetheless, the procedure can be used to check whether the extracted flux is of the expected order of magnitude. The results of the four CZT detectors using the data with the lowest amplification settings reported in Tab. 7.7 are depicted in Fig. 7.30.

The average expected muon flux at sea level covers a range of $\Phi_\mu = 100 - 150 \text{ m}^{-2}\text{s}^{-1}$ depending on the chosen reference and the location of the related experiment (see summary in [PDG18]). According to a commonly used rule of thumb, the maximum flux is expected to be approximately one muon per square-centimeter and minute, which translates to $\Phi_\mu^{\max} = 1 \text{ cm}^{-2}\text{min}^{-1} = 166.7 \text{ m}^{-2}\text{s}^{-1}$ [PDG18]. Given those expectations, the measurements are able to reproduce the expected flux by setting the lower energy threshold to $E_{\text{th}} \approx 3 \text{ MeV}$ for all detectors. It should be noted that the number of selected events has been corrected by

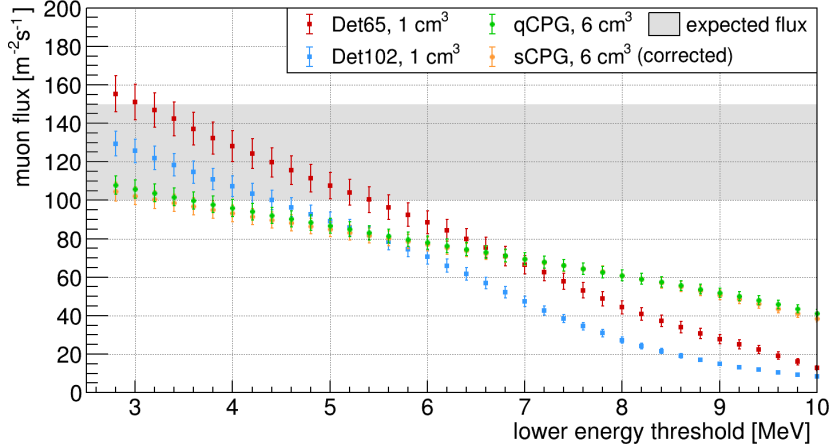


Figure 7.30: Estimate of the cosmic muon flux using laboratory long-term background measurements with different CZT detector types. While Det65 was operated with LA(99), the other three detectors share a linear amplification of LA(77). For a lower energy threshold of about 3 MeV all measurements are in agreement with the expected muon flux covering a range of $\Phi_\mu = 100 - 150 \text{ m}^{-2}\text{s}^{-1}$. The assigned uncertainties are a combination of the statistical uncertainty due to number of selected events and an additional systematic uncertainty introduced by the restriction of the z -range. The number of selected events for the 6 cm^3 sCPG detector was corrected by 20% to compensate its poor performance and depth resolution (see also Fig. 7.32).

20% for the 6 cm^3 sCPG detector in order to take into account its overall poor quality and reconstruction capability. After the correction of the sCPG rate there is a perfect agreement with the qCPG detector result and the threshold dependency. The offset between the extracted muon rates of the small CZT detectors is likely due to the different shielding concepts as pointed out in the first part of this section. Another potential effect could be the seasonal variation of the cosmic muon flux. Because of the variation of the atmospheric temperature, a maximum flux is expected in the summer period as the density of the atmosphere decreases with the average temperature. The measurement campaign of Det65 was performed in beginning of June, while Det102 was operated from mid-August until beginning of October. However, the maximum differences averaged over large time scales are expected to be on the order of only a few percent (see e.g. Ref. [OPE19]).

The uncertainties are derived as a combination of the statistical uncertainty and a systematic effect introduced by the depth restriction. The latter alters the overall muon detection probability as the angular acceptance depends on the effective height of the CZT crystal. This leads to a systematic uncertainty of about 4%, which dominates most of the depicted measurements. In the next step, the collected experimental data will be compared to the predictions of the developed analytic muon reconstruction model.

Comparison to analytic reconstruction model

At first the impact of the linear signal amplification based on the data obtained with the small CZT detectors labeled as Det65 and Det102 will be discussed. The data are depicted in Fig. 7.31 in form of z -versus- E plots with an overlay corresponding to the expected muon ranges according to Eqn. (7.17) and Eqn. (7.19).

The presence and shape of the saturation features in Fig. 7.31 provide a validation of the analytical treatment of the FADC saturation limits discussed in section 7.4.2. Moreover, the event population above the γ -ray dominated energy region can be described very accurately by the analytic muon reconstruction model for the measurements with a lower LA setting. The most prominent event population is found close to the tip area of the triangle indicating

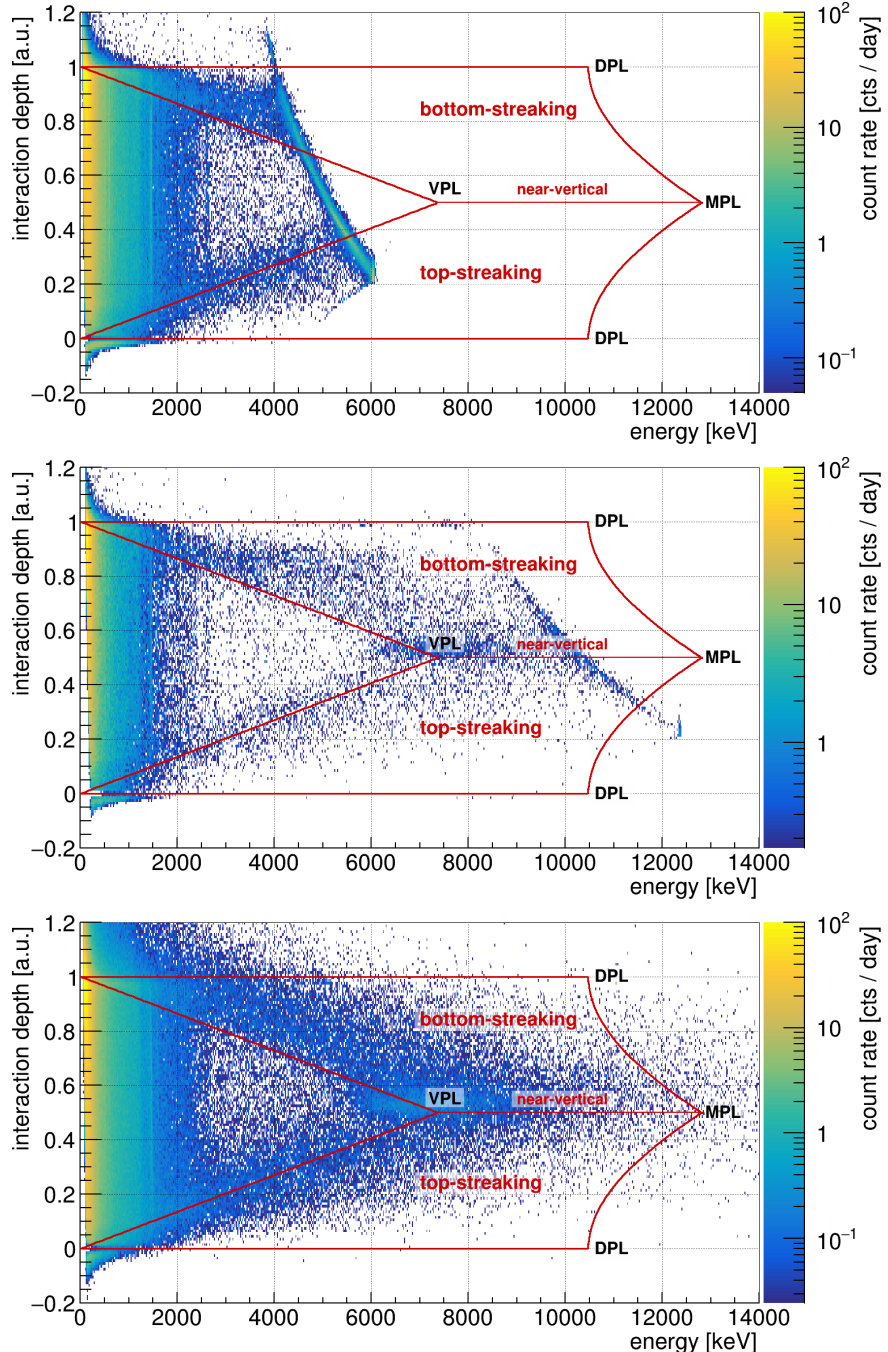


Figure 7.31: Illustration of the analytic muon reconstruction model for long-term laboratory background measurements using 1cm^3 CPG-CZT detectors. *Top:* Det65 with LA(BB). *Middle:* Det65 with LA(99). *Bottom:* Det102 with LA(77). Only events that pass the standard DCCs enter the z -versus- E plots. Each spectrum is normalized to the live-time reported in Tab. 7.7 and features a binning of 20 keV along the energy axis. The labeled areas correspond to characteristic muon path lengths: VPL (vertical path length), DPL (diagonal path length) and MPL (maximum path length). Nearly vertically incoming muons are expected to appear along the indicated $z = 0.5$ line. Muons passing through only a fraction of the z -range would appear in the framed areas indicating the range of events where muons streak either the top or the bottom of the CZT detector. As the linear amplification decreased from top to bottom, the maximum energy that can be reconstructed properly without reaching the FADC saturation limits increases accordingly. The saturation effect can be clearly seen for the first two measurement campaigns performed with Det65, while the shape of the saturation curve in the first example agrees qualitatively with the saturation model presented in Fig. 7.28.

muon interactions with small incident angles with respect to the vertical. Because of their small incident angles, the traveled path length is close to the VPL. Furthermore, there is an excellent agreement between the predicted and observed low and high z -bands corresponding to top- and bottom-streaking muons. A comparison of the analytic muon model and the laboratory data obtained with the larger CZT detectors is depicted in Fig. 7.32.

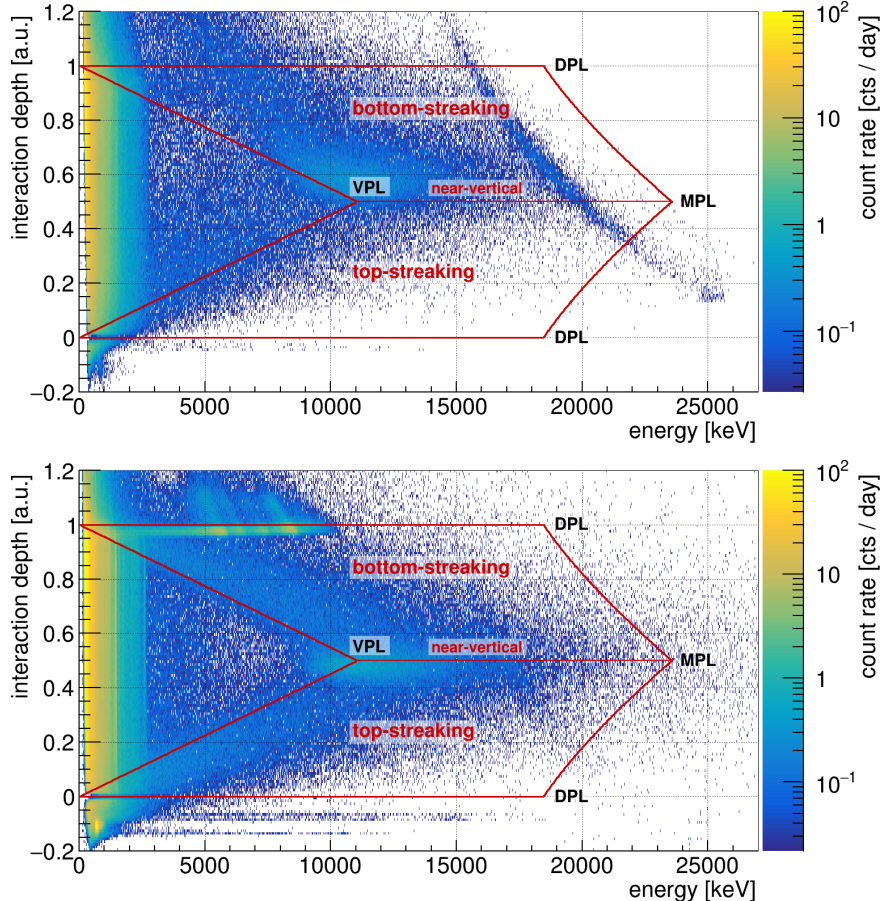


Figure 7.32: Illustration of the analytic muon reconstruction model for long-term laboratory background measurements using two different 6 cm^3 CPG-CZT detectors. *Top:* Redlen sample detector equipped with a up-scaled CPG electrode. *Bottom:* Redlen qCPG detector. Both background measurement campaigns were performed with LA(77). The resulting spectra are normalized to the live-time reported in Tab. 7.7 and feature a binning of 20 keV along the energy axis. In contrast to Fig. 7.31, only a subset of the full DCCs are applied as most of the criteria have not yet been optimized for the new prototype detectors. This why there are some artifacts around $z \approx 1$ for the qCPG detector data. In the upper example, the saturation of the pre-amplifier stage can be observed, which leads to a similar saturation curve as observed for the FADC saturation limit depicted in Fig. 7.28. The overlay indicates again the expected muon ranges while the characteristic path lengths (VPL, DPL, MPL) have been adjusted to the corresponding values of the larger detectors. In both cases there is a good agreement between the predicted ranges and the observed event population, whereas the event distribution indicates a dominance of nearly vertically incoming muons.

In contrast to Fig. 7.31, a slightly adjusted event selection is applied because the standard DCCs discussed in section 7.1.1 are not optimized for the new prototype detectors. Moreover, the reconstruction algorithms used for the qCPG are only preliminary and might still have some flaws. This is also why there are some artifacts around $z \approx 1$ for this detector type. Another particularity is found for the data of the large sCPG. Because of its overall poor performance, a special low-noise charge-sensitive pre-amplifier module was used for its signal readout in order to partly compensate the negative ramifications. While the intrinsic signal

amplification is about the same compared to COBRA's standard pre-amplifiers, the capacity of those modules is lower, causing a similar saturation curve as for reaching the FADC saturation limit (see Fig. 7.28).

Regarding the expected muon ranges, the detector dimensions entering the underlying equations of the model were adjusted to make use of the correct values. It should be noted that for the case of the 6 cm^3 detectors with a height of about 1.5 cm an additional correction factor is needed to achieve a rescaling of the reconstructed z to the usual range of $z \in [0, 1]$. Again, most events are found in the area corresponding to an almost vertical incident angle of the incoming muons which follows the expectation of their angular distribution. Some particular applications of the experimentally confirmed muon reconstruction model will be discussed in the next section.

7.4.4 Analysis of muon-induced events

By confirming the analytic event reconstruction with the dedicated laboratory measurements in the previous section, the developed model can be used to address some elaborate analysis topics. The first concerns a characterization of the typical pulse-shapes encountered for muon-induced interactions. This subject is also of particular interest in the context of the double beta decay search with the COBRA demonstrator array as there is no active muon veto system for the LNGS setup. Moreover, the signature of nearly vertically incoming muons can be used to estimate the contribution of holes as charge carriers with respect to the signal amplitudes. Both topics will be briefly discussed in the following section. Finally, some potential follow-up analysis topics will be summarized in a concluding section.

Prospects of a muon pulse-shape study

Besides the characteristic appearance of minimum-ionizing muon interactions with respect to the interaction depth and the expected energy regions, additional information might be encoded in the corresponding pulse-shapes. The available laboratory data provide access to a statistical set of muon-induced events, including two 6 cm^3 prototype detectors. Some examples of the recorded pulse-shapes can be found in Fig. D.5 of the appendix.

In a previous pulse-shape study performed in [Zat14] it could be shown that the derivative of the difference pulse features multiple peaks for events that were collected from the area of vertically incoming muons (see Fig. D.6 in the appendix). The maximum number of peaks was found to be related to the number of anode rails of the CPG electrode. From this it was concluded that the derivative peaks indicate the delayed collection of the expanded charge cloud by different rails of the CPG anode. Moreover, the same characteristics could be reproduced by a simple toy Monte-Carlo based on a VENOM simulation using a single 1 cm^3 detector geometry (see Fig. D.7 in the appendix).

The same observations are made for the present data and apply to all type of investigated CZT detectors. However, at lower energies it gets more and more challenging to distinguish muon-like interactions from MSE and bulk events. For central muon interactions close to $z_\mu = 0.5$ and $E_\mu > 6\text{ MeV}$ using the LNGS amplification setting LA(99), the fraction of SSE-like interactions was determined to about 3% [Zat14]. For lower energies, the fraction of SSEs is found to be even smaller as only non-vertically incoming muons are expected in this region. Because of the higher incident angle with respect to the vertical, the chance of creating an extended charge cloud that is collected by more than anode rail increases. Consequently, the existing PSD methods would be able to identify such muon-induced events. Based on those findings the development of a dedicated muon identification algorithm was not further pursued in the present thesis.

Moreover, the observed muon energy spectrum at deep underground laboratories such as the LNGS in Italy is shifted to higher energies compared to the surface level due to the absorption of less energetic muons by the typical rock overburden of several kilometers. While this leads at first order to an increase of the mean deposited energy per path length via ionization, the presumed treatment of muons as minimum-ionizing particles might reach a point where it is not justified anymore. Instead, alternative processes such as Bremsstrahlung as well as nuclear and spallation reactions will become more dominant for increasing particle energies. Although the ionization loss could still be estimated with the help of the Bethe-Bloch formula, correction factors would be needed based on the actual muon spectrum observed in the underground. The modeling of the residual muon flux is another non-trivial task and would require elaborate Monte-Carlo studies. Nonetheless, the application of the analytic muon model in the context of the evaluation of the COBRA demonstrator’s physics data will be discussed in section 8.2.5.

With respect to the collected laboratory data at the surface level it could be particularly interesting to take a closer look at the data of the 6 cm^3 qCPG detector. Given the orientation of its four single coplanar grids, which are rotated by 90° to each other, there might be some potential to reconstruct the angular distribution of the muon flux. This would be a great achievement considering the compact size of the experimental setup. However, due to the preliminary nature of the applied qCPG reconstruction algorithms, the idea was not further pursued in the course of the present work. Instead, a quantitative analysis of the collected laboratory data with the aim to estimate the signal contribution of the positive charge carriers, usually referred to as holes, will be discussed in the next section.

Estimate of hole shift correction

One of the fundamental principles of the CPG signal readout is the treatment of CZT detectors as effective single-charge-carrier devices. By following this approach the signal reconstruction only relies on the electron signal, while the contribution of the created positively charged holes is treated as a second order effect. In the current implementation of the event reconstruction there is no explicit correction of the hole contribution (see e.g. section 5.2). Moreover, for the energy reconstruction the effective hole contribution is expected to be absorbed in the energy calibration process. This leaves only the depth reconstruction affected by the unaccounted hole contribution.

The magnitude of the hole contribution can be estimated with the collected laboratory measurements using the signature of nearly vertically incoming muons. As their reconstructed depth is expected to appear close to $z_\mu \approx 0.5$ referring to Eqn. (7.19), an enhancement with respect to this value can be interpreted as a direct measure of the hole contribution. The following analytic treatment of the hole shift is based on the original work reported in [Zat14].

The first step is to determine the so-called ρ parameter which refers to the mean trapping length for holes in analogy to the λ parameter introduced for the treatment of electron trapping effects in section 5.2.3. Although ρ is expected to be small compared to the typical order of $\lambda \approx 4 - 40$, a notable deviation from $z_\mu = 0.5$ is expected due to the hole shift. As a starting point the reconstructed muon depth z_μ can be expressed as an energy weighted value assuming single energy depositions over the muon path as a function of the true z . This leads to

$$z_\mu = \frac{\sum_i E_\mu^i \cdot F(z_i)}{\sum_i E_\mu^i}. \quad (7.21)$$

with E_μ^i being the deposited energy at the measured depth $F(z_i)$. For the case of a continuous

energy deposition via ionization loss along the z -dimension, assuming

$$E_z \equiv \left\langle \frac{dE}{dz} \right\rangle_{\min} = \text{constant} \quad (7.22)$$

for minimum-ionizing particles, Eqn. (7.21) can be written as

$$z_\mu = \frac{\int_0^1 \left\langle \frac{dE}{dz} \right\rangle_{\min} \cdot F(z) dz}{\int_0^1 \left\langle \frac{dE}{dz} \right\rangle_{\min} dz} \quad (7.23)$$

$$\stackrel{(7.22)}{=} \int_0^1 F(z) dz. \quad (7.24)$$

For zeroth-order behavior without distortions and trapping effects it follows $F(z) = z$, thus, $z_\mu = 0.5$ for the present scenario of vertically incoming muons. A first naive option to incorporate the hole shift contribution is to assume $F(z) = z + \rho$, which alters the general expression Eqn. (7.24) to

$$z_\mu = \int_0^1 (z + \rho) dz \quad (7.25)$$

$$= \frac{1}{2} + \rho. \quad (7.26)$$

However, this is an oversimplification as the hole shift is expected to strongly depend on the interaction depth. In fact, the hole shift should be negligible far away from the anode as the depth reconstruction for e.g. cathode events at $z = 1$ agrees perfectly with the expectation using solely the electron trapping correction (see e.g. the depth distributions presented in section 7.1.2). By considering those boundary conditions, a more elaborate treatment of the hole shift was proposed in [Zat14]. The idea is to introduce a z -dependent term according to

$$F(z) = z + s(z), \quad (7.27)$$

$$\text{with } s(z) = \rho \left(1 - e^{-\frac{(1-z)}{\rho}} \right). \quad (7.28)$$

This way, the hole shift contribution $s(z)$ gets reduced for increasing depths, while the maximum effect would be observed for near-anode events close to $z = 0$. By inserting the new expression for the measured depth $F(z)$ into the general expression Eqn. (7.24), the following expression for the reconstructed depth of nearly vertically incoming muons can be derived.

$$z_\mu = \int_0^1 \left[z + \rho \left(1 - e^{-\frac{(1-z)}{\rho}} \right) \right] dz \quad (7.29)$$

$$= \frac{1}{2} + \rho \left[1 - \rho \left(1 - e^{-\frac{1}{\rho}} \right) \right] \quad (7.30)$$

$$\approx \frac{1}{2} + \rho - \rho^2. \quad (7.31)$$

The approximation in the last step is justified by the smallness of the exponential term, which gets negligible for an expected ρ parameter on the order of $\mathcal{O}(0.1)$.

At this stage it is possible to derive another correction based on the near-anode *double-energy effect*, which is caused by the distortions in the weighting potential for events close to the anode surface. The effect results in a doubling of the reconstructed energy while the reconstructed depth is close to zero (see e.g. Fig. 8.4 in section 8.2). Its effective area can be characterized by assuming a typical range of $z < \varepsilon$ with $\varepsilon > 0$. This makes it possible to

express the measured depth $F(z)$ and the expected energy deposition $E(z)$ in the vicinity of the anode as

$$F(z) = \begin{cases} 0 & z < \varepsilon, \\ z + \rho & z > \varepsilon, \end{cases} \quad (7.32)$$

$$E(z) = \begin{cases} 2E_z & z < \varepsilon, \\ E_z & z > \varepsilon. \end{cases} \quad (7.33)$$

Note that for the near-anode region the implemented naive hole shift in Eqn. (7.32) is a valid approximation. By inserting Eqn. (7.32) – (7.33) into the general expression Eqn. (7.24), the following expression is found for the reconstructed interaction depth of vertically incoming muons considering the near-anode reconstruction artifacts.

$$z_\mu = \frac{\int_0^\varepsilon 2E_z \cdot 0 dz + \int_\varepsilon^1 E_z \cdot (z + \rho) dz}{\int_0^\varepsilon 2E_z dz + \int_\varepsilon^1 E_z dz} \quad (7.34)$$

$$= \frac{\frac{1}{2}(1 - \varepsilon^2) + \rho(1 - \varepsilon)}{1 + \varepsilon} \quad (7.35)$$

$$= \frac{1}{2}(1 - \varepsilon) + \rho \left(\frac{1 - \varepsilon}{1 + \varepsilon} \right) \quad (7.36)$$

$$\stackrel{1}{1+\varepsilon} \approx \stackrel{1-\varepsilon}{1-\varepsilon} = \frac{1}{2}(1 - \varepsilon) + \rho(1 - 2\varepsilon + \varepsilon^2), \quad \mathcal{O}(\varepsilon^2) \rightarrow 0 \quad (7.37)$$

$$\approx \frac{1}{2} + \rho - \varepsilon \left(\frac{1}{2} + 2\rho \right) \quad (7.38)$$

The last term in Eqn. (7.38) represents the contribution of the near-anode *double-energy effect* to the overall hole shift $s(z_\mu)$ for near-vertical muon signatures. In combination with the former result presented in Eqn. (7.28), incorporating a realistic z -dependence for the bulk of the detector volume, the overall hole shift results in

$$s(z_\mu) = \rho - \rho^2 - \varepsilon \left(\frac{1}{2} + 2\rho \right). \quad (7.39)$$

The final expression in Eqn. (7.39) connects the experimentally accessible hole shift $s(z_\mu)$ with the mean trapping length ρ and the parameter ε that indicates the depth region which is affected by the near-anode distortions. The latter parameter can be determined with the help of electric field line simulations using e.g. COMSOL multiphysics (see section 5.3.4). Based on the results presented in the Master thesis of J.-H. Arling [Arl16] it is estimated as $\varepsilon \approx 0.025 \pm 0.008$. The assigned uncertainty takes into account that ε depends on the applied grid bias (GB), whereas the central value was estimated for GB = 90 V. This GB setting is a representative value for the laboratory measurements performed in the course of the present work (compare to the DAQ settings in Tab. 7.7).

The estimate of $s(z_\mu)$ for the four investigated CZT detectors is depicted in Fig. 7.33. It makes use of a 2σ -Gaussian fit of the z -distribution according to Eqn. (5.7) to determine $z_\mu = 0.5 + s(z_\mu)$. The energy range is restricted to the area of expected muon interactions with only small incident angles with respect to the vertical (see Fig. 7.31 and Fig. 7.32). An overview of the resulting fit parameters is given in Tab. 7.8.

Finally, Eqn. (7.39) can be solved for ρ to determine the mean trapping length for holes as positive charge carriers in CZT. The extraction of ρ leads to a quadratic equation with two possible solutions. However, only one of those yields a non-negative physical value and

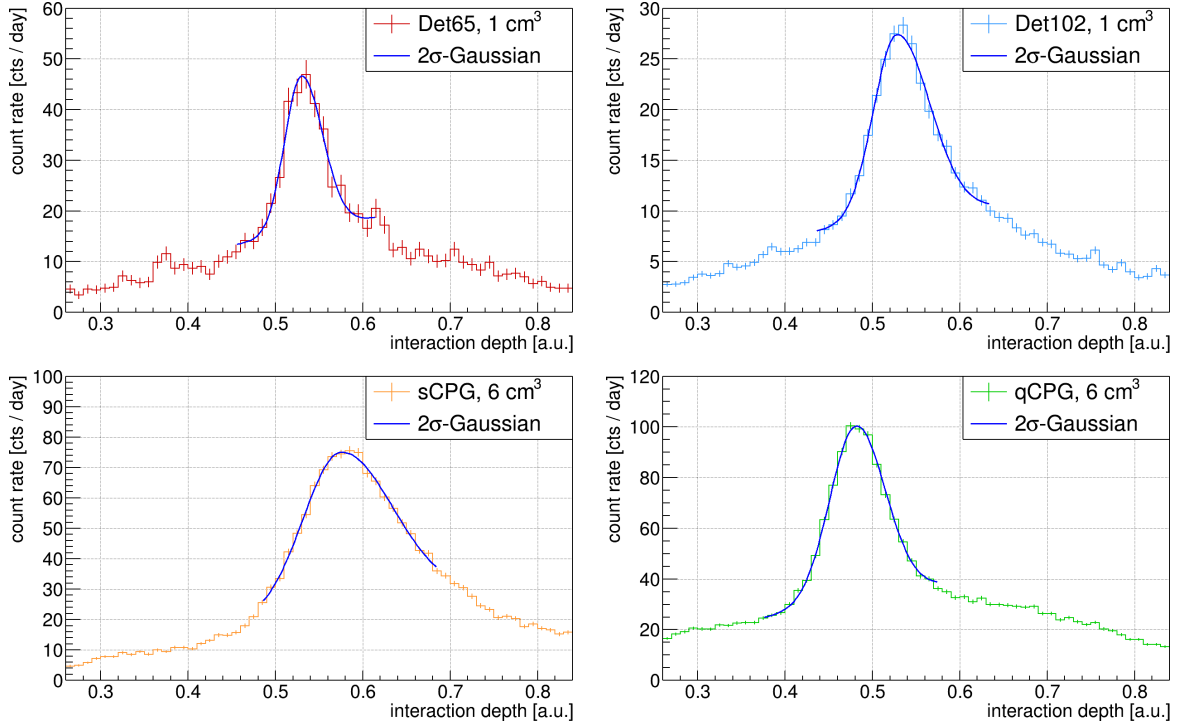


Figure 7.33: Determination of the hole shift $s(z_\mu)$ for vertically incoming muons using laboratory background measurements with different CZT detector types. Besides the applied standard event selection as discussed in section 7.4.3 the energy range is restricted to the expected area of vertical muon signatures as depicted in Fig. 7.31 and Fig. 7.32. Each of the z -peaks around $z_\mu \approx 0.5$ is approximated with a 2σ -Gaussian according to Eqn. (5.7). The fit results are summarized in Tab. 7.8 and confirm an excellent agreement between the fit model and the data with respect to the corresponding χ^2_{red} parameter. The relative depth resolution in terms of FWHM yields 9.6% for Det65, 14.4% for Det102 and 15.6% for the 6 cm^3 qCPG detector. Due to its poor performance, the 6 cm^3 sCPG detector only achieves a resolution of about 21.1% for the present z -peak.

Table 7.8: Results of the hole shift determination based on vertically incoming muon interactions observed in laboratory background measurements with different CZT detector types. The fit of the z -distributions depicted in Fig. 7.33 result in $\mu(z_\mu) = z_\mu + s(z_\mu)$, whereas the fit model achieves for all detector types adequate χ^2_{red} values. The mean trapping length ρ of holes in CZT is determined with Eqn. (7.40). The assigned uncertainties on ρ follow from a Gaussian error propagation based on the uncertainties on $\mu(z_\mu)$ and ε . For the qCPG prototype detector $s(z_\mu)$ turns out to be negative which hints to an imperfect treatment of other more dominant effects in the current implementation of the reconstruction algorithms.

label	det. type	$E_\mu^{\min} - E_\mu^{\max}$ [MeV]	$\mu(z_\mu)$	χ^2_{red}	ρ
Det65	1 cm^3 , CPG	5.8–10.0	0.530 ± 0.004	0.973	0.046 ± 0.009
Det102	1 cm^3 , CPG	5.8–10.0	0.528 ± 0.002	1.058	0.044 ± 0.009
Redlen	6 cm^3 , sCPG	8.0–15.0	0.574 ± 0.002	1.139	0.102 ± 0.005
Redlen	6 cm^3 , qCPG	8.0–15.0	0.481 ± 0.001	1.011	-

results in the following expression

$$\rho = \frac{1}{2} \left(1 - 2\varepsilon - \sqrt{1 - 4s(z_\mu) - 6\varepsilon + 4\varepsilon^2} \right). \quad (7.40)$$

The final values of the hole trapping length according to Eqn. (7.40) can be found in Tab. 7.8. The assigned uncertainties are derived by a Gaussian error propagation of the uncertainties on the hole shift $s(z_\mu)$ and the ε parameter. For the two small 1 cm^3 detectors there is a perfect agreement of the respective ρ values while the relative uncertainties are

on the level of 20%. Regarding the previously discussed uniform depth distribution of the intrinsic ^{113}Cd β -decay (see Fig. 7.5 in section 7.1.2), the derived magnitude of the hole trapping length can only explain part of the observed z -shift. However, the energy scale of the ^{113}Cd β -decay is limited by its Q -value of only 320 keV. Because of the large deviation in the probed energy scales, a direct comparison might already be corrupted by a weak energy dependence. Potential follow-up investigations might be able to resolve the discrepancy and help in the interpretation of the results.

For the background measurements performed with the 6 cm³ prototypes, the hole trapping parameter could only be determined for the sCPG detector as the hole shift would be negative in case of the qCPG detector applying the same analysis procedure. This result might be a consequence of the non-optimal event reconstruction, which is currently still under development. Regarding the large sCPG detector, the trapping length seems to be about twice as high as determined for the small detectors. This result could be explained with the much higher applied bulk voltage, although such a finding has to be taken with caution because of the detector's poor overall performance. However, a certain BV dependency of the ρ parameter would be expected as the same is observed for the λ parameter and the associated weighting factor (see e.g. the parameters listed in Tab. E.1–E.4 of the appendix).

In future laboratory experiments the ρ parameter could be studied with an irradiation of the near-anode region using an α -emitter. For a penetration depth $z > \varepsilon$ the barrier of the *double-energy* effect could be overcome. In that case, at least part of the events should be reconstructed at the true interaction depth allowing for a direct measurement of the hole shift. A similar study based on the prominent α -decay of the platinum isotope ^{190}Pt , which is part of the electrode metalization of the demonstrator detectors, will be discussed in section 8.5 in the course of the LNGS data analysis.

Summary and outlook

The performed long-term laboratory background measurements served well in the development of the presented analytic muon reconstruction model. Furthermore, the data could be used to confirm the origin of high-energy events that lead to a saturation of the DAQ electronics. A comparison of the predicted model ranges with respect to the physics data of the COBRA demonstrator at the LNGS will be discussed in section 8.2.5.

One of the most important findings in the evaluation of the collected laboratory data is a first experimental approach to address the hole contribution to the signal amplitudes. More specifically, the magnitude of the shift of the reconstructed interaction depth due to the hole's signal contributions could be determined by utilizing the signature of vertically incoming atmospheric muons. During the evaluation of those data, a general procedure could be established to estimate the mean trapping length for holes in CZT for different detector types. The results might be used for an improved depth reconstruction in the future.

Moreover, the collected data could be used to investigate the feasibility of reconstructing the muon angular distribution with a single CZT detector, which might be especially interesting for the new qCPG detector type. Furthermore, the data could be scanned for muon capture events. For a statistical sample of such events, a muon lifetime measurement could be performed. Ultimately, a large statistical sample could be used to search for exotic bound states forming short-lived muonic atoms. In those cases a low-energetic muon is expected to trigger the emission of x-rays of characteristic energies during its capture process, which would be the smoking gun signature for the formation of a muonic atom.

Chapter 8

Rare nuclear decay searches with the COBRA demonstrator

In the following chapter some results of the operation of the COBRA demonstrator at the LNGS as well as results obtained by dedicated Monte-Carlo studies will be presented. The first part consists of an overview regarding the LNGS data management and the different steps of the data evaluation procedure. In the second section a characterization of the evaluated physics data with an emphasis on the identified background features will be presented.

One of the most prominent nuclear decays is the β -decay of ^{113}Cd , which dominates the low-energy region. The analysis of the ^{113}Cd β -decay's spectrum-shape is the main subject of the present thesis and allows for the investigation of quenching effects leading to a reduced value of the weak axial-vector coupling g_A in nuclear processes. This investigation is based on a dedicated low-threshold run with optimized operation conditions prior to the upgrade to COBRA XDEM. The data analysis is performed in the context of three nuclear model frameworks to address and quantize the discussed quenching of g_A .

Besides the analysis of the dedicated ^{113}Cd low-threshold data, a first evaluation of the full exposure of the COBRA demonstrator has been performed focusing on the $2\nu\beta\beta$ -decay of ^{116}Cd . In the course of this study the A/E criterion was applied to the LNGS data to improve the selection of potential double beta decay events. Furthermore, a partitioning of the data was performed in order to identify periods with higher background rates.

At higher energies, the data evaluation of the demonstrator's full exposure makes it possible to study the long-lived α -decay of ^{190}Pt as a localized contaminant in the CZT detectors' electrode metalization. The analysis involves a MC modeling of the platinum layer and results in a half-life that is compatible with recent and previous measurements.

Finally, a feasibility study addressing the prospects of performing a search for double beta decays via excited state transitions with the COBRA demonstrator has been performed. This study is purely based on MC simulations and the updated implementation of the experiment's geometry. It focuses on the lowest excited state transitions of the isotopes ^{116}Cd and ^{130}Te .

The last section is an outlook regarding the half-life sensitivity of the COBRA demonstrator given its full exposure and the current background level for all of the accessible $\beta^-\beta^-$ ground-state-to-ground-state transitions. Moreover, the sensitivity projections is compared to the prospects of the next stage of the experiment involving the COBRA XDEM upgrade.

8.1 LNGS data management

The following section is a brief introduction into COBRA’s data management at the LNGS and the corresponding data notation. Firstly, the data obtained with the demonstrator array is divided into *physics* and *calibration* data. In both cases the initial data contain the full pulse-shapes of each recorded event and are referred to as *raw data*. Details on the raw data will be discussed in the subsequent section 8.1.1. After the signal processing with MAnTiCORE as discussed in section 5.1, the data are referred to as *processed data* and allows for its evaluation in order to perform an energy calibration or to conduct an analysis of the physics data. Furthermore, the complete physics data set is divided into several so-called *calibration periods*, each indicated by an evaluated pre- and post-calibration of the demonstrator. Each of the calibration periods consists usually of multiple physics runs (PRs), which are defined by a change of the experiment’s thresholds or other measures taken by COBRA’s remote and on-site shifters. An overview of the physics data-taking is given in section 8.1.4.

8.1.1 Raw data

Due to the general purpose concept of COBRA’s DAQ hardware and software tools, the structure of the raw data is the same for compact laboratory setups used for the CZT crystal’s characterization as for the demonstrator at the LNGS. A description of the DAQ hardware can be found in section 4.3.3. For the same reason all raw data can be processed with the same version of MAnTiCORE. However, the processing tool has to be provided with the correct meta data such as the detector configuration, e.g. which detector is connected to which channel, the thresholds and trigger settings of each channel and a so-called UUID (universally unique identifier), which is a 128-bit number. This UUID is automatically created by COBRA’s DAQ software DAQCorE and partly contained in each data-taking period’s label. Those labels usually start with the date of the measurement followed by the first eight characters of the UUID. This way, it is ensured that multiple measurements on the same date can still be distinguished. Moreover, the full UUID is unique among all measurements and can be used to identify a certain period within COBRA’s LNGS database. An overview of this database is given in section 8.1.3.

In both PRs and calibration runs the data are stored in the ROOT file format with an internal structure according to section 4.3.3. In case of a PR, the typical duration of a single ROOT file, containing the data of one of the 16 FADCs, is 4 h. Those single files are simply referred to as *runs* and present the basic unit of COBRA’s raw data. This is also the level on which the so-called *pre-selection* takes place before the actual processing. It is meant to identify and reject single runs of much too high trigger rate without the need to process the data beforehand. This is done by monitoring the trigger rate as explained in the following.

The expected trigger rate per channel can be estimated by calculating the number of ^{113}Cd decays within a certain time. The fourfold forbidden β -decay of ^{113}Cd is the most prominent signal for the COBRA demonstrator and makes up for more than 99% of all triggered events. At first the actual amount of ^{113}Cd atoms, labeled as N_{113} , contained in a single CZT detector with an average mass of $m_{\text{CZT}} = 5.95 \text{ g}$ needs to be calculated. This is done via

$$N_{113} = a_{113} \cdot s_{\text{Cd}} \cdot m_{\text{CZT}} \cdot \frac{N_A}{M_{\text{CZT}}} \quad (8.1)$$

$$= 0.1222 \cdot 5.95 \text{ g} \cdot \frac{6.022 \cdot 10^{23} \text{ mol}^{-1}}{235.31 \text{ g/mol}} \quad (8.2)$$

$$= 1.675 \cdot 10^{21} \quad (8.3)$$

with a_{113} being the isotopic abundance, s_{Cd} the stoichiometry factor for cadmium in $\text{Cd}_{0.9}\text{Zn}_{0.1}\text{Te}$, M_{CZT} the respective weighted molar mass and the Avogadro constant N_A . The number of source atoms can now be plugged into the radioactive decay law following Eqn. (8.4) to estimate the number of expected ^{113}Cd decays per year and detector using a half-life of $T_{1/2} = 8.04 \times 10^{15}$ yr according to Ref. [BBB⁺07].

$$N(t) = N_{113} \cdot \exp\left(-\frac{\ln 2}{T_{1/2}} \cdot t\right) \quad (8.4)$$

$$\Rightarrow N_{113}^{\text{exp}}(1 \text{ yr}) = N_{113} - N(t = 1 \text{ yr}) = N_{113} \cdot \left[1 - \exp\left(-\frac{\ln 2}{T_{1/2}} \cdot 1 \text{ yr}\right)\right] \quad (8.5)$$

$$= 1.86 \cdot 10^5. \quad (8.6)$$

The contribution to the single detector trigger rate, averaged over the usual run duration of 4 h, is expected to be $N_{113}^{\text{exp}}(4 \text{ h}) \approx 85$, respectively. Furthermore, there are artificial signals contributing to the overall trigger rate, which are injected simultaneously into all channels every 10 min using a pulse generator (see section 4.3.3) to monitor the DAQ electronics' stability and to allow for the synchronization of the individual FADC clocks. Every 23rd injected pulse is exchanged by a burst of 100 pulses following directly after each other to provide a distinct reference point for each 4 h run. This results in a total of 123 injected pulses per detector and run. However, as the injected pulses are true coincidences and get flagged as non-physical signals, they do not contribute to the single detector trigger rate. Besides the ^{113}Cd decay rate, there is only a negligible contribution of other physical signals (see section 8.2). The rate in the $0\nu\beta\beta$ -decay ROI is referred to as the background index (BI) in units of counts per detector mass, per energy window and per live-time. For the COBRA demonstrator the BI is on the order of a few cts/(kg keV yr).

A conservative measure of the expected single detector trigger rate is about ~ 150 events per 4 h run. This value is well above the expected ^{113}Cd rate to take into account potential noise triggers as usually observed during the low-threshold operation, as well as statistical fluctuations due to the Poisson nature of radioactive decays. Moreover, only a part of the ^{113}Cd energy range up to its Q -value of about 320 keV is accessible while operating at a typical threshold of 100 – 150 keV. This makes the expected single detector rate quoted before even more conservative. The effect of the threshold adjustments and its optimization is further elaborated in section 8.2.2 and 8.3.3.

After closing a physics run by a COBRA shifter, every 4 h run undergoes a set of consistency checks as part of the pre-selection of the raw data. During the operation of the COBRA demonstrator starting in Sept.'11 until Nov.'19, a total of 581 PRs were performed. Those PRs contain 228 637 runs of which 94.8% pass the first step of the pre-selection in which obviously too high rates up to several orders of magnitude above the expected rate and corrupt files are removed. The threshold for the removal is set to at least ten times the expected rate. In a second step, a tiny fraction of 0.1% of the remaining runs gets removed because they do not contain any valid event according to the data-cleaning cuts presented in section 7.1.1. This can happen for very short runs at the end of a PR, where the full duration of 4 h has not been reached. The same key concept of the pre-selection as explained for the physics raw data applies also towards the calibration data.

8.1.2 Calibration parameters

An energy calibration of the COBRA demonstrator array consists of multiple calibration measurements and processing steps. The data-taking usually lasts for about two days to achieve sufficient statistics with each detector of the array. An overview of the radionuclides

and their characteristic γ -lines used in the energy calibration is given in section 8.3.4. During the demonstrator’s operation the calibration procedure has been optimized by performing several calibration runs with changing thresholds and positioning of the calibration sources. In the beginning, after completing the four layer array in Nov.’13, the wired sources have been only placed in the central position between the innermost layers. This way, the edge and corner detectors of the top and bottom layer were not only much farther away but also shielded by the inner detectors. To partly overcome this problem, the procedure was adjusted by placing the sources by turns between the two lower (L1/L2) and upper layers (L4/L3) (see also Fig. A.5 in the appendix). In contrast to the physics data-taking, the applied thresholds are fixed and only differ between the radionuclides, but usually not between the detectors in the same calibration run.

Tab. 8.1 contains a list of all the calibration parameters that are determined for each detector in the evaluation process of a LNGS calibration run. During the operation of the COBRA demonstrator, a total of 56 calibration measurements were performed. An overview can be found in appendix D.2.3. Each of those has been evaluated with the same software tool developed in the course of this thesis, which involves multiple steps as will be pointed out in the following.

Table 8.1: Short description of LNGS calibration parameters. A combination of several calibration runs with different radionuclides, including usually ^{22}Na and ^{228}Th , is used to extract the calibration parameters for each detector individually. A third optional calibration source containing ^{152}Eu provides additional low-energy γ -lines, but has been available only in some recent calibrations. The evaluation of a calibration measurement requires multiple processing steps as some of the parameters depend on each other and can only be determined subsequently. The parameters are listed according to the order of their determination.

parameter	short description	standard radionuclide(s)
w	weighting factor	^{22}Na (tuned with ^{228}Th)
g_b	gain-balancing correction	^{228}Th (^{22}Na as cross-check)
c_0	offset of linear energy calibration	^{22}Na , ^{228}Th , (^{152}Eu)
c_1	slope of linear energy calibration	^{22}Na , ^{228}Th , (^{152}Eu)
p_0	constant parameter in energy resolution	^{22}Na , ^{228}Th , (^{152}Eu)
p_1	square root parameter in energy resolution	^{22}Na , ^{228}Th , (^{152}Eu)
p_2	linear parameter in energy resolution	^{22}Na , ^{228}Th , (^{152}Eu)
$\mu_{A/E}$	mean of A/E distribution	^{228}Th (DEP of ^{208}Tl)
$\sigma_{A/E}$	sigma of A/E distribution	^{228}Th (DEP of ^{208}Tl)
m_{det}	detector mass in kg	
uncertainties	recorded for c_0 , c_1 and $p_0 - p_2$	

The evaluation of the calibration data requires a first signal processing with MAnTiCORE to access e.g. the pulse heights of the raw signals (see signal processing in section 5.1 and event reconstruction in section 5.2). The first step of the energy calibration is the determination of the optimum weighting factor w (see section 5.1.2). This is done by assuming different values of w to optimize the energy resolution of a prominent γ -line, usually the one of ^{22}Na at 1274.5 keV. The spectrum of ^{22}Na features an even more prominent γ -line originating from the positron annihilation of its initial β^+ -decay, which is used as a reliable first estimate of the energy scale with respect to its peak position in FADC channels (see also Fig. 8.2). At the same time, the more energetic events of the ^{228}Th data are used to perform the gain-balancing in order to extract the NCA correction factor g_b (see section 5.1.2).

With the first two parameters a second iteration of the MAnTiCORE processing is performed to make use of the MWA branch (see Fig. 5.4), which provides a higher energy

resolution. The resulting spectra are then used to perform the actual energy calibration by fitting each γ -line with Eqn. (5.7) to assign a tabulated energy E_γ (see Tab. 8.6) to the determined peak position μ in FADC channels (see also section 5.2.2). The fit range of each γ -line is optimized iteratively depending on the achieved χ^2 of the fit and the width of the initial Gaussian peak approximation.

Finally, the tabulated γ -line energies over the determined peak positions are fit with a linear function according to

$$E_{[\text{keV}]} = c_0 + c_1 \cdot \mu_{[\text{ADC}]} \quad (8.7)$$

to determine the calibration offset c_0 and the linear conversion factor c_1 . An impression of the linearity of the energy response for three detectors of the COBRA demonstrator is shown in Fig. 8.1.

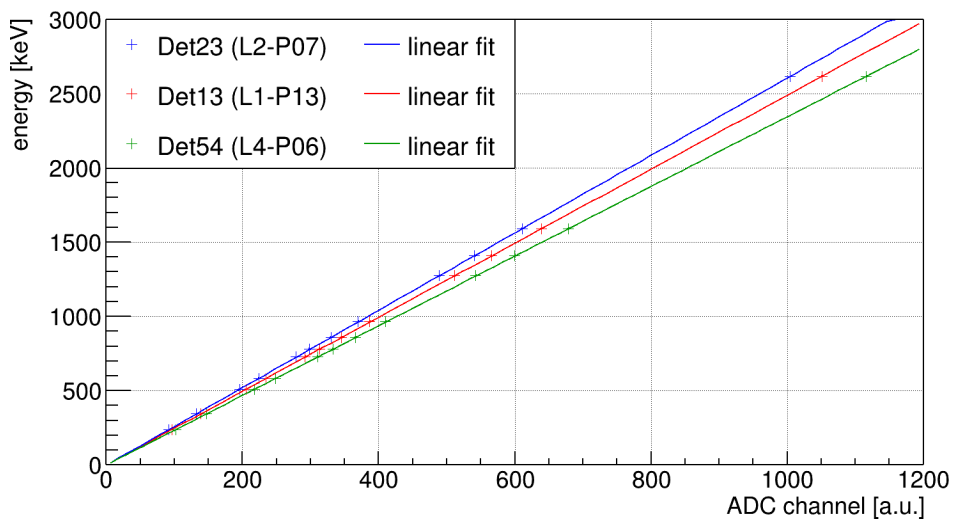


Figure 8.1: Exemplary results of an energy calibration of the COBRA demonstrator. The examples are taken from a special calibration run involving the exposition to ^{22}Na , ^{228}Th as well as ^{152}Eu . All three detectors show a perfect linearity of the detector response over the accessible energy range from 121.6 keV to 2614.5 keV defined by the γ -lines of the radionuclides.

The parameters c_0 and c_1 allow for another MAnTiCORE iteration, which results among other terms in energy equivalent pulse-height spectra such as shown in Fig. 8.2.

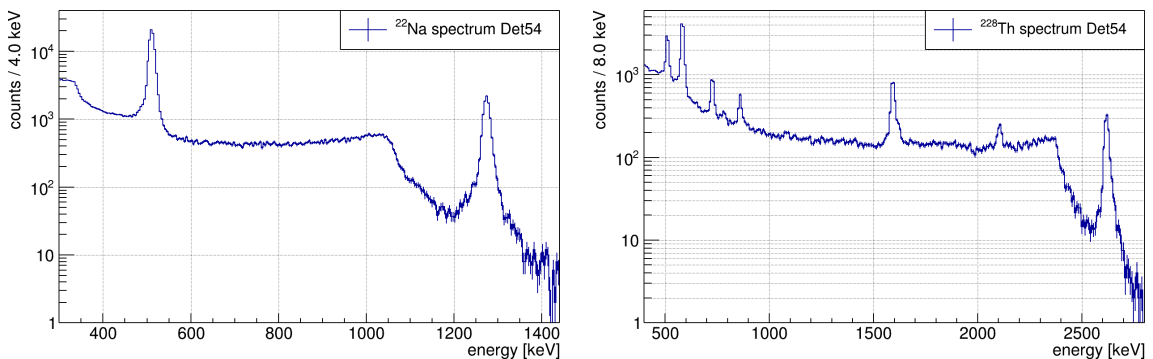


Figure 8.2: Examples of energy calibrated single detector spectra. *Left:* ^{22}Na . *Right:* ^{228}Th . The calibration spectra are from Det54 (L4-P06). The position of the very prominent annihilation peak at 511 keV, which originates from the β^+ -decay of ^{22}Na , provides a reliable estimate of the energy scale for the automatized calibration tool.

The γ -lines in the energy calibrated spectra are again fit with the two-sided Gaussian function according to Eqn. (5.7) to determine their widths in terms of FWHM. This allows to fit the energy resolution function $\text{FWHM}(E)$, which is based on the parameters $p_0 - p_2$ as presented later in section 8.3.4. One application of the detector-dependent $\text{FWHM}(E)$ is the selection of events in a certain energy range around a γ -line based on the energy resolution of this line. This procedure is applied in the calibration of the A/E pulse-shape discrimination variable, which has been discussed in section 7.2.4. The respective mean $\mu_{A/E}$ and $\sigma_{A/E}$ of the A/E distribution of events corresponding to the double-escape peak of the ^{208}Tl γ -line at 2614.5 keV complete the list of calibration parameters. A complete set of those parameters makes it possible to process physics data in a single step rather than following the progressive calibration procedure. That is also why the detector masses, which usually do not vary between the calibrations for the same crystal, are included in Tab. 8.1. If the detector masses are provided to the processing tool along with the calibration parameters, it is possible to compare e.g. single detector rates based on their exposure rather than their ordinary live-time in all further analysis steps and efficiency calculations.

In conclusion, the developed calibration tool and deployed optimization routines achieve great robustness and reliability in the evaluation of all calibration runs. In fact, the failure rate of the peak fitting turns out to be well below 0.1%, which is an impressive result considering the differences in the single detectors' performance as will be reported in section 8.3.4 and 8.3.5. An usual calibration measurement requires to perform several hundred peak fits due to the maximum of 64 detectors of the COBRA demonstrator and the number of γ -lines per radionuclide. Hence, an automatized calibration tool as sketched out in the previous section is absolutely necessary. Furthermore, all calibration parameters are uploaded into an online database, which will be discussed in the next section.

8.1.3 COBRA CouchDB

The automatized processing of COBRA's physics data requires the compilation of the correct meta data consisting of the configuration of the detector array, e.g. which detectors have been switched on and their threshold settings, as well as the respective calibration parameters applicable to the current PR. This is done by providing the UUIDs of the PR to an online database, which is referred to as *COBRA's CouchDB*. The database has been developed in the course of the PhD thesis of O. Schulz [Sch11] at the TU Dortmund in 2011. It complies well with the need of COBRA in its current prototype stage, where the requirements of the data structure change rather frequently. A conventional relational database, featuring a fixed scheme of its data structure, is not suitable in that case. Moreover, the underlying CouchDB package [Apa20] is freely available on multiple platforms and can be easily accessed via web applications such as *CouchAPP* [Var16] and terminal commands (e.g. *curl*) using the Hypertext Transfer Protocol (HTTP) for communicating with the database. The flexible data structure of CouchDB is achieved by storing JSON (JavaScript Object Notation) documents. The JSON format [ECM17] defines a small set of structuring rules for the portable representation of structured data, whereas a JSON string is a sequence of tokens formed from Unicode code points that conforms to the JSON value grammar.

Furthermore, CouchDB makes it possible to run simple JavaScript procedures in the database that allow for arbitrary indexing and lookup of the stored JSON documents without requiring a fixed structure scheme. Moreover, the data can be reformatted on the server side, thus, provide e.g. a compilation of parameters in a format specified by the client rather than the original server structure. This includes simple mathematical calculations such as averaging parameters or if-else statements. In fact, this feature is used to compose the MAnTiCORE configuration file in order to process PRs with their corresponding calibration

parameters in an automatized and standardized way. This includes an averaging of all the parameters presented in Tab. 8.1 for the pre- and post-calibration that are valid for the respective PR (see also appendix D.2.3). One prerequisite and potential disadvantage is, however, that each PR and calibration run has to be first uploaded to CouchDB in order to use this feature. Since there are usually multiple PRs in between the secluding pre- and post-calibration runs, the correct and final processing of the physics data can only be done after the evaluation of the respective calibration measurements. Hence, systematic problems with the configuration of the data-taking or the DAQ electronics might only be discovered with some delay.

In 2014 COBRA's CouchDB was moved, updated and rehosted at TU Dresden, whereas the support and maintenance has been carried out by the TUD collaboration members. More recently, in Jan.'19, the support and host of the system has been outsourced towards the central IT service “Center for Information Services and High Performance Computing (ZIH)” of TU Dresden. Nonetheless, the data access and the content of the database is maintained by the collaboration's TUD members. The current installation of COBRA's CouchDB is based on the software version 3.0.0.

8.1.4 Overview of physics data-taking

The amount of data collected by a double beta decay experiment is usually referred to as its exposure in units of source mass times the respective live-time. In case of the COBRA demonstrator a typical unit is kg days because of the rather small mass of the detector array of about 380 g. Fig. 8.3 illustrates the exposure accumulation of the demonstrator for the complete period of its operation from 2011-09-29 till 2019-11-04.

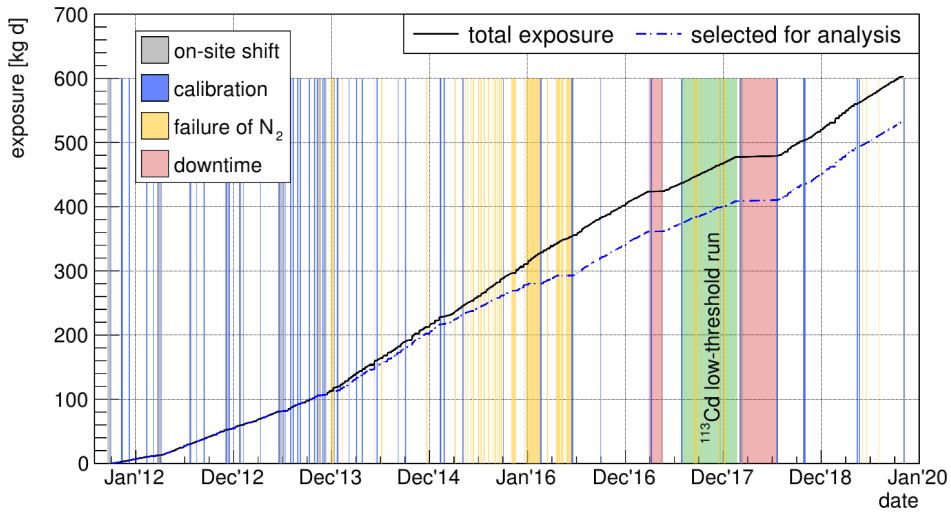


Figure 8.3: Exposure accumulation for the COBRA demonstrator at the LNGS. During its operation a total of 604.2 kg d has been collected, from which 533.3 kg d are considered for analysis purposes. Periods that were affected by a failure of the nitrogen flushing (indicated in yellow) feature an increased background index and are usually excluded from the physics data analysis. Further indicated are the dates of on-site shifts (grey), calibration runs (blue) and two major downtimes in which the demonstrator could not be operated. The preparation, evaluation and data analysis of the special ^{113}Cd low-threshold run (indicated in green) is the main subject of the present thesis and will be presented in section 8.3.

During its operation at the LNGS, a total of 20 on-site shifts have been performed, starting with the installation of the first detector layer in Sept.'11. In advance, two preparation shifts were carried out to install the experiments shielding and to move the predecessor setup to its current location (see section 4.3.1). The exposure graph in Fig. 8.3 clearly shows the increase

of the exposure rate after the installation of the second layer in Apr.'12 and the third and fourth layer in Nov.'13. In total an exposure of 604.2 kg d was collected by the demonstrator array. The initial data of the third layer from Jul.'13 to Nov.'13 is not considered for any analyses due to its unstable operation during the commissioning phase. Moreover, the L3 detector's BV had to be limited to 1 kV in this period, which alters not only their performance but affects also the required efficiency calculations. The problems could be resolved in the L4 installation shift by reworking the BV supply of L3 on-the-fly.

The demonstrator array's performance has been checked regularly with calibration runs. A summary of all 56 performed calibration measurements can be found in section D.2.3 of the appendix. Unfortunately, the experiment suffered several times from failures of the nitrogen flushing, which is meant to prevent radon from diffusing into the inner shield. The nitrogen flow is monitored by several humidity sensors within the setup (see section 4.3.3), which indicate a clear correlation between the relative humidity and an increase of the trigger rate for periods without proper N₂ flushing (see Fig. D.9 in the appendix). Because of this, a data partitioning is performed in order to separate those periods from the rest of the data. The data partitioning will be discussed in section 8.4.2 with the aim to improve the sensitivity to the 2νββ-decay of ¹¹⁶Cd.

Besides the partitioning, a pre-selection of the raw data is performed as mentioned previously in section 8.1.1. A summary of the pre-selection and further consecutive data selection steps is shown in Tab. 8.2.

Table 8.2: Summary of the physics data-taking with the COBRA demonstrator at the LNGS. The pre-selection is performed on the raw data level and consists of two steps to remove corrupt files and runs with unphysically high trigger rates. The second part of the table refers to the standard selection cuts on the event level as introduced in section 7.1. The amount of physics data gets reduced by more than ten times using the below-threshold cut and the DCCs, as indicated by the survival fraction.

description	absolute number	survival fraction [%]
total number of PRs	581	100.00
total number of runs	228 637	100.00
after pre-selection	216 639	94.75
after processing PRs	216 385	94.63
total number of events	229 369 591	94.63
after below-threshold cut	46 659 382	20.34
after DCCs	17 495 065	7.63
after FADC coincidence cuts	17 445 422	7.61

The pre-selection removes about 5.3% of the data, which do not contribute to the total exposure presented in Fig. 8.3. Furthermore, the standard event selection continues on the event level after the processing of the 581 PRs, containing the quoted number of runs (usually a file of 4 h of data-taking per FADC). Those event selection cuts have been introduced in section 7.1 and consist of the below-threshold cut and the DCCs. In combination, the physics data are reduced by more than a factor of ten, indicating that the raw data are dominated by unphysical low-energy signals. For most of the data the offline synchronization of the single FADC clocks (see section 7.1.5) is an ongoing effort. That is why it is only possible to reject coincident events between detectors which are read out with the same FADC device at the time of this thesis. However, the effect turns out to be only marginal with respect to the survival fraction of the total data. This is partly due to the fact that certain noise patterns cause coincidences, which are already flagged by the DCCs, or appear as below-threshold events. A more detailed report on the characteristic features of coincident signal noise and

its potential origin is given in section 8.3.3.

The main subject of the present thesis is the analysis of a dedicated low-threshold run in order to investigate the spectrum-shape of the fourfold forbidden non-unique β -decay of ^{113}Cd . This measurement has been performed prior to the upgrade to COBRA XDEM, following an intensive threshold study and optimization campaign. The preparation, evaluation and data analysis will be presented in section 8.3. After the commissioning of the COBRA XDEM layer, the demonstrator array remained switched off for several months, before it accumulated another 100 kg d along with the XDEM setup. However, in Nov.'19 it was decided to finally end the operation of the four layer demonstrator array to focus entirely on the promising new prototype XDEM detectors in the future.

8.2 Background characterization

This section contains a description of the characteristic background features identified for the COBRA demonstrator and summarizes the knowledge about their presumed origins. The identification and reduction of crucial backgrounds in the $0\nu\beta\beta$ -decay's region of interest (ROI), that might mimic the expected signal, is one of the key objectives of the demonstrator phase. A powerful tool to identify such features in the combined physics data of the experiment is the combination of the reconstructed energy and the interaction depth. The interaction depth z is defined as the normalized distance between the anode side with the CPG at $z = 0$ and the planar cathode electrode at $z = 1$ (see the event reconstruction in section 5.2). Fig. 8.4 illustrates the combined physics data of the COBRA demonstrator for the full exposure of 604.2 kg d in form of a multi-dimensional plot. The x -axis refers to the deposited energy while the y -axis denotes the corresponding interaction depth. The color-coding indicates the decay rate, which has been normalized by the total exposure.

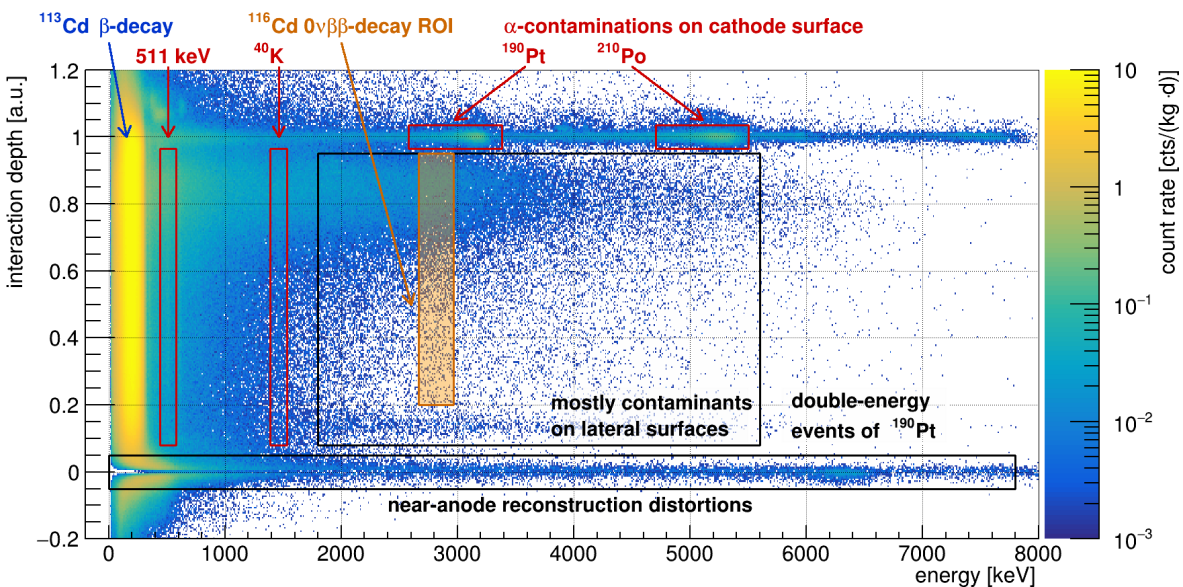


Figure 8.4: Illustration of prominent background features identified for the COBRA demonstrator during its operation at the LNGS. The full exposure of 604.2 kg d has been used in the multi-dimensional display of the reconstructed energy deposit (x -axis), interaction depth (y -axis) and the normalized decay rate (color-coding). While the intrinsic radioactive decays, such as the β -decay of ^{113}Cd at low energies and potential double beta decays, as well as external or internal γ -lines are expected to be homogeneously distributed over the entire z -range, external α -radiation appears much more localized. A preliminary version of this plot with only a fraction of the total exposure has been published in [Zat15].

The most prominent signal arises from the β -decay of ^{113}Cd at low energies, which is clearly dominating the overall decay rate. Due to the uniform distribution of the ^{113}Cd atoms within the sensitive CZT volume, the decay rate follows a flat distribution along z in this energy range. The same uniformity is expected for external contaminations emitting characteristic γ -lines, which will be discussed in section 8.2.3.

On the contrary, external α -particle emitting contaminations are expected to be much more localized due to their short characteristic penetration depth. The observed contaminations on the cathode side, which are caused by the α -decays of ^{190}Pt ($Q_\alpha = 3.2\text{ MeV}$) and ^{210}Po ($Q_\alpha = 5.4\text{ MeV}$), will be discussed in more detail in section 8.2.4. Since the low- z range of $z < 0.2$ is strongly affected by near-anode reconstruction artifacts, the area is removed as part of the standard DCCs in the physics data analysis. This also includes the so-called *double-energy events* of ^{190}Pt , which are explained as well in section 8.2.4.

An one-dimensional projection of the interaction depth spectrum above the ^{113}Cd endpoint has been shown in Fig. 7.4 of section 7.1.2. In both Fig. 7.4 and Fig. 8.4 there is a clear indication for the so-called z -hump region, which refers to the area of $z > 0.6$ with a significantly increased event rate. By splitting the total data according to the detector layers, it is found that the z -hump is most prominent for the layer L3, which is situated at the top of the array (see e.g. Fig. A.5 in the appendix). The same distribution as observed for the one-dimensional z -spectra is found for the multi-dimensional display of each detector layer's total exposure as depicted in Fig. 8.5.

Although there is not yet a complete and validated background model of the COBRA demonstrator, there seems to be a quite plausible explanation for the present z -hump feature. Before the installation of the third and fourth layer took place, it was necessary to upgrade the signal cables' feed-through in order to transmit the detector signals from the lower to the upper floor where the main DAQ electronics are operated (see section 4.3.3). Even though special care has been taken in cleaning the laboratory at the lower floor, both layers might still be contaminated with tiny amounts of dust. Since L3 has been installed directly after those mechanical works, the contamination level is expected to be higher.

After finishing the integration of L3 and L4 into the inner shielding of the experiment, with L3 being the uppermost layer, those contaminants are expected to settle, thus, to concentrate to some degree on the Delrin support frames (see schematic drawing Fig. 4.7 in section 4.3.3). While the top part of the detectors, which corresponds to low- z values, is shielded by the upper Delrin frame, radioactive decays of a potential dust layer on the bottom frame might penetrate the sensitive volume. Moreover, a small part close to the cathode at $z = 1$ would be covered by the Delrin as well. This could explain the small gap observed in the multi-dimensional illustrations as shown in Fig. 8.4 and Fig. 8.5. Furthermore, the presence of the z -hump fades from the top to the bottom of the array. This might be explained by the dust settling hypothesis as well. Without further knowledge about the exact composition of the dust contamination it can be assumed that it contains a significant amount of elements occurring in the natural decay chains of uranium and thorium (see Fig. D.8 in the appendix). The decay series involve multiple highly energetic β - and α -decays, whereas only electrons are expected to pass through the encapsulation lacquer of about $20\text{ }\mu\text{m}$ thickness.

One promising candidate decay to explain the z -hump is the β^- -decay of ^{214}Bi with $Q_\beta = 3269\text{ keV}$ and a half-life of about 20 min [NDS20]. The shape as well as the endpoint of the decay fit quite well to the observed z -hump. Furthermore, the maximum deposited energy in this depth range as seen in Fig. 8.5 is the highest for L4, which features the smallest amount of the encapsulation lacquer, hence, the thinnest layer of shielding material. While the average lacquer mass per detector is about 16.5 mg for L1 – L3, it is only 11.3 mg for the L4 detectors (see Tab. E.1 – E.4 in the appendix).

However, this explanation has to be seen as preliminary and requires more detailed stud-

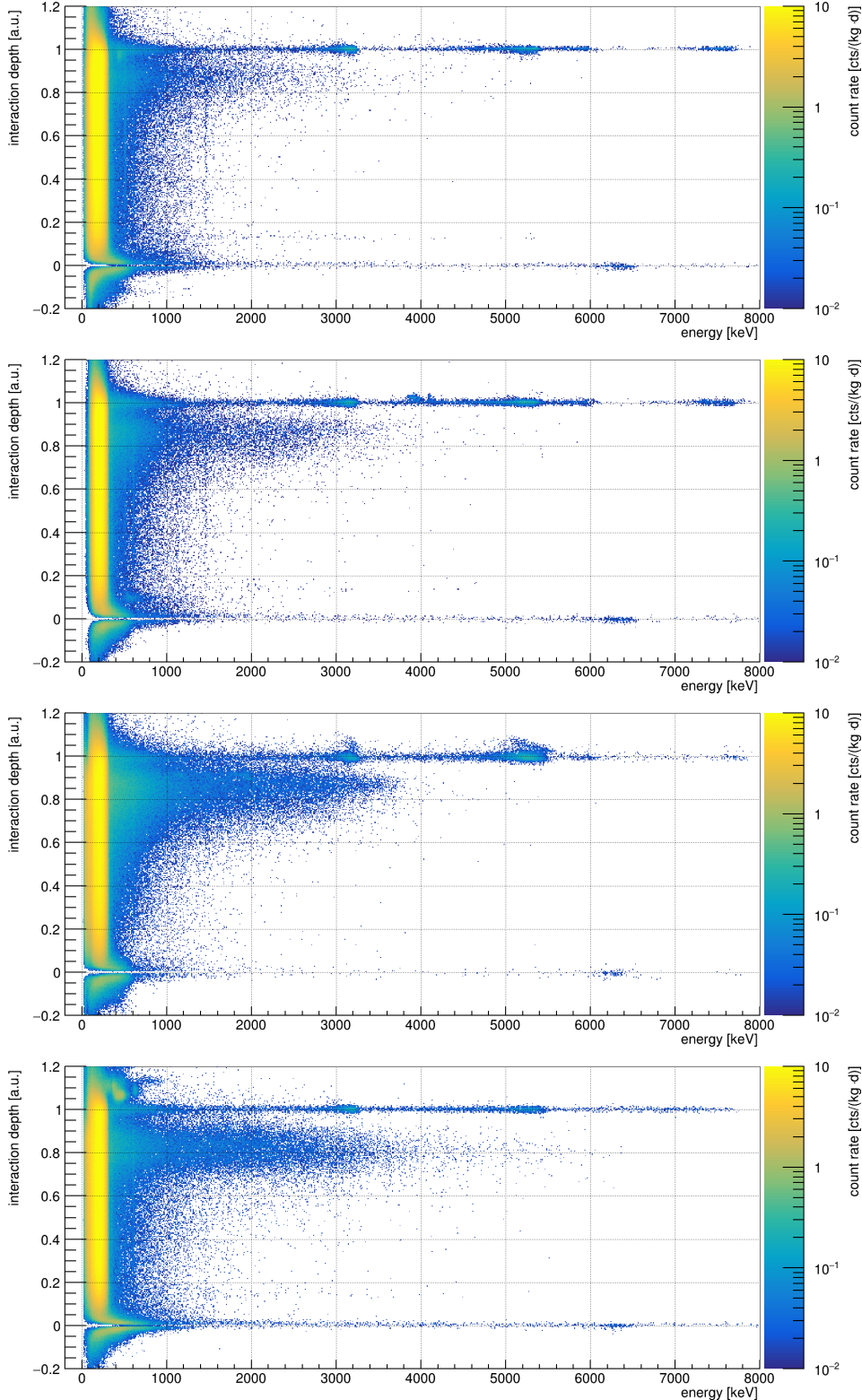


Figure 8.5: Multi-dimensional illustration of the full data set accumulated with the COBRA demonstrator. From top to bottom the data of L1 – L4 are shown, whereas only the DCCs have been applied. Each layer's z -versus- E spectrum has been normalized by its respective exposure as reported in Tab. 8.14 of section 8.4.2. While the z -hump region around $z \approx 0.8$ is much more prominent for L3/L4 than for L1/L2, the other background features highlighted in the combined spectrum of Fig. 8.4 look rather similar for all four layers.

ies based on Monte-Carlo (MC) simulations. One particular challenge of the background projection at higher energies is the modeling of the encapsulation lacquer as it deteriorates the observable endpoint of the presumed β -spectrum contribution of ^{214}Bi as well as the peak position of characteristic α -decays of the natural decay chains as will be discussed in section 8.3.7. In the same section a MC background model for the low-energy region close to the ^{113}Cd β -decay will be presented that might be extended in the future to give a realistic background projections at higher energy scales as well.

In the following sections a more detailed discussion of the impact of the PSD cuts, which have been introduced in section 7.1, as well as their application towards further characterizing the identified background features will be presented.

8.2.1 Performance of PSD cuts

In Fig. 8.6 the effect of several stages of the event selection for the combined energy spectrum of the COBRA demonstrator array and its full exposure is shown. The standard event selection includes the DCCs, the FADC coincidence cut as well as a rather mild restriction of the interaction depth according to $0.2 < z \leq 1.1$. These three selections are applied for all of the depicted spectra.

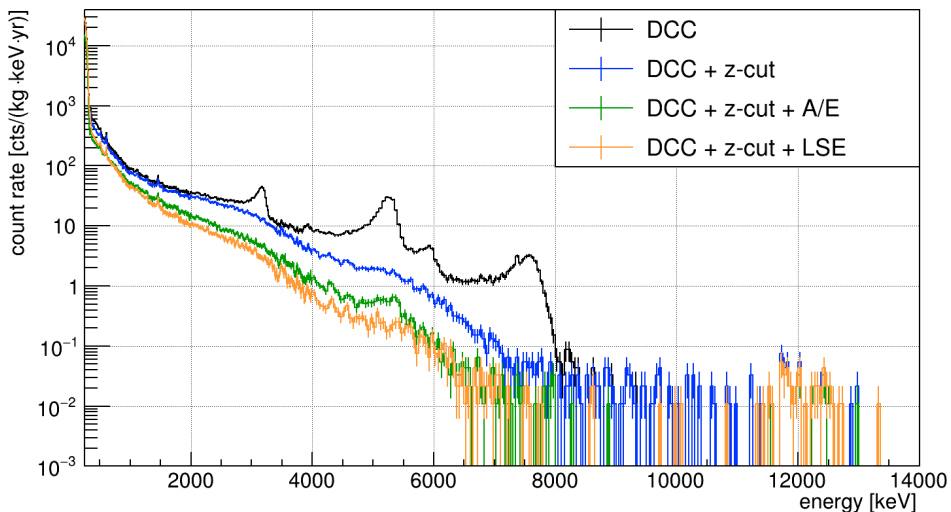


Figure 8.6: Effect of consecutively applied event selections on the combined energy spectrum obtained with the COBRA demonstrator at the LNGS. The data correspond to the full exposure of 604.2 kg d and include the standard analysis cuts (DCCs, FADC coincidence cut, $0.2 < z \leq 1.1$) for all spectra. The additional z -cut removes near-cathode events with $z > 0.97$ (see section 7.1.2). The actual PSD cuts are sensitive to LSEs and MSEs, but feature different signal efficiencies for signal-like SSEs.

At higher energies above the already mentioned α -decay contaminations of ^{190}Pt and ^{210}Po , there are indications for further α -particle emitting contaminations. However, all the α -contaminations are effectively reduced by a cut on the interaction depth to exclude the cathode region. The effect will be further elaborated in section 8.2.4.

In combination with the previous cuts, the application of the actual PSD cuts, referred to as the LSE selection (see section 7.1.3) and the revised $(A/E)_{90\%}$ criterion (see section 7.2.2), further reduces the background in the double beta decay ROI below the α -peaks. A more detailed discussion of this energy range with emphasize on the presence of characteristic γ -lines will follow in section 8.2.3. Although it seems that the LSE cut reduces the background more strongly than the $(A/E)_{90\%}$ selection, one has to take the respective survival fraction of signal events into account. The average signal efficiency of the LSE cut has been determined

to $\varepsilon_{\text{LSE}} = (76 \pm 2)\%$ [COB16a] using the DEP events of ^{208}Tl as a proxy for signal-like SSE. The same method results in a signal efficiency of $\varepsilon_{A/E} = (90.0 \pm 1.5)\%$ for the calibrated $(A/E)_{90\%}$ criterion (see section 7.2.4). Furthermore, the calibration of the A/E parameter ensures that the efficiency should be constant for a fixed cut value across the entire detector ensemble. As a result the calibrated $(A/E)_{90\%}$ shows great robustness, stability and in general a similar performance for all detectors of the demonstrator array. The LSE cut on the other hand has neither been calibrated at the detector level, nor was it optimized for each calibration period separately. That is why in the following chapters and analyses the calibrated A/E parameter is being used as the default PSD cut.

The events above ~ 9 MeV of the combined spectrum are assumed to be caused by the residual muon flux in the LNGS underground complex and sum up to about 170 events for the total exposure after applying the standard analysis cuts without PSD. Further information on the muon-induced background will be given in section 8.2.5. To further reduce the background in the double beta decay region of interest, a partitioning of the full exposure into a background-enriched and a background-reduced data set has been performed. This topic will be presented in section 8.4.2 in order to investigate the potential to observe the $2\nu\beta\beta$ -decay of ^{116}Cd and to reduce the BI in the $0\nu\beta\beta$ -decay ROI around the Q -value at 2.8 MeV for the same isotope.

In the following, a more detailed description of the background characteristics starting from the low-energy region up to the 10 MeV scale will be given.

8.2.2 Low-energy features

As explained in previous section, the low-energy spectrum is dominated by the highly forbidden β -decay of ^{113}Cd . A detailed analysis and a summary of previous studies on this subject is given in section 8.3. The typical decay rate is so high that there are hardly any other low-energy features observable in the projected energy or z -versus- E spectra. Any x-ray or γ -line below the ^{113}Cd Q -value would be hidden by its continuous β -decay spectrum.

However, besides the physical signals caused by ^{113}Cd , the low-energy region is affected by signal noise and distortions of every form. The typical energy thresholds of the experiment are chosen in a way that ensures a conservative coverage of the ^{113}Cd decay range (see section 8.1.1), but at the cost of triggering also on noise. In fact, a large fraction of the physics data is removed by the dedicated below-threshold and data-cleaning cuts as reported in Tab. 8.2 of section 8.1.4. Due to the variety of possible unphysical signals such as high- and low-frequency baseline noise, micro-discharges, or electromagnetic interference (EMI) in general, there is no unique form or origin of those signals. Furthermore, there have been several approaches to describe the near-threshold features in the past (see e.g. the theses [Hom12], [Hei13], [Kan17] and [Hei18]). It turned out that there is no universal model to describe the noise edge analytically and that in some cases also the efficiency of the standard DCCs might be not well-defined.

The efficiency issue could be partly overcome by improving the definition of the reconstructed threshold as pointed out in section 5.2.4, which led to the definition of the already mentioned below-threshold cut. Additionally, after the installation of the cooling system for the pre-amplifier stage (see section 4.3.3), a reduction of the thermal noise component could be reported. The effect of the mild cooling of the electronics (and indirectly of the detectors) will be summarized in section 8.3.3. In the end, the efficiency issues of the standard DCCs turned out to be not as severe as reported in [Kan17] (see section 7.1.1). Nonetheless, special care has to be taken when combining the data of multiple runs and detectors. Because the individual detectors' thresholds might change between runs according to the optimum trigger rate, each energy bin of the final spectrum has to be normalized with its corresponding

exposure. Moreover, this has to be done separately for each detector to take into account the individual detector masses as listed in Tab. E.1–E.4 of the appendix. All physics spectra shown before or about to be presented in the following analysis sections have been prepared accordingly.

8.2.3 Prominent γ -lines

Besides the prominent α -contaminants identified in Fig. 8.4, there are indications for weak γ -lines in the physics data of the COBRA demonstrator. While some of them originate again from the natural decay chains (see section D.2.1 of the appendix) and show a uniform distribution over the detector array and the experiments live-time, there are a few more exotic cases, which will be discussed in the following.

Tab. 8.3 contains a list of the most prominent and the usually expected γ -lines, as well as their corresponding signal strength expressed as the signal-to-background ratio (S/B). In the present case, the S/B ratio refers to the number of peak entries N_{peak} reduced by the number of estimated background counts N_{SB} and normalized by the Poisson variation $\sqrt{N_{\text{SB}}}$ of the background. Because of the presumed weakness of the γ -lines, a simple *cut and counting* method is applied to express their signal strength and to compare their intensities.

For each γ -line, N_{peak} is determined as the integral over $E_\gamma \pm 2\sigma$, whereas $\sigma = \sigma(E_\gamma)$ follows from the known average resolution curves FWHM(E) (see section 8.1.2). This integral corresponds to a Gaussian coverage of 95.45% (see appendix C.2 for more details about the coverage). An exception is the lowest γ -line associated to the decay of ^{210}Pb . In this case the integral range has been modified to $[E_\gamma - 1\sigma, E_\gamma + 2\sigma]$ to avoid contributions from the endpoint of the ^{113}Cd β -decay. The decreased range reduces the Gaussian coverage to 81.86%. As the peak integral also includes events of the underlying background, which is assumed to consist of Compton scattered photons and degraded α - and β -particles, it has to be corrected for those contributions. This is done by defining two side-band (SB) regions around the center of a γ -line, that cover the same range as the peak window, but are shifted by half of the integration range. The procedure is similar to the optimization of the A/E criterion discussed in section 7.2.3. For the present scenario outlined above, the left SB would cover $[E_\gamma - 4\sigma, E_\gamma - 2\sigma]$ and the right SB $[E_\gamma + 2\sigma, E_\gamma + 4\sigma]$, respectively. Moreover, a one-bin-offset ensures that there is no double counting of events. Again, the case of ^{210}Pb is treated separately to avoid the ^{113}Cd β -decay at lower energies.

The analysis of the γ -lines is carried out for the full data set and after removing the so-called HRP partition. This partition contains the high-rate periods (HRPs), where the nitrogen flushing of the air-tight acrylic box as part of the inner shield failed and radon was able to diffuse into it. The appearance of those periods is indicated in Fig. 8.3. Further details on the data partitioning will be given in section 8.4.2. Furthermore, the surveillance of the γ -induced background is done for the combined spectrum of all detectors and split according to the four detector layers in order to investigate its local distribution.

The most prominent γ -line with the highest intensity according to the determined S/B ratio is found to be the 511 keV annihilation line. The observed relative signal strength is rather independent of the performed data partitioning, thus, not related to an increased radon exposure. While muons are able to produce electron-positron pairs via bremsstrahlung in the vicinity of the detector array, the magnitude of the signal cannot be explained by this effect alone (see also section 8.2.5). In fact, the signal strength is found to vary strongly between the four detector layers hinting to an origin at the bottom of the array. In accordance with the position of the layers in the real experiment – from top to bottom L1-L2-L4-L3 (see Fig. A.5 in the appendix) – the local distribution follows roughly a $1/r^2$ behavior.

Table 8.3: Overview of identified or expected γ -lines for the combined spectrum of the COBRA demonstrator and each of its detector layers. For each spectrum a cut on the interaction depth has been performed to remove near-cathode events. The intensity of the presumed γ -lines is evaluated with a *cut and counting* method to estimate the S/B ratio. Moreover, the analysis is performed for the full data set and after the removal of the so-called HRP partition (high-rate periods, see section 8.4.2). Because of the background correction, the signal strength might turn out to be negative but close to zero, which indicates the absence of the associated γ -line in the present data set.

partitioning	E_γ [keV]	S/B = $(N_{\text{peak}} - N_{\text{SB}})/\sqrt{N_{\text{SB}}}$									
		full data set					HRP removed				
		L1	L2	L3	L4	total	L1	L2	L3	L4	total
	511.0	29.0	13.5	2.3	7.2	11.9	32.7	15.2	3.7	9.6	14.1
^{22}Na	1274.5	< 0	< 0	< 0	< 0	< 0	< 0	< 0	< 0	< 0	< 0
^{40}K	1460.8	16.9	9.2	5.7	0.0	7.0	19.7	17.0	5.6	1.4	9.4
^{214}Pb	351.9	10.9	22.1	1.4	21.4	13.0	< 0	< 0	< 0	< 0	< 0
^{214}Bi	609.3	21.3	28.7	18.1	27.4	22.9	4.4	2.1	2.1	3.2	2.8
	1120.3	2.0	4.3	6.0	4.7	4.3	0.0	0.0	2.5	1.4	1.1
^{208}Tl	583.2	< 0	< 0	< 0	< 0	< 0	< 0	< 0	< 0	< 0	< 0
	2614.5	< 0	< 0	< 0	< 0	< 0	< 0	< 0	< 0	< 0	< 0

Moreover, there are indications for a correlation of the annihilation line and another γ -line at about 1275 keV, which would be consistent with the β^+ -decay of the artificial sodium isotope ^{22}Na . As this γ -line is only observed by a few detectors, it disappears in the sum of multiple detectors such as reported in Tab. 8.3. While ^{22}Na is also one of the standard radionuclides used in the energy calibration of the detector array, there is absolute clarity that the observed background contribution is not related to a hypothetical leak of the source's encapsulation as there are regular leakproofness tests by the safety authorities at the LNGS. A typical energy calibration spectrum can be found in Fig. 8.2. The associated γ -line energies as well as their absolute intensities are listed in Tab. 8.6. The absolute intensities suggest that the 511 keV should be much more prominent than the ^{22}Na full energy line, which is perfectly consistent with the observation. While the origin of such a contamination remains unclear, it has been already quite well characterized in the past (see e.g. Ref. [Hom13]).

The intensity distribution of the presumed γ -lines of ^{22}Na of the first two detector layers are found to be consistent with a point-like contamination of about 3.3 mBq within the copper nest [Hom13]. The highest intensity is found for Det4 (L1-P04), which is at a corner position of the 4×4 layer, followed by its neighboring detectors (L1-P03, L1-P07 and L1-P08). The corresponding L2 detectors right above are already quite far away from the supposed origin of the ^{22}Na contamination and only show it much more reduced. An impression of the single detector spectra compared to the combined spectrum of L1 is depicted in Fig. 8.7.

The identification of the ^{22}Na contamination, which is associated with a half-life of 2.6 yr [NDS20], triggered an intensive cleaning of the copper nest prior to the installation of L3 in Jul.'13. However, the effect of the cleaning remains inconclusively as Det4 has been disabled due to its rather unstable performance in most of the data-taking runs. Moreover, during almost eight years of operation, the initial activity of ^{22}Na should have faded away leaving almost no trace in the more recent data.

All the other considered γ -lines listed in Tab. 8.3 feature a much weaker S/B ratio and are more challenging to be observed. However, their presence can be enhanced by inverting the PSD cuts as shown in Fig. 8.8, because a significant contribution to full energy depositions of γ -lines at the energy scale of interest are caused by multiple interactions. Those are typically

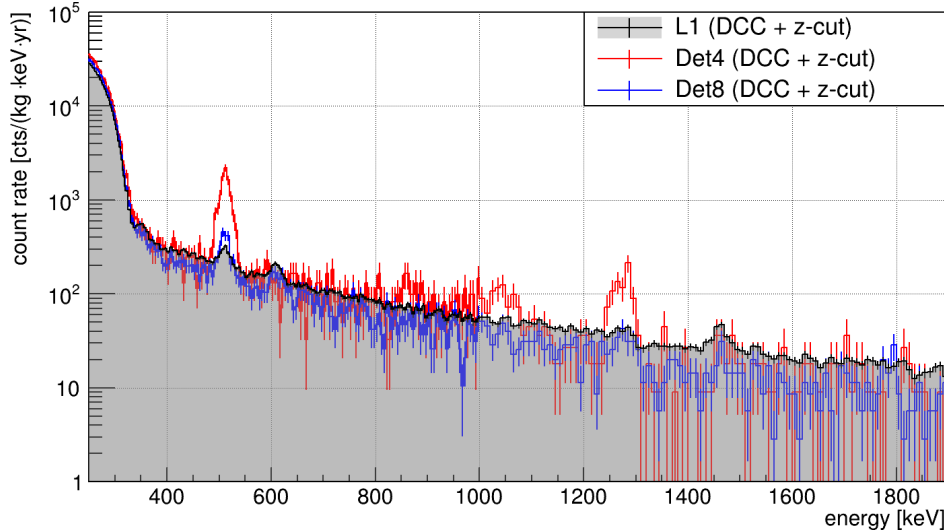


Figure 8.7: Example detector spectra with a clear indication for a localized ^{22}Na contamination of the COBRA demonstrator setup. The two γ -lines at 511 keV and 1275 keV are clearly visible for Det4 (L1-P04), but are already strongly reduced for its next neighbors (e.g. L1-P08). Moreover, in case of Det4 there is also a clear indication for the Compton edge of the full energy ^{22}Na line at $E_C = 1062$ keV. For comparison, the combined spectrum of L1 is shown, where hardly any indication for the ^{22}Na full energy line can be observed. Each spectrum corresponds to the full data of the respective detectors without making use of the data partitioning and only includes the DCCs and the cathode z -cut.

an initial Compton scatter process and the subsequent photoelectric absorption. This leads to a significant fraction of multi-site interactions for full energy depositions, similar to the optimization procedure of the A/E criterion in section 7.2.3. By inverting the PSD cuts meant to select single-site interactions, an effective enhancement of the full energy peaks over the Compton background is achieved. The effect is stronger for the MSE selection because of the $(A/E)_{90\%}$ cut being sensitive to LSEs as well.

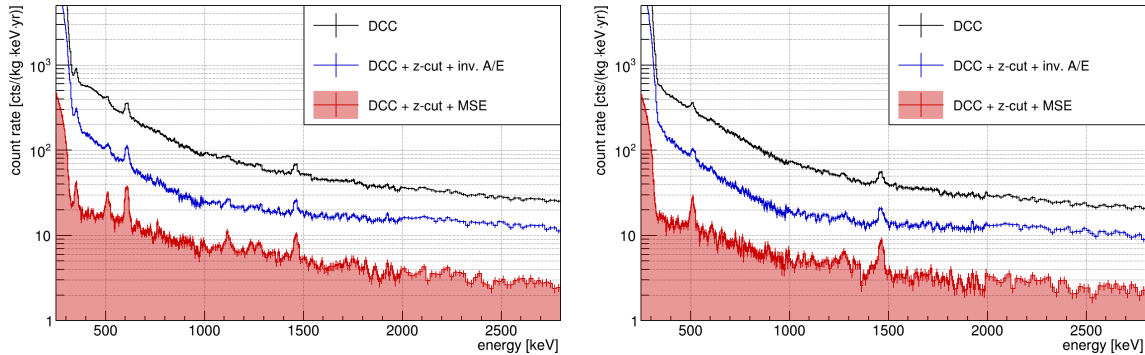


Figure 8.8: Comparison of the inverted $(A/E)_{90\%}$ selection and the MSE flagging algorithm to enhance weak γ -lines in the combined spectrum of the COBRA demonstrator. *Left:* total exposure including the HRP partition. *Right:* reduced exposure after HRP removal. The spectra in both plots have been scaled according to the exposure of the selected data (see Tab. 8.14 in section 8.4.2). As the $(A/E)_{90\%}$ selection is also sensitive to LSEs, the γ -line enhancement is more prominent in the MSE spectra.

In the full exposure plot there are clear indications for the high intensity γ -lines of the primordial radionuclide ^{40}K at $E_\gamma = 1460.8$ keV as well as from prominent nuclides of the natural decay chains. One prominent radionuclide is the radon isotope ^{222}Rn as part of the natural ^{238}U decay series (see Fig. D.8 in the appendix), which features a rather short half-life

of 3.8 d. A reliable trace marker for a temporary increase of the ^{222}Rn activity is the presence of γ -lines of its short-lived daughter nuclei such as ^{214}Pb (351.9 keV) and ^{214}Bi (609.3 keV and 1120.3 keV). The γ -line of ^{214}Pb appears to be less prominent for L3, but this is only due to the overall higher background arising from the prominent z -hump as pointed out in the introduction part of the background characterization section. By removing the data of the HRP partition, the associated radon-induced γ -lines are strongly suppressed and almost disappear entirely. According to the S/B ratio in Tab. 8.3, the suppression turns out to be about one order of magnitude for $E_\gamma = 609.3$ keV of ^{214}Bi . For the α -decay region the effect of the partitioning will be discussed in the next section.

As the ^{40}K and the 511 keV annihilation γ -lines are not related to the radon exposure, their signal strength is not much affected by the partitioning. The S/B ratio of the ^{40}K γ -line shows that it is more prominent for the first two detector layers, but it is present for all four. However, no clear point-like origin as for ^{22}Na can be inferred in the case of ^{40}K . A potential contribution arises from the encapsulation lacquer that covers each CZT detector (see e.g. Tab. 8.8 in section 8.3.7) and the conventional glue used to strengthen the mechanical connection of the electrodes' wire contacts. Moreover, the construction and instrumentation of the first two detector layers involved larger quantities of potentially radioactive materials, especially on the HV side. For L3 and L4 a more careful material selection had been performed based on the experience gathered with the previous layers' designs. An impression of the evolution of the layer design is shown in Fig. A.3 of the appendix.

Finally, another well-defined indication for the presence of traces of the natural decay chains near the sensitive detector array would be the characteristic γ -lines of ^{208}Tl at 583.2 keV and 2614.5 keV. The β^- -decay of ^{208}Tl is part of the ^{232}Th decay chain. No indication for those γ -lines has been found in the demonstrator's physics data, independently of the selected detector ensemble or data partition. Further restrictions on the contribution of the natural uranium and thorium decay series to the overall background will be shortly addressed in section 8.3.7.

8.2.4 Identified α -decay contaminants

Above the energy range of the sought double beta decay signals, with the ^{116}Cd ROI around $Q_{\beta\beta} = 2.8$ MeV being the uppermost signal region, there are α -particle emitting surface contaminations that dominate the energy spectrum. Due to their localized position and their short range, a large fraction of those events can be removed by a cut on the interaction depth to exclude near-cathode events (see e.g. section 7.1.2). An overview of the identified α -decays, which contribute to the cathode contamination, is given in Tab. 8.4. Due to the nuclear recoil, the emitted α -particles do not carry the full Q -value of the nuclear reaction but a reduced energy E_α , which depends on the masses of the mother and daughter nuclei.

Table 8.4: Overview of identified α -decays as background for the COBRA demonstrator. The isotopes are ordered according to their Q -values from low to high. The Q -values and the corresponding maximum energies of the emitted α -particles are taken from Ref. [NDS20] and have been rounded to three digits. The half-lives are quoted from the same reference and feature a broad variety.

isotope	Q_α [MeV]	E_α [MeV]	half-life	origin
^{190}Pt	3.269	3.175	6.5×10^{11} yr	part of electrode metalization
^{210}Po	5.408	5.304	138.4 d	initial exposure + produced by ^{222}Rn
^{222}Rn	5.590	5.489	3.8 d	prompt exposure (failure of N_2 flushing)
^{218}Po	6.115	6.001	3.1 min	produced by ^{222}Rn
^{214}Po	7.834	7.687	$164.3 \mu\text{s}$	produced by ^{222}Rn

The observed α -contaminations are the result of two different source decays. The first is the long-lived α -decay of ^{190}Pt . Platinum is part of the detector's electrode metalization and contains naturally about 0.01% of ^{190}Pt . Moreover, the platinum layer is expected to have only a thickness of about 40–50 nm as per information by the CZT detector supplier. The maximum depth reached by the α -particles can be estimated with the ASTAR database [NIS17]. As CZT is not available in the database's list of 74 materials, tin with a similar nuclear charge of $Z = 50$ has been used to estimate the α -particles CSDA range using the continuous-slowing-down approximation as an estimate for the maximum penetration depth R_{\max}^α . Scaled to the density of CZT, an α -particle of 3.2 MeV is expected to have $R_{\max}^\alpha \approx 12 \mu\text{m}$. Similar values are obtained for the α -particle energies E_α listed in Tab. 8.4. Thus, the energy deposition of those particles is limited to the surfaces and cannot penetrate deeply into the bulk region.

Another feature caused by the α -decay of ^{190}Pt can be seen in the z -versus- E display of the physics data such as shown in e.g. Fig. 8.4. For interactions that appear close to the anodes, there is an additional signal contribution from the holes' drift as charge carriers. In the proximity of the CPG anode, the holes are able to be collected, which is not foreseen by the detector's design and event reconstruction (see section 4.1.3). Due to the additional hole contribution, the charge signal is roughly twice as high, which is why the ^{190}Pt events in this region appear at roughly twice their original energy E_α in the z -versus- E illustration. Because of the doubling of E_α , the events are also referred to as *double-energy events* (see Fig. 8.4). However, this is usually not an issue since the near-anode region is removed as part of the data-cleaning. A dedicated investigation of the ^{190}Pt α -decay including the determination of its half-life will be presented in section 8.5.

The second group of α -peaks at higher energies E_α (see Tab. 8.4) are induced by the decay of ^{222}Rn . Radon is a noble gas and features a high mobility, which allows it to diffuse rather easily out of the surrounding rocks and into the setup in case of a failure of the nitrogen flushing. More information on the radon level at the LNGS underground laboratory will be given in section 8.3.7. Besides the initial α -decay of ^{222}Rn , the decay series contains three α -decaying isotopes of polonium, whereas ^{218}Po and ^{214}Po have very short half-lives. On the other hand, ^{210}Po has a half-life of about 138.4 d, which builds up as a long-lasting contamination. Usually, the daughter atoms remain in a positively ionized state after an α -decay for a time being, hence, might get attracted by the negative bulk voltage applied between the anode at ground potential and the cathode of the detectors. Moreover, polonium is a metal and has only a poor mobility after it has settled to a surface. That is why there is a concentration of the α -contaminants on the cathode side, but not exclusively. As indicated in the previous z -versus- E display of the demonstrator data in Fig 8.4, it is expected that most events in the double beta decay ROI are caused by α -particle emitting contaminations on the lateral surfaces. Although their presence can be suppressed by using pulse-shape discrimination (see e.g. section 7.1), the remaining fraction of events still dominates the background in this region. The effect of the cathode z -cut and the combination with the $(A/E)_{90\%}$ selection is shown in Fig. 8.9.

While there are clear α -peaks at the corresponding α -particle energies E_α in case of the cathode contaminations, which are removed by the cathode z -cut, the spectrum of the remaining events is rather continuous. The observed absence of the α -peaks is an indication for the location and composition of the α -contaminations on the lateral detector sides. If there would only be the relatively long-lived ^{210}Po situated directly on the CZT, without a passive absorber material in between, a clear α -peak at 5.4 MeV could be expected after removing the near-cathode events. The same applies to other α -emitters with higher Q -values. In fact, the combined spectrum after removing the HRP partition and applying the $(A/E)_{90\%}$ cut features an indication for ^{210}Po on the side walls. However, there is a much stronger population of

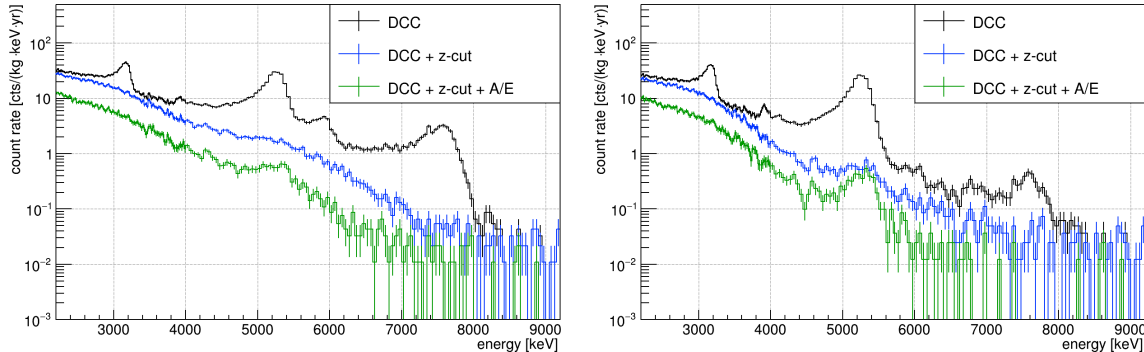


Figure 8.9: Suppression of α -contaminants for the COBRA demonstrator. *Left:* total exposure including the HRP partition. *Right:* reduced exposure after HRP removal. In both cases, the cathode z -cut removes efficiently the α -peaks. Furthermore, the removal of the HRP partition clearly reduces the prompt exposure of ^{222}Rn and its daughter nuclei above the α -peak of the long-lived ^{210}Po at 5.4 MeV before the z -cut. The residual background below 3 MeV is further reduced by about two times by the $(A/E)_{90\%}$ selection.

events with lower energies. The reason for this is assumed to be caused by the encapsulation lacquer, which shields the detectors on their lateral sides in case of a prompt ^{222}Rn exposure. Because of the different amounts of the lacquer per detector and its inhomogeneity across the lateral surfaces, the expected high-energy α -peaks are strongly deteriorated. On the other hand, at least part of the observed ^{210}Po contamination of the CZT detector's sides is presumed to be present on the actual detector surfaces below the encapsulation. This can be concluded from the clear presence of the ^{210}Po α -peak after the application of the full event selection. The events at lower energies might be caused by a later unintended exposure to radon or further contaminants in the encapsulation lacquer (see also section 8.3.7).

In fact, during the characterization of the demonstrator's detectors, they have been operated under a normal air atmosphere, not only in the collaboration's surface laboratories, but also for the quality tests performed by the manufacturer. In such an environment, the same decay mechanisms could take place as pointed out above. Furthermore, even without biasing the detectors, there is the chance to attract radon daughters leading to a rather long-lived ^{210}Po contamination on all detector surfaces. Since the α -contaminants have been found to be the dominating background contribution for the demonstrator array, special care has been taken in the preparation of the COBRA XDEM upgrade (see section 4.3.4). All pre-commissioning steps by the manufacturer and the characterization measurements of the final XDEM detector pool have been done under a strict nitrogen atmosphere in clean-room like environments to prevent the build-up of radon-induced surface contaminations. Moreover, the shipment of the detectors was only done with double-layered air-tight sealed packaging. Further details on the commissioning of the COBRA XDEM setup can be found in the PhD thesis of R. Temminghoff [Tem19].

8.2.5 Muon-induced background

The operation of the COBRA demonstrator at the LNGS underground laboratory has the advantage that the cosmic muon flux is reduced by more than six orders of magnitude compared to the surface level (see e.g. section 4.3.1). The residual muon flux in the underground is monitored continuously by several experiments and has been precisely measured by e.g. the Borexino collaboration. The average flux is found to be $\Phi_\mu = (3.41 \pm 0.01) \times 10^{-4} \text{ m}^{-2}\text{s}^{-1}$ with a seasonal amplitude modulation of only $(1.29 \pm 0.07)\%$ [Bor12]. This flux corresponds to about 30 muons passing through an area of one square-meter per day.

Based on the laboratory measurements presented in section 7.4.2 and the developed analytic model for the reconstruction of muon-induced events, it is possible to interpret the high energy region of the COBRA demonstrator’s physics data. While the imprints of the muon-induced events would also be visible at lower energies, their presence is hidden by the other, more frequent background processes discussed previously.

Fig. 8.10 illustrates the application of the analytic muon model and its predicted muon ranges for the z -versus- E spectrum corresponding to the total exposure of 604.2 kg d. Vertically incoming muons following a path that traverses the complete bulk volume of a single CZT detector would be expected to appear between the points labeled as VPL (vertical path length) and MPL (maximum path length) along the $z = 0.5$ line. The VPL corresponds to the detectors’ average height, hence the minimum path between the anode and cathode side leading to $\langle E_{\mu}^{\min} \rangle = 7.4$ MeV, while the MPL is found for the connection between two corners on the diagonal opposite sides, resulting in an energy deposition of $\langle E_{\mu}^{\max} \rangle = 12.8$ MeV (see section 7.4.2). Similarly, in case of the xy -planes close to the electrodes at $z = 0$ (anode, top) and $z = 1$ (cathode, bottom) a maximum energy deposition is expected for the diagonal path lengths (DPLs). If a muon passes through only a part of a crystal, its energy deposition with respect to the interaction depth would fall into either the *top-streaking* or *bottom-streaking* area. The derivation of this model and the respective equations are discussed in section 7.4.2.

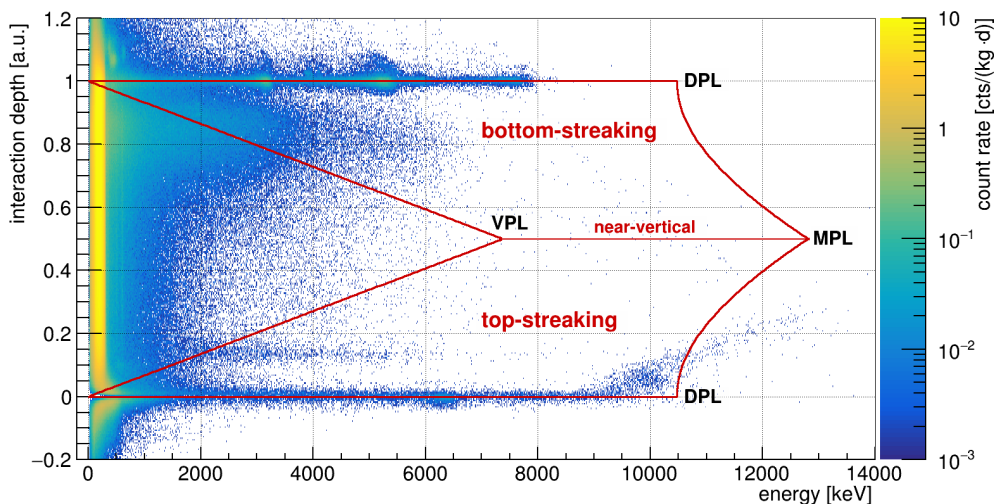


Figure 8.10: Illustration of the analytic muon model with respect to the physics data obtained by the COBRA demonstrator at the LNGS. Only events that pass the standard data-cleaning cuts enter the z -versus- E plot, which represents the total exposure of 604.2 kg d. The labeled areas correspond to the expected energy depositions of minimum-ionizing muons for certain path lengths: VPL (vertical path length), DPL (diagonal path length) and MPL (maximum path length). Nearly vertically incoming muons are expected to appear along the indicated $z = 0.5$ line. Muons passing through only a fraction of the z -range would appear in the framed areas indicating the range of events where muons streak either the top or the bottom of a crystal.

As there is no clear clustering of events along the $z = 0.5$ line, indicating vertically incoming muons, it is hardly possible to characterize e.g. the angular distribution of the muon flux. Moreover, given the small size of the demonstrator array and the residual flux of cosmic muons as reported by the Borexino experiment, the expected number of muon interactions is very low. In fact, by considering the Borexino result for the average muon flux, only about 312 muon-induced events would be expected for the total exposure of the COBRA demonstrator assuming an effective area of $64 \times 1 \text{ cm}^2$. It should be noted that is an upper limit as not all detectors have been operational during all physics runs and there might be coincidences between several crystals for vertical incoming muons, which would lead to the exclusion of those events from the usual double beta decay searches. On the other hand,

it is very unlikely that a single muon would produce coincidences between detectors of the same layer, if it is passing through the setup. This allows for the estimate of a lower limit using an effective area of only $16 \times 1 \text{ cm}^2$ which results in 78 expected muon hits.

The clustering of events in the lower right corner of Fig. 8.10 for $z < 0.2$ and $E \approx 10 \text{ MeV}$ is probably an artifact of the event reconstruction of surface contaminations on the CPG anode. As discussed in the previous section, near-anode events are affected by a doubling of the reconstructed energy because of the unaccounted hole contribution to the charge signal. Furthermore, the saturation of the FADC range causes an upwards slope in the z -versus- E plane. The double-energy distribution of the near-anode clustering is compatible with the expected signal of the long-lived ^{210}Po α -decay with $E_\alpha = 5.3 \text{ MeV}$ (see Tab. 8.4).

By excluding this area using the standard depth selection according to $0.2 < z < 0.97$ together with a lower energy threshold based on $E_\mu^{\min} = 7.4 \text{ MeV}$, an integrated number of $N_\mu = 266 \pm 16$ potential muon interaction events are found. This number is in agreement with the previously estimated expectation of 78–312 events depending on the chosen effective area. By scaling N_μ to the total exposure and the energy range limited by E_μ^{\min} and E_μ^{\max} , a background index of about $0.03 \text{ cts}/(\text{kg keV yr})$ is found. Regarding the ROI of the ^{116}Cd $0\nu\beta\beta$ -decay around 2.8 MeV , the contribution of muon-induced events is negligibly small compared to the rates of the previously discussed α -decays of surface contaminants. However, the analytic model is based on the assumption that muons pass the detector bulk completely and are not absorbed in the CZT volume. Given the hardening of the muon’s energy spectrum due to the overburden of about 3400 m.w.e. at the LNGS (see section 4.3.1), this should be a well-justified assumption. Nonetheless, due to potential secondary effects or the decay of muons in the vicinity of the CZT detectors, it might be possible to observe muon-induced events outside the boundaries defined by the analytic event reconstruction model.

In a future evaluation of the current set of PSD cuts, the application of the A/E criterion might prove suitable to remove muon-induced events according to their imprints on the pulse-shapes. Of particular interest could be the number of observed peaks in the current pulse, which is derived as the first derivative of the charge pulse (see section 7.2.1). A peak in the current pulse corresponds to the collection of charges by a single rail of the CPG anode, hence, the number of peaks is a measure for the extension of the charge cloud and its orientation within the CZT bulk volume (see section 7.4.2).

A preliminary study based on such a method is presented in [Zat14]. It uses the demonstrator’s initial exposure consisting of 84.4 kg d obtained in the two-layer period. However, one drawback of the approach is that there are only multiple peaks in the charge pulse’s derivative, when the muon comes at a certain angle with respect to the verticality. Only for highly non-vertical incident angles there are paths that lead to the collection of extended charge clouds causing such imprints in the pulse-shapes. In fact, only about 10% of the potential muon-induced events that were investigated in the previous study revealed multiple peaks in the current pulse. That is why an iteration of the analysis based on the improved A/E criterion might be worthwhile to be considered in a follow-up campaign.

8.3 Quenching of g_A deduced from the ^{113}Cd β -decay

For the theoretical description of the $0\nu\beta\beta$ decay, nuclear structure effects play an important role as they may affect considerably the expected decay rate. The nuclear effects are summarized in the nuclear matrix elements (NMEs) containing information about the initial and final states of the nuclei and the mechanism triggering the decay. By assuming the exchange of a light Majorana neutrino in the decay process, the inverse half-life scales with the fourth power of the weak axial-vector coupling strength g_A as pointed out in Eqn. (3.6) of section 3.2.3. Hence, potential quenching effects that lead to significantly smaller values of g_A in nuclear processes as discussed in section 3.2.5 might have a dramatic impact on the half-life prediction and, thus, on the sensitivity estimate for experiments to reach a certain neutrino mass range. Such quenching effects are discussed in order to match theoretical calculations and experimental results from β -decay and $\beta\beta$ -decay studies [Suh17].

The following sections are dedicated to the direct study of g_A quenching by investigating the electron momentum distribution of the ^{113}Cd β -decay and represent the main part of the thesis at hand. This investigation is driven by nuclear model calculations which show that the β -spectrum shape of the fourfold forbidden non-unique decay of ^{113}Cd strongly depends on an effective value of g_A . Firstly, a brief summary of the proposed method to access g_A quenching in strongly forbidden β -decays and an overview of previous studies on ^{113}Cd will be given. Following this, the task of optimizing the COBRA demonstrator for a dedicated low-threshold run as well the detector pool and event selection will be discussed. The section describing the analysis method is followed by a careful discussion of the results including the evaluation of considered systematic uncertainties. In the end, a short outlook and preliminary results based on new insights from the theoretical treatment of some of the involved NMEs will be presented in the last part of this chapter. The main concept of the analysis and the extracted effective values of g_A in the framework of three different nuclear models have been published recently in *Physics Letters B* [COB20]. This publication is also the basis for the introductory section of this chapter.

8.3.1 The spectrum-shape method

Different methods are being investigated to determine an effective value of g_A at low energies, typically at the order of a few MeV as the energy scale of nuclear decays (see review [Suh17]). In Ref. [HSS16] it was proposed that the shapes of β -electron spectra could be used to determine the values of the weak coupling strengths g_V (vector part) and g_A (axial-vector part) by comparing the shape of the computed spectrum with the measured one for forbidden non-unique β -decays. This method was coined the spectrum-shape method (SSM) and its potential in determining the values of the weak coupling strengths is based on the complexity of the β -electron spectra. The corresponding β -decay shape factor $C(w_e)$, w_e being the total energy of the emitted electron (β^- -decay) or positron (β^+ -decay) in units of m_e , is an involved combination of different NMEs and phase-space factors [MAS06]. According to Ref. [HSS16] it can be decomposed into several parts (vector, axial-vector, mixed) in the form of

$$C(w_e) = g_A^2 \left[\left(\frac{g_V}{g_A} \right)^2 C_V(w_e) + C_A(w_e) + \frac{g_V}{g_A} C_{VA}(w_e) \right]. \quad (8.8)$$

In the same reference it was noticed that the β -spectrum shape for the fourfold forbidden non-unique ($\Delta J^\pi = 4^+$) ground-state-to-ground-state transition $^{113}\text{Cd}(1/2^+) \rightarrow ^{113}\text{In}(9/2^+)$ is highly sensitive to the ratio g_V/g_A in Eqn. (8.8) and an ideal candidate for the SSM to determine this ratio experimentally. Assuming vector-current conservation, where $g_V = 1$, as predicted by the Standard Model, there is a direct g_A dependence of the spectrum-shape.

In Ref. [HSS16] the theoretical electron spectra were computed by using the microscopic quasiparticle-phonon model (MQPM) [TS98] and the ISM, including also the next-to-leading-order corrections to $C(w_e)$. This work was extended in [HKS17] to include a comparison with the results of a third nuclear model, the microscopic interacting boson-fermion model (IBFM-2) [II91]. The original studies [HSS16, HKS17] were continued by the works [KHS17] and [KS17] where the evolution of the β -spectra with changing value of g_V/g_A was followed for a number of highly-forbidden β^- -decays of odd- A nuclei (MQPM and ISM) and even- A nuclei (ISM). An impression of the predicted g_A dependence of the ^{113}Cd spectrum-shape in the context of the SSM and the previously mentioned nuclear models is shown in Fig. 8.11.

Challenges and shortcomings

However, there are also challenges and shortcomings related to the SSM. One potential problem is the delicate balance of the vector, axial-vector and mixed vector-axial-vector parts in Eqn. (8.8), especially in the range where the SSM is the most sensitive to the ratio g_V/g_A . At this point one has to rely on results which require cancellations at a sub-percent level (see review [Suh17]). On the other hand, this point of cancellation seems to be similar for different nuclear models and to be quite insensitive to the parameters of the adopted model Hamiltonians and the details of the underlying mean field. Nevertheless, quantification of the associated uncertainties is non-trivial and rarely discussed in the available literature. This problem is addressed in section 8.3.9 by using three different nuclear-model frameworks (ISM, MQPM, IBFM-2) in the spectrum-shape analysis to extract effective values of g_A . Potential variations of the analysis results are taken as a measure for the model dependence and the agreement of experiment and model prediction can be used to express a model preference.

One particular problem of the present calculations is that the nuclear models cannot predict the half-life of ^{113}Cd and the electron spectral shape for consistent values of g_A and g_V simultaneously. This was already pointed out in the original references [HSS16] and [HKS17]. Fig. 8.12 shows the comparison of the predicted half-life for the ^{113}Cd decay branch as a function of g_A and the experimental half-life of about $8 \cdot 10^{15}$ years [BBB⁺07]. Moreover, it illustrates the relative second-order corrections to the shape factor $C(w_e)$ in Eqn. (8.8).

The reason for the observed mismatch between predicted and experimental half-life could be associated with the deficiencies of the adopted nuclear Hamiltonians in the discussed nuclear mass region $A \sim 110$ and/or a need for a more nuanced treatment of the effective renormalization of the weak coupling constants. The review [Suh17] includes a compilation of examples that demonstrate how the renormalization can be done separately for different transition multipoles in the context of first-forbidden non-unique transitions. Moreover, new insights in the theoretical description of the involved NMEs based on the conserved vector current (CVC) hypothesis allow to resolve the issue of the observed mismatch, at least to some degree. Although the current status is very preliminary, first results will be presented in the last section of this chapter. However, one has also to bear in mind that the half-life depends on the values of both g_A and g_V whereas the normalized spectrum-shape depends only on the ratio of them. That is why the SSM can be used to fix the ratio g_V/g_A whereas the half-life can be used to fix the absolute value of e.g. the axial-vector coupling g_A .

The basis of the intended ^{113}Cd spectrum-shape analysis has been developed in collaboration with A. Heimbolt in the course of his Master thesis [Hei18]. In the thesis it was pointed out that the theoretical templates for different values of g_A get the less distinctive, the higher the energy threshold is chosen. In order to compare the predicted ^{113}Cd shape for an assumed value of g_A with experimental data, both spectra have to be normalized to unity over the available energy range. It is limited by the experiment's threshold and the ^{113}Cd

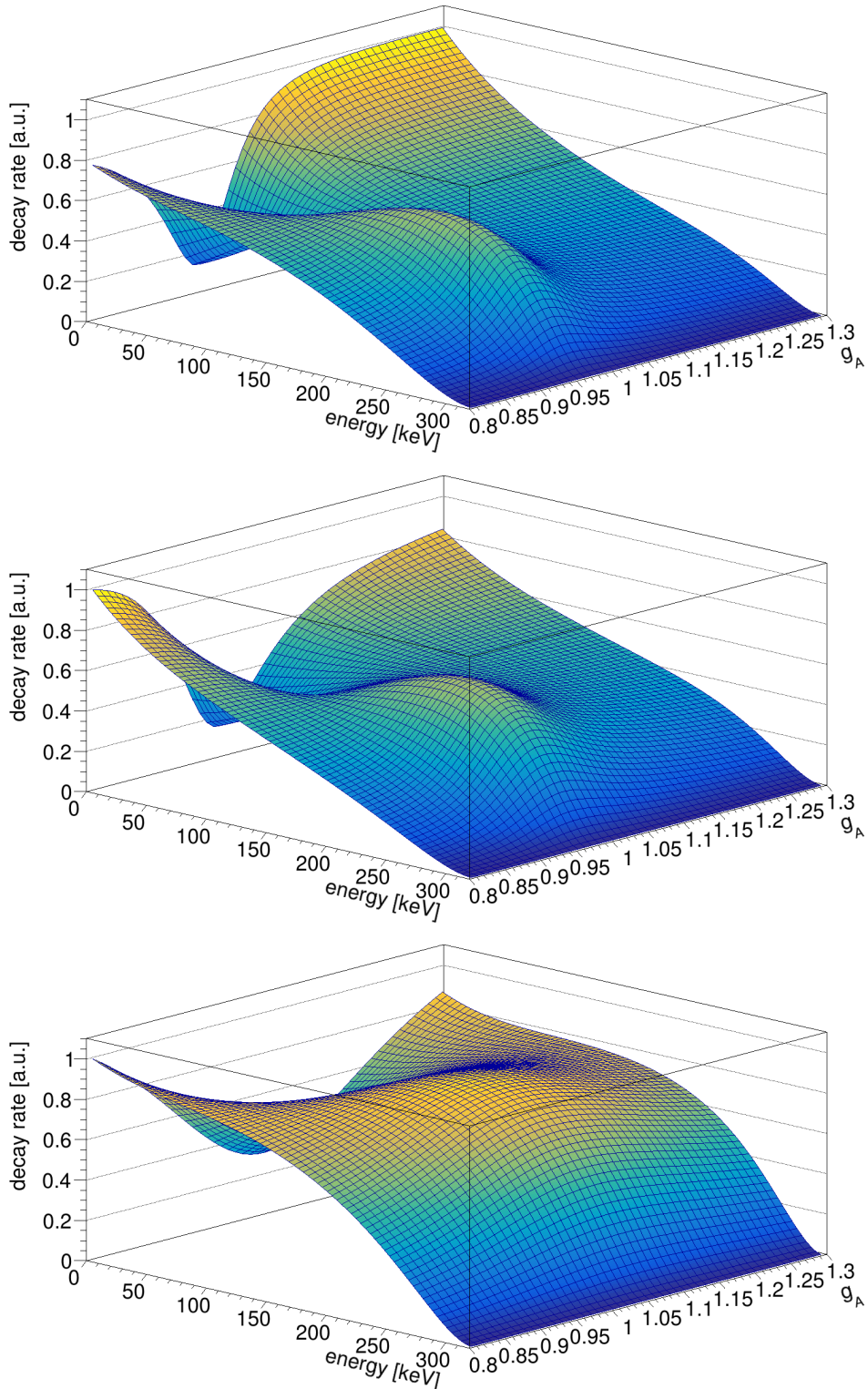


Figure 8.11: Nuclear model predictions for the ^{113}Cd spectrum-shape dependence on the effective value of the axial-vector coupling g_A . The free value of the coupling has been determined to $g_A^{\text{free}} = 1.276(4)$ [UCN10]. *Top:* interacting shell model (ISM). *Middle:* microscopic quasiparticle-phonon model (MQPM). *Bottom:* interacting boson-fermion model (IBFM-2). The predicted g_A dependency is quite similar for the ISM and MQPM calculations but not so strongly evolved for the IBFM-2.

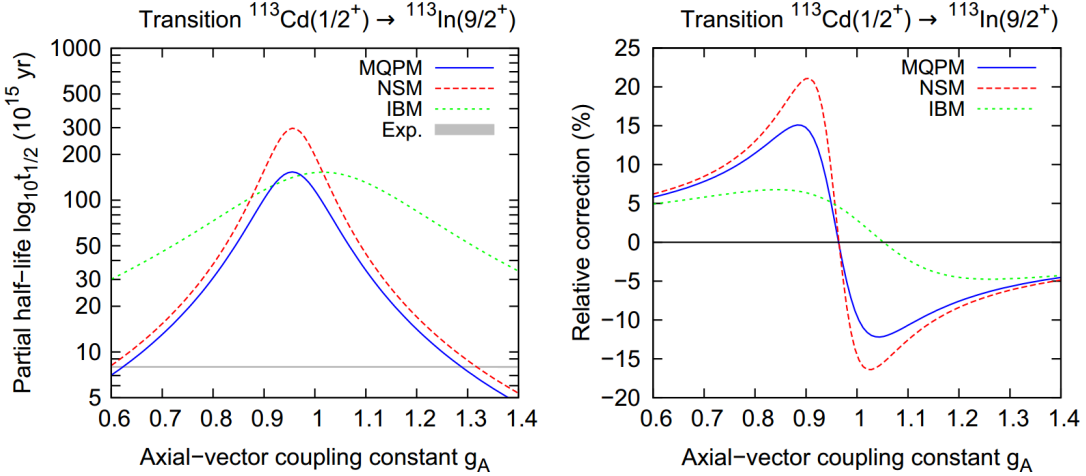


Figure 8.12: Shortcomings and details of the present nuclear model calculations (taken from [HKS17]). *Left:* Comparison of the second-order partial half-life of the ^{113}Cd decay branch as a function of the axial-vector coupling strength g_A and experimental half-life (gray horizontal band). *Right:* Dependence of the next-to-leading-order contributions on g_A . The graphs represent the relative correction to the partial half-life stemming from the second-order terms of the shape factor $C(w_e)$ according to Eqn. (8.8).

Q -value, which is why the threshold is a crucial parameter for the SSM. The preparation of the theoretical templates and the effect of the threshold on their normalization is discussed in section 8.3.8.

Before getting to the details of the developed analysis framework to address the potential quenching of g_A in low-energy nuclear processes, a detailed discussion of previous experiments on ^{113}Cd and their characteristics will be given in the following section.

8.3.2 Previous studies on ^{113}Cd

The fourfold forbidden non-unique β -decay of ^{113}Cd has already been studied by several groups using different experimental techniques with the main focus on the determination of its Q -value and half-life. Among them are the COBRA collaboration using CZT semiconductor detectors and low-background experiments based on CdWO_4 crystals used as scintillators or bolometers. A summary of the most recent studies is given in Tab. 8.5.

Table 8.5: Compilation of previous studies on ^{113}Cd . Listed are the detection threshold E_{th} , the isotopic exposure based on the actual amount of ^{113}Cd atoms, the energy resolution quoted as FWHM at the accepted AME2016 Q -value [AME17], the signal-to-background ratio (S/B) as well as the experimentally determined half-life $T_{1/2}$. Statistical and systematic uncertainties were added in quadrature, if quoted separately.

detector material	$E_{\text{th}} / \text{keV}$	isotop. exp.	FWHM / keV	S/B	$T_{1/2} / 10^{15} \text{ yrs}$	Ref.
CdWO_4 , 58 g	~20	0.03 kg d	~ 5	~ 2	9.3 ± 1.1	[ABC ⁺ 94a]
CdWO_4 , 454 g	~44	0.31 kg d	~ 49	~ 50	7.7 ± 0.3	[DGK ⁺ 96]
CZT, 3×5.9 g	~100	0.05 kg d	~ 43	~ 8	$8.2^{+0.3}_{-1.0}$	[COB05]
CdWO_4 , 434 g	~28	1.90 kg d	~ 47	~ 56	8.04 ± 0.05	[BBB ⁺ 07]
CZT, 11×6.5 g	~110	0.38 kg d	~ 20	~ 9	8.00 ± 0.26	[COB09b]
CZT, 23×5.9 g	~50	2.04 kg d	~ 17	~ 40	7.91 ± 0.22	[Hei13]
CZT, 45×6.0 g	~84	2.89 kg d	~ 17	~ 47	-	[COB20]

Cadmium tungstate studies

First results on the use of CdWO₄ as a cryogenic thermal particle detector to search for double beta decays in cadmium isotopes were reported in [ABC⁺94b]. The data of a small bolometer setup at LNGS were also used to determine the Q -value and half-life for the β -decay of ¹¹³Cd with rather small statistics resulting in $Q_\beta = 318.8 \pm 1.4(\text{stat.}) \pm 5.0(\text{syst.})$ keV and $T_{1/2} = (9.3 \pm 0.5(\text{stat.}) \pm 1.0(\text{syst.})) \times 10^{15}$ years [ABC⁺94a]. The low-background operation at cryogenic temperatures is challenging, which has been pointed out in section 3.3.2, and is one reason for the bad signal-to-background ratio (S/B) of approximately 2. Moreover, the authors of the respective reference used a very simplified analysis without a sufficient discussion of systematic uncertainties or background contributions. Further they assumed that the determined energy resolution of ~ 5 keV at 2.6 MeV is constant over the whole energy range. An extrapolation of the exponential fit of the data above the Q -value was used to take into account potential background and noise near the threshold without further elaboration. Given the lack of information and details of the analysis procedure, the results should be taken with caution.

The most precise half-life measurement was achieved by Belli *et al.* [BBB⁺07] in 2007 with a CdWO₄ scintillator crystal of 434 g installed in the low-background DAMA/R&D setup at LNGS. It is noteworthy that the exact same CdWO₄ crystal was already used ten years before in a similar study at the Solotvina underground laboratory [DGK⁺96]. However, it was necessary to refurbish the surface of the crystal for the usage of the same crystal in the more recent study, leading to a loss of about 20 g in mass. CdWO₄ scintillators reach typically lower thresholds, but feature a worse energy resolution compared to CZT solid state detectors as used for COBRA.

CZT studies by COBRA

Already in 2005, the ¹¹³Cd β -decay was investigated with an early predecessor of the COBRA demonstrator at LNGS consisting of an array of 2×2 crystals of about 5.9 g [COB05]. However, the crystal's quality was rather poor at that time, which is also indicated by the energy resolution in terms of FWHM as quoted in Tab. 8.5. Also the S/B ratio has been much worse compared to the former Solotvina experiment. Due to the small available isotopic exposure, the determined half-life is dominated by the statistical uncertainty.

An improved value for the half-life was published by COBRA in 2009 [COB09b] using the first iteration of the demonstrator's layer approach with 4×4 crystals. The resolution could be enhanced by more than a factor of two while the exposure was increased eight times until the data release. Both the energy threshold as well as the S/B ratio could not be improved with respect to the previous COBRA result. The latter case has been found to be caused by contaminants in the standard encapsulation lacquer of the manufacturer *eV Products* (now *Kromek*) [Kro20]. Such an encapsulation improves the mechanical handling and prevents damages and degradation by the exposure to humidity, which is why all detectors that were installed at LNGS are coated by default to ensure a stable performance over the time scale of several years. Nonetheless, the iterations of the COBRA experiment investigated different coatings of increasing radiopurity as will be briefly summarized in section 8.3.7.

The combination of the eleven best-performing detectors, which were analyzed independently from each other, resulted in a ¹¹³Cd half-life of $(8.00 \pm 0.11 \text{ (stat.)} \pm 0.24 \text{ (syst.)}) \times 10^{15}$ years and a Q -value of $322.2 \pm 0.3 \text{ (stat.)} \pm 0.9 \text{ (syst.)}$ keV. It is noteworthy that this Q -value is in perfect agreement with the accepted AME2016 value of $Q_\beta = 323.83 \pm 0.27$ keV [AME17] based on precise Penning trap measurements, while it is several 10 keV off for Ref. [BBB⁺07] ($Q_\beta = 343.1 \pm 0.6$ keV). However, the determined half-lives of both studies agree very well.

The first ^{113}Cd data of the actual COBRA demonstrator equipped with half of the final 64 detectors was analyzed in the Bachelor thesis of F. Heiße [Hei13]. The experiment's detectors, read-out and electronics were updated as discussed before in section 4.3.3. The analysis makes use of the event selection and cut definitions available at that time and focuses on a subset of 23 detectors with an isotopic exposure that is similar to the study resulting in the most precise half-life. Unfortunately, it misses an adequate discussion of the cut efficiencies, potential near-threshold effects, a background projection and additional systematic uncertainties besides the energy calibration, which is why the results have to be taken again with a grain of salt. This time, the ^{113}Cd spectra of the selected detectors were combined and analyzed together, neglecting individual detector effects that were already known to exist. Nevertheless, the extracted half-life of $(7.91 \pm 0.09 \text{ (stat.)} \pm 0.21 \text{ (syst.)}) \times 10^{15}$ years and the Q -value of $323.6 \pm 0.2 \text{ (stat.)} \pm 1.2 \text{ (syst.)}$ keV are in good agreement with former results.

COBRA stability study

More recently, the ^{113}Cd β -decay was used to investigate the demonstrator's detector stability by monitoring the average decay rate over the time scale of several years between Oct.'11 and Feb.'15 [COB16d]. This topic is also part of the PhD thesis of D. Gehre [Geh17]. Fig. 8.13 illustrates the relative rate change observed in the ^{113}Cd energy region for all four layers of the COBRA demonstrator.

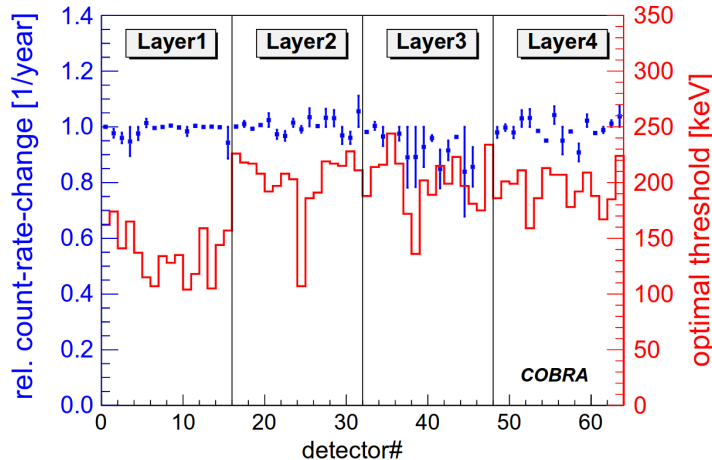


Figure 8.13: Results of the COBRA demonstrator's stability study [COB16d]. The observed relative rate change is negligible for the detectors of the demonstrator's first two layers during the complete period from Oct.'11 to Feb.'15. Due to the later installation of layer three and four and problems in the commissioning phase, there are larger error bars on the blue data points. The optimal threshold of each detector is shown as red bar. It was chosen in a way that prevents threshold dependent exposure for each single detector.

The average analysis threshold for this particular study was ~ 170 keV and relatively high compared to E_{th} given in Tab. 8.5. Usually the individual detector thresholds of the COBRA demonstrator are evaluated regularly about once a week by checking the data rate per detector. The procedure will be described in more detail in section 8.3.3. Each detector's optimal threshold was chosen as the highest common threshold during the data-taking period in order to perform the stability study without the need to correct for a change of it (see Fig. 8.14). On the other hand, such a high threshold drastically limits the available ^{113}Cd energy range and exposure. The stability study triggered modifications on the hardware and software level to optimize the demonstrator setup for a dedicated low-threshold run prior to the planned upgrade to COBRA XDEM with the aim to investigate the ^{113}Cd spectrum-shape with high precision at low energies.

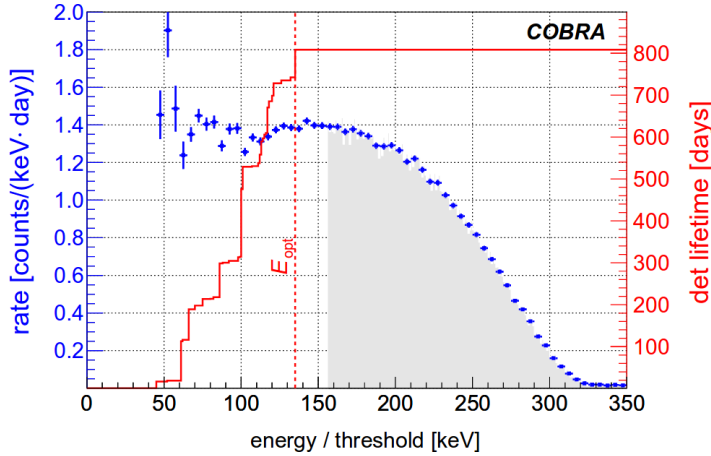


Figure 8.14: Example of a single detector ^{113}Cd spectrum used in the COBRA demonstrator’s stability study [COB16d]. The solid red line represents the threshold dependent lifetime of the detector. To ensure that all energy bins have the same exposure, the optimal threshold E_{opt} was chosen as the highest common value indicated by the vertical dashed line. The value of E_{opt} was optimized for each detector individually.

Spectrum-shape studies

First attempts to describe the β -spectrum shape with conventional shape factors were also pursued in the past 25 years. In all the studies discussed so far, leading to a ^{113}Cd half-life or Q -value, it was assumed that the ^{113}Cd β -decay can be described approximately with shape factors corresponding to a threefold forbidden unique transition ($\Delta J^\pi = 4^-$) as provided e.g. by Ref. [BJ69]. This is a clear oversimplification probably due to the lack of accurate nuclear model calculations at that time. Furthermore, the extracted shape factors of former experiments are inconclusive as pointed out in Ref. [BBB⁺07] and [COB09b]. Fig. 8.15 shows a comparison of the experimentally determined ^{113}Cd spectra based on the shape factors as quoted by the previous CdW₀₄ experiments in Tab 8.5. It should be noted that the authors of Ref. [BBB⁺07] already mentioned that they observe a discrepancy between the assumed polynomial fit and the experimental spectrum above 250 keV, if their Q -value is fixed to the accepted value of the AME.

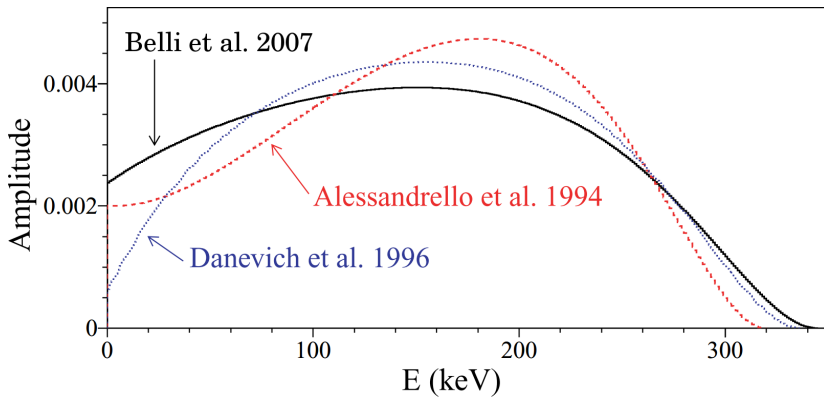


Figure 8.15: Comparison of ^{113}Cd spectra based on the shape factors as determined with previous CdW₀₄ experiments (adapted from [BBB⁺07]). The latest measurement by Belli *et al.* coincides practically with a predicted shape according to Ref. [BJ69] for a threefold forbidden unique transition ($\Delta J^\pi = 4^-$) as stated by the authors. The spectrum-shapes deviate significantly at low energies, which might be caused by an insufficient treatment in the previous analyses and unregarded near-threshold effects.

Nowadays there is no justification to assume such an oversimplified parametrization with accurate nuclear model calculations at hand. The key features of the recent article [COB20] and the analysis presented in this thesis are the best S/B ratio of all previous COBRA studies, high statistics and a good energy resolution while providing 45 independent β -spectra of the transition $^{113}\text{Cd}(1/2^+) \rightarrow ^{113}\text{In}(9/2^+)$ with moderate lower energy thresholds. The single detector data will be evaluated with the SSM as introduced in section 8.3.1 by using recent calculations of the full expression Eqn. (8.8) in the context of three nuclear models (ISM, MQPM, IBFM-2). In the first analysis presented in [Hei18] only the ISM is used as the basis for the SSM. The improvements achieved since then will be covered in the following sections.

8.3.3 Threshold study and optimization

In preparation of a dedicated ^{113}Cd run, the potential of optimizing the COBRA demonstrator towards minimum threshold operation was studied in detail. The main reason is the expected threshold dependency of the normalization needed to compare the theoretical templates and the actual COBRA data. The lower the accessible energy range, the more distinguishable are the theoretical templates after their normalization as shown later in Fig. 8.22.

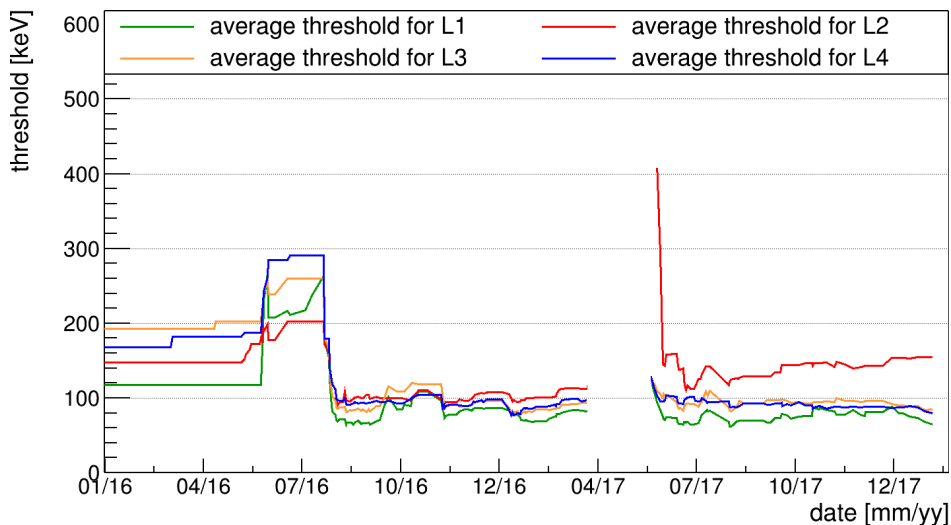


Figure 8.16: Evolution of the average threshold of the four layers of the COBRA demonstrator. After resolving some problems with the nitrogen flushing of the inner shield that allowed only for an operation at rather high threshold above 200 keV, a campaign to find optimal operation conditions was started by the end of Jul.'16. The effort had to be interrupted due to a global noise problem that prevented the operation of the experiment from April 7th to May 20th 2017. In parallel, the ambient temperature was optimized by changing the cooling power of the pre-amplifier stage. Finally, the dedicated ^{113}Cd was started in Jul.'17 and lasted until Feb.'18.

A first attempt to optimize the individual detector thresholds was started in Jul.'16 after finalizing the demonstrator's stability study [COB16d]. At the end of the stability study, the individual thresholds were mostly kept at the same level for a single detector. Fig. 8.16 illustrates the evolution of the average energy threshold for all four layers of the demonstrator in the period of Jan.'16 to Feb.'18. Unfortunately, the experiment suffered several times in the past from problems with part of the electronics and the nitrogen flushing (see hardware description in section 4.3.3). An overview of periods indicating a fail of the N_2 flushing is presented in section 8.1.4. Usually a fail of the N_2 flushing system coincides with an increase of the detector's trigger rate (see Fig. D.9 in the appendix). This is not exclusively caused by an increase of radon decays and its daughters (see also section 8.2), but mainly due to an

altered performance as direct consequence of the higher humidity level. A similar behavior of the trigger rate is partly seen when the liquid nitrogen is biweekly refilled. During the refill, the dewar vessel has to be disconnected in order to get it to one of the main tanks in the LNGS underground complex. The time without active N₂ flushing is too short to affect the nitrogen atmosphere in the inner shield, but there is a noticeable rapid change in the humidity at the moment when the dewar vessel is attached again. Some detector channels are very sensitive to such rapid changes of the ambient humidity and cause the trigger rate to go up by more than ten times. The effect is assumed to be related to the increase of leakage currents that benefit from the humid environment. The temperature and humidity surveillance as well as the average trigger rate is checked by online shifters in order to ensure a stable operation. The trigger rate can be adjusted accordingly by raising or lowering the experiment's individual detector thresholds to match the expected rate of about 900 single channel events per detector and day as estimated in section 8.1.1. The adjustment of the thresholds is done manually based on a shifter's judgment.

Initial threshold optimization campaign – noise problems

After a complete rework of the N₂ flushing, including the exchange of its tube system in Jul.'16, a campaign was started to optimize the trigger thresholds of all 64 CZT detectors. This was done by monitoring the trigger rate per channel on a day-by-day basis. In parallel, the cooling power of the pre-amplifier stage has been varied to find the ideal ambient operation temperature and to study the effect of different temperatures on the detector performance. Unfortunately, the effort had to be interrupted due to a global noise problem that suddenly occurred shortly after an on-site shift in Apr.'17. The shift was meant to prepare the upgrade to COBRA XDEM by installing a new cable tree for the signal transmission via CAT6 Ethernet cables between the lower and upper floor of the experiment's location at LNGS. Furthermore, it was planned to replace a faulty uninterruptible power supply (UPS) unit whose battery broke some weeks in advance. As all of the UPS devices used for the experiment are double conversion units, the power supply of the electronics was still ensured, but due to the missing galvanic filtering of the LNGS input power line, there was a significant increase of the signal noise. The noise was found to originate from the linear amplifier stage, which was powered by the faulty UPS unit. The operation of some detectors was only possible at very high trigger thresholds of several hundred keV in this period. Moreover, the DAQ electronics suffered from several short power shortages, which are normally covered by the UPS system. This caused additional problems with some of the FADCs. In the end, all the electronic problems could be resolved and the demonstrator detectors were calibrated by the end of the on-site shift. The evaluation of the calibration data revealed that the measures were successful and the noise induced by the faulty UPS had finally vanished.

All the more incomprehensible was that shortly afterwards there was another problem with a different kind of noise disturbance. While the previous data period suffered from noise that mainly increased the baseline fluctuations, thus, could be handled by increasing the trigger threshold, the situation was completely different after the on-site shift. Right after its discovery, a lot of effort was spent to identify the origin of the sudden noise incident via the remote control of the experiment. A closer look into the data revealed that the overall trigger rate of all channels had increased by several orders of magnitude and that most triggered events were occurring in coincidence. It was found that the operation with a reasonably low trigger rate was only possible for arbitrary high thresholds of about 1-2 MeV, which made it impossible to continue with the preparations of the planned ¹¹³Cd measurement.

The data-taking had to be suspended for several weeks while the origin of the noise remained unclear until another maintenance shift could resolve the issue. On-site the origin

was found to be related to the bias supply of the detectors. The outlets of the HV modules hosted in the *WIENER* MPOD crate are made for REDEL multi-pin connector cables. These are attached to custom-made converter boxes that support the Sub-D 8w8 cable standard used for the feedthrough cables towards the pre-amplifier boxes inside the outer shield. As the electronic rack in the lower floor had to be moved during the previous shift to install the XDEM's Ethernet signal cable read-out, there might have been some unintended stress on the cabling of those converter boxes. When the rack was moved to its original position by the end of it, after finishing the calibration measurement, some of the pins might have moved as well, resulting in faulty contacts to the actual HV modules. Those contacts probably caused micro-sparks and induced crosstalk on all supply channels resulting in the coincident noise pattern as observed in the data. To fix and avoid this problem in the future, the converter boxes have been reworked on-the-fly to support connectors that can be tightly screwed to the modules using M3 distance bolts.

Second threshold optimization campaign – temperature studies

After the issue was finally resolved, the demonstrator went back to smooth operation, thus, the preparation of the dedicated ^{113}Cd run could be continued by immediately starting another threshold optimization campaign in the end of May'17. Unfortunately, it was not possible to reach the same threshold levels as achieved before with layer two (see Fig. 8.16). The reason for this might be related to the specific temperature behavior of the setup components. The remaining three detector layers did not show an altered performance.

During the preparation phase, the cooling of the pre-amplifier stage was intensified to lower the overall ambient temperature inside the shielding successively (see Fig. 8.17). In general, the direct cooling of the first stage of the electronics dramatically reduces the thermal component of the signal noise, while at the same time the detector performance benefits from an ambient temperature slightly below room temperature. As a reminder, the crystals themselves are not cooled directly, but through convection and radiation cooling they are kept at the same temperature as the surrounding shielding components. The cooling power can be controlled remotely by setting a target temperature for the cooling unit (model *Julabo FL 601*). The liquid coolant inside the closed cooling cycle gets circulated via insulated tubes through aluminum plates located between the pre-amplifier boxes. The environment inside the shield is monitored with several temperature and humidity sensors (model *DHT22*) at different positions. A full documentation of COBRA's Arduino-based slow-control system can be found in the Bachelor thesis of A. Hemmetter [Hem16]. One sensor is located next to the pre-amplifier stage, one inside the radon sealing on top of the lead castle and one is used to monitor the ambient temperature in the surrounding laboratory. The temperature of the lead castle, housing the copper nest and the detectors, is a measure for the operation temperature of the detectors due to the thermal contact of all components. For each target temperature set, the optimum trigger threshold for every channel had to be determined after reaching the thermal equilibrium.

In agreement with previous studies on CPG-CZT detectors [COB09a], an optimal temperature was found to be around 9°C (2°C for the pre-amplifier stage). The criteria to quantify the temperature behavior on the basis of the demonstrator's individual detectors have been worked out in the Bachelor thesis of T. Kreße [Kre17]. Although most detectors were benefiting from lowering the ambient temperature, the trend was not so obvious for others, especially the crystals of layer two. This could be seen as a hint for the origin of the observed higher noise level of those crystals, which seemed to be dominated by temperature independent effects.

At that time the accessible temperature range was limited by the coolant's properties, which was pure water only. This prevented to lower the target temperature of the system below the freezing point of water and led to a minimum operation temperature of the detectors of about 15°C as can be seen in Fig. 8.17.

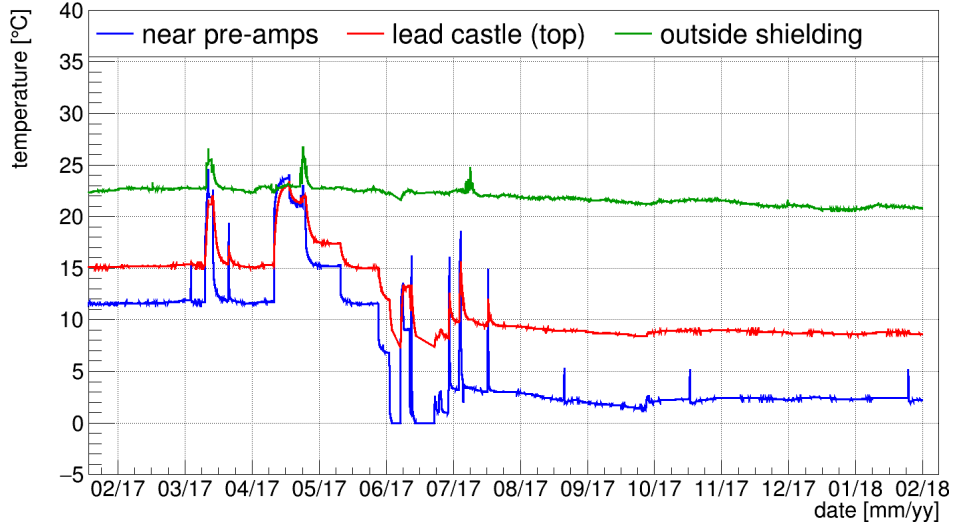


Figure 8.17: Temperature surveillance of the COBRA demonstrator prior and during the dedicated ^{113}Cd run. The sensor on top of the lead castle (red graph) is a measure for the detector operation temperature. Before the exchange of the coolant in Apr.'17, a minimum operation temperature of about 15°C was reached without crossing the freezing point of water anywhere in the cooling cycle. Afterwards, the target temperature could be lowered down to -20°C, which caused the sensor nearest to the pre-amplifier stage (blue graph) to partly fail. It was found that the detector performance is optimal for about 9°C, which is well below the temperature of the ambient laboratory (green graph). This temperature is achieved by setting the target temperature of the cooling device to -10°C.

Shortly after finishing the investigations in [Kre17], it was decided to exchange the pure water with a special coolant offered by the manufacturer of the cooling device (referred to as *Thermal G liquid*). The exchange was performed during the maintenance shift in Apr.'17 and enabled to probe lower temperature ranges down to a target temperature of -20°C. This temperature range was fully covered in several steps. No benefits of an operation below a target temperature of -10°C were found. In fact, the slow-control sensor's failed at temperatures below 0°C, which is why the ultimate lower temperature limit could not be accessed directly.

Final threshold optimization campaign – cooling effects

At the ideal operation temperature, a final iteration of the threshold optimization was performed. It was found that the intensified cooling allowed for another lowering of the thresholds by a few keV for the detectors with the lowest thresholds. This is due to the reduction of the thermal noise component leading to smoother baselines of the signals. For signal amplitudes on the order of the variance of the baseline, it is not possible to discriminate between an actual detector signal and a random fluctuation due to thermal noise or electromagnetic interferences. Furthermore, a mild detector cooling is expected to reduce surface and bulk leakage currents, which are a limiting factor for the achievable energy resolution of CZT detectors [ALL06]. A reevaluation of the laboratory data reported in [Sch12] revealed that the formerly observed improvement of the energy resolution for gently cooled CZTs is mainly due to an unaccounted drift of the weighting factor used in the signal reconstruction. If the optimal

weighting factor is determined for each temperature separately, there is hardly a noticeable effect on the energy resolution. A more detailed discussion can be found in [Kre17].

As can be seen in Fig. 8.17, the detector's operation temperature was constant for the entire ^{113}Cd run starting by the end Jul.'17 (sensor on top of lead castle). This was partly achieved by developing a software-based temperature surveillance that checked the state of the cooling unit on a regular basis. Unfortunately there are times, where power shortages of less than a second appear several times a day at the LNGS. Such blackouts can occur when the underground laboratory's main power is switched between the L'Aquila and the Teramo side, especially during thunderstorms. The main infrastructure of the COBRA setup is backed up by several UPS units, but not the cooling device due to its high power consumption. A dedicated UPS for the pre-amplifier cooling was only installed after the upgrade to COBRA XDEM. The software solution took care of the restarting of the cooling device in case of a power failure and its proper configuration. Only a few short temperature increases for the sensor the nearest to the pre-amplifier stage can be seen in Fig. 8.17, while the temperature of the lead castle containing the detectors was not affected.

Achieved thresholds in dedicated ^{113}Cd data-taking

While the last threshold optimization was accomplished, the worst-performing detector channels were switched off to prevent potential sources of electromagnetic interferences and crosstalk. The final detector pool selection will be discussed in section 8.3.5. The COBRA demonstrator was then calibrated at the point of best performance and the dedicated ^{113}Cd data-taking period was started. It lasted from Jul.'17 until Feb.'18.

During this period, the individual trigger thresholds E_{th} were mostly kept at the same level resulting in an average of $\bar{E}_{\text{th}} = 83.9 \pm 14.5$ keV, including the average energy resolution in terms of FWHM at this energy. Without considering the L2 detectors, the average threshold turns out to be significantly lower and results in 72.5 keV. An impression of the variation of the individual detector's energy thresholds E_{th} and the average threshold achieved per detector layer is shown in Fig. 8.18. It is based on the data of the last run of the dedicated ^{113}Cd data-taking period. In comparison, it is found that L2 features much higher thresholds than the other three layers.

It should be noted that the quoted thresholds are not the minimum amounts of energy, denoted as E_0 in the following, that can be measured by the detectors, but include a correction function $f_{\text{cor}}(z)$ depending on the interaction depth z to ensure that the spectrum-shape is not distorted by the event reconstruction

$$E_{\text{th}} = E_0 \cdot f_{\text{cor}}(z), \quad \text{with } f_{\text{cor}}(0) \approx 1.6. \quad (8.9)$$

A more detailed discussion of COBRA's energy threshold definition is given in section 5.2.4. Moreover, an analysis threshold \tilde{E}_{th} is introduced by modifying Eqn. (8.9) to $\tilde{E}_{\text{th}} = E_{\text{th}} + 8$ keV as will be motivated in section 8.3.9. Such a careful and conservative threshold correction has not been discussed in the previous studies summarized in Tab. 8.5.

The lowest E_{th} reached per detector during the entire ^{113}Cd run cover a range from 44 keV to 124 keV, whereas the 18 best detectors were operated for the most time below or around 70 keV and only the four worst-performing never crossed a value below 124 keV. For comparison, the threshold quoted in Ref. [BBB⁺07], which achieved the most precise ^{113}Cd half-life measurement using a CdWO₄ scintillator, can be referred to as 28 ± 14 keV considering the given energy resolution. This is not far away from what has been achieved in the present COBRA study, where in addition a much higher number of detector channels could be used. The information and illustrations presented in this section have been provided by the author to A. Heimbolt for the usage in his Master thesis [Hei18].

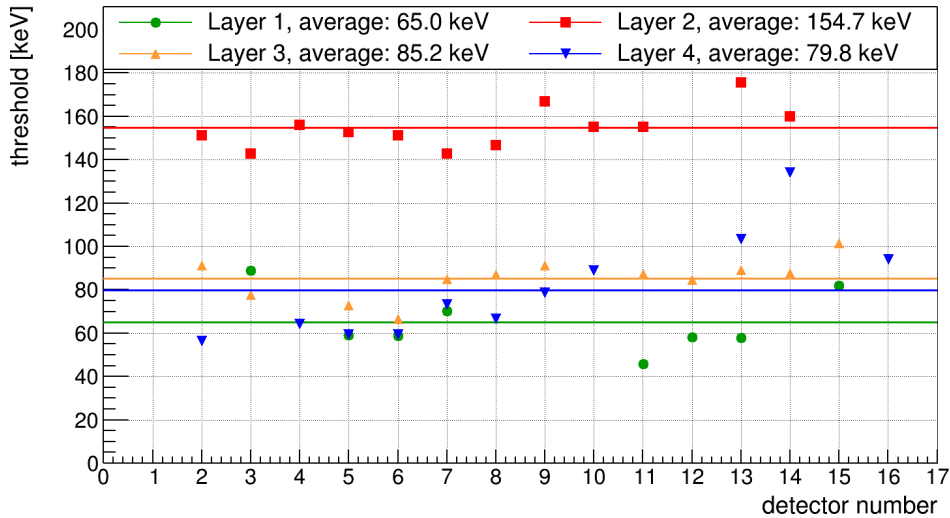


Figure 8.18: Variation of the individual detector thresholds by the end of the dedicated ^{113}Cd run. Shown are all 45 detectors that were selected for the final spectrum-shape analysis (see section 8.3.5) and the average per detector layer (solid lines). The thresholds of the layer two detectors had to be increased significantly since the start of the ^{113}Cd run, but were at higher values from the beginning (see Fig. 8.16). The lowest thresholds were achieved for layer one and four detectors.

8.3.4 Detector calibration

The energy calibration of each detector was done using the radionuclides ^{22}Na , ^{152}Eu and ^{228}Th providing γ -lines in the range from 121.8 keV to 2614.5 keV. All γ -lines that were used are listed in Tab. 8.6.

Table 8.6: List of γ -lines used for the energy calibration of the COBRA demonstrator in the ^{113}Cd run. The ^{152}Eu calibration source has been purchased specifically to provide additional calibration points in the low energy range. The γ -line energies and their absolute intensities have been taken from [NDS20] and were rounded to two digits. The reference date used to calculate the source's activities is 2019-05-27.

nuclide (decay)	E_γ / keV	abs. intensity / %	activity / kBq	$T_{1/2}$ / yr
^{22}Na (100% β^+ /EC)	511.00 1274.54	<180.76 99.94	2.90	2.60
^{152}Eu (27.9% β^-) (72.1% β^+ /EC)	121.78 344.28 778.90 964.06 1408.01	28.53 26.59 12.93 14.51 20.87	4.74	13.52
^{228}Th (100% α) (decay chain)	238.63 583.19 727.33 860.56 1592.51 2614.51	43.60 85.00 6.67 12.50 DEP 99.75	5.08	1.91

The sodium isotope ^{22}Na undergoes a β^+ /EC transition with a probability of 90.3% for the β^+ -decay and 9.6% for the electron capture (EC) [NDS20]. Due to the dominance of the β^+ -decay and the involved positron emission, the absolute intensity of the 511 keV

annihilation radiation is very high. Although the annihilation peak is broadened by the Doppler shift [NHTV05], the effect turns out to be negligibly small for most of COBRA's CZT detectors (see also Fig. 8.19). The decay scheme for ^{152}Eu is rather complex and involves both β^- (27.9%) and β^+/EC transitions (72.1%) [NDS20]. In the latter case the EC has a probability of $\sim 99.98\%$ and clearly dominates over the β^+ -decay [NDS20].

The ^{152}Eu source was specifically purchased in preparation of the intended low-threshold run to provide additional calibration points at low energies (121.8 keV, 344.3 keV). Previously, the lowest energetic γ -line (238.6 keV) was originating from the de-excitation of ^{212}Pb as part of the ^{228}Th decay chain. This decay chain also involves the de-excitation of ^{208}Tl , providing a prominent γ -line at 2614.5 keV close to the ^{116}Cd Q -value at 2813.5 keV. Such a highly energetic γ -line has a high chance to produce an electron-positron pair by interacting with the detector material and can cause the already mentioned single-escape peak (SEP) and double-escape peak (DEP) (see section 7.2.3). The ^{208}Tl DEP is a well-suited calibration point right in the middle of the energy range of interest.

Since the product of available γ -lines and detector channels easily exceeds several hundred potential calibration fits, even without using the optional ^{152}Eu low-energy points, an automatized and robust procedure is needed. The key features of the calibration tool are discussed in section 5.2.2. Each γ -line is fit with a two-sided Gaussian function according to Eqn. (5.7), which also takes into account the underlying Compton continuum, to extract its position and width (see also section 8.1.2). The fit procedure automatically determines an optimum fit range by varying the default one based on the preliminary width of the Gaussian part and searches for the fit with the minimum reduced χ^2 . If the reduced χ^2 is larger than a defined threshold, the fit is discarded in the following calibration routine. This χ^2_{red} threshold is defined for each detector individually and based on the experience gained during the demonstrator's operation. For most detectors it is set to $\chi^2_{\text{red}} \leq 1.3$.

The actual energy calibration is done by a linear fit of the peak position in channel numbers versus the known γ -line energy as listed in Tab. 8.6. Using the fit results, the energy resolution quoted as full-width at half-maximum (FWHM) can be parametrized for each detector separately as

$$\text{FWHM}(E) = \sqrt{p_0 + p_1 \cdot E + p_2 \cdot E^2}, \quad p_i > 0. \quad (8.10)$$

The parameter p_0 is independent of the deposited energy and accounts for a constant contribution from noise. The second term scales with \sqrt{E} and is motivated by the Poisson fluctuations of the charge carrier production while the third term is a rather small correction for detector effects. All three parameters are constrained to have non-negative contributions to the energy resolution. An example of the resolution fit according to Eqn. (8.10), taking into account the γ -lines that are listed in Tab. 8.6, is shown in Fig. 8.19.

Unfortunately, the lowest available γ -line at 121.8 keV from ^{152}Eu is only visible for a couple of detectors due to strong absorption effects in the detector array and the dominance of the underlying Compton continuum of the higher energetic lines. Also the position of the calibration source has to be taken into account. If the radiation of the low-energy line is penetrating a detector crystal from the top, its energy is likely deposited close to the CPG anode. As part of the standard pulse-shape cuts, the area close to the anodes is usually discarded with a restriction on the reconstructed interaction depth (see section 7.1.2). Without using the anode z -cut, the energy reconstruction suffers from distortions of the weighting potential near the coplanar grid, which worsens the energy resolution significantly. The situation is not so severe for the irradiation from the bottom side of the crystals due to the less restrictive cathode z -cut and the uniformity of the weighting potential in this area. Especially for the detectors on the edges of the 4×4 layers there was hardly any sign for the

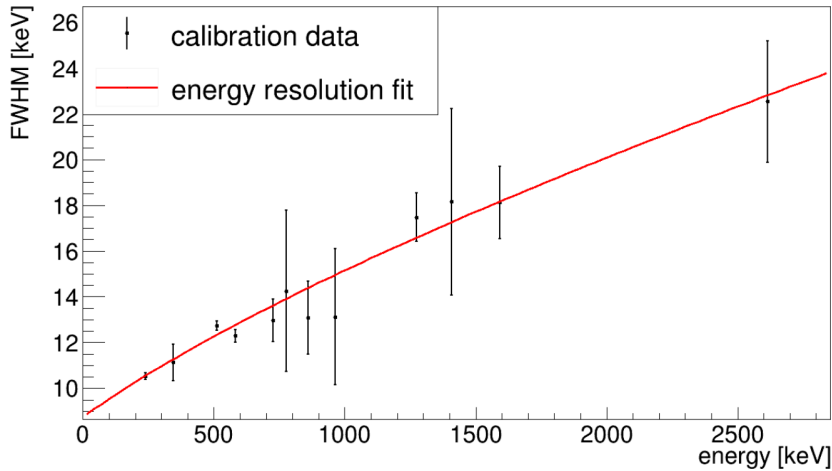


Figure 8.19: Example of an energy resolution fit to extract $\text{FWHM}(E)$ for one detector (taken from [Hei18]). The calibration data is coming from Det54 (L4-P06), which is one of the best performing detectors in the ^{113}Cd run. The broadening of the 511 keV annihilation peak due to the Doppler shift is only marginal and still consistent with the overall statistical fluctuations. The ^{152}Eu γ -line at 121.8 keV was removed by the calibration tool in this example due to an insufficient χ^2_{red} . The shape of the $\text{FWHM}(E)$ fit is similar for all detectors of the final selection. The error bars correspond to the combined uncertainties of the fit parameters of the two-side Gaussian peak approximations.

^{152}Eu γ -line at 121.8 keV. Moreover, some detectors have not been operated at low enough thresholds during the calibration runs to get a measure of this line.

The evaluation of the calibration runs performed during the ^{113}Cd data-taking was also used to define the final detector pool of the anticipated spectrum-shape analysis. As will be discussed in the following section 8.3.5, it comprises 45 crystals. With the parametrization given in Eqn. (8.10) the achieved mean relative resolution $\text{FWHM}(E)/E$ obtained with this ensemble of detectors ranges from $12.5 \pm 0.6\%$ at 121.8 keV to $1.7 \pm 0.1\%$ at 2614.5 keV, considering the uncertainty on the mean. The spread of the $\text{FWHM}(E)/E$ distribution can be expressed by the respective standard deviations of 4.0% (121.8 keV) and 0.7% (2614.5 keV).

8.3.5 Selection of detector pool

The following section is an update on the information given in [Hei18]. As mentioned earlier, only a subset of the 64 detectors of the COBRA demonstrator collected data in the ^{113}Cd run or qualified for the final spectrum-shape analysis. The main reason for this was to ensure a stable operation over the anticipated data-taking period until the planned upgrade to COBRA XDEM. The selection of the best performing detectors, focusing on their low-energy performance, consist of four major steps which will be discussed in the following.

Hardware and contacting issues

After years of operation there are some detectors that suffer from either issues with the data acquisition (DAQ) electronics or their electrode contacting. Those detectors are typically not operational in all runs, while the related hardware problems are not easily resolvable at the same time. For the dedicated ^{113}Cd run it was decided to switch off such faulty detectors in order to prevent crosstalk and potential sources of electromagnetic interference at low energies, even if the detectors could still be used to search for double beta decay modes at higher energy scales.

The functionality of the DAQ electronics can be checked independently of the detectors using an external signal generator (see section 4.3.3). The signal generator provides a well-defined charge signal that is injected directly into the pre-amplifier stage. This way, the entire signal transmission chain can be checked, even without powering a corresponding detector. Furthermore, it is possible to identify whether an observed problem is related to the electrode contacting. As a reminder, each detector's coplanar grid anode is connected to a flexible PCB readout cable via two $50\ \mu\text{m}$ thick gold wires, which also supply the grid bias (GB). On the opposite side, there is another gold wire contacting the planar cathode electrode. The gold wires are fixed to the electrodes with a silver-based conductive glue of only low mechanical strength. This is why an additional fixation by a conventional glue spot is needed to reduce the wires' tension (see section 4.3.2). Each detector layer has its own PCB signal readout and routing for the high voltage cables, that are then connected to the pre-amplifier boxes outside the lead castle and radon shield.

The design of both bias supply stages (GB, HV) was improved between the successive installation of the demonstrator's detector layers, following the technology progress and the experience gained with previous iterations. However, the aging of the conductive silver glue or its mechanical counterpart can cause the electrode contacts to become loose or electrically unreliable over time. Micro-vibrations as caused by the passing of trucks near the COBRA location in the LNGS underground complex (see Fig. 4.5 in section 4.3.1) or weak earthquakes in the vicinity of the laboratory might then cause a contact to fail completely. An unreliable electric contact might still cause a detector to be operational from time to time, but this has to be checked regularly with calibration runs.

If the HV contact on the cathode side is not working probably anymore, the detector is only sensitive in a small volume close to the CPG anode. The effect can be easily identified in a calibration run by the related dramatic reduction of the count rate, accompanied by a worsened energy resolution. If only the GB supply is missing, but still both signal channels are working, the detector is still sensitive in the full bulk volume. But due to the missing bias voltage between the interleaved grids, the electrons will be collected by both anode rails, thus, there is no clear assignment of CA and NCA anymore. This affects the count rate as well, since the trigger system expects a CA-like (NCA-like) signal on its even (odd) channel numbers. As a consequence, the overall trigger rate is roughly cut in half and the resulting energy spectrum features again a worsened energy resolution.

Three detectors were known to suffer from such problems with the DAQ electronics and unreliable contacting prior to the ^{113}Cd run: Det4 (no GB), Det9 (no HV) and Det10 (no HV). It is noteworthy to mention that all three are part of the first detector layer (L1), which was installed in Sept.'11, and that the improvements towards the more recent iterations of the layer's design (L2-L4) seem to be more robust and allow for a more reliable operation. The mentioned detectors were switched off in the very beginning of the ^{113}Cd run preparation, before starting to optimize the individual thresholds.

Threshold optimization

During the threshold optimization as reported in section 8.3.3, it was noticed that certain detectors can only be operated at comparably high thresholds to ensure a reasonably low trigger rate. Some of those suspicious detectors also showed an unstable trigger rate that affected the other detectors connected to the same FADC or nearby channels on the layer's PCB signal readout. This effect is referred to as electronic crosstalk and can be caused by various origins. The design of the demonstrator's pre-amplifier stage includes a meandering metallic shielding between the pre-amplifiers to minimize the low-level crosstalk between the channels (see Ref. [Sch11] and [Teb11]). Previous studies revealed that crosstalk is a minor,

but not critical, concern for the electronic readout of the COBRA demonstrator and can be neglected at the MeV energy scale.

Nonetheless, it was decided to switch off detectors that have to be operated at higher thresholds than 200 keV to prevent potential sources of crosstalk and noise affecting the low energy region during the ^{113}Cd run. This applies to the following detectors:

- L1: Det16,
- L2: Det28, Det31, Det32,
- L3: Det33, Det36, Det42, Det48,
- L4: Det51, Det59, Det63.

It is remarkable that most of those are either the first or last unit of a layer consisting of 16 detectors. The root cause might be related to the 32-channel PCB signal readout cables that are used to transmit the detector signals from inside the lead castle to the pre-amplifiers. The first and last detectors of a layer occupy the outer lying signal lanes on the flexible Kapton cables. If the signal transmission is altered by the contact of the cables with the edge of the lead castle or the copper nest, the outer channels should be affected the most.

This issue, as well as the previously described problems with some unreliable electrode contacts, cannot be fixed without reworking the related part of the passive lead and copper shield. However, in the planning of the upgrade towards the COBRA XDEM setup, special care was taken to design the signal and HV cable feedthroughs with additional spacing towards the edges. This measure should at least partly eliminate the observed abnormality related to the outermost signal lanes in the future.

Evaluation of calibration data

The calibration measurements performed during the ^{113}Cd run were used to check the general operation and performance of the remaining active detectors. The calibration at the point of best performance, referring to the optimum operation temperature of the detectors and their optimized thresholds, marks the beginning of the ^{113}Cd run. It was used to crosscheck the determined calibration parameters (see section 8.1.2) against previous results for each detector. Prior to the comparison, a set of quality criteria was defined to identify detectors whose calibration parameters differ more than the conservatively estimated parameter range (see also section 8.1.2). This includes bounds on the variation of the gain-balancing, the weighting factor, the energy calibration and the energy resolution. If either of those parameters would turn out to be out of range, the respective detector would be switched off, too.

This was the case for the gain-balancing correction of Det49 (L3-P01), which was off by more than a factor of two in the initial calibration. The reason for such a change might be a sudden damping of either the CA or NCA signal over the differential signal transmission, caused by a faulty wire or contact of the corresponding CAT6 Ethernet cable. More unusual would be a broken linear amplifier or a pre-amplifier channel, respectively. However, the root cause is repairable during an on-site maintenance shift and will not be discussed any further.

By comparing the results of the initial and final calibration run, it was decided which detectors qualify for the ^{113}Cd spectrum-shape analysis. It was found that four detectors showed a worsened energy resolution due to a distortion of the signal traces' baselines induced by low-frequency noise. Moreover, it was not possible to include the low-energetic γ -lines covering the ^{113}Cd energy range into their energy calibration. Even though there was a valid pre-calibration at the beginning of the physics data-taking, it was decided to exclude the following detector numbers from the final data set due to their altered performance:

Det1, Det2, Det8 (all L1) and Det17 (L2). Again, the removed detector numbers correspond dominantly to the outer signal lanes on the PCB signal readout cables.

In between the physics data-taking, the electronics stability was monitored with the help of artificially injected charge pulses from the signal generator at a rate of one pulse every ten minutes. These measures revealed no notable performance alteration or other problems.

Interaction depth distribution

Lastly, the z -distribution of the final ^{113}Cd data of each detector was checked prior all analysis cuts. The event selection will be discussed in the subsequent section 8.3.6. The energy spectrum, on the other hand, is not a criteria for the detector selection in order to prevent introducing a bias into the ^{113}Cd spectrum-shape analysis.

The z -spectrum was limited to the energy range determined by the detectors' individual thresholds and the ^{113}Cd Q -value. It was found that four detectors show additional peak features besides the expected flat distribution between $z = 0$ (anode side) and $z = 1$ (cathode side). An example of the z -distribution that matches the expectation according to the homogeneously distributed ^{113}Cd inside the CZT detectors is shown in Fig.7.5 of section 7.1.2,. In addition to the detector-specific rather smooth rise for $0 < z \leq 0.2$, which is related to the hole collection near the coplanar grid, and the steep fall for $z > 1$, the peak features show up close to the anode or cathode side. Even after applying the data-cleaning cuts (DCCs) (see section 7.1.1), the peak features remain due to their specific characteristics on the pulse-shape level. For example a peak close to the cathode can be explained by signals where the CA amplitude is much higher than its corresponding NCA. Such events can be caused by noise that only affects one anode channel. In the reconstruction, the dominant amplitude of the CA would lead to a positive energy entry, potentially in the ^{113}Cd energy range, independently of the exact value of the NCA amplitude. Following the depth reconstruction according to Eqn. (5.6) and Eqn. (5.21) in section 5.2.3, such events would also lead to $z \approx 1$. Similarly, a peak feature for $z \leq 0$ can be explained.

The following detector numbers were found to have such features in their ^{113}Cd depth spectra: Det3 (for $z \leq 0$) and Det14, Det52 and Det60 (for $z > 1$). Fortunately, the peaks are in all cases well separated from the expected ^{113}Cd plateau and can be easily removed by a cut on the interaction depth. Moreover, there is no need to discard those detectors from the spectrum-shape analysis since the observed z -features do not affect the region of interest. Some examples of the ^{113}Cd depth distribution can be found in the appendix D.4.3.

Summary

In the end, 45 out of 49 operated detectors qualified for the spectrum-shape analysis with an average exposure of 1.10 kg d per detector. A list of the removed detector numbers and the reasoning behind their removal according to the categories discussed above is given in Tab. 8.7. Two detectors were partly disabled and feature a reduced exposure of 0.79 kg d (Det14) and 0.29 kg d (Det60), respectively. Both of them featured the previously explained high- z peak. Due to its well-defined occurrence, only the runs passing the criteria explained above were included into the final data set. The effect of the reduced exposure on the single detector results of the spectrum-shape analysis will be discussed in section 8.3.10.

Using the natural abundance of ^{113}Cd of 12.227% [IUP16] in combination with the molar mass fraction of cadmium in the detector material, referred to as $\text{Cd}_{0.9}\text{Zn}_{0.1}\text{Te}$, it follows that the ^{113}Cd isotopic exposure makes up for 5.84% of the total exposure. The combined isotopic exposure of all selected detectors adds up to 2.89 kg d and represents the largest statistical sample of all previous studies on the β -decay of ^{113}Cd (see Tab. 8.5).

Table 8.7: Summary of the detector pool selection for the ^{113}Cd spectrum-shape analysis. Three detector units were disabled prior to the start of the dedicated ^{113}Cd run because of known electrode contacting issues. During the threshold optimization a set of eleven CZT crystals, including detectors of all four layers, has been switched off due to their high threshold operation. Finally, five additional units failed to match the stability criteria demanded for the respective pre- and post-calibration measurements.

category	detector number	notes
contacting issues	L1: 4	disabled, unstable GB supply
	L1: 9	disabled, unstable HV supply
	L1: 10	disabled, unstable HV supply
threshold optimization	L1: 16	disabled due to $E_{\text{th}} > 200 \text{ keV}$
	L2: 28, 31, 32	
	L3: 33, 36, 42, 48	
	L4: 51, 59, 63	
calibration data	L1: 1, 2, 8	altered resolution in post-calibration
	L2: 17	altered resolution in post-calibration
	L3: 49	disabled, high gain in pre-calibration

8.3.6 Event selection

The event selection for the ^{113}Cd spectrum-shape analysis is based on the cuts presented in section 7.1. The actual cut sequence, the related optimization as well as the efficiency estimates will be presented in the following.

Data-cleaning cuts

The first stage of the event selection consists of the data-cleaning cuts (DCCs) to remove distorted and unphysical pulse-shapes (see section 7.1.1). The validity of those cuts was checked with a special trigger run in the end of the ^{113}Cd data-taking. In contrast to the normal trigger mode, all channels belonging to the same FADC unit were read out, if the trigger condition was fulfilled for a single channel. The triggered event trace was then rejected and only the remaining baseline pulses were analyzed. Those baseline pulses were treated as a proxy for noise-only signals. It was found that $99.8 \pm 0.1\%$ of the untriggered events are rejected by the DCCs, while there is no significant variation among the different channels. The signal acceptance of the DCCs is sufficiently constant over the ^{113}Cd energy range and has been determined to $87.5 \pm 0.6\%$ (see section 7.1.1). After applying the DCCs the remaining events of the noise-only data are limited to the energy range below $\sim 40 \text{ keV}$, which is already well below the average trigger threshold of 84 keV and the anticipated analysis thresholds of each detector. That is why the influence of any residual noise in the low energy region can be neglected in the spectrum-shape analysis.

Coincidence veto

In a second step coincidences between all operational detectors are rejected, which is possible after synchronizing the individual FADC clocks (see section 7.1.5). The coincidence time window τ_c , which is used to declare two events as simultaneous, is set to $\tau_c = 0.1 \text{ ms}$. It refers to the achieved accuracy of the synchronization as pointed out in the Master thesis of J. Volkmer [Vol18]. The ^{113}Cd data-taking run is the first period that was processed with the recently finalized time synchronization tool and the evaluation of the remaining data is an ongoing effort.

After the synchronization with $\tau_c = 0.1\text{ ms}$ it is possible to reject background events caused by e.g. multiple Compton scatterings of photons across the active detector array, while at the same time the loss of events due to random coincidences of potential ^{113}Cd decays in different source crystals is minimized. The longer the coincidence time window, the higher the chances to accidentally declare two unrelated ^{113}Cd decays as a coincidence. However, it turns out that the COBRA demonstrator's data contain only a small fraction of true coincidences in general. In the present case of the ^{113}Cd data sample only about 0.05% of the cleaned data are removed by the coincidence veto. At the same time a conservative estimate of the potential live-time loss leads to a value of less than 10^{-2} percent.

Compared to the previous CdWO₄ study reported in [BBB⁺07], quoting 3.16 ms for the minimum time between the signals that can be recorded by their DAQ system, an improvement of at least a factor of 30 has been achieved in the recent investigation. This is a very conservative estimate since the actual single channel timing resolution of COBRA's DAQ is even better. However, the expected total ^{113}Cd decay rate scales with the number of atoms and is comparable for both experiments. Since the COBRA DAQ system allows for continuous data-taking with a single pulse length of $10\ \mu\text{s}$, two consecutive events in the same detector are only recorded as a single event, if they appear within those $10\ \mu\text{s}$. On the other hand, the timing accuracy cannot be compared directly between an experiment using only a single CdWO₄ crystal and the COBRA approach with multiple but smaller detectors. That is why the referred synchronization accuracy of 0.1 ms is quoted as a more conservative measure of the experiment's timing resolution, regardless of the fact whether they occur in the same detector or in separated ones.

Interaction depth restrictions

The DCCs are usually applied in combination with a mild cut on the interaction depth z to remove near-anode reconstruction artifacts (see section 7.1.2). The interaction depth is further restricted to remove events with an unphysically high z . The final depth selection is optimized for each detector individually and covers, for the majority, the range $0.2 < z \leq 0.97$. The detectors that were affected by the additional near-anode or near-cathode peak features, as mentioned in section 8.3.5, are treated separately to exclude those unphysical z -regions (see also Fig. D.20). Besides the ^{113}Cd spectrum-shape investigation, the obtained low-threshold data was also used to study the depth cut's volume selection and its implication for the efficiency to measure double beta decay events as discussed before in section 7.1.2.

In the course of the spectrum-shape method (SSM), no further pulse-shape discrimination (PSD) cuts are necessary since the ^{113}Cd decay is by far the strongest signal for the COBRA demonstrator at low energies. The overwhelming dominance of the fourfold forbidden β -decay of ^{113}Cd could be verified by comparing the combined experimental spectrum to the average background expectation using a Monte-Carlo based low-energy background model as discussed in the next section.

8.3.7 Low-energy background model

In order to estimate the signal-to-background ratio (S/B) and to quantify the effect of potential background contributions coming from radioactive contaminants within the demonstrator's shielding and construction materials, especially at low energies, a survey among the available radiopurity measurements has been performed. In principle, background contributions can be divided into external and internal (intrinsic) sources. As semiconductor detectors, such as COBRA's CZTs, are only functional if they are already intrinsically very clean, the

external background is usually much higher than the intrinsic one, especially in conventional surface laboratories. However, it turns out that the expected external background for the COBRA demonstrator is so low that the intrinsic contaminants become non-negligible. The external background can be reduced by first selecting known to be radiopure materials and, secondly, by reducing the amount of material close to the detectors as far as possible.

Radiopurity assessment campaigns

A compilation of recent radiopurity campaigns and the resulting specific activities for a variety of materials is shown in Tab. 8.8. The materials have been chosen according to their presence in the vicinity of the CZT detectors. Besides the detector material itself, which is already made from very pure base materials with impurities of foreign elements on the ppb level (see section 4.1.1, Tab. 4.3), the most critical parts are the crystal’s encapsulation lacquer and the detector holders made of Delrin. Further out from the detector array, the inner shield consisting of oxygen-free high-conductivity (OFHC) copper and ultra low-activity (ULA) lead is located (see section 4.3.3).

Table 8.8: List of material impurities considered for the low-energy background modeling. The specific activities quoted for single isotopes result mainly from low-background γ -spectroscopy campaigns at LNGS [INF20] and LSM [CNR20]. For the detector holder material Delrin the overall activities of the thorium and uranium decay chains have been determined with low-level α -spectroscopy at TUD. The ICP-MS measurements for Delrin and one of the CZT crystal’s encapsulation coatings (referred to as *eV clear*) were performed at LNGS. The required conversion from ppb to mBq/kg was done by using the factors in Tab. 8.9. Supplement data for ULA lead has been taken from [LCCP20] and the provider of COBRA’s ULA lead (*Plombum*, Poland). The measurements are given with a Gaussian standard distribution quantile $k_\alpha = 1$ (68.3% central C.L.) and upper limits with $k_\alpha = 1.645$ (95% upper C.L.). For further information see also appendix C.2.

material reference / campaign	eV clear [Köt12]	Glyptal LNGS	Delrin LNGS, TUD	ULA lead Plombum	OFHC copper LSM
element / decay chain	isotope	activity in mBq/kg			
^{232}Th	^{40}K	< 1000	32 ± 11	< 31	0.32 ± 0.08
	^{56}Co				0.06 ± 0.02
	^{58}Co				0.24 ± 0.05
	^{60}Co		< 2	< 1.1	< 0.02
				< 43	0.12 ± 0.03
	^{228}Ra	< 180	< 7.4	< 5	< 6.6
	^{228}Th	< 190	5 ± 1	< 5	< 1.6
				< 43	0.14 ± 0.05
	^{226}Ra	< 140	16 ± 2	< 5	< 5.7
	^{234}Th	< 1500	< 91		
$^{238}\text{U}/^{235}\text{U}$	^{234m}Pa	< 4300	< 0.1	< 700	
	^{235}U	< 15	< 1.2	< 3	< 51
ICP-MS					
potassium		51 ± 12		-	2.1 ± 0.78
thorium		0.59 ± 0.06		0.12 ± 0.02	< 0.16
uranium		1.4 ± 0.1		2.3 ± 0.4	0.36 ± 0.15

Different experimental techniques were used to quantify the near-detector materials’ radiopurity. The first method is based on low-background γ -spectroscopy using typically HPGe detectors in underground laboratories such as the LNGS [INF20] and the Laboratoire Souterrain de Grenoble [CNR20]. The second method is based on low-level α -spectroscopy using a Ge(Li) detector at the Technical University of Darmstadt (TUD) [Köt12]. The third method is based on ICP-MS measurements of Delrin samples at the University of Regensburg [LCCP20].

rain de Modane (LSM) [CNR20]. Due to the unique energy signature of γ -lines for a certain nuclide, it is possible to put a number on the specific activity for single isotopes. From the single isotope activities, the total expected activity for the natural ^{232}Th and ^{238}U decay chains can be deduced assuming a secular equilibrium. Although this is a common approach, special care has to be taken in cases where additional contaminants of involved daughter nuclei are present.

Another way to address the decay chains' total activity, is the inductively coupled plasma - mass spectrometry (ICP-MS). Since it is a destructive method, a sample is lost in the measuring process. Due to its fundamentally different approach, it is expected that the results might differ from the γ -spectroscopy. For example the activity of ^{40}K can be measured directly with γ -spectroscopy, but because ^{40}Ar is used to produce a plasma torch in ICP-MS, only the content of ^{39}K can be determined directly. From this, the ^{40}K content can only be deduced assuming its natural abundance in the isotopic composition of the sample. Furthermore, the thorium and uranium activities from γ -spectroscopy are obtained from daughter nuclei of the chain, while ICP-MS determines the contamination levels of the initial isotopes ^{232}Th and ^{238}U . If the chains are not in an equilibrium, there might be significant deviations between the techniques, even for the same material sample.

In the beginning of COBRA's low-background operation, a first test array consisting of four bare CZT detectors was operated at LNGS (see e.g. Ref. [COB05]). It was found that the detector performance suffered from leakage currents due to moisture and the overall high humidity level in the underground complex. Following this, the CZT detectors of the first iteration of the COBRA demonstrator were coated with a red encapsulation lacquer in order to provide a highly resistive surface (see e.g. Ref. [COB09b]). This measure was meant to improve the long-term stability and mechanical handling of the CZT crystals. Both setups were used to investigate the ^{113}Cd β -decay and the results are part of the compilation of previous studies in Tab. 8.5. The red lacquer was the standard encapsulation of the detector manufacturer *eV Products* at that time and was found to contain contaminations on the order of 1 Bq/kg for the long-lived radionuclides ^{232}Th and ^{238}U , and about 10 Bq/kg of ^{40}K .

After identifying the red lacquer as a major source of background, different alternative clear encapsulations were investigated with γ -spectroscopy and ICP-MS (see compilation in [Köt12]). The clear lacquer offered by the manufacturer, referred to as *eV clear*, has been measured with both methods at LNGS by M. Laubenstein. The γ -spectroscopy resulted in only poor upper limits due to the small sample mass of about 4.2 g. At that time the exact receipt of the lacquer was treated as a corporate secret and only little was known to the collaboration about its composition. Later it was found that the encapsulation used by the manufacturer is referred to as *Glyptal* and a large sample of it was prepared by R. Temminghoff (TU Dortmund) to repeat the radiopurity measurements with the help of M. Laubenstein at LNGS in 2016 [Tem19]. Due to its high sample mass of 148.1 g, the results of the γ -spectroscopy could be improved by several orders of magnitude. The same sample has been also measured at LSM but with higher upper limits, which is why the results are not included in Tab. 8.8.

The detector holder material Delrin has been probed with γ -spectroscopy by M. Laubenstein at LNGS already in 2006. Only upper limits on the specific activity could be set at that time. Another Delrin sample has been provided to S. Nisi at LNGS in order to perform an ICP-MS measurement in 2017. This campaign confirmed the good radiopurity and resulted in initial activities on the order of mBq/kg for thorium and uranium. At the same time, a large Delrin sample of the exact same material batch with a mass of about 100 g was prepared for the study of its radiopurity by using low-level α -spectroscopy in-house at TUD. The measurement was carried out by H. Wilsenach and sets a limit for the total activity of the ^{232}Th and ^{228}U chains of < 43 mBq/kg [Wil20]. As the expected α -peaks of the corre-

sponding decays are close together in energy and they are affected by the energy smearing due to the sample's thickness, there is no discrimination power between the two chains and the same limit applies to both of them.

The impurities related to the inner ULA layer of the lead castle are taken from the manufacturer's documentation (*Plombum*, Poland). This applies to the ICP-MS results. Those values have been supplemented with data from the radiopurity.org website [LCCP20] for the single isotopes as quoted in Tab. 8.8. The radiopurity.org project has been serving the low-background physics community since 2014 [LCC⁺16] and is supported by many experiments in the field of double beta decay and dark matter searches. Its recent status and a detailed description of the data formatting is described in [CLP18]. It should be noted that the tabulated ULA lead activities strongly depend on the selected database entry and can serve only as a rough indicator for the actual contamination level. The same applied to other materials listed in the database.

Lastly, the results of the OFHC copper sample's γ -spectroscopy, whose preparation is discussed in section 4.3.4, are included in Tab. 8.8. The measurement was performed at the LSM in France by E. Rukhadze (CTU Prague) in 2018 using the Obelix HPGe detector (600 cm^3 , 160% relative efficiency) [LBP⁺15]. Although the LSM is rather small compared to the LNGS (see section 4.3.1, Fig. 4.4), it is one of the world's best facilities for low-level γ -spectroscopy due to its overburden of 4800 m.w.e. and the Obelix HPGe setup. All copper contamination levels are well below 1 mBq/kg, while it is expected that the cosmogenic activation products ^{56}Co (EC/ β^+ , $T_{1/2} = 77.24\text{ d}$) and ^{58}Co (EC/ β^+ , $T_{1/2} = 70.86\text{ d}$) [NDS20] should not be present anymore in the copper housing of the demonstrator. For the long-lived isotope ^{60}Co (β^- , $T_{1/2} = 5.27\text{ yr}$) [NDS20] only an upper limit was found.

As ICP-MS is only sensitive to the concentration of elements in units of ppb and similar definitions, it is only possible to estimate the respective activity for single isotopes or a decay chain of interest. Assuming that a decay chain is in equilibrium and the isotopic abundance in a sample matches the natural abundance a of the isotope of interest, the concentration in ppb can be converted into the specific activity of a long-lived nuclide with half-life $T_{1/2}$ and atomic mass M via

$$1 \text{ [ppb]} = \frac{\ln 2}{T_{1/2}} \cdot \frac{a \cdot N_A}{M} \cdot 10^{-3} \text{ [mBq/kg]} \quad (8.11)$$

using the Avogadro constant N_A . The corresponding conversion factors for ^{40}K , ^{232}Th and ^{238}U based on the parameters of Eqn. (8.11) from recent references are listed in Tab. 8.9.

Table 8.9: Conversion factors from [ppb] to [mBq/kg]. The procedure is described in [Köt12] and follows Eqn. (8.11). The half-lives, natural abundances and atomic masses (rounded to three digits) have been taken from Ref. [IUP16], [NDS20] and [AME17]. The decay chains have to be assumed to be in equilibrium in order to perform the conversion.

conversion	$T_{1/2} / 10^9\text{ yr}$	nat. abund. / %	atomic mass / u	[ppb] \rightarrow [mBq/kg]
$\text{K} \rightarrow {}^{40}\text{K}$	1.248	0.0117(1)	39.964	0.031
$\text{Th} \rightarrow {}^{232}\text{Th}$	14.05	99.98(2)	232.038	4.056
$\text{U} \rightarrow {}^{238}\text{U}$	4.468	99.2742(10)	238.051	12.346

In general, the ICP-MS measurements result in lower activities and stricter limits compared to the ones obtained via γ -spectroscopy. However, this only indicates the fundamentally different measurement techniques as explained before. More concerning would be a significant difference in the activities of different isotopes within the same decay chain. Such an effect would hint to an imbalance within the chain, contradicting the assumed secular equilibrium.

From the sequence of half-lives it should be certainly stronger for the ^{238}U chain because it contains several isotopes with half-lives on the order of several hundred years. However, the γ -spectroscopy results reported in Tab 8.8 are consistent with the assumed secular equilibrium of the primordial decay chains.

The discussed radiopurity measurements are the basis to estimate the background contribution to the ^{113}Cd region with a Monte-Carlo (MC) simulation using COBRA's VENOM simulation toolkit (see section 5.3.1). VENOM is based on GEANT4 [GEA16] and uses the *shielding* physics list, which is recommended for low-background experiments. Compared to the contribution of the external background sources, the concentration of the expected intrinsic contaminations within the CZT detectors (see Tab. 4.3) cannot be neglected. Following Eqn. (8.11) the impurities on the ppb level convert to specific activities on the order of a few mBq/kg. However, the respective ICP-MS measurement returned only upper limits, even though a material sample from the spent solvent was used, where it is expected that impurities will concentrate due to the details of the CZT crystal's growth process. The detection limits are therefore a very conservative estimate of the actual contamination level. That is why, although the sample was provided by a different manufacturer (*Redlen Technologies*) compared to the demonstrator's CZT crystals (*eV Products*), it should be justified to consider those values in the recent background estimate.

Background description

As has been pointed out earlier, the recent ^{113}Cd analysis features the highest exposure of all previous studies listed in Tab. 8.5. Nevertheless, the statistics per single detector are not sufficient to estimate the background on the individual detector level. Instead, the background is modeled as an average projection based on the combined experimental data. The combined energy spectrum of the final detector pool, comprising 45 crystals, and after applying the event selections as described in section 8.3.6, is shown in Fig. 8.20.

The combined spectrum reveals that the measured count rate drops by at least two orders of magnitude above the ^{113}Cd Q -value, which is about a factor of ten better than what has been achieved in the previous COBRA ^{113}Cd analysis [COB09b]. The maximum count rate of the combined spectrum is about 175 cts/(kg keV d) at 150 keV and drops sharply to below 1.5 cts/(kg keV d) at 400 keV. The background decreases exponentially for higher energies and is recorded up to ~ 10 MeV (see e.g. Fig. 8.4). The ratio of the integrals over the ^{113}Cd energy region and the total combined spectrum up to its endpoint at 10 MeV results in 99.84%, indicating the overwhelming dominance of the ^{113}Cd decay in the COBRA data. A detailed description of the general background features, especially at higher energies, can be found in section 8.2. The previous CdWO₄ studies limited the background observation to much lower energies, e.g. in Ref. [BBB⁺07] for a first background run up to 1.7 MeV and for the ^{113}Cd data-taking to 0.6 MeV.

Near the ^{113}Cd ROI there are only two prominent γ -lines visible in the combined spectrum of all detectors. These lines originate from the decays of ^{214}Pb (351.9 keV) and ^{214}Bi (609.3 keV) as short-living ^{222}Rn daughters and correspond to the dominant de-excitation processes. In Sept.'17 and Dec.'17 there were short periods without proper N₂ flushing of the inner shield of the experiment that increase the overall radon exposure (see Fig. 8.3). Nevertheless, their effect on the ^{113}Cd spectrum-shape is completely negligible since the γ -lines only produce weak Compton continua in this region.

It should be noted that the background composition of the dedicated ^{113}Cd run is different compared to the latest $0\nu\beta\beta$ -decay analysis using data of the same setup from Oct.'11 to Sept.'16 [COB16a] and the description of the general features in section 8.2. The ^{113}Cd data shows no indication for the previously observed annihilation line at 511 keV or the ^{40}K γ -line

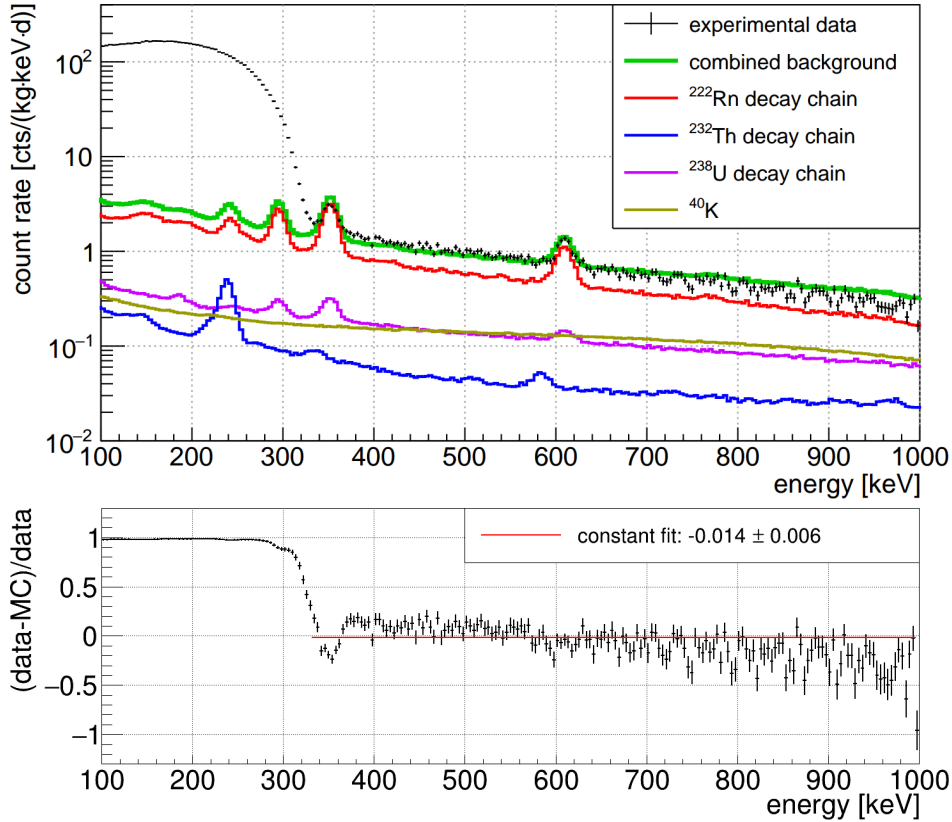


Figure 8.20: Results of the low-energy background characterization. *Top:* Comparison of the combined experimental data of the ¹¹³Cd run (45 detectors) and the low-energy Monte-Carlo background model. Considered are the ²²²Rn, ²³²Th and ²³⁸U decay chains as well as ⁴⁰K with different origins of the primary decays. The background composition has been determined by using the *TFractionFitter* class of ROOT. The fit range extends from 320 keV to 1200 keV. *Bottom:* Residuals of the data and the MC model normalized to the data. The background contribution in the ¹¹³Cd energy range is only marginally and results in a S/B ratio of ∼ 47. The constant approximation of the residuals over the fit range of the model is sufficiently consistent with zero. Its slightly negative value indicates a conservative overestimation of the background level at low energies.

at 1460.8 keV. One reason might be the absence of PSD cuts to remove LSEs in the present analysis because of their rather poor efficiency at low energies. Moreover, only a subset of the 64 installed CZT detectors qualified for the spectrum-shape analysis. In the detector selection process, described in section 8.3.5, about half of the L1 detectors were discarded, which featured the highest amount of potentially radioactive material near them. Especially prior the installation of the third and fourth layer, there was a significant progress to further decrease the amount of material in the vicinity of the detectors by improving the detector layer concept [Teb16].

Furthermore, there is no sign for a contribution of the ^{113m}Cd β-decay ($Q_\beta = 585.7$ keV, $T_{1/2} = 14.1$ yr) as considered in Ref. [BBB⁺07]. As the detectors have been underground at the LNGS since at least 3.5 years (installation of L1 in Sept.'11, L4 in Nov.'13), short-lived cosmogenics, potentially affecting the low-energy region, have already decayed.

Due to the presence of the radon-induced γ-lines of ²¹⁴Pb and ²¹⁴Bi, the decay chain of ²²²Rn is taken as starting point for the background model. Further components are near-detector contaminants from the ²³²Th and ²³⁸U decay chains as well as the presence of ⁴⁰K. For simplicity, only one near-detector component is defined as source of the background decays. The reason behind is that it is hardly possible to constrain the contributions of either internal or external sources since the background is rather featureless besides the

already mentioned γ -lines. That applies to the impurities of the primordial radionuclides that can only contribute marginally to the combined spectrum due to the observed absence of characteristic prompt γ -lines, such as the de-excitation lines of ^{208}Tl at 583.2 keV and 2614.5 keV or ^{40}K at 1460.8 keV.

Simulation of background components

The VENOM simulation of the contaminants makes use of the complete demonstrator geometry as described in section 5.3.3. All considered contaminants were confined to specific volumes of the geometry according to Tab. 8.10 in order to create template spectra of their contribution to the overall background spectrum.

Table 8.10: List of simulated material impurities from inner- to outermost. The total mass is the sum of all detector parts of the same material. The available gas volume surrounding the CZT crystals has been calculated from the inner dimension of the copper nest, corrected for the placed Delrin frames and detectors. The simulation includes all 64 crystals, but only the 45 active detectors in the ^{113}Cd spectrum-shape analysis are considered for the background estimate.

material	total mass	volume / cm ³	contaminants
CZT (64 crystals)	381.31 g	64.63	^{40}K , ^{232}Th , ^{238}U
CZT (45 crystals)	268.11 g	45.44	
Glyptal (64 crystals)	978.6 mg		^{40}K , ^{232}Th , ^{238}U
Glyptal (45 crystals)	688.1 mg		
gas volume		370.44	^{222}Rn
Delrin frames	101.4 g	70.91	^{40}K , ^{232}Th , ^{238}U
copper shield	65.69 kg	7348.16	^{40}K , $^{56,58,60}\text{Co}$, ^{232}Th , ^{238}U
ULA lead	86.47 kg	7625.00	^{40}K , ^{232}Th , ^{238}U

The detector masses, which are treated as variables inside VENOM, were fixed to the average of the ^{113}Cd detector pool of 5.96 g. The same is done for the lacquer volume of the Glyptal encapsulation, whereby an average mass per detector of 15.29 mg has been determined from the freight documents of the manufacturer. The resulting average thickness is about 20 μm assuming a coverage of five sides (cathode side left blank) and a density of 1.441 g/cm³. Since the lacquer masses vary strongly between the detectors, from about 9 to 20 mg per detector, and it is rather inhomogeneously distributed on the detectors' sides, one has to rely on such averaged values.

For each nuclide 10^7 events have been simulated with either VENOM's single isotope *bkggen* or *chaingen* generators. The initial decay's energy deposit in the active CZT volume was summed for each detector and event separately. This way, multi-detector hits can be identified and discarded as has been done with the experimental data after the FADC synchronization. Moreover, it is possible to smear the simulated MC energy deposit E_{MC} according to the finite detector resolution of the experiment, denoted as the parameter σ_{det} , by assigning a randomized value following Eqn. (8.12)

$$E_{\text{det}}(E_{\text{MC}}) = \text{RNDM} \left\{ \frac{1}{\sqrt{2\pi\sigma_{\text{det}}^2}} e^{-\frac{1}{2} \left(\frac{E_{\text{det}} - E_{\text{MC}}}{\sigma_{\text{det}}} \right)^2} \right\} \quad (8.12)$$

assuming a Gaussian normal distribution around the true Monte-Carlo energy. The randomization is done with the *TRandom3* package of ROOT. For each energy deposit the parameter $\sigma_{\text{det}}(E_{\text{MC}})$ is obtained from the known energy resolution functions $\text{FWHM}(E)$

(see section 8.3.4). In the present case, the average $\text{FWHM}(E)$ of all 45 considered detectors is used for the energy smearing of each simulated background template.

Since the combined spectrum of the experimental data already includes a cut on the interaction depth, there is no need to mimic the cathode contaminations explicitly. The final template spectra consist only of the single detector events of the 45 selected crystals. One detail that should be mentioned is that the detector numbering in VENOM differs from the real experiment due to the present switch of the positions of L3 and L4 (see section 4.3.3). This is taken into account by converting the respective detector numbers into the MC naming scheme prior to their removal from the simulated data.

It was found that the energy smeared template spectrum of the ^{222}Rn decay chain, which was confined to the gas volume surrounding the CZT crystals, is already a good match to the experimental data by applying only a rough normalization (see final result in Fig. 8.20). Furthermore, the width of the radon-induced γ -lines agree quite well between the data and the smeared MC template. However, the γ -line intensities turn out to be too high solely considering ^{222}Rn .

The evaluation of the ^{232}Th and ^{238}U template spectra revealed that there is hardly any discrimination power between an associated intrinsic (CZT) or external (e.g. Glyptal encapsulation) contribution at low energies. At higher energies, on the order of 10 MeV, the intrinsic contaminations cause prominent α -peaks in the MC, which are not observed in the data. Hence, the intrinsic contributions will be neglected completely in the following.

The remaining external near-detector impurities of ^{40}K , ^{232}Th and ^{238}U result in very similar template spectra at low energies. Due to the absence of any additional γ -lines, the combined contribution of the ULA lead, the copper shield as well as the Delrin holder can only be on the order of a few percent in the energy range of interest. Any other contributions from α - or β -radiation, that might be emitted by those materials, will have to pass through the encapsulation coating and result in similar featureless template spectra. In fact, it turned out that the required weakening of the simulated γ -lines of ^{214}Pb and ^{214}Bi with respect to the data could be achieved by considering solely the encapsulation lacquer as source of external contaminations in the low-energy region. An accurate modeling of the expected high-energy α -peaks of the primordial decay chains is very challenging because of the inhomogeneity of the lacquer and its unknown thickness profile, even for a single crystal. The encapsulation causes external α - and β -particles to lose a significant portion of their initial energy before they can penetrate the sensitive CZT volume. Due to the thickness variation there is no noticeable peak position in the combined experimental spectrum of the selected 45 detectors. The same applies to α - and β -particles, which have been started within the encapsulation lacquer's volume following a nuclear decay. This justifies to consider only the radiopurity of the Glyptal coating to represent a measure of the near-detector contaminants.

Construction of background model

The relative composition of the background below 2 MeV is determined via an instance of the *TFractionFitter* class of the ROOT software package. It uses the template spectra for ^{222}Rn , ^{40}K , ^{232}Th and ^{238}U which were confined to the previously discussed volumes. A prerequisite of the method is that the simulated templates and the experimental data have to be binned in the same way. Furthermore, the Glyptal contamination levels in Tab. 8.8 are used as priors in the *TFractionFitter* to constrain the contribution of ^{40}K , ^{232}Th and ^{238}U according to their relative activities. From this it is expected to encounter three times more ^{238}U than ^{232}Th and a multiple more of ^{40}K . Those constraints coincide with the relative activities deduced from the older ICP-MS measurement of the lacquer referred to as *eV clear* (which is assumed to be Glyptal as well).

The best fit of the templates to the combined data, as shown in Fig. 8.20, results in the following fractions for a fit range of 320 keV to 1200 keV:

$$\begin{aligned} ^{222}\text{Rn} : & \quad 65.7\%, \\ ^{238}\text{U} : & \quad 15.3\%, \\ ^{40}\text{K} : & \quad 14.7\%, \\ ^{232}\text{Th} : & \quad 4.3\%. \end{aligned}$$

The total integral of the accordingly scaled templates can be used to express the contamination levels of the near-detector components. In a first step the normalization of the experimental data by the known detector exposure in units of kg d and the bin width of 4 keV has to be taken into account. Secondly, the ratio of the numbers of detected and originally simulated decays, referred to as the simulation efficiency ε_{sim} , allows to estimate the total activity of the considered background components. For the Glyptal contaminations the following values of ε_{sim} have been found: 58.4% (^{40}K), 56.2% (^{232}Th) and 55.7% (^{238}U). As the simulation efficiency is mainly a geometric effect, the values are very similar to each other for the same confined volume. In case of ^{222}Rn in the gas volume surrounding the detectors an efficiency of $\varepsilon_{\text{sim}} = 23.7\%$ is obtained.

Finally, the actual contamination levels can be calculated from the template integral, the exposure normalization and the simulation efficiency. For the decay chain of ^{222}Rn an activity of about 6.7 Bq/m³ is found. This value is well below the monitored radon concentration at the LNGS, which ranges from 25 – 250 Bq/m³ strongly depending on the position in the underground complex. For COBRA's detector location it was measured to be 84 Bq/m³ in 2015. According to Ref. [WZ05], describing a nitrogen flushing system as in use by the experiment, an ultimate radon level of about 0.5 – 1.3 mBq/m³ could be achieved with unpurified evaporated nitrogen. Due to the failure of the nitrogen flushing during the ^{113}Cd data-taking, an increased ^{222}Rn exposure was to be expected. However, the average level over the complete run duration was reduced by more than one order of magnitude compared to the radon concentration in the ambient laboratory.

The resulting contamination levels for the Glyptal encapsulation exceed several hundred mBq/kg, if scaled to its total mass of only about 700 mg for 45 detectors with about 15.3 mg each. Nonetheless, the expected activity ratios of the ^{40}K , ^{232}Th and ^{238}U contributions are recovered again. Compared to Tab. 8.8 it is clear that those high activity levels are due to the simplified approach of considering solely the CZT crystal's encapsulation as source of external background. If the template integrals are scaled to the combined mass of the Delrin frames and the encapsulation (see Tab. 8.8), the contamination levels end up in the expected range on the order of a few mBq/kg. Furthermore, there are additional potential sources of external backgrounds. One of those is the additional glue used to fix the gold wires of the electrode contacting. An original sample of the conventional industry glue has been analyzed with γ -spectroscopy in the Dortmund low-background facility (DLB) by M. Gerhardt (TU Dortmund) in 2018. It resulted in upper limits on the order of 100 mBq/kg for the ^{232}Th and ^{238}U decay chains and a rather high ^{40}K concentration of about 910 ± 120 mBq/kg. However, due to the glue spot's tiny mass the expected background contribution turns out to be negligible.

Conclusion and results

From the combined background projection it is finally possible to calculate the S/B ratio. It is taken as the ratio of the integrals over the ^{113}Cd ROI of the experimental data and the MC prediction. The ^{113}Cd ROI is defined by the average threshold of $\bar{E}_{\text{th}} = 84$ keV

and the Q -value (see Tab. 4.4). This leads to $S/B \approx 47$, which is on the same order of the previous CdWO_4 experiments and about a factor of five better compared to former COBRA studies (see Tab. 8.5). The determined S/B ratio is only slightly worse compared to the more simplified approaches of assuming a constant ($S/B \approx 60$) or an exponentially decreasing background ($S/B \approx 52$). Both cases are discussed in Fig. D.21 of the appendix. Because of such a superior S/B ratio, there is no need to take the background projection into account for the intended single detector spectrum-shape analysis. However, the combined MC background prediction will be used to compare the single detector results to the ones obtained for the combined spectrum after the subtraction of the background. The deviation between both approaches is then taken as a measure of the systematic uncertainty related to the negligence of the background modeling on the single detector basis.

8.3.8 Preparation of templates

The general procedure to prepare the theoretical ^{113}Cd templates for the spectrum-shape comparison is well documented in [Hei18] for one nuclear model (ISM). However, some improvements have been achieved since then, which will be covered in the following section.

As mentioned before in section 8.3.1, the SSM is based on the comparison of the measured β -spectra to an ensemble of ^{113}Cd template spectra, which were calculated in different nuclear models (ISM, MQPM, IBFM-2) in dependence on g_A . The template calculations have been performed by Suhonen *et al.* for $g_A \in [0.8, 1.3]$ in steps of 0.01 with an energy binning of about 1 keV. Those templates will be referred to as $t(E_j, g_A)$, with j being the index of the energy bin E_j and the corresponding effective value of g_A . The upper bound of the g_A range is motivated by the free value of the axial-vector coupling $g_A^{\text{free}} = 1.276(4)$ [UCN10].

An improvement with respect to the previous work in [Hei18] is the availability of three different nuclear model calculations, which can be used to study model dependencies. Moreover, the g_A step width could be improved by a factor of five, resulting in a total of 50 input templates $t(E_j, g_A)$ for each model. The total set of original g_A values is denoted as \hat{g}_A in the following. Before that, only a varying g_A step width between 0.05 and 0.01 had been available to reduce the number of input templates in the outer g_A range due to their time consuming computation at that time. In order to overcome the limitation of the number of available $t(E_j, g_A)$, an interpolation procedure has been developed in cooperation with A. Heimbolt to produce ^{113}Cd template for arbitrary g_A values in the range given by the original calculations. As pointed out in [Hei18], the first attempt to find an analytic description of the three-dimensional planes spanned by the nuclear model calculations (see Fig. 8.11) failed due to the complexity of the problem. Any two-dimensional approximation $f_{2d}(E_j, \hat{g}_A)$ showed significant deviations from the original data points $P(E_j, \hat{g}_A)$ making an accurate interpolation impossible. The two-dimensional problem could be simplified by projecting the g_A dependence for a fixed energy $E_j = E_{\text{const}}$, which creates a one-dimensional slice denoted as $s(E_{\text{const}}, \hat{g}_A)$. However, also the one-dimensional slices could not be described with a unique parametrization. The reason for this is the variety of the expected shapes that cannot be described sufficiently with a single conventional polynomial (see Fig. 8.21).

In the end it was found that an accurate description of $s(E_{\text{const}}, \hat{g}_A)$ can be achieved by making use of so-called *splines*. A spline is a collection of several polynomial functions. In contrast to a conventional parameter fit, no optimization process is involved in the construction of a spline since it is uniquely defined by the involved data points (x_n, y_n) , which are referred to as *knots*, and a set of boundary conditions on the polynomials connecting them. The knots divide the spline's definition range into intervals, whereby two neighboring intervals share exactly one data point. The boundary conditions define the polynomial in between two neighboring knots. For the polynomials $g(x)$ defined in $[x_{n-1}, x_n]$ and $h(x)$ defined in

$[x_n, x_{n+1}]$ they can be expressed as

$$g(x_n) = h(x_n) = y_n, \quad (8.13)$$

$$g'(x_n) = h'(x_n), \quad (8.14)$$

$$g''(x_n) = h''(x_n). \quad (8.15)$$

The first condition Eqn. (8.13) demands the knots to be part of the polynomials while the other two boundaries Eqn. (8.14) and Eqn. (8.15) ensure the continuity between two neighboring polynomials using the first and second derivatives. Per definition the original data points of the slices $s(E_{\text{const}}, \hat{g}_A)$ form the knots, hence, are contained in the spline and can be recovered perfectly at any time.

For the spline description of $s(E_{\text{const}}, \hat{g}_A)$, the *TSpline3* class of the ROOT software package is used, which utilizes polynomials of grade three. Besides the grade of the polynomials, the spacing between the knots characterizes the class of a spline. If the knots are equidistant, it is called a *uniform spline*, which applies to the present case. Fig. 8.21 illustrates some examples of the spline construction.

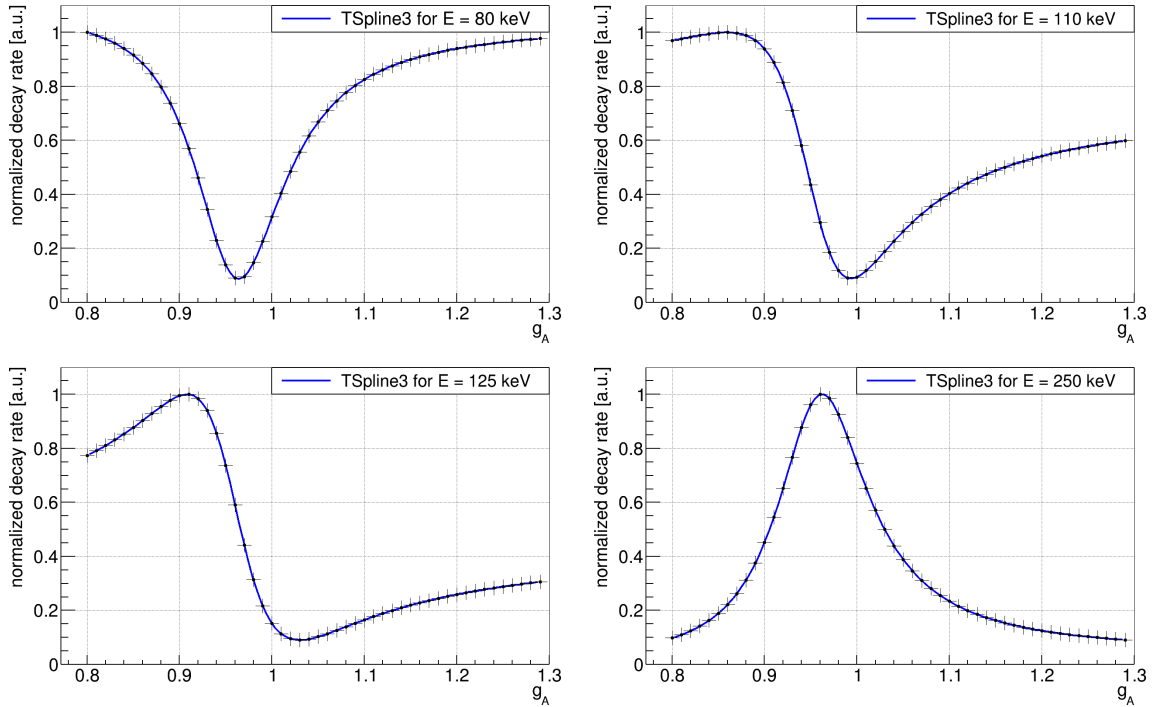


Figure 8.21: Compilation of spline examples for a constant energy slice of the original set of ^{113}Cd templates. Each spline was scaled to a maximum of one. The splines' knots are shown as black crosses. The examples are shown for the energy bins $E_j = 80\text{ keV}$ (top left), $E_j = 110\text{ keV}$ (top right), $E_j = 125\text{ keV}$ (bottom left) and $E_j = 250\text{ keV}$ (bottom right).

The spline approximation of the constant energy slices is used to interpolate the decay rate for an arbitrary g_A by evaluating the spline at this value. If done for all energy slices $s(E_{\text{const}}, \hat{g}_A)$, a new ^{113}Cd template can be constructed for the previously inaccessible value of g_A . The method is used to construct interpolated templates $\tilde{t}(E_j, g_A)$ with a g_A spacing in units of $2.5 \cdot 10^{-3}$, which increases the total number of ^{113}Cd templates for the spectrum-shape analysis by a factor of four. The final set of templates, including the originally calculated ones, is again converted into a set of splines based on the *TSpline3* class. An instance of this set is referred to as $\tilde{s}(E_j, g_A)$ for a fixed value of g_A and a running value of E_j . Those splines build the basis of the spectrum-shape comparison, but before they have to be further prepared.

The accuracy of the spline interpolation and its effect on the results of the spectrum-shape analysis is discussed in section 8.3.11.

Threshold and template normalization

For the comparison of each $\tilde{s}(E_j, g_A)$ with the single detector data it is necessary to take into account the experimental characteristics such as the detector-dependent threshold, the finite energy resolution, as well as the intrinsic electron detection efficiency. The first affects the normalization of the calculated spectrum-shape templates. Both the experimental and predicted ^{113}Cd spectra are supposed to be normalized to unity in order to perform the spectrum-shape comparison. But because of the typical detection threshold E_{th} , which is discussed in section 8.3.3 and has a different value for each detector, it is only possible to perform the normalization over the accessible energy range. It is limited by the value of E_{th} and the ^{113}Cd Q -value. The effect of the lower energy threshold on the template normalization is depicted in Fig. 8.22 for a subset of the original ISM calculations.

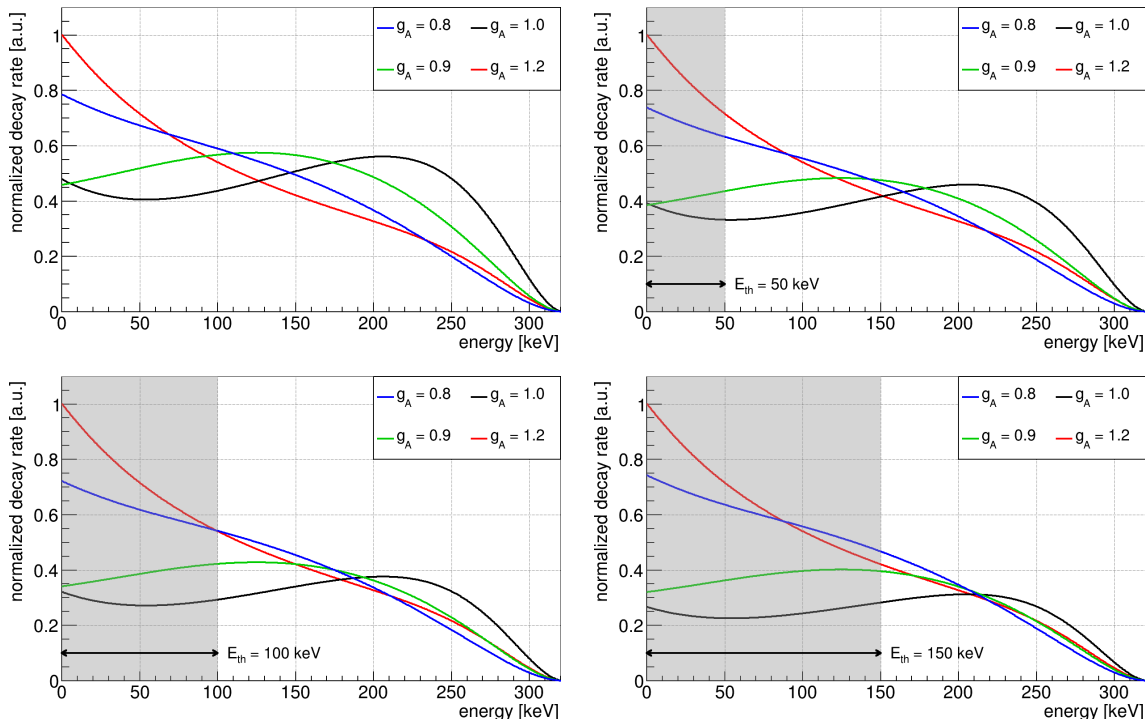


Figure 8.22: Threshold dependence of the template normalization exemplarily shown for the ISM. The smaller the accessible energy range gets by increasing the threshold, the less distinctive are the theoretical ^{113}Cd templates for different values of g_A at higher energies. In each case the maximum of the $g_A = 1.2$ template is set to unity, while the threshold is step-wise increased: no threshold (top left), $E_{\text{th}} = 50 \text{ keV}$ (top right), $E_{\text{th}} = 100 \text{ keV}$ (bottom left) and $E_{\text{th}} = 150 \text{ keV}$ (bottom right).

The distinction of the spectrum-shape features at higher energies gets the less prominent, the higher the threshold of the corresponding experimental data gets. As each of the 45 detectors has been operated at slightly different thresholds, it is not possible to use the same $\tilde{s}(E_j, g_A)$ set for all of them in the spectrum-shape analysis. Furthermore, the finite energy resolution in terms of $\text{FWHM}(E)$ differs for each detector and has to be incorporated, respectively. This is why each detector features its own set of interpolated templates in the final analysis.

Energy resolution smearing

After its normalization over the accessible energy range, the set of splines is folded with the detectors' individual resolution functions. Those have been extracted from the calibration measurements as discussed in section 8.3.4. The Gaussian energy smearing follows Eqn. (8.12) and the general procedure as described in the previous section 8.3.7 about the background modeling. However, the usage of the spline approximation allows to perform the smearing in an analytical way rather than following the statistical procedure as described before. The mathematics behind the convolution of two functions $f(t)$ and $g(t)$ can be expressed as

$$(f \star g)(t) = \int_{-\infty}^{+\infty} f(\tau)g(t - \tau)d\tau \quad (8.16)$$

$$= \int_{-\infty}^{+\infty} f(t - \tau)g(\tau)d\tau \quad (\text{commutativity}). \quad (8.17)$$

In this case $g(t)$ would be the Gaussian energy smearing according to Eqn. (8.12) and $f(t)$ a representative of the set of interpolated splines.

Electron detection efficiency

The last effect that needs to be incorporated into the set of $\tilde{s}(E_j, g_A)$ arises from the energy-dependent detection efficiency of the CZT detectors for the electrons released in the ^{113}Cd β -decay. Depending on its origin and momentum, it is possible that an emitted electron will not deposit its full energy in the source crystal. This is described by the intrinsic full-energy detection efficiency (FEE) $\varepsilon_{\text{int}}(E)$ and can be studied with MC simulations. The higher the electron momentum, the higher the chances to escape the CZT crystal with only a partial energy deposition. That is why the effect is expected to be most severe for electrons carrying the full Q -value. From a simulation of 10^6 mono-energetic electrons, which were distributed homogeneously over the volume of an average-sized cuboidal CZT detector with an xy -dimension of 10.2 mm and a height of 10.0 mm, it follows to be $\varepsilon_{\text{int}}(Q_\beta) = 97.7(1)\%$. For lower energies $\varepsilon_{\text{int}}(E)$ is expected to continuously increase.

However, a correction based solely on $\varepsilon_{\text{int}}(E)$ neglects that all the electrons with partial energy deposition will still contribute to the spectrum at lower energies. Instead, the normalized detector response function $\varepsilon_{\text{det}}(E)$ has to be used to incorporate the effect of partial energy depositions. Although it is expected to be a rather small effect, this circumstance has not been addressed properly in the previous analyses, e.g. [Hei18] and [BBB⁺07]. In fact, the authors of Ref. [BBB⁺07] used an even more simplified approach to correct for the efficiency of their CdWO₄ scintillator setup and introduced an energy independent scaling factor of $\varepsilon = 99.97\%$. It is quite certain that this mistreatment should affect the spectrum-shape at low energies and is another indication for taking such previous results with caution.

In order to determine and compare the energy-dependent FEE $\varepsilon_{\text{int}}(E)$ and the full response function $\varepsilon_{\text{det}}(E)$, a MC campaign was performed. It utilizes 10^6 electrons for initial energies $E_j \in [4, 340]$ keV in steps of 4 keV and follows the same approach as discussed for the case of electrons carrying the full Q -value. The energy steps are chosen according to the binning of the experimental data. The number of entries in the full-energy bin with respect to the total number of simulated events are taken as $\varepsilon_{\text{int}}(E_j)$. A polynomial fit of the resulting efficiency values leads to an analytic expression for $\varepsilon_{\text{int}}(E)$.

Moreover, the normalized detector response function $\varepsilon_{\text{det}}(E)$ can be extracted from the same batch of MC data. For each energy bin E_j of the respective template $\tilde{t}_j = \tilde{t}(E_j, g_A)$

obtained from the set of splines $\tilde{s}(E_j, g_A)$, the detector response spectrum can be calculated from the MC simulations with starting energies E_j . The normalization of the resulting detector response spectra is achieved by dividing each bin content by the number of simulated events. This way the so-called detector response matrix R_{jk} can be constructed, with R_{jk} being the j -th normalized detector response spectrum, obtained for electrons with starting energy E_j . In this case, the k -th energy bin of R_{jk} corresponds to the detected energy $E_k \in [4, E_j]$ keV in steps of 4 keV. The detector response matrix R_{jk} obtained for the MC simulations, based on the average crystal dimensions as quoted before, is shown in Fig. 8.23.

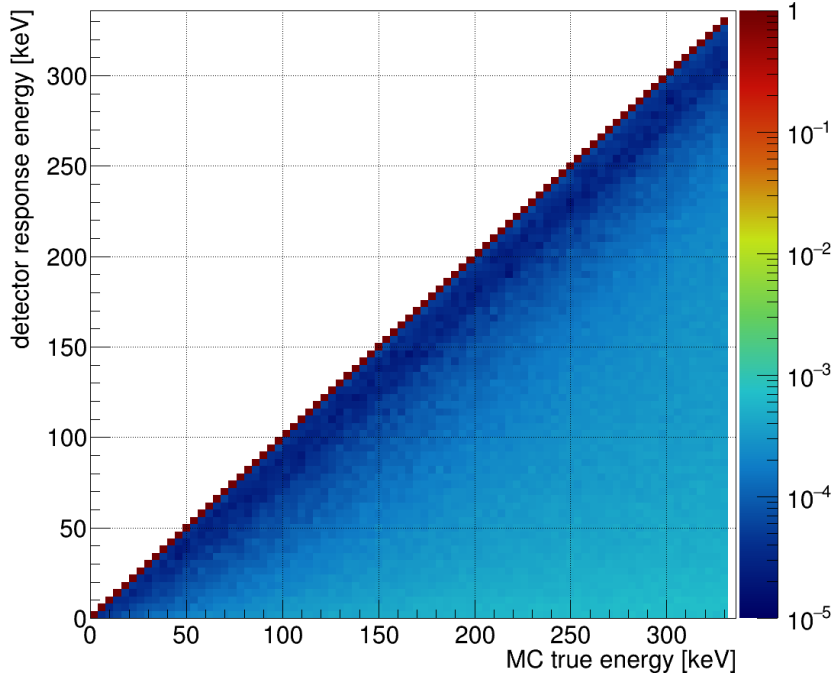


Figure 8.23: Simulated detector response matrix for an average-sized CZT detector with $x = y = 10.2$ mm and $z = 10.0$ mm dimensions. The x -axis represents the MC true electron energy in steps of 4 keV. The normalized detector response matrix R_{jk} takes into account the contributions to the k -th energy bin coming from only partially detected electrons with starting energies $E_j > E_k$. The diagonal elements represent the full-energy detection efficiency (FEE).

Finally, each template spectrum \tilde{t}_j has to be convoluted with R_{jk} according to Eqn. (8.18).

$$\tilde{t}'_k = \sum_{j \geq k} \tilde{t}_j \cdot R_{jk} \quad (8.18)$$

The resulting template spectra \tilde{t}'_k take into account the contribution to the k -th energy bin coming from only partially detected electrons with starting energies $E_j > E_k$. Using the spline formalism allows again to perform the convolution process analytically by following the procedure as introduced in Eqn. (8.16). According to Eqn. (8.18) the normalized detector response $\varepsilon_{\text{det}}(E_j)$ can be extracted for each energy bin E_j from the summation over the entries of R_{jk} . Following this, an analytic expression for $\varepsilon_{\text{det}}(E)$ can be found by fitting the single points with a polynomial function. It should be noted that the previously discussed intrinsic FEE $\varepsilon_{\text{int}}(E_j)$ follows from the same equation by setting $j = k$ in the summation. This way, only the diagonal elements would be taken into account. A comparison of the energy dependency of the intrinsic FEE $\varepsilon_{\text{int}}(E)$ and the full normalized detector response function $\varepsilon_{\text{det}}(E)$ is shown in Fig. 8.24.

The observed discrepancies for energies between the minimum threshold of all detector channels at 52 keV and the ^{113}Cd Q -value at 320 keV are on the order of only a few percent.

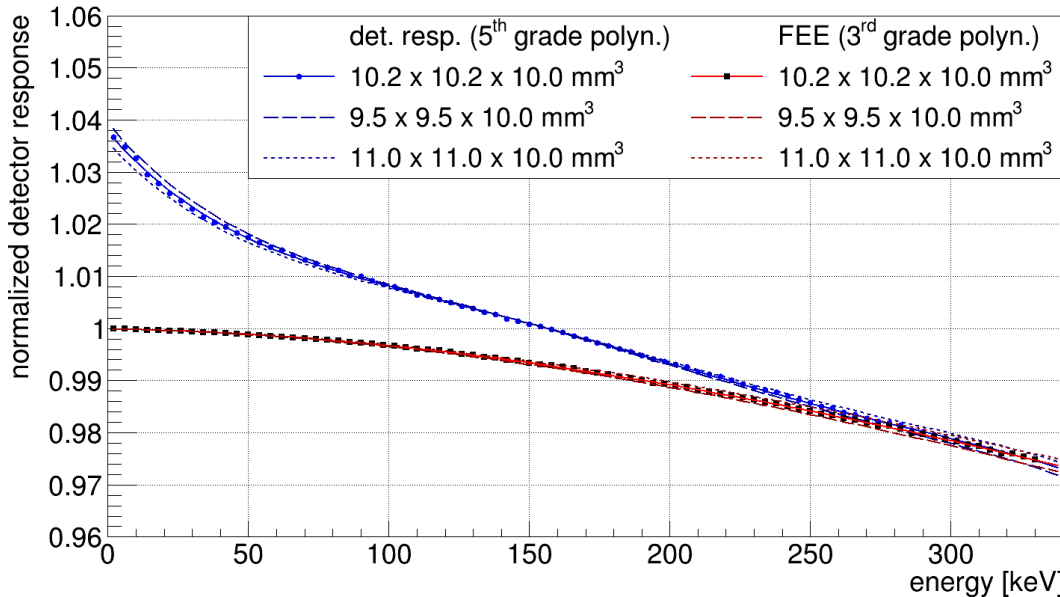


Figure 8.24: Comparison of the simulated detector response function $\varepsilon_{\text{det}}(E)$ and the intrinsic full-energy detection efficiency $\varepsilon_{\text{int}}(E)$. Due to the contribution of partially detected electron energies, the normalized $\varepsilon_{\text{det}}(E)$ curve exceeds a maximum of one. For electron energies close to the ^{113}Cd Q -value, there is a convergence of both quantities. An analytic approximation can be achieved by using different polynomial functions, e.g. for $\varepsilon_{\text{det}}(E)$ of grade five and for $\varepsilon_{\text{int}}(E)$ of grade three. Three sets of varying CZT crystal dimensions were simulated to quantify the systematic uncertainties related to the variance of the observed xy -dimensions in the ^{113}Cd detector pool.

For higher energies, the difference gets less prominent before there is a convergence near the Q -value. In order to access the systematic uncertainty related to the efficiency convolution of the template spectra, the complete MC campaign has been repeated for the minimum and maximum values of the crystals' xy -dimensions in the ^{113}Cd detector pool. It was found that although changing the xy -dimensions by up to 10%, there is hardly any difference in the normalized detector response function. A detailed discussion of all the systematic uncertainties considered in the spectrum-shape analysis is given in section 8.3.11.

By folding the set of interpolated splines $\tilde{s}(E_j, g_A)$ with the detector-dependent energy resolution $\text{FWHM}(E)$ and the normalized detector response function $\varepsilon_{\text{det}}(E)$, the preparation of the spectrum-shape comparison is almost complete. The final step consists of a renormalization of each convolved template spectrum in order to ensure the normalization to unity over the accessible energy range. With the final set of template spectra that follow from the convoluted splines $\tilde{s}(E_j, g_A)$, the comparison with the actual single detector data can be pursued as discussed in the following section.

8.3.9 Spectrum-shape analysis

The procedure to analyze the ^{113}Cd spectrum-shape data follows the approach developed by A. Heimbold [Hei18] in the course of his Master thesis. However, the present work includes significant improvements such as a more nuanced treatment of the individual detector's threshold (see section 8.3.3), an optimized energy calibration (see section 8.3.4) and event selection (see section 8.3.6), and finally the convolution of the predicted ^{113}Cd template spectra with the full detector response function as discussed in the previous section 8.3.8. In the same section it was already mentioned that the theory basis of the spectrum-shape comparison within the SSM could be improved as well by including three different nuclear

models (ISM, MQPM, IBFM-2) with a much finer g_A binning. Furthermore, a low-energy background model (see section 8.3.7) has been developed to confirm the superior S/B ratio and to complement the single detector analysis with the results obtained by combining the data into an average experimental spectrum including a subtraction of the MC background prediction. For both approaches – single detector versus combined spectrum analysis – an extensive study of systematic effects contributing to the overall uncertainty has been performed. This subject will be covered in one of the subsequent sections after presenting the results of the spectrum-shape analysis.

Following the preparation of the theoretical templates as discussed in the previous section, the experimental data have to be prepared in a similar way. As the individual detector thresholds had to be adjusted slightly over the run time of the ^{113}Cd data-taking, it is necessary to normalize each energy bin of the experimental spectra with its corresponding exposure. All energy bins below a temporary threshold do not contribute to the spectrum over the complete live-time of the measurement. If the spectrum would then be scaled only to the total live-time, without acknowledging the bin-to-bin variations, the effect of the changing threshold would result in characteristic steps in the energy spectrum. The careful bin-wise normalization prevents such artifacts. Accordingly, the lower energy bins feature larger statistical uncertainties, which is why the bin uncertainties should be taken into account in the spectrum-shape analysis.

Analysis methods

Two methods have been investigated in [Hei18] to perform the spectrum-shape comparison: a standard χ^2 test and a so-called *run method* meant as an additional control. Both of them follow from the examples described in one of the standard textbooks about statistics by R. J. Barlow [Bar89]. While the χ^2 test accounts for the absolute value of the differences between the data and the template prediction, the run method focuses entirely on the sign of those. In this sense the both methods are very complementary to each other.

Using the experimental values m_i of the energy bins i to N with Poisson uncertainties σ_i and the corresponding predictions t_i based on the template for a certain g_A , the χ^2 quantity can be derived as

$$\chi^2 = \sum_{i=1}^N \left(\frac{m_i - t_i}{\sigma_i} \right)^2 \quad (8.19)$$

for each of the interpolated g_A templates. A good match would be indicated by $\chi^2 \approx N$, due to the differences per bin ($m_i - t_i$) approaching the order of the assigned experimental uncertainty σ_i . This would mean that the observed fluctuations are consistent with the underlying Poisson statistic. In this case, each term in the sum would be on average on the order of $\mathcal{O}(1)$, leading to the approximative numerical agreement of χ^2 and N . On the other hand, the case $\chi^2 \ll N$ would suggest that there is on average an overestimation of the uncertainties and $\chi^2 \gg N$ would either indicate an underestimation, respectively, or a mismatch of data and prediction.

A derived quantity is the so-called reduced χ^2 , denoted as χ^2_{red} , following from Eqn. (8.19) by dividing it with the number of degrees of freedom (NDF). In the present case it follows $\text{NDF} = (N - 1)$ due to the normalization of each spectrum's integral to unity which fixes one of the degrees of freedom. For a large quantity N , $\chi^2_{\text{red}} \approx 1$ is a measure for a good match.

The complementary run method relies on a specific labeling of the spectrum's energy bins to classify the relation of the data and the predictions. If the experimental data exceeds the predicted decay rate in a bin, it is labeled as category *A*. In the other case, where the

predicted bin content is higher than the measured value, it is labeled as category *B*. The comparison of all energy bins i to N results in a sequence of those labels, whereby the number of label changes is referred to as the number of runs r . A large value of r indicates that the data fluctuate statistically around the prediction, hence, is a measure for their agreement. By comparing r to the expected number of runs according to Eqn. (8.20) [Bar89]

$$\langle r \rangle = 1 + \frac{2N_A \cdot N_B}{N_A + N_B}, \quad (8.20)$$

with N_A and N_B being the number of assigned labels of both categories, it is possible to express a certain model preference. However, this is only a qualitative statement and the performance of the run method turned out to be not as robust and reliable as for the χ^2 procedure (see [Hei18] for more details). An example of the run method can be found in section D.4.1 of the appendix. In contrast, an quantitative statement about the absolute difference between the model predictions and the data can be accessed via the χ^2 test, which is why it is chosen as the default method in the spectrum-shape analysis.

Application on COBRA's ^{113}Cd data

The bin width of the data is set to 4 keV, which is a compromise between a large number of bins N – beneficial for the anticipated χ^2 test – and the assigned bin uncertainties arising from the number of entries per bin, scaled by the corresponding exposure. The fixed binning requires to remove the lowest bin of each spectra, because E_{th} is not necessarily a multiple of 4 keV. This might cause a loss of events in the lowest bin, e.g. for a bin ranging from 88 – 92 keV in case of $E_{\text{th}} = 90$ keV. Additionally, as a conservative approach to address that some noise contribution might still be leaking into the ^{113}Cd spectra for certain periods where the thresholds had to be increased along with a potential signal loss due to the limited DCCs' efficiency (see sections 7.1.1 and 8.3.6), the final analysis thresholds are set to $\tilde{E}_{\text{th}} = E_{\text{th}} + 8$ keV for each detector spectra. This removes the lowest two energy bins and increases the average threshold \bar{E}_{th} of the present analysis to 91.9 keV. Following this, the experimental spectra are normalized by the integral over the accessible energy range. The assigned bin uncertainties are scaled accordingly. This way, there is no arbitrary offset between the experimental data and the interpolated ^{113}Cd template spectra and their shape can be compared directly.

In contrast to the conservative data treatment described above, Ref. [BBB⁺07] used a much finer binning in the data analysis, while their detector's energy resolution is at least two times worse. The noise influence was corrected using a PSD technique along with the deduced signal efficiency of the PMT setup, which was estimated from calibration data. However, there are doubts about the robustness of the presented method and the claimed negligible effect on the signal acceptance, especially at such low energies. That is why the quoted threshold of $E_{\text{th}} = 28 \pm 14$ keV (see Tab. 8.5) has to be taken with caution and is by no means conservatively estimated.

Following the preparation of the data, the χ^2 test is performed for each detector spectrum and its accordingly prepared sets of interpolated templates, covering the full g_A range for the three considered nuclear models. Fig. 8.25 illustrates exemplarily a comparison between one of the COBRA single detector measurements and a compilation of each model's interpolated ^{113}Cd templates around the best match g_A . Each spectrum-shape comparison results in a χ^2_{red} value corresponding to a fixed value of g_A . Depending on the threshold, the NDF used for the normalization ranges from 45 – 67 with a mean of ~ 56 . A graphical representation of the resulting $\chi^2_{\text{red}}(g_A)$ curve in the given g_A range is shown in Fig. 8.26 for the same example detector as used for Fig. 8.25 and the three nuclear model calculations.

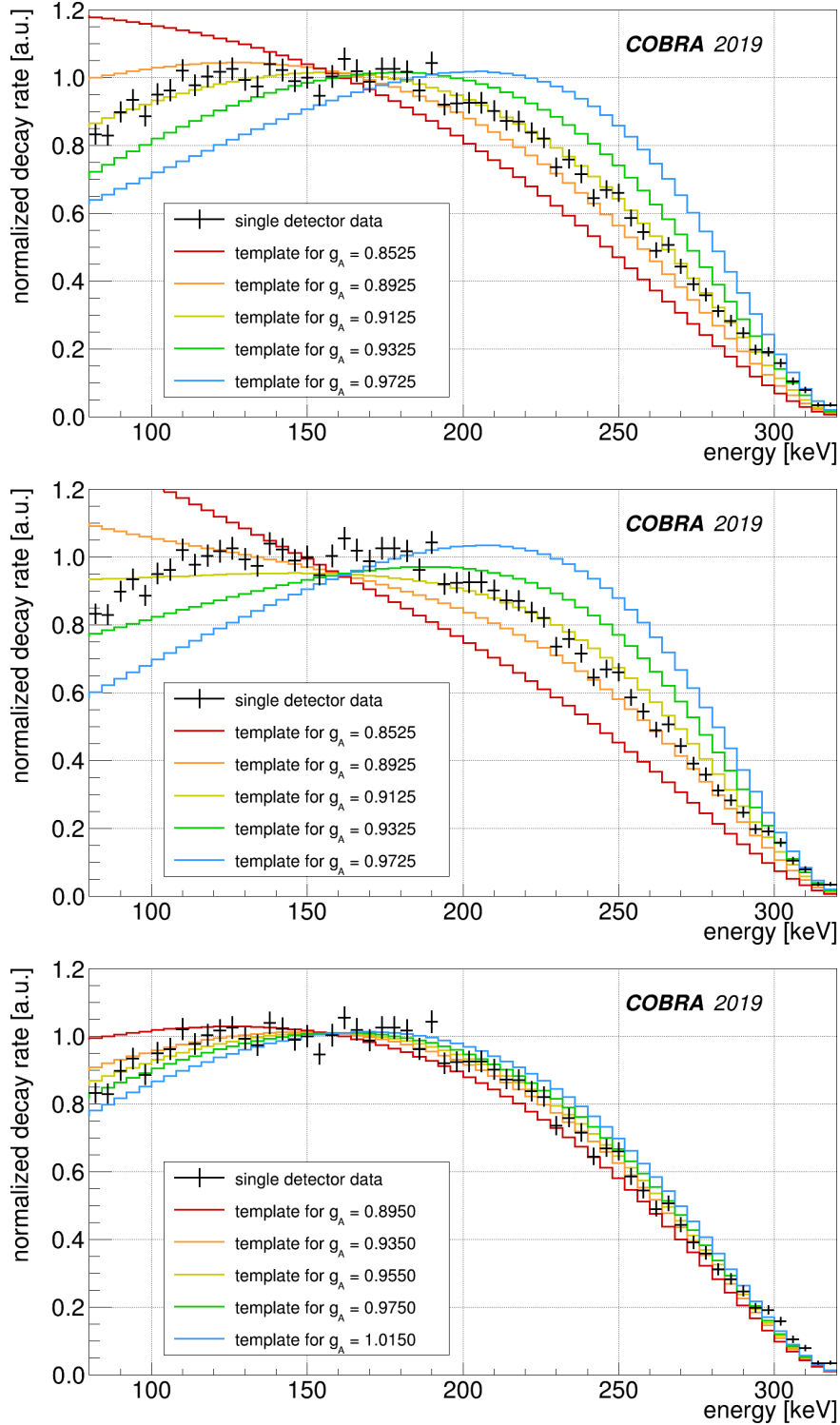


Figure 8.25: Example of a COBRA single detector spectrum compared to a set of five interpolated ^{113}Cd templates. *Top:* ISM (taken from [COB20]). *Middle:* MQPM. *Bottom:* IBFM-2. The experimental data is shown for Det54 (L4-P06) with a binning of 4 keV. The bin-to-bin fluctuations are consistent with the statistical uncertainties indicated by the black crosses. The interpolated templates have been prepared according to section 8.3.8 by folding in the detector's energy resolution and response function. The present compilation has been selected symmetrically around the centroid marked by the g_A template that is the closest to the best match for each nuclear model according to the χ^2 test.

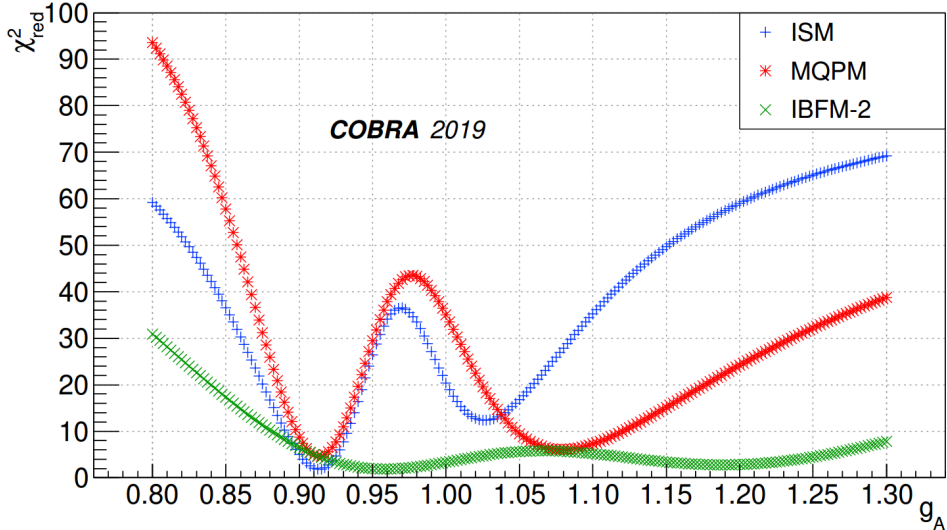


Figure 8.26: Example $\chi^2_{\text{red}}(g_A)$ curves of the spectrum-shape comparison for one COBRA single detector spectrum and the interpolated templates based on the ISM (blue), MQPM (red) and IBFM-2 (green) calculations (taken from [COB20]). Again, the results are shown for the example of Det54 (L4-P06). The shape of the $\chi^2_{\text{red}}(g_A)$ curves is representative for the complete ensemble of 45 detectors and the combined spectrum.

The observed features in the $\chi^2_{\text{red}}(g_A)$ curves are not uniquely connected to the chosen example detector but are representative for the complete ensemble of 45 crystals, as well as for their combined experimental spectrum. One particular problem of the recent SSM realization is that there are two competing minima for each of the three models. In some cases their depth is rather similar, in others they are well separated. However, only the global minima are taken into account in the further analysis. The location of the lower minima is very similar for the ISM and MQPM, while the IBFM-2 is in general less sensitive to g_A resulting in less prominent features in the corresponding $\chi^2_{\text{red}}(g_A)$ curve. Nevertheless, none of the curves favors the free g_A value of about 1.27, not even with the upper minima.

The global minimum of each $\chi^2_{\text{red}}(g_A)$ curve is fit with a parabola to extract the best match g_A from the minimum of the fit. The fit is optimized by varying its fit range to achieve a robust approximation. The variation of the fit range is considered as a source of systematic uncertainty in section 8.3.11.

Exemplarily, the best match g_A values presented in Eqn. (8.21)–(8.23) can be extracted for the single detector data depicted in Fig. 8.26.

$$g_A^{\min}(\text{ISM}) = 0.91352 \pm 0.00091 \text{ (stat.)} \quad \text{at} \quad \chi^2_{\text{red}} = 1.85, \quad (8.21)$$

$$g_A^{\min}(\text{MQPM}) = 0.91354 \pm 0.00084 \text{ (stat.)} \quad \text{at} \quad \chi^2_{\text{red}} = 4.63, \quad (8.22)$$

$$g_A^{\min}(\text{IBFM-2}) = 0.95850 \pm 0.00371 \text{ (stat.)} \quad \text{at} \quad \chi^2_{\text{red}} = 1.88. \quad (8.23)$$

The statistical uncertainty on the 1σ level is defined as the $(\chi^2 + 1)$ deviation from the minimum and follows directly from the statistical interpretation according to Ref. [Bar89] of the underlying χ^2 distribution (see Eqn. (C.4) in the appendix). It is determined by an iteration of the fit of the original $\chi^2(g_A)$ curve around the minimum $(g_A^{\min}, \chi^2_{\min})$ to find the points $(g_A^L, \chi^2_{\min} + 1)$ and $(g_A^R, \chi^2_{\min} + 1)$ to the left and right, respectively. Following this, the statistical uncertainty on g_A^{\min} can be expressed as

$$\Delta g_A^{\text{stat}} = \text{Max}(|g_A^{\min} - g_A^R|, |g_A^{\min} - g_A^L|). \quad (8.24)$$

The derivation of Δg_A^{stat} according to Eqn. (8.24) is also a conservative estimate for asymmetrically shaped parabola around the global minimum. However, referring to the determined

minimum χ_{red} values listed in Eqn. (8.21)–(8.23), the assigned statistical uncertainties are not sufficient to express any model preference on the level of the single detector data. A statistical interpretation can be derived from the so-called *p*-value, which denotes the probability to achieve the same or an even larger χ^2 by chance, even when the correct model is used. In the present case the *p*-values turn out to be $< 5 \cdot 10^{-5}$ for the ISM and IBFM-2 and considerably worse in case of the MQPM. Since the calculation of the *p*-values only includes the determined minimum χ^2 and the NDF, it can be interpreted solely in the context of the statistical compatibility of the data and the considered models. Hence, a discussion of systematic effects related to the analysis procedure should be done as will be presented in section 8.3.11.

Finally, the analysis procedure based on the χ^2 test is applied to all 45 independent detector spectra in order to extract the best match g_A value from the minimum of the $\chi^2_{\text{red}}(g_A)$ curves for each of the nuclear models. Moreover, the analysis is performed for the combination of the single detector data in form of a combined ^{113}Cd spectrum. The respective set of interpolated templates is prepared by using average values of the input parameters. This applies to the energy resolution and the evaluation of some of the systematic uncertainties as will be discussed in the next sections. Due to the careful normalization of each energy bin according to its exposure, the combined spectrum also extends down to the lowest threshold of all channels. The spectrum-shape analysis of the combined spectrum is meant as an additional control for the single detector results and is used to crosscheck the systematic uncertainties. A compilation of all the experimental ^{113}Cd spectra with the final analysis threshold \tilde{E}_{th} compared to the combined spectrum can be found in the appendix (see Fig. D.15–D.19).

8.3.10 Discussion of results

The results of the ^{113}Cd spectrum-shape analysis, as presented in this section, have been published recently in the journal of *Physics Letters B* [COB20]. As mentioned earlier, two strategies were pursued to combine the single detector data. The first and default procedure is based on a combination of the single detectors' best match g_A values following from the corresponding χ^2 tests. An example of the single detector results has been shown in Eqn. (8.21)–(8.23). From those $N = 45$ single detector values a weighted mean according to

$$\bar{g}_A = \frac{\sum_i w_i \cdot g_{A,i}}{\sum_i w_i} \quad (8.25)$$

with $i \in [1, N]$ can be constructed by using the statistical uncertainty as the weight $w_i = 1/(\Delta g_{A,i}^{\text{stat}})^2$ in Eqn. (8.25). The statistical uncertainty on the weighted mean \bar{g}_A can then be expressed as the square root of the summed weights $1/\bar{\sigma}_{\text{stat}}^2 = \sum_i w_i$. In fact, the statistical uncertainty $\bar{\sigma}_{\text{stat}}$ on \bar{g}_A turns out to be negligibly small considering the overall systematic uncertainties $\bar{\sigma}_{\text{sys}}$ as discussed in section 8.3.11 and summarized in Tab. 8.11. They are on the order of $\bar{\sigma}_{\text{stat}} \sim 2 \cdot 10^{-4}$ for the ISM and MQPM and a factor of four higher for the IBFM-2, respectively. The extracted weighted means including the dominating systematic uncertainties yield the following results

$$\bar{g}_A(\text{ISM}) = 0.915 \pm 0.007, \quad (8.26)$$

$$\bar{g}_A(\text{MQPM}) = 0.911 \pm 0.013, \quad (8.27)$$

$$\bar{g}_A(\text{IBFM-2}) = 0.955 \pm 0.022. \quad (8.28)$$

The second method follows the analysis procedure as described in section 8.3.9, but instead for only a single detector spectrum, the analysis is performed for the combination of all 45 detector spectra. From the combined ^{113}Cd spectrum as shown in Fig. 8.20, the spectrum

of the MC background projection can be subtracted. Both the background corrected as well as the original spectrum combination are used for the spectrum-shape analysis to access the systematic uncertainty related to the background modeling. Due to the normalization of the combined spectra's integral to unity, the exact same procedure as for the single detector spectra can be applied. The resulting best match g_A value of the background corrected combined spectrum is denoted as \tilde{g}_A in the following. Again, it turns out that the statistical uncertainties are on the order of $\tilde{\sigma}_{\text{stat}} \sim 2 \cdot 10^{-4}$ and can be neglected in the final results compared to the respective systematics. The combined spectrum-shape analysis including the background correction results in

$$\tilde{g}_A(\text{ISM}) = 0.915 \pm 0.010, \quad (8.29)$$

$$\tilde{g}_A(\text{MQPM}) = 0.914 \pm 0.016, \quad (8.30)$$

$$\tilde{g}_A(\text{IBFM-2}) = 0.967 \pm 0.044. \quad (8.31)$$

These values are in perfect agreement with the weighted means Eqn. (8.26) – Eqn. (8.28) following from the single detector analysis, but feature about 30% higher relative uncertainties. This is also due to the general drawback of the combined spectrum approach, because the present detector differences are only poorly taken into account. As a result of the averaging of the input parameters, the corresponding minimum $\chi^2_{\text{red}} \approx 15$ is much worse compared to the single detector examples in Eqn. (8.21) – (8.23) and the distribution of the 45 values for the single detector analysis (see Fig. 8.28). However, it can be confirmed that the combined spectrum after the background subtraction results in significantly lower minimum χ^2_{red} values than the original combined spectrum without it. The observed reduction is about 10% and differs slightly for the three nuclear models. Again, it should be noted that the background model is not used explicitly in the single detector analysis, but that this issue is treated as a systematic uncertainty in the end.

Fig. 8.27 shows the distributions of the best match g_A values for the 45 independent measurements, which were evaluated in the context of the three considered nuclear models. While the ISM and MQPM results are tightly distributed around a common mean value, the IBFM-2 distribution is much wider. This is due to the fact that the latter model is in general less sensitive to g_A as could already be seen in the $\chi^2_{\text{red}}(g_A)$ curve shown in Fig. 8.26.

Compared to the results reported in [Hei18], there are no outliers observed for the ISM after achieving the improvement of the analysis procedure as summarized in the beginning of this section. The same applies to the MQPM distribution. Only for the templates following from the IBFM-2 calculations there are two prominent outliers resulting from the $\chi^2_{\text{red}}(g_A)$ curve's upper minima being selected in the course of the χ^2 test. The respective detectors are Det40 (L3-P08) and Det43 (L3-P11). Their minimum χ^2_{red} values are consistent with the characteristic spread of those values as observed for the total detector pool. The distribution of the minimum χ^2_{red} corresponding to the 45 best match g_A values is shown in Fig. 8.28

Compared to the g_A distribution depicted in Fig. 8.27 it is somewhat surprising that the distribution of the corresponding minimum χ^2_{red} values is rather flat for MQPM, while it is very similar in case of the ISM and IBFM-2. Before that, a good agreement of the g_A distributions was found for the ISM and MQPM. Moreover, the two outliers (Det40, Det43) observed for the IBFM-2 in Fig. 8.27 do not coincide with the detectors corresponding to the highest minimum χ^2_{red} in Fig. 8.28 for the same model. While Det40 ($\chi^2_{\text{red}} = 1.25$) and Det43 ($\chi^2_{\text{red}} = 1.84$) are found inside the bulk of the values, the IBFM-2 outliers correspond to Det12 ($\chi^2_{\text{red}} = 3.55$) and Det57 ($\chi^2_{\text{red}} = 5.00$). The same detectors feature a rather high minimum χ^2_{red} for their best match g_A in case of the ISM (Det12: $\chi^2_{\text{red}} = 2.46$, Det57: $\chi^2_{\text{red}} = 4.08$) and the MQPM (Det12: $\chi^2_{\text{red}} = 7.09$, Det57: $\chi^2_{\text{red}} = 10.08$). At least for Det12 there is the hypothesis that the detector might suffer from an insufficient grid bias supply as has been

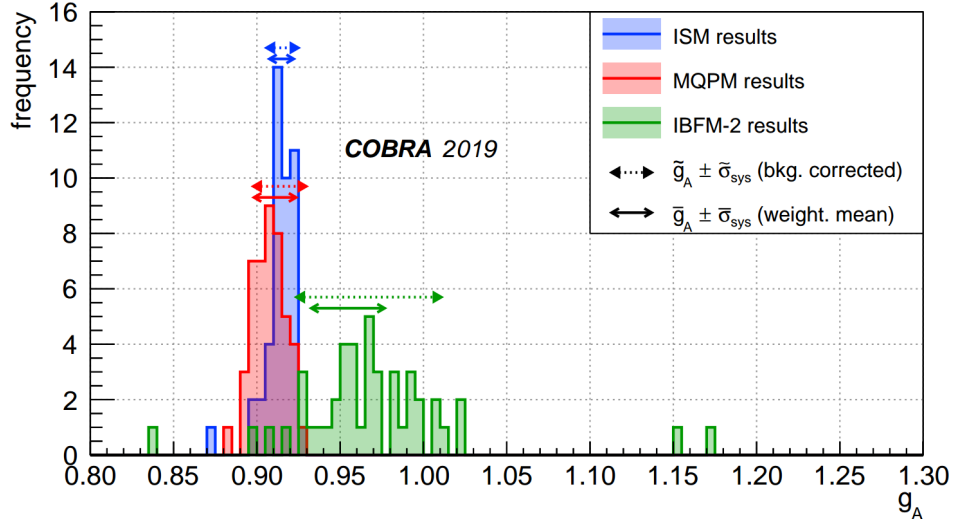


Figure 8.27: Distribution of the 45 best match g_A values for the ISM, MQPM and IBFM-2 (taken from [COB20]). Additionally, the weighted mean $\bar{g}_A \pm \bar{\sigma}_{\text{sys}}$ as well as the result of the spectrum-shape comparison for the combined spectrum $\tilde{g}_A \pm \tilde{\sigma}_{\text{sys}}$ including the background correction are highlighted.

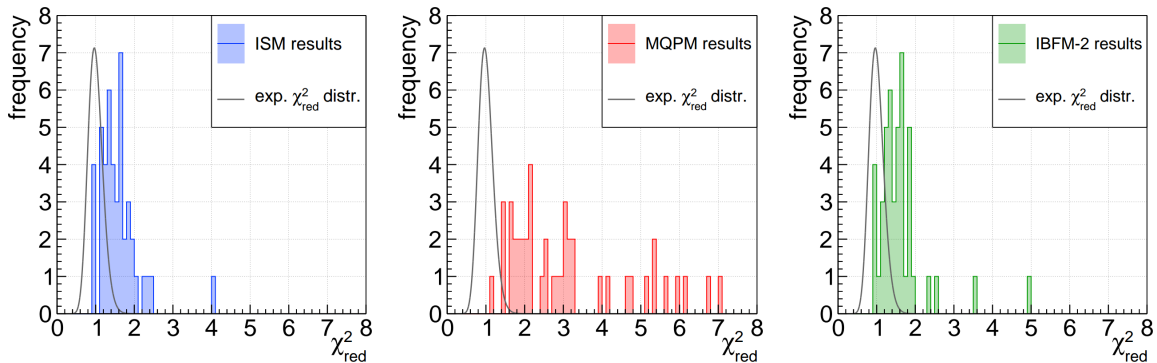


Figure 8.28: Distribution of the minimum χ^2_{red} values of the 45 best match g_A values for the single detector spectrum-shape comparison (adapted from [COB20]). While the χ^2 test results dominantly in minimum $\chi^2_{\text{red}} < 2$ with an approximately Gaussian shape for the ISM and IBFM-2, the distribution is rather flat for MQPM indicating on average less agreement with the underlying model prediction of the ^{113}Cd spectrum-shape. For comparison, the expected χ^2_{red} distribution for the average NDF ~ 56 is shown. The observed disagreement is likely an indication for the dominance of systematic uncertainties, which are not taken into account in the evaluation of the χ^2_{red} .

observed in past data-taking runs. However, there was no indication for this in the evaluation of the calibration data prior and after the ^{113}Cd data-taking. Nonetheless, the normalized energy spectrum of Det12 differs the most from the combined spectrum comparing all the 45 individual measurements (see Fig. D.15 in the appendix). Such obvious deviations cannot be reported for any other of the mentioned outliers. Furthermore, the spectrum-shape analysis of Det12 resulted for each of the three nuclear models in the lowest g_A values of the distribution shown in Fig. 8.27. This might hint again to an unaccounted systematic effect related to this specific detector. Finally, the results for the detectors with significantly reduced exposure compared to the average of 1.10 kg d per detector (Det14: 0.79 kg d, Det60: 0.29 kg d), which is due to their partly disabled operation state over the ^{113}Cd run, turn out to be perfectly consistent with the bulk of the g_A and corresponding χ^2_{red} distributions.

Considering the mean of the χ^2_{red} distributions and its respective uncertainty, the following

average numbers are found for the distributions in Fig. 8.28.

$$\bar{\chi}_{\text{red}}^2(\text{ISM}) = 1.57 \pm 0.08, \quad (8.32)$$

$$\bar{\chi}_{\text{red}}^2(\text{MQPM}) = 3.27 \pm 0.28, \quad (8.33)$$

$$\bar{\chi}_{\text{red}}^2(\text{IBFM-2}) = 1.62 \pm 0.10. \quad (8.34)$$

The average values indicate that there is less agreement between the MQPM predictions and the experimentally determined spectrum-shapes than for the ISM and IBFM-2. Moreover, the p -values corresponding to Eqn. (8.32)–(8.34) and the average NDF lead to $p \sim 4 \cdot 10^{-3}$ (ISM), $p \sim 2 \cdot 10^{-3}$ (IBFM-2) and $p \sim 2 \cdot 10^{-15}$ (MQPM). The observed deviation from the ideal case $\chi_{\text{red}}^2 \approx 1$ might be related to an underestimation of the bin uncertainties, which solely follow from the Poisson fluctuations of the data. However, an estimate of the nuclear models' uncertainties seems to be out of reach due to the elaborate template computation and the number of related input parameters such as the NMEs. In the original reference introducing the SSM [HKS17], the computation of the ^{113}Cd electron momentum distribution consists of ~ 45 numerically different NMEs, whereby some of them are connected to each other in a non-trivial way. Changing the NMEs within their model constraints, as done for the experimental parameters, fails either due to the absence of any meaningful constraints in the first place or, if accessible, indirectly through the interplay of the some of the NMEs, due to the oversized dimensionality of such a variation problem. Nonetheless, a potential combination of the experimental and model uncertainties might reduce the χ_{red}^2 in a future follow-up analysis. Due to the unknown contribution arising from the theoretical predictions, the estimate of the analysis' systematic uncertainties and their impact on the extracted average values of g_A has been done in a very conservative way. Details on the study of the systematics will be discussed in the upcoming section 8.3.11.

Finally, the average g_A values in combination with their determined experimental uncertainties can be used to illustrate the allowed spectrum range for the ^{113}Cd β -decay as shown in Fig. 8.29. This is done by using the weighted means as the default results of the single detector spectrum-shape analysis according to Eqn. (8.26)–Eqn. (8.28). The spline interpolation technique as discussed in section 8.3.8 allows to construct template spectra for the experimentally determined $\bar{g}_A \pm \bar{\sigma}_{\text{sys}}$ based on the original model calculations. This way, the allowed spectrum range is independent of the present detector effects such as the finite energy resolution and detection efficiency.

While the spectrum-shape is very similar for the ISM and IBFM-2, the trend at low energies is contrary for the MQPM prediction. The same agreement between the ISM and IBFM-2 has been seen for the distribution of the minimum χ_{red}^2 values in Fig. 8.28. Nonetheless, the spectrum-shapes agree well for energies above 120 keV for all three considered nuclear models. Even though the IBFM-2 result is associated with the highest experimental uncertainty, a comparable spectrum range follows from the spline interpolation in Fig. 8.29. This is only achieved due to the fact that the model turns out to be less sensitive to g_A .

In conclusion it can be stated that there is a slight preference for the ISM due to the following three observations. Firstly, the best match g_A results following from the preferred single detector analysis are tightly distributed around a common mean value (see Fig. 8.27). This is also due to the well-separated minima in the corresponding $\chi_{\text{red}}^2(g_A)$ curve (see Fig. 8.26). Secondly, the assigned systematic uncertainty for the ISM turns out to be the lowest for the weighted means \bar{g}_A as presented in Eqn. (8.26)–Eqn. (8.28) as well as for the combined spectrum results \tilde{g}_A in Eqn. (8.29)–Eqn. (8.31) incorporating the background subtraction. Lastly, the distribution of the minimum χ_{red}^2 values is of almost Gaussian shape and features a mean value that is the closest to the ideal case of $\chi_{\text{red}}^2 \approx 1$ among the three models. The

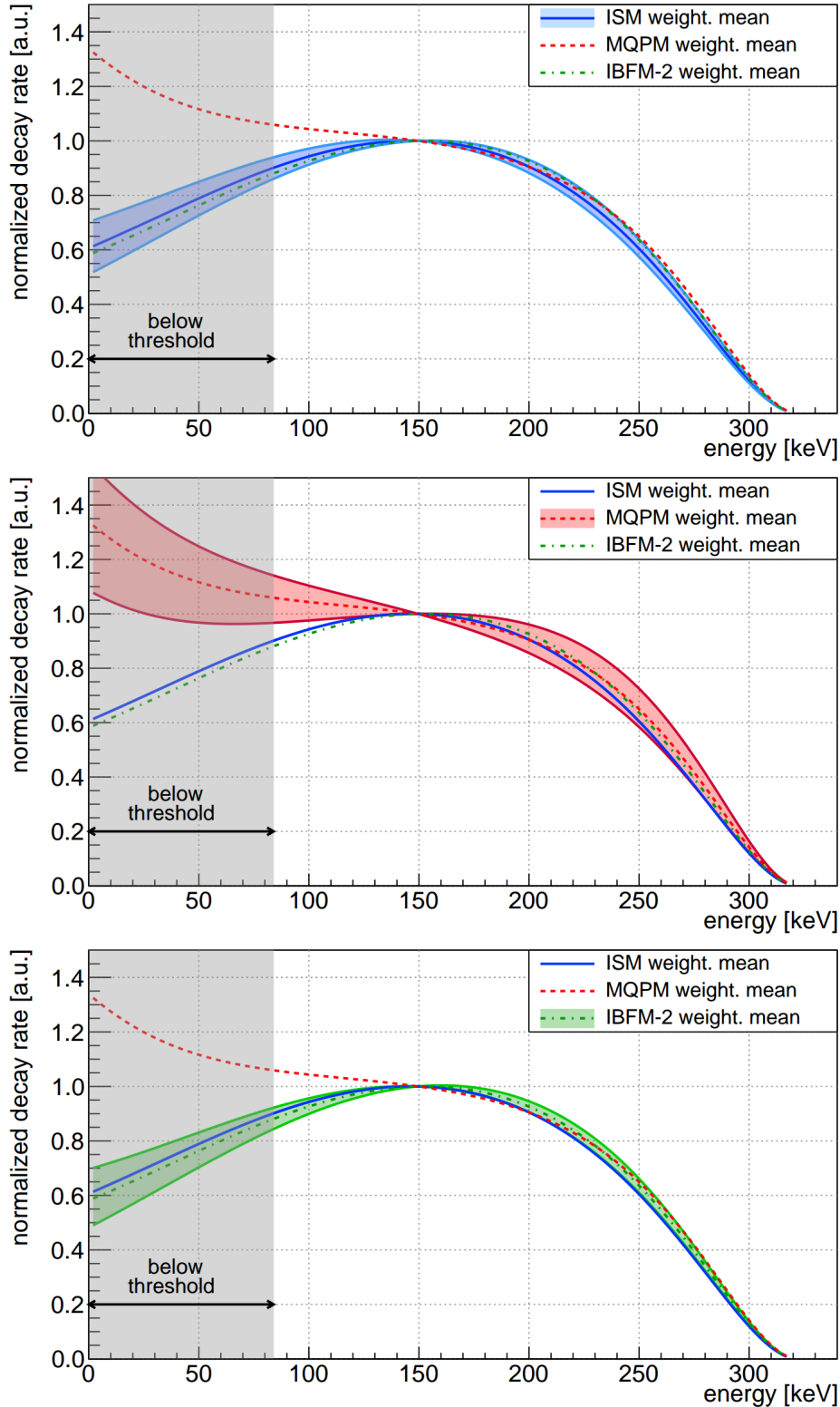


Figure 8.29: Allowed spectrum range for the ^{113}Cd β -decay according to the spectrum-shape results (adapted from [COB20]). *Top:* ISM. *Middle:* MQPM. *Bottom:* IBFM-2. The spline interpolation technique was used to construct template spectra for $\bar{g}_A \pm \bar{\sigma}_{\text{sys}}$ from the originally provided theoretical templates including the experimental uncertainties for each model. For comparison the templates corresponding to the weighted means are shown in each graph for the respective other models.

assessment of the systematic uncertainties, which contribute to the ISM model preference just discussed, is the subject of the subsequent section.

8.3.11 Systematic uncertainties

As pointed out in the previous sections, there is a list of parameters that are needed as an input for the spectrum-shape analysis. Some of them arise from the analysis procedure itself, like the optimum fit range to find the minimum of the $\chi^2_{\text{red}}(g_A)$ curves, while others are affecting the template preparation, independently from the actual analysis procedure. All the considered sources of systematic uncertainties have been investigated after fixing the input parameters of the spectrum-shape analysis to their default values. Each respective systematic effect on the results referred to as the weighted mean \bar{g}_A or the average \tilde{g}_A of the combined spectrum has been evaluated separately. This is done by modifying only one parameter at a time within conservative limits while the other parameters are fixed to their default values in the spectrum-shape analysis. The modulus of the difference between the altered and the default g_A results are then taken as a measure for the systematic uncertainty. None of the considered parameters turns out to be negligible as they all lead to deviations which are significantly larger than a corresponding 3σ deviation of the statistical uncertainties.

The total systematic uncertainty for each model is obtained as the square root of the sum of squared uncertainties (see Eqn. (C.3) in the appendix). A summary of the considered systematics and their corresponding impact on the average g_A results is given in Tab. 8.11.

Table 8.11: List of systematic uncertainties considered in the ^{113}Cd spectrum-shape analysis. For each nuclear model (ISM, MQPM, IBFM-2) two analysis strategies were pursued to extract an effective value of g_A . The results obtained with the combined experimental spectrum, leading to \tilde{g}_A , are meant as an additional control for the default results, referred to as \bar{g}_A , following as the weighted mean of the single detectors' best match g_A according to the χ^2 comparison. The latter values have been published in [COB20]. It turns out that in both cases the systematic uncertainty introduced by the variation of the energy calibration is the dominating one, followed by the limitation of the analysis threshold and the z -cut selection.

model parameter	uncertainty [%]					
	ISM		MQPM		IBFM-2	
	\bar{g}_A	\tilde{g}_A	\bar{g}_A	\tilde{g}_A	\bar{g}_A	\tilde{g}_A
template interpolation	0.002	0.002	0.002	0.001	0.001	0.001
detector response $\varepsilon_{\text{det}}(E)$	0.010	0.012	0.011	0.009	0.033	0.049
resolution FWHM(E)	0.060	0.055	0.032	0.022	0.226	0.179
energy calibration	0.751	0.983	0.796	0.977	2.130	4.201
analysis threshold	0.131	0.297	1.120	1.433	0.714	1.529
z -cut selection	0.120	0.146	0.192	0.097	0.457	0.390
χ^2_{red} fit range	0.102	0.042	0.058	0.015	0.034	0.003
background modeling	0.042	0.042	0.016	0.016	0.068	0.067
total	0.798	1.040	1.389	1.737	2.306	4.492

In the following, the variation of the input parameters will be briefly summarized. The first three systematic uncertainties are expected to arise from the template preparation. The accuracy of the developed spline interpolation technique can be evaluated by removing parts of the original input templates. In fact, this is what has been done in [Hei18]. Based on this approach, one input template after each other was removed from the ensemble with the objective to predict the missing template with the remaining information. It was found that the largest deviation occurs for the removal of the template that is the closest to the best match g_A . Following this, only the most critical template was removed from the given

ensemble to assess the related systematic uncertainty. It follows as the difference between the results using the reduced and the full spline interpolation. As the removed template is still part of the final spline, the whole uncertainty estimate is an exceedingly conservative approach. However, the effect is negligibly small in the end. This is mainly due to the increased number of input templates as reported in section 8.3.8.

The next step in the template preparation is the incorporation of the detector response in form of the simulated $\varepsilon_{\text{det}}(E)$ and the energy resolution. The first effect has been studied by changing the crystal size in the MC simulation to the minimum and maximum physical xy -dimensions of the selected detector pool (see Fig. 8.24). The systematic differences obtained after following the complete spectrum-shape analysis are then added in quadrature to obtain a conservative measure of the respective uncertainty contribution. Similarly, the influence of the resolution smearing has been studied. The corresponding detector-dependent resolution functions $\text{FWHM}(E)$ were fixed for all of them to the worst and best resolution curves, which was evaluated for the ^{113}Cd Q -value of about 320 keV. Following this, the spectrum-shape analysis has been repeated with the fixed $\text{FWHM}(E)$ to obtain the difference with respect to the default parameters. The systematic differences following from the two extreme cases were again added in quadrature. All the systematics discussed so far turn out to have a rather small contribution to the total systematic uncertainty.

According to Tab. 8.11, the variation of the energy calibration leads to the dominating uncertainty contribution for the ISM and IBFM-2. The influence of a misaligned energy calibration is studied by shifting the experimental data according to the uncertainty of the calibration. To assess the calibration uncertainty, the energy calibrated γ -spectrum of each detector's ^{228}Th calibration has been evaluated. As a measure of the potential energy misalignment the shift of the γ -line at 238.6 keV of ^{212}Pb as part of the ^{228}Th decay chain has been determined. The modulus of the average peak shift results in an conservative uncertainty of ± 1.3 keV for the combined calibration data. The experimental spectra were shifted accordingly to asses the effect on the g_A results following from the SSM. Again, the systematic differences were added in quadrature to produce the values quoted in Tab. 8.11. The magnitude of the calibration uncertainty allows to neglect the quoted uncertainty of ± 0.27 keV for the accepted ^{113}Cd Q -value as an additional uncertainty of the energy scale.

The second largest contribution to the overall uncertainty for the ISM and IBFM-2 and the largest for the MQPM is related to the choice of the analysis threshold and its variation. It follows from a conservative approach to estimate the effect of the individual detector thresholds by increasing it for all channels to at least 120 keV, which is more than two FWHM on average. The effect turns out to be different for the three nuclear models and ensues from the change of the predicted shape at low energies for the MQPM compared to the other two models (see Fig. 8.29) and the generally weaker g_A dependence of the IBFM-2 calculations.

Another potential systematic effect arises from the z -cut selection as discussed in section 8.3.6. For the assessment of the respective uncertainty contribution each detector is sliced into two disjunct depth ranges to perform the spectrum-shape analysis for both slices independently. The lower part covers the range $0.25 \leq z < 0.5$ while the top includes events with $0.5 \leq z < 0.75$. The resulting systematic differences in the average g_A values are again added in quadrature and lead to relative contributions on the same order of magnitude for all three models. This can be seen as an indication for the homogeneity of the distribution of the ^{113}Cd isotopes inside the crystal's volume and the resulting uniform z distribution.

The second to last considered systematic uncertainty is related to the fitting of the $\chi^2_{\text{red}}(g_A)$ around the global minimum. The default range of the parabola fit function, which is defined symmetrically around this minimum, is optimized iteratively by an algorithm based on the resulting fit's χ^2_{red} . To evaluate a potential systematic effect, the default range is changed to arbitrary upper and lower boundaries, giving the algorithm the freedom to select

an increased or decreased optimized fit range in the end. The corresponding differences in the extracted average g_A values are then added in quadrature to estimate the systematic uncertainty of the $\chi^2_{\text{red}}(g_A)$ fitting procedure. It turns out that the effect is significantly smaller for the combined spectrum approach, probably because of the increased statistics compared to a single detector spectrum affecting the fit's χ^2_{red} .

Finally, the effect of neglecting the developed low-energy background model (see section 8.3.7) in the single detector analysis is inferred from the analysis results of the combined spectrum with and without the background subtraction. The observed difference in the average g_A values is a direct measure of the corresponding contribution to the overall systematic uncertainty. As expected from the superb S/B ratio, the effect is only marginal for all three models, which justifies the procedure in the end.

Additional systematics as considered in previous studies (e.g. [BBB⁺07] and [COB09b]), such as the exact amount of ^{113}Cd atoms in the crystals, potential dead layer effects or a varying elemental composition of the detector material CZT due to the complex crystal growth, are not expected to have an influence on the spectrum-shape analysis. The reason for this is the careful normalization prior to the spectrum-shape comparison. However, those effects would be important for extracting the total decay rate, which is needed to determine the decay's half-life in a conventional way.

In total, the systematic uncertainties add up to values on the percent level and agree well with the observed spread of the g_A distributions as seen in Fig. 8.27. Furthermore, the single detector results are consistent with the analysis results obtained for the combined spectrum, which feature about 30% higher uncertainties. After finishing the presented ^{113}Cd spectrum-shape analysis and publishing the results in *Physics Letters B* [COB20], supporting the idea of a significantly quenched g_A in low-momentum exchange nuclear processes, there was an announcement regarding a deeper insight into the correct treatment of the related NMEs by the theory colleagues involved in the template calculations. The impact of the claimed breakthrough on the present ^{113}Cd results will be covered in the following section, but have to be taken as preliminary due to the theory basis, which is only provisionally and reflects the most recent progress available in the course of this thesis.

8.3.12 Preliminary results under the CVC hypothesis

In Sept.'19 there was the announcement of a fundamental breakthrough by the theory colleagues of the university of Jyväskylä (Finland), providing the predicted ^{113}Cd template spectra for the SSM, and some of their collaborators. It was found that one of the main shortcoming of the SSM, the observed mismatch between the ^{113}Cd literature reference half-life and the value predicted for an effective g_A well below its free value, could be resolved by studying the implications of the underlying conserved vector current (CVC) hypothesis in a more general scope. Since there is no peer-reviewed publication explaining the details of the new insights, the following summary is based on the private communication between J. Suhonen, J. Kostensalo and the members of the COBRA collaboration.

As mentioned in the introduction section 8.3.1, the β -decay shape factor $C(w_e)$ according to Eqn. (8.8) can be decomposed into a vector, axial-vector and mixed vector-axial-vector part containing the ratio of the weak couplings g_V/g_A . Under the assumption of the conserved vector current, as predicted by the Standard Model of particle physics, it follows that g_V is equal to unity. This way, the spectrum-shape predicted by $C(w_e)$ solely depends on the effective value of the axial-vector coupling g_A . However, applying the CVC hypothesis within the SSM framework also affects the calculation of the related nuclear matrix elements (NMEs) in a non-trivial way. The reasons for this are related to the mixed VA component $C_{VA}(w_e)$ of the shape factor Eqn. (8.8) and the constraints put in place for the different nuclear models.

In fact, the calculations presented in the original reference of the SSM [HKS17] were based on different assumptions regarding the model spaces of the three considered nuclear models. In order to gain information about the involved NMEs in case of the interacting shell model (ISM) and the interacting boson-fermion model (IBFM-2), there is the need to constrain the respective model space, while for the microscopic quasiparticle-phonon model (MQPM) it is unlimited. Due to the limitation of the model space, one of the NMEs involved in the vector part of the calculation turns out to be exactly zero for the first two models. Following the label scheme of Ref. [HKS17] for the ~ 45 involved leading-order and next-to-leading-order NMEs, it is referred to as $V\mathcal{M}_{KK-11}^{(0)}$ in (see [HKS17], Tab. II). For the same NME a non-zero value of ~ 0.37 is found in case of the MQPM in the same reference. The recent objection raised by the founders of the SSM is that all three models should result in the same numerical value of the corresponding NME under the CVC hypothesis. It is claimed that the result of $V\mathcal{M}_{KK-11}^{(0)}$ being exactly zero for the ISM and IBFM-2 is only due to the required model constraints in order to access the other involved NMEs. That is why it should be well justified to estimate the value of the NME for both of the models by using the one following from the MQPM calculations.

Nowadays, according to the claimed breakthrough, it has been found that the model space for the MQPM is not exactly unlimited, but has to be constrained in the case of the CVC hypothesis as well. On the other hand, the constraints can be performed rather freely without breaking any other bounds of the nuclear model. In its current implementation the bounds on the MQPM’s model space are tuned towards reproducing the most accurate ^{113}Cd half-life measurement as reported in Ref. [BBB⁺07] (see Tab. 8.5). The resulting value of the leading-order NME denoted as $V\mathcal{M}_{KK-11}^{(0)}$ of the MQPM is then used as an estimate for the same NME of the ISM and IBFM-2.

Based on this procedure, it is possible to predict the ^{113}Cd spectrum-shape under the improved CVC hypothesis within the SSM. Again, the predictions were provided in the form of template spectra covering the range of $g_A \in [0.6, 1.4]$ in units of 0.01 and an energy binning of about 1 keV. The step size in g_A as well as the energy binning of the theory input are the same as before, but the g_A range has been extended slightly in both directions. An illustration of the predicted g_A dependence of the ^{113}Cd spectrum-shape under the CVC hypothesis can be found in Fig. D.22 of the appendix.

Results of the spectrum-shape analysis

In the following, the results of the once more applied spectrum-shape analysis based on the χ^2 comparison between the COBRA data and the new ^{113}Cd template spectra will be summarized. The template preparations follows the exact same procedure as presented in section 8.3.8 as well as all subsequent analysis steps. However, it was decided to exclude one additional detector from the final detector pool due to its suspicious ^{113}Cd spectrum-shape as found in the previous analysis. This applies to Det12 (L1-P12), because of the findings reported in section 8.3.10 such as the systematic smallest g_A results of the complete detector ensemble accompanied by comparably large minimum χ_{red}^2 values for the best match g_A . Furthermore, the decision takes into account the observed mismatch of the detector’s ^{113}Cd spectrum compared to the normalized combined spectrum of all detectors (see Fig. D.15) and the presumption of a faulty grid bias supply, which might have altered its energy resolution during the data-taking.

The resulting distributions of the remaining 44 best match g_A values, as evaluated in the context of the nuclear models under the CVC hypothesis, are depicted in Fig. 8.30. An apparent drawback of the CVC breakthrough is the observed weakening of the g_A dependence

for all models. This causes the best match g_A values to be distributed over a wider range, whereby the IBFM-2 distributions turns out to be rather flat, but without clear outliers.

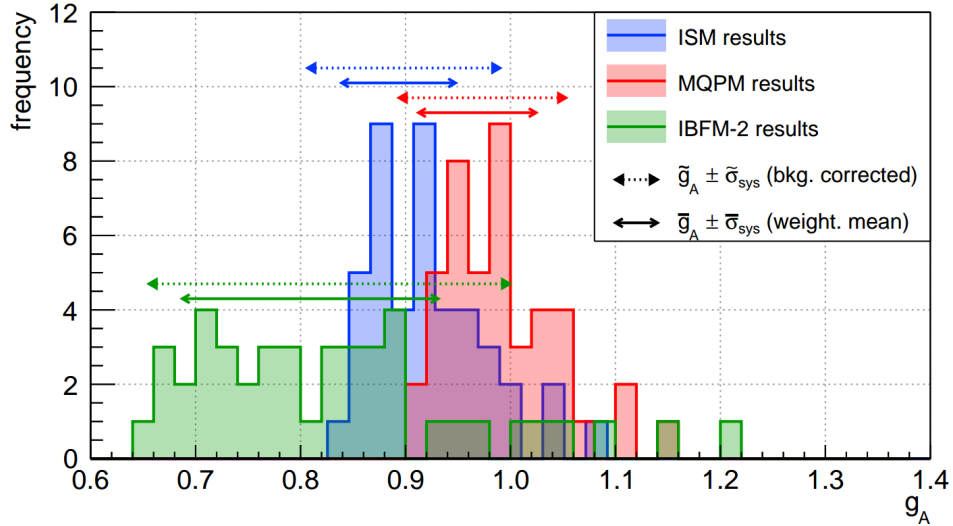


Figure 8.30: Distribution of the 44 best match g_A values for the ISM (blue), MQPM (red) and IBFM-2 (green) under the CVC hypothesis. Again, the respective weighted mean $\bar{g}_A^{\text{cvc}} \pm \bar{\sigma}_{\text{sys}}^{\text{cvc}}$ as well as the result of the spectrum-shape comparison for the combined spectrum $\tilde{g}_A^{\text{cvc}} \pm \tilde{\sigma}_{\text{sys}}^{\text{cvc}}$ including the background correction are highlighted. In contrast to Fig. 8.27 the bin width has been increased to take into account the observed larger spread of the best match g_A values.

Following the previous analysis steps, two procedures are used to assess an average g_A for each nuclear model. The first method is again used to construct a weighted mean of the single detector results, denoted as \bar{g}_A^{cvc} , using the $(\chi^2 + 1)$ deviation from the minimum of the $\chi^2(g_A)$ curves as the weight and a measure of the statistical uncertainty. It turns out that the absolute statistical uncertainty from the sum of weights is on the order of $\bar{\sigma}_{\text{stat}} \sim 1 \cdot 10^{-3}$ for the ISM and MQPM and, as before, about a factor of four higher for the IBFM-2. While the statistical uncertainties are found to be increased significantly, they can still be neglected compared to the overall systematic uncertainties such as shown in the results according to Eqn. (8.35) – (8.37).

$$\bar{g}_A^{\text{cvc}}(\text{ISM}) = 0.893 \pm 0.054, \quad (8.35)$$

$$\bar{g}_A^{\text{cvc}}(\text{MQPM}) = 0.968 \pm 0.056, \quad (8.36)$$

$$\bar{g}_A^{\text{cvc}}(\text{IBFM-2}) = 0.809 \pm 0.122. \quad (8.37)$$

These are again the default results of the spectrum-shape analysis. Secondly, the analysis is repeated for the combination of the single detector data in form of a normalized combined spectrum. A slightly modified low-energy background model, excluding Det12, is used to subtract the predicted background from the default combined spectrum. The resulting average \tilde{g}_A^{cvc} values for the three nuclear models are shown in Eqn. (8.38) – (8.38) using the total systematic uncertainties.

$$\tilde{g}_A^{\text{cvc}}(\text{ISM}) = 0.898 \pm 0.092, \quad (8.38)$$

$$\tilde{g}_A^{\text{cvc}}(\text{MQPM}) = 0.973 \pm 0.079, \quad (8.39)$$

$$\tilde{g}_A^{\text{cvc}}(\text{IBFM-2}) = 0.827 \pm 0.172. \quad (8.40)$$

The associated statistical uncertainties arising from the $(\chi^2 + 1)$ deviation are on the same level as for the weighted means, thus, can be neglected compared to the combined systematic

uncertainties. Moreover, the observed increase of the systematics coincides again with about a factor of five, which is in accordance to the comparison of the previous weighted means and the recent results. The main reason for the uncertainty increase is the already mentioned decreased g_A sensitivity of the SSM under the CVC hypothesis. Another indication for this effect can be seen in Fig. 8.31, where the corresponding $\chi^2_{\text{red}}(g_A)$ curves for the example of Det54 (L4-P06) are depicted.

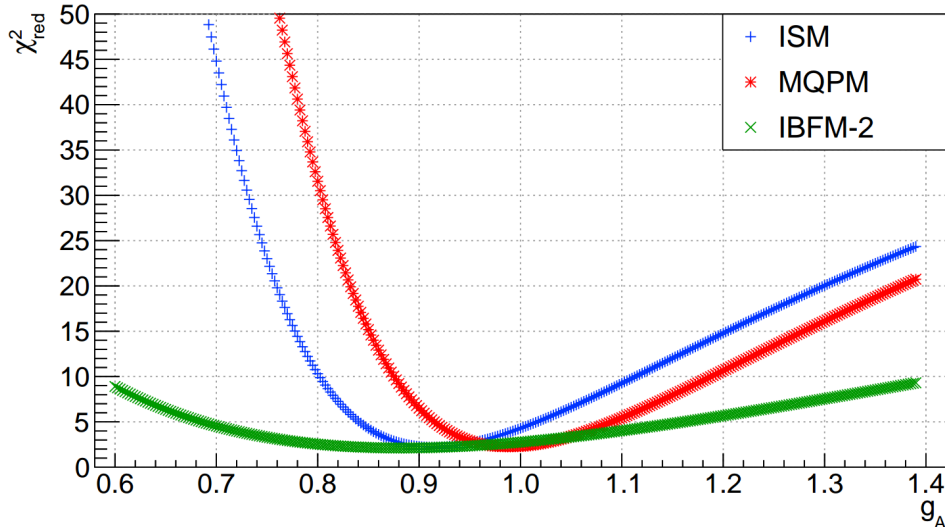


Figure 8.31: Example $\chi^2_{\text{red}}(g_A)$ curves of the spectrum-shape comparison for one COBRA single detector spectrum and the interpolated templates based on the ISM (blue), MQPM (red) and IBFM-2 (green) calculations under the CVC hypothesis. The curves are shown for the same example of Det54 (L4-P06) as in Fig. 8.26. In contrast to the previously shown results of the χ^2 comparison, there is only one minimum for each of the models. Moreover, the shape of the $\chi^2_{\text{red}}(g_A)$ curves is again representative for the other detectors of the complete ensemble and the combined spectrum.

The presented $\chi^2_{\text{red}}(g_A)$ curves are again representative for the complete detector ensemble as well as their combination. Compared to the previously shown curves in Fig. 8.26 of the same example detector, there is only one global minimum for each of the nuclear models. Even though this is in general a favorable outcome of the χ^2 test, it comes at the cost of a less distinctive location of the corresponding minimum. Moreover, the shape of the $\chi^2_{\text{red}}(g_A)$ curves turn out to be less symmetrically around the minimum. However, the estimate of the statistical uncertainty according to Eqn. (8.24) is also valid for asymmetric parabola and should not affect the spectrum-shape analysis in a negative way.

Following the analysis steps further, the distribution of the minimum χ^2_{red} values for the single detector's best match g_A can be taken as an indication for the agreement between the COBRA data and the provided nuclear model predictions. The distributions are shown in Fig. 8.32. In comparison, the corresponding minimum χ^2_{red} values for the combined spectrum analysis turn out to be about ten times worse, which matches the previous observations.

The most prominent outlier can be identified as Det57 (L4-P09). The corresponding $\chi^2_{\text{red}} \gtrsim 5$ for each of the three models are the highest values among all 44 detectors and correspond at the same time to the maximum values of the g_A distributions as shown in Fig. 8.30. The same detector number was found to be an outlier in the previous results reported in section 8.3.10. By comparing the shape of its ^{113}Cd spectrum to the combined one of all detectors (see Fig. D.19 of the appendix), the differences are found to be not as dramatic as for Det12. The second highest outliers with respect to the minimum χ^2_{red} are Det56 (L4-P08) for the ISM and MQPM and Det43 (L3-P11) in case of the IBFM-2. Both of them feature a minimum $\chi^2_{\text{red}} \gtrsim 3$ in the respective models. While Det56 results in a best

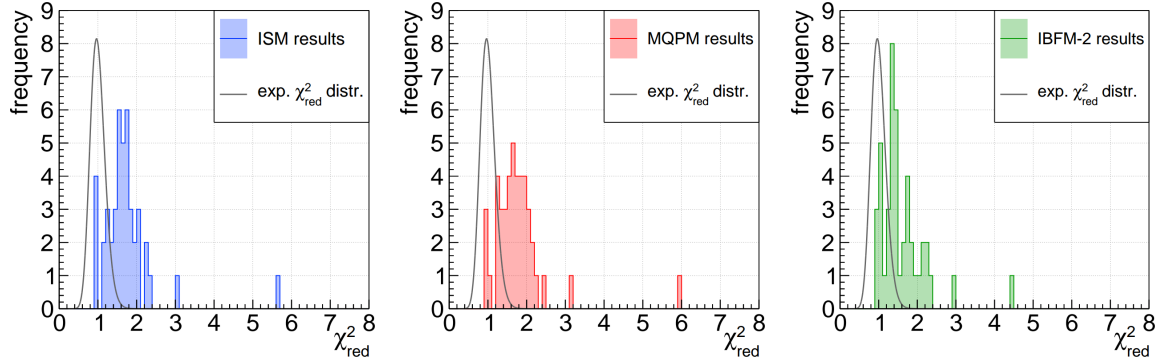


Figure 8.32: Distribution of the minimum χ^2_{red} values of the best match g_A values for the single detector spectrum-shape comparison under the CVC hypothesis. In contrast to Fig. 8.28, all three nuclear models show a similar distribution around a common mean value of approximately Gaussian shape. While this indicates a similar degree of agreement between the experimental data and the model predictions, most values do not comply with the expected χ^2_{red} distribution for the average NDF ~ 56 . Again, the observed disagreement is an indication for the dominance of systematic uncertainties.

match of $g_A \gtrsim 1.1$ for all three models, Det43 prefers a rather small best match of $g_A \approx 0.7$ in the IBFM-2. For comparison, the χ^2 test for Det12, which has been excluded from the final analysis as mentioned before, resulted in a high minimum $\chi^2_{\text{red}} \approx 5$ as well. However, for the other discussed outliers there is no clear argument to exclude them from the final results.

Although the underlying distributions of the best match g_A values changed quite a lot, the shape of the corresponding χ^2_{red} distributions is very similar for all three nuclear models and turns out to be approximately Gaussian. It can be further characterized by the extracted mean values and the respective uncertainty on the mean as shown in Eqn. (8.41) – (8.43).

$$\bar{\chi}^2_{\text{red}}(\text{ISM}) = 1.73 \pm 0.11, \quad (8.41)$$

$$\bar{\chi}^2_{\text{red}}(\text{MQPM}) = 1.77 \pm 0.12, \quad (8.42)$$

$$\bar{\chi}^2_{\text{red}}(\text{IBFM-2}) = 1.61 \pm 0.09. \quad (8.43)$$

The mean values are found to agree well with each other, too. This is an indication for the general agreement between the data and the model predictions, but fails to reproduce the optimum case of $\chi^2_{\text{red}} \approx 1$. Furthermore, there is no clear model preference anymore combining the observations of the smeared out best match g_A distributions and the corresponding minimum χ^2_{red} distributions under the CVC hypothesis. The degree of agreement based on the mean values Eqn. (8.41) – (8.43) for the updated nuclear model calculations is comparable to the previous results obtained for the ISM and IBFM-2. However, the p -values corresponding to Eqn. (8.41) – (8.43) and the average NDF ~ 56 result in $p \sim 6 \cdot 10^{-4}$ (ISM), $p \sim 3 \cdot 10^{-4}$ (MQPM) and $p \sim 3 \cdot 10^{-3}$ (IBFM-2).

Since the MQPM has been used as the basis to tune the related NMEs in order to reproduce the ^{113}Cd reference half-life, the model results, such as the distribution of the minimum χ^2_{red} , have changed the most. Furthermore, it should be mentioned again that the χ^2 test only considers the Poisson uncertainties assigned to the energy bins of the data, which might explain the deviation from $\chi^2_{\text{red}} \approx 1$ as well as the low p -values. As pointed out in section 8.3.10, an incorporation of model uncertainties to counter the potential underestimation of the bin uncertainties is not feasible in the current implementation of the SSM due to the complexity of the involved NME calculations. Given those restrictions, there is no clear statement whether the deviations from $\chi^2_{\text{red}} \approx 1$ are related to a potential underestimation

of the uncertainties or a fundamental mismatch between the data and the predicted ^{113}Cd spectrum-shape of the available nuclear models.

Evaluation of systematic uncertainties

A summary of the updated contributions to the overall systematic uncertainties according to the discussion in section 8.3.11 is given in Tab. 8.12. By comparing the total uncertainties between the previous results listed in Tab. 8.11 and Tab. 8.12, an overall increase of the systematics by about a factor of five is found. The root cause is assumed to be related to the less localized minima of the corresponding $\chi^2_{\text{red}}(g_A)$ curves under the CVC hypothesis.

Table 8.12: List of systematic uncertainties considered in the preliminary ^{113}Cd spectrum-shape analysis based on the CVC update. Again, two analysis strategies were pursued to extract an effective value of g_A for each nuclear model. The default results based on the single detector χ^2 comparison are referred to as \bar{g}_A^{CVC} , the control results based on the combined spectrum of all detectors are denoted as \tilde{g}_A^{CVC} . Similarly to the previously discussed systematics listed in Tab. 8.11, it turns out that the variation of the energy calibration is the dominating one, followed by the limitation of the analysis threshold and the z -cut selection.

model parameter	uncertainty [%]					
	ISM		MQPM		IBFM-2	
	\bar{g}_A^{CVC}	\tilde{g}_A^{CVC}	\bar{g}_A^{CVC}	\tilde{g}_A^{CVC}	\bar{g}_A^{CVC}	\tilde{g}_A^{CVC}
template interpolation	0.001	0.001	0.001	0.001	0.001	0.001
detector response $\varepsilon_{\text{det}}(E)$	0.044	0.046	0.044	0.043	0.125	0.124
resolution FWHM(E)	0.159	0.197	0.150	0.187	0.438	0.467
energy calibration	5.248	9.240	4.811	6.822	14.312	20.993
analysis threshold	2.601	4.240	2.842	4.431	0.739	3.082
z -cut selection	1.626	0.700	1.494	0.645	4.581	2.135
χ^2_{red} fit range	0.002	0.002	0.003	0.002	0.003	0.002
background modeling	0.063	0.062	0.038	0.038	0.568	0.556
total	6.081	10.192	5.786	8.162	15.064	21.338

Due to the preliminary nature of the template predictions using the SSM based on the CVC breakthrough, it might be that changes on the theory level will affect the systematic effects in a significant way. That is why the results presented in this section have to be labeled as preliminary as well. The relative composition of the total systematic uncertainties changed only marginally and follows the same trend as reported in section 8.3.11. The variation of the energy calibration scale turns out to be the dominant contribution for all models, followed by the analysis threshold and the z -cut selection.

Finally, the default results of the spectrum-shape analysis following the weighted means $\bar{g}_A^{\text{CVC}} \pm \sigma_{\text{sys}}^{\text{CVC}}$ as reported in Eqn. (8.35)–(8.37), including the total systematic uncertainties, can be used to illustrate once more the allowed ^{113}Cd spectrum range for all three nuclear models. Again, an interpolation of the original template calculations has been used for this. While the overall behavior of the resulting spectrum-shapes is very similar for the previous results shown in Fig. 8.29 in case of the ISM and IBFM-2, there is a completely different trend at low energies for the MQPM. In fact, the spectrum-shapes agree now perfectly for all three models considering their associated experimental uncertainties under the SSM and CVC hypothesis. Even though the overall uncertainties have increased by about five times, the effect is not as dramatic for the respective ranges of the allowed spectrum-shape. Especially the new results evaluated in the context of the ISM and MQPM turn out to be almost identically. Nonetheless, a lower experimental threshold would be beneficial in a future follow-up campaign.

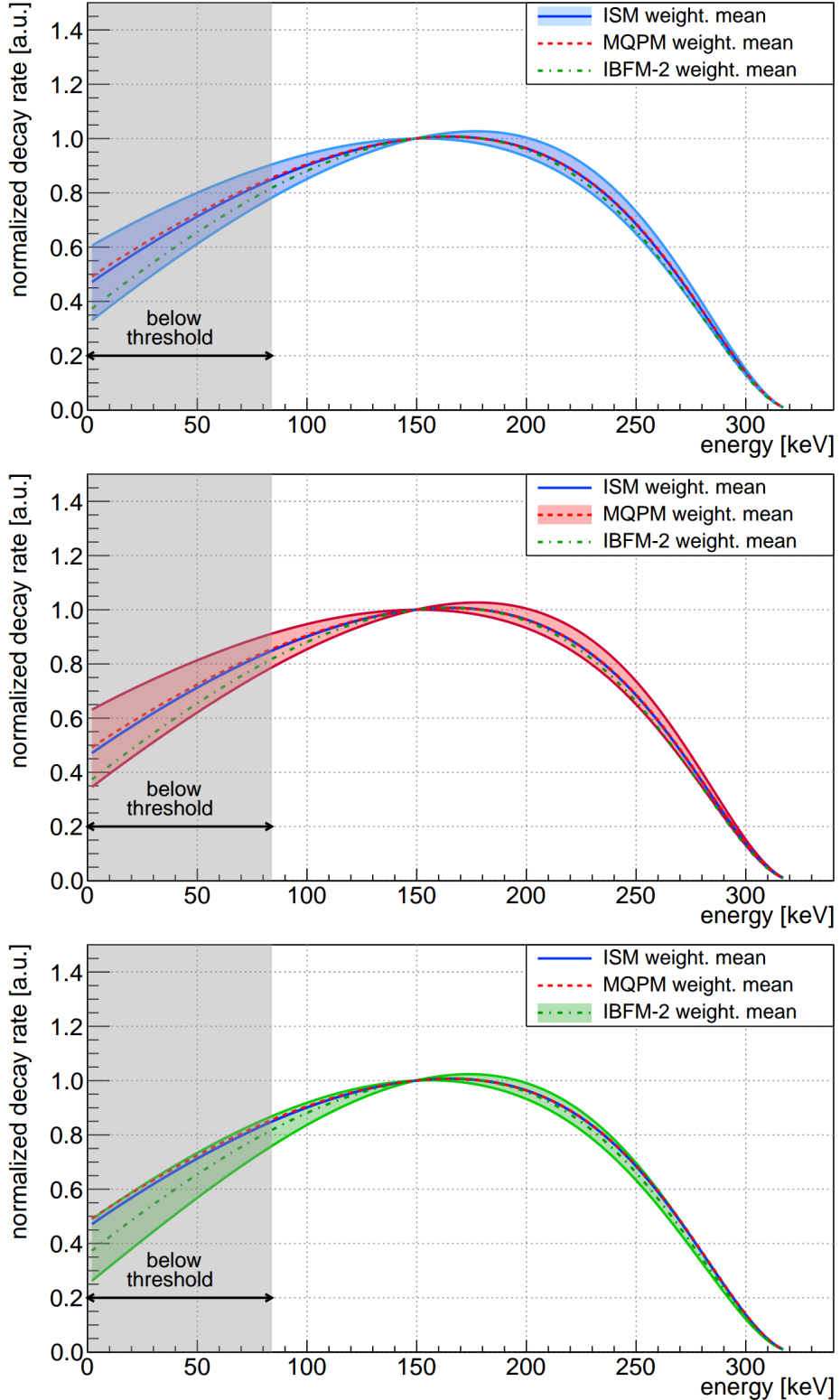


Figure 8.33: Allowed spectrum range for the ^{113}Cd β -decay according to the spectrum-shape results under the CVC hypothesis. *Top:* ISM. *Middle:* MQPM. *Bottom:* IBFM-2. The spline interpolation technique was used to construct template spectra for $\bar{g}_A \pm \bar{\sigma}_{\text{sys}}$ from the originally provided theoretical templates including the experimental uncertainties for each model. For comparison the templates corresponding to the weighted means are shown in each graph for the respective other models.

In conclusion, the preliminary spectrum-shape analysis performed for the most recent implementation of the SSM under the conserved vector current hypothesis leads to first promising results. Both sets of average g_A values – the weighted means of the single detector results Eqn. (8.35) – (8.37) and the combined analysis results according to Eqn. (8.38) – (8.40) – agree well with each other considering the total systematic uncertainties. Besides some tensions that are present for the comparison of the previous IBFM-2 results with the update under the CVC hypothesis, the two analyses are found to be compatible on the 1σ level. Although this agreement is mainly due to the increase of the overall uncertainties, the results of the SSM under the CVC hypothesis should still be seen as a major improvement in the study of g_A quenching in low-momentum exchange processes. The reasoning behind this statement will be clarified in the last section dedicated to the ^{113}Cd analysis.

8.3.13 Half-life determination via the SSM

As discussed in the introduction to the spectrum-shape method in section 8.3.1, one of the critical shortcomings of the approach is the observed mismatch between the predicted ^{113}Cd half-life considering a quenching of the weak axial-vector coupling and the respective deviation from its free value of $g_A^{\text{free}} = 1.276(4)$ [UCN10]. The nuclear model calculations used for the prediction of the ^{113}Cd templates as the basis of the SSM failed to produce consistent results in the past. This issue has already been pointed out in the original reference [HKS17] of the SSM and is depicted in Fig. 8.12 of section 8.3.1. Using today’s most precise ^{113}Cd half-life measurement of Ref. [BBB⁺07], quoting $T_{1/2} = (8.04 \pm 0.05) \times 10^{15}$ yr, as a literature reference, it is only possible to reproduce the experimental half-life for $g_A \lesssim 0.6$ or for the case of $g_A \approx g_A^{\text{free}}$ with the ISM and MQPM. Moreover, the IBFM-2 fails to reproduce the reference half-life for any $g_A \in [0.6, 1.4]$ by more than a factor of four.

However, under the CVC hypothesis it is possible to tune the NMEs with the objective to reproduce the ^{113}Cd reference half-life for consistent effective values of g_A . The general procedure behind the CVC approach has been pointed out in the previous section. Based on the constrained nuclear models, an updated correlation between the ^{113}Cd half-life and the effective value of g_A has been obtained by the group of J. Suhonen *et al.* and has been provided to the COBRA collaboration. The predicted correlation is provided in form of data pairs covering the extended g_A range from 0.6 to 1.4 in steps of $\Delta g_A = 0.02$. An illustration of the predicted half-life in dependence on the effective g_A for all three nuclear models is shown in Fig. 8.34.

In contrast to Fig. 8.12, showing the original correlation between the ^{113}Cd half-life and g_A , the new correlation turns out to be unambiguously in the sense that for $g_A > 0.7$ there is only a single g_A pointing to a unique $T_{1/2}$ for each of the models and vice versa. Before that, a predicted half-life was pointing almost always to two separate effective g_A values (see Fig. 8.12). Only for the MQPM there is a small range of $0.6 < g_A < 0.7$ for which the new correlation reproduces the predicted half-life for multiple effective g_A . For higher values of g_A close the free one, the correlation gets rather flat for all models, whereby the IBFM-2 prediction seems to be repeatedly less sensitive to g_A in general.

The discrete data points of the correlation can be analytically described using once more the *TSpline3* class of ROOT to access arbitrary half-life values in the given range by evaluating the spline $T_{1/2}(g_A)$ for a certain g_A . Again the argument applies, that $T_{1/2}(g_A)$ contains per definition the original data points forming the knots of the spline and that no optimization algorithm is involved in the spline’s construction. It is based on the boundary conditions presented in Eqn. (8.13) – (8.15). A more detailed description of the spline interpolation can be found in section 8.3.8.

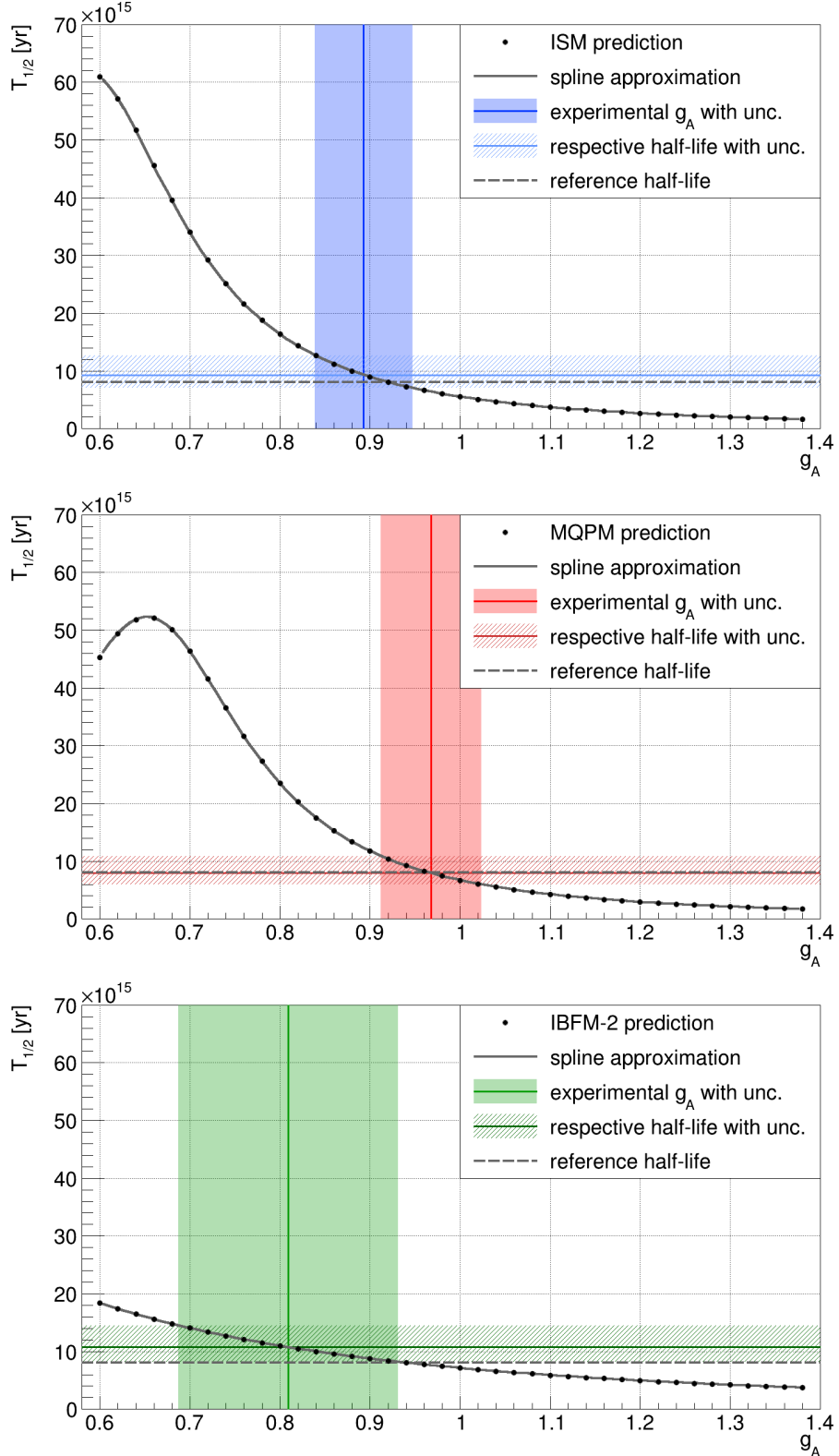


Figure 8.34: Conversion of the experimental results $\bar{g}_A^{\text{cvc}} \pm \bar{\sigma}_{\text{sys}}^{\text{cvc}}$ into the corresponding half-life range following the SSM prediction under the improved CVC hypothesis. *Top:* ISM. *Middle:* MQPM. *Bottom:* IBFM-2. All three nuclear model results are consistent with the reference half-life of $(8.04 \pm 0.05) \times 10^{15}$ yr [BBB⁺07] considering the uncertainty following from the average g_A results presented in Eqn. (8.35)–(8.37).

With the spline approximation it is possible to convert the experimental \bar{g}_A^{CVC} results Eqn. (8.35) – (8.37), following the single detector spectrum-shape analysis under the CVC hypothesis, into a respective half-life range (see Fig. 8.34). Even though the precision of the SSM is reduced under the CVC hypothesis, the resulting bounds on $T_{1/2}$ turn out to be consistent for the three nuclear models and cover the reference half-life quoted before. As the NMEs of the MQPM were tuned to reproduce the exact same reference half-life, the achieved perfect match is not so much of an surprise, but can be seen as an indication for the reliability of the developed spectrum-shape analysis. Finally, using the symmetric uncertainties $\sigma_{\text{sys}}^{\text{CVC}}$ assigned to the weighted mean values \bar{g}_A^{CVC} , the corresponding half-lives in Eqn. (8.44) – (8.46) can be deduced from Fig. 8.34.

$$T_{1/2}(\text{ISM}) = 9.3_{-2.3}^{+3.4} \times 10^{15} \text{ yr}, \quad (8.44)$$

$$T_{1/2}(\text{MQPM}) = 7.9_{-2.0}^{+3.0} \times 10^{15} \text{ yr}, \quad (8.45)$$

$$T_{1/2}(\text{IBFM-2}) = 10.7_{-2.5}^{+3.8} \times 10^{15} \text{ yr}. \quad (8.46)$$

Due to the shape of the predicted $T_{1/2}(\bar{g}_A^{\text{CVC}})$ correlation, the assigned uncertainties are not symmetric around the central value and turn out to be less restrictive for higher rather than lower values. In relative units, the half-life uncertainties are on the order of $\sim 30\%$ for all models. An improvement in the experimental determination of g_A would directly affect the achievable precision of the half-life conversion with the current procedure. As mentioned before, the largest contribution to the systematic uncertainty on the average g_A values arise from the particularly conservative variation of the energy calibration scale and the arbitrarily increased analysis threshold. While the same relative composition of the total systematic uncertainties on the experimentally determined g_A values has been found for the original SSM predictions, their increase by about five times comparing Tab. 8.11 and Tab. 8.12 hints to some unresolved issues. As essentially the same data has been used in both analyses, it is more probable to assume that the uncertainty increase originates from the rather dramatic changes of the nuclear model predictions. Even though the corresponding $\chi^2(g_A^{\text{CVC}})$ curves turn out to contain only one global minimum for each model, which is a preferable and more conclusive result of the spectrum-shape analysis, they turn out to be less localized. This allows for much more variation of the analysis results based on the location of the minimum, even for only small changes of the input parameters.

Conclusion and outlook

However, the current status of the SSM is an impressive step towards resolving the main shortcomings and theoretical issues related to the details of the description of strongly forbidden beta decays such as ${}^{113}\text{Cd}$ following from first principles. It should be mentioned that the SSM can be also used to predict the electron momentum distribution for several other nuclear transitions. For a recent compilation regarding the experimental confirmation of g_A quenching in weak interactions and an overview over potentially interesting nuclear decays see Ref. [ESZ19]. Among the list of nuclear decays are non-unique as well as unique transitions up to an angular momentum exchange of $\Delta J = 4$, for which the effect of an effectively quenched g_A is expected to be the most prominent.

The only other known candidate available for the investigation of a fourfold forbidden non-unique β -decay ($\Delta J^\pi = 4^+$) is the decay branch of ${}^{115}\text{In}(9/2^+) \rightarrow {}^{115}\text{Sn}(1/2^+)$ with a Q -value of $Q_\beta = 497.489 \pm 0.010 \text{ keV}$ [AME17] and a half-life of $(4.41 \pm 0.25) \times 10^{14} \text{ yr}$ [NDS20]. Compared to the present case of ${}^{113}\text{Cd}$, the half-life of ${}^{115}\text{In}$ turns out to be 20 times lower while the Q -value is about 1.6 times higher, reducing the need to reach ultra-low thresholds and background conditions. Moreover, the natural abundance of ${}^{115}\text{In}$ is

found to be 95.719(52)% [IUP16], which is much higher than the natural ^{113}Cd abundance of 12.227(7)% [IUP16]. This makes the highly forbidden β -decay of ^{115}In a perfect follow-up candidate for the SSM to confirm the quenching of g_A independently.

Recently, a group from the MIT (U.S.), CSNSM (France) and the university of Jyväskylä (Finland) started a collaborative effort to investigate the β -decay of ^{115}In . The analysis is assumed to be based on the methods developed in the course of this thesis and the related COBRA publication [COB20]. First results have been shown at several conferences (e.g. [Suh19]) but so far there is no journal publication of the involved groups explaining the experimental details and possible challenges of the study of ^{115}In . However, the preliminary results seem to be consistent with an effective value of $g_A \approx 0.9$, if the data is evaluated in the context of the same three nuclear models as done for ^{113}Cd .

Any additional experimental input helps to constrain the related model spaces and their specific assumptions in the NME calculations and might trigger similarly positive developments as achieved by improving the conserved vector current hypothesis, at least in the case of predicting the half-life of ^{113}Cd for a matching g_A range. Furthermore, dedicated studies help to strengthen the acceptance of the approach in the nuclear physics community and might ultimately lead to an universal theoretical framework to predict the spectrum-shapes and half-lives for rare nuclear decays involving also the various modes of double beta decays.

In the mean time, the mass dependence of the quenching of the weak axial-vector coupling could be investigated by studying nuclear transitions of suitable light ($A < 100$) and heavy nuclei ($A > 200$). This could help to gather more information about the involved processes on the nucleon level and to obtain deeper insights into the different kinds of nuclear medium effects (see the review [Suh17]). The only candidate for the heavy mass range is found to be the onefold forbidden unique β -decay of ^{210}Bi [ESZ19] with $Q_\beta = 1161.2 \pm 0.8$ [AME17] and a rather short half-life of only five days [NDS20]. In this case, the short half-life requires to produce an active ^{210}Bi sample via e.g. neutron capture reactions on natural bismuth. According to its isotopic composition, there is almost only ^{209}Bi present in natural bismuth despite traces of other isotopes. Recently, the spectrum-shape of the ^{210}Bi β -decay has been measured with high precision at TUD in the course of the PhD thesis of J. Thurn [Thu20] using Passivated Implanted Planar Silicon (PIPS) detectors. Those detector are specifically developed for β -spectroscopy and offer a good energy resolution. An analysis based on the SSM and the methods presented in the previous sections is currently ongoing and will be published in a scientific journal in the near future.

One important issue, that might not have been addressed appropriately in the past, is that the comparison of a theory prediction and an experimental result requires to take into account detector effects and the experiment's systematics. This can either be achieved by unfolding the data or, as has been done in the course of this thesis, by folding the prediction with the respective detector response, which is usually the easier approach. The unfolding procedure has the advantage that the experimental results between several experiments could be compared directly to each other and that they could be used as input for e.g. Monte-Carlo generators on the truth level. However, the approach followed by the COBRA collaboration also leads to a result on the truth level by projecting the experimental uncertainty onto the original theory input. In the end the preferred analysis procedure, whether to unfold the data or to incorporate detector effects into the prediction, depends also on the cooperation between the theory and the experimental side. However, the ongoing follow-up studies of several groups, targeting ^{115}In and ^{210}Bi , are expected to rely on some degree on the successful analysis procedure presented in this thesis and the related article [COB20].

8.4 Conventional double beta decay of ^{116}Cd

The following section is an update on the analysis results presented in the Master thesis of J. Küttler [Küt19] for the conventional $2\nu\beta\beta$ -decay of ^{116}Cd into the ground-state of ^{116}Sn . The improvements achieved since then comprise an automation of the developed data partitioning, the application of the calibrated $(A/E)_{90\%}$ selection as well as the availability of the full exposure of the COBRA demonstrator array.

In the previous thesis, only the physics data between Sept.'11 and Sept.'16 were fully evaluated and could be analyzed. Moreover, there was only a preliminary implementation of the A/E criterion in the processing tool MAnTiCORE and no support of the A/E calibration by the CouchDB database, which is a central element of the whole data processing chain (see section 8.1.3). After finalizing the implementation of the A/E criterion into all platforms, a reevaluation of all 56 calibration runs was performed to optimize the $(A/E)_{90\%}$ selection on the detector level as discussed in section 7.2.4. Before the key concepts and improvements of the ^{116}Cd $2\nu\beta\beta$ -decay sensitivity study will be discussed, a brief overview of past experiments on this subject is given in the next section.

8.4.1 Previous experiments

In the past 25 years there have been multiple experiments searching for the $0\nu\beta\beta$ -decay of ^{116}Cd and were able to determine the half-life of its $2\nu\beta\beta$ -decay mode. An overview is given in Tab. 8.13 with emphasis on the $T_{1/2}^{2\nu}$ results.

Table 8.13: Overview of previous experiments to determine the $2\nu\beta\beta$ -decay half-life of ^{116}Cd (adapted from [Aur18]). Two main experimental approaches have been followed in the past: enriched ^{116}Cd -foils surrounded by tracking calorimeters (ELEGANT V, NEMO-2, NEMO-3) and enriched $^{116}\text{CdWO}_4$ crystal scintillators (Solotvina, Aurora). The uncertainties on $T_{1/2}^{2\nu}$ could be reduced with each new generation of experiments.

experiment	detection approach	$T_{1/2}^{2\nu} [10^{19} \text{ yr}]$	reference
ELEGANT V	^{116}Cd -foils, drift chambers, plastic scintillators	$2.6^{+0.9}_{-0.5}$	[EFH ⁺ 95]
Solotvina	$^{116}\text{CdWO}_4$ scintillators	$2.7^{+0.5}_{-0.4} (\text{stat})^{+0.9}_{-0.6} (\text{sys})$	[DGK ⁺ 95]
		$2.6 \pm 0.1 (\text{stat})^{+0.7}_{-0.4} (\text{sys})$	[DGK ⁺ 00]
NEMO-2	^{116}Cd -foils, Geiger cells for track reconstruction	$2.9 \pm 0.06 (\text{stat})^{+0.4}_{-0.3} (\text{sys})$	[DGK ⁺ 03]
NEMO-3	same as NEMO-2	$3.75 \pm 0.35 (\text{stat}) \pm 0.21 (\text{sys})$	[NEM96]
Aurora	$^{116}\text{CdWO}_4$ scintillators	$2.9 \pm 0.3 (\text{stat}) \pm 0.2 (\text{sys})$	[Bar10]
		$2.74 \pm 0.04 (\text{stat}) \pm 0.18 (\text{sys})$	[NEM17a]
		$2.63 \pm 0.01 (\text{stat})^{+0.11}_{-0.12} (\text{sys})$	[Aur18]

The first experimental approach followed by the ELEGANT V and NEMO-2 experiments involves enriched ^{116}Cd -foils that were placed inside a tracking calorimeter. The same procedure has been applied in one of the direct successor experiment, referred to as NEMO-3. A second group of experiments, consisting of multiple stages at the Solotvina underground laboratory and a follow-up experiment at the LNGS, is based on enriched $^{116}\text{CdWO}_4$ crystal scintillators. A quite similar approach has been already discussed in section 8.3.2 for the study of the ^{113}Cd β -decay with a natural CdWO_4 crystal. In fact, the so-called Aurora experiment has been performed in the same low-background DAMA/R&D setup at the LNGS.

However, an observation of the $2\nu\beta\beta$ -decay of ^{116}Cd by COBRA would be the first measurement using semiconductor detectors and could verify previous results based on different detection techniques. Moreover, a high precision measurement of the spectrum-shape allows

for an investigation of alternative decay scenarios involving so-called Majoron emission modes (see e.g. Ref. [GER15b] and [Aur18]). In case of such more exotic models, a distortion of the continuous $2\nu\beta\beta$ -spectrum is predicted, which might be challenging to be observed for scintillator based experiments due to their limited energy resolution.

A comparison of the previous $2\nu\beta\beta$ -decay half-life measurements for ^{116}Cd and their uncertainties is depicted in Fig. 8.35. The most precise measurements have been performed by the NEMO-3 and the Aurora experiment (see also Tab. 8.13). Although applying fundamentally different experimental techniques, the results turn out to be completely consistent. One way to compare the two experiments is to point out their immanent advantages and disadvantages. At first, the achieved isotopic exposure can be considered, which is the exposure scaled to the amount of deployed ^{116}Cd and usually determines the statistical uncertainty. While the NEMO-3 experiment accumulated about 2.16 kg yr of isotopic exposure – twice as much compared to Aurora with 0.91 kg yr – its total signal acceptance is rather poor and estimated with only 1.8% [NEM17a]. On the other hand, the Aurora experiment reports a signal efficiency of about 98.4% after all analysis cuts, which is mainly due to the chosen source-equals-detector approach. The product of the isotopic exposure and signal efficiency corresponds to about 5 k events for the entire $2\nu\beta\beta$ -spectrum range in case of NEMO-3 and about 126 k events for Aurora. In terms of the achievable statistics, the COBRA demonstrator is somewhat comparable to NEMO-3 and is expected to produce a ^{116}Cd $2\nu\beta\beta$ -decay rate of about $3.65 \cdot 10^3$ cts/(kg yr) as estimated in [Küt19].

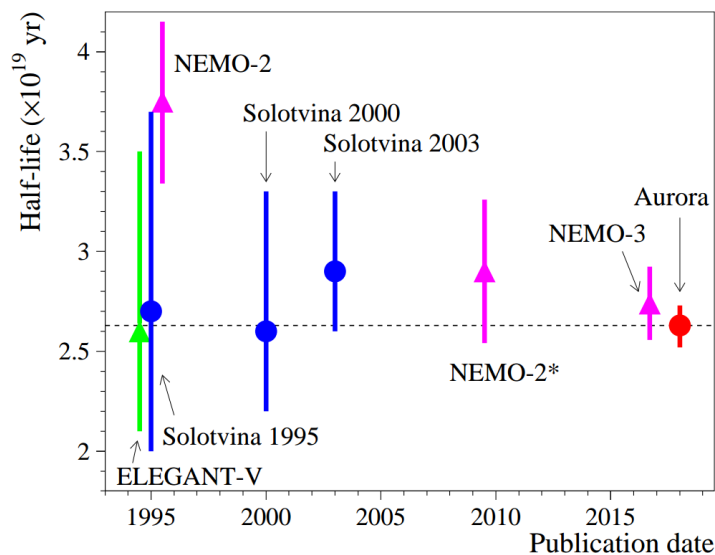


Figure 8.35: Comparison of experimentally determined half-lives for the $2\nu\beta\beta$ -decay of ^{116}Cd (adapted from [Aur18]). The originally reported half-life of the NEMO-2 experiment has been re-estimated in 2010, resolving the tension with previous and follow-up experiments. The most precise measurement has been achieved by the Aurora experiment using isotopically enriched $^{116}\text{CdW}_4$ crystal scintillators.

However, one of the main advantages of the NEMO-3 experiment is its tracking capability, which allows for an unprecedented background reduction. In the latest publication listed in Tab. 8.13 a signal-to-background ratio of $S/B \sim 12$ is quoted for NEMO-3, while Aurora achieves $S/B \sim 1.5$ in comparison. Both experiments developed a detailed Monte-Carlo background model to estimate their residual backgrounds. In contrast to this, most of the other past studies listed in Tab. 8.13 and Fig. 8.35 feature a simplified analysis procedure. Nonetheless, after an adjustment of the originally reported NEMO-2 half-life [Bar10] there is an agreement of all past experiments within their quoted total uncertainties on the 1σ level.

8.4.2 Data partitioning and event selection

The main motivation for a partitioning of the data is the observed correlation between an increase of the average decay rate and the humidity level inside the inner shield, which acts as a monitor for the nitrogen flushing (see Fig. D.9 in the appendix). Without the nitrogen flushing, radon is more likely to able to diffuse into the shield, leading to a prompt background contribution induced by the ^{222}Rn decay chain (see section 8.2.3 and 8.2.4). By identifying and removing those so-called high-rate periods (HRPs), an effective background reduction can be achieved. Moreover, the background-enriched periods might be useful in the future modeling of the radon-related background contribution, especially with emphasis on the long-lived α -decay of ^{210}Po .

The preliminary results presented in [Küt19], based on about 400 kg d of exposure from the demonstrator array, triggered a careful revision of the raw data, which culminated in the pre-selection routine as discussed in section 8.1.1 (see also Tab. 8.2). This measure greatly reduces the occurrence of very short HRPs of single channels, with typical timescales of the order of the duration of a single run of 4 h. These were found to be the most problematic periods to be identified with the methods developed in the previous thesis. The reason is keyed to the problem of defining a meaningful expected rate in order to decide whether a data period should be considered in the analysis without introducing a strong bias. As pointed out before in section 8.1.1, the trigger rate is optimized based on the expected ^{113}Cd decay rate per channel. However, a change of the thresholds also changes the expected decay rate, thus, there is no fixed average expected rate over the complete lifetime of the experiment. Moreover, because of the typical threshold differences between the detectors, there is usually no universal expectation for the individual channels during the same physics run (PR). In fact, for some PRs the thresholds had to be pushed above the ^{113}Cd Q -value for a few channels in order to maintain a reasonably low trigger rate. Above the ^{113}Cd energy region, the typical trigger rate decreases by more than two orders of magnitude, which requires an integration over the time scale of several days to reach sufficient statistics. However, this comes with the danger of averaging out the effect of very short HRPs and has to be optimized.

All in all, that is why the originally anticipated automation of the identification of suspicious data periods turned out to be challenging and could only be resolved recently in the course of the present work. Nevertheless, the methods and tools developed in the first collaborative effort could be used as a starting point. The evolution of the observed data rate for the 64 detectors of the COBRA demonstrator array is depicted in Fig. 8.36 for subsequently more restrictive event selections.

Following the original procedure and the aim to improve the sensitivity for the $2\nu\beta\beta$ -decay of ^{116}Cd , the data partitioning is based on the standard event selection including the DCCs, the standard z -cut according to $0.2 < z \leq 0.97$ and the weak FADC coincidence cut. The cathode z -cut removes the remaining single detector HRPs after the pre-selection of the raw data as shown in Fig. 8.36. In a next step, the energy range is limited to $350\text{ keV} < E < 2800\text{ keV}$, excluding the ^{113}Cd region, which leaves the necessity to integrate over a certain time scale to reach sufficient statistics. The shortest reasonable integration window with respect to the low statistics is found to be two days for the single detector rates and half a day for the combination of all detectors. The previously reported risk of averaging out short-term HRPs of single channels could be resolved by applying the pre-selection on the raw data level before performing the data partitioning.

The actual algorithm to identify short HRPs, caused by a failure of the nitrogen flushing, is based on the combined rate of all detectors as the projection of Fig. 8.36 in units of half a day. Moreover, an average critical rate R_{crit} is calculated separately for each period in between two data-taking interruptions, indicating calibration measurements or a switch-off

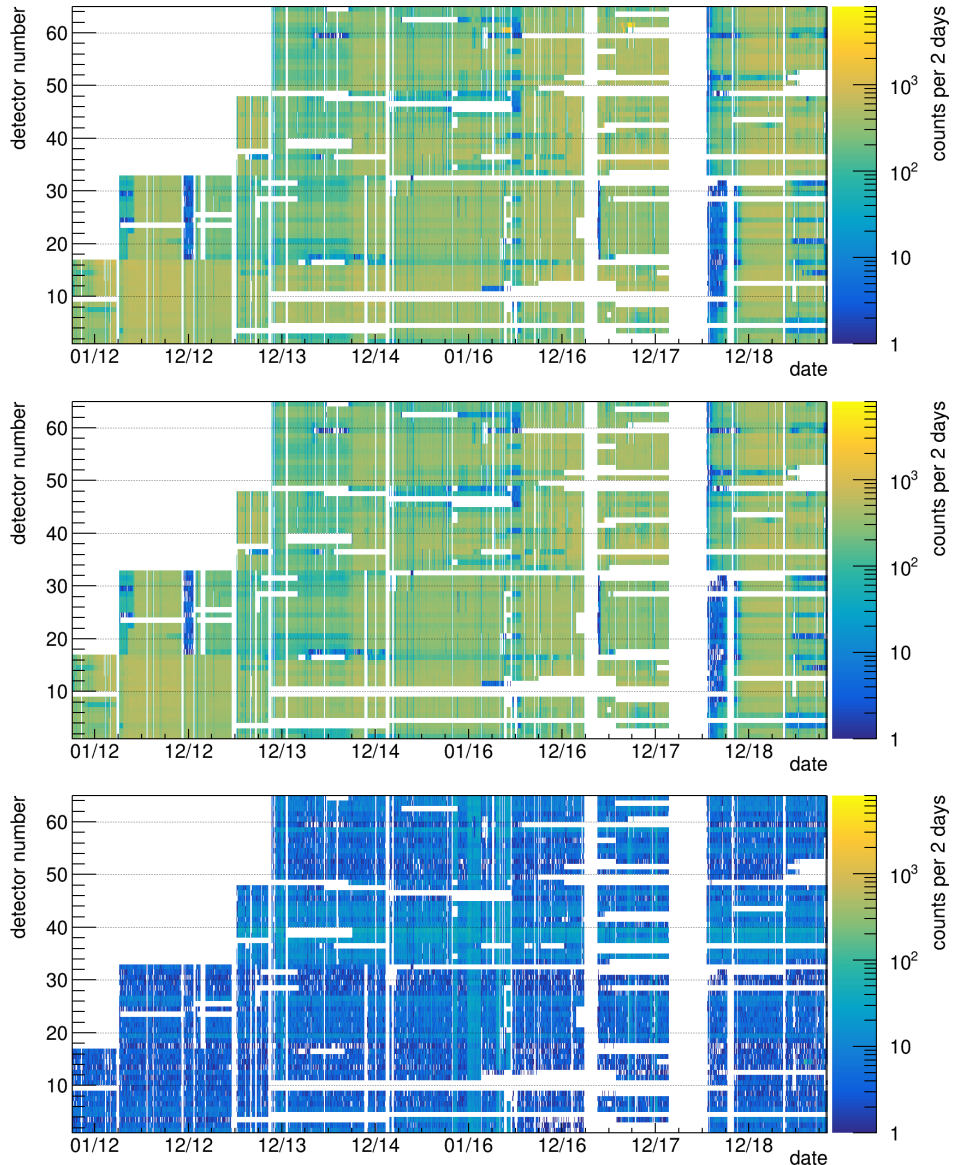


Figure 8.36: Evolution of the observed data rate for the COBRA demonstrator over the lifetime of the experiment (updated versions of the illustrations in [Küt19]). The rate is encoded in color and shown for each detector (1–64) separately. In the beginning, the successive installation of the detector layers can be seen. Horizontal white spaces indicate whether a detector has been disabled temporarily, while vertical ones indicate offline periods of the complete detector array (see also Fig. 8.3). *Top:* full data including the standard event selection (DCCs + low- z cut + FADC coincidence). The observed rate is dominated by the ^{113}Cd β -decay. *Middle:* application of the additional cathode z -cut. The stricter z -cut removes the short-term high-rate periods (HRPs) observed for Det60 (L4-P12) and Det61 (L4-P13). *Bottom:* application of an additional energy restriction according to $350\text{ keV} < E < 2800\text{ keV}$. This limits the energy range to the expected region of the $2\nu\beta\beta$ -decay of ^{116}Cd . The projection of the multi-dimensional display is used to identify global HRPs, high-rate detectors (HRDs) and, respectively, medium-rate detectors (MRDs).

of the experiment to perform maintenance tasks (see also Fig. 8.3 in section 8.1.4). This way, instead of using a fixed R_{crit} for all PRs, which usually differ in the number of active detectors and their trigger thresholds, a much more elaborate treatment can be performed. If the rate associated to a certain unix timestamp is found to be higher than two times the corresponding R_{crit} for more than two consecutive timestamps, it gets flagged as the start of a HRP. As soon as the rate falls again below R_{crit} , the end of the current HRP is assumed to be reached.

As an additional conservative measure, an offset of ± 0.5 days is added to the start and end of a HRP timestamp. The same procedure is repeated for the average rate per layer and the single detector rates to provide a crosscheck for potential localized origins of the sudden rate increase. While in principle it should be possible to perform an additional crosscheck by comparing the HRPs timestamps with the data of the humidity sensors monitoring the nitrogen flow, there are periods for which the sensor data is not available. Nonetheless, if the sensor data is available, it might provide additional information that could be used in a future iteration of the automated data partitioning. The conservatively defined offset of ± 0.5 days is expected to prevent an underestimation of a HRP’s duration. The time scale of half a day is found to be sufficient to reach the minimum humidity level in case the nitrogen flow could be restored after a failure of the system.

In the end, the flagging algorithm removes 250 d of live-time, corresponding to about 9% of the total live-time in relative terms. Another 435.5 d are labeled as downtime, which is mainly caused by the period before the dedicated ^{113}Cd data-taking run and the shutdown of the demonstrator after the upgrade to COBRA XDEM. Besides the global HRPs, where all detectors feature an increased rate because of a failure of the nitrogen flushing, there are only three more exceptional periods. The first concerns the initial data of the third layer, as pointed out before in section 8.1.4. The other two are triggered by Det14 (L1-P14) and Det47 (L3-P15). Both detectors feature a temporary high- z peak in their interaction depth spectra similar to the examples reported for the ^{113}Cd run (see Fig. D.20 in the appendix). Those single detector periods are also included into the final HRP partition.

Compared to the previous work, the evaluation of the automatized routine reveals a great overlap with the semi-manual partitioning performed in [Küt19]. Moreover, it allows to extend the selection towards the full data set comprising about 1.5 times more data. The effect of the complete partitioning on the data of the COBRA demonstrator and its accumulated exposure is summarized in Tab. 8.14 and Fig. 8.37.

The first partitioning step related to the previously discussed HRPs removes the prompt γ -lines of the short-lived radon daughters ^{214}Pb and ^{214}Bi (see also Fig. 8.8 in section 8.2.3) and the high-energy part of the z -hump above 4 MeV. Furthermore, the high-energy cathode contaminations above the signal of ^{210}Po at $E_\alpha = 5.3$ MeV get strongly reduced (see e.g. Tab. 8.4 in section 8.2.4). In combination with the $(A/E)_{90\%}$ selection, a strong suppression of the remaining z -hump region can be achieved.

Besides the definition of the HRP partition, an even more restrictive measure includes the separation of single detectors with an overall increased background index (BI) compared to the average value (see also Fig. 8.36). In the present case the BI is calculated as the integral over the $0\nu\beta\beta$ -decay ROI of ^{116}Cd defined as $Q_{\beta\beta} \pm 300$ keV. At first, all detectors with $\text{BI} \gtrsim 10.0 \text{ cts}/(\text{keV kg yr})$ have been identified, which are referred to as HRDs (high-rate detectors) in the following and comprise the following detector numbers

$$\text{HRD : } 19, 34, 37, 38, 39, 43, 44, 54, 58, 62, 63, 64. \quad (8.47)$$

The HRD selection contains six detectors from L3 and five of L4, where the z -hump has been found to be most prominent (see e.g. Fig. 8.5). Secondly, another set of detectors with $\text{BI} \gtrsim 5.0 \text{ cts}/(\text{keV kg yr})$, referred to as MRDs (medium-rate detectors), can be defined. It contains the following detector numbers, additionally to the ones listed in Eqn. (8.47)

$$\text{MRD : } \text{HRD} + 12, 23, 25, 36, 40, 42, 46, 48, 50, 51, 61. \quad (8.48)$$

The final MRD selection according to Eqn. (8.48) contains one detector of L1, three of L2, eleven of L3 and eight of L4. This leaves 41 out of 64 detectors in the low-rate partition. The effect of the single partitioning steps and their combination on the exposure is shown

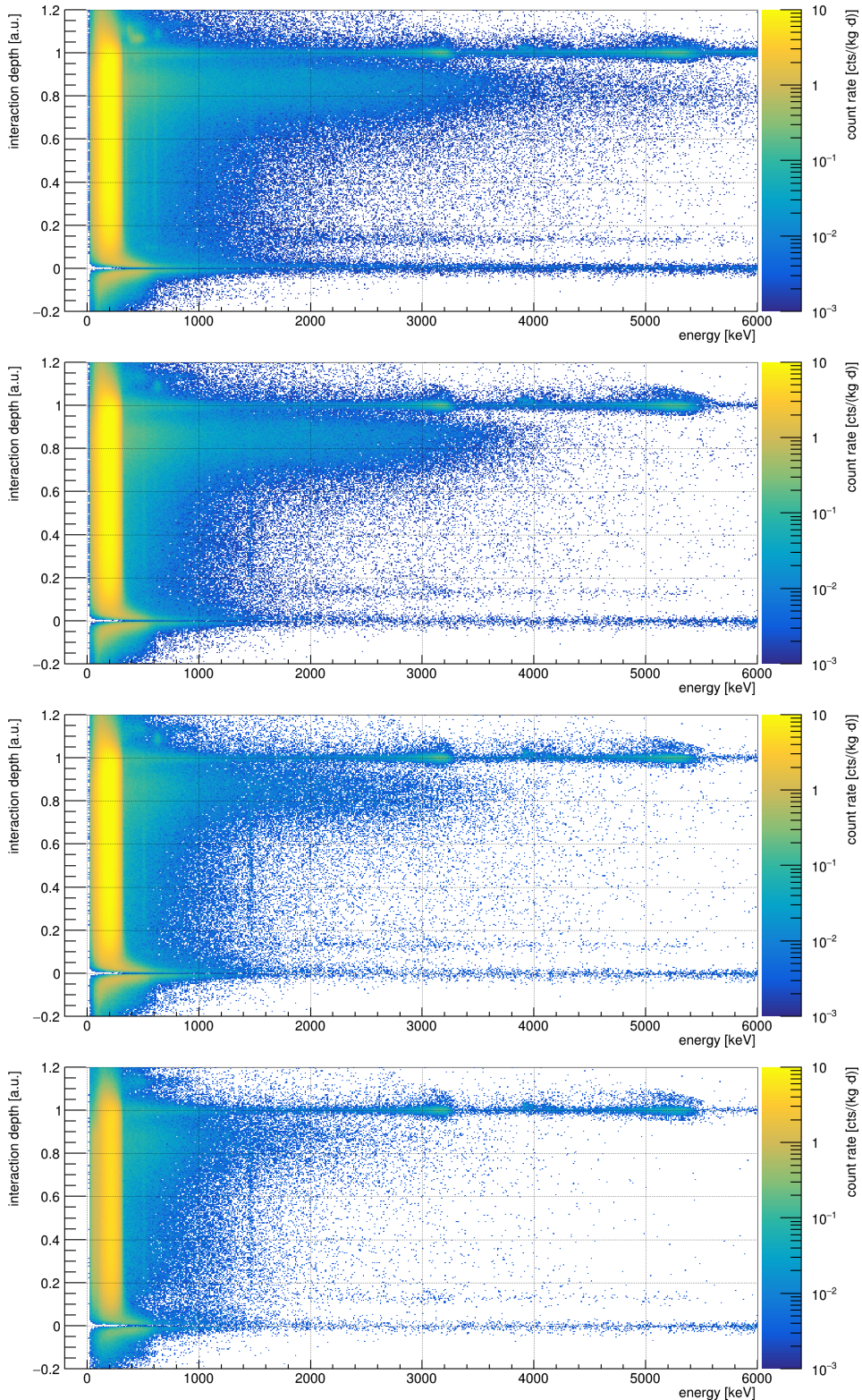


Figure 8.37: Combined effect of the data partitioning and the PSD event selection on the z -versus- E display of the physics data of the COBRA demonstrator. All plots include the DCCs and the FADC coincidence cut. *Top:* full data without partitioning. *Upper middle:* after HRP removal. *Lower middle:* after HRP removal and $(A/E)_{90\%}$ selection. *Bottom:* after HRP+MRD removal and $(A/E)_{90\%}$ selection. The range of the color-axis is the same for all plots and each has been normalized according to its exposure (see Tab. 8.14).

in Tab. 8.14. The most restrictive combination HRP+MRD reduces the total exposure by about 40.0%, while at the same time a significant reduction of the BI is achieved.

Table 8.14: Effect of the data partitioning on the exposure accumulated with the COBRA demonstrator. The HRP partition reduces the total exposure by about 11.7%, the HRD by 18.3% and the MRD by 32.6%, if applied individually. Because there is an overlap between the three categories, the combinations HRP+HRD and HRP+MRD result in an exposure loss of 27.6% and 40.0%, respectively.

selection	exposure after partitioning in kg d					
	none	HRP	HRD	MRD	HRP+HRD	HRP+MRD
L1	165.2	149.6	165.2	157.4	149.6	142.7
L2	176.6	157.3	164.3	142.7	146.4	127.4
L3	134.2	116.4	79.1	46.0	69.0	40.1
L4	128.2	110.0	85.2	61.3	72.8	52.3
total	604.2	533.3	493.9	407.4	437.7	362.4

The impact on the BI in the ^{116}Cd ROI with respect to the different partitions has been analyzed quantitatively. The results using the HRP and the combined HRP+MRD partition as well as several stages of the PSD selection are presented in Tab. 8.15. It should be pointed out that each BI is normalized by the exposure of its respective data partition. Because of this, the corresponding exposure loss as reported in Tab. 8.14 is already taken into account.

Table 8.15: Impact of the data partitioning and the PSD cuts on the ^{116}Cd background index achieved with the COBRA demonstrator. The PSD selections get stricter from left to right. All BIs are quoted after applying the standard cuts (DCCs + low- z cut + FADC coincidence). It has been determined as the integral over $Q_{\beta\beta} \pm 300$ keV for the respective detector and event selection. The strictest combination reduces the initial BI by more than two orders of magnitude, which already includes the exposure loss according to Tab. 8.14.

partitioning	background index [cts/(kg keV yr)]								
	none			w/o HRP			w/o HRP+MRD		
	selection	DCC	z -cut	A/E	DCC	z -cut	A/E	DCC	z -cut
L1	14.4	6.1	2.3	12.0	4.1	1.7	11.5	3.8	1.4
L2	19.9	11.1	1.9	17.0	8.6	1.3	12.6	4.5	0.7
L3	44.9	34.1	17.3	40.6	31.4	15.9	14.1	6.1	3.2
L4	38.1	30.0	9.8	29.3	22.8	7.0	20.6	15.5	1.2
total	27.5	18.6	7.0	23.0	15.1	5.7	13.3	6.0	1.3

As seen before, the highest background level without any partitioning is found for L3 followed by L4. Only after removing the HRP+MRD selection the BI is almost the same for all four layers. However, there seems to be an excess of events for L4 before applying the $(A/E)_{90\%}$ cut. The reason for this might be again the thinner encapsulation layer as mentioned before in section 8.2. The thinner encapsulation allows for a higher contribution of surface contaminations on the lateral detector walls, which turn out to be effectively reduced by the revised $(A/E)_{90\%}$ selection covering both MSEs and LSEs (see section 7.2.2).

With the finalization of the data partitioning, a comparison of the COBRA demonstrator’s physics data and a Monte-Carlo simulation of the $2\nu\beta\beta$ -decay of ^{116}Cd can be performed. The results will be discussed in the next section.

8.4.3 Comparison of LNGS data and MC simulation

An impression of the current sensitivity to observe the continuous $2\nu\beta\beta$ -spectrum of ^{116}Cd with the COBRA demonstrator is depicted in Fig. 8.38. The VENOM simulation of the expected spectrum-shape comprises 10^7 events and is based on the full detector geometry as introduced in section 5.3.3. The initial conditions of the decay kinematics were provided by the DECAY0 generator (see section 5.3.2).

In order to compare the MC spectrum with the final low-background partition of the data (HRP+MRD removed), it has to be first normalized to the detector units of cts/(kg keV yr) and, secondly, needs to be smeared according to the average energy resolution. The first step is done by applying the experimentally determined half-life of Ref. [Aur18] (see Tab. 8.13) and the average detector mass of 5.95 g to convert the number of simulated events into the corresponding exposure. The Gaussian resolution smearing follows the procedure presented in Eqn. (8.12) of section 8.3.7. Furthermore, the simulated spectrum is scaled according to the efficiency of the data selection, denoted as ε_{sel} , which differs for the four presented cases because of the applied PSD cuts. Lastly, the FADC coincidence cut, which has been applied for the data, is taken into account as well, whereas only coincidences between detectors of the same FADC are removed from the simulation.

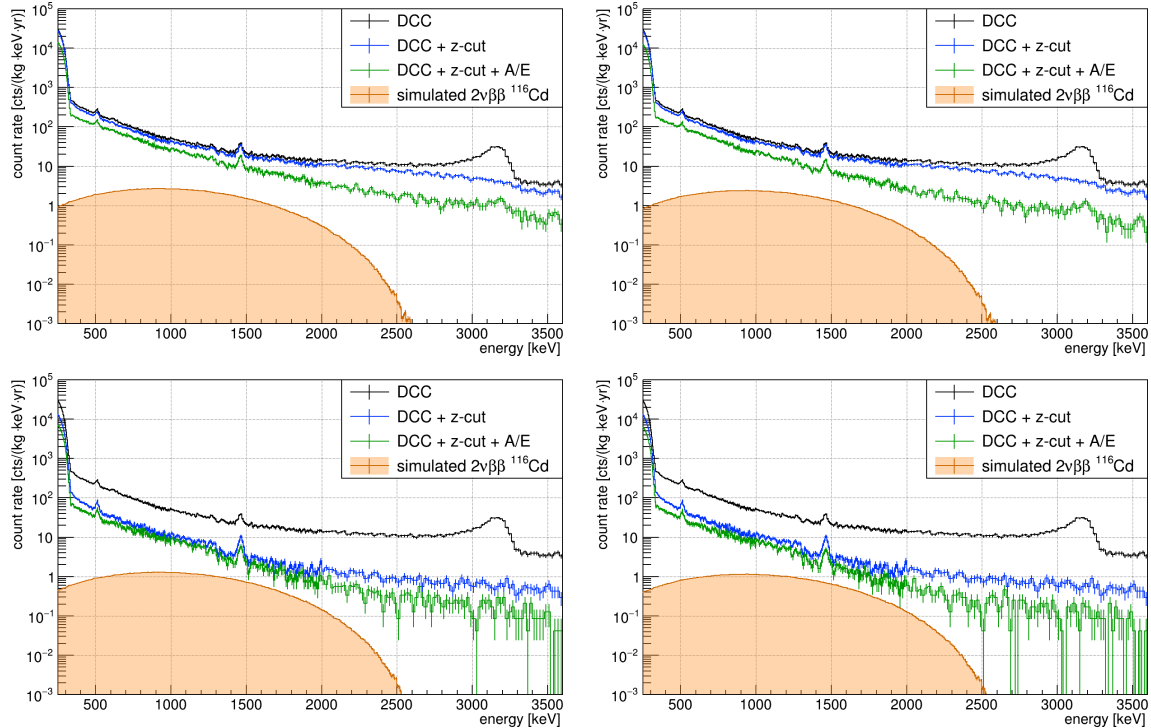


Figure 8.38: Comparison of the combined COBRA demonstrator data and the MC prediction for the $2\nu\beta\beta$ -decay of ^{116}Cd . The experimental spectra are based on the HRP+MRD partitioning and include the standard event selection (DCCs + low- z cut + FADC coincidence). Several combinations of cathode z -cuts and the A/E criterion are applied, whereas the MC spectra are scaled according to the combined signal acceptance ε_{sel} of the selection and a half-life of $T_{1/2}^{2\nu} = (2.63 \pm 0.12) \times 10^{19}$ yr [Aur18]. *Top left:* $0.2 < z \leq 0.97$, $(A/E)_{90\%} > 0.872$ and $\varepsilon_{\text{sel}} = 78.8\%$. *Top right:* $0.2 < z \leq 0.97$, $(A/E)_{80\%} > 0.916$ and $\varepsilon_{\text{sel}} = 70.0\%$. *Bottom left:* $0.2 < z \leq 0.6$, $(A/E)_{90\%} > 0.872$ and $\varepsilon_{\text{sel}} = 37.5\%$. *Bottom right:* $0.2 < z \leq 0.6$, $(A/E)_{80\%} > 0.916$ and $\varepsilon_{\text{sel}} = 33.4\%$.

For the first example selection depicted in Fig. 8.38, the standard z -cut with an efficiency of $\varepsilon_z = (87.52 \pm 0.07)\%$ (see Tab. 7.2 in section 7.1.2) and the $(A/E)_{90\%}$ cut is applied, leading to a total selection efficiency of $\varepsilon_{\text{sel}} = 78.8\%$. The other cases are combinations of a stricter A/E selection, denoted as $(A/E)_{80\%}$, and a stricter z -cut to remove the region of the z -hump.

The $(A/E)_{80\%}$ selection is motivated by the combined efficiency of the previous LSEs cuts of $\varepsilon_{\text{LSE}} = (76 \pm 2)\%$ [COB16a], but turns out to improve the situation only marginally. A much higher effect is achieved by applying a stricter depth selection of $0.2 < z \leq 0.6$, which reduces the signal acceptance to $\varepsilon_z = (41.70 \pm 0.05)\%$, following the procedure presented in section 7.1.2 based on the data of the dedicated ^{113}Cd run.

The results of a more quantitative sensitivity analysis are summarized in Tab. 8.16. It is based on a derived measure of the inverse signal-to-background ratio $(S/B)^{-1}$ for each of the four cases presented in Fig. 8.38. The signal counts follow from the integral of the MC spectrum, while the data result in $N_{\text{exp}} = S + B$. The highest sensitivity has been found for an integration window of $1500 - 2500$ keV. The lower edge avoids the ^{40}K line at 1460.8 keV, while the upper limit arises from the low signal rate close to $Q_{\beta\beta} = 2.8$ MeV of ^{116}Cd .

Table 8.16: Summary of the quantitative sensitivity study regarding the observation of the $2\nu\beta\beta$ -decay of ^{116}Cd with the COBRA demonstrator. Four combinations of two different z -cuts and A/E selections have been investigated. The results are presented as the inverse S/B ratio, with S being derived from the MC spectra and $N_{\text{exp}} = S + B$ from the experimental data. The integration of the respective spectra is done for $1500 - 2500$ keV. The stricter z -cut improves the inverse S/B ratio by about three times for the combined spectrum and results in similar values for all four layers. Due to the binning of the data, there are small variations comparing the sum of N_{exp} between the single layers and the total spectra results.

z -cut A/E	$0.2 < z \leq 0.97$				$0.2 < z \leq 0.6$			
	$(A/E)_{90\%}$		$(A/E)_{80\%}$		$(A/E)_{90\%}$		$(A/E)_{80\%}$	
	N_{exp}	$(S/B)^{-1}$	N_{exp}	$(S/B)^{-1}$	N_{exp}	$(S/B)^{-1}$	N_{exp}	$(S/B)^{-1}$
L1	1957	9.5	1560	8.4	348	2.9	275	2.5
L2	902	4.5	666	3.6	251	2.2	214	2.1
L3	830	14.2	621	11.8	88	2.4	81	2.5
L4	749	9.4	524	7.2	198	4.8	157	4.1
total	4363	8.1	3308	6.8	867	2.8	712	2.5

By applying the standard z -cut and the $(A/E)_{90\%}$ selection, L2 is found to have the highest sensitivity with respect to the determined $(S/B)^{-1}$. After the stricter z -cut, the first three layers show a similar sensitivity and result in $(S/B)^{-1} \sim 2.5$. In agreement with the impression following from Fig. 8.38, the stricter $(A/E)_{80\%}$ selection only has a small impact on the inverse S/B ratio. Moreover, it has been found that L4 features the worst $(S/B)^{-1}$ under the strictest combination, which again is likely due to the effect of the significantly thinner encapsulation layer as pointed out before.

In the end, the current evaluation of the full data set of the COBRA demonstrator confirms that the double beta ROI is dominated by more frequent background processes other than the $2\nu\beta\beta$ -decay of ^{116}Cd . However, the estimated $(S/B)^{-1} \lesssim 2.8$ of the combined spectrum could still allow for the determination of the decay's half-life given a background model to account for the main background contributions. Some concluding remarks and prospects will be given in the following section.

8.4.4 Concluding remarks

Although an independent determination of the $T_{1/2}^{2\nu}$ half-life of ^{116}Cd has not yet been successful with the current stage of the data evaluation of the COBRA demonstrator, there are good prospects to accomplish this by a more elaborate analysis. Most urgently, a background model is needed to constrain the residual background in a combined fit to the data including the well-understood ^{116}Cd $2\nu\beta\beta$ -decay MC template as a free parameter.

While the data partitioning has already been performed in a very conservative way, among other things by increasing the unix timestamps of HRPs by ± 0.5 days, the full PSD capabilities might not have been reached yet. Nevertheless, it could be investigated whether removing the initial data of each layer would turn out beneficial with respect to the long-lived contamination of ^{210}Po on the lateral detector sides (see section 8.2.4). An established contamination of ^{210}Po before the detector's installation at the LNGS would be expected to fade away according to its half-life of 138.4 days (see Tab. 8.4). This circumstance is currently not explicitly considered in the partitioning, except for the initial data of L3.

An improvement of the pulse-shape discrimination involves only the definition of the A/E criterion, because the alternative z -cut to remove the z -hump region is already exceedingly strict. In its current implementation the A/E selection is not only sensitive to MSEs, but expected to flag LSEs as well (see also section 7.1.3). However, the sensitivity to the LSEs might only be due to the ERT criterion of CA-side lateral surface events, which is expected to show a strong overlap with the A/E distribution of multi-site interactions. The second LSE criterion, referred to as DIP of the difference pulse below its baseline for NCA-side interactions, might not be flagged as efficiently by A/E . In fact, the sensitivity could be improved by including the minimum of the difference pulse's derivative in the cut definition. At the moment, only the maximum of the derivative, denoted as A , enters the definition of the A/E parameter. Thus, the effect of such a measure on the ^{208}Tl DEP's signal acceptance has not been studied in detail.

Furthermore, additional advanced analysis techniques could be applied to reduce the currently unaccounted background, especially due to true detector coincidences. Such a measure requires to synchronize the FADC's timestamps in the full data set, which is an ongoing effort at the time of this thesis. Besides coincidences at the timescale of the expected synchronization accuracy of about 0.1 ms [Vol18], being sensitive to prompt events such as γ -ray scattering across the array, it would allow for the investigation of delayed coincidences such as e.g. the $^{214}\text{Bi} - ^{214}\text{Po}$ sequence of the ^{222}Rn decay series. The particular example involves the β -decay of ^{214}Bi ($Q_\beta = 3.3$ MeV), which is followed by the α -decay of ^{214}Po ($Q_\alpha = 7.8$ MeV) with a half-life of only $164.3\ \mu\text{s}$ [NDS20]. As both decays might lead to an entry in the ROI of the $2\nu\beta\beta$ -decay of ^{116}Cd , e.g. because of the attenuation by the encapsulation, the time correlation provides an additional measure to reject $^{214}\text{Bi} - ^{214}\text{Po}$ coincidences. On the other hand, the misidentification of signal processes as delayed coincidences is very unlikely and should be a negligible effect.

Moreover, the synchronized FADC data open the door towards other double decay modes involving positron emission (e.g. $\beta^+\beta^+$ or EC/ β^+) or transitions via excited states, which are accompanied by a single or cascade of de-excitation photons. The latter subject will be discussed in the next analysis section. Finally, the study of coincidences might allow to refine the background model of the COBRA demonstrator by further constraining the activity distribution of contaminants within the setup.

With the current status of the analysis there is no doubt that the spectrum of the $2\nu\beta\beta$ -decay of ^{116}Cd would be observable for isotopically enriched CZT detectors. Previous experiments such as NEMO-3 and Aurora (see Tab. 8.13) achieved enrichment factors of more than ten times the natural abundance of ^{116}Cd , which immediately increases the expected decay rate and improves the S/B ratio, respectively.

Besides the discussed approaches to improve the demonstrator's sensitivity, the COBRA XDEM setup is in a very promising situation to detect the $2\nu\beta\beta$ -spectrum and should be able to measure its half-life reaching the aimed exposure of $1\ \text{kg yr}$. According to a preliminary analysis of about $0.1\ \text{kg yr}$ presented in [Tem19], an inverse S/B of about 2.1 ± 0.3 could be reached. The analysis involved a slightly different definition of the $2\nu\beta\beta$ -decay ROI and combined the simulations of the $2\nu\beta\beta$ -decay spectra of ^{116}Cd and ^{130}Te . Moreover, a z -cut

of $0.2 < z \leq 0.9$, but no additional PSD has been used. As will be further elaborated in section 8.7.3, the instrumentation of the guard-ring electrode results in a background reduction of more than one order of magnitude compared to the demonstrator’s background level after all analysis cuts. The analysis methods developed in the course of this thesis, involving the calibrated A/E criterion and the automated data partitioning, are expected to serve well in the upcoming COBRA XDEM analyses. A comparison of the $0\nu\beta\beta$ -decay half-life sensitivities reached by the demonstrator array and a projection based on the first data evaluation of COBRA XDEM will be presented in section 8.7.

8.5 Long-lived α -decay of ^{190}Pt

Platinum is part of the CZT detectors’ electrode metalization and contains a small fraction of the long-lived radioactive isotope ^{190}Pt , which undergoes an alpha decay. Its presence has been already mentioned in section 8.2.4 in the course of characterizing the background composition of the COBRA demonstrator at the LNGS. This section is dedicated to an analysis of the demonstrator’s physics data with the aim to confirm already existing half-life measurements using complementary experimental approaches. The main challenge is to determine the number of source nuclei, which is needed to convert the observed ^{190}Pt decay rate into the corresponding half-life. As an external investigation of the platinum layers of the CZT detectors is currently not possible because they are hosted inside the LNGS setup, a characterization of the Pt-layers can only be done indirectly. This includes the review of previous laboratory measurements, the evaluation of the demonstrator’s physics data as well as Monte-Carlo simulations using COBRA’s VENOM toolkit.

8.5.1 Motivation and introduction

The main motivation for the investigation of the ^{190}Pt α -decay is an independent, internal characterization of the platinum layers including a crosscheck of recent half-life measurements. Of particular interest is the actual thickness of the Pt-layer as it enters the GDML implementation of the COBRA setup as a not well-known parameter. Due to their characteristic penetration depths, there is a strong dependence of the imprints of α - and β -radiation with respect to potential layers of insensitive materials such as platinum in the cathode metalization of the CZT detectors.

Moreover, ^{190}Pt is not only a prominent background for the COBRA demonstrator, but is also present in the CUORE experiment searching for the $0\nu\beta\beta$ -decay of ^{130}Te (see e.g. Ref. [CUO19b]). CUORE uses TeO_2 crystals as bolometric detectors at a temperature of approximately 10 mK. Due to the applied crystal growth procedure there is a bulk contamination with ^{190}Pt originating from the calcination process using a Pt-coated crucible [ABB⁺10].

In a more general scope, the study of long-lived α -decays such as the ^{190}Pt - ^{186}Os series has proven as powerful tool for the understanding of nuclear physics. A prominent example is the observed relation between the Q -value of an α -decay transition and its respective $T_{1/2}$, which is known as the Geiger-Nuttall law [GN11] and its more recent formulation referred to as the Viola-Seaborg relation [SB16]. The platinum isotope ^{190}Pt undergoes a decay series according to the sequence listed below.



The respective Q -values of the transitions in Eqn. (8.49) – (8.50) are rather low compared to the prominent α -decays of the natural decay series (see Tab. 8.4 in section 8.2.4). They

are quoted as $Q_\alpha(^{190}\text{Pt}) = 3268.6 \pm 0.6 \text{ keV}$ and $Q_\alpha(^{186}\text{Os}) = 2821.2 \pm 0.9 \text{ keV}$ in the *Live Chart of Nuclides* [NDS20] and the recent AME database [AME17]. Although the Q -values are of the same order, the half-lives of the two consecutive decay branches are found to differ by almost four orders of magnitude. The half-life differences in the ^{190}Pt - ^{186}Os system can also be used as a cosmochronometer to date geological samples and meteorites (see e.g. Ref. [WMB⁺97]). Moreover, it allows to investigate the chronology and evolution of those samples at time scales on the order of the respective half-lives.

Recently, the ^{190}Pt half-life has been determined to $(4.97 \pm 0.16) \times 10^{11} \text{ yr}$ using a low-background twin Frisch-grid ionization chamber in a surface laboratory [BGS⁺17]. The working principle of such an ionization chamber is rather similar to COBRA's CPG-CZT detectors. The recent half-life result is one of the most precise measurements for ^{190}Pt involving a direct counting experiment and is in agreement with the half-life obtained using so-called geological comparison methods. In those methods the isotopic abundances of the ^{190}Pt - ^{186}Os system are determined, while the age of the sample, which is usually an ore or meteorite, can be inferred from radiometric dating methods using e.g. the U-Th-Pb geochronology [Sch14]. The differences in the relative isotopic composition allow for the evaluation of the ^{190}Pt half-life with high precision. A compilation of previous measurements is given in Ref. [TTM06], quoting a weighted average for the geological comparison method of $(4.78 \pm 0.05) \times 10^{11} \text{ yr}$.

According to the same reference there are severe deviations up to a factor of 2-3 between the half-life results of past direct counting experiments. As an example the ^{190}Pt half-life is quoted as $(6.5 \pm 0.3) \times 10^{11} \text{ yr}$ in Ref. [NDS20], which disagrees with the previously quoted half-lives by more than five standard deviations. A more detailed discussed can be found in a recent review article [BBD⁺19]. However, the source of the discrepancies is still unclear, which is why further direct counting measurements are required to help resolving those deviations and to interpret the results.

In general, the contribution of the secondary ^{186}Os α -decay can be neglected in direct counting experiments using pure platinum samples, because of its much longer half-life of $(2.0 \pm 1.1) \times 10^{15} \text{ yr}$ [VRM75], even though it is not yet measured very precisely. Consequently, only the initial decay of the ^{190}Pt - ^{186}Os series is considered in the present study, which uses the Pt-layer of COBRA's CZT detectors as platinum sample. The current knowledge regarding the thickness and uniformity of the Pt-layer will be addressed in the next section.

8.5.2 Pre-characterization of platinum layer

The characterization of the electrode material is a long-lasting issue in the course of the COBRA experiment. As per information of the crystal supplier the total thickness of the cathode's metalization is around 80 – 100 nm. However, it is known that the actual thickness of the electro-chemical plated layers of gold and platinum can deviate significantly from those default values, especially for detector of different production batches. This is why the collaboration performed several non-destructive measurement campaigns in order to investigate the potential thickness variations. The results are partly discussed in the PhD thesis of D. Gehre [Geh17] and will be briefly summarized in the following. The same reference includes already a rough estimate of the ^{190}Pt decay rate for the COBRA demonstrator.

External characterization measurements

The first characterization measurements were performed by external laboratories in the beginning of the construction of the COBRA demonstrator. The main objective at that time was to determine the zinc concentration and its potential gradient for CZT crystals of the same batch. As zinc can replace cadmium in the crystal structure of CZT, which is usually

referred to as $\text{Cd}_{1-x}\text{Zn}_x\text{Te}$ with $x \approx 0.1$, the variance of its concentration is an important systematic uncertainty in any intended double beta decay search.

In a first characterization attempt energy-dispersive X-ray spectroscopy (EDX) was applied on a single CZT detector that was originally coated with a red encapsulation lacquer [GW12]. The entire detector batch was used in a predecessor stage of the current demonstrator array and revealed a much too high contamination level due to the present color particles of the red lacquer (see also the discussion of the radiopurity assessment in section 8.3.7). The entire detector batch has been reworked by the supplier to replace the red encapsulation with a colorless version, in order to reuse the same detectors in the COBRA demonstrator. Given the sensitivity of the EDX, a variation of the zinc concentration of about 20% was found (see e.g. [COB16a]). Unfortunately, it turned out the method is not able to discriminate between the gold and platinum plating, hence, could not determine their thicknesses.

An alternative approach applied for the same material sample was x-ray fluorescence (XRF). In contrast to EDX there is an increased depth information for the XRF. The zinc concentrations was found to agree with the previous EDX results within the respective experimental uncertainties. Furthermore, the thickness of the Pt-layer could be determined to about 40 nm with an uncertainty on the 10% level [Raj12]. About the same thickness was found for the gold layer on top of the platinum, which confirmed the total thickness of the CZT detector’s cathode metalization as quoted by the manufacturer for the first detector batch. However, in comparison to samples of other batches a variation of about 20% was found. As those characterizations involved only a rather small set of material samples, the results should be taken with some caution. Moreover, it cannot be excluded that the production routines changed since the first characterizations based on the EDX and XRF measurements.

Internal characterization based on ^{190}Pt

With the long-term operation of the COBRA demonstrator and its presently performed data evaluation of its full exposure, it is now possible to characterize the Pt-layer based on the intrinsic α -decay of ^{190}Pt . A first impression of the demonstrator’s physics data is depicted in Fig. 8.39. The underlying event selection will be discussed in section 8.5.4.

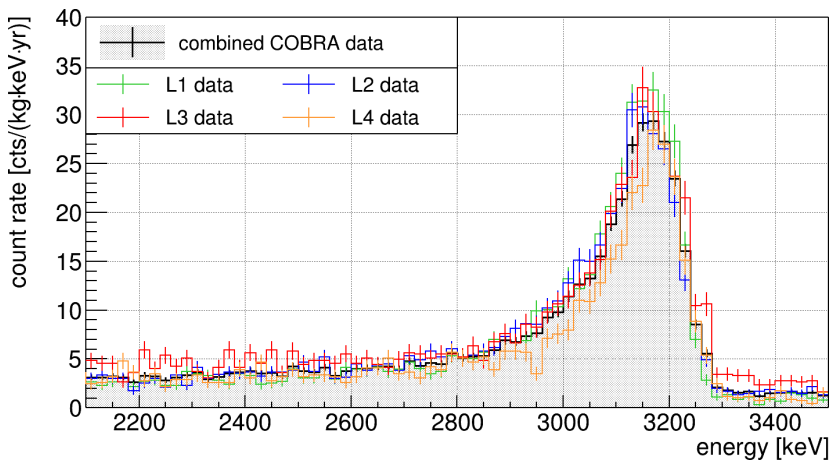


Figure 8.39: Comparison of the combined energy spectrum of the COBRA demonstrator and its four detector layers with respect to the α -decay of ^{190}Pt . The physics data has been normalized according to the selected exposure of 533.3 kg d after applying the HRP partitioning (see section 8.4.2 and Tab. 8.14). Moreover, the energy bin width of 16 keV enters the normalization. The interaction depth is limited to $0.97 < z \leq 1.03$ in order restrict the energy spectra to near-cathode events. It is found that the spectra of the individual detector layers agree well with each other and the combined spectrum of all detectors.

The normalized energy spectra of the individual detector layers agree well with each other, which hints to a rather uniform Pt-layer although the detectors are from different production batches. Moreover, the α -peak's position is consistent with the expected energy deposit of the decay. Because of the nuclear recoil, the emitted α -particles do not carry the full Q_α of the ^{190}Pt transition, but a reduced energy of $E_\alpha = 3183 \pm 6 \text{ keV}$ [BGS⁺17]. The energy deposit by the nuclear recoil is not expected to be observed as the decay does not take place within the sensitive detector material (in contrast to the ^{190}Pt bulk contamination for the CUORE TeO₂ crystals). Due to the typical ionization losses in CZT, a perpendicularly incoming α -particle carrying E_α is expected to have only a range on the micrometer scale. While the CSDA range is found to be about $12 \mu\text{m}$ (see section 8.2.4), a simulation using SRIM results in a maximum range of about $1.2 \mu\text{m}$ [Geh17], which is even one order of magnitude less. In any case, the sensitive volume can be restricted to the near-cathode region.

However, the limited statistics are not sufficient to allow for an analysis on the single detector level. Instead, the combined spectrum will be used in the analysis of the ^{190}Pt α -decay. While this approach minimizes the statistical uncertainties, it requires to rely on average values that enter the analysis, which might not perfectly describe the combined data of the single detectors and their characteristic features.

Even though the thickness of the planar cathode's Pt-layer is not yet well-characterized, its xy -dimension can be determined from the known physical size of each detector. By using the tabulated crystal dimensions of the cuboidal CZT crystals and the exposure per detector under the given data selection (see section 8.5.4), an exposure weighted average results in $\bar{xy} = 10.14 \pm 0.12 \text{ mm}$, which is taken as representative value for the combined spectrum. The quoted uncertainty is an indication for the variation of the crystals' dimensions with respect to the mean value. By fixing the xy -dimensions of the Pt-layer, only the thickness denoted as d_{Pt} remains as a free parameter. In the following section, the dependency of the ^{190}Pt α -decay's spectrum-shape with respect to d_{Pt} will be studied with MC simulations.

8.5.3 Monte-Carlo simulation of ^{190}Pt α -decay

As outlined in the motivation given in section 8.5.1, one of the main interests of the present study is the determination of the Pt-layer's thickness to improve the GDML implementation of the COBRA demonstrator setup. Moreover, its determination is also required to calculate the number of ^{190}Pt source nuclei, which is needed to convert the measured decay rate into the corresponding half-life. The implementation of platinum into the existing framework will be addressed in the following.

Implementation of platinum

In preparation of the MC simulations, a custom platinum material has been added to COBRA's *material.xml* (see also section 5.3.3). This approach ensures the full control over the material properties, independently of the underlying version of the GEANT4 packages and related databases. The isotopic composition of the implemented material is defined in Tab. 8.17.

All naturally occurring isotopes of platinum besides ^{190}Pt are assumed to be stable. The isotopes corresponding to the atomic mass numbers $A = 188 - 200$ that are not listed in Tab 8.17 can only be produced artificially and decay with half-lives on the order of hours up to several days. The present status of the search for unknown α -decays of the assumed to be stable platinum isotopes is summarized in Ref. [BBD⁺19].

The definition of platinum as a solid component is attributed by setting its density to 21.45 g/cm^3 . Regarding the radioactive decay of ^{190}Pt , it could be verified that the uptodate Q -value, as quoted in the introduction, is available in the physics list used by COBRA's

Table 8.17: Isotopic composition and atomic masses of natural platinum. The atomic masses have been taken from [AME17] and the natural abundances from [IUP16]. The quoted molar mass for the element is the weighted average of the atomic masses and needed for the conversion of the measured decay rate into the half-life of the ^{190}Pt α -decay. The primordial isotope ^{190}Pt is only present in traces in natural platinum and features a comparably high uncertainty of about 8.3% with respect to the quoted abundance.

isotope	abundance [%]	atomic mass [u]
^{190}Pt	0.012(1)	189.9599499(7)
^{192}Pt	0.782(24)	191.9610427(28)
^{194}Pt	32.864(410)	193.9626835(5)
^{195}Pt	33.775(240)	194.9647944(5)
^{196}Pt	25.211(340)	195.9649547(5)
^{198}Pt	7.356(130)	197.9678967(23)
element	-	195.0844294(2)

simulation tool. As only the initial decay of the ^{190}Pt - ^{186}Os system is of interest, the second part of the decay series has been disabled in all simulations by modifying VENOM’s *chaingen* generator. Finally, the Pt-layer’s thickness d_{Pt} has been added as a global parameter in the GDML implementation of the demonstrator geometry and can now be set via a macro command. The maximum thickness is limited to about $1\ \mu\text{m}$ to avoid an overlap with other parts of the geometry and a shift of the CZT crystals’ positions.

Investigation of platinum layer thickness

For the investigation of the shape of the ^{190}Pt spectrum by assuming different thicknesses of the Pt-layer, a first simulation campaign with a step size of 100 nm for the range of 100 – 800 nm has been performed. Each simulation run includes 10^6 events using a slightly modified version of VENOM’s *chaingen* generator (see section 5.3.1). In a second MC campaign the step size was reduced to 10 nm for the complementary range of 10 – 400 nm. Some examples of the resulting MC spectra are shown in Fig. 8.40 for different normalization procedures.

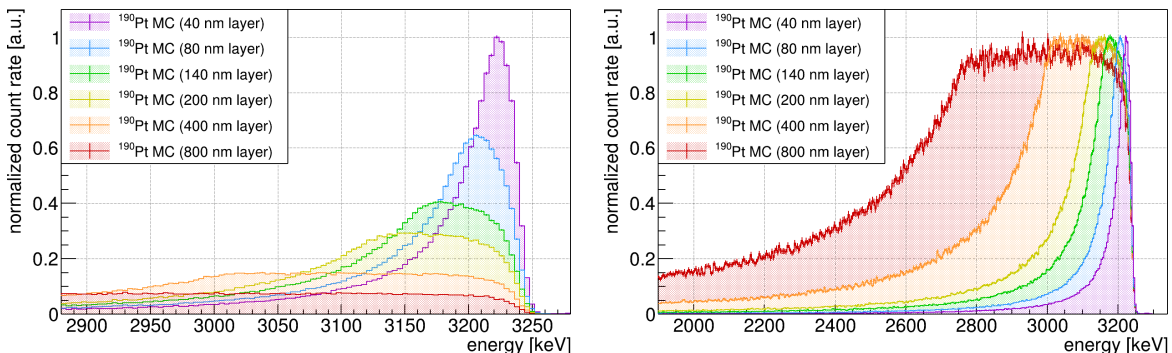


Figure 8.40: Normalized MC spectra of the ^{190}Pt α -decay for different thicknesses of the platinum layer using the COBRA demonstrator geometry. *Left:* normalization according to the maximum of the thinnest layer with $d_{\text{Pt}} = 40\ \text{nm}$. In this case the integral over each spectrum covers an area, which reflects the same number of simulated primary events. *Right:* normalization according to each spectrum’s maximum. Under this normalization the effect of the peak tailing towards lower energies for thicker Pt-layers can be seen more clearly. However, the integrals do not reflect the number of simulated events anymore. The effect of an energy smearing due to the finite energy resolution of the detectors is discussed separately in Fig. 8.41.

As pointed out in Ref. [BGS⁺17] the peak tailing towards lower energies is only a minor effect for thin layers, but gets rather prominent for $d_{\text{Pt}} \gtrsim 200\ \text{nm}$ in the case of the simulated

CZT detectors. Because of this feature α -spectroscopy requires in general thin targets to minimize the energy losses within the target and to maintain the discrimination of potential backgrounds in the ROI of the expected α -peak. The previous study [BGS⁺17] used several platinum targets of about 400 nm thickness each. However, the two experimental approaches cannot be compared directly to each other. Furthermore, it is noteworthy to mention that the simulation results presented in Fig. 8.40 have not been folded with the average energy resolution of the demonstrator detectors. This step will be discussed in the next section.

Energy resolution smearing

The effect of applying the average detector resolution to the output of the VENOM simulations of the ^{190}Pt α -decay is shown exemplarily in Fig. 8.41. This step is necessary to compare the simulated energy spectra to the COBRA data as will be discussed in section 8.5.4. The procedure follows the steps outlined in section 8.3.7 for the ^{113}Cd low-energy background model. It consists of a randomization of the simulation data using a Gaussian distribution with the true MC energy as mean and a width according to the average energy resolution function $\text{FWHM}(E)$, which has been obtained from the calibration measurements during the dedicated ^{113}Cd low-threshold run. Consequently, the Gaussian energy resolution smearing is applied to all VENOM simulations before proceeding with the data analysis as presented in the following section.

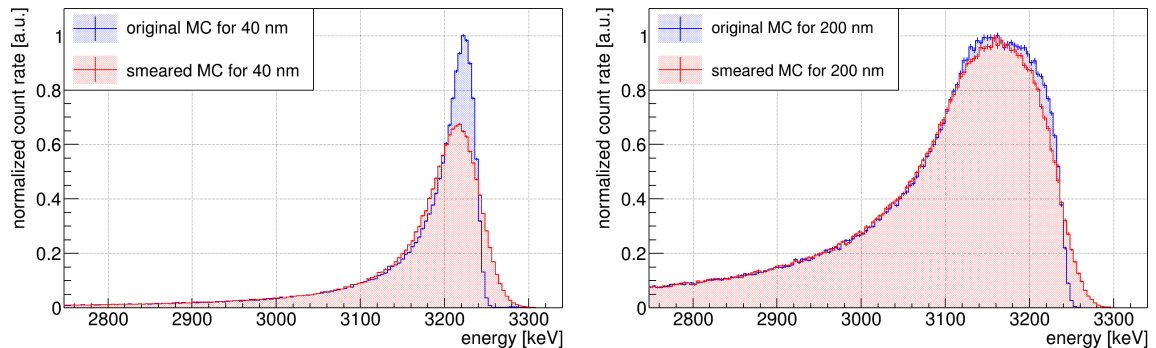


Figure 8.41: Effect of a Gaussian energy smearing for two example simulations of the ^{190}Pt α -decay for different platinum thicknesses. *Left:* $d_{\text{Pt}} = 40 \text{ nm}$. *Right:* $d_{\text{Pt}} = 200 \text{ nm}$. In both cases there is a small shift of the α -peak's mean position towards lower energies and an expected broadening of its width. However, the effect is more prominent for thinner Pt-layers and only marginal for $d_{\text{Pt}} \gtrsim 200 \text{ nm}$ as the spectra are getting more and more continuous due to the increasing likelihood of prior energy losses in the Pt-layer.

8.5.4 Analysis of COBRA's LNGS data

The analysis of the available physics data of the COBRA demonstrator is based on a *cut and counting* method and consists of three steps. At first the event selection with respect to the α -decay of ^{190}Pt needs to be fixed. Secondly, the thickness of the Pt-layer can be determined using the simulated MC templates for different d_{Pt} in a spectrum-shape comparison of the normalized experimental spectra and the MC spectra. This step of the analysis is inspired by the procedure applied in the PhD thesis of H. Wilsenach [Wil20] for various α -spectroscopy measurements using a twin Frisch-grid ionization chamber. Moreover, the intended spectrum-shape comparison is partly based on the techniques developed for the analysis of the ^{113}Cd β -spectrum as discussed in before in section 8.3.

Finally, the ^{190}Pt half-life can be extracted from the measured decay rate, which needs to be corrected for the signal efficiency. The conversion formula also requires to fix the Pt-layer's

thickness in order to determine the number of ^{190}Pt source nuclei. All of the parameters involved in the half-life conversion are going to be evaluated regarding their effect on the systematic uncertainty on the final analysis result.

Event selection

As usual, the first step of the even selection consists of the application of the standard data-cleaning cuts (DCCs) (see section 7.1.1). At the energy scale of the α -decay of ^{190}Pt the signal efficiency of the DCCs is about 100%, hence, requires no correction with respect to the total decay rate. The second step is a restriction of the interaction depth to only select near-cathode events. Based on the z -cut characterization presented in section 7.1.2, a $\pm 3\sigma$ range with a Gaussian coverage of 99.87% around the cathode position at $z = 1$ corresponds to a selection of the range $0.97 < z \leq 1.03$. The same selection covers about $6.72 \pm 0.02\%$ of the total sensitive CZT volume (see Tab. 7.2).

With respect to data partitioning discussed in section 8.4.2 in the course of the analysis of the ^{116}Cd $2\nu\beta\beta$ -decay, it makes sense to reject the identified high-rate periods (HRPs) in the present analysis, as they contribute to the near-cathode contamination. Fortunately, the Q -values of the involved α -decays of the radon isotope ^{222}Rn and its long-lived daughters are much higher in energy and rather well separated from the ^{190}Pt ROI (see e.g. Fig. 8.9 in section 8.2.4). The total exposure that remains after removing the HRP partition is 533.3 kg d and corresponds to about 88.3% of the full exposure (see Tab. 8.14 in section 8.4.2).

Because of the strict depth selection there is no need to exclude detector numbers with an increased background index for bulk events as done for the ^{116}Cd $2\nu\beta\beta$ -decay analysis. Another indication for this non-necessity is the observed similarity of the energy spectra of the detector layers under the discussed event selection (see Fig. 8.39), which is quite different from the previous analysis where the rate of the single layers deviated up to a factor of three under similar selections. It should be noted that the average xy -dimensions of the Pt-layer, which were determined in the second half of section 8.5.2, depend slightly on the chosen data partition. However, the actual determination has been done under the final event selection and the observed deviations are much smaller than the assigned systematic uncertainties.

Determination of platinum thickness

As mentioned in the introduction to this section, the analysis procedure to determine the platinum thickness d_{Pt} is based on a spectrum-shape comparison between the combined spectrum obtained by the COBRA demonstrator and the performed MC simulations. The actual spectrum-shape comparison is partly based on the methods of the ^{113}Cd β -decay study and involves again a standard χ^2 test to asses the degree of agreement. In order to compare the two types of energy spectra, a normalization by the integral over the energy range of 2400–3300 keV is done, which fixes the integrals over this energy range to unity. All energy spectra have a fixed bin width of 16 keV, which is motivated by the statistics per bin in the combined experimental spectrum (see also Fig. 8.39). This choice results in $N = 50$ degrees of freedom for the energy range quoted above.

In the present case the *Chi2Test* function of the ROOT framework for histograms of the *TH1* class is used to determine the best match. The key principle is the same as discussed for the case of the ^{113}Cd spectrum-shape analysis following Eqn. (8.19). However, ROOT’s *Chi2Test* function includes several modifications to address bins with low-statistics and offers different built-in scaling attributes. Details of those modifications with respect to the conventional χ^2 test procedure are discussed in Ref. [Gag06]. One of the features used in the analysis is the definition of an offset to take into account the background level above

the Q -value of ^{190}Pt . The background level is constrained by the integral over the data for $3300\text{--}3600\,\text{keV}$ and assumed to be constant over the ROI defined above. Moreover, the option *norm* is used in the present analysis to address the normalization of both spectra, which affects the effective number of degrees of freedom (NDF).

The resulting χ^2_{red} curve in dependence on d_{Pt} for the range of $10\text{--}400\,\text{nm}$ is depicted in Fig. 8.42. The best match is found for $d_{\text{Pt}} = 180 \pm 10\,\text{nm}$ and corresponds to a minimum of $\chi^2_{\text{red}} = 4.51$. The comparably high χ^2_{red} value of the best match, given a NDF of $N = 50$, is an indication for an imperfect modeling of the data. Potentially, a more nuanced treatment of the individual detectors could resolve this situation. One idea for a follow-up analysis would be to define a multivariate fit to determine the ratio of detectors that feature a low, medium or high thickness of the Pt-layer instead of assuming a uniform thickness distribution.

Nonetheless, the χ^2 test result reveals that the average Pt-layer is somewhat thicker than expected from the pre-characterization measurements discussed in section 8.5.2. Compared to the previous laboratory measurement presented in [BGS⁺17], the Pt-layer thickness is about half the size of their platinum samples. The thinner samples have the advantage of being less affected by the peak-tailing towards lower energies, but come at the cost of a reduced ^{190}Pt decay rate.

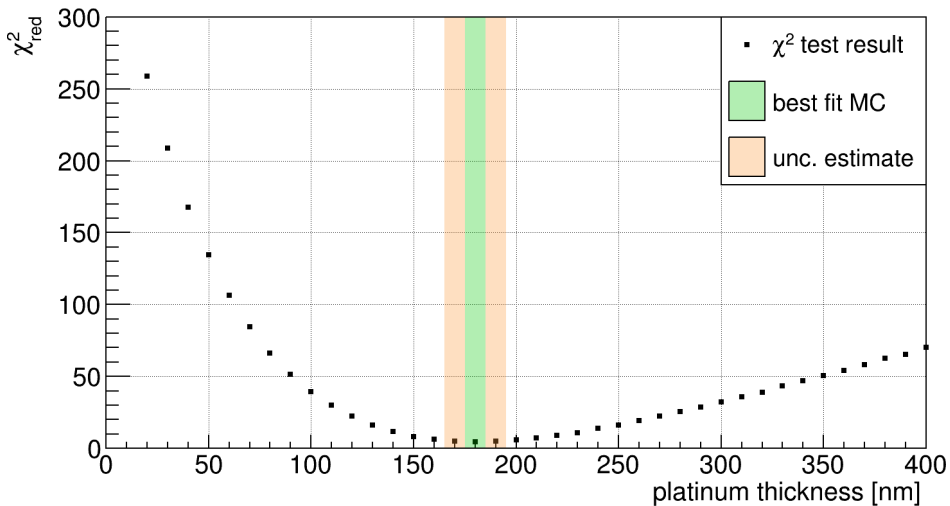


Figure 8.42: Results of the χ^2 test procedure to determine the best match MC spectra with respect to the average thickness of the CZT detectors' Pt-layer. The best match is found for $d_{\text{Pt}} = 180 \pm 10\,\text{nm}$ at $\chi^2_{\text{red}} = 4.51$. As the minimum χ^2_{red} value indicates some tensions between the MC modeling and the data, a conservative estimate of the systematic uncertainty has been performed.

Because of the rather unsatisfying minimum χ^2_{red} value, a conservative estimate of the uncertainty on the Pt-layer's thickness has been performed. Instead of choosing the $(\chi^2 + 1)$ deviation as estimate of the $\pm 1\sigma$ uncertainty, the systematic uncertainty is conservatively estimated as $\pm 10\,\text{nm}$. The χ^2_{red} values corresponding to the increased, respectively decreased, platinum thicknesses are $\chi^2_{\text{red}}(170\,\text{nm}) = 5.09$ and $\chi^2_{\text{red}}(190\,\text{nm}) = 4.86$. While those values are on the same order as for the best match, the uncertainty estimate indicates a deviation from the standard $(\chi^2 + 1)$ uncertainty by about 20 times considering the given NDF.

A comparison of the best match MC spectrum and the combined data of the COBRA demonstrator is shown in Fig. 8.43. While there is a good agreement near the maximum of the α -peak, there are deviations for the modeling of the peak-tailing towards lower energies and close to the endpoint of the peak. The latter deviations might be caused by the energy resolution smearing according to the average $\text{FWHM}(E)$, which does not necessarily apply to the detectors with the worst energy resolution. The mismatch in the tailing part of the

α -peak could be caused by unaccounted background contributions or the superposition of the ^{190}Pt spectra of varying thicknesses. For the energy range above the peak there is again a good agreement between the two spectra due to the background level constraint, which is taken as a constant offset in the spectrum-shape comparison.

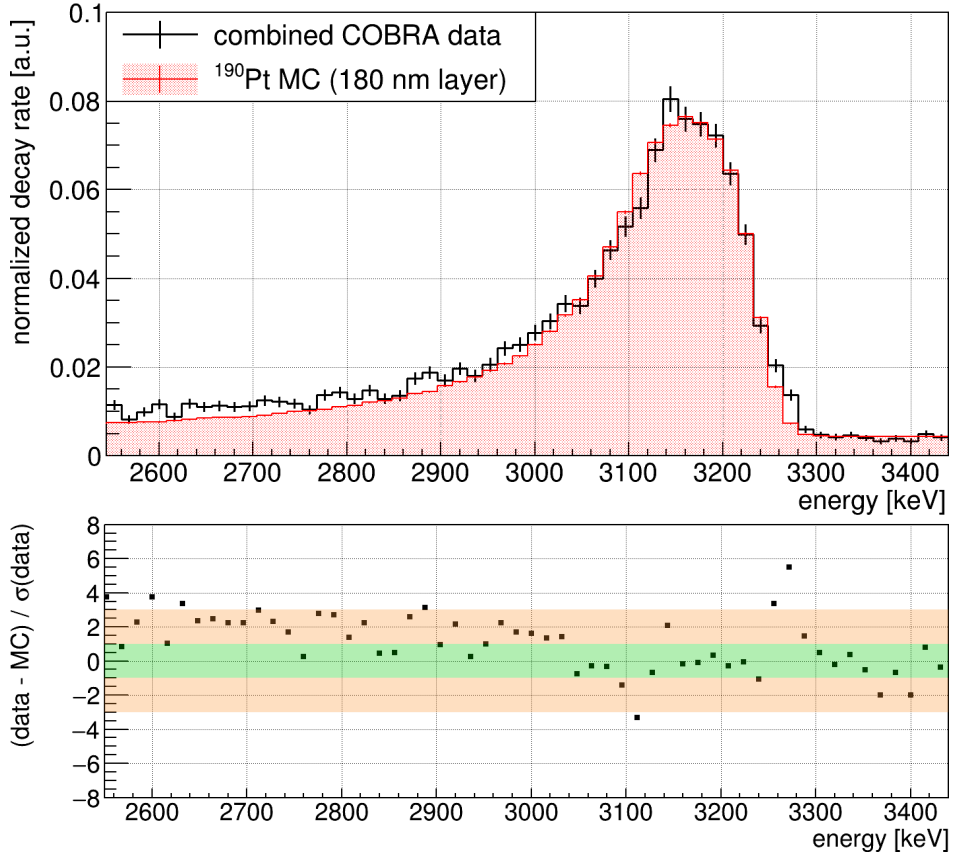


Figure 8.43: Comparison of the combined data of the COBRA demonstrator and the MC spectrum corresponding to the best match of the χ^2 test. *Top:* illustration of the normalized energy spectra. The background level above the ^{190}Pt α -peak is taken as a constant offset for the MC spectrum. *Bottom:* distribution of the residuals between data and Monte-Carlo. The residuals are scaled by the statistical uncertainties of the data. The observed deviations are largely compatible with fluctuations on the $\pm 3\sigma$ level (orange band). However, for the peak-tailing towards lower energies there is a slight over fluctuation in the data, which is likely caused by the simplified modeling of the Pt-layer using average values for all of the individual CZT detectors. The $\pm 1\sigma$ level is shown for comparison (green band) and indicates a sufficient match for the bulk of the α -peak.

In the final step of the analysis of the ^{190}Pt α -decay, the half-life corresponding to the observed decay rate and its uncertainty will be determined. The analysis procedure is based on Ref. [BGS⁺17] and presented in the next section.

Determination of ^{190}Pt half-life

The conversion of the measured decay rate into the corresponding half-life is based on Eqn. (8.51) and relies on the number of ^{190}Pt source nuclei N_{190} and the corrected decay rate R_{true} , which takes into account the involved efficiencies and a background correction.

$$T_{1/2} = \frac{\ln(2) \cdot N_{190}}{R_{\text{true}}} \quad (8.51)$$

The platinum mass corresponding to the volume formed by the determined d_{Pt} and the average xy -dimensions is about 400 μg per detector. As the number of active detectors

changes over the lifetime of the experiment and consequently the number of available source nuclei N_{190} do as well, a scaling according to the selected exposure towards a virtual single CZT detector with an increased observational live-time is performed. The accumulated total exposure of 533.3 kg d (HRP partition removed) is equal to an observational live-time of about 255.8 yr assuming a single CZT detector with the previously quoted average dimensions. These numbers still represent the achieved statistics by using up to 64 CZT crystals in parallel in the period of Sept.'11 – Nov.'19 (see e.g. Fig. 8.3).

Due to the scaling procedure described above only the effective N_{190} for a single Pt-layer of the average dimensions enters the half-life conversion in Eqn. (8.51). It follows as

$$N_{190} = \frac{d_{\text{Pt}} \cdot \bar{x}y^2 \cdot \varrho}{M_{\text{Pt}}} \cdot N_A \cdot a_{190} = (1.47 \pm 0.21) \times 10^{14} \quad (8.52)$$

using the platinum density $\varrho = 21.45 \text{ g/cm}^3$ as well as the molar mass M_{Pt} and the ^{190}Pt abundance listed in Tab. 8.17. The quoted uncertainty originates from the systematics of the respective parameters in Eqn. (8.52) and will be derived in the next section, whereas the uncertainties on the molar mass M_{Pt} and the Avogadro constant N_A are negligible.

The ^{190}Pt decay rate is determined by a direct counting approach and corrected for all involved efficiencies to obtain the quantity R_{true} entering Eqn. (8.51). Firstly, the number of counts in the ROI is determined. The ROI is defined as an energy interval covering the range of 2000–3300 keV. This energy range is found to have a high coverage of the α -peak based on the MC simulations for different d_{Pt} (see e.g. Fig. 8.39). The background level above the ^{190}Pt Q -value is taken as an estimate of a flat and constant background (see Tab. 8.18). The total number of counts in the ROI after background correction is 26814 ± 164 , with a statistical uncertainty of 0.6%. Compared to the previous study reported in Ref. [BGS⁺17] the statistics achieved in the present analysis are about 2.6 times higher.

The same ROI is applied for the MC simulation corresponding to the best match d_{Pt} to determine the efficiency of detecting an α -decay of ^{190}Pt with respect to the geometry of the experiment. The geometric efficiency is found to be $\varepsilon_{\text{MC}} = 49.05 \pm 0.06\%$, which agrees with the expectation of observing roughly half of the decays for an isotropic emission probability. Finally, a corrected decay rate of $R_{\text{true}} = 213.72 \pm 0.77 \text{ cts/yr}$ is found by using the observational live-time following from the accumulated exposure, the efficiency of the depth selection as well as the determined ε_{MC} . The systematic effects resulting in the quoted uncertainty will be discussed in the next section.

With the determined values of N_{190} and R_{true} the half-life of the ^{190}Pt α -decay can be derived from Eqn. (8.51). The conversion results in

$$T_{1/2} = (4.77 \pm 0.03 \text{ (stat.)} \pm 0.69 \text{ (syst.)}) \times 10^{11} \text{ yr.} \quad (8.53)$$

The half-life result is in agreement with the previous studies discussed in section 8.5.1 and dominated by systematic effects, which will be addressed in the following.

Systematic uncertainties

An overview of the parameters that are considered as systematic uncertainties with respect to the quantities N_{190} and R_{true} , which enter the half-life conversion formula Eqn. (8.51) and the result presented in Eqn. (8.53), is given in Tab. 8.18.

In the case of N_{190} the largest contribution arises from the ^{190}Pt abundance according to Ref. [IUP16]. The quoted value of a_{190} corresponds to a relative uncertainty of 8.3%. Compared to Ref. [BGS⁺17] a much more precise value of $a_{190} = 0.01125(21)\%$ with a relative uncertainty of 1.9% could be achieved by performing a dedicated investigation of the isotopic

Table 8.18: Overview of the systematic uncertainties of the half-life determination of the ^{190}Pt α -decay with the COBRA demonstrator. The two quantities N_{190} and R_{true} entering the half-life conversion formula Eqn. (8.51) depend on several parameters, which are treated as systematic uncertainties. The last column refers to the relative uncertainty on the determined half-life. The single contributions are added in quadrature to determine the combined systematic uncertainty for the three quantities of interest.

quantity	parameter	absolute value	rel. unc. [%]
N_{190}	Pt-layer thickness	$180 \pm 10 \text{ nm}$	7.86
	Pt-layer xy -dimension	$10.14 \pm 0.12 \text{ mm}$	3.35
	Pt-density	$21.45 \pm 0.05 \text{ g/cm}^3$	0.33
	^{190}Pt abundance	$0.012 \pm 0.001\%$	11.79
R_{true}	^{190}Pt atoms	$(1.47 \pm 0.21) \times 10^{14}$	14.55
$T_{1/2}$	z -cut efficiency	$99.87 \pm 0.30\%$	0.30
	geometric efficiency ε_{MC}	$49.05 \pm 0.06\%$	0.13
	background variation	$0.23 \pm 0.12 \text{ cts/yr}$	0.16
R_{true}	corrected decay rate	$213.72 \pm 0.77 \text{ cts/yr}$	0.36
$T_{1/2}$	half-life	$(4.77 \pm 0.69) \times 10^{11} \text{ yr}$	14.56

composition of the respective platinum samples. Such a measure would only be possible after the decommission of the COBRA demonstrator in a later stage of the experiment. The same applies to the second highest contribution which is related to the determination of the Pt-layer's thickness. Using XRF to determine d_{Pt} for each of the CZT detectors of the COBRA demonstrator would help to reduce the conservatively estimated uncertainty.

With respect to the total uncertainty the contribution of R_{true} , as the second quantity that enters the half-life conversion, turns out to be small. The uncertainty of the z -cut efficiency follows from the variation of the depth resolution as reported in section 7.1.2. The geometric efficiency's uncertainty is derived by varying d_{Pt} within its constraints. Consequently, the modulus of the deviations are added in quadrature and taken as the uncertainty on ε_{MC} . The largest variation is performed for the assumed flat background. In this case a variation of 50% of the nominal value is applied to estimate the contribution to the overall uncertainty. The uncertainty on the observational live-time can be neglected.

In summary, the total systematic uncertainty on the determined ^{190}Pt half-life in Eqn. (8.53) is about 14.56%. Hence, there is a clear dominance of the systematic effects over the uncertainty resulting from the accumulated statistics of the present study. A short outlook and some concluding remarks are given in the last paragraph of this section.

Conclusion and outlook

The determined half-life of the ^{190}Pt α -decay agrees perfectly with the result presented in Ref. [BGS⁺17] and the weighted mean of previous studies based on the geological comparison method (see e.g. Ref. [TTM06]). However, previous measurements had a better control of their systematic uncertainties. As already addressed in the discussion of the systematic contributions to the overall uncertainty, the most critical parameters are the ^{190}Pt natural abundance and the thickness of the CZT detectors' Pt-layer. The latter one was determined indirectly by a spectrum-shape comparison between the combined data of the COBRA demonstrator and MC spectra for different assumed thicknesses. Both related systematic uncertainties could be reduced by performing a depth-resolved investigation of the Pt-layer, e.g. by XRF or similar methods, as soon as the CZT detectors are available for such measures. Furthermore, variations between the single detectors could be treated in a more nuanced way, which could improve the agreement between the data and the MC modeling.

The observed mismatch between the determined platinum thickness of $180 \pm 10 \text{ nm}$ and the statement by the manufacturer, that the total thickness of the cathode's metalization is about $80 - 100 \text{ nm}$, could also be caused by potentially unaccounted dead layer effects. However, this is unlikely as the experimental half-life result agrees well with previous measurements and would scale with the platinum thickness, accordingly.

A potential internal crosscheck could be to repeat the direct counting analysis for near-anode events. The CPG electrode consists also of a platinum layer of probably similar thickness. However, the event reconstruction is not perfectly in this depth region and strongly affected by distortions of the weighting potential. Moreover, only part of the anode sides is covered by the CPG electrode, hence, an additional coverage factor needs to be considered in the analysis. Especially the *double-energy events* of ^{190}Pt (see e.g. Fig. 8.4) might be worthwhile to be considered for such a measure or, on the contrary, could be used to estimate the magnitude of the underlying double-energy effect using the platinum coverage of the anode's CPG electrode compared to the planar cathode.

For the next stage of the experiment, involving the XDEM detector layer, there are prototype detectors of two different suppliers. Due to improved surface finalization methods it is now possible to relinquish the additional platinum layer in the electrode's metalization without altering the long-term performance of the detectors. This approach is applied for a part of the COBRA XDEM detectors. Those detectors allow for a direct measurement of the background in the ^{190}Pt ROI in a potential follow-up campaign using the new detector array.

Finally, there are experiments with a large target mass that feature a prominent contamination with ^{190}Pt such as the CUORE experiment at the LNGS. If the systematics could be controlled, it might be possible for CUORE to produce an outmost precise ^{190}Pt half-life measurement by analyzing their data in a similar fashion as presented in this thesis.

8.6 Double beta decays into excited states

Besides the possibility of observing double beta transitions directly into the ground-state (g.s.) of the daughter nuclei, as discussed in the previous section, double beta decays can also occur into excited states. Although excited state transitions are expected to have a significantly reduced rate compared to the g.s. due to a smaller phase-space, they provide an enhanced experimental signature because of the accompanied cascade of γ -rays as result of the relaxation of the excited daughter nuclei. This opens a new analysis window involving multi-detector hits, which are usually treated as background in most of the conventional double beta decay searches. Because of its rather high granularity the COBRA demonstrator array might be competitive with respect to the current experimental data situation, despite the fact that the most frequent decay mode – the g.s.-to-g.s. $2\nu\beta\beta$ -decay of ^{116}Cd – has not yet been observed by the experiment.

In the following sections a feasibility study based on Monte-Carlo simulations of the COBRA demonstrator array will be presented. This includes the most promising decay modes with and without the emission of neutrinos for the isotopes ^{116}Cd and ^{130}Te and assumes a *best-case scenario* without any external contaminations such as described in section 8.2. In fact, only the $2\nu\beta\beta$ -decay of ^{116}Cd into the ground-state will be considered as an intrinsic, irreducible background. However, under those assumptions, the MC study allows to fathom the potential of COBRA to confirm already existing experimental results or to even improve the overall experimental data situation by setting stronger limits for some of the decay modes. The recent experimental situation will be briefly discussed in the next sections.

Some very preliminary results with a rather simple MC implementation of the COBRA demonstrator have been provided to L. Dathe for the usage in a high school thesis [Dat16]. Furthermore, some of the illustrations in the analysis part of this section are based on the visualization tool developed in the course of this work.

8.6.1 Motivation and recent experimental results

The main motivation to search for excited state transitions is related to the theoretical description of the involved nuclear physics in form of the nuclear matrix elements (NMEs) (see section 3.2.3). Because of their specific nuclear configuration, the ground-states of $\beta\beta$ -nuclides and their daughter nuclei are characterized as spin states with $J^\pi = 0^+$. Neutrino-accompanied double beta decays are only possible via intermediate 1^+ states and typically limited to the lowest energetic ones, while $0\nu\beta\beta$ -decays involve also other intermediate states up to ~ 100 MeV (see also section 3.2.3). That is why the involved NMEs are inherently different for $2\nu\beta\beta$ - and $0\nu\beta\beta$ -decay modes. However, the underlying nuclear models rely on similar assumptions and are expected to share a certain parameter space. Hence, experimental results for $2\nu\beta\beta$ -decay transitions can be used to validate nuclear model calculations, which were performed in a specific framework. This includes not only the determination of the half-life for a transition via a specific excited state, but also the confirmation of the excited states' energy levels as well as their branching ratios in case of γ -ray cascades. Moreover, it might be possible to constrain unknown or free parameter that enter the NME calculations such as e.g. a quenching of g_A in low-momentum exchange nuclear reactions. In combination, this might help to identify superior nuclear models and, indirectly, improve the theoretical predictions for $0\nu\beta\beta$ -decay modes into the ground-state.

Ultimately, the discovery of $0\nu\beta\beta$ -decay excited state transitions could help to distinguish the various discussed decay mechanisms by shedding light on the involved nuclear physics. The additional γ -ray signature provides the opportunity to perform topological measurements involving the angular correlation between the emitted γ -rays, which are otherwise only pos-

sible with suitable tracking detectors (like e.g. the NEMO detectors) that are able to resolve the electrons spatially. Furthermore, $0\nu\beta\beta$ -decays via excited states are expected to be sensitive to certain right-handed coupling parameters, independently of the effective Majorana neutrino mass. However, the presently available experimental results already rule out most of those discussed resonance effects involving enhanced signatures due to right-handed currents.

From the spin configuration of the $\beta\beta$ -nuclides' ground-state, the most probable excited state transition is expected for the first 0^+ state (0_1^+). Final states other than 0_1^+ are suppressed by their spin combinations. However, the 0_1^+ state cannot decay directly into the ground-state, denoted as $0_{\text{g.s.}}^+$, because of the angular momentum conservation. That is why the lowest accessible state in a daughter nucleus is typically a 2^+ state. The de-excitation from the first 2^+ state (2_1^+) features only a single γ -ray emission while the transition from the 0_1^+ state produces a γ -ray cascade involving all intermediate states. The signature of a 0_1^+ state transition consists typically of at least two γ -rays, which is in addition to the two electrons a very distinct signal.

An overview of recent experimental results is given in Tab. 8.19. Further results and an overview of the experimental activity over the past decades with emphasis on excited state searches can be found in Ref. [Bar17]. As already discussed in sections 3.2.3 and 3.3.2 for both the theoretical and experimental aspects regarding the investigation of double beta decay processes, there is no clear favorite nuclide or experimental approach. The same applies to searches for excited state transitions.

Table 8.19: Overview of experimental results involving excited state transitions in $2\nu\beta\beta$ -decays. The table includes a selection of the world-leading $0\nu\beta\beta$ -decay experiments and is ordered according to the atomic mass of the $\beta\beta$ -nuclides. The Q -values and experimental results are taken from the references listed in the last column. Limits on $T_{1/2}^{2\nu}$ are at 90% C.L. (see Tab. 3.2 in section 3.3.3 for the respective limits on the $0\nu\beta\beta$ -decay g.s. transitions). For the reported half-life measurements only the most recent ones have been included for each nuclide and transition. The originally quoted statistical and systematic uncertainties were added in quadrature, if quoted separately, and rounded to two digits.

nuclide	experiment	transition	$Q_{\beta\beta}$ [keV]	$T_{1/2}^{2\nu}$ [yr]	reference
^{76}Ge	GERDA	$0_{\text{g.s.}}^+ \rightarrow 0_{\text{g.s.}}^+$	2039.1	$(1.93 \pm 0.09) \times 10^{21}$	[GER15b]
		$0_{\text{g.s.}}^+ \rightarrow 2_1^+$	1480.0	$> 1.6 \times 10^{23}$	[GER15a]
		$0_{\text{g.s.}}^+ \rightarrow 0_1^+$	916.8	$> 3.7 \times 10^{23}$	
	MAJORANA	$0_{\text{g.s.}}^+ \rightarrow 0_1^+$	1480.0	$> 9.6 \times 10^{23}$	[MAJ19]
		$0_{\text{g.s.}}^+ \rightarrow 2_1^+$	916.8	$> 6.8 \times 10^{23}$	
^{100}Mo	NEMO-3 γ -spectroscopy	$0_{\text{g.s.}}^+ \rightarrow 0_{\text{g.s.}}^+$	3034.4	$(6.81 \pm 0.40) \times 10^{18}$	[NEM19]
		$0_{\text{g.s.}}^+ \rightarrow 2_1^+$	2494.9	$> 2.5 \times 10^{21}$	[NEM14]
		$0_{\text{g.s.}}^+ \rightarrow 0_1^+$	1904.1	$(7.50 \pm 0.85) \times 10^{20}$	
^{136}Xe	KamLAND-Zen	$0_{\text{g.s.}}^+ \rightarrow 0_{\text{g.s.}}^+$	2457.8	$(2.21 \pm 0.07) \times 10^{21}$	[Kam16c]
		$0_{\text{g.s.}}^+ \rightarrow 2_1^+$	1639.3	$> 4.6 \times 10^{23}$	[Kam16b]
		$0_{\text{g.s.}}^+ \rightarrow 0_1^+$	878.8	$> 8.3 \times 10^{23}$	
	EXO-200	$0_{\text{g.s.}}^+ \rightarrow 0_1^+$	878.8	$> 6.9 \times 10^{23}$	[EXO16]
^{150}Nd	NEMO-3 γ -spectroscopy	$0_{\text{g.s.}}^+ \rightarrow 0_{\text{g.s.}}^+$	3367.3	$(9.34 \pm 0.64) \times 10^{18}$	[NEM16]
		$0_{\text{g.s.}}^+ \rightarrow 2_1^+$	3033.4	$> 2.2 \times 10^{20}$	[BHNU09]
		$0_{\text{g.s.}}^+ \rightarrow 0_1^+$	2626.9	$(1.33 \pm 0.36) \times 10^{20}$	

From the experimental point of view there are two complementary approaches to search for excited state transitions in $\beta\beta$ -nuclides. The first one is based on conventional low-background γ -spectroscopy using e.g. an array of HPGe detectors surrounding a sample that

contains the $\beta\beta$ -nuclide of interest. The same technique has been briefly discussed in 8.3.7 in order to assess the radiopurity of COBRA’s near detector materials. While γ -spectroscopy is sensitive to the monoenergetic γ -lines from the de-excitation processes, it cannot distinguish between the $2\nu\beta\beta$ -decay and $0\nu\beta\beta$ -decay modes. Hence, only effective half-lives $T_{1/2}^{2\nu+0\nu}$ and branching ratios can be determined. Although the $0\nu\beta\beta$ -decay into excited states is expected to be exceedingly more rare than its $2\nu\beta\beta$ -decay counter part, the $T_{1/2}^{2\nu}$ and $T_{1/2}^{0\nu}$ half-lives as well as the involved branching ratios can only be disentangled with dedicated $0\nu\beta\beta$ -decay experiments. This is why the second approach to search for excited state transitions makes use of the large target mass of those experiments. An overview of the underlying experimental techniques is given in Tab. 3.1 of section 3.3.2.

The current experimental situation is summarized in Tab. 8.19 with emphasis on the more frequent $2\nu\beta\beta$ -decay modes. The only two observations of excited state transitions have been achieved by γ -spectroscopy for the $0_{\text{g.s.}}^+ \rightarrow 0_1^+$ transitions of the isotopes ^{100}Mo and ^{150}Nd . While ^{100}Mo has been studied several times in the past decades (see e.g. [Bar17]), the confirmation of the excited state transition in ^{150}Nd has only been achieved rather recently [KEFT14]. Both $\beta\beta$ -nuclides feature a beneficial combination of the nuclides’ internal structure and their Q -values with $Q_{\beta\beta}(\text{g.s.}) > 3$ MeV, which is comparably high with respect to the other candidates in Tab. 8.19. In fact, for ^{100}Mo and ^{150}Nd the $T_{1/2}^{2\nu}(0_1^+)$ half-lives turn out to be lower than the $T_{1/2}^{2\nu}(\text{g.s.})$ half-lives for the ground-state transitions of the world-leading $0\nu\beta\beta$ -decay experiments based on ^{76}Ge and ^{136}Xe . Because of the much smaller $Q_{\beta\beta}(0_1^+)$ for the latter isotopes and the strong dependency of the related phase-space factor on the Q -value (see e.g. section 3.2.3), which predetermines the decay rate, the expected half-lives are much higher. Even though there are some advantages related to the isotopes ^{100}Mo and ^{150}Nd in terms of excited states, they are not considered for a near-future large-scale $0\nu\beta\beta$ -decay experiment due to other concepts proving to be more promising.

Until today there is no experimental evidence for excited state transitions involving 2_1^+ states, which are suppressed by their spin configuration despite having larger Q -values and related phase-spaces compared to 0_1^+ transitions. However, with larger $0\nu\beta\beta$ -decay experiments in operation or going online, new results are expected to be established in the near future. Current experimental lower limits are on the order of $10^{20} - 10^{24}$ years for various $2\nu\beta\beta$ -decay modes (see Tab. 8.19). The recent upgrade of the GERDA experiment [GER18b] provides excellent prospects to discover the first excited state transition in ^{76}Ge . First results and updated limits on both $2\nu\beta\beta$ -decay and $0\nu\beta\beta$ -decay excited state transitions can be found in the PhD thesis of T. Wester [Wes19]. The two most promising candidate isotopes that are accessible with the COBRA demonstrator will be discussed in the following section.

8.6.2 COBRA’s isotopes of interest

In case of COBRA’s detector approach using CZT semiconductors the double beta transitions of ^{116}Cd and ^{130}Te are the most promising ones because of their high Q -values (see e.g. section 4.2). Furthermore, both isotopes are of general interest in the double beta decay community due to their comparably low $T_{1/2}^{2\nu}(\text{g.s.})$ half-lives, which are roughly in between the ones for ^{100}Mo and ^{150}Nd , proven to be beneficial in terms of excited states, and the world-leading experiments focusing on ^{76}Ge and ^{136}Xe (see Tab. 8.19). The level schemes of the potential excited state transitions for ^{116}Cd and ^{130}Te are illustrated in Fig. 8.44.

Recently, the most likeliest excited state transitions have been investigated by the LNGS experiments Aurora [Aur18] and CUORE [CUO19b]. An overview of the experimental results and predicted half-live values according to Ref. [PS15] is given in Tab. 8.20. The Aurora project has already been discussed previously in section 8.4.1 with emphasis on the ^{116}Cd

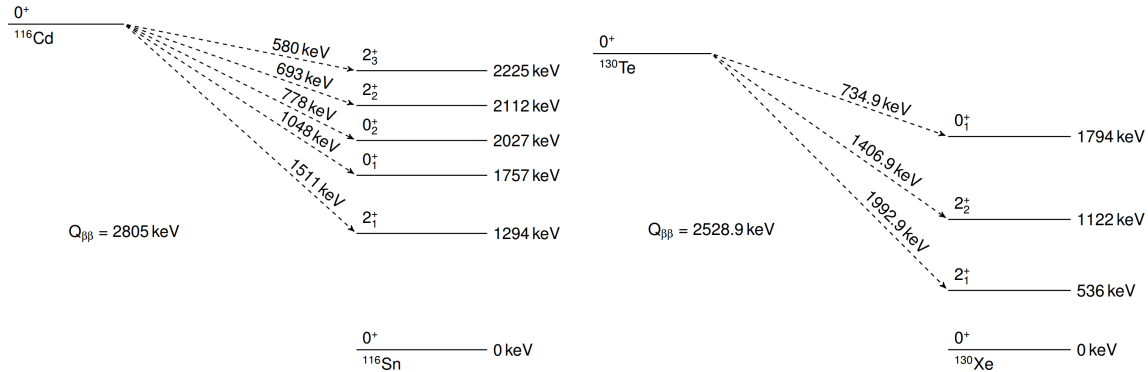


Figure 8.44: Decay schemes of the double beta transitions of ^{116}Cd and ^{130}Te via potential excited states. *Left:* $^{116}\text{Cd}(0^+) \rightarrow ^{116}\text{Sn}(0^+)$. *Right:* $^{130}\text{Te}(0^+) \rightarrow ^{130}\text{Xe}(0^+)$. The energy levels of the excited states in ^{116}Sn and ^{130}Xe as well as the Q -values are taken from the DECAY0 source code and differ slightly from the most recent literature values (see e.g. Tab. 4.4 in section 4.2). Only the states up to the first excited 0^+ state (0_1^+) will be considered in the feasibility study. This includes one 2^+ state for ^{116}Cd and two in the case of ^{130}Te .

$2\nu\beta\beta$ -decay into the ground-state. In case of ^{130}Te there are results from several stages of the CUORE experiment, whereas the most recent study with the full-size CUORE detector array only focuses on the 0_1^+ transitions with and without neutrino emission. That is why especially the limit on $T_{1/2}^{2\nu}(2_1^+)$ is so much weaker compared to the limit on $T_{1/2}^{2\nu}(0_1^+)$ using a much higher exposure.

Each transition via an excited state is accompanied by the emission of characteristic γ -rays. In the case of the $0_{\text{g.s.}}^+ \rightarrow 0_1^+$ transition there is at least one intermediate 2^+ state that forms a γ -ray cascade by populating the state from the initial 0^+ level (see Fig. 8.44). However, the neutrino-accompanied as well as the neutrinoless decay modes share the same excited state levels, hence, can be identified by observing the same γ -lines in an experiment.

The theoretical half-life predictions in Tab. 8.20 include quenching effects of the weak axial-vector coupling g_A as motivated in section 3.2.5 and further elaborated in the course of the ^{113}Cd analysis reported in section 8.3. For the $2\nu\beta\beta$ -decay of ^{130}Te into the 0_1^+ state, the CUORE experiment reports a 90% C.L. lower limit that is rather close to predicted half-life. However, at the same time the predicted $T_{1/2}^{2\nu}$ for the ground-state is off by more than four times. In case of the other $2\nu\beta\beta$ -decay modes there are at least two orders of magnitude difference between the current experimental limits and the recent calculations. The quoted predictions for the $T_{1/2}^{0\nu}$ half-lives are based on an effective neutrino mass of 50 meV and a weighting of the ground-state value with the ratio of the corresponding $T_{1/2}^{2\nu}$ predictions. Conservatively speaking, none of the potential $0\nu\beta\beta$ -decays via excited state transitions will be accessible with the current generation of experiments reporting sensitivities on the order of $\tilde{T}_{1/2}^{0\nu} \sim 10^{26}$ years for the expected g.s. transitions.

Although the sensitivity of the COBRA demonstrator is rather low compared to large experiments such as CUORE, the granularity of the detector array might turn out beneficial in the search for excited states. Because of the involved γ -rays, excited state transitions are expected to appear as coincident events between multiple detectors, which provides distinct experimental signatures. Moreover, as soon as the existence of the $0\nu\beta\beta$ -decay has been confirmed, more experimental input is needed to identify the underlying decay mechanism. Preferably, a confirmation with a different kind of detector concept should be performed. In case of COBRA multiple isotopes could be considered for a construction of a large-scale enriched detector array. Furthermore, the lower limits on the ^{116}Cd $2\nu\beta\beta$ -decays into excited states could already be improved with an experiment of the size of the COBRA demonstrator, while future stages are still under development. The Monte-Carlo simulation of the double

Table 8.20: Experimental results and half-life predictions for excited state transitions in ^{116}Cd and ^{130}Te . The Q -values and energy levels of the excited states in the daughter nuclei have been taken from the DECAY0 source code [PTZ00]. Multiple γ -line energies within a line indicate that a γ -ray cascade is associated with the respective transition (e.g. for the de-excitation from a 0_1^+ state). The γ -line energies are the same for $2\nu\beta\beta$ -decay and $0\nu\beta\beta$ -decay modes of the same isotope. For ^{130}Te there are two intermediate 2^+ states, whereas both states can undergo two decay branches labeled as B1 and B2. However, for the de-excitation from the 0_1^+ state the second branch involves three γ -rays and is expected to have a rather small branching ratio (indicated by the brackets). While $T_{1/2}^{2\nu}(\text{g.s.})$ is already precisely known for ^{116}Cd and ^{130}Te , there are only lower limits (90% C.L.) on the half-lives for excited state transitions. For the half-life measurements the statistical and systematic uncertainties were added in quadrature. The experimental ^{116}Cd results originate from the Aurora experiment at the LNGS using CdWO₄ scintillator crystals [Aur18]. The ^{130}Te results have been obtained by the CUORE experiment [CUO19b] and several predecessor stages (CUORE-0 [CUO19a], CUORICINO [CUO12]). A detailed summary of previous experiments can be found in the review article [Bar17]. The $2\nu\beta\beta$ -decay half-life predictions are taken from Ref. [PS15]. In contrast to the majority of other references, the present calculations consider a quenching of the weak axial-vector coupling g_A with effective values of about 0.6 – 0.7. For the prediction of $T_{1/2}^{0\nu}$ an effective neutrino mass of 50 meV has been assumed, indicating the top of the inverted mass ordering (see Fig. 2.2). Instead of using dedicated calculations to predict $T_{1/2}^{0\nu}$ for the excited state transitions, a scaling according to the ratio of the $T_{1/2}^{2\nu}$ between the g.s. and the respective excited states has been performed. In any case, the discovery of those $0\nu\beta\beta$ -decay modes is out of reach with the given sensitivity of the current generation of experiments.

transition	$Q_{\beta\beta}$ [keV]	E_γ [keV]	mode	$T_{1/2}^{\text{exp}}$ [yr]	$T_{1/2}^{\text{theo}}$ [yr]
^{116}Cd					
$0_{\text{g.s.}}^+ \rightarrow 0_{\text{g.s.}}^+$	2805	-	2ν	$(2.63 \pm 0.12) \times 10^{19}$	2.4×10^{19}
			0ν	$> 2.2 \times 10^{23}$	$\sim 2.0 \times 10^{26}$
$0_{\text{g.s.}}^+ \rightarrow 2_1^+$	1511	1294	2ν	$> 9.8 \times 10^{20}$	2.5×10^{24}
			0ν	$> 7.1 \times 10^{22}$	$\sim 2.1 \times 10^{31}$
$0_{\text{g.s.}}^+ \rightarrow 0_1^+$	1048	1294, 463	2ν	$> 5.9 \times 10^{20}$	1.6×10^{24}
			0ν	$> 4.5 \times 10^{22}$	$\sim 1.3 \times 10^{31}$
^{130}Te					
$0_{\text{g.s.}}^+ \rightarrow 0_{\text{g.s.}}^+$	2529	-	2ν	$(7.9 \pm 0.2) \times 10^{20}$	1.6×10^{20}
			0ν	$> 1.5 \times 10^{25}$	$\sim 2.0 \times 10^{26}$
$0_{\text{g.s.}}^+ \rightarrow 2_1^+$	1993	536	2ν	$> 2.8 \times 10^{21}$	4.2×10^{23}
			0ν	$> 1.3 \times 10^{23}$	$\sim 5.3 \times 10^{29}$
$0_{\text{g.s.}}^+ \rightarrow 2_2^+$	1407	B1: 586, 536 B2: 1122	2ν	-	1.0×10^{27}
			0ν	-	$\sim 1.3 \times 10^{33}$
$0_{\text{g.s.}}^+ \rightarrow 0_1^+$	735	B1: 1258, 536 B2: (672, 586, 536)	2ν	$> 2.5 \times 10^{23}$	7.2×10^{23}
			0ν	$> 1.4 \times 10^{24}$	$\sim 8.8 \times 10^{29}$

beta decay processes just discussed and first results regarding the feasibility of performing an excited state search with the COBRA demonstrator will be presented in the next section.

8.6.3 Monte-Carlo simulation of excited state transitions

The simulation of the excited state transitions of ^{116}Cd and ^{130}Te is done with COBRA’s simulation tool VENOM. The initial kinematics of the double beta decay modes are once more created via the DECAY0 event generator, which is why the Q -values and energy levels of the excited states are taken directly from the source code rather than from the latest literature databases. For each decay mode listed in Tab. 8.19 a total of 10^8 events have been simulated with a confinement of the initial vertex to the 64 sensitive CZT crystal volumes. This includes all $2\nu\beta\beta$ -decay as wells as $0\nu\beta\beta$ -decay modes up to the first excited 0^+ states. As the creation of the DECAY0 input files is rather time and storage consuming, especially for

the excited 2^+ states because of the complexity of the underlying decay schemes and angular correlation functions, only a reduced set of 10^7 initial events has been used in those cases. By comparing the simulation results, no statistical abnormalities have been found for the decay modes with the reduced pool of initial conditions. However, this statement only holds for the present case of reusing the same DECAY0 input pool ten times. In previous iterations based on only 10^6 initial events, statistical artifacts have been discovered in the final VENOM simulation of up to 10^8 events, in case the limited initial kinematics were reused 100 times.

It should be noted again that the following analysis is based on a best-case scenario without consideration of any external background. Instead, the $2\nu\beta\beta$ -decay of ^{116}Cd into the ground-state of ^{116}Sn is treated as intrinsic background for all excited state transitions. Although the ground-state transition is only on the edge to be observed with the demonstrator array, there might already be good prospects to crosscheck the present experimental results. Furthermore, as long as no signal is observed, the decay modes can be treated separately, neglecting possible ambiguities due to lower states also being populated by higher excited state transitions.

Event multiplicities

When searching for excited state transitions, there are a couple of promising signal selection opportunities due to the additional γ -ray emission from the de-excitation of the daughter nucleus. While the two electrons that are released in the initial double beta decay are expected to remain in the source crystal, the de-excitation radiation has a rather high probability to escape. That is why searching for coincidences between several detectors is a natural choice to identify excited state transitions. Multi-detector hits can be characterized by the number of involved crystals, which is referred to as the *multiplicity* m of an event. Single detector events are classified as multiplicity $m = 1$ (M1), two detector hits as multiplicity $m = 2$ (M2) and so on for higher multiplicities.

Another point of consideration is that the COBRA demonstrator's background is dominated by surface contaminations undergoing dominantly rather long-lived α -decays, which are mostly limited to a single detector and do not trigger coincidences (see also section 8.2.4). Because of this, the background for the combined energy spectrum of multiple detector hits is expected to be much lower compared to the results of the previously presented investigation of the $2\nu\beta\beta$ -decay of ^{116}Cd using the preliminary M1 data set (see section 8.4). A preliminary data evaluation of the demonstrator's M2 physics data between 2014 and 2016 with about 230 kg d exposure, which is presented in the Master thesis of J. Volkmer [Vol18], confirms this expectation. Based on the results obtained in [Vol18], a background level of about $\sim 0.06 \text{ cts}/(\text{keV kg yr})$ can be expected for the sum spectrum of M2 events above 2 MeV. However, the statistics of the M2 data set are very limited and consist of only a couple of ten events in this energy region. At lower energies only the prominent ^{40}K γ -line at 1460.8 keV has been identified in the preliminary sum spectrum of M2 events [Vol18], which is in agreement with the background characterization presented in section 8.2.

An illustration of the multiplicity distribution for the simulated double beta decay modes of ^{116}Cd is shown in Fig. 8.45. While the $2\nu\beta\beta$ -decay and $0\nu\beta\beta$ -decay ground-state transitions are dominantly single detector events, they also produce a significant fraction of higher multiplicity events. In case of the excited state transitions, the difference between M1 and higher multiplicities is less prominent. Another observation is that the fraction of $m > 1$ events is larger for the investigated $0\nu\beta\beta$ -decay modes, while the differences between ground-state and excited state transitions get diminished compared to the $2\nu\beta\beta$ -decay modes. The reason for this behavior is related to the likelihood of producing bremsstrahlung by the initial electrons. In the case of $0\nu\beta\beta$ -decays the electrons share the full Q -value while for a $2\nu\beta\beta$ -

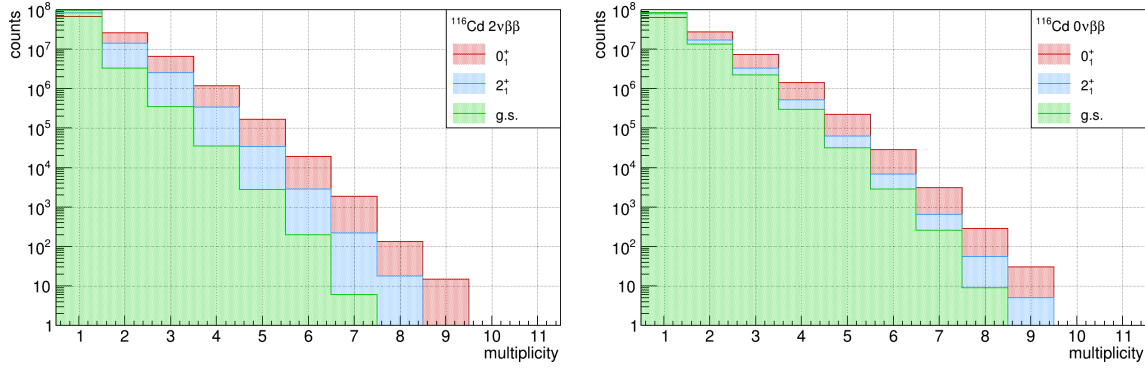


Figure 8.45: Multiplicity distribution for double beta decay transitions of ^{116}Cd simulated for the COBRA demonstrator. *Left:* $2\nu\beta\beta$ -decay modes. *Right:* $0\nu\beta\beta$ -decay modes. The latter decay modes are more likely to produce bremsstrahlung, which explains the overall higher rate of $m > 1$ events as well as the less prominent differences between ground-state and excited state transitions in terms of the event multiplicity. The transition via the 0_1^+ state produces higher multiplicity rates compared to the 2_1^+ state because of its γ -ray cascade and the emission of two de-excitation photons per decay (see also Fig. 8.44).

decay part of the energy is carried away by the neutrinos, which reduces the mean electron energy, thus, the probability of producing bremsstrahlung inside the detector material CZT.

Table 8.21: Relative multiplicity fractions for the simulated ^{116}Cd double beta decay modes using the COBRA demonstrator. While all decay modes feature a high fraction of M1 events, the excited state transitions clearly show an excess of events with higher multiplicities. Based on the determined relative multiplicity composition, M2 events seem to provide a promising tool to discriminate ground-state and excited state transitions. Higher multiplicities only make up for a small fraction of the simulated events and are likely to contribute even less for the case of applying an energy threshold in the analysis.

decay mode	$^{116}\text{Cd } 2\nu\beta\beta$			$^{116}\text{Cd } 0\nu\beta\beta$			
	state	g.s.	2_1^+	0_1^+	g.s.	2_1^+	0_1^+
$f(m = 1) / \%$		96.2	83.0	66.0	84.1	79.3	63.9
$f(m = 2) / \%$		3.3	14.1	26.1	13.3	16.8	27.3
$f(m \geq 3) / \%$		0.4	2.9	7.9	2.5	3.9	9.0

The fraction of events that fall under a certain multiplicity category for the different decay modes are presented in Tab. 8.21. For M1 events the ground-state transitions are clearly dominating. In agreement with the original motivation, the determined multiplicity fractions confirm an increased amount of $m > 1$ events in case of excited state transitions. From the relative rates in Tab. 8.21, M2 events are found to provide a promising signature to discriminate ground-state and excited state transitions, whereas the discrimination seems not as strong for the $0\nu\beta\beta$ -decay modes. The investigation of higher multiplicities would not only be more complex, but would depend more strongly on further analysis steps such as limiting the available energy range or introducing an energy threshold. That is why higher multiplicity events will not be investigated further. Instead, the feasibility study focuses on M2 events.

The same analysis procedure is applied to the ^{130}Te decay modes with the only difference being that there is an additional transition via the intermediate 2_2^+ state of ^{130}Xe . The distribution of the event multiplicities and the corresponding relative multiplicity fractions are shown in Fig. 8.46 and Tab. 8.22. The same conclusions as drawn from the first analysis of the ^{116}Cd decay modes apply to the case of ^{130}Te . Only small differences are found, which are due to the altered decay scheme as depicted in Fig. 8.44.

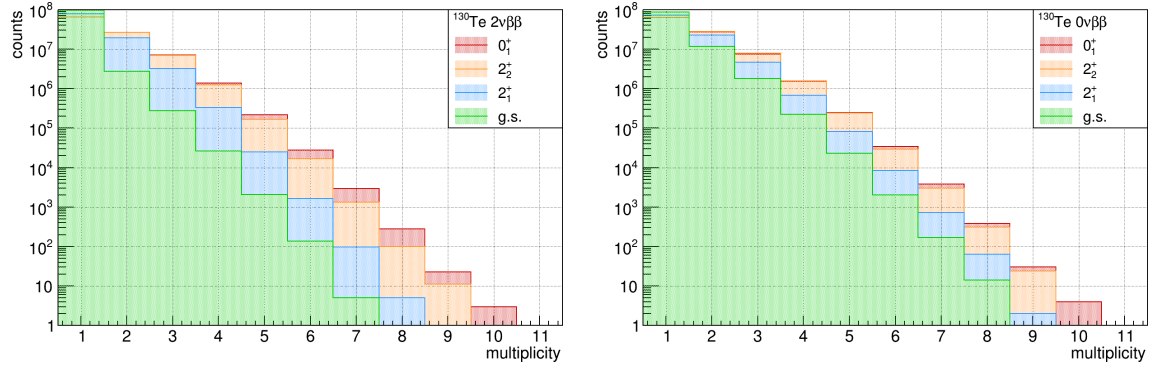


Figure 8.46: Multiplicity distribution for double beta decay transitions of ^{130}Te simulated for the COBRA demonstrator. *Left:* $2\nu\beta\beta$ -decay modes. *Right:* $0\nu\beta\beta$ -decay modes. The differences between the single decay modes coincide with the observations for the already discussed transitions of ^{116}Cd . The increased multiplicity rates for $m > 1$ for the investigated $0\nu\beta\beta$ -decays with respect to the neutrino-accompanied modes is due to the energy dependence of the probability to produce bremsstrahlung. The transitions via the 2_2^+ and 0_1^+ state produce higher multiplicity rates because of the involved γ -ray cascades (see also Fig. 8.44).

Table 8.22: Relative multiplicity fractions for the simulated ^{130}Te double beta decay modes using the COBRA demonstrator. Again, the same conclusion apply as drawn for the already discussed ^{116}Cd decay modes. The focus of the feasibility study is on M2 events, while higher multiplicities only make up for a rather small fraction of the simulated events and can be neglected.

decay mode	$^{130}\text{Te} 2\nu\beta\beta$				$^{130}\text{Te} 0\nu\beta\beta$				
	state	g.s.	2_1^+	2_2^+	0_1^+	g.s.	2_1^+	2_2^+	0_1^+
$f(m = 1) / \%$		97.0	77.2	65.2	65.1	86.2	72.2	62.6	63.8
$f(m = 2) / \%$		2.7	19.2	26.4	26.2	11.8	22.4	27.7	26.9
$f(m \geq 3) / \%$		0.3	3.5	8.4	8.7	2.0	5.4	9.7	9.3

Because of the multiplicity distributions' similarity between the double beta decay modes of ^{116}Cd and ^{130}Te , the prioritization of the M2 analysis approach will be continued in the following. One of the next steps is to investigate the local distribution of M2 events over the detector array of the COBRA demonstrator.

Detector pair distribution

By limiting the analysis to M2 events, it is possible to analyze the simulated decay modes in form of two-dimensional distributions such as discussed in the following. The first series of plots depicted in Fig. 8.47 illustrates the local distribution of the M2 detector pairs for several double beta decay modes of ^{116}Cd and the complete demonstrator array.

As it is not possible to distinguish in the actual physics data whether a detected energy deposition corresponds to the initial decay or a secondary hit by e.g. escaping de-excitation γ -rays or bremsstrahlung, but those processes could be differentiated in the simulation, a randomization of the fixed ordering of the M2 instances is performed. This way, the first detector hit is not necessarily related to the initial decay anymore and, vice versa, for the second detector hit, which was originally referring to the interaction of the secondary radiation. While the total number of simulated events has been distributed equally between the single detectors of the four layers of the demonstrator, there is a clear clustering of events in the M2 detector maps. Because of the randomization of the simulated M2 data, the patterns are symmetric with respect to the counter diagonal.

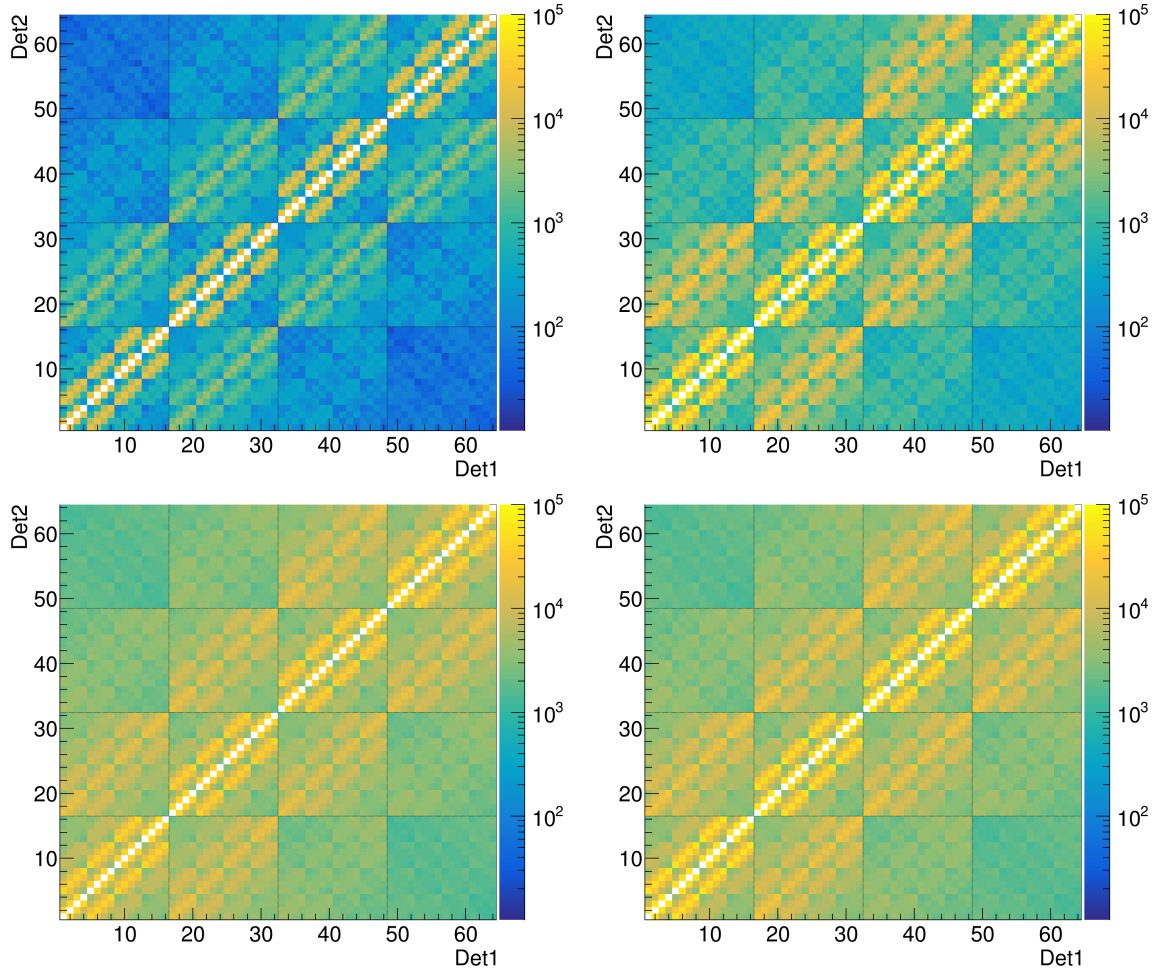


Figure 8.47: Examples of the M2 detector pair distribution for simulated double beta transitions of ^{116}Cd with the COBRA demonstrator. *Top:* $0_{\text{g.s.}}^+ \rightarrow 0_{\text{g.s.}}^+$ transitions via $2\nu\beta\beta$ -decay (*left*) and $0\nu\beta\beta$ -decay (*right*). *Bottom:* $0_{\text{g.s.}}^+ \rightarrow 2_1^+$ transitions via $2\nu\beta\beta$ -decay (*left*) and $0\nu\beta\beta$ -decay (*right*). The grid lines highlight the structure of the detector array consisting of four layers with 4×4 detectors. The counter diagonal elements are empty as they would correspond to coincidences between the same detector numbers. Within a layer, the highest M2 rates are caused by the $0\nu\beta\beta$ -decay into the g.s. (*top right*). Again, the reason for this is the rather high probability to produce bremsstrahlung via the two electrons in the detector material CZT. The observed patterns are very similar for all four example cases and do not allow to identify superior detector pairs.

It is found that the rate of M2 events is higher for direct neighbors within the same layer and gets the lower, the farther the detectors are apart. However, the patterns are very similar for all four considered cases of double beta decay modes and do not show clear preferences of certain detector pairs. Moreover, to discriminate the excited state transitions from the background process (^{116}Cd $2\nu\beta\beta$ -decay into g.s.) a normalization of the rates with respect to the half-lives of the transitions is required.

One particular effect that has not been expected to occur in such a prominent fashion is backscattering. A better impression of the backscattering effect is depicted in Fig. 8.48 comparing the M2 detector pairs of the $0_{\text{g.s.}}^+ \rightarrow 2_1^+$ transition for the $0\nu\beta\beta$ -decay of ^{116}Cd between L1 and L2. The plots are a zoomed version of the illustrations shown before in Fig. 8.47 and feature a linear color axis. While one would expect the pairs of the innermost detectors (e.g. L1: 6, 7, 10, 11 and L2: 22, 23, 26, 27) to feature the highest M2 rates, higher rates are observed for the pairs of outer lying detectors (e.g. L1: 1-4, and L2: 17-21). Furthermore, there are more M2 coincidences of the respective detector pairs for the outer

layers (e.g. L1) than for the inner ones (e.g. L2). This effect is caused by the backscattering of the de-excitation γ -rays and bremsstrahlung from the copper and lead shield surrounding the CZT detector array. Previous simulation studies neglected the artificial shielding of the experiment, which is why the effect of backscattering has not been taken into account before.

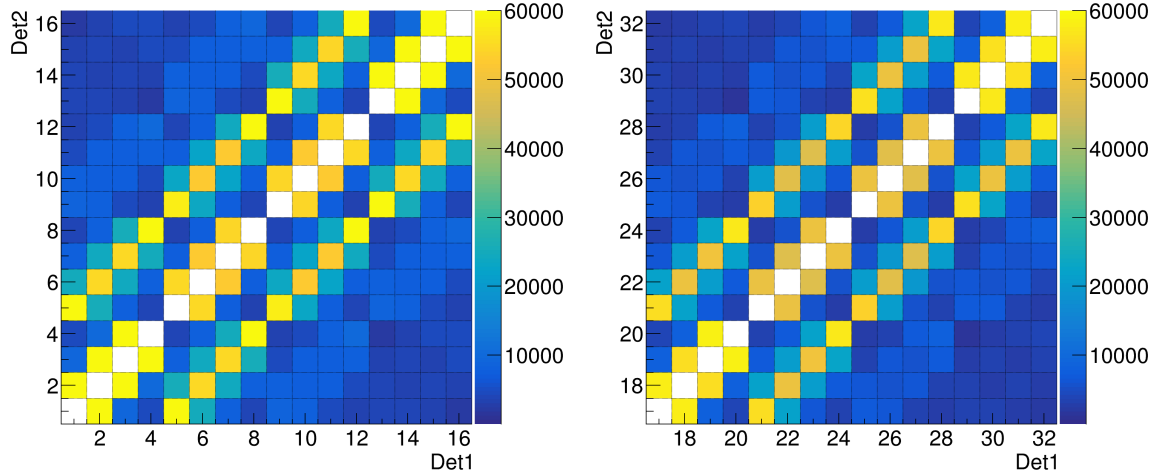


Figure 8.48: Comparison of the M2 detector pair distribution for the $0\nu\beta\beta$ -decay of ^{116}Cd via the 2_1^+ state of ^{116}Sn . *Left:* L1 detectors (1–16). *Right:* L2 detectors (17–32). Due to the backscattering of bremsstrahlung and de-excitation radiation from the surrounding copper and lead castle, pairs involving detectors that are close to the outer shield produce higher M2 rates compared to inner pairs. The effect is stronger for L1 as it is located closer to the bottom of the shield. The same effects are seen for L3 (inner pos.) and L4 (outer pos.).

Finally, the M2 detector pair investigation is repeated for the double beta transitions of ^{130}Te . In agreement with the previously discussed similarity of the multiplicity distributions, the same patterns of M2 detector pairs are found. An illustration of the M2 detector pair distribution of all simulated transitions can be found in section D.5.1 of the appendix.

Energy resolution smearing

The output of the VENOM simulation needs to be folded with the average detector resolution in order to be able to use the same selection cuts in a potential analysis of the physics data. The Gaussian resolution smearing is performed according to the procedure discussed in section 8.3.7 for the ^{113}Cd low-energy background model. It makes use of the average energy resolution function $\text{FWHM}(E)$ which has been obtained from the calibration measurements during the dedicated ^{113}Cd low-threshold run. An illustration of the resolution smearing for some examples for the double beta decay modes of ^{116}Cd is depicted in Fig. 8.49. While the continuous spectra of the $2\nu\beta\beta$ -decay modes are not affected by the applied Gaussian energy smearing, the effect is clearly visible for the $Q_{\beta\beta}$ peaks and γ -lines in the selected $0\nu\beta\beta$ -decay transitions. The discussed energy resolution smearing is applied to all VENOM simulations before performing further analysis steps.

Coincident M2 energy spectra

Naturally, the investigation of the M2 energy spectra of the double beta decays of interest provides deeper insights on how to distinguish potential excited state transitions from the ^{116}Cd $2\nu\beta\beta$ -decay into the ground-state. However, there are several options for the display and characterization of the respective energy spectra. The first option is a two-dimensional representation of the energy depositions of the first and second detector, similarly to the

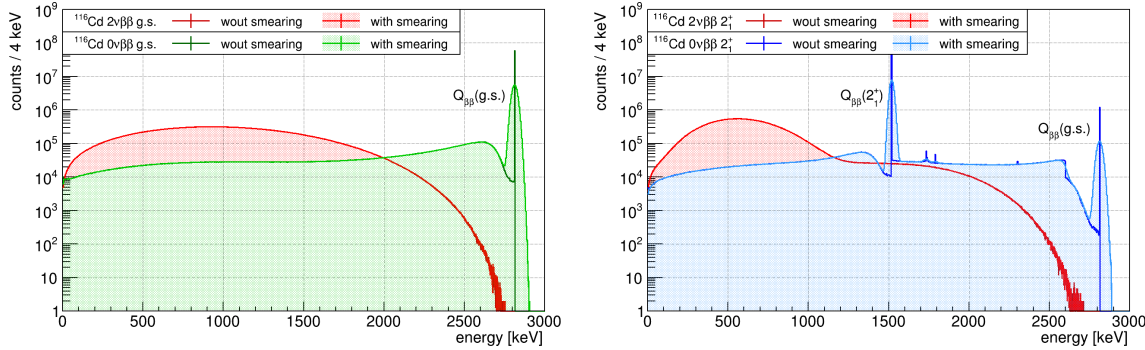


Figure 8.49: Effect of a Gaussian energy smearing onto the VENOM simulations of several double beta decay processes. *Left:* double beta decay transitions of ^{116}Cd into the ground-state of ^{116}Sn . *Right:* double beta decay transitions of ^{116}Cd into the first excited 2^+ state of ^{116}Sn . Each spectrum results from a full detector simulation of the COBRA demonstrator array with 10^8 events and only includes single detector events. The continuous $2\nu\beta\beta$ -decay spectra (indicated in red) are only marginally affected by the applied resolution smearing and are almost congruent with each other. On the contrary, a broadening of the discrete peaks corresponding to different Q -values can be seen for the $0\nu\beta\beta$ -decay modes.

maps of the M2 detector pairs (see e.g. Fig. 8.50). Secondly, a projection of the two-dimensional plots lead to a conventional energy spectrum, which is referred to as the M2 single-spectrum (M_{2s}). Because of the randomization of the M2 energy depositions, referring to the indistinguishability of the first and second detector hit, only one projection onto either the x - or y -axis is needed. Finally, the sum spectrum of the two energy depositions, denoted as $M_{2\Sigma}$, will be used to characterize the simulated transitions. It should be noted that all energy spectra that will be discussed in the following have been randomized to mimic the energy depositions in a real world experiment and were folded with the average energy resolution as pointed out in the previous paragraph.

The two-dimensional representations of the simulated M2 spectra for the double beta decay modes of ^{116}Cd are shown in Fig. 8.50. The respective plots for ^{130}Te can be found in Fig. 8.51. As a result of the post-processing of the simulations including the randomization of the M2 energy depositions, the two-dimensional energy spectra turn out to be mirror-symmetric with the counter diagonal being the symmetry axis. The observed horizontal and vertical lines correspond to the cases where one detector registers a fixed energy (e.g. the full deposition of E_γ), while the second detector observes the sum of the electrons' energy deposit up to the corresponding $Q_{\beta\beta}$. In the case of $2\nu\beta\beta$ -decays into excited states, these lines provide a promising tool to distinguish the transitions from the continuous spectrum of the respective ground-state transition. Their presence and distinctiveness from the considered background process will be studied in the $2\nu\beta\beta$ -decay's M_{2s} projections.

The same can be done for the $0\nu\beta\beta$ -decay modes of the respective isotopes. One particular difference is, however, that the detection of E_γ in one detector coincides dominantly with the detection of the Q -value of the corresponding excited state transition in the second detector in case of an excited state transition. The potential summation effects of the combination $E_\gamma + Q_{\beta\beta}$ cause additional patterns in the two-dimensional M2 representations such as the prominent summation points. Furthermore, this increases the number of vertical and horizontal lines with respect to the $2\nu\beta\beta$ -decay modes. Besides the already discussed features there are additional diagonal lines, which do also correspond to summation effects. The diagonal line with the highest intensity indicates events where the full $Q_{\beta\beta}$ of the respective transition has been deposited as the sum of two detectors. One common feature of all $0\nu\beta\beta$ -decay modes is a diagonal line for $Q_{\beta\beta}(\text{g.s.})$ as all neutrinoless decay modes have the potential to deposit the full ^{116}Cd Q -value of 2.8 MeV according to their decay schemes (see Fig. 8.44). The summation peaks are expected to appear in the $M_{2\Sigma}$ spectra.

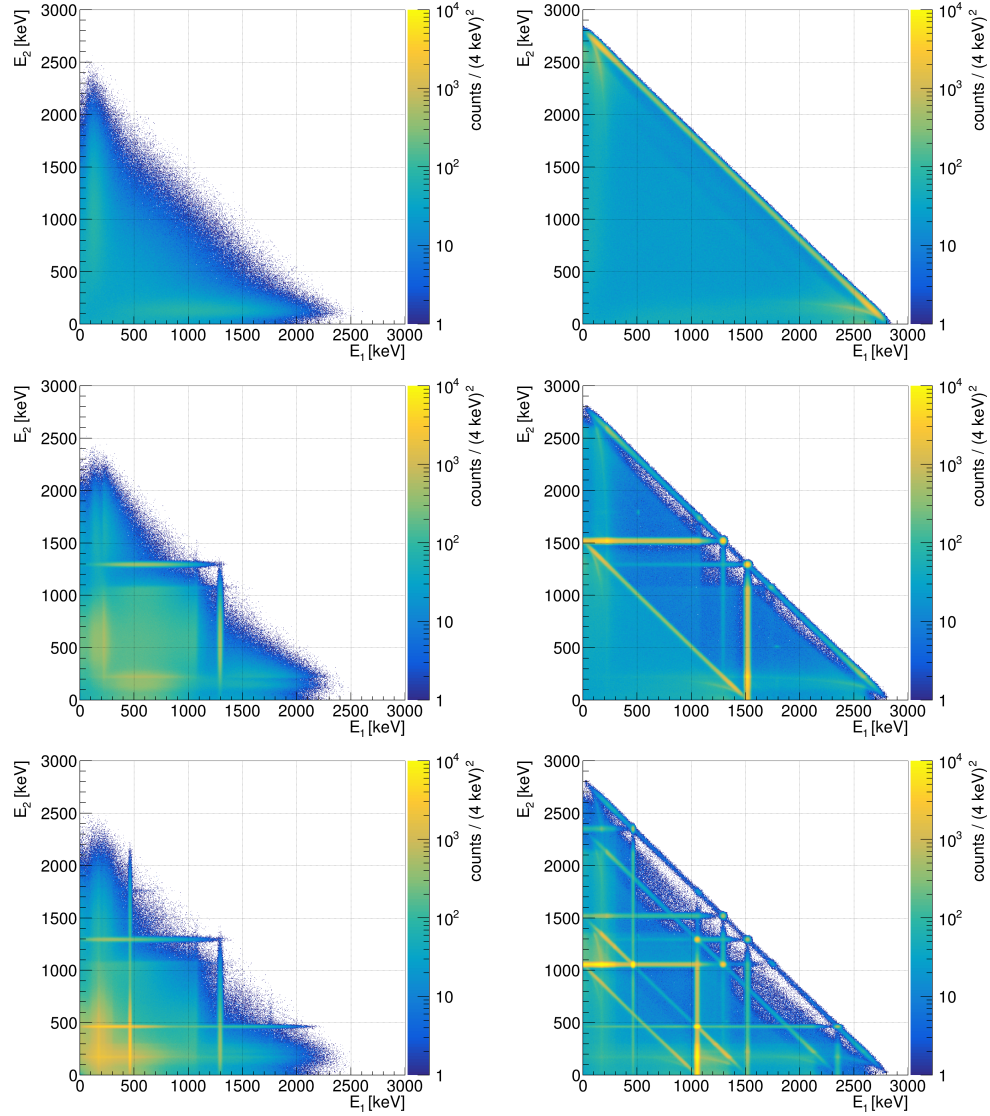


Figure 8.50: Representation of coincident energy spectra of M2 events for double beta transitions of ^{116}Cd . Left: $2\nu\beta\beta$ -decay modes via ground-state (top), 2_1^+ state (middle) and 0_1^+ state (bottom). Right: $0\nu\beta\beta$ -decay modes via ground-state (top), 2_1^+ state (middle) and 0_1^+ state (bottom). The randomization of the M2 energy deposits ensures a symmetric distribution with respect to the counter diagonal. For the excited state transitions, areas of increased count rate (e.g. horizontal, vertical and diagonal lines) can be identified.

Normalization of Monte-Carlo spectra

In order to quantify the intensity of the previously presented features of the two-dimensional M2 spectra, the one-dimensional M_{2S} and $M_{2\Sigma}$ spectra will be used in the following. However, a comparison with respect to the ^{116}Cd $2\nu\beta\beta$ -decay into the ground-state as an estimate of the intrinsic, irreducible background requires a normalization of the MC spectra according to the half-lives of the transitions. Moreover, the normalization depends on the number of source atoms $N_{\beta\beta}$ per mass unit in CZT, the number of simulated events $N_{\text{MC}} = 10^8$ and the width of the energy bins $\Delta b = 4 \text{ keV}$ to express the decay rate in the usual units of $\text{cts}/(\text{keV kg yr})$. This way it would also be possible to compare the normalized MC spectra to the physics data of the COBRA demonstrator in a future analysis attempt.

The value of $N_{\beta\beta}$ can be calculated according to Eqn. (8.1). Because of the half-lives being much longer than the observation time and $N_{\text{MC}} \ll N_{\beta\beta}$, a Taylor expansion of the

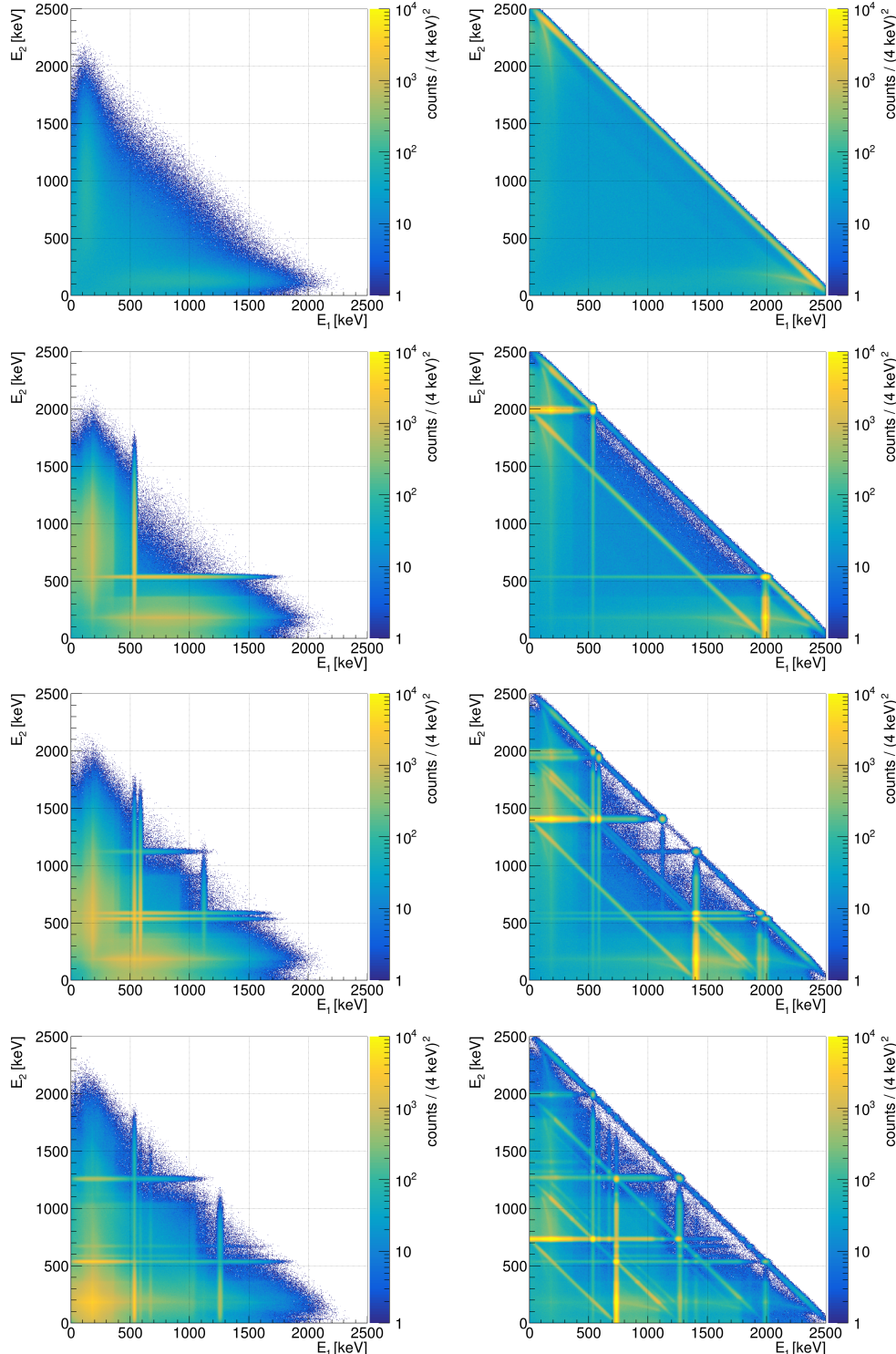


Figure 8.51: Representation of coincident energy spectra of M2 events for double beta transitions of ^{130}Te . Left: $2\nu\beta\beta$ -decay modes via ground-state (top), 2_1^+ state (upper middle), 2_2^+ state (lower middle) and 0_1^+ state (bottom). Right: $0\nu\beta\beta$ -decay modes via ground-state (top), 2_1^+ state (upper middle), 2_2^+ state (lower middle) and 0_1^+ state (bottom). The randomization of the M2 energy deposits ensures a symmetric distribution with respect to the counter diagonal. For the excited state transitions, areas of increased count rate (e.g. horizontal, vertical and diagonal lines) can be identified.

radioactive decay law can be used to calculate the scaling factors f_s . This leads to an expression of the following form

$$f_s = \frac{\ln(2) \cdot N_{\beta\beta}}{N_{\text{MC}} \cdot T_{1/2} \cdot \Delta b}. \quad (8.54)$$

Considering the most recent experimental results for ^{116}Cd and ^{130}Te , the lower limits at 90% C.L. of the Aurora and CUORE experiments (see Tab. 8.20) are used as an estimate of the respective half-lives entering Eqn. (8.54). For ^{130}Te it was decided to estimate the half-lives for the transitions via the two excited 2^+ states with the lower limits on the 0_1^+ transitions due to the lack of recent analysis results that could compete with the much stricter limits set by the full-size CUORE experiment in case of the 0_1^+ transitions.

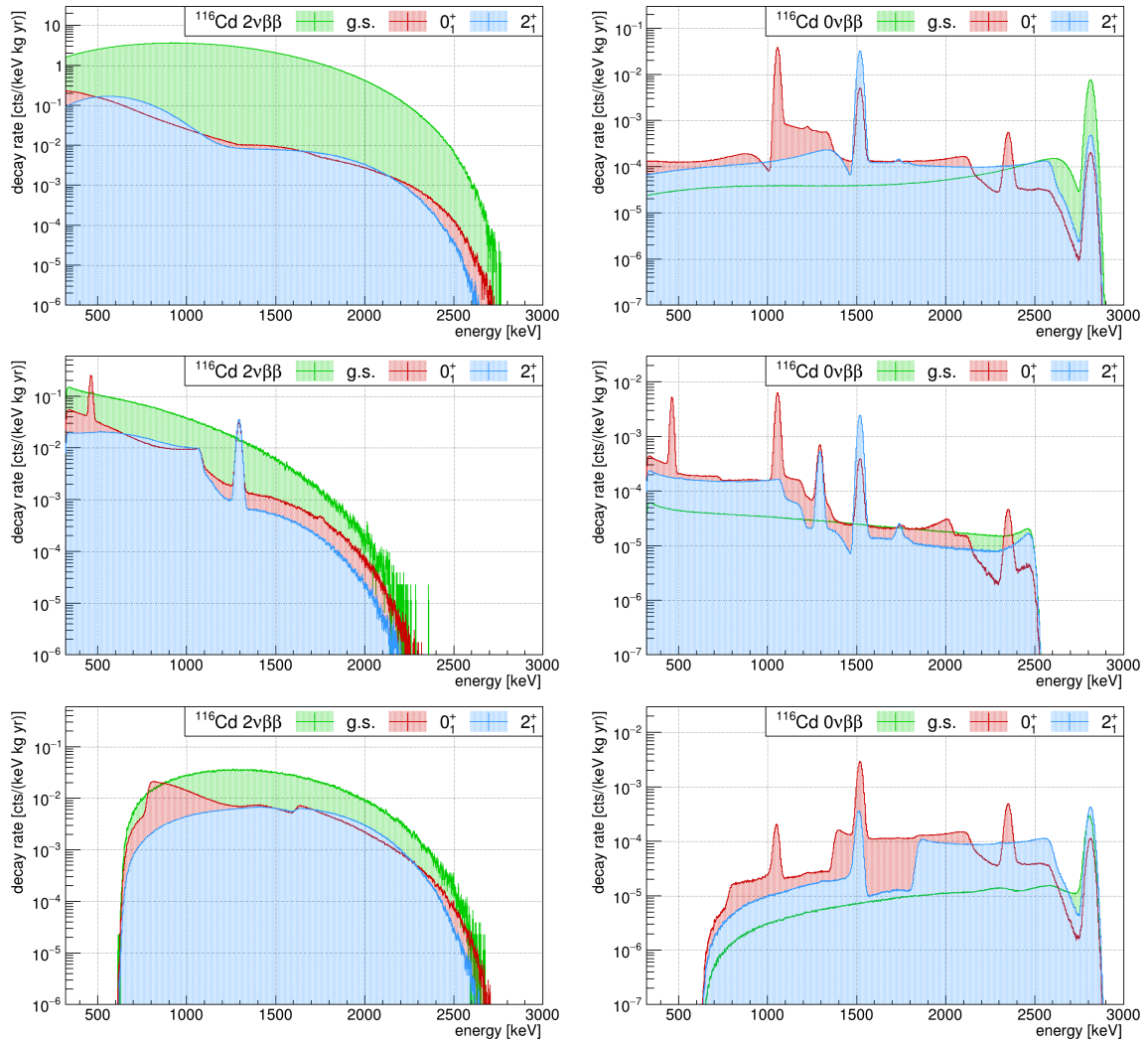


Figure 8.52: Comparison of normalized MC spectra for the investigated double beta transitions of ^{116}Cd . Left: $2\nu\beta\beta$ -decay modes. Right: $0\nu\beta\beta$ -decay modes. The three rows correspond to the M1 spectra (top), the $M2_s$ spectra (middle) and the $M2_\Sigma$ spectra (bottom). The normalization according to Eqn. (8.54) is based on the lower half-life limits at 90% C.L. obtained by the Aurora experiment (see Tab. 8.20). The y-axis features different scales for a better visibility. While the $2\nu\beta\beta$ -decay modes are dominated by the ground-state transition in case of the M1 channel, the additional γ -line signatures are clearly visible in the $M2_s$ spectra. The signatures of the $0\nu\beta\beta$ -decays via the intermediate excited states would be largely hidden by the $2\nu\beta\beta$ -decay into the g.s. as an estimate of the intrinsic background.

The accordingly scaled energy spectra of the simulated double beta decay transitions of ^{116}Cd are presented in Fig. 8.52. Besides the $M2_s$ and $M2_\Sigma$ spectra, which have been introduced before, the spectra based on M1 events are shown for comparison. All spectra are subject to a restriction of the energy range to remove events with an energy deposit below the Q -value of the β -decay of ^{113}Cd . As pointed out before in several sections, the ^{113}Cd decay rate dominates the physics data of the COBRA demonstrator at low energies. In fact, the rate is about six orders of magnitude higher than expected for the $2\nu\beta\beta$ -decay of ^{116}Cd . While the chance of random coincidences between unrelated ^{113}Cd decays in different detectors is still negligibly small for the COBRA demonstrator, the probability increases in the light of a potential large-scale COBRA experiment with several thousand CZT crystals and an increasing target mass (see section 4.3.5). As such a size would be needed to really compete with the currently running and proposed $0\nu\beta\beta$ -decay experiments, it makes sense to define such a threshold from the very beginning. In the present case the single detector threshold is set to $E_{\text{th}} = 320 \text{ keV}$. Consequently, the threshold for the displayed $M2_\Sigma$ spectra is twice as high. Details regarding the effect of choosing a threshold instead of taking all M2 events into account in the construction of the M2 spectra will be discussed in section 8.6.4.

For the M1 spectra there is a overwhelming dominance of the $2\nu\beta\beta$ -decay g.s. transition of ^{116}Cd for the $2\nu\beta\beta$ - and $0\nu\beta\beta$ -decay modes, which prevents any imprints of the potential excited states transitions to appear in the combined spectrum of all decay modes. This confirms once more the need to perform a search for excited state transitions for events with a higher multiplicity. Even though the situation is similarly challenging for the $M2_s$ and $M2_\Sigma$ channels, applying the normalization according to the latest Aurora results on $T_{1/2}^{0\nu}$ (see Tab. 8.20), the prospects of the COBRA demonstrator are quite promising for the $2\nu\beta\beta$ -decay modes. Here, the $M2_s$ channel is expected to provide a noticeable signature under the assumption of the lower half-life limits and the g.s. $2\nu\beta\beta$ -decay as an estimate of the intrinsic background. The case of normalizing the MC spectra according to the predicted double beta decay half-lives reported in Tab. 8.20 can be found in section D.5.2 of the appendix. In this case it will be extremely unlikely to discover any excited state signature with an experiment of the size of the COBRA demonstrator array.

The normalized MC spectra for the double beta transitions of ^{130}Te are depicted in Fig. 8.53. Because of the stronger half-life limits set by the CUORE experiment and the assumed universality of the 0_1^+ result as estimate for the intermediate 2^+ states, no decay mode is expected to provide a clear signature given the intrinsic background of the $2\nu\beta\beta$ -decay ground-state transitions and the exposure that could be reached with the demonstrator array. It should be noted that the expected $2\nu\beta\beta$ -decay rate of ^{116}Cd is almost a magnitude higher than for ^{130}Te , which worsens the experimental starting point even more. For the sake of completeness, a compilation of the normalized ^{130}Te spectra based on the predicted half-lives according to Tab. 8.20 can be found in section D.5.2 of the appendix.

The evaluation of potential event selection criteria that might improve the identification of the excited states features in the normalized M2 spectra will be discussed in the following section. The aim is to determine the selection efficiency for excited state transitions as a guide line for future analysis approaches as well as to estimate a best-case signal-to-background ratio (S/B) in order to investigate the feasibility of such attempts given the size and geometry of the COBRA demonstrator.

8.6.4 Event selection based on M2 spectra

An overview of the potential signatures that are unique for the double beta decays of ^{116}Cd and ^{130}Te via the excited states of their daughter nuclei and might be able to distinguish them from the ground-state transitions is given in Tab. 8.23. The criteria are based on the

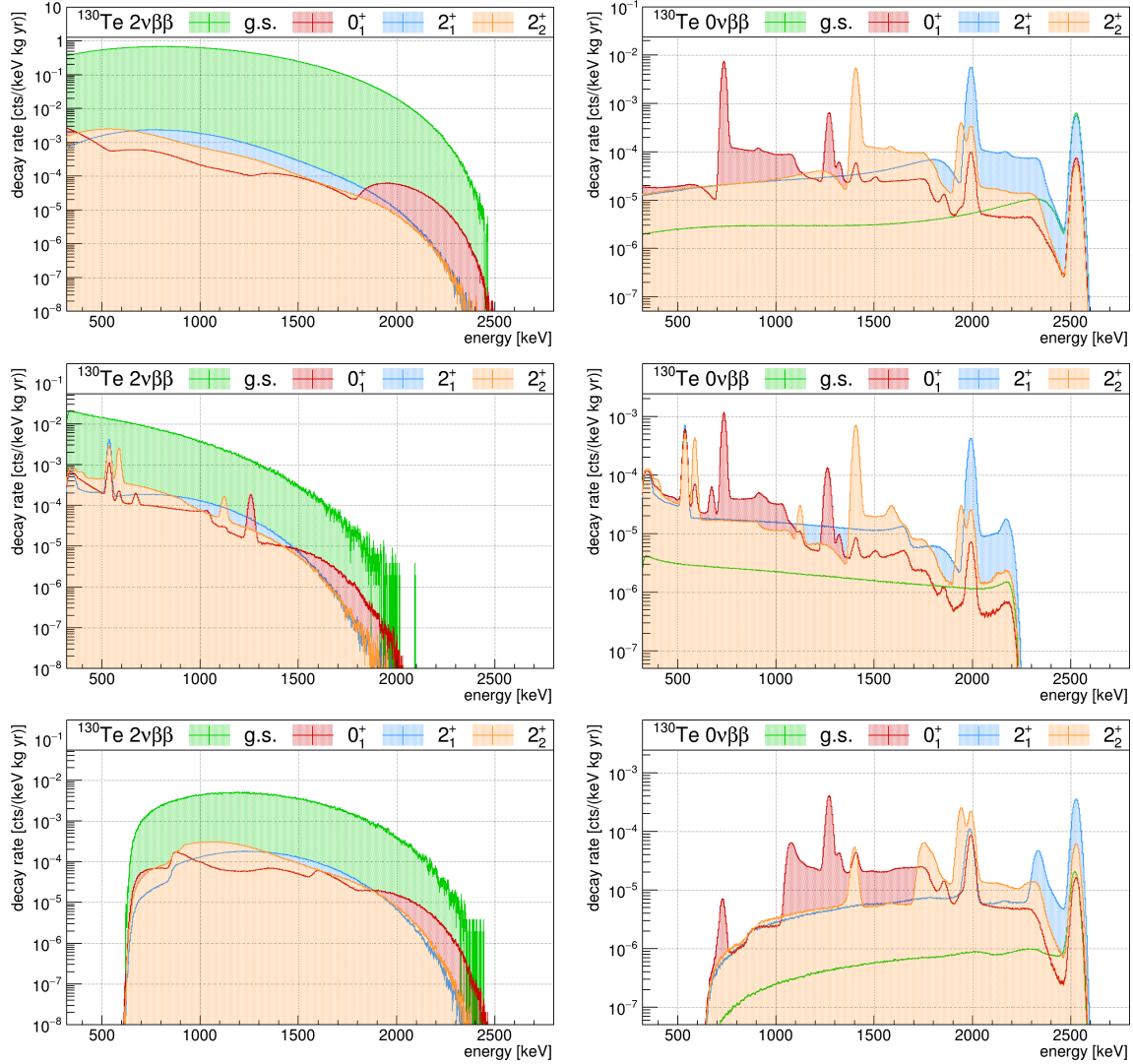


Figure 8.53: Comparison of normalized MC spectra for the investigated double beta transitions of ^{130}Te . *Left:* $2\nu\beta\beta$ -decay modes. *Right:* $0\nu\beta\beta$ -decay modes. The three rows correspond to the M1 spectra (*top*), the M 2_s spectra (*middle*) and the M 2_Σ spectra (*bottom*). The normalization according to Eqn. (8.54) is based on the lower half-life limits at 90% C.L. obtained by the CUORE experiment (see Tab. 8.20). The *y*-axis features different scales for a better visibility. Because of the very restrictive CUORE results there is hardly a chance to improve the current experimental situation with the COBRA demonstrator, not even by assuming the presently applied best-case scenario.

previously discussed M2 spectra and originate from the characteristic, discrete energy levels of the corresponding decay schemes depicted in Fig. 8.44.

In several iterations of the analysis it was found that the results depend on the construction of the required M2 spectra. In the first iteration no artificial threshold for the energy deposition of a single detector has been used. By comparing the two-dimensional representation of the irreducible background process – the ground-state $2\nu\beta\beta$ -decay of ^{116}Cd – with the excited state transitions in Fig. 8.50, it is clear that applying a threshold improves the S/B ratio exceptionally for the projection of the M 2_s spectra. The same applies for the application of dedicated energy restrictions to limit the ROI as summarized in Tab. 8.23, which are found to provide the best prospects in terms of the achievable S/B ratio.

Table 8.23: Overview of selection criteria to identify excited state transitions for the isotopes ^{116}Cd and ^{130}Te in the M2 channel. While for the $2\nu\beta\beta$ -decay modes only the M2_s spectra are of interest, there are additional information in case of the $0\nu\beta\beta$ -decay transitions due to summation effects which are visible in the M2_Σ spectra. Moreover, the $2\nu\beta\beta$ -decay transitions can only be identified via the de-excitation γ -lines, whereas the spectra of the $0\nu\beta\beta$ -decays contain also imprints of the respective Q -values and potential summation effects (see also Fig. 8.52 and Fig. 8.53). The potential ROIs are highlighted below as $E_\gamma(\text{e.s.})$ and $Q_{\beta\beta}(\text{e.s.})$ and could be selected via a suitable energy window. The corresponding central values can be found in Fig. 8.44 and Tab. 8.20. The criteria indicated with † are expected to have a rather low efficiency as they are either only effective for direct neighbors (shared $Q_{\beta\beta}$) or involve suppressed γ -line cascades, which usually applies to the B2 branch (see Tab. 8.20). That is also why the criteria for the $0\nu\beta\beta$ -decays only consider γ -lines from the B1 branches. As an estimate of the irreducible background the same selection rules are applied to the $2\nu\beta\beta$ -decay of ^{116}Cd into the ground-state of ^{116}Sn .

decay mode	$2\nu\beta\beta$		$0\nu\beta\beta$	
	spectrum	M2 _s	M2 _s	M2 _Σ
^{116}Cd				
$0_{\text{g.s.}}^+ \rightarrow 2_1^+$		$E_\gamma(2_1^+)$	$E_\gamma(2_1^+)$ $Q_{\beta\beta}(2_1^+)$	$Q_{\beta\beta}(2_1^+)^\dagger$ $Q_{\beta\beta}(\text{g.s.})$
^{116}Cd				
$0_{\text{g.s.}}^+ \rightarrow 0_1^+$		$E_\gamma(0_1^+)$ $E_\gamma(2_1^+)$	$E_\gamma(0_1^+)$ $E_\gamma(2_1^+)$ $Q_{\beta\beta}(0_1^+)$ $Q_{\beta\beta}(0_1^+) + E_\gamma(0_1^+)$ $Q_{\beta\beta}(0_1^+) + E_\gamma(2_1^+)$	$Q_{\beta\beta}(0_1^+)^\dagger$ $Q_{\beta\beta}(0_1^+) + E_\gamma(0_1^+)$ $Q_{\beta\beta}(0_1^+) + E_\gamma(2_1^+)$ $Q_{\beta\beta}(\text{g.s.})$
^{130}Te				
$0_{\text{g.s.}}^+ \rightarrow 2_1^+$		$E_\gamma(2_1^+)$	$E_\gamma(2_1^+)$ $Q_{\beta\beta}(2_1^+)$	$Q_{\beta\beta}(2_1^+)^\dagger$ $Q_{\beta\beta}(\text{g.s.})$
^{130}Te				
$0_{\text{g.s.}}^+ \rightarrow 2_2^+$		B1: $E_\gamma(2_1^+)$ B1: $E_\gamma(2_2^+)$ B2: $E_\gamma(2_2^+)^\dagger$	$E_\gamma(2_1^+)$ $E_\gamma(2_2^+)$ $Q_{\beta\beta}(2_2^+)$ $Q_{\beta\beta}(2_2^+) + E_\gamma(2_1^+)$ $Q_{\beta\beta}(2_2^+) + E_\gamma(2_2^+)$	$Q_{\beta\beta}(2_2^+)^\dagger$ $Q_{\beta\beta}(2_2^+) + E_\gamma(2_1^+)$ $Q_{\beta\beta}(2_2^+) + E_\gamma(2_2^+)$ $Q_{\beta\beta}(\text{g.s.})$
^{130}Te				
$0_{\text{g.s.}}^+ \rightarrow 0_1^+$		B1: $E_\gamma(0_1^+)$ B1: $E_\gamma(2_1^+)$ B2: $E_\gamma(0_1^+)^\dagger$ B2: $E_\gamma(2_2^+)^\dagger$ B2: $E_\gamma(2_1^+)^\dagger$	$E_\gamma(2_1^+)$ $E_\gamma(0_1^+)$ $Q_{\beta\beta}(0_1^+)$ $(Q_{\beta\beta}(0_1^+) + E_\gamma(2_1^+))^\dagger$ $Q_{\beta\beta}(0_1^+) + E_\gamma(0_1^+)$	$Q_{\beta\beta}(0_1^+)^\dagger$ $Q_{\beta\beta}(0_1^+) + E_\gamma(2_1^+)$ $Q_{\beta\beta}(0_1^+) + E_\gamma(2_1^+)$ $Q_{\beta\beta}(\text{g.s.})$

Some analysis approaches for the $\beta\beta$ -decay transitions of ^{116}Cd are depicted in Fig. 8.54 and Fig. 8.55. Each plot contains three pairs of spectra corresponding to the different analysis approaches. For each pair, the signal process of an excited state transition is compared to the $2\nu\beta\beta$ -decay ground-state of ^{116}Cd . The first of the three options is to apply no restriction on the energy spectra, thus, to use all simulated events. Alternatively, a minimum threshold of e.g. $E_{\text{th}} > 320\text{ keV}$ can be defined for the M2_s and M2_Σ spectra, whereas the example spectra in Fig. 8.54 and Fig. 8.55 are the same as shown before in Fig. 8.52. Compared to the spectra containing all events, without applying an energy threshold, a clear improvement of the intensity of the signal peaks with respect to the corresponding background estimate

can be seen for all decay modes. The third option consists of a combination of the threshold cut and the dedicated energy restrictions according to the ROIs listed in Tab. 8.23. The respective ROIs as well as the related side-bands (SBs) have been highlighted for each of the displayed examples. Their definitions are based on the average energy resolution.

The extraction of the signal selection efficiency and an estimate of the achievable S/B ratio for the present best-case scenario will be discussed in the next section.

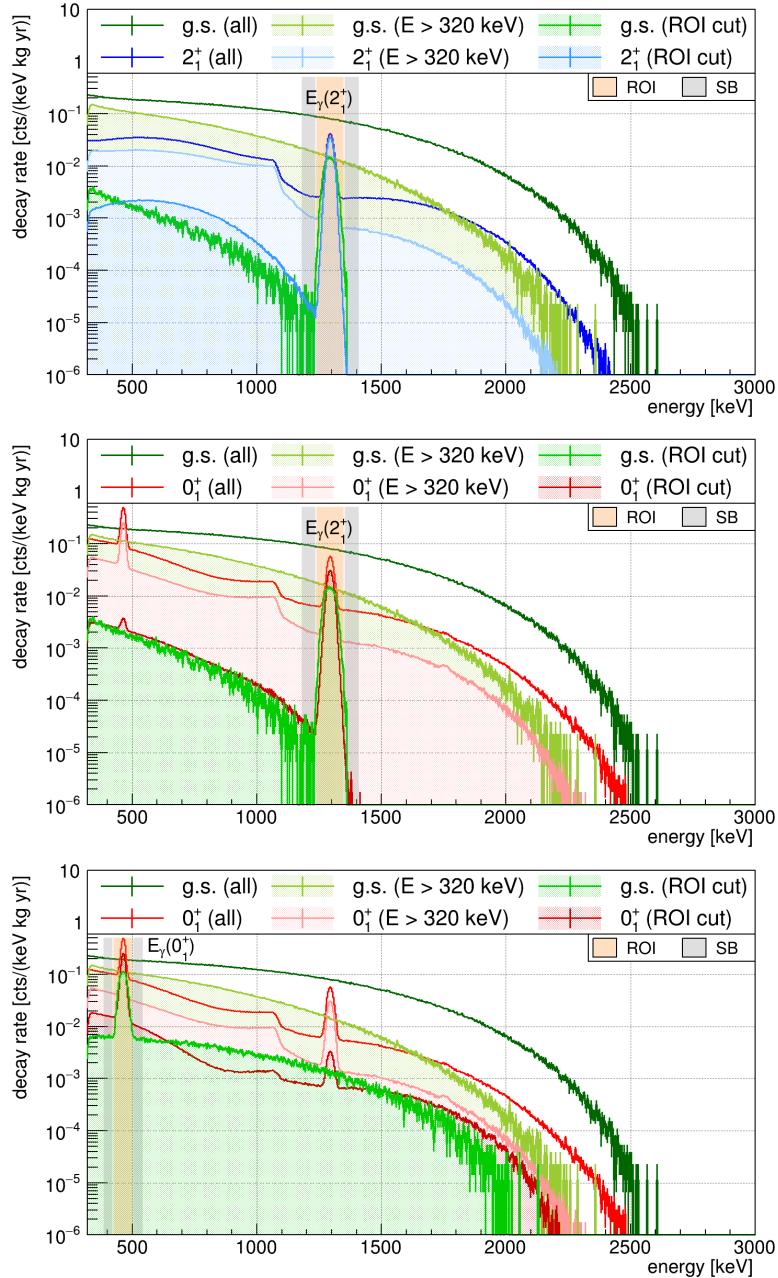


Figure 8.54: Examples for the selection of excited state signatures for $2\nu\beta\beta$ -decays of ^{116}Cd based on the M2_s spectra. *Top:* $0_{\text{g.s.}}^+ \rightarrow 2_1^+$ transition with $E_\gamma(2_1^+) = 1294 \text{ keV}$. *Middle:* $0_{\text{g.s.}}^+ \rightarrow 0_1^+$ transition with $E_\gamma(2_1^+) = 1294 \text{ keV}$. *Bottom:* $0_{\text{g.s.}}^+ \rightarrow 0_1^+$ transition with $E_\gamma(0_1^+) = 463 \text{ keV}$. The three pairs of energy spectra in each plot correspond to the underlying event selections to construct the M2 spectra. The first option is to use all events, the second to only use events above $E_{\text{th}} = 320 \text{ keV}$ and the third to apply an additional energy restriction to only select the highlighted ROI (see also Tab. 8.23). The ROI covers a range of $\pm 2 \cdot \text{FWHM}(E)$ around the discrete energy of interest, providing an almost 100% coverage. The corresponding SBs are placed symmetrically around the ROI with a 4 keV offset and cover the same width.

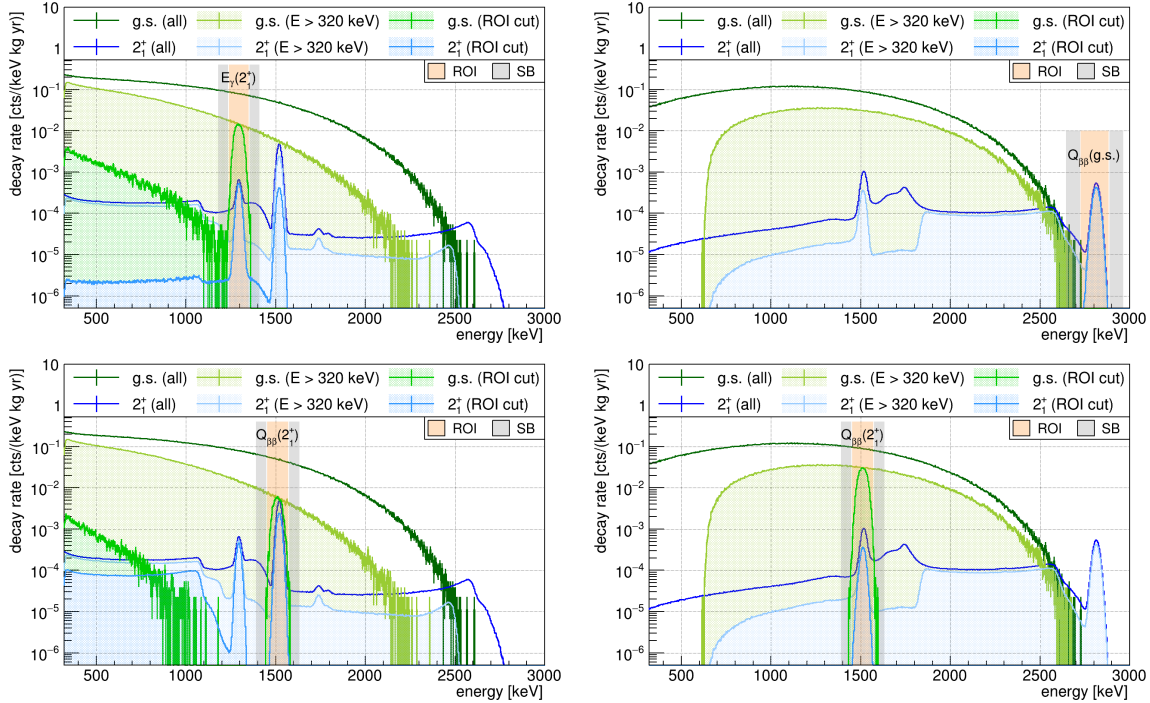


Figure 8.55: Examples for the selection of excited state signatures for $0\nu\beta\beta$ -decays of ^{116}Cd based on the M 2_s spectra (*left*) and the M 2_Σ spectra (*right*). *Top left*: $0^+_{\text{g.s.}} \rightarrow 2^+_1$ transition with $E_\gamma(2^+_1) = 1294$ keV. *Top right*: $0^+_{\text{g.s.}} \rightarrow 2^+_1$ transition with $Q_{\beta\beta}(\text{g.s.}) = 2805$ keV. In this case the g.s. spectrum remains empty for the application of the ROI selection. *Bottom*: $0^+_{\text{g.s.}} \rightarrow 2^+_1$ transition with $Q_{\beta\beta}(2^+_1) = 1511$ keV. The three pairs of energy spectra in each plot correspond to the underlying event selections to construct the M2 spectra. The first option is to use all events, the second to only use events above $E_{\text{th}} = 320$ keV and the third to apply an additional energy restriction to only select the highlighted ROI (see also Tab. 8.23). The ROI covers a range of $\pm 2 \cdot \text{FWHM}(E)$ around the discrete energy of interest, providing an almost 100% coverage. The corresponding SBs are placed symmetrically around the ROI with a 4 keV offset and cover the same width.

8.6.5 Determination of signal selection efficiency

The determination of the signal selection efficiency is based on the analysis procedure described in the previous section. Firstly, for each ROI listed in Tab. 8.23 the projected M2 spectra are prepared by restricting the energy range to $\pm 2 \cdot \text{FWHM}(E)$ using the known average energy resolution function. In previous iterations, without the energy restrictions to the ROIs, it was found that some of the excited state signatures could not be resolved (see e.g. the M 2_s and M 2_Σ spectra in Fig. 8.53 for the 2^+_2 transition of ^{130}Te). However, by following the described procedure it is possible to analyze each decay mode and ROI independently. Furthermore, the Gaussian coverage of the ROIs has been improved to about 100% by increasing the width from $\pm \text{FWHM}(E)$ (98.15% coverage) to twice its original size in the final iteration.

The advanced treatment of the ROIs also affects the reasoning behind the usage of the side-bands. Originally, they were supposed to estimate the flat background in the ROI due to coincidences of underlying events which were not caused by the intended excited state signatures. An impression of the continuous background can be found in the two-dimensional M2 spectra displayed in Fig. 8.50 and Fig. 8.51 and the corresponding M 2_s spectra in Fig. 8.52 and Fig. 8.53. In the latter example plots the signal peaks are situated on top of a rather flat and continuous background. However, by restricting the energy range to the defined ROIs, the signal peaks become much more prominent in the respective M2 spectra (see the examples

shown in Fig. 8.54 and Fig. 8.55). For some cases, like for instance the $0\nu\beta\beta$ -decay selections that are based on the $Q_{\beta\beta}$ criteria listed in Tab. 8.23, the signal regions are well separated from the residual background, which make the SBs kind of obsolete (see Fig. 8.55). On the other hand, there are cases with a strong overlap of the signal regions (e.g. the $2\nu\beta\beta$ -decay of ^{116}Cd via the 2_1^+ state). In those cases, the consideration of the SBs provides a measure to estimate the overlap with the second signal region.

Finally, the application of the SB approach allows for a crosscheck of the background contribution from the ^{116}Cd ground-state $2\nu\beta\beta$ -decay. In the present best-case scenario, the irreducible background can be directly determined by applying the ROI selection criteria onto the ^{116}Cd ground-state M2 spectra. The deviation between the integral over the ROI and the SBs is $0.1 - 4.6\%$ for the investigated signatures that are well below the ^{116}Cd Q -value of $Q_{\beta\beta}(\text{g.s.}) = 2805 \text{ keV}$. For the highest ROI below the Q -value of the ground-state transition, corresponding to $Q_{\beta\beta}(0_1^+) + E_\gamma(2_1^+) = 2342 \text{ keV}$, the deviation increases to about 20% due to the sharply falling edge of the $2\nu\beta\beta$ -decay spectrum. However, those numbers only indicate once more the limitation of the present feasibility study without having access to an actual background model.

In preparation for a future analysis attempt, any template spectrum could be used as an input in order to incorporate a more complete background projection. Moreover, the position of the SBs could be shifted to avoid known γ -lines or other prominent background features in a given model. These are essential features for a potential excited state search using the physics data of the COBRA demonstrator and have been implemented into the analysis software. The same applies to the widths of the signal regions.

A summary of the intermediate results obtained in the course of the present thesis will be given in the following. The first parameter that has been determined separately for each decay mode is the selection efficiency $f_{\text{M}2}^{\text{sig}}$ for the considered excited state signatures in the M2 channel. It is defined as the ratio of the corrected ROI counts and the total number of simulated events N_{MC} according to

$$f_{\text{M}2}^{\text{sig}} = \frac{N_{\text{ROI}} - N_{\text{SB}}}{N_{\text{MC}}}. \quad (8.55)$$

The number of counts in the ROI and SBs, denoted as N_{ROI} and N_{SB} in Eqn. (8.55), result from the integration over the corresponding energy ranges. The $f_{\text{M}2}^{\text{sig}}$ efficiency only depends on the MC geometry and could be compared to other $0\nu\beta\beta$ -decay experiments (see e.g. the references listed in Tab. 8.19 and Tab. 8.20). Moreover, it provides a figure of merit that could be used to optimize the detector design and arrangement of the CZT crystals in a potential future large-scale COBRA experiment.

The second quantity, which can be derived from the $f_{\text{M}2}^{\text{sig}}$ efficiency, is an estimate of the achievable S/B ratio under the assumed best-case scenario. It requires the determination of the M2 fraction for the background process according to Eqn. (8.55), which results in $f_{\text{M}2}^{\text{bg}}$ for each ROI. As a reminder, in case of the $2\nu\beta\beta$ -decay of ^{116}Cd into the g.s. as the only considered background there is no need to correct for the SB entries. The quotient of the two scaled M2 selection efficiencies, $f_{\text{M}2}^{\text{sig}}/T_{1/2}^{\text{exp}}$ and $f_{\text{M}2}^{\text{bg}}/T_{1/2}^{2\nu}(\text{g.s.})$, is taken as a measure of the S/B ratio. Again, the experimental half-life limits $T_{1/2}^{\text{exp}}$ as listed in Tab. 8.20 and the respective measurement of $T_{1/2}^{2\nu}(\text{g.s.})$ by the Aurora experiment are applied in the scaling.

The results of the conducted feasibility study for the double beta transitions of the isotopes ^{116}Cd and ^{130}Te are summarized in Tab. 8.24 and Tab. 8.25. For the $0\nu\beta\beta$ -decay modes there is a differentiation between the signatures in the $\text{M}2_s$ and the $\text{M}2_\Sigma$ spectra, while there is no clear preference for any of the two considered options.

As has been already expected from the impression of the normalized MC spectra shown in Fig. 8.52 and Fig. 8.53, the only reasonable channels to be considered for an analysis with

Table 8.24: Results of the excited states feasibility study based on MC simulations of potential double beta transitions of ^{116}Cd with the COBRA demonstrator. The selection of the decays' signatures is based on the M2_s spectra for the $2\nu\beta\beta$ -decay and $0\nu\beta\beta$ -decay modes as well as the M2 _{Σ} spectra for only the latter ones. The analysis includes a threshold of $E_{\text{th}} = 320$ keV and a dedicated energy restriction for each considered ROI in the M2 spectra. The M2 signal selection efficiency $f_{\text{M2}}^{\text{sig}}$ is the result of Eqn. (8.55). The quoted S/B ratio takes into account the respective $f_{\text{M2}}^{\text{bg}}$ fraction considering the ^{116}Cd g.s. transition via the $2\nu\beta\beta$ -decay mode as irreducible background as well as the recent experimental results listed in Tab. 8.20.

decay mode	transition	M2 event selection				
		signature	$f_{\text{M2}}^{\text{sig}} [\%]$	S/B	0 <i>ν</i> $\beta\beta$ -decay	$f_{\text{M2}}^{\text{sig}} [\%]$
^{116}Cd	$0_{\text{g.s.}}^+ \rightarrow 0_{\text{g.s.}}^+$	$Q_{\beta\beta}(\text{g.s.})$		background	M2 _{Σ}	2.469
^{116}Cd	$0_{\text{g.s.}}^+ \rightarrow 2_1^+$	$E_{\gamma}(2_1^+)$	0.879	1.337	M2 _s	0.955
		$Q_{\beta\beta}(2_1^+)$	-	-	M2 _s	4.626
		-	-	-	M2 _{Σ}	0.802
		$Q_{\beta\beta}(\text{g.s.})$	-	-	M2 _{Σ}	1.105
^{116}Cd	$0_{\text{g.s.}}^+ \rightarrow 0_1^+$	$E_{\gamma}(0_1^+)$	2.595	1.177	M2 _s	4.162
		$E_{\gamma}(2_1^+)$	0.468	1.183	M2 _s	0.840
		$Q_{\beta\beta}(0_1^+)$	-	-	M2 _s	6.568
		-	-	-	M2 _{Σ}	0.266
		$Q_{\beta\beta}(0_1^+) + E_{\gamma}(0_1^+)$	-	-	M2 _s	0.488
		-	-	-	M2 _{Σ}	3.844
		$Q_{\beta\beta}(0_1^+) + E_{\gamma}(2_1^+)$	-	-	M2 _s	0.070
		-	-	-	M2 _{Σ}	0.787
		$Q_{\beta\beta}(\text{g.s.})$	-	-	M2 _{Σ}	0.186
						108.763

respect to excited state transitions are the $2\nu\beta\beta$ -decay modes of ^{116}Cd . While there are a few $0\nu\beta\beta$ -decay modes of ^{116}Cd whose M2 selection efficiencies are significantly higher, the corresponding S/B ratios are much worse. The same applies to the decay modes of ^{130}Te . Even though some decay modes profit from a beneficial $f_{\text{M2}}^{\text{sig}}$ efficiency, the half-life scaling to the current limits of the CUORE experiment clearly indicates the dominance of the expected $2\nu\beta\beta$ -decay of ^{116}Cd .

Furthermore, it should be noted that the determined S/B ratio for the $0\nu\beta\beta$ -decay modes involving the $Q_{\beta\beta}(\text{g.s.})$ selection criterion is only an artifact of the applied best-case scenario. Since the simulated 10^8 events fail to produce a single entry in the corresponding ROI of the background spectrum, an upper limit of $< 1/N_{\text{MC}}$ has been assumed. Given the lack of an accurate background model for the M2 channel, the present results are only a first rough and outmost preliminary projection and very likely the subject to extensive changes in the future. Nevertheless, an outcome of the feasibility study is that the $2\nu\beta\beta$ -decay modes of ^{116}Cd should be prioritized in an upcoming analysis attempt.

In the following section, the prospects of a M2 detector pair optimization will be discussed in order to improve the sensitivity towards the excited state transitions. This step is motivated by the typical mean free paths of the involved γ -rays. While the M2 events caused by the ground-state transitions involve the emission of bremsstrahlung of the initial electrons, which is effectively limited to only a few hundred keV in case of the $2\nu\beta\beta$ -decay modes (see e.g. the

Table 8.25: Results of the excited states feasibility study based on MC simulations of potential double beta transitions of ^{130}Te with the COBRA demonstrator. The selection of the decays' signatures is based on the M2_s spectra for the $2\nu\beta\beta$ -decay and $0\nu\beta\beta$ -decay modes as well as the M2 _{Σ} spectra for only the latter ones. The analysis includes a threshold of $E_{\text{th}} = 320$ keV and a dedicated energy restriction for each considered ROI in the M2 spectra. The M2 signal selection efficiency $f_{\text{M2}}^{\text{sig}}$ is the result of Eqn. (8.55). The quoted S/B ratio takes into account the respective $f_{\text{M2}}^{\text{bg}}$ fraction considering the ^{116}Cd g.s. transition via the $2\nu\beta\beta$ -decay mode as irreducible background as well as the recent experimental results listed in Tab. 8.20.

decay mode	transition	M2 event selection					
		signature	$2\nu\beta\beta$ -decay		$0\nu\beta\beta$ -decay		
			$f_{\text{M2}}^{\text{sig}} [\%]$	S/B	spectrum	$f_{\text{M2}}^{\text{sig}} [\%]$	S/B
^{130}Te	$0_{\text{g.s.}}^+ \rightarrow 0_{\text{g.s.}}^+$	$Q_{\beta\beta}(\text{g.s.})$	-	-	M2 _{Σ}	2.215	0.019
^{130}Te	$0_{\text{g.s.}}^+ \rightarrow 2_1^+$	$E_\gamma(2_1^+)$	3.659	0.004	M2 _s	3.614	0.001
		$Q_{\beta\beta}(2_1^+)$	-	-	M2 _s	3.557	0.005
		-	-	-	M2 _{Σ}	1.048	0.001
		$Q_{\beta\beta}(\text{g.s.})$	-	-	M2 _{Σ}	3.464	0.325
^{130}Te	$0_{\text{g.s.}}^+ \rightarrow 2_2^+$	B1: $E_\gamma(2_2^+)$	2.269	0.003	M2 _s	2.254	< 0.001
		B1: $E_\gamma(2_1^+)$	2.642	0.003	M2 _s	2.665	0.001
		B2: $E_\gamma(2_2^+)$	0.235	0.001	M2 _s	0.231	< 0.001
		$Q_{\beta\beta}(2_2^+)$	-	-	M2 _s	5.112	0.002
		-	-	-	M2 _{Σ}	0.466	< 0.001
		$Q_{\beta\beta}(2_2^+) + E_\gamma(2_2^+)$	-	-	M2 _s	0.223	< 0.001
		-	-	-	M2 _{Σ}	2.005	0.003
		$Q_{\beta\beta}(2_2^+) + E_\gamma(2_1^+)$	-	-	M2 _s	0.254	< 0.001
		-	-	-	M2 _{Σ}	2.278	0.003
		$Q_{\beta\beta}(\text{g.s.})$	-	-	M2 _{Σ}	0.592	0.056
^{130}Te	$0_{\text{g.s.}}^+ \rightarrow 0_1^+$	$E_\gamma(0_1^+)$	0.240	0.001	M2 _s	1.042	0.001
		$E_\gamma(2_1^+)$	1.033	0.001	M2 _s	3.145	0.001
		$Q_{\beta\beta}(0_1^+)$	-	-	M2 _s	6.370	0.015
		-	-	-	M2 _{Σ}	0.051	< 0.001
		$Q_{\beta\beta}(0_1^+) + E_\gamma(0_1^+)$	-	-	M2 _s	0.064	< 0.001
		-	-	-	M2 _{Σ}	0.793	0.001
		$Q_{\beta\beta}(0_1^+) + E_\gamma(2_1^+)$	-	-	M2 _s	1.042	< 0.001
		-	-	-	M2 _{Σ}	3.095	0.001
		$Q_{\beta\beta}(\text{g.s.})$	-	-	M2 _{Σ}	0.157	0.015

M2 energy distribution in Fig. 8.50), the excited state transitions are accompanied by the emission of γ -rays of much higher energies. Hence, the distribution of M2 events across the detector array might provide additional information to distinguish both type of transitions.

8.6.6 Prospects of detector pair optimization

Based on the motivation given in the outlook of the previous section and the results of the conducted feasibility study, the focus of the detector pair optimization is on the double beta

decay modes of ^{116}Cd . Moreover, especially the transitions via the intermediate 2_1^+ state with $E_\gamma(2_1^+) = 1294 \text{ keV}$ is of interest for the detector pair optimization. The corresponding γ -line appears to be the most suitable option to crosscheck the potential differences because of the typical energy scales of the involved γ -rays and their related mean free path. Furthermore, there is a special interest in the $2\nu\beta\beta$ -decays, as they turned out to feature the highest S/B ratio in the previous analysis.

Interplay of M2 detector pairs and energy restrictions

As a starting point the interplay of the M2 detector pairs and the previously discussed selection criteria for the M2 energy spectra has been studied. The results are depicted in Fig. 8.56 for the three different cases and the $2\nu\beta\beta$ -decay modes of ^{116}Cd .

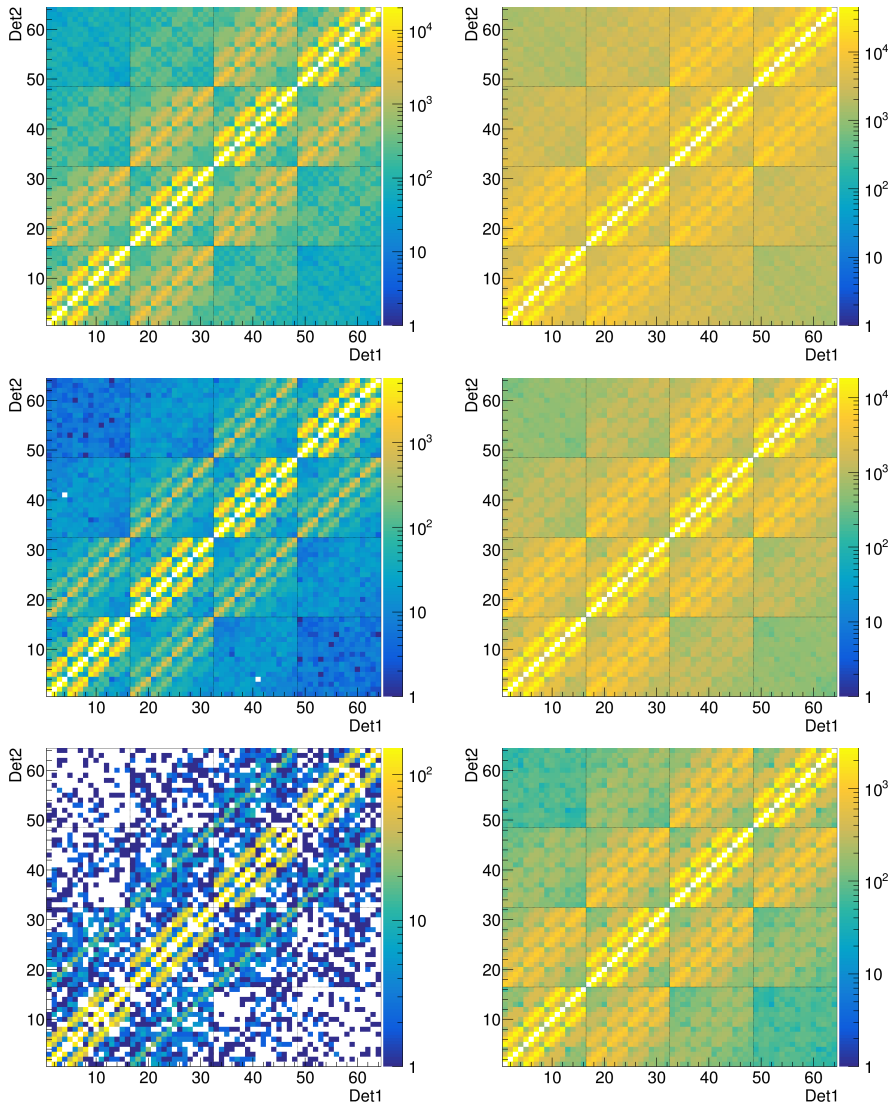


Figure 8.56: Effect of the excited states' event selections with respect to the M2 detector pair distribution for two examples of the simulated $2\nu\beta\beta$ -decay transitions of ^{116}Cd . *Left:* $0_{\text{g.s.}}^+ \rightarrow 0_{\text{g.s.}}^+$ transition. *Right:* $0_{\text{g.s.}}^+ \rightarrow 2_1^+$ transition. The three rows correspond to the iterations of the event selection as discussed in section 8.6.4. *Top:* all events without energy restriction. *Middle:* application of an energy threshold of $E_{\text{th}} = 320 \text{ keV}$ for both detector hits. *Bottom:* combination of energy threshold and ROI selection. In the present case the ROI covers a range of $E_\gamma \pm 2 \cdot \text{FWHM}(E_\gamma)$ for $E_\gamma(2_1^+) = 1294 \text{ keV}$. The prominent patterns along the counter diagonal is preserved in all cases. Note that the maximum of the color axis changes between the plots.

By comparing the different cases no significant changes of the main patterns can be reported. In fact, the same characteristics as discussed before in the second part of section 8.6.3 applies to all three iterations. Of particular interest is the pattern of the coincidence rate between detector pairs of the same layer, which dominates each of the depicted examples and seems to be similar for the ground-state transitions and the transitions involving the population of the 2_1^+ state in ^{116}Sn . However, the observed maximum rate of M2 events decreases more strongly for the ground-state than for the 2_1^+ state transitions. This can be seen as a first hint regarding the potential of a detector pair optimization. Since the most prominent M2 detector pair patterns are rather similar for the two presented example transitions of ^{116}Cd , a closer investigation into the subject needs to be performed.

Detector pair optimization

Based on the previous results obtained for the complete detector array of the COBRA demonstrator, it seems particularly promising to have a closer look on certain detector pairs. As a matter of statistics and given the lack of an accurate background model, it does not make sense to perform such an investigation for each of the potential $64 \cdot 63/2 = 2016$ detector combinations. In fact, because of the demonstrator's uniformity it is possible to define topological group of detectors to investigate the potential of a detector pair selection. This approach also helps to overcome the issue of dealing with detector pairs without a single entry in the M2 detector maps, which are already based on the simulation of 10^8 events. By combining detectors with a similar position relation with respect to the other members of the array, the effect of empty detector pairs is expected to even out.

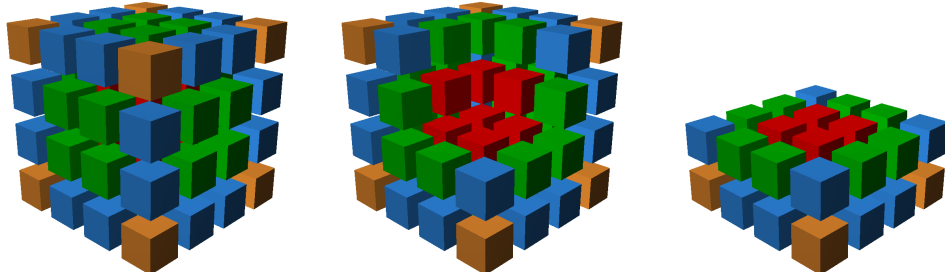


Figure 8.57: Illustration of the topological detector classifications based on their position in the COBRA demonstrator. Because of its regular structure, the array can be divided into four categories: center (red), side (green), edge (blue) and corner (orange). An overview of the respective detector numbers for each category is given Tab. 8.26. The visualization is based on a simplified MC implementation via an instance of ROOT's *TGeoManager* class, which neglects the actual distances between the CZT crystals (see e.g. Fig. A.5 in the appendix). The visualization has been developed in the course of the high school thesis of L. Dathe [Dat16].

An illustration of the topological detector classes is shown in Fig. 8.57. Each detector can be classified as either a *center*, *side*, *edge* or *corner* detector according to its position in the detector array of $4 \times 4 \times 4$ cuboidal CZT crystals. A complete list of the detector numbers that fall under a certain category is given in Tab. 8.26. With those four classes it is possible to divide the M2 detector pairs according to the following naming scheme.

- 1) center-center (Ce-Ce), center-side (Ce-Si), center-edge (Ce-Ed), center-corner (Ce-Co)
- 2) side-side (Si-Si), side-edge (Si-Ed), side-corner (Si-Co)
- 3) edge-edge (Ed-Ed), edge-corner (Ed-Co)
- 4) corner-corner (Co-Co)

Table 8.26: Overview of the detectors that belong to one of the four topological detector classes. Each detector number from 1 to 64 only appears once. In contrast to the detector label scheme in the real experiment (see Fig. A.5 in the appendix) the GDML implementation applied for the VENOM simulations follow a strict counting from the bottom to the top according to 1–16 (L1), 17–32 (L2), 33–48 (L3) and 49–64 (L4).

category	N_{det}	detector numbers
center	8	22, 23, 26, 27, 38, 39, 42, 43
side	24	6, 7, 10, 11, 18, 19, 21, 24, 25, 28, 30, 31, 34, 35, 37, 40, 41, 44, 46, 47, 54, 55, 58, 59
edge	24	2, 3, 5, 8, 9, 12, 14, 15, 17, 20, 29, 32, 33, 36, 45, 48, 50, 51, 53, 56, 57, 60, 62, 63
corner	8	1, 4, 13, 16, 49, 52, 61, 64

Table 8.27: Overview of the topological detector pairs based on the categorization of the detectors according to their position in the demonstrator array (see Fig. 8.57 and Tab. 8.26). As there are no coincidences between the same detector numbers, the total number of possible pairs is $N_{\text{pairs}} = 64 \cdot 63/2 = 2016$. However, the exclusion of M2 events for the same detector is the only boundary condition for the entirety of possible combinations. Moreover, the M2 combinations do not distinguish between an ordering of the involved detectors and apply vice versa, which is why the labeling of the first and second detector number is arbitrary.

1 st detector	2 nd detector	label	N_{pairs}
center	center	Ce-Ce	28
	side	Ce-Si	192
	edge	Ce-Ed	192
	corner	Ce-Co	64
side	side	Si-Si	276
	edge	Si-Ed	576
	corner	Si-Co	192
edge	edge	Ed-Ed	276
	corner	Ed-Co	192
corner	corner	Co-Co	28
total			2016

The combinatorics of the topological detector pairs and the composition with respect to the total number of possible combinations is presented in Tab. 8.27. The number of detector pairs N_{pairs} is used as an additional normalization in the subsequent plots of the M2 coincidence rate for each of the considered combinations. The distributions presented in Fig. 8.58 correspond to the first two analysis approaches based on all M2 events independently from their minimum energy deposition and, secondly, to the case of requiring a minimum energy deposit of $E_{\text{th}} = 320 \text{ keV}$ for each detector. All distributions are normalized to the corresponding experimental half-life results reported in Tab. 8.20. Furthermore, the Ce-Ce category is taken as a fixed reference and set to unity for the $2\nu\beta\beta$ -decay of ^{116}Cd into the ground-state, which is taken as an estimate of the irreducible background in all four cases.

For the $2\nu\beta\beta$ -decay modes there is a dominance of the g.s. transition for almost all channels. Only the Co-Co category selects more M2 events for excited states than for the ground-state. By following the second analysis approach including the threshold condition

for the single detectors' energy depositions, also the Ce-Ed, Ce-Co and Si-Co channels feature a comparable S/B ratio. On the contrary, the improvements with respect to the first approach are only marginal for all the other categories. Most of them do not benefit from the introduction of the threshold requirement at all.

A similar trend is observed for the $0\nu\beta\beta$ -decay modes. While it seems that the background process is suppressed in all channels with respect to the excited state transitions, which contradicts the expectation from the predicted half-lives, this is only an artifact of the half-life scaling based on the experimental results. The deviation between the predicted half-lives and the current experimental sensitivities (see Tab. 8.20) encompasses more than nine orders of magnitude, which nullifies the effect to the extreme. However, the overall shape of the distributions of the relative M2 rates is very similar compared to the $2\nu\beta\beta$ -decay modes.

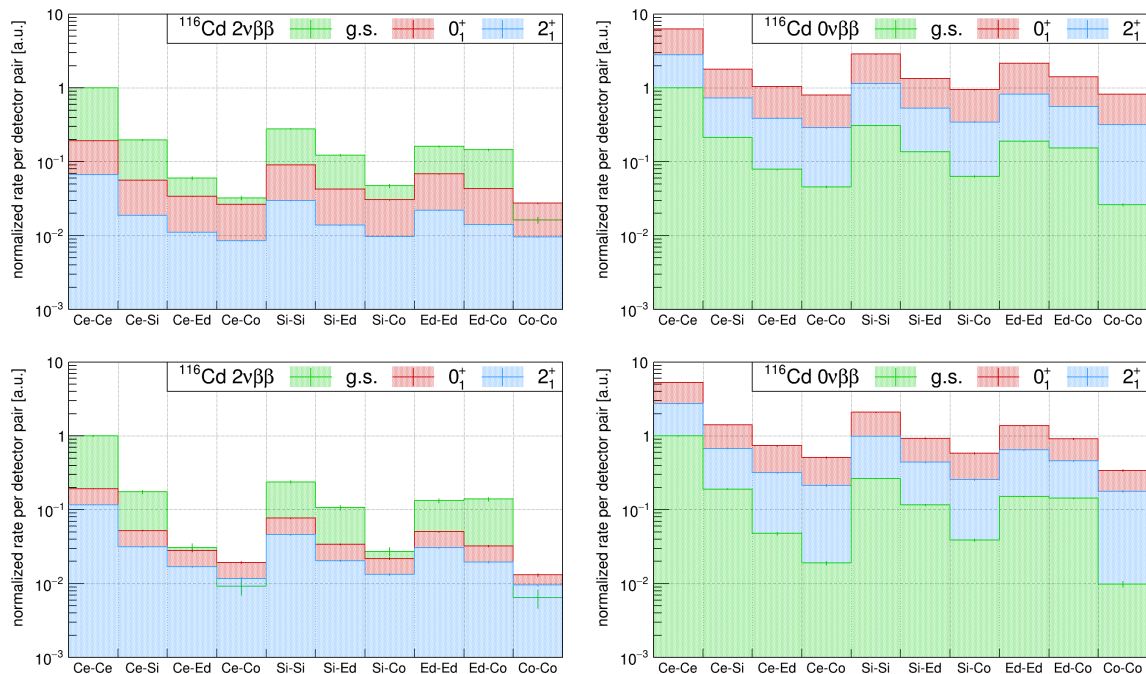


Figure 8.58: Distribution of the topological M2 detector pairs for the simulated double beta decay transitions of ^{116}Cd with the COBRA demonstrator. *Left:* $2\nu\beta\beta$ -decay modes for all M2 events (*top*) and after applying a threshold of $E_{\text{th}} = 320$ keV on the energy deposition of each detector (*bottom*). *Right:* $0\nu\beta\beta$ -decay modes for the same two cases. It should be noted that the depicted g.s. transitions (green) are the same for all cases and correspond to the $2\nu\beta\beta$ -decay of ^{116}Cd , which is taken as an estimate of the irreducible background. Each decay mode has been scaled with the experimental half-life results of the Aurora experiment according to Tab. 8.20. Moreover, the Ce-Ce category is chosen as a fixed reference and set to unity. The other categories have been scaled with respect to this reference.

The respective distributions of the M2 rates for the double beta decay modes of ^{130}Te can be found in Fig. D.27 of the appendix. While the ^{130}Te distributions feature in general the same characteristics as discussed for the ^{116}Cd decay modes, there is no topological detector pair category for which the excited state transitions could compete with the background process of the ^{116}Cd $2\nu\beta\beta$ -decay into the ground-state. Because of this, the prospects of the third analysis procedure are rather poor for the ^{130}Te decay modes, as well as for the $0\nu\beta\beta$ -decay modes of ^{116}Cd , and are not discussed any further. Instead, the final step of only selecting M2 events that fulfill the energy restrictions according to the excited states' ROIs, as discussed in section 8.6.4, is solely performed for the $2\nu\beta\beta$ -decay modes of ^{116}Cd .

For the final comparison of the M2 coincidence rates an additional classification of the detector pairs has been developed, which is based on the previous observations and more

advanced than the presently used categories. The new class only considers detector pairs that do not have a side wall in direct sight, thus, removes pairs of next neighbors, which is why it is denoted as the *no next neighbor* (no-NN) category. Exemplarily, for an edge detector such as L1-P1, three detector numbers (L1-P2, L1-P5, L2-P1) would be removed from the set of possible detector pairs (see also the numbering of the detector array in Fig. A.5 of the appendix). In case of a center detector, all six sides face another detector in direct sight, hence, would require to exclude six detector pair combinations. Because of the limited size of the demonstrator array and the corresponding exposure loss, it seems not beneficial to also remove detector pairs with a diagonal position relation. However, such a measure, which would be much more restrictive, could be studied in a future campaign.

By following the procedure introduced above, there is either at least one detector in between the two involved detectors of a M2 event or the pair of detectors is in a diagonal position relation. Either way, the chance of direct hits gets reduced, which is expected to turn out beneficially in terms of avoiding bremsstrahlung and M2 events caused by secondary hits from escaping $\beta\beta$ -electrons. Moreover, such a detector pair selection is also expected to be of great use regarding an analysis of the demonstrator's physics data. As pointed out before in section 8.2.4, one of the dominating M1 background components is caused by the decay of radon-induced contaminants. Part of the decay series of the radon isotope ^{222}Rn (see also Fig. D.8 in the appendix) is the ^{214}Bi - ^{214}Po sequence, which could also contribute to the M2 background. However, by removing neighboring detector pairs the chance of observing events of the ^{214}Bi - ^{214}Po sequence in the M2 channel is expected to be dramatically reduced.

The new detector pair selection no-NN removes 288 pairs from the total number of M2 combinations according to Tab. 8.27. This corresponds to a rather high acceptance of 85.7% of all pairs compared to the other categories (e.g. for Ce-Ce/Co-Co $\sim 1.4\%$). Finally, the distributions of the relative M2 rates for all combinations of the topological pairs, based on the ROI restrictions for the ^{116}Cd $2\nu\beta\beta$ -decay modes, are depicted in Fig. 8.59.

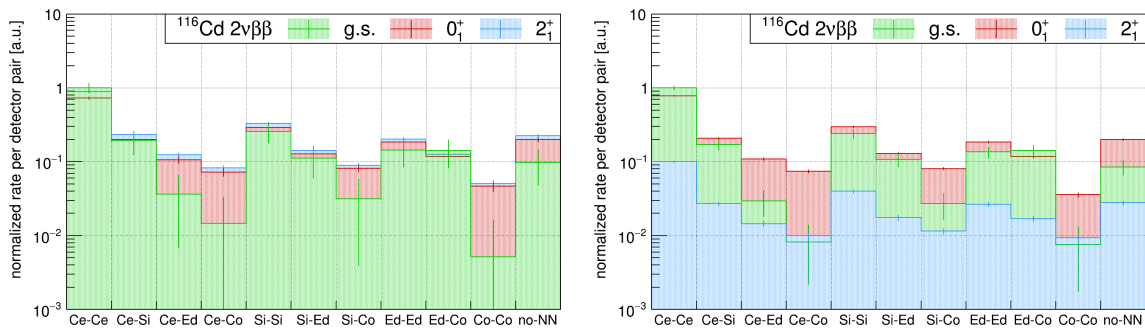


Figure 8.59: Distribution of the topological M2 detector pairs for the $2\nu\beta\beta$ -decay modes of ^{116}Cd using the ROI restrictions based on the excited states' γ -lines. *Left:* ROI restriction according to the $0_{\text{g.s.}}^+ \rightarrow 2_1^+$ transition with $E_\gamma(2_1^+) \pm 2 \cdot \text{FWHM}(E_\gamma)$. As the γ -cascade of the $0_{\text{g.s.}}^+ \rightarrow 0_1^+$ transition involves the same energy level as for the $0_{\text{g.s.}}^+ \rightarrow 2_1^+$ transition, the distributions of the excited states are very similar to each other (see also the decay scheme in Fig. 8.44 and Tab. 8.20). *Right:* ROI restriction according to the $0_{\text{g.s.}}^+ \rightarrow 0_1^+$ transition with $E_\gamma(0_1^+) \pm 2 \cdot \text{FWHM}(E_\gamma)$. In both cases, the g.s. transition is again treated as an irreducible background. The scaling according to the half-lives follows the procedure described before (see Fig. 8.58).

The similarity of the detector pair distributions for the ROI restrictions regarding the γ -line signature of the 2_1^+ de-excitation between the two excited state transitions is due to the fact that the 0_1^+ decay branch is also able to populate the 2_1^+ state (see Fig. 8.44). On the contrary, when the unique ROI restriction based on the intermediate de-excitation from $0_1^+ \rightarrow 2_1^+$ within ^{116}Sn is applied for the $0_{\text{g.s.}}^+ \rightarrow 2_1^+$ transition, the resulting M2 rates turn out to be even lower than for the ground-state transition in all detector pair categories.

Again, the Ce-Ce category of the ground-state transition is used as a reference and set to unity. In agreement with the previous results reported in Fig. 8.58, the Ce-Ed, Ce-Co, Si-Co and Co-Co detector pairs provide good prospects to improve the S/B ratio in the signature search for the excited state transitions. However, the statistical uncertainties for the background process become rather high as the ROI selection leads to a significant fraction of empty detector pairs in the M2 detector map based on 10^8 simulated events (see Fig. 8.56).

Fortunately, also the newly introduced detector pair selection (no-NN) provides excellent prospects and maintains at the same time a high acceptance of the total number of pairs. Without an actual M2 background projection besides the rough expectation of potential contributions (e.g. the ^{214}Bi - ^{214}Po sequence), it is reasonable to rely on this detector selection in order to evaluate the benefits of a detector pair optimization. Consequently, the selection will be used for a final iteration of the analysis procedure with the aim to distinguish the excited states' signatures of the $2\nu\beta\beta$ -decay modes of ^{116}Cd from its ground-state.

Preliminary results of M2 detector pair optimization

In a final iteration of the present excited state study, the previous ROI event selection is complemented with the no-NN criterion in order to asses the impact on the S/B ratio. The impact on the M2 detector pair distributions corresponding to the combined event selections for the $2\nu\beta\beta$ -decay decay modes of ^{116}Cd is shown in Fig. 8.60.

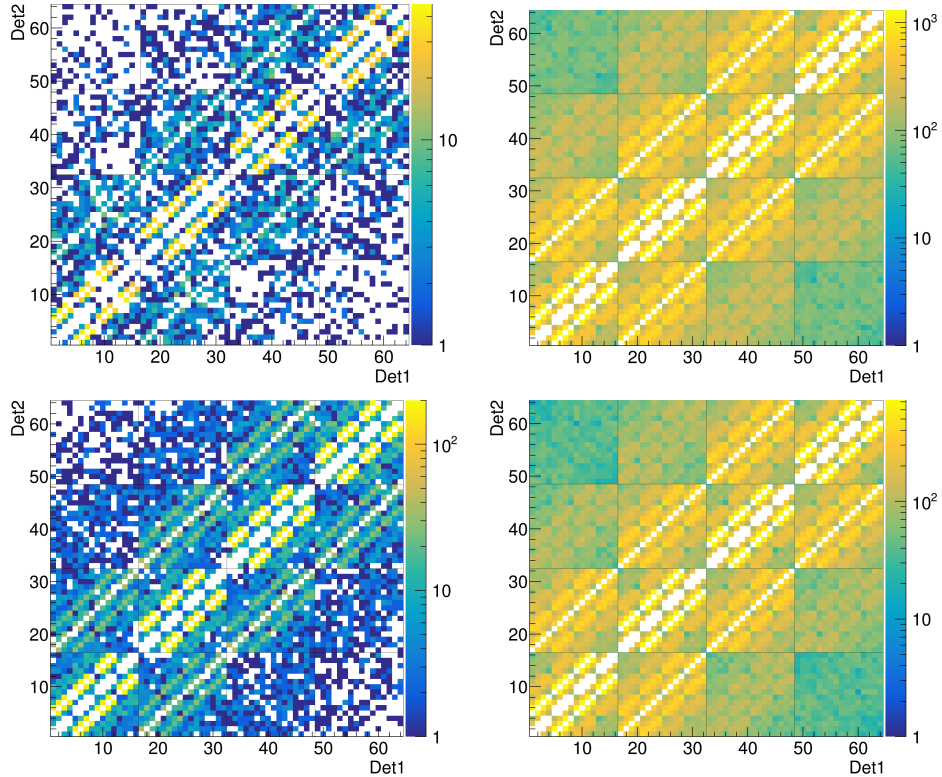


Figure 8.60: M2 detector pair distributions for the simulated $2\nu\beta\beta$ -decay modes of ^{116}Cd under the ROI energy restrictions and the optimized detector pair selection no-NN. *Left:* $0_{\text{g.s.}}^+ \rightarrow 0_{\text{g.s.}}^+$ transition with selection for $E_\gamma(2_1^+) = 1294$ keV (*top*) and $E_\gamma(0_1^+) = 463$ keV (*bottom*). *Top right:* $0_{\text{g.s.}}^+ \rightarrow 2_1^+$ transition with $E_\gamma(2_1^+) = 1294$ keV. *Bottom right:* $0_{\text{g.s.}}^+ \rightarrow 0_1^+$ transition with $E_\gamma(0_1^+) = 463$ keV. The corresponding M2 detector maps of the 2_1^+ transition for the different stages of the previous event selections can be found in Fig. 8.56. In comparison, the main counter diagonals with the highest M2 rates are removed by the optimized detector pair selection, which rejects pairs of next neighbors. The additional, randomly distributed blank spots in the representation of the ground-state transitions result from low statistics due to the applied ROI selections.

In comparison with Fig. 8.56, showing the different steps of the energy restrictions based on the excited state signature of the 2_1^+ transition, the main counter diagonal entries are removed by the no-NN criterion. As already mentioned before, the additional blank spots in the M2 detector pair maps for the ground-state transitions are simply due to the low statistics for the ROI selection and are not related to the detector pair optimization. Furthermore, besides the maximum observed M2 rates, which is almost a factor of two higher for the $2_1^+ \rightarrow 0_{\text{g.s.}}^+$ de-excitation compared to the $0_1^+ \rightarrow 2_1^+$ decay branch, the same patterns are observed for both excited state transitions. However, because of the different energy scales of the corresponding γ -lines, $E_\gamma(2_1^+) = 1294 \text{ keV}$ and $E_\gamma(0_1^+) = 463 \text{ keV}$, the maximum M2 rate of the background process turns out to be about twice as high for the lower one.

The final M2_s spectra, which are used to extract the number of ROI and SB counts, are depicted in Fig. 8.61. It should be noted that the three cases are an updated version of the spectra shown before in Fig. 8.54 and highlight the same ROI and SB regions. The only difference is the application of the combined ROI selection and the first implementation of an optimized M2 detector pair selection.

Finally, the M2 signal fractions $f_{\text{M2}}^{\text{sig}}$ and the corresponding background fractions $f_{\text{M2}}^{\text{bg}}$ can be calculated according to Eqn. (8.55) based on N_{ROI} , N_{SB} and N_{MC} . The results of the evaluation of the excited state signatures are summarized in Tab. 8.28. It is found that the detector pair optimization reduces the $f_{\text{M2}}^{\text{sig}}$ fraction by about 35% compared to the previous values reported in Tab. 8.24. However, based on $f_{\text{M2}}^{\text{sig}}$ and $f_{\text{M2}}^{\text{bg}}$ it is possible to assess the S/B ratio, which includes a scaling with respect to the corresponding experimental half-life results of the Aurora experiment and the predictions following Ref. [PS15] (see Tab. 8.20). The first scaling option results in $(\text{S}/\text{B})_{\text{exp}}$, which can be compared to the S/B ratio reported in Tab. 8.24, and the latter based on the predicted $T_{1/2}^{2\nu}$ in $(\text{S}/\text{B})_{\text{theo}}$. While the $(\text{S}/\text{B})_{\text{exp}}$ could be improved on average by more than a factor of 2.4 for the three evaluated ROIs, the potential to observe the $2\nu\beta\beta$ -decay excited state transition of ^{116}Cd with the current stage of the experiment is still completely out of reach for the case of the predicted half-lives. Some concluding remarks and a brief outlook will be given in the subsequent section.

Table 8.28: Updated analysis results for the simulation of the $2\nu\beta\beta$ -decay modes of ^{116}Cd via the first excited states with the COBRA demonstrator array. The signal and background fractions of M2 events, $f_{\text{M2}}^{\text{sig}}$ and $f_{\text{M2}}^{\text{bg}}$, have been calculated according to Eqn. (8.55). The S/B ratios, $(\text{S}/\text{B})_{\text{exp}}$ and $(\text{S}/\text{B})_{\text{theo}}$, are based on the scaling of the M2 fractions according to the experimental $T_{1/2}^{2\nu}$ results of the Aurora experiment and, respectively, of the predictions following Ref. [PS15] (see Tab. 8.20).

transition	signature	E_γ [keV]	$f_{\text{M2}}^{\text{sig}}[\%]$	$f_{\text{M2}}^{\text{bg}}[\%]$	$(\text{S}/\text{B})_{\text{exp}}$	$(\text{S}/\text{B})_{\text{theo}}$
^{116}Cd	$0_{\text{g.s.}}^+ \rightarrow 2_1^+$	$E_\gamma(2_1^+)$	1294	0.574	0.005	3.151
						0.001
^{116}Cd	$0_{\text{g.s.}}^+ \rightarrow 0_1^+$	$E_\gamma(0_1^+)$	463	1.652	0.024	3.071
		$E_\gamma(2_1^+)$	1294	0.305	0.005	2.781
						0.001

8.6.7 Conclusion and outlook

The present feasibility study based on the MC simulations of the first excited state transitions of the isotopes ^{116}Cd and ^{130}Te for the COBRA demonstrator array reveals that only the $2\nu\beta\beta$ -decay transitions of ^{116}Cd provide reasonable signatures that might be distinguished from the irreducible background caused by the ground-state transition of ^{116}Cd . Moreover,

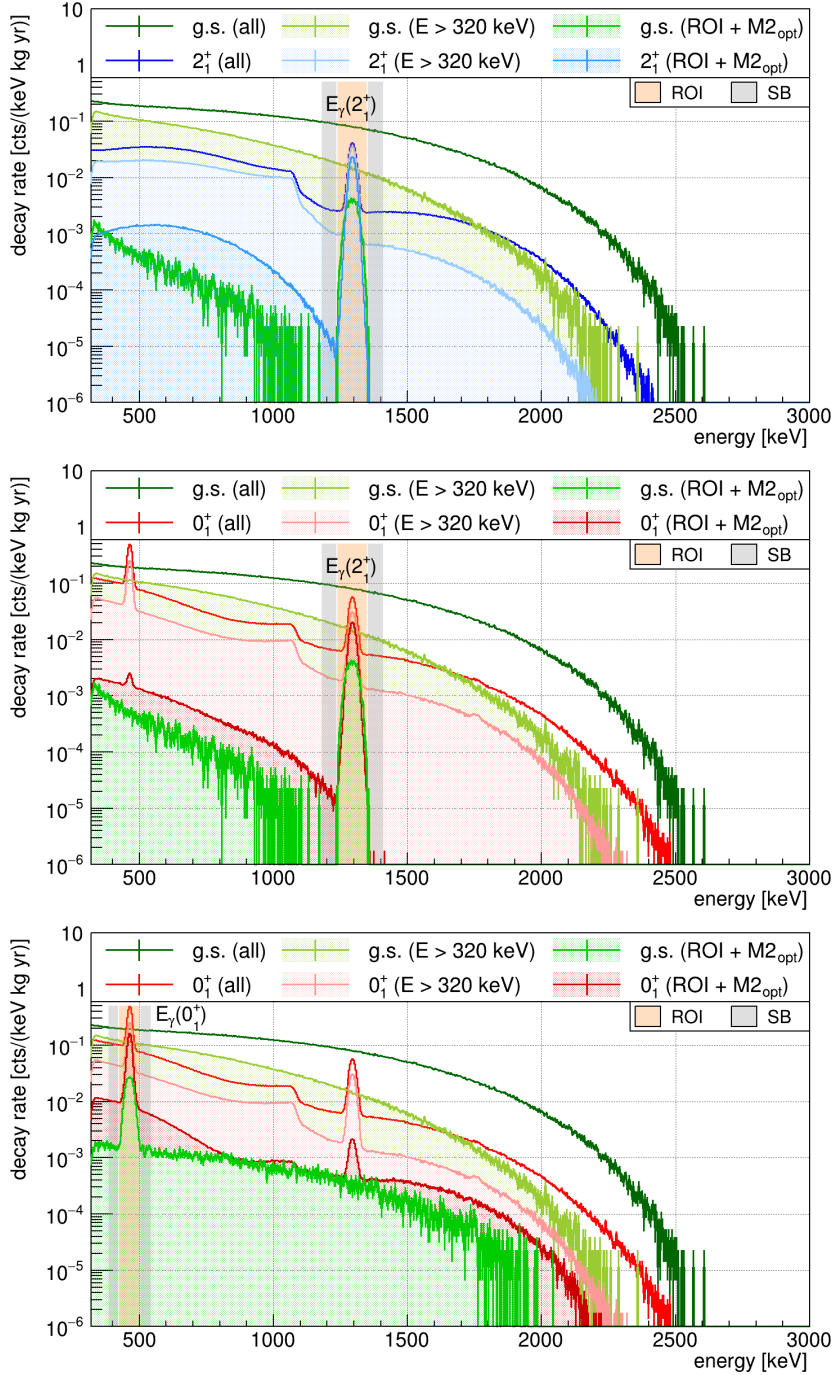


Figure 8.61: Updated analysis examples for the selection of the $2\nu\beta\beta$ -decay excited state signatures of ^{116}Cd . Top: $0_{\text{g.s.}}^+ \rightarrow 2_1^+$ transition with $E_\gamma(2_1^+) = 1294$ keV. Middle: $0_{\text{g.s.}}^+ \rightarrow 0_1^+$ transition with $E_\gamma(2_1^+) = 1294$ keV. Bottom: $0_{\text{g.s.}}^+ \rightarrow 0_1^+$ transition with $E_\gamma(0_1^+) = 463$ keV. In comparison to the previous results presented in Fig. 8.54, the ROI selection has been complemented by the optimized M2 detector pair selection.

this statement only holds for the assumed best-case scenario and might turn out less confidently as soon as external background will be considered.

Based on the evaluation of the MC campaigns, the current experimental situation is comparable to the status of the Aurora experiment. However, the available exposure of the COBRA demonstrator is much lower. Although there might be some potential to perform an almost background-free search for excited state transitions by focusing on the M2 data

set, which is currently under evaluation, the achievement of competitive limits will be rather challenging. Among the most advisable next steps is the development of a background model. Here, the combined fit of the M1 and M2 data could provide a better understanding of its isotopic composition and position dependence within the experiment.

Considering an enrichment of the detector material with respect to the isotope of interest, there is no improvement expected regarding the results of the performed feasibility study. An enrichment would not affect the determined S/B ratio as only the irreducible background has been taken into account for now, which would also scale with the enrichment factor. Nevertheless, the use of enriched CZT is one of the requirements to improve the overall sensitivity of the experiment in a future iteration.

One topic completely uncovered in the present study are systematic effects and their impact on the analysis results such as the determined M2 signal fraction f_{M2}^{sig} . Since f_{M2}^{sig} would be treated as an efficiency in a potential limit setting analysis, its systematic uncertainty needs to be known. However, the determination is non-trivial and requires prior knowledge regarding the active volume of the CZT crystals (e.g. dead layer effects) as well as their position uncertainty in the real experiment. The monitoring of the intrinsic ^{113}Cd decay rate could help to provide a measure for the active volume. Furthermore, dedicated laboratory measurements have been performed for each CZT crystal that has been operated at the LNGS, prior to its installation. Those measurement could be repeated now that the operation of the demonstrator array has been stopped to evaluate potential changes over time by e.g. a growing of the dead layer.

Finally, a potential medium-scale COBRA experiment could be optimized concerning the search for double beta decays via excited states, without inferring with the prioritized $0\nu\beta\beta$ -decay search. In this light, the analysis strategies described in the course of the performed feasibility study could act as a guideline. For a larger detector array it would also make sense to look for higher multiplicity events, especially for the transitions involving a cascade of γ -rays. Opening up to higher multiplicities would also allow to develop more advanced analysis strategies based on the event topology of the excited state transitions. This could include the development of a more advanced detector pair optimization or the application of pulse-shape discrimination. Already in the previously discussed M2 channel, one additional requirement in the selection of excited state transitions could be that one of the energy deposits should have single-site character as it is caused by the two emitted electrons, while the second detector would see a full energy deposition of the γ -ray, which could be either single- or multi-site.

In the near future, the prospects of the COBRA XDEM array are going to be evaluated. While the analysis priority is first on the M1 data, the applied detector approach based on the qCPG concept with its four independent sectors might also turn out suitable for excited state searches, independently of the actual configuration of the detector array.

8.7 Update on COBRA's $0\nu\beta\beta$ -decay modes

The final analysis section of this thesis is a brief update on the half-life sensitivity for five neutrinoless $\beta^- \beta^-$ ground-state-to-ground-state transitions achieved with the full exposure of the COBRA demonstrator. The first part consists of the determination of the intrinsic signal efficiencies based on dedicated MC simulations of the double beta decay processes. Furthermore, the results of the previously discussed analyses of the demonstrator's physics data are used to determine the total signal efficiency for each decay mode. Following this, a conservative estimate of the half-life exclusion sensitivity at 90% C.L. will be discussed, including the application of the data partitioning developed in the course of the presented $2\nu\beta\beta$ -decay study of ^{116}Cd in combination with the $(A/E)_{90\%}$ selection. Finally, an outlook and a sensitivity projection in the light of the COBRA XDEM upgrade will be presented.

8.7.1 Determination of intrinsic efficiency

The intrinsic full-energy detection efficiency ε_{int} is a measure for the fraction of $0\nu\beta\beta$ -decays that deposit their full Q -value within the initial source crystal. It can be determined by simulating the detector response for the intrinsically abundant $\beta\beta$ -emitters using the COBRA simulation toolkit VENOM and the DECAY0 package to provide the initial kinematics of the decays (see section 5.3.1 and 5.3.2). As ε_{int} depends strongly on the crystal geometry and the related surface-to-volume ratio, it is expected to vary for the different types of CZT detectors under investigation (see e.g. Fig. 6.1). Moreover, because of the expected non-linearity of the efficiency scaling with the detector's volume, respectively mass, and the decay's Q -value, it has to be studied for each detector type and decay mode individually.

The results of the performed Monte-Carlo campaign using the standard libraries of VENOM and the *shielding* physics list are summarized in Tab. 8.29. For each of the considered decay modes, 10^6 events were simulated using either the full demonstrator array's geometry or the XDEM setup (see section 5.3.3). The number of simulated events is sufficiently large enough to neglect the statistical contribution compared to the quoted systematic uncertainties.

Table 8.29: Comparison of the intrinsic full-energy detection efficiency ε_{int} for several $\beta^- \beta^-$ -decays and detector geometries investigated by COBRA. The list of isotopes is ordered according to their Q -values reported in Tab. 4.2 of section 4.2. The CPG-CZT detectors of about 1 cm^3 volume are installed in the demonstrator array. The larger detector geometries with a volume of about 6 cm^3 are prototypes for a future large-scale experiment. The qCPG detector design is applied for the COBRA XDEM module and can be treated as either four independent sectors, which reduces the overall efficiency, or be combined to form a virtual single CPG-CZT detector. For each decay mode 10^6 events have been simulated. The quoted uncertainties on ε_{int} follow from a systematic variation of the crystal size according to their observed xy -variations in the available detector pool. The parameter f_{coin} refers to the total fraction of coincidences involving hits between multiple detectors (or sectors in the case of the qCPG detector design).

isotope	CPG (1 cm^3)		CPG (6 cm^3)		qCPG (6 cm^3)	
	ε_{int} [%]	f_{coin} [%]	ε_{int} [%]	f_{coin} [%]	ε_{int} [%]	f_{coin} [%]
^{114}Cd	96.2 ± 0.2	1.15	96.6 ± 0.2	1.46	96.6 ± 0.2	2.91
^{128}Te	91.9 ± 0.3	2.60	92.5 ± 0.3	3.22	92.6 ± 0.3	6.43
^{70}Zn	90.1 ± 0.3	3.21	90.7 ± 0.3	3.97	90.8 ± 0.3	7.94
^{130}Te	66.2 ± 0.5	12.63	75.9 ± 0.6	15.96	67.3 ± 0.5	30.11
^{116}Cd	62.0 ± 0.9	14.43	73.2 ± 0.8	17.22	63.2 ± 0.8	30.45

The higher the Q -value of the initial $0\nu\beta\beta$ -decay, the smaller ε_{int} turns out in the simulation. This matches with the expectation referring to the likelihood to contain an increasing

amount of energy in a constant volume. The $0\nu\beta\beta$ -decays with a full energy deposition in the source crystal have to be single detector events as there is no energy left to be spread over multiple detectors. On the other hand, the coincidence fraction f_{coin} is an expression for the number of expected coincidences caused by multi-detector events. Such events can occur in cases where an initial $0\nu\beta\beta$ -decay deposits only part of its Q -value in the source crystal. However, the dominant process leading to multi-detector hits is not the escape of the originally emitted electrons, but the creation of bremsstrahlung. Moreover, because of the heavy copper and lead shield around each of the detector arrays, there is a high chance for backscattering, increasing the chance for a second crystal hit. While f_{coin} turns out to be rather similar for both single CPG setups (1 cm^3 versus 6 cm^3), it is about twice as high for the qCPG approach. Because of the segmented approach, it is more likely to detect e.g. bremsstrahlung in two sectors of the same device. In full anti-coincidence mode, this would reduce the achievable ε_{int} in a way that almost nullifies the beneficial surface-to-volume ratio of the larger crystals compared to the demonstrator’s detectors. That is why the combination of the four sectors should be considered as the default reconstruction approach for the search for the $0\nu\beta\beta$ -decay. Nevertheless, the internal coincidence veto might be advantageous for other physics searches involving more exotic decay modes.

The determined $0\nu\beta\beta$ -decay efficiencies for the large CZT detectors agree well with the results presented in [Tem19] considering the systematic uncertainties, which have been determined by varying the crystal size in the present work. However, the small deviations between the two similar approaches might arise from different Q -value definitions in the applied version of DECAY0. A previous iteration of the simulation results obtained for the 1 cm^3 detectors of the COBRA demonstrator has been used for the latest $0\nu\beta\beta$ -peak search based on a Bayesian analysis approach [COB16a]. In the following section the resulting limits on the five $\beta^- \beta^-$ decay modes are compared to the sensitivity achieved with the full exposure of the COBRA demonstrator.

8.7.2 Half-life sensitivity estimate

Besides the intrinsic efficiency derived in the previous section, additional experimental parameters are needed to estimate the half-life sensitivity for the full exposure of the COBRA demonstrator. This includes the energy resolution in terms of FWHM at the respective $Q_{\beta\beta}$ as well as the background index (BI) and the total selection efficiency. The energy resolution has been determined from the combination of several calibration runs and can be found in Tab. 8.30. Moreover, Tab. 8.30 contains the nuclid-specific number of source atoms per kilogram mass of CZT, denoted as $N_{\beta\beta}$, which is calculated according to the procedure outlined in Eqn. (8.1) of section 8.1.1 for the case of ^{113}Cd .

Table 8.30: List of additional experimental parameters required for the $0\nu\beta\beta$ -decay half-life sensitivity estimate. The energy resolution at the corresponding $Q_{\beta\beta}$ (see Tab. 4.4 in section 4.2) and the quoted uncertainties are taken from a combination of several calibration measurements. The number of source atoms $N_{\beta\beta}$ per mass unit of the detector material CZT contains the natural isotopic abundance according to Tab. 4.4 and the corresponding stoichiometry factor of the element composition of CZT.

nuclide	FWHM @ $Q_{\beta\beta}$ [keV]	$N_{\beta\beta}$ per kg
^{114}Cd	19.2 ± 0.3	$6.62 \cdot 10^{23}$
^{128}Te	22.4 ± 0.3	$2.28 \cdot 10^{22}$
^{70}Zn	23.7 ± 0.3	$1.56 \cdot 10^{21}$
^{130}Te	38.7 ± 0.5	$8.72 \cdot 10^{23}$
^{116}Cd	41.5 ± 0.6	$1.73 \cdot 10^{23}$

The total $0\nu\beta\beta$ -decay selection efficiency ε_{tot} is the product of the intrinsic efficiency ε_{int} and the combined cut efficiency of the PSD selection according to the standard z -cut (see Tab. 7.2 in section 7.1.2) and the $(A/E)_{90\%}$ criterion. Finally, the background index for each $0\nu\beta\beta$ -decay's ROI is needed. It is calculated for the combined spectrum of all detectors by applying once more a *cut and counting* method using the side-band approach as introduced before. The central SBs cover the energy range of $Q_{\beta\beta} \pm 2 \cdot \text{FWHM}$ while the signal region of $Q_{\beta\beta} \pm 1 \cdot \text{FWHM}$ around the Q -value is excluded. Because of the beneficial results obtained by the data partitioning in the analysis of the ^{116}Cd $2\nu\beta\beta$ signal region, the same method is applied for the $0\nu\beta\beta$ -decay sensitivity estimate. The results of the half-life exclusion sensitivity approximation according to Eqn. (3.10) at 90% C.L. is shown in Tab. 8.31, including the values of the determined background indices and total efficiencies. Furthermore, the same experimental parameters and the results of the Bayesian analysis reported in Ref. [COB16a] are shown for comparison.

Table 8.31: Half-life sensitivity estimate for five neutrinoless $\beta^- \beta^-$ g.s. to g.s. transitions and the full exposure of the COBRA demonstrator after the HRP+MRD partitioning. Besides the selected exposure of 362.4 kg d , the estimate of the half-life exclusion sensitivity $\tilde{T}_{1/2}^{0\nu}$ (90% C.L.) according to Eqn. (3.10) depends on the FWHM at $Q_{\beta\beta}$ and the number of source nuclei $N_{\beta\beta}$ (see Tab. 8.30), the BI in units of $\text{cts}/(\text{keV kg yr})$ and the total efficiency ε_{tot} as the combination of ε_{int} (see Tab. 8.29) and the PSD cut efficiencies (see section 7.1). The quoted uncertainty on ε_{tot} follows from a Gaussian uncertainty propagation of the contributing efficiencies. For comparison, the parameters of a Bayesian analysis using 216.1 kg d (212.8 kg d in case of ^{114}Cd due to some high-threshold runs) and the resulting lower limits on $T_{1/2}^{0\nu}$ at 90% credibility are listed.

nuclide	full set (HRP+MRD+PSD)			COBRA'16 [COB16a]		
	BI	$\varepsilon_{\text{tot}} [\%]$	$\tilde{T}_{1/2}^{0\nu} @ 90\% \text{ C.L.}$	BI	$\varepsilon_{\text{tot}} [\%]$	$T_{1/2}^{0\nu} @ 90\% \text{ C.L.}$
^{114}Cd	123.9 ± 1.0	75.8 ± 1.3	$\sim 3.91 \times 10^{21} \text{ yr}$	213.9 ± 1.7	48 ± 7	$> 1.6 \times 10^{21} \text{ yr}$
^{128}Te	42.2 ± 1.0	72.4 ± 1.2	$\sim 7.28 \times 10^{21} \text{ yr}$	65.5 ± 1.6	46 ± 7	$> 1.9 \times 10^{21} \text{ yr}$
^{70}Zn	28.6 ± 0.6	70.9 ± 1.2	$\sim 1.62 \times 10^{19} \text{ yr}$	45.1 ± 1.0	45 ± 7	$> 6.8 \times 10^{18} \text{ yr}$
^{130}Te	1.7 ± 0.1	52.1 ± 1.0	$\sim 2.13 \times 10^{22} \text{ yr}$	3.6 ± 0.3	34 ± 5	$> 6.2 \times 10^{21} \text{ yr}$
^{116}Cd	1.3 ± 0.1	48.8 ± 1.1	$\sim 4.38 \times 10^{21} \text{ yr}$	2.7 ± 0.2	33 ± 5	$> 1.1 \times 10^{21} \text{ yr}$

Between [COB16a] and the present work, a reduction of the BI of about a factor of two has been achieved using the advanced PSD cuts and the full data partitioning. Moreover, a higher total efficiency could be preserved by switching from the LSE cut approach (see section 7.1.3) to the advantageous A/E criterion with an average signal acceptance of 90% (see section 7.2.2). The higher value of ε_{tot} is also due to the newly evaluated volume selection efficiency of the standard z -cut, which revealed a higher selection efficiency based on the data of the dedicated ^{113}Cd low-threshold run (see section 7.1.2). No significant improvement can be reported for the previously determined values of the intrinsic $0\nu\beta\beta$ -decay efficiency and the energy resolution FWHM at $Q_{\beta\beta}$, which are found to be comparable for both approaches and rely on similar methods. In fact, preliminary values were provided by the author to assist the accomplishment of the Bayesian analysis at that time. By comparing the achieved lower half-life limits $T_{1/2}^{0\nu}$ at 90% credibility with $\tilde{T}_{1/2}^{0\nu}$ according to Eqn. (3.10), an improvement of about three to four times can be expected for the results of an updated $0\nu\beta\beta$ -decay analysis using the COBRA demonstrator's full exposure.

The previous $0\nu\beta\beta$ -decay analysis was done by using the Bayesian Analysis Toolkit (BAT) [CKK09] and driven by T. Quante (TU Dortmund). The software package BAT is based on Bayes' theorem (see appendix C.3) and designed to help solve statistical problems encountered in Bayesian inference. It provides a set of algorithms which enable straightforward parameter estimation, limit setting and uncertainty propagation. The implementation of BAT is done

in C++ and features an interface to ROOT and its related data formats.

In addition to the already discussed efficiencies, there is another correction factor taken into account in the Bayesian analysis based on the experimentally determined absolute full-energy detection efficiencies $\varepsilon_{\text{FE}}(^{137}\text{Cs})$ as explained in section 6.2.2 and listed in Tab. E.1–E.4 of the appendix. Nonetheless, by performing the same estimate of the half-life sensitivity according to Eqn. (3.10) for the parameters of the Bayesian analysis, about 20% lower values of $\tilde{T}_{1/2}^{0\nu}$ are obtained with respect to the actually achieved Bayesian lower half-life limits at the 90% credibility level. This can be seen as an indication for Eqn. (3.10) being even more conservative than the conducted Bayesian analysis, for which all considered uncertainties were already addressed and treated thoughtfully in form of nuisance parameters.

8.7.3 Outlook and future projection

At first, the same concluding remarks as quoted for the potential of observing the $2\nu\beta\beta$ -decay of ^{116}Cd in section 8.4.4 can be applied to improve the $0\nu\beta\beta$ -decay half-life sensitivity given the data of the COBRA demonstrator. This includes an update of the A/E selection to make use of the expected dip feature of the difference pulse for NCA-side LSEs, the offline synchronization of the FADC time stamps to identify multi-detector hits, as well as the tagging of delayed coincident events caused e.g. by the ^{214}Bi - ^{214}Po series. Moreover, a Monte-Carlo based background model could improve the previously used Bayesian analysis procedure. Given a background model, it might be beneficial to perform a reevaluation of the data partitioning to maximize the overall exposure. An update on the $0\nu\beta\beta$ -decay search with the COBRA demonstrator array is expected to appear in the PhD thesis of J. Volkmer.

Furthermore, as already pointed out in previous sections, the knowledge gained during the operation of the demonstrator setup provided valuable input for the preparation and construction of the COBRA XDEM setup. Because of the intended universality of COBRA’s analysis tools, it is expected that all the developed analysis techniques should be rather easily adaptable for the case of the XDEM qCPG detectors.

A first analysis of the physics data of the XDEM array with about 0.1 kg yr of exposure has been performed in [Tem19]. The instrumentation of the GR electrode proved to be very effective and reduced the background level by more than one order of magnitude in the double beta decay ROI compared to the demonstrator, even without applying any pulse-shape discrimination other than the standard z -cut. However, the GR instrumentation already comes with the cost of reducing the fiducial volume to about 85.3% [COB17] and might affect the energy and depth reconstruction, which is currently still under investigation. In general, the concept of the qCPG-CZT detector design is still a rather novel approach and most of the involved efficiencies have not been studied in all details. Moreover, the XDEM setup suffered from various technical problems since its commissioning in Mar.’18 and has not yet reached a state of optimum performance. Since the ending of the demonstrator phase in Nov.’19, the operation of the XDEM setup is one of the collaboration’s priorities and the efficiency of the physics data-taking is continuously increasing.

Fig. 8.62 illustrates a projection of the half-life sensitivity of COBRA XDEM for the $0\nu\beta\beta$ -decay of ^{116}Cd . The projection of $\tilde{T}_{1/2}^{0\nu}$ according to Eqn. (3.10) at 90% C.L. is based on the experimental parameters determined in [Tem19].

The estimate of the background level results in $B \approx 0.08 \pm 0.04 \text{ cts}/(\text{keV kg yr})$ for an energy range of $Q_{\beta\beta} \pm 300 \text{ keV}$, excluding the signal region defined as $Q_{\beta\beta} \pm 3 \cdot \text{FWHM}$. This background level is about 16 times lower than for the final partition of the demonstrator and its full pulse-shape discrimination. The average energy resolution at the Q -value, as deduced from calibration data, yields $\text{FWHM} = 26.1 \text{ keV}$ and corresponds to 0.93% in relative terms. This is an improvement of about a factor of 1.6 compared to the demonstrator results listed

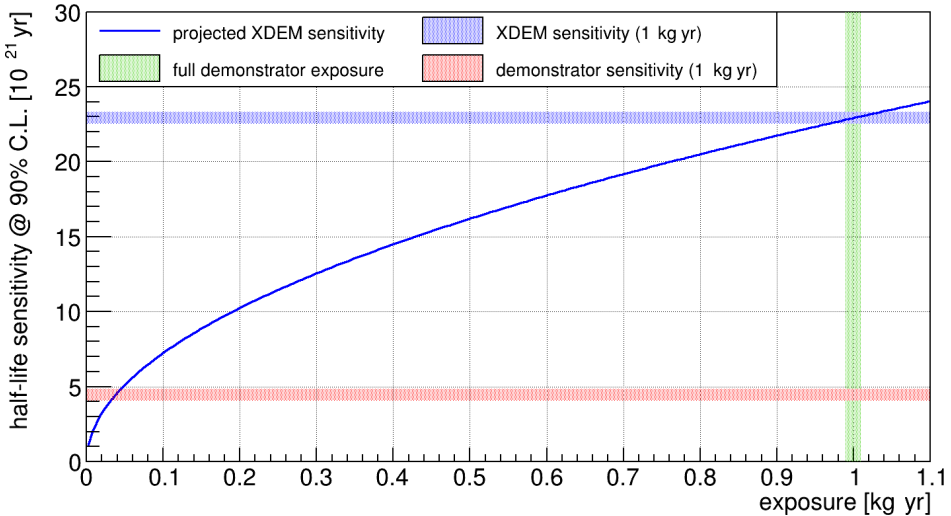


Figure 8.62: Projected half-life sensitivity of COBRA XDEM for the $0\nu\beta\beta$ -decay of ^{116}Cd . The projection according to Eqn. (3.10) at 90% C.L. is based on a background index of $0.08 \pm 0.04 \text{ cts/(keV kg yr)}$, a total $0\nu\beta\beta$ -decay detection efficiency of $\varepsilon_{\text{tot}} = (50 \pm 3)\%$ and a relative energy resolution of 0.93% in terms of FWHM at $Q_{\beta\beta} = 2.8 \text{ MeV}$. For an exposure of about 1 kg yr, the projected sensitivity of the XDEM setup is expected to reach $\tilde{T}_{1/2}^{0\nu} \sim 2.3 \times 10^{22} \text{ yr}$, which surpasses the demonstrator projection (see also Tab. 8.31) by about a factor of five.

in Tab. 8.30. Furthermore, also the quoted total selection efficiency of $\varepsilon_{\text{tot}} = (50 \pm 3)\%$ for the $0\nu\beta\beta$ -decay of ^{116}Cd turns out to be slightly higher for the XDEM detectors. This results in an overall increase of the sensitivity rate by about a factor of five. However, it should be noted that there might still be some unattended efficiency issues as pointed out before, which could not be addressed so far due to a lack of data, e.g. for the ^{113}Cd β -decay as an universal monitor of the detector performance.

Because of its superior background level and energy resolution, the projected half-life sensitivity of the XDEM setup might already surpass the final sensitivity of the demonstrator array with only about 20 kg d of exposure. However, due to the limited statistics that were available for the first analysis of the XDEM physics data, the results should be seen as preliminary. In fact, the SB region contains only two events, whereas an additional event is found in the excluded signal region close to the Q -value. Ultimately, by reaching the full demonstrator exposure of about 1 kg yr, the sensitivity of COBRA XDEM might reach $\tilde{T}_{1/2}^{0\nu} \sim 2.3 \times 10^{22} \text{ yr}$ for the $0\nu\beta\beta$ -decay of ^{116}Cd . This would be an improvement of more than one order of magnitude compared to the previous Bayesian analysis results presented in Tab. 8.31. Although this ultimate sensitivity would still one order of magnitude below the most stringent lower limit set by the Aurora experiment for the same decay – resulting in $T_{1/2}^{0\nu} \geq 2.2 \times 10^{23} \text{ yr}$ at 90% C.L. [Aur18] – it would be a major milestone for the COBRA experiment. In fact, the Aurora experiment used two CdWO_4 crystal scintillators with a combined mass of 1.162 kg and an isotopic enrichment of 82% in ^{116}Cd , while the XDEM setup is not only much lighter but relies on non-enriched source materials with a natural ^{116}Cd abundance of only 7.5% (see Tab. 4.4). An enrichment on the level of the Aurora experiment would directly boost the sensitivity by about one order of magnitude, pushing it to the level of the world-leading experiment in case of ^{116}Cd , and should be considered as one of the next steps towards a large-scale COBRA experiment.

Chapter 9

Conclusions

The aim of the COBRA experiment is to search for the existence of the hypothesized $0\nu\beta\beta$ -decay with room temperature semiconductor CZT detectors. The present work contributed significantly to the progress of the project and can be sectioned into three main parts – CZT detector characterization, pulse-shape discrimination and physics data analysis.

In the first part, the characterization of the prioritized monolithic CPG-CZT detector approach has been reviewed. The characterization procedure has been improved substantially by implementing a new standardized optimization routine for the weighting factor and gain-balancing correction. This method is not only applied in the determination of the optimal working point biases and the evaluation of localized γ -ray scanning measurements, but has been also implemented into the data processing scheme of the LNGS calibration and physics data. For each of the characterized 1 cm^3 CZT crystals that were selected for the COBRA demonstrator array, the absolute full-energy efficiency at $E_\gamma = 661.7\text{ keV}$ has been determined from ^{137}Cs irradiation measurements at different distances. The extracted efficiencies entered as correction factors into the latest $0\nu\beta\beta$ -peak search analysis reported in [COB16a].

Furthermore, the entire crystal characterization procedure has been adapted for prototype CZT detectors with an increased volume of 6 cm^3 that became available in recent years. The characterization measurements of the first prototypes, including the extensive characterization of an up-scaled version of a conventional CPG detector, provided valuable input for the decision making process regarding the future orientation of the project. In particular, the decision to focus on the qCPG-CZT detector approach for the COBRA XDEM upgrade out of the available design options was made based on the characterization results obtained in the present work. Moreover, the performed localized γ -ray scanning measurements made it possible to perform a quantitative validation of the interaction depth reconstruction and are expected to serve well in ongoing and future studies aiming to improve the event reconstruction for the novel qCPG-CZT detector approach.

The second part, dedicated to pulse-shape discrimination techniques applicable to conventional CPG-CZT detectors such as deployed in the demonstrator array, contains a review of past and recent developments focusing on the standard data-cleaning cuts, the depth restrictions to veto surface events and the A/E criterion. For all of these, reliable efficiencies have been derived by making use of physics data of the LNGS setup or dedicated calibration measurements. The determined efficiencies provide the basis for future analyses. Particularly, the combination of the previous LSE and MSE algorithms in form of the A/E parameter proved to be beneficial. Moreover, an optimization routine has been developed which results in a unique cut value of $(A/E)_{90\%}$ for each of the demonstrator detectors after a delicate calibration of the A/E distribution for signal-like SSEs. The A/E optimization has been complemented by

performing a dedicated laboratory experiment to create a pulse-shape library of SSEs via the Compton coincidence technique for different energy regimes. The accumulated data might be used in future applications involving deep learning techniques or neural networks for the discrimination between signal-like and background-like event signatures.

Regarding the investigation of high-energy events, multiple long-term laboratory measurements were performed with three different CZT detector types to collect statistical samples of muon-induced events for varying DAQ settings. The interpretation of the collected data culminated in an analytic reconstruction model for muon-induced events, which was also applied in the background characterization of the data taken by the COBRA demonstrator. Furthermore, the derived model allows for a qualitative evaluation of the contribution of holes as secondary charge carriers in CZT detectors. This makes it possible to incorporate the holes' contribution as second order correction in future iterations of COBRA's event reconstruction.

In the third and main part of the present thesis, several analysis topics were addressed. This includes an elaborate characterization of the background of the COBRA demonstrator using the updated PSD techniques as well as an automatized data partitioning to identify periods with an increased background index during its operation from Sept.'11 to Nov.'19. In this time, a total exposure of 1.72 kg yr has been collected, whereas a carefully selected low-background partition of about 1 kg yr has been used to evaluate the potential of observing the $2\nu\beta\beta$ -decay of ^{116}Cd . The developed techniques will serve well in the data analysis of the COBRA XDEM setup. In general, it could be confirmed that the COBRA design allows for stable long-term operation under low-background conditions, which has been monitored with regular calibration measurements and the intrinsic decay rate of the ^{113}Cd β -decay.

The spectrum-shape investigation of the fourfold forbidden non-unique β -decay of ^{113}Cd with a subset of the best-performing CPG-CZT detectors has been the major analysis project in the present thesis. Each individual ^{113}Cd β -spectrum was evaluated in the context of three nuclear models to extract average values of the effective axial-vector coupling g_A . The data support the idea that g_A is quenched in the low-momentum-exchange β -decay of ^{113}Cd , independently of the underlying nuclear model, as published in [COB20]. Moreover, the main criticism of the applied spectrum-shape method, referring to a severe mismatch between the predicted spectrum-shape and the ^{113}Cd half-life in dependence on g_A , could be resolved by using updated template calculations based on the CVC hypothesis. The accordingly tuned NME calculations allow for a consistent determination of the spectral shape and the respective half-life in agreement with previous literature values.

At higher energy scales, the prominent signature of the α -decay of ^{190}Pt observed with the COBRA demonstrator has been used to determine the poorly known thickness of the cathode's electrode metalization. Furthermore, the accumulated statistics and MC studies made it possible to determine the half-life of this long-lived α -decay with an uncertainty of about 15%, which turned out to be compatible with existing literature values. As the uncertainty is dominated by systematic effects, whereas the natural abundance of ^{190}Pt being by far the largest unknown, the results might be significantly improved in follow-up campaigns.

With the updated Monte-Carlo implementation of the COBRA demonstrator, a feasibility study regarding the search for excited state transitions of the most promising $\beta\beta$ -candidates ^{116}Cd and ^{130}Te has been performed. The elaborate signal MC study revealed good prospects for improving the current experimental limits for the $2\nu\beta\beta$ -decay modes of ^{116}Cd , considering solely the respective ground-state transitions as an irreducible background.

Finally, an outlook and update on the accessible $\beta^- \beta^-$ decay modes of several isotopes of cadmium, zinc, and tellurium based on the newly evaluated efficiencies, background levels and the available full exposure of the demonstrator array has been presented. The projection of the half-life sensitivity has been compared to the results achieved in the commissioning phase of the COBRA XDEM setup and confirmed the excellent prospects of the new prototype detector module as the potential base unit for a large-scale COBRA experiment.

Appendix A

Impressions of LNGS setup

A.1 COBRA demonstrator setup



Figure A.1: Overview of the COBRA demonstrator setup at the LNGS. The outer shield consists of borated polyethylene sheets surrounding a steel EMI box with a copper-granulate-filled chute as cable feed-through. The inner shield is enclosed in an acrylic box that is constantly flushed with evaporated dry nitrogen to prevent radon from diffusing into the setup. The CPG-CZT detectors are operated in a copper housing in the center of a multi-layer lead castle. Several sensors on top of the lead castle and inside the EMI shield monitor the temperature and humidity (see also the schematic drawing in Fig. 4.6).



Figure A.2: Inner parts of the COBRA demonstrator array. The detector array consists of four layers of 4×4 CPG-CZT detectors with each a volume of 1 cm^3 that are placed into a housing made of OFHC copper.

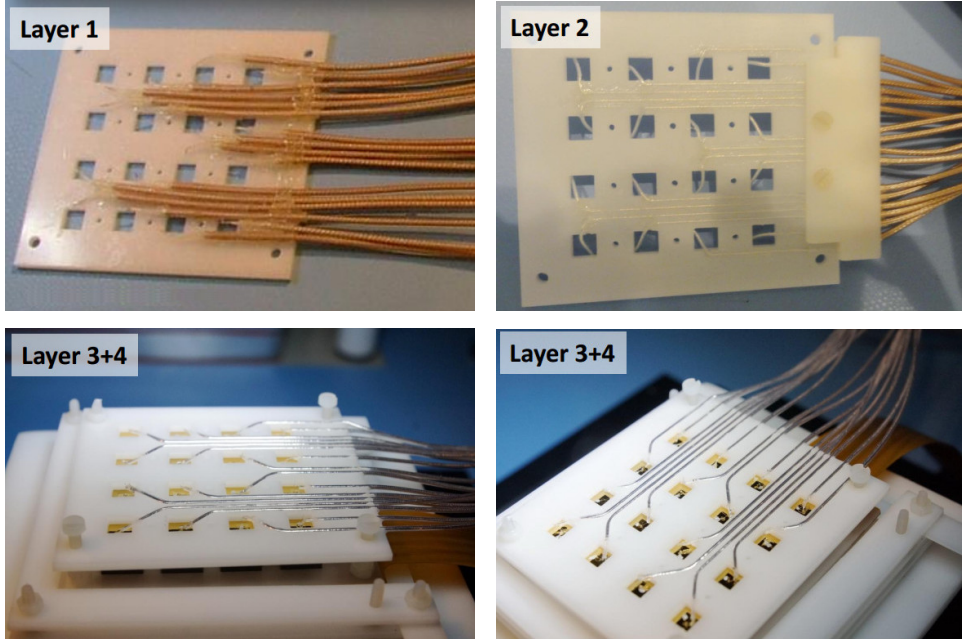


Figure A.3: Evolution of the detector layer concept (adapted from [Raj13]). *Top row:* design of L1 (Sept.'11) and L2 (Apr.'12) with only small differences on the HV side. *Bottom row:* improved design for L3 (Jul.'13) and L4 (Nov.'13). Each layer consists of multiple sheets made from POM (see Fig. 4.7 in section 4.3.3).

A.2 Installation of XDEM upgrade

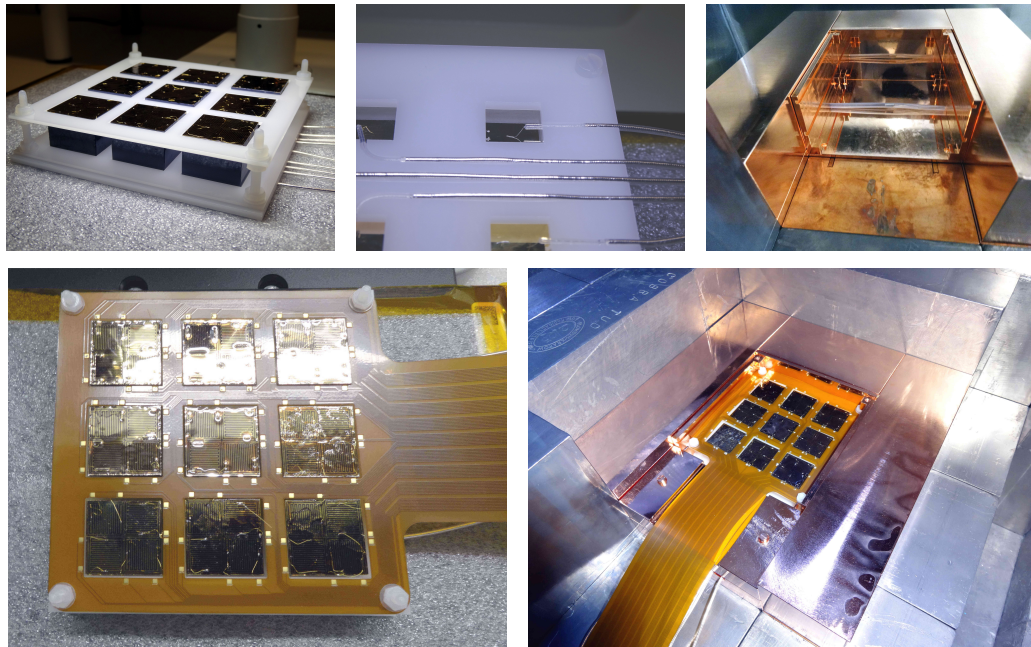


Figure A.4: Impressions of the COBRA XDEM installation at the LNGS in March 2018. *Top:* POM holder (*left*), electrode contacts on HV side (*middle*), new electro-polished copper nest on top of the original demonstrator setup (*right*). *Bottom:* fully equipped XDEM layer containing 3×3 qCPG-CZT detectors of 6 cm^3 volume. *Left:* electrode wiring of the anode side. *Right:* integration into the inner shield.

A.3 Detector arrangement

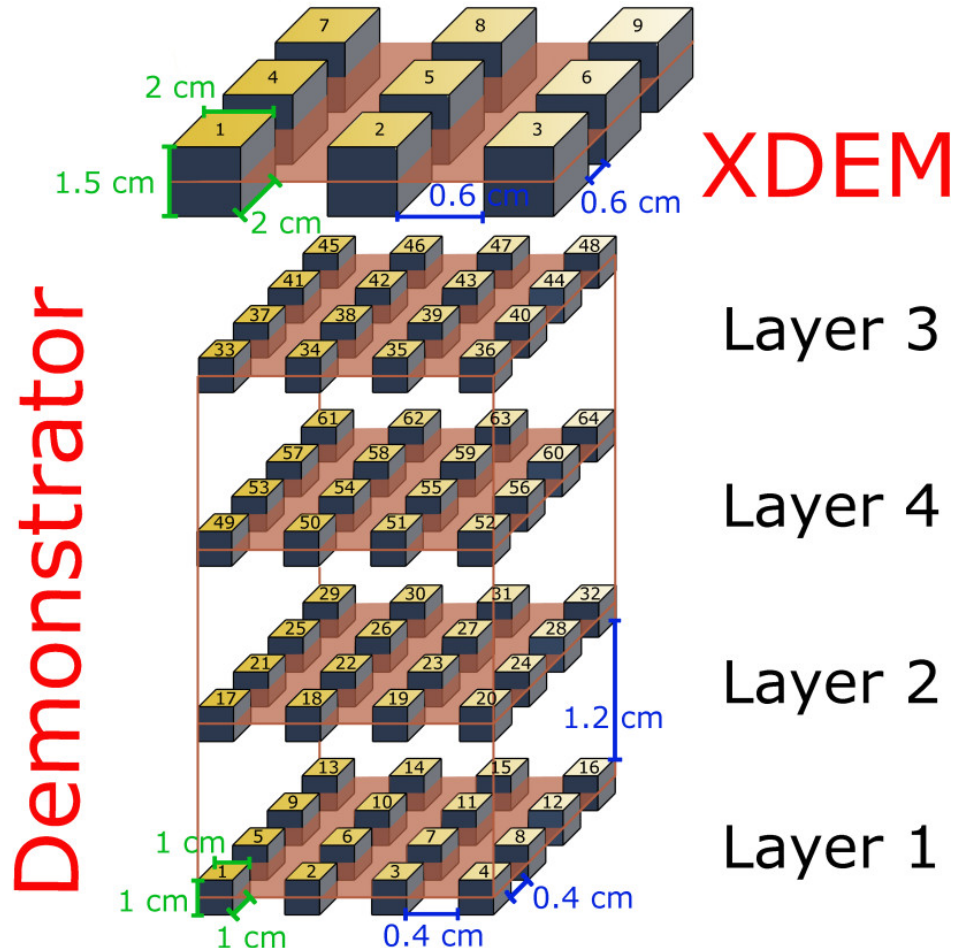


Figure A.5: Overview of the detector arrangement and numbering scheme for the COBRA demonstrator and the XDEM layer (taken from [Vol18]). Each layer of the demonstrator array consists of 4×4 CZT crystals of 1 cm^3 size. During the crystals' characterization, it was found that the detectors meant for L4 show a better performance than the ones already installed at the third layer's position. Because of this, both layers were switched during the installation of the fourth layer to increase the performance of the array in potential coincidence studies. The XDEM layer holds nine qCPG detectors with a size of 6 cm^3 . Each qCPG is divided into four sectors that can be treated individually in the event reconstruction. The sectors' numbering starts from 1–36, while the XDEM detectors are labeled as X1–X9.

Appendix B

Experimental equipment at TUD

B.1 Localized crystal characterization

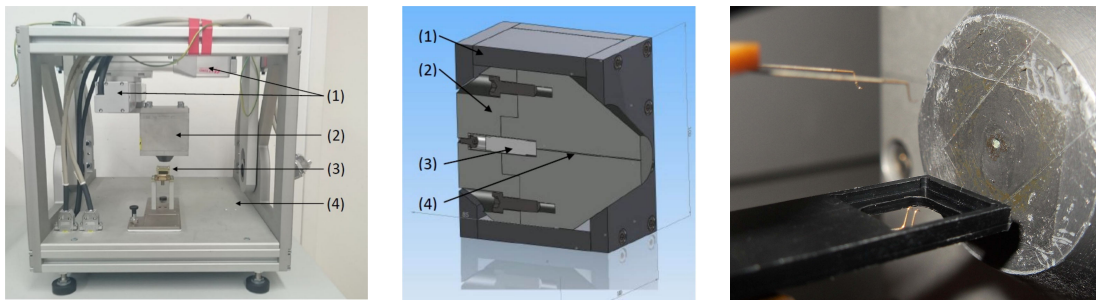


Figure B.1: Experimental apparatus for the localized γ -ray irradiation measurements (adapted from [Geh17] and [Zat14]). *Left:* two-dimensional scanning table with motorized axis (1), collimated source container (2), CPG-CZT detector mount (3) and rotatable base holder (4). *Middle:* collimated γ -ray source consisting of aluminum housing (1), lead shield of 4–6 cm thickness (2), active LAA type ^{137}Cs sample (3) and open collimator channel with $d = 0.5$ mm and $l = 60$ mm (4). *Right:* close-up of the collimator channel pointing to the empty CPG-CZT detector mount and its needle probes for the electrode contacting.

B.2 Long-term background measurements



Figure B.2: Overview of the long-term background measurement setup. *Left:* inside view of the EMI box with a complete lead castle containing the CPG-CZT detector setup. *Top right:* acrylic box around the CPG-CZT detector mount that is flushed with evaporated nitrogen from the dewar vessel of the nearby HPGe detector system. *Bottom right:* test assembly of the lead castle around the acrylic box.

B.3 Compton scattering experiment



Figure B.3: Overview of the Compton scattering experiment's shielding and electronics. *Left:* readout electronics and EMI box containing the CPG-CZT detector setup (see Fig. B.4). *Right:* multi-layer shield of the HPGe detector system made of copper and lead.

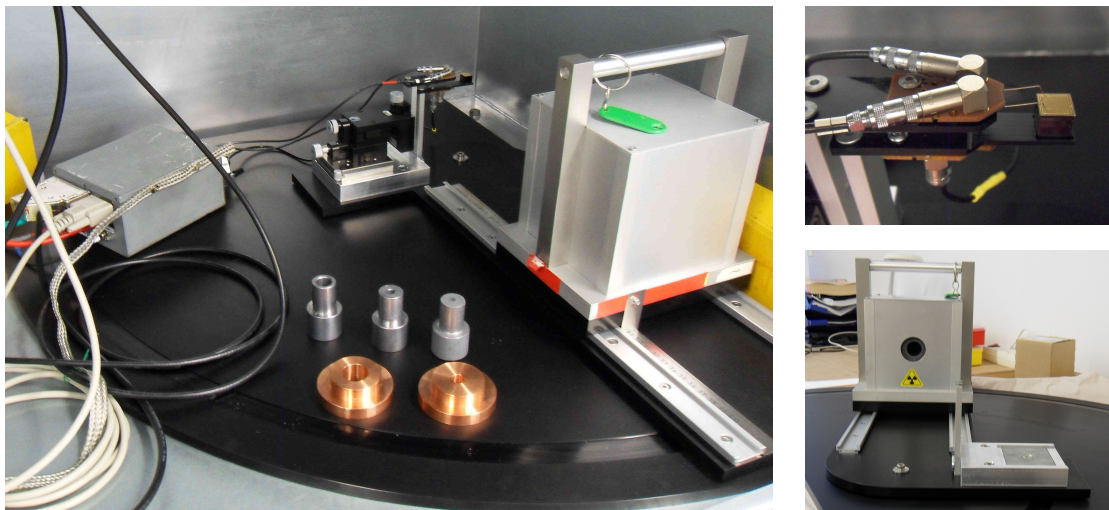


Figure B.4: Details of the CPG-CZT detector setup of the Compton scattering experiment. *Left:* inside view of EMI box. *Top right:* contacting of CPG-CZT detector using needle probes. *Bottom right:* front view of the source container pointing to the pivot position of the goniometer table.

Appendix C

Statistics and limits

C.1 Basic equations

- Gaussian normal distribution with mean μ and standard deviation σ

$$P(x) = \frac{1}{\sqrt{2\pi\sigma^2}} \exp\left\{-\frac{1}{2}\left(\frac{x-\mu}{\sigma}\right)^2\right\}. \quad (\text{C.1})$$

- Propagation of Gaussian uncertainties for $f(x, y, z)$ without correlations

$$\sigma_f = \sqrt{\left(\frac{\partial f}{\partial x}\right)^2 \sigma_x^2 + \left(\frac{\partial f}{\partial y}\right)^2 \sigma_y^2 + \left(\frac{\partial f}{\partial z}\right)^2 \sigma_z^2}. \quad (\text{C.2})$$

- Combination of standard deviations

$$\sigma_{\text{tot}} = \sqrt{\sum_{i=1}^N (\sigma_i)^2}. \quad (\text{C.3})$$

- Probability density function of χ^2 distribution with n degrees of freedom and $x > 0$

$$f(x; n) = \frac{x^{\frac{n}{2}-1} \cdot e^{-\frac{x}{2}}}{2^{\frac{n}{2}} \cdot \Gamma\left(\frac{n}{2}\right)}. \quad (\text{C.4})$$

- Gamma function $\Gamma(\frac{n}{2})$ appearing in Eqn. (C.4)

$$\Gamma\left(\frac{n}{2}\right) = \int_0^\infty x^{\frac{n}{2}-1} \cdot e^{-x} dx. \quad (\text{C.5})$$

For high degrees of freedom $n > 100$, the χ^2 distribution converges to a normal Gaussian distribution with mean $\mu = n$ and $\sigma = \sqrt{2n}$.

C.2 Coverage factor for sensitivity and limit setting

In section 3.3.1, an approximation formula to estimate the half-life sensitivity of a $0\nu\beta\beta$ -decay experiment according to Eqn. (3.10) has been introduced. This formula has been applied to project the sensitivity for a future large-scale COBRA experiment (see Fig. 4.11) and the XDEM setup (see Fig. 8.62), which is currently under operation at the LNGS.

The first part of Eqn. (3.10), the so-called *coverage factor* k_α , results from the underlying statistics and is also referred to as the *quantile* of the corresponding distribution. Assuming a Gaussian normal distribution with mean μ and standard deviation σ according to Eqn. (C.1), the probability to measure a variable with value x can be derived by integrating $P(x)$ within a certain range based on the standard deviation. In case of $\mu = 0$ and $\sigma = 1$, the total integral of the Gaussian distribution is normalized to unity. This makes it possible to directly access the probability P as shown in the following examples in Eqn. (C.6)–(C.8).

$$|\mu - x| \leq 1\sigma \longrightarrow P = 0.6827, \quad (\text{C.6})$$

$$|\mu - x| \leq 2\sigma \longrightarrow P = 0.9545, \quad (\text{C.7})$$

$$|\mu - x| \leq 3\sigma \longrightarrow P = 0.9973. \quad (\text{C.8})$$

On the other hand, a so-called *confidence interval* can be obtained by fixing the probability to a certain value and determining the respective σ -range. As an example, the interval corresponding to the probability $P(x) = 0.9$ to measure the value x is found for

$$|\mu - x| \leq 1.645\sigma \quad (\text{C.9})$$

and referred to as the 90% confidence interval. It should be noted that this is a so-called central confidence interval. However, the analysis techniques applied to extract lower limits in $0\nu\beta\beta$ -decay searches or upper limits in case of radioactive impurities, such as reported in section 8.3.7, are based on one-sided upper, respectively lower, confidence intervals. Fig. C.1 illustrates the difference between a central and an one-sided confidence interval for the example of a normalized Gaussian distribution and the case of the 90% confidence level (C.L.).

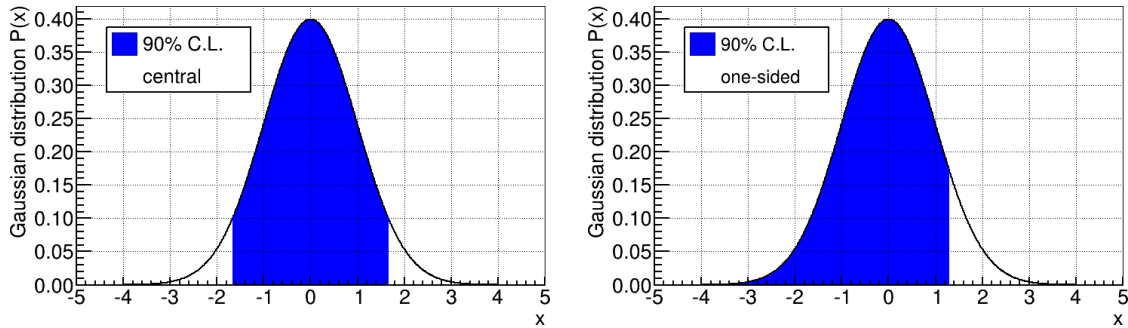


Figure C.1: Example for a central (left) and one-sided (right) confidence interval for a normalized Gaussian distribution (taken from [Zat14]). In both cases, the corresponding σ -ranges for the 90% C.L. are indicated, which means that the filled areas cover the exact same 90% fraction of the total integrals.

The one-sided confidence interval corresponds to

$$-\infty < \mu - x \leq 1.282\sigma @ 90\% \text{ C.L.} \quad (\text{C.10})$$

with an upper limit of 1.282σ of the integration. The upper integration limit in units of σ yields the quantile or coverage factor k_α . Usually, a coverage factor of $k_\alpha = 1.282$ enters Eqn. (3.10) to estimate the experimental half-life exclusion sensitivity at 90% C.L.

C.3 Bayes' theorem and Bayesian statistics

Bayes' theorem can be expressed mathematically as the following

$$P(A|B) = \frac{P(B|A) \cdot P(A)}{P(B)}, \quad (\text{C.11})$$

relating the probabilities $P(A)$ and $P(B) \neq 0$ of observing the events A and B with the conditional probabilities $P(A|B)$ and $P(B|A)$, respectively. More explicitly, the conditional probability $P(A|B)$ refers to the likelihood of event A occurring given that B is true and vice versa for $P(B|A)$. The probabilities $P(A)$ and $P(B)$ are denoted as the *marginal probabilities* of observing A and B .

One of the key applications of Bayes's theorem is Bayesian inference, e.g. to infer the conditional probability $P(A|B)$ from the knowledge or estimates of the probabilities on the right-hand side of Eqn. (C.11). Following the Bayesian interpretation of Eqn. (C.11), $P(A)$ can be interpreted as the initial degree of belief to observe the event A , which is denoted as the *prior probability*. The result of Bayes' theorem, the term $P(A|B)$, is referred to as the *posterior probability* and can be seen as the degree of belief in A having accounted for B . In this sense the quotient $P(B|A)/P(B)$ represents the support B provides for A . Moreover, Bayes' theorem states that it is usually not possible to conclude $P(A|B)$ from $P(B|A)$ without any knowledge about the *a-priori* probability $P(A)$. Such a statement would only hold, if $P(A)$ and $P(B)$ would be about the same.

In Bayesian statistics, the concept of Bayes' theorem is used to convert an estimate of the *a-priori* probability distribution into an *a-posteriori* probability distribution. Usually, previous experimental results enter as so-called *prior knowledge* into a Bayesian analysis to construct the posterior distribution based on the observed data and the prior. The resulting posterior probability distribution provides new insights and could be used as an updated prior for following experiments. An example case is shown in Fig. C.2.

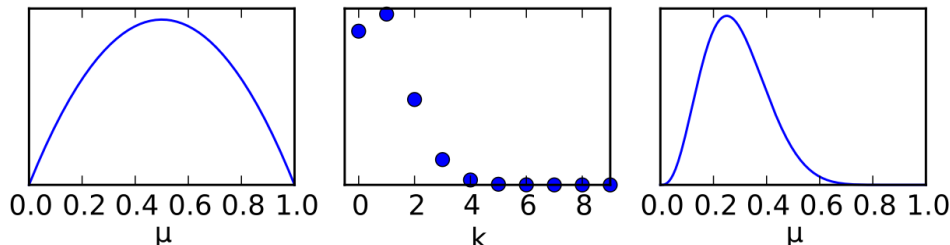


Figure C.2: Example for the application of Bayes' theorem in Bayesian statistics (adapted from Ref. [Wikb]). *Left:* prior probability distribution around $\mu = 0.5$. *Middle:* pseudo-data following from a binomial distribution. The data can be described by a standard Likelihood. *Right:* posterior probability distribution as result of a Bayesian interpretation of the pseudo-data and the prior distribution. The posterior provides new insights about the distribution of μ and could be used as an updated prior in a follow-up observation.

Appendix D

Supplementary material

D.1 Pulse-shape discrimination

D.1.1 Lateral surface events

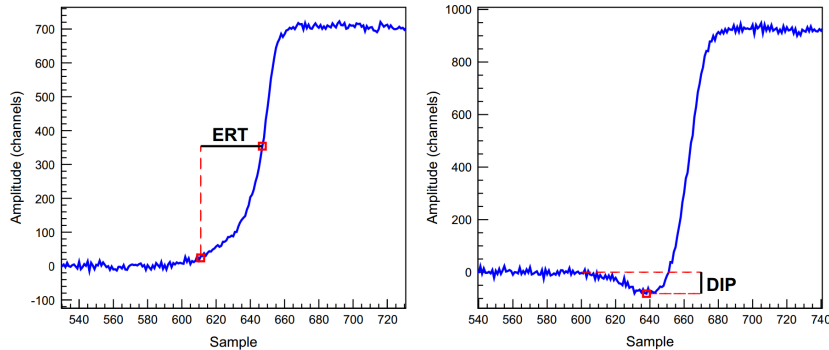


Figure D.1: Illustration of the definitions of the LSE identification quantities (taken from [COB14]). Both of the criteria are based on the shape of the difference pulse for interactions near the lateral detector walls. *Left:* the early rise time (ERT) is defined as the number of samples between the points, where the pulse-height reaches 3%, respectively 50%, of its nominal amplitude. One sample unit is equal to 10 ns. *Right:* the DIP criterion is defined as the minimum amplitude below the pre-baseline in a 30-sample-wide window with the right edge at the 50% point of the full amplitude.

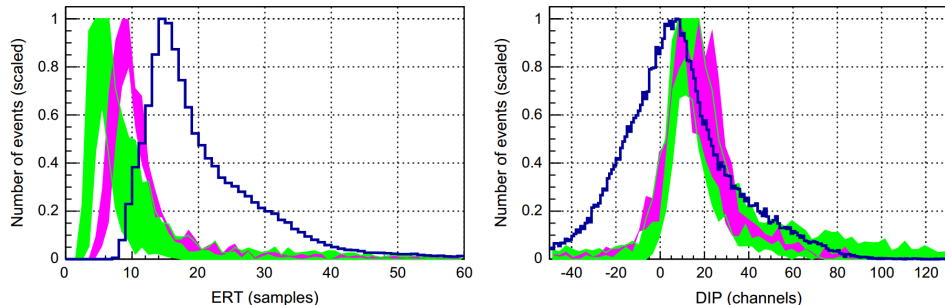


Figure D.2: Distribution of the LSE identification quantities for γ -ray interactions in an energy range of 1.7–2.0 MeV using calibration data of the COBRA demonstrator from the two-layer period and a laboratory measurement (taken from [COB14]). *Left:* ERT distribution. *Right:* DIP distribution. The broader curves correspond to the LNGS data which are split into 30 high-resolution (green) and two lower-resolution detectors (magenta), namely Det24 (L2-P08) and Det28 (L2-P12). While the two curves agree rather well for the DIP criterion, there are deviations due to the crystals' performance in case of the ERT quantity. The widths of the curves indicate the full range of values for the included detectors. In comparison, the laboratory measurement (blue) uses the same detector design as applied in the demonstrator array, but a lower quality crystal from a different batch. This is why the distributions of the LSE parameters turn out to be different.

D.1.2 A/E criterion

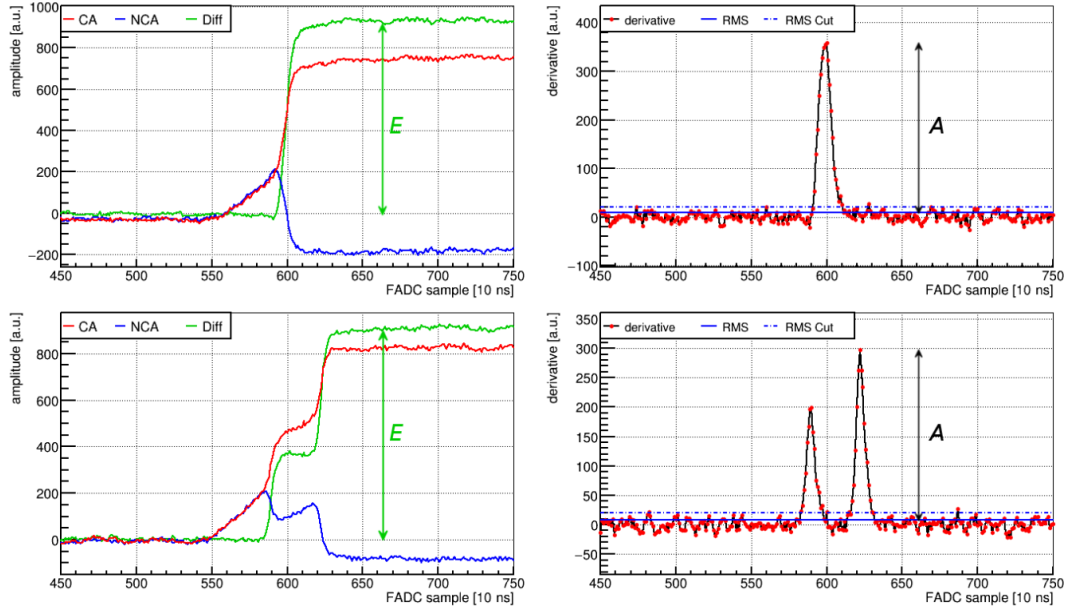


Figure D.3: Illustration of the definition of the A/E parameter (adapted from [Küt19]). *Left:* pulse-shapes of a single-site (*top*) and a multi-site event (*bottom*). The reconstructed energy deposition based on the pulse-height of the difference pulse is about $E = 2$ MeV in both examples. *Right:* corresponding current pulses as the derivatives of the difference pulses. The maximum amplitude A of the current pulse is significantly lower for the MSE compared to the SSE example, which is why MSEs are expected to feature lower A/E values.

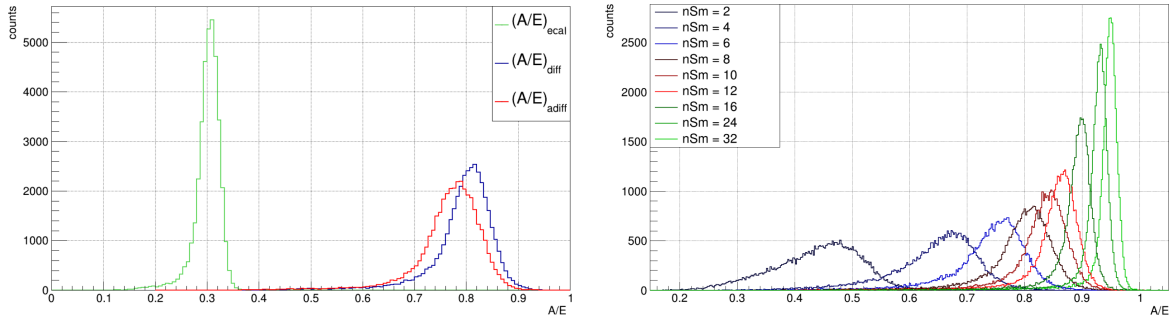


Figure D.4: Comparison of different A/E definitions and the influence of the smoothing window size in the construction of the current pulse (taken from [Küt19]). The distributions of A/E values are based on the calibration data of Det23 (L2-P07) with an energy restriction to the ^{208}Tl double-escape peak, which is taken as a proxy for single-site interactions (see section 7.2.3). *Left:* the three depicted options are based on different definitions of the involved parameters. The indices *diff* and *adiff* refer to the difference signal with and without the usage of an optimized weighting factor in the construction of the A/E parameter. Furthermore, the *ecal* option includes the actual energy calibration for the pulse-height of the difference pulse, which is why the distribution is shifted to lower values. All three options apply a smoothing window of $n_{\text{sm}} = 8$. By comparing all detectors of the demonstrator array, the $(A/E)_{\text{diff}}$ definition is found to be the most robust option. *Right:* effect of the smoothing window size n_{sm} on the parameter distribution for the standard $(A/E)_{\text{diff}}$ definition.

D.1.3 Muon-induced events

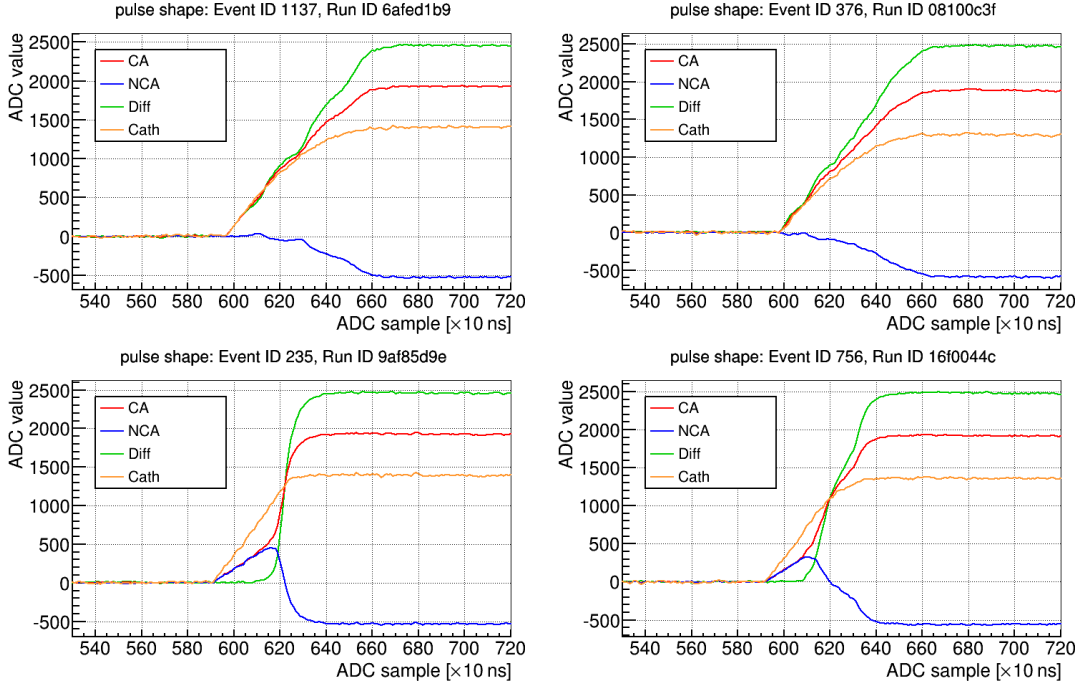


Figure D.5: Typical pulse-shape examples of muon-induced events (taken from [Zat14]). The selected events are from the laboratory background measurement of Det65 with a linear amplification setting of LA(99) (see Fig. 7.31 in section 7.4.3). The selection is based on the area of nearly vertically incoming muons with $E_\mu > 6$ MeV and $z_\mu \approx 0.5$. The corresponding derivatives of the difference pulse can be found in Fig. D.6.

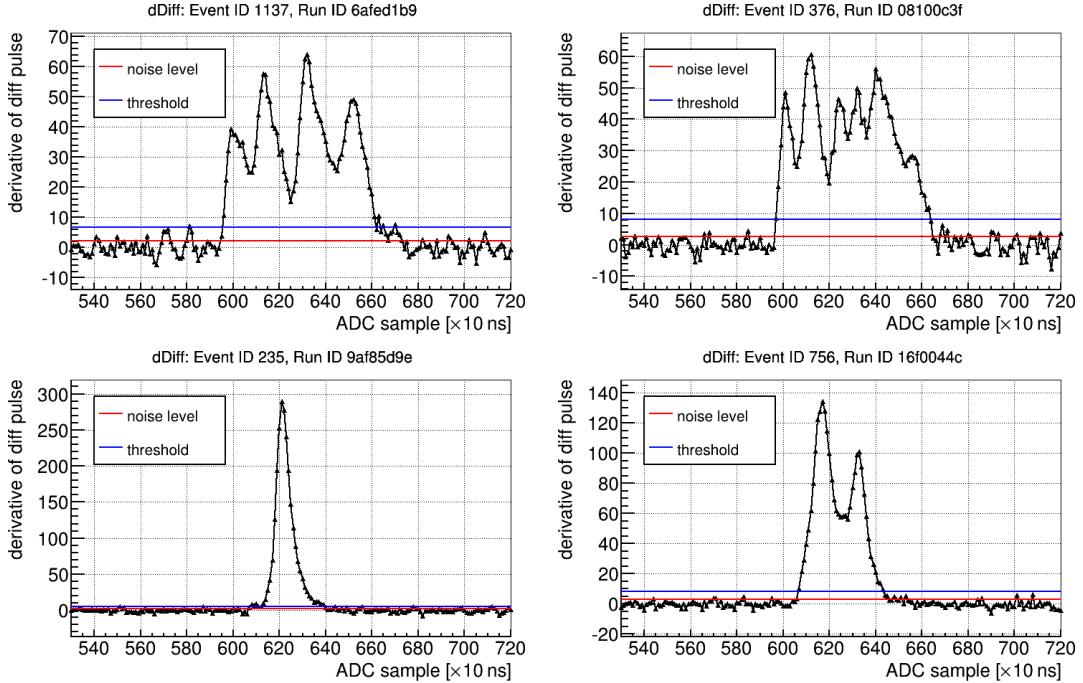


Figure D.6: Derivatives of the difference pulse for muon-induced events (taken from [Zat14]). The examples correspond to the pulse-shapes depicted in Fig. D.5, which were collected by Det65 in a laboratory background measurement. The varying number of peaks results from the delayed collection of the extended charge cloud by different rails of the CPG electrode. About 3% of all investigated events show single-site character with only a single peak in the derivative. The plots show the derivative as defined for the PSA method (see section 7.2).

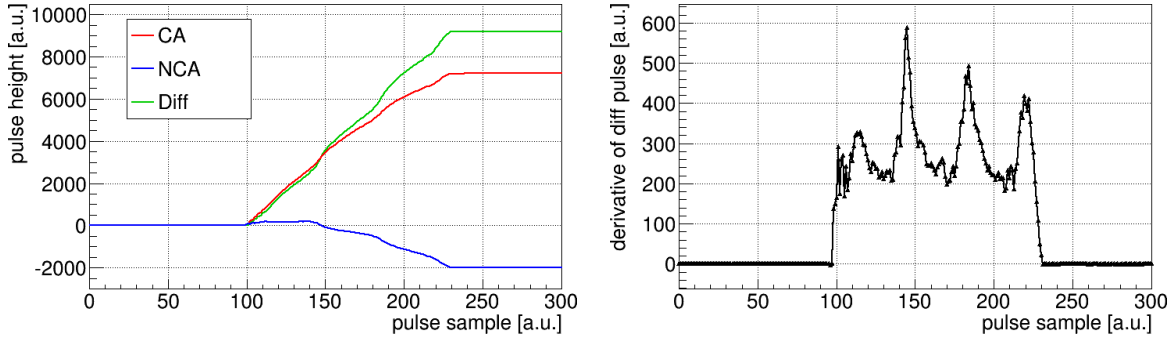


Figure D.7: Results of a detector simulation for a traversing muon with a highly non-vertical incident angle for a 1 cm^3 CPG-CZT detector (taken from [Zat14]). *Left:* pulse-shapes of the CA, NCA and difference signal. *Right:* derivative of the difference pulse based on the PSA method (see section 7.2). The muon interaction process was simulated with COBRA’s VENOM toolkit, while the charge propagation is done via a simple toy Monte-Carlo tool developed by M. Fritts. In comparison to the real detector signals depicted in Fig. D.5 and Fig. D.6 the same features are observed in the detector simulation.

D.2 LNGS data evaluation

D.2.1 Natural decay chains

Long-lived nuclides are the starting point of series of radioactive decays, which are naturally present since the forming of the Earth and the entire solar system. There are three main decay chains observed in nature, referred to as the uranium series, the actinium series and the thorium series. A fourth decay chain, denoted as the neptunium series, is already extinct on Earth due to the relatively short half-life of 2.14×10^6 yr of its initial isotope ^{237}Np [NDS20]. As only the α -decay changes the atomic mass number A , considering the most common radioactive decay modes, the natural decay chains are closely related to their starting nuclides. From those starting nuclides, an α -decay decreases A by $\Delta A = 4$, therefore, all nuclides within a chain share the same residue mod 4. Because of this, the natural decay chains are also labeled as $A = 4n$ (^{232}Th), $A = 4n + 1$ (^{237}Np), $A = 4n + 2$ (^{238}U) and $A = 4n + 3$ (^{235}U). The last one is referred to as the actinium series. All of the decay chains end with one of the stable isotopes of lead. An overview of the involved radionuclides, the most probable decay modes as well as their half-lives can be found in Fig. D.8.

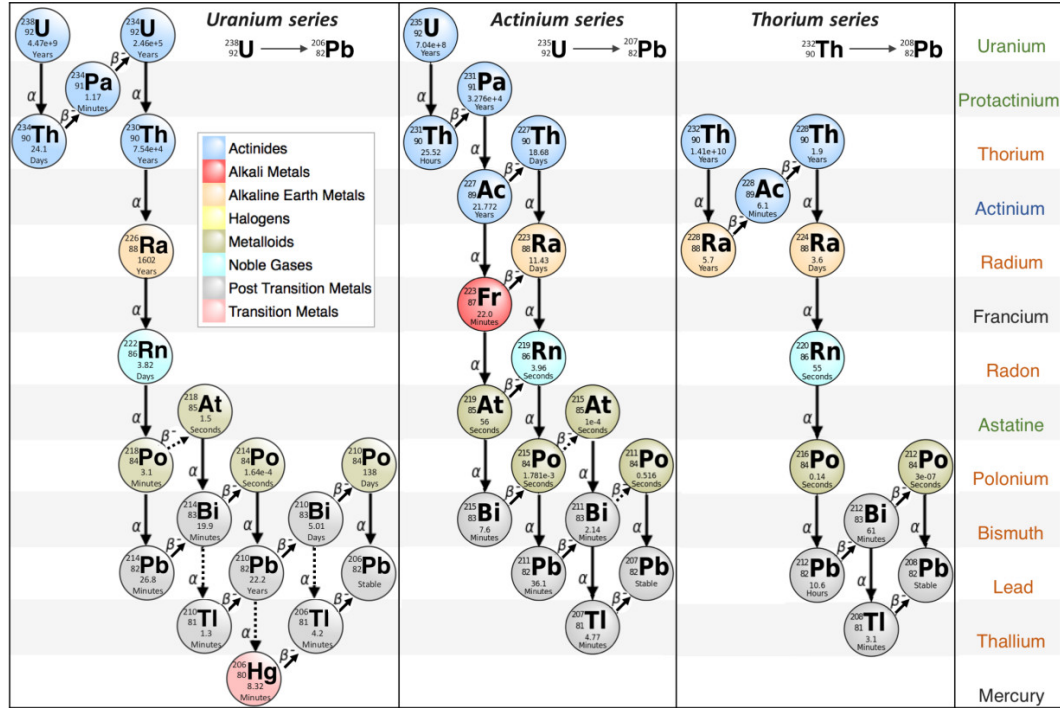


Figure D.8: Illustration of the natural decay chains (adapted from [Tan16], originally referring to [Wikd]). The fourth series related to ^{237}Np is already extinct on Earth, which is why it does not play a role in low-background experiments and the search for rare events.

D.2.2 Failure of nitrogen flushing at LNGS

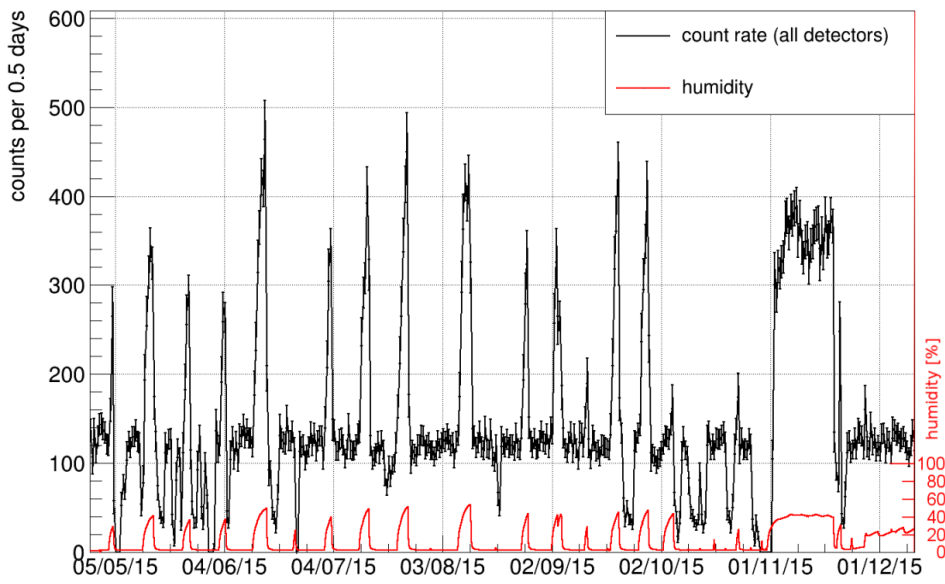


Figure D.9: Correlation of the COBRA demonstrator's total count rate and the relative humidity level as monitored on top of the lead castle inside the air-sealed radon enclosure (taken from [Küt19]). The humidity is a clear indication for the nitrogen flow and provides an indirect measure of the radon concentration. The data of the demonstrator array refers to the energy range of $350 < E < 2800 \text{ keV}$ as the ROI of the $2\nu\beta\beta$ -decay of ^{116}Cd . The data-taking suffered from multiple failures of the nitrogen flushing during the presented six month period in 2015. There is a clear correlation between the humidity level and the observed count rate.

D.2.3 Overview of the demonstrator’s LNGS calibrations

Table D.1: Overview of calibrations runs of the COBRA demonstrator at LNGS between 2011–2013. The labels *pre* and *post* indicate whether the calibration measurement indicates the start or the end of a physics period. If there was no hardware change in between, a calibration run is taken as both. The third column contains the detector numbers (1–64) that have been either disabled during the data-taking or could not be calibrated sufficiently. A normal calibration is based on ^{22}Na and ^{228}Th (high + low threshold).

date	label	missing/removed detectors	notes
2011-09-29	pre	9	start of 1-layer period
2011-11-07	post	9	
2011-11-11	pre	9	
2011-12-06	post/pre	9	
2012-02-09	post/pre	9	
2012-03-06	post/pre	9	
2012-03-23	post	9	end of 1-layer period
2012-04-04	pre	-	first 2-layer calibration
2012-07-19	post	-	
2012-07-23	pre	17-32	missing ^{22}Na + ^{228}Th for L2
2012-08-14	post/pre	-	
2012-09-11	post/pre	-	
2012-12-02	post	-	
2012-12-13	pre	23	missing ^{228}Th low-thresh for L1
2013-01-20	post	-	missing ^{228}Th low-thresh for ADC1, ADC2, ADC7
2013-01-25	pre	25	
2013-02-03	post/pre	23, 25	
2013-04-09	post/pre	23, 25	
2013-06-17	post	25	end of 2-layer period
2013-07-05	pre	3, 36, 37, 48	first 3-layer calibration
2013-07-10	post/pre	3, 37, 48	
2013-07-31	post/pre	3, 37, 48	
2013-08-09	post/pre	3, 36, 37, 48	
2013-08-26	post/pre	3, 37, 48	
2013-09-04	post/pre	3, 37, 48	
2013-10-08	post/pre	3, 28, 37, 48	
2013-10-28	post/pre	3, 28, 31, 37, 48	
2013-11-07	post	3, 28, 31, 37, 48	end of 3-layer period
2013-11-20	pre	3, 4, 9, 10, 28, 31, 36	first 4-layer calibration
2013-11-28	post/pre	3, 4, 9, 10, 28, 31, 48	
2013-12-05	post/pre	3, 4, 9, 10, 28, 31, 48	missing ^{22}Na for L4

Table D.2: Overview of calibrations runs of the COBRA demonstrator at LNGS between 2014–2019. The labels *pre* and *post* indicate whether the calibration measurement indicates the start or the end of a physics period. If there was no hardware change in between, a calibration run is taken as both. The third column contains the detector numbers (1–64) that have been either disabled during the data-taking or could not to be calibrated sufficiently. A normal calibration is based on ^{22}Na and ^{228}Th (high + low threshold).

date	label	missing/removed detectors	notes
2014-01-09	post/pre	3, 4, 9, 10, 28, 31, 48	missing ^{22}Na for L4, missing ^{228}Th for ADC7 and ADC12
2014-01-22	post/pre	3, 4, 9, 10, 28, 31, 38, 39, 48	missing ^{228}Th for ADC7 and ADC12
2014-03-05	post/pre	3, 4, 9, 10, 16, 38, 39	
2014-04-02	post/pre	3, 4, 9, 10, 38, 39	
2014-04-24	post/pre	3, 4, 9, 10, 16, 38, 39	
2014-06-18	post/pre	3, 4, 9, 10, 16, 38, 39, 47	
2014-09-04	post/pre	3, 4, 9, 10, 16, 38, 39, 47	
2014-10-01	post/pre	3, 4, 9, 10, 36, 47	
2015-02-08	post	3, 4, 9, 10	
2015-02-23	pre	4, 9, 10, 32, 46	
2015-05-04	post/pre	4, 9, 10, 46, 62	
2015-10-28	post/pre	4, 9, 10, 32, 45, 46	
2016-02-19	post/pre	4, 9, 10, 32, 36, 45	
2016-06-13	post	4, 9-12, 32, 36, 45, 54-56	missing ^{22}Na for all layers
2016-06-17	pre	9-11, 32	
2016-09-29	post/pre	4, 9-12, 32, 49	
2017-04-05	post/pre	1-4, 9-12, 32, 36, 41, 48, 49, 52, 56	preparation of ^{113}Cd run
2017-07-28	post/pre	1, 2, 4, 8-10, 16, 17, 28, 31-33, 36, 42, 48, 49, 51, 59, 63	start of ^{113}Cd run, additional ^{152}Eu low-energy calibration
2018-03-05	post	1, 2, 4, 8-10, 12, 16, 17, 28, 31-33, 36, 38-40, 42, 43, 48, 49, 51, 59, 63	end of ^{113}Cd run, additional ^{152}Eu low-energy calibration
2018-07-19	pre	9, 32, 36	red. calib. factors for ADC1, ADC3, ADC13 and ADC16 due to FADC exchange
2018-10-25	post	4, 12, 28, 31, 32, 36, 48, 57	red. calib. factors for ADC1, ADC3, ADC13 and ADC16 due to FADC exchange
2018-10-30	pre	4, 12, 28, 31, 32, 36, 43, 48	exchanged L2's FADCs to compensate red. calib. factors by higher signal amplification
2019-05-13	post	4, 12, 28, 32, 36, 43, 48, 49	
2019-05-22	pre	4, 12, 28, 32, 36, 48, 49	
2019-11-04	post	4, 12, 28, 32-34, 36, 48, 49	end of 4-layer period

D.3 Characterization of qCPG-CZT prototype detector

The following plots illustrate the single sector results of the working point characterization of one of the very first qCPG-CZT prototype detectors labeled as Redlen-33556. The global working point has been chosen as $BV/GB = 1300/100$ V (see Fig. 6.5 in section 6.2.1). Besides the energy resolution in terms of FWHM at 661.7 keV and the integral count rate in the full-energy peak (FEP), the asymmetry of the FEP is taken into account.

$$A = \frac{\sigma_L - \sigma_R}{\sigma_L + \sigma_R} \quad (\text{D.1})$$

The parameters σ_L and σ_R are part of the two-sided Gaussian fit in Eqn. (5.7). The single sector results turn out to be very similar to each other, whereas the higher asymmetry for low GB values is an indication for charge sharing. The observed drop of the FEP count rate for $BV = 1700$ V is due to the occurrence of leakage currents that cause a higher fraction of events to be flagged by the standard data-cleaning cuts.

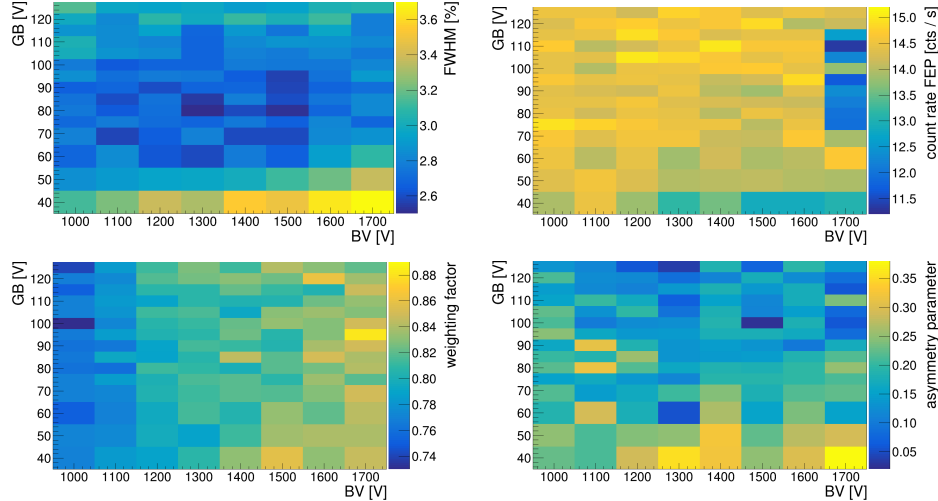


Figure D.10: Results of the working point measurements for sector 1 of one of the first qCPG-CZT prototype detectors (Redlen-33556). The global working point has been determined to $BV/GB = 1300/100$ V.

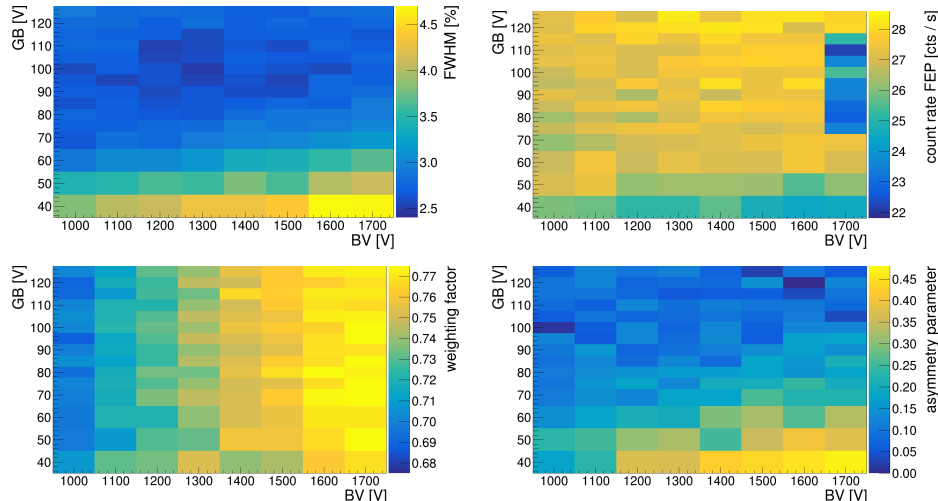


Figure D.11: Results of the working point measurements for sector 2 of one of the first qCPG-CZT prototype detectors (Redlen-33556). The global working point has been determined to $BV/GB = 1300/100$ V.

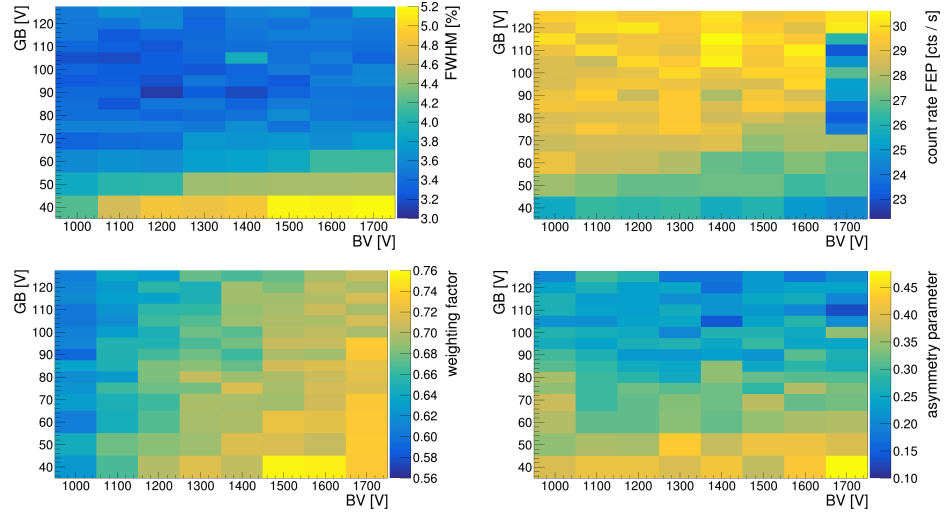


Figure D.12: Results of the working point measurements for sector 3 of one of the first qCPG-CZT prototype detectors (Redlen-33556). The global working point has been determined to $BV/GB = 1300/100$ V.

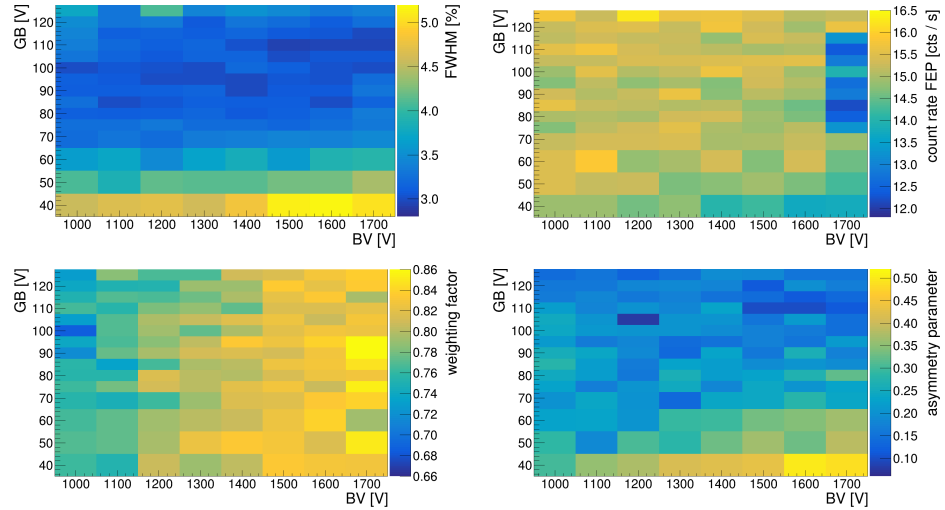


Figure D.13: Results of the working point measurements for sector 4 of one of the first qCPG-CZT prototype detectors (Redlen-33556). The global working point has been determined to $BV/GB = 1300/100$ V.

D.4 ^{113}Cd spectrum-shape analysis

D.4.1 Run method example

Originally, the so-called *run method* was meant as an additional control for the χ^2 test in order to compare the COBRA data with predicted ^{113}Cd template spectra for varying effective values of the weak axial-vector coupling g_A . The complete analysis procedure is presented in section 8.3 including a reference to the run method in section 8.3.9. The following example is taken from the Master thesis of A. Heimbold [Hei18].

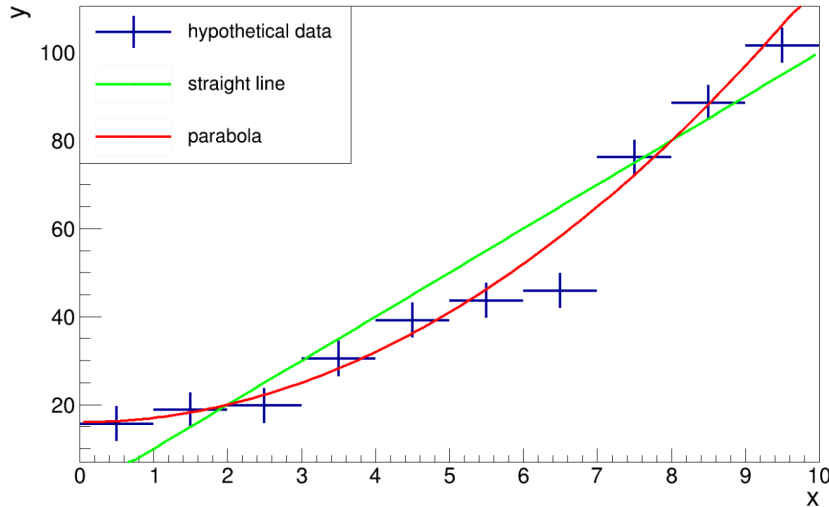


Figure D.14: Example case to illustrate the ability of expressing a model preference based on the run method (taken from [Hei18]). In the present example, ten pseudo data points are compared to two models: a straight line (green) and a parabola (red).

As a reminder, the run method relies on a specific labeling of the data points to classify the relation between the data and a model prediction. If the data exceeds the prediction in a certain data point, it is labeled as category *A*. In the other case, where the prediction is larger than the value of the data, the corresponding data point is labeled as category *B*. According to this procedure, the example shown in Fig. D.14 results in the following sequences for the two model predictions

$$\text{straight line: } AABBBBAA, \quad (\text{D.2})$$

$$\text{parabola: } BABAAABAAB. \quad (\text{D.3})$$

The number of runs r is referred to as the number of label changes in the complete sequences and results in $r = 3$ for the straight line model and in $r = 7$ assuming the parabola as the true distribution. In general, a large value of r indicates that the data fluctuate statistically around the prediction, which would mean on average a good agreement between the data and the compared model. However, this is only a qualitative statement and more or less a rule of thumb. A more accurate statement follows from the number of expected runs $\langle r \rangle$ according to Eqn. (8.20) in section 8.3.9 and Ref. [Bar89]. The same reference quotes the following expression for the expected variance of r

$$V(r) = \frac{2N_A N_B \cdot (2N_A N_B - N)}{N^2 \cdot (N - 1)} \quad (\text{D.4})$$

using the number of data points N_A and N_B with the respective labels. For the sequences in Eqn. (D.2) and Eqn. (D.3) it follows $N_A = N_B = 5$ for both models. This corresponds

in both cases to $\langle r \rangle = 6$ with a variance of $V(r) \approx 2.22$. The square root of the variance leads to a standard deviation of $\sigma = \sqrt{V(r)} \approx 1.49$. The observed number of runs can now be interpreted as more than 2σ deviation in case of the straight line model ($r = 3$), while the parabola is compatible with the data within 1σ . However, in case of the ^{113}Cd spectrum-shape analysis a more accurate statement could be achieved by using the χ^2 test.

D.4.2 Single detector spectra

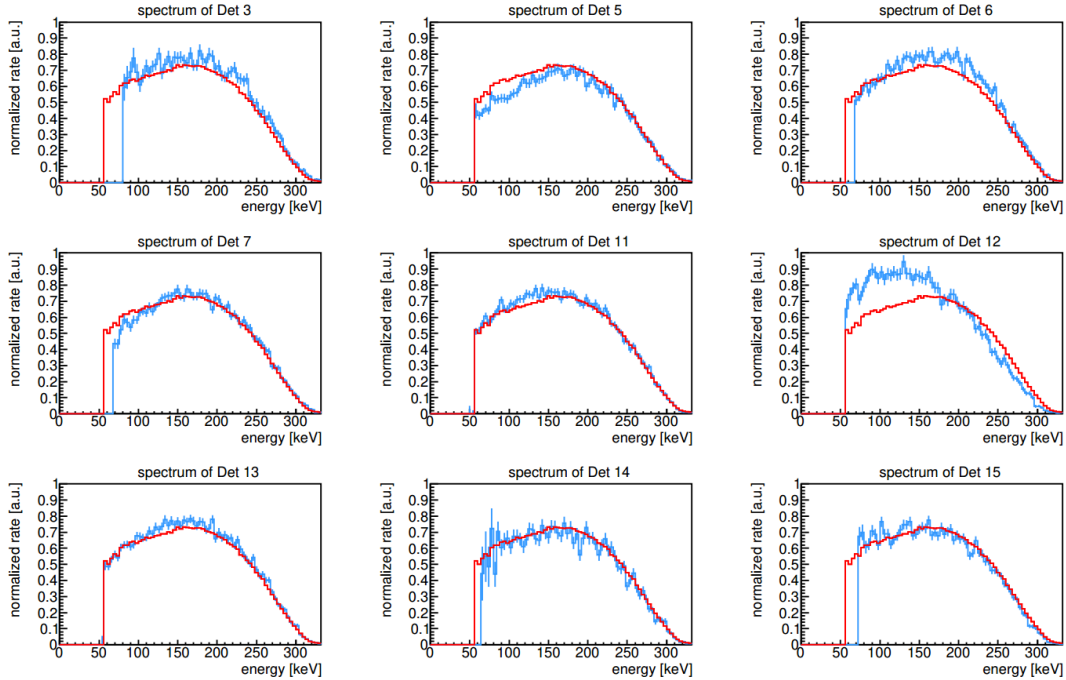


Figure D.15: Compilation of the experimental ^{113}Cd spectra measured with (Det3 – Det15) of the COBRA demonstrator (taken from [COB20]). Each spectrum is normalized by the integral from the respective threshold to the Q -value of ^{113}Cd . The combination of all detectors is shown for comparison (red solid histogram).

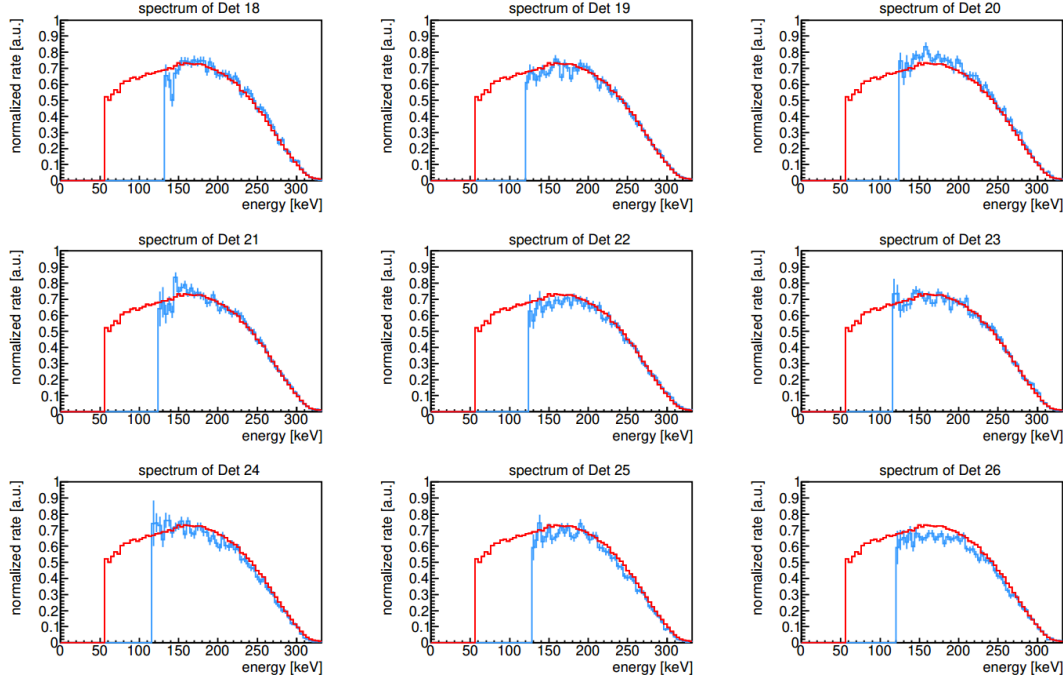


Figure D.16: Compilation of the experimental ^{113}Cd spectra measured with (Det18 – Det26) of the COBRA demonstrator (taken from [COB20]). Each spectrum is normalized by the integral from the respective threshold to the Q -value of ^{113}Cd . The combination of all detectors is shown for comparison (red solid histogram).

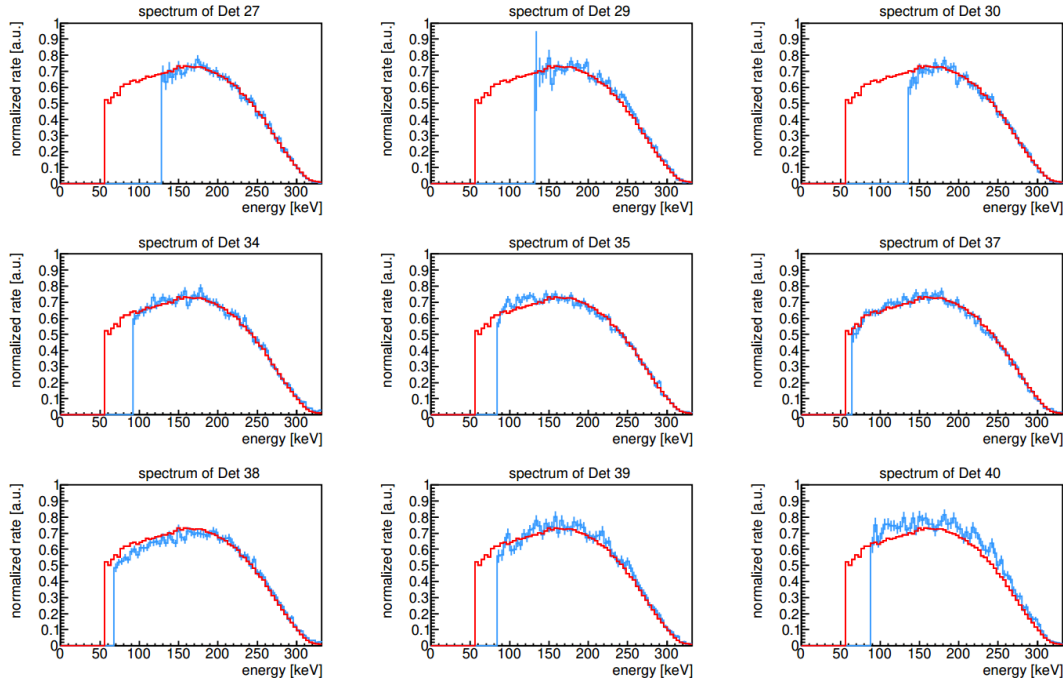


Figure D.17: Compilation of the experimental ^{113}Cd spectra measured with (Det27– Det40) of the COBRA demonstrator (taken from [COB20]). Each spectrum is normalized by the integral from the respective threshold to the Q -value of ^{113}Cd . The combination of all detectors is shown for comparison (red solid histogram).

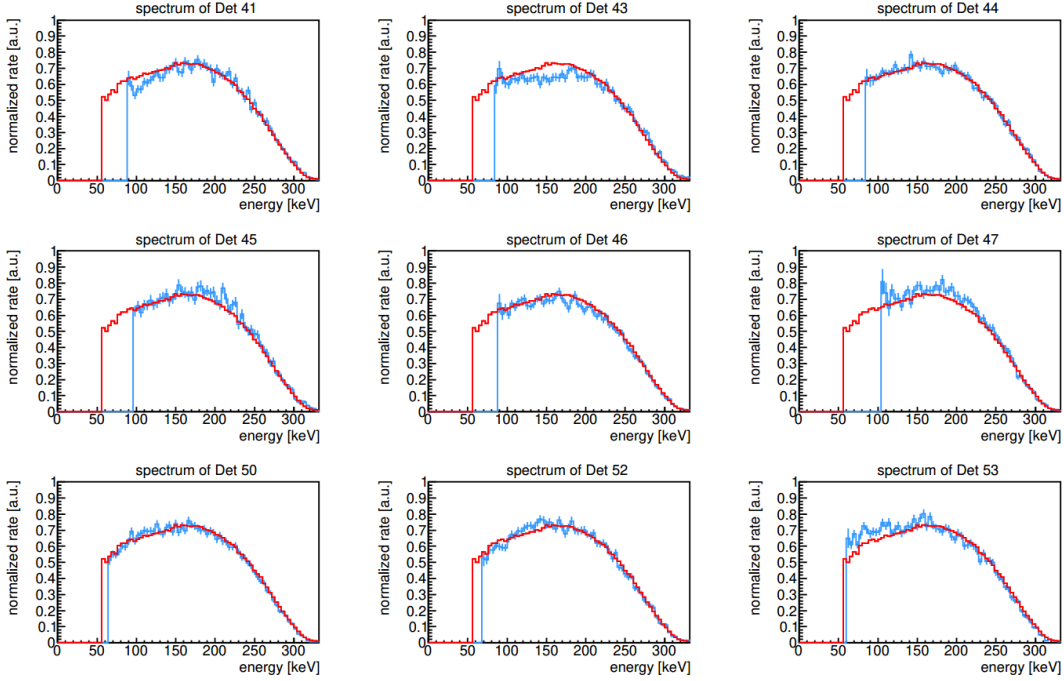


Figure D.18: Compilation of the experimental ^{113}Cd spectra measured with (Det41 – Det53) of the COBRA demonstrator (taken from [COB20]). Each spectrum is normalized by the integral from the respective threshold to the Q -value of ^{113}Cd . The combination of all detectors is shown for comparison (red solid histogram)..

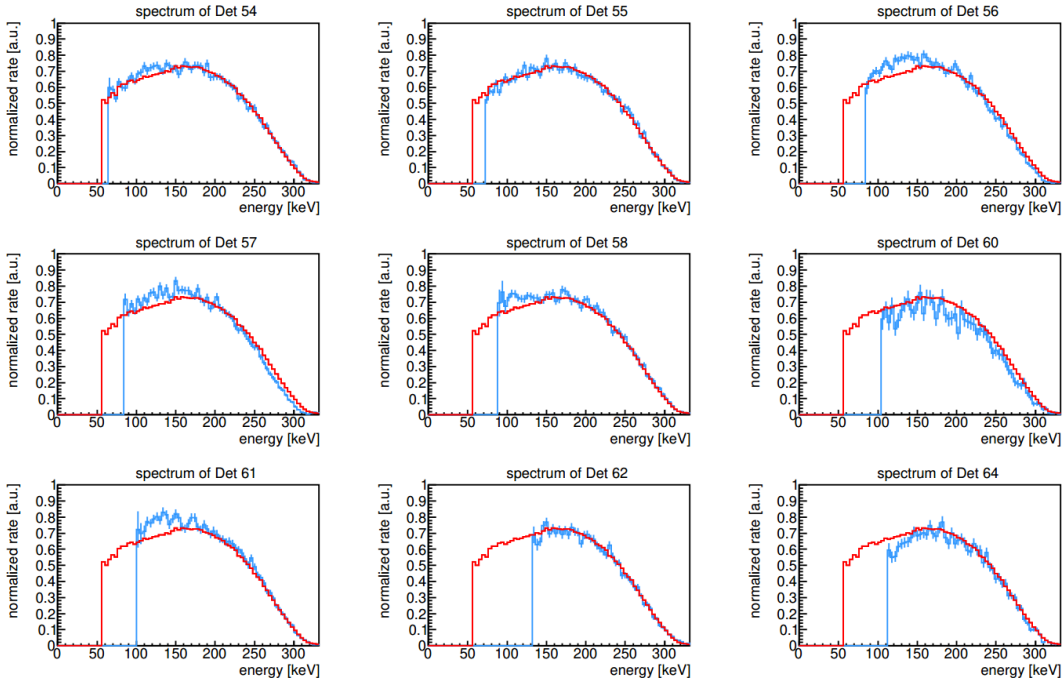


Figure D.19: Compilation of the experimental ^{113}Cd spectra measured with (Det54 – Det64) of the COBRA demonstrator (taken from [COB20]). Each spectrum is normalized by the integral from the respective threshold to the Q -value of ^{113}Cd . The combination of all detectors is shown for comparison (red solid histogram).

D.4.3 Interaction depth distribution for ^{113}Cd

The following plot compilation contains some examples of the single detector's z -distribution recorded during the dedicated ^{113}Cd data-taking period from Jul.'17 till Feb.'18. The energy range has been limited to the ^{113}Cd region of interest. An explanation of the characteristic z -features is given in section 7.1.2 and section 8.3.5.

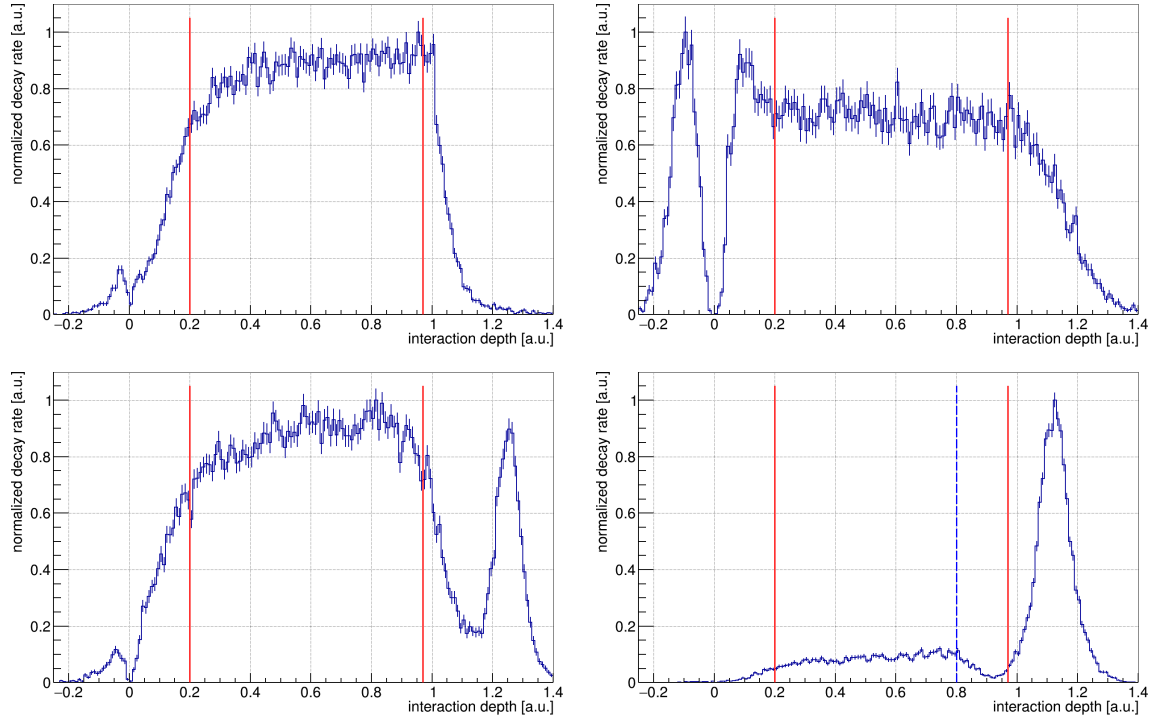


Figure D.20: Compilation of examples for the ^{113}Cd depth distribution. The vertical red lines indicate the default cut on the interaction depth: $0.2 < z \leq 0.97$. *Top left:* expected shape of the z -distribution according to the homogeneously distributed source decays. The example is shown for Det50 (L4-P02). *Top right:* Det3 (L1-P03) featuring a prominent low- z peak for $z < 0$, which assumed to be caused by unflagged noise. The peak is removed by the standard z -cut. *Bottom:* both examples, Det52 (L4-P04) (*left*) and Det60 (L4-P12) (*right*), feature a high- z peak for $z > 1$, which is also assumed to be caused by unflagged noise. In the first case the peak is sufficiently removed by the standard z -cut. For Det60 a stricter upper z -cut of $z < 0.8$ has been used in the ^{113}Cd spectrum-shape analysis, which is indicated by the vertical dashed blue line.

D.4.4 Analytic low-energy background model

As a crosscheck of the Monte-Carlo based low-energy background model developed for the ^{113}Cd spectrum-shape analysis in section 8.3.7, two analytic alternatives have been investigated. Both are based solely on the combined experimental spectrum of the 45 selected detectors and are depicted in Fig. D.21. The S/B ratio turns out to be slightly higher for both alternatives, but is on the same order as for the much more advanced MC model.

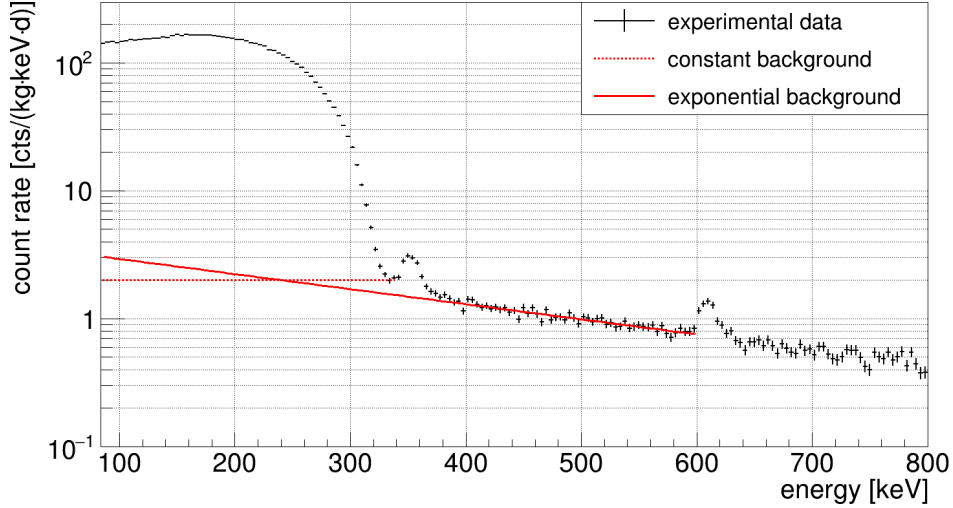


Figure D.21: Analytic models for the low-energy background description of the ^{113}Cd energy range. Two scenarios are investigated: a constant approximation based on the background level at the ^{113}Cd Q -value (dotted line) and an exponential fit over 400–600 keV (solid line), which avoids the prominent γ -lines of ^{214}Pb (351.9 keV) and ^{214}Bi (609.3 keV). The S/B ratio is determined for the energy range of $\bar{E}_{\text{th}} = 84$ keV to the Q -value of 320 keV and leads to $S/B \approx 60$ assuming a constant background of 2 cts/(kg keV d) and $S/B \approx 52$ in case of the exponential background fit.

D.4.5 Prediction under the CVC hypothesis

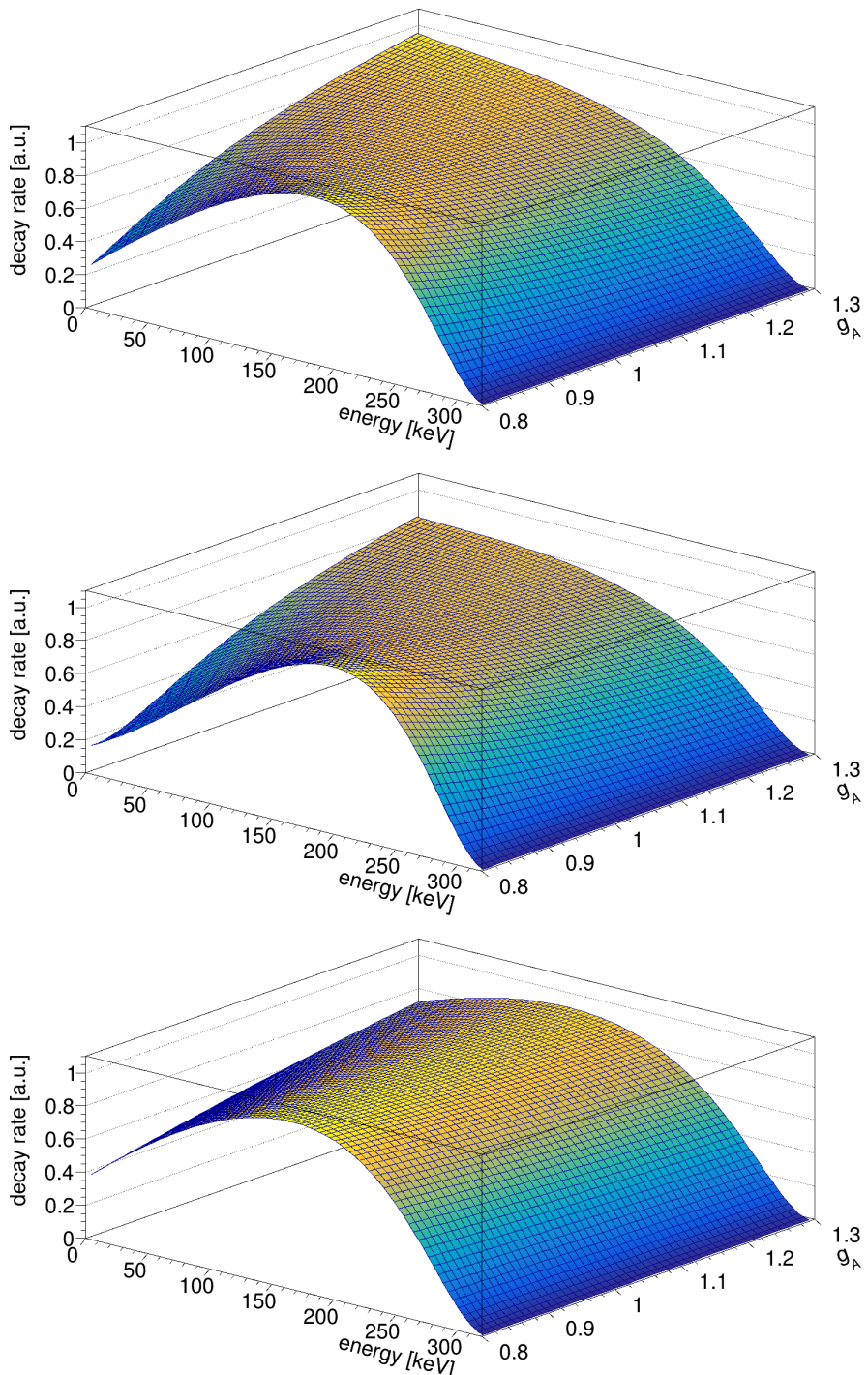


Figure D.22: Nuclear model predictions for the ^{113}Cd spectrum-shape dependence on g_A under the CVC hypothesis. *Top:* interacting shell model (ISM). *Middle:* microscopic quasiparticle-phonon model (MQPM). *Bottom:* interacting boson-fermion model (IBFM-2). The predicted g_A dependency is quite similar for all three nuclear models and differs significantly from the previous results depicted in Fig 8.11 of section 8.3.1.

D.5 Double beta decays into excited states

D.5.1 Detector pair distributions

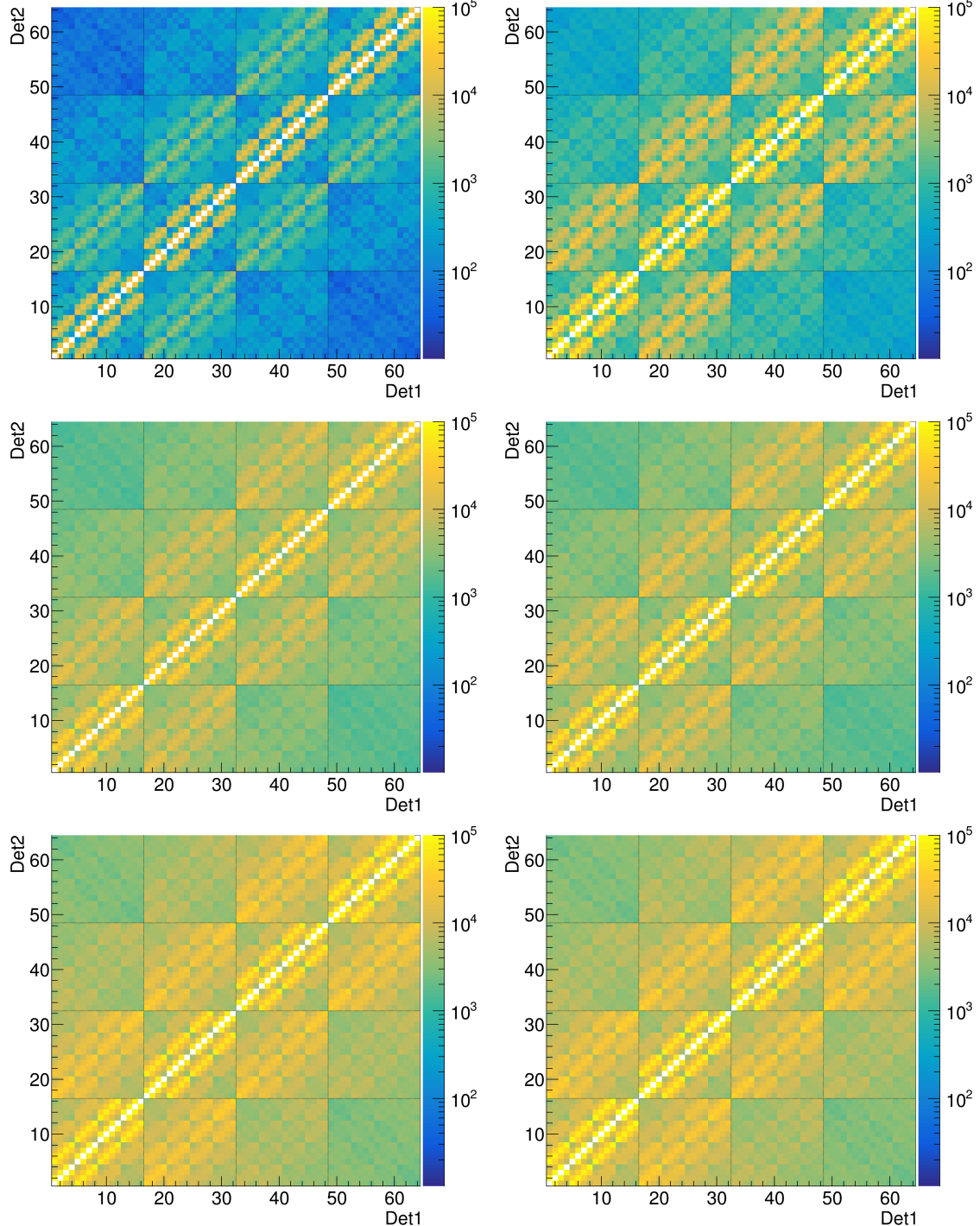


Figure D.23: M2 detector pair distributions for simulated double beta transitions of ^{116}Cd with the COBRA demonstrator. Top: $0_{\text{g.s.}}^+ \rightarrow 0_{\text{g.s.}}^+$ transitions via $2\nu\beta\beta$ -decay (left) and $0\nu\beta\beta$ -decay (right). Middle: $0_{\text{g.s.}}^+ \rightarrow 2_1^+$ transitions via $2\nu\beta\beta$ -decay (left) and $0\nu\beta\beta$ -decay (right). Bottom: $0_{\text{g.s.}}^+ \rightarrow 0_1^+$ transitions via $2\nu\beta\beta$ -decay (left) and $0\nu\beta\beta$ -decay (right). The grid lines highlight the structure of the detector array consisting of four layers with 4×4 detectors. The counter diagonal elements are empty as they would correspond to coincidences between the same detector numbers.

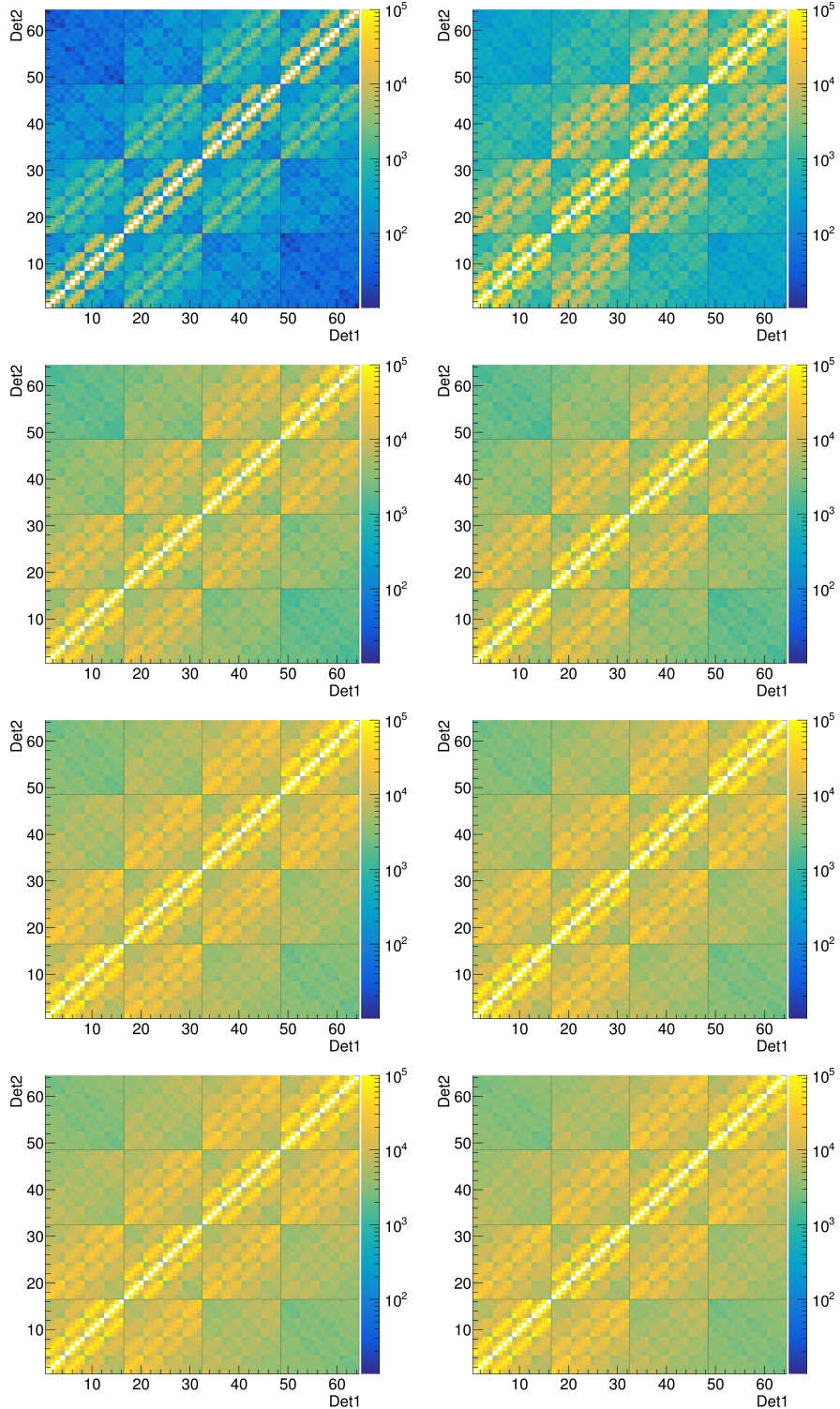


Figure D.24: M2 detector pair distributions for simulated double beta transitions of ^{130}Te with the COBRA demonstrator. Top: $0_{\text{g.s.}}^+ \rightarrow 0_{\text{g.s.}}^+$ transitions via $2\nu\beta\beta$ -decay (left) and $0\nu\beta\beta$ -decay (right). Upper middle: $0_{\text{g.s.}}^+ \rightarrow 2_1^+$ transitions via $2\nu\beta\beta$ -decay (left) and $0\nu\beta\beta$ -decay (right). Lower middle: $0_{\text{g.s.}}^+ \rightarrow 2_2^+$ transitions via $2\nu\beta\beta$ -decay (left) and $0\nu\beta\beta$ -decay (right). Bottom: $0_{\text{g.s.}}^+ \rightarrow 0_1^+$ transitions via $2\nu\beta\beta$ -decay (left) and $0\nu\beta\beta$ -decay (right). The grid lines highlight the structure of the detector array consisting of four layers with 4×4 detectors. The counter diagonal elements are empty as they would correspond to coincidences between the same detector numbers.

D.5.2 Normalized Monte-Carlo spectra

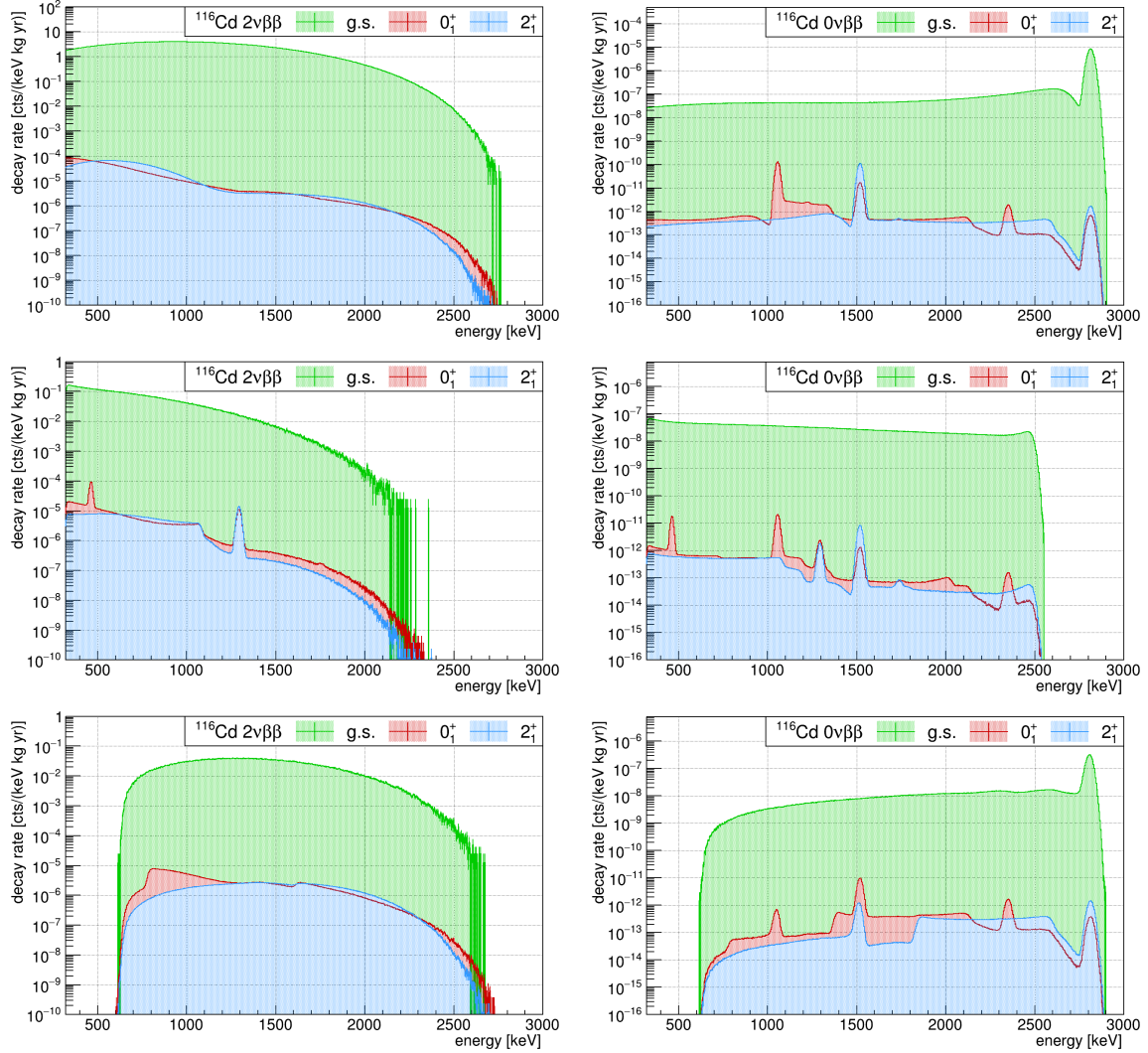


Figure D.25: Comparison of normalized MC spectra for the investigated double beta transitions of ^{116}Cd . *Left:* $2\nu\beta\beta$ -decay modes. *Right:* $0\nu\beta\beta$ -decay modes. The three rows correspond to the M1 spectra (*top*), the M2_s spectra (*middle*) and the M2_Σ spectra (*bottom*). The normalization according to Eqn. (8.54) is based on the predicted half-lives taken from Ref. [PS15] (see Tab. 8.20).

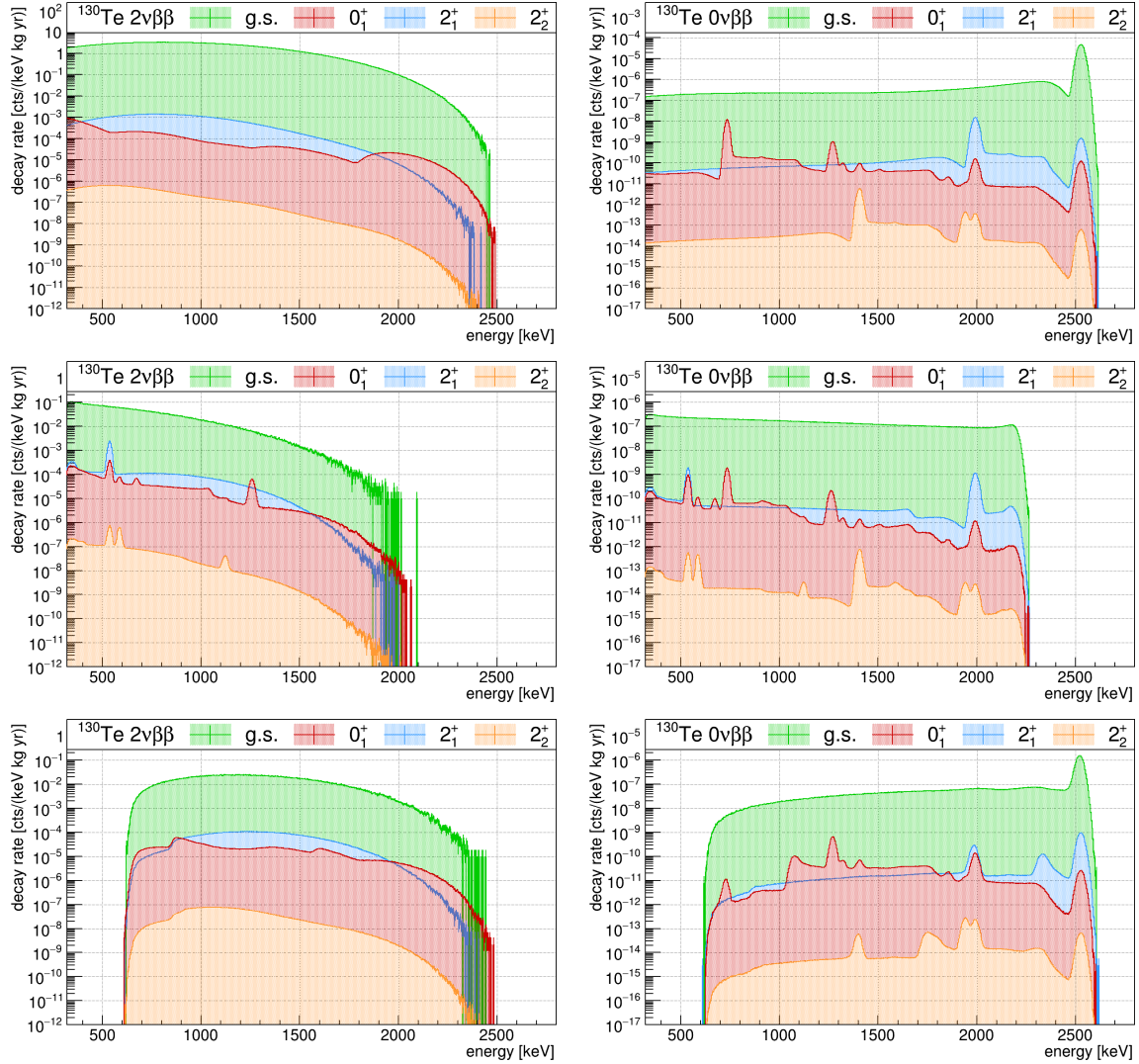


Figure D.26: Comparison of normalized MC spectra for the investigated double beta transitions of ^{130}Te . *Left:* $2\nu\beta\beta$ -decay modes. *Right:* $0\nu\beta\beta$ -decay modes. The three rows correspond to the M1 spectra (*top*), the M2_s spectra (*middle*) and the M2_Σ spectra (*bottom*). The normalization according to Eqn. (8.54) is based on the predicted half-lives taken from Ref. [PS15] (see Tab. 8.20).

D.5.3 Detector pair optimization

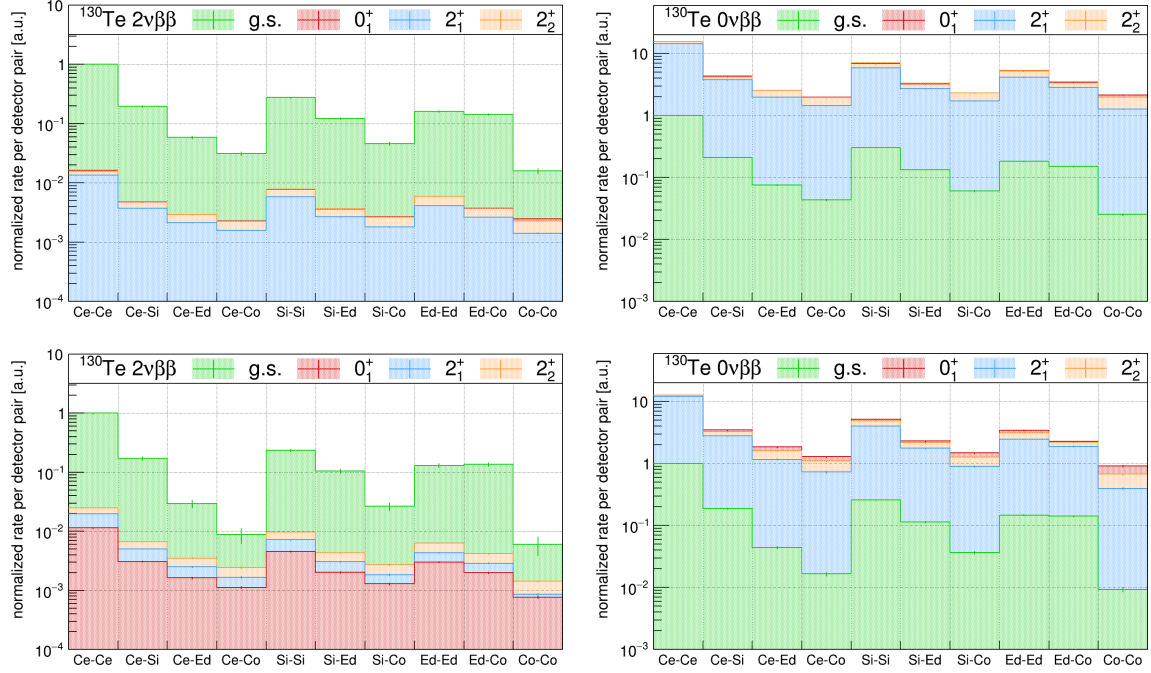


Figure D.27: Distribution of the topological M2 detector pairs for the simulated double beta decay transitions of ^{130}Te with the COBRA demonstrator. *Left:* $2\nu\beta\beta$ -decay modes for all M2 events (*top*) and after applying a threshold of $E_{\text{th}} = 320$ keV on the energy deposition of each detector (*bottom*). *Right:* $0\nu\beta\beta$ -decay modes for the same two cases. It should be noted that the depicted g.s. transitions (green) are the same for all cases and correspond to the $2\nu\beta\beta$ -decay of ^{116}Cd , which is taken as an estimate of the irreducible background. Each decay mode has been scaled with the experimental half-life results listed in Tab. 8.20. In case of the excited state transitions, all decay modes have been scaled with the latest CUORE limits obtained for the 0_1^+ state. Moreover, the Ce-Ce category of the background process is chosen as a fixed reference and set to unity. The other categories have been scaled with respect to this reference. The improvements achieved by introducing a threshold are only marginal. In fact, the ^{116}Cd background process dominates the $2\nu\beta\beta$ -decay modes via excited state transitions for all categories. For the $0\nu\beta\beta$ -decay modes the situation seems to be more beneficial, which is only an artifact of the half-life scaling based on the current experimental sensitivities. Given the latest predictions according to Ref. [PS15] (see also Tab. 8.20), there is at least a deviation of five orders of magnitude with respect to the current experimental sensitivities.

Appendix E

Characterization of LNGS detectors

Table E.1: Compilation of the COBRA demonstrator's L1 detector parameters. The first columns refer to the detector labels according to the LNGS position, the characterization at TUD and the original ID provided by the manufacturer *eV Products*. The next columns contain the specific working point settings: bulk voltage (BV), grid bias (GB) and weighting factor w as well as the obtained relative resolution FWHM at $E_\gamma = 661.6\text{ keV}$ with ^{137}Cs . The detector masses and the amount of the applied encapsulation lacquer have been provided by the manufacturer. If those values were missing in the freight documents, average values of the respective detector batch are used. The depth selection efficiency $\varepsilon_z(^{113}\text{Cd})$ has been determined based on the dedicated ^{113}Cd data-taking run (see section 7.1.2). For the detectors that were non-available in this period, the average of all detectors is quoted. The uncertainty refers to the Poisson statistics of the selected number of events. The full energy detection efficiency ε_{FE} at $E_\gamma = 661.6\text{ keV}$ has been extracted from the characterization measurements at TUD (see section 6.2.2). This efficiency has been corrected by $\varepsilon_z(^{113}\text{Cd})$. The uncertainty is dominated by the uncertainty of the $1/r^2$ fit, but takes also into account the uncertainty on $\varepsilon_z(^{113}\text{Cd})$. The last column contains the total exposure over the entire live time of the COBRA demonstrator and the exposure gained during the ^{113}Cd run.

position	TUD ID	ev ID	BV/GB [V]	w	FWHM	m_{det} [g]	m_{lac} [mg]	$\varepsilon_z(^{113}\text{Cd})$	$\varepsilon_{\text{FE}}(^{137}\text{Cs})$	total/ ^{113}Cd exp. [kg d]
L1-P01	Det44	668004-06	1300/90	0.7961	3.88%	5.9002	12.6	87.52±0.07 ¹	5.67±0.28	11.09 / -
L1-P02	Det48	668007-01	1300/90	0.8746	2.78%	5.8887	15.2	87.52±0.07 ¹	5.48±0.26	11.07 / -
L1-P03	Det37 ²	667615-02	1300/30	0.8734	3.30%	5.8509	20.5	87.52±0.07 ¹	5.42±0.26	- / -
L1-P03	Det72	681165-17	1500/80	0.8342	3.58%	6.2420	16.0	77.45±0.58	6.28±0.31	9.32 / 1.08
L1-P04	Det42	668004-02	1300/90	0.8294	3.60%	5.9063	19.5	87.52±0.07 ¹	5.79±0.29	3.70 / -
L1-P05	Det03	667467-05	900/60	0.9026	2.65%	5.8578	20.0	87.20±0.56	5.32±0.25	13.09 / 1.07
L1-P06	Det10	667470-03	1200/70	0.9530	2.38%	5.8780 ³	15.3	87.01±0.51	5.34±0.25	13.07 / 1.07
L1-P07	Det04	667467-03	1200/80	0.9093	3.21%	5.8330	15.9	86.91±0.46	5.48±0.26	13.03 / 1.07
L1-P08	Det05	667467-04	1200/90	0.8824	2.69%	5.8524	17.8	87.52±0.07 ¹	5.36±0.25	11.72 / -
L1-P09	Det12	668005-01	1200/70	0.8278	2.96%	5.8930	16.6	87.52±0.07 ¹	5.54±0.27	4.54 / -
L1-P10	Det08	668007-05	1100/100	0.8244	2.47%	5.9046	16.2	87.52±0.07 ¹	5.55±0.27	5.84 / -
L1-P11	Det09	667470-02	1100/90	0.9525	2.37%	5.8780 ³	15.3	85.35±0.40	5.57±0.27	10.98 / 1.10
L1-P12	Det06	668006-01	1300/100	0.8363	2.68%	5.9029	18.4	85.09±0.54	5.79±0.29	7.79 / 1.11
L1-P13	Det11	667617-03	1400/50	0.8773	3.69%	5.8607	18.5	88.46±0.42	5.47±0.27	13.14 / 1.05
L1-P14	Det07	668007-02	1300/80	0.8924	2.81%	5.9064	17.1	77.35±0.44	5.94±0.28	12.97 / 0.79
L1-P15	Det13	668005-03	1100/70	0.8613	2.70%	5.8667	17.9	87.33±0.53	5.48±0.26	13.15 / 1.05
L1-P16	Det43	668004-04	1300/90	0.8301	3.46%	5.9053	17.4	87.52±0.07 ¹	5.74±0.29	10.69 / -
average of layer		3.33%	5.9048	16.9	85.92±0.31	5.61±0.27			10.32 / 1.04	

¹ average value due to absence of detector in dedicated ^{113}Cd run

² exchange of detector units during the LNGS on-site shift in Oct.'13

³ average mass of the same detector batch with an uncertainty of about 0.022 g due to missing information in original freight documents

Table E.2: Compilation of the COBRA demonstrator’s L2 detector parameters. The first columns refer to the detector labels according to the LNGS position, the characterization at TUD and the original ID provided by the manufacturer *eV Products*. The next columns contain the specific working point settings: bulk voltage (BV), grid bias (GB) and weighting factor w as well as the obtained relative resolution FWHM at $E_\gamma = 661.6$ keV with ^{137}Cs . The detector masses and the amount of the applied encapsulation lacquer have been provided by the manufacturer. If those values were missing in the freight documents, average values of the respective detector batch are used. The depth selection efficiency $\varepsilon_z(^{113}\text{Cd})$ has been determined based on the dedicated ^{113}Cd data-taking run (see section 7.1.2). For the detectors that were non-available in this period, the average of all detectors is quoted. The uncertainty refers to the Poisson statistics of the selected number of events. The full energy detection efficiency ε_{FE} at $E_\gamma = 661.6$ keV has been extracted from the characterization measurements at TUD (see section 6.2.2). This efficiency has been corrected by $\varepsilon_z(^{113}\text{Cd})$. The uncertainty is dominated by the uncertainty of the $1/r^2$ fit, but takes also into account the uncertainty on $\varepsilon_z(^{113}\text{Cd})$. The last column contains the total exposure over the entire live time of the COBRA demonstrator and the exposure gained during the ^{113}Cd run.

position	TUD ID	eV ID	BV/GB [V]	w	FWHM	m_{det} [g]	m_{lac} [mg]	$\varepsilon_z(^{113}\text{Cd})$	$\varepsilon_{\text{FE}}(^{137}\text{Cs})$	total/ ^{113}Cd exp. [kg d]
L2-P01	Det38	667617-02	1100/50	0.8611	3.50%	5.8690	20.5	87.52 ± 0.07^1	5.32 ± 0.25	10.86 / -
L2-P02	Det46	668005-05	1300/90	0.7880	2.56%	5.8738	20.1	88.91 ± 0.55	5.25 ± 0.25	12.23 / 1.10
L2-P03	Det36	667470-01	1500/90	0.9137	2.76%	5.8780 ³	15.3	87.55 ± 0.50	5.24 ± 0.24	12.24 / 1.10
L2-P04	Det45	668005-02	1300/70	0.8114	3.11%	5.8771	16.0	87.99 ± 0.51	5.44 ± 0.26	12.13 / 1.10
L2-P05	Det44	668005-04	1100/50	0.8097	2.73%	5.8664	18.6	89.36 ± 0.52	4.98 ± 0.22	12.08 / 1.10
L2-P06	Det33	667467-02	1000/70	0.9041	2.44%	5.8536	17.0	88.34 ± 0.55	5.33 ± 0.25	12.05 / 1.10
L2-P07	Det47	668005-06	1200/70	0.8348	2.70%	5.9046	17.4	88.33 ± 0.50	5.14 ± 0.23	10.18 / 1.10
L2-P08	Det51 ²	631937-03	1200/80	0.6456	5.44%	6.4590	28.0	87.52 ± 0.07^1	4.41 ± 0.17	- / -
L2-P08	Det108	682872-05	1500/60	0.8200	3.27%	5.7240	10.0	89.13 ± 0.56	5.24 ± 0.25	12.11 / 1.07
L2-P09	Det40	667989-02	1150/60	0.8518	2.54%	5.8780 ³	15.3	88.78 ± 0.56	5.54 ± 0.28	11.51 / 1.10
L2-P10	Det35	667468-02	1100/70	0.8907	2.54%	5.8780 ³	15.3	88.52 ± 0.51	5.41 ± 0.26	12.15 / 1.10
L2-P11	Det34	667468-01	1300/80	0.9161	2.27%	5.8780 ³	15.3	88.38 ± 0.54	5.17 ± 0.24	12.15 / 1.10
L2-P12	Det50	632083-02	1100/80	0.6378	4.96%	6.5290	21.0	87.52 ± 0.07^1	5.05 ± 0.22	8.74 / -
L2-P13	Det41	667989-03	1200/70	0.7984	3.65%	5.8780 ³	15.3	88.88 ± 0.55	5.50 ± 0.27	12.25 / 1.10
L2-P14	Det01	667615-04	1000/40	0.8945	3.10%	5.8597	19.4	88.56 ± 0.56	5.30 ± 0.25	12.21 / 1.10
L2-P15	Det39	667989-01	1300/110	0.8583	2.86%	5.8853	17.9	87.52 ± 0.07^1	5.02 ± 0.22	8.78 / -
L2-P16	Det02	667467-01	1200/110	0.7886	3.62%	5.8669	17.4	87.52 ± 0.07^1	5.04 ± 0.22	4.91 / -
average of layer		3.18%	5.9062	17.0	88.31 ± 0.42	5.25	± 0.25		11.04 / 1.10	

Table E.3: Compilation of the COBRA demonstrator's L3 detector parameters. The first columns refer to the detector labels according to the LNGS position, the characterization at TUD and the original ID provided by the manufacturer *eV Products*. The next columns contain the specific working point settings: bulk voltage (BV), grid bias (GB) and weighting factor w as well as the obtained relative resolution FWHM at $E_\gamma = 661.6\text{ keV}$ with ^{137}Cs . The detector masses and the amount of the applied encapsulation lacquer have been provided by the manufacturer. If those values were missing in the freight documents, average values of the respective detector batch are used. The depth selection efficiency $\varepsilon_z(^{113}\text{Cd})$ has been determined based on the dedicated ^{113}Cd data-taking run (see section 7.1.2). For the detectors that were non-available in this period, the average of all detectors is quoted. The uncertainty refers to the Poisson statistics of the selected number of events. The full energy detection efficiency ε_{FE} at $E_\gamma = 661.6\text{ keV}$ has been extracted from the characterization measurements at TUD (see section 6.2.2). This efficiency has been corrected by $\varepsilon_z(^{113}\text{Cd})$. The uncertainty is dominated by the uncertainty of the $1/\eta^2$ fit, but takes also into account the uncertainty on $\varepsilon_z(^{113}\text{Cd})$. The last column contains the total exposure over the entire live time of the COBRA demonstrator and the exposure gained during the ^{113}Cd run.

position	TUD ID	eV ID	BV/GB [V]	w	FWHM	m_{det} [g]	m_{lac} [mg]	$\varepsilon_z(^{113}\text{Cd})$	$\varepsilon_{\text{FE}}(^{137}\text{Cs})$	total/ ^{113}Cd exp. [kg d]
L3-P01	Det64	681165-09	1000/50	0.7094	3.23%	6.241	15.0	87.52±0.07 ¹	5.72±0.29	8.35 / -
L3-P02	Det74	681165-19	1200/40	0.8249	2.89%	6.133	16.0	85.45±0.44	5.56±0.27	9.62 / 1.20
L3-P03	Det75	681165-20	1500/90	0.7970	3.06%	6.232	16.0	87.47±0.39	4.96±0.22	10.79 / 1.22
L3-P04	Det66	681165-11	1100/40	0.7404	3.12%	6.195	15.0	87.52±0.07 ¹	5.63±0.28	3.14 / -
L3-P05	Det65	681165-10	1500/100	0.7621	2.77%	6.275	17.0	88.71±0.39	4.86±0.21	10.19 / 1.21
L3-P06	Det67	681165-12	1400/80	0.7520	2.65%	6.226	17.0	88.44±0.42	4.90±0.21	8.18 / 1.20
L3-P07	Det71	681165-16	1500/90	0.8097	2.27%	6.253	15.0	89.07±0.47	4.87±0.21	8.22 / 1.21
L3-P08	Det69	681165-14	1400/110	0.7409	2.67%	6.243	15.0	86.25±0.56	4.99±0.23	9.58 / 1.20
L3-P09	Det60	681165-05	1500/70	0.7483	2.77%	6.251	19.0	90.27±0.52	5.48±0.26	9.35 / 1.21
L3-P10	Det57	681165-02	1500/80	0.7794	2.66%	6.204	16.0	87.52±0.07 ¹	5.43±0.26	8.89 / -
L3-P11	Det62	681165-07	1400/100	0.7385	2.52%	6.262	17.0	87.92±0.52	4.97±0.22	8.18 / 1.21
L3-P12	Det73	681165-18	1400/80	0.7395	2.70%	6.314	15.0	88.50±0.41	5.12±0.23	10.67 / 1.22
L3-P13	Det63	681165-08	1300/50	0.7777	3.28%	6.226	18.0	86.34±0.57	5.83±0.30	8.45 / 1.20
L3-P14	Det56	681165-01	1500/100	0.7109	2.86%	6.206	18.0	89.20±0.44	4.91±0.22	8.18 / 1.20
L3-P15	Det59	681165-04	1100/40	0.7478	3.04%	6.262	17.0	87.06±0.54	5.82±0.30	9.06 / 1.21
L3-P16	Det58	681165-03	1300/50	0.8035	3.11%	6.222	17.0	87.52±0.07 ¹	5.45±0.26	3.35 / -
average of layer		2.85%	6.2341	16.4	87.80±0.37	5.26±0.25	8.39 / 1.21			

Table E.4: Compilation of the COBRA demonstrator’s L4 detector parameters. The first columns refer to the detector labels according to the LNGS position, the characterization at TUD and the original ID provided by the manufacturer *eV Products*. The next columns contain the specific working point settings: bulk voltage (BV), grid bias (GB) and weighting factor w as well as the obtained relative resolution FWHM at $E_\gamma = 661.6$ keV with ^{137}Cs . The detector masses and the amount of the applied encapsulation lacquer have been provided by the manufacturer. If those values were missing in the freight documents, average values of the respective detector batch are used. The depth selection efficiency $\varepsilon_z(^{113}\text{Cd})$ has been determined based on the dedicated ^{113}Cd data-taking run (see section 7.1.2). For the detectors that were non-available in this period, the average of all detectors is quoted. The uncertainty refers to the Poisson statistics of the selected number of events. The full energy detection efficiency ε_{FE} at $E_\gamma = 661.6$ keV has been extracted from the characterization measurements at TUD (see section 6.2.2). This efficiency has been corrected by $\varepsilon_z(^{113}\text{Cd})$. The uncertainty is dominated by the uncertainty of the $1/r^2$ fit, but takes also into account the uncertainty on $\varepsilon_z(^{113}\text{Cd})$. The last column contains the total exposure over the entire live time of the COBRA demonstrator and the exposure gained during the ^{113}Cd run.

position	TUD ID	eV ID	BV/GB [V]	w	FWHM	m_{det} [g]	m_{ac} [mg]	$\varepsilon_z(^{113}\text{Cd})$	$\varepsilon_{\text{FE}}(^{137}\text{Cs})$	total/ ^{113}Cd exp. [kg d]
L4-P01	Det99	682871-02	1500/50	0.8247	3.11%	5.679	14.0	87.52 ± 0.07^1	5.38 ± 0.25	4.26 / -
L4-P02	Det112	682873-02	1100/40	0.9266	2.01%	5.711	12.0	86.57 ± 0.41	4.77 ± 0.20	8.31 / 1.11
L4-P03	Det104	682872-01	1300/60	0.9086	2.04%	5.673	11.0	87.52 ± 0.07^1	4.63 ± 0.19	6.23 / -
L4-P04	Det115	682873-07	1200/80	0.8990	2.19%	5.630	12.0	85.81 ± 0.43	4.15 ± 0.15	7.03 / 1.10
L4-P05	Det110	682872-07	1500/90	0.7974	2.58%	5.755	11.0	91.35 ± 0.43	3.19 ± 0.09	9.49 / 1.12
L4-P06	Det114	682873-04	1200/40	0.9342	1.86%	5.682	11.0	86.49 ± 0.40	5.01 ± 0.22	8.88 / 1.10
L4-P07	Det96	668364-03	1100/60	0.8956	1.71%	5.882	9.0	86.72 ± 0.41	5.01 ± 0.22	9.19 / 1.14
L4-P08	Det97	682046-02	1400/60	0.8736	2.23%	5.982	10.0	88.25 ± 0.43	3.47 ± 0.11	8.10 / 1.16
L4-P09	Det100	682871-03	1500/50	0.8083	2.57%	5.740	11.0	89.02 ± 0.43	4.11 ± 0.15	8.61 / 1.10
L4-P10	Det107	682872-04	1200/40	0.8994	1.89%	5.756	11.0	89.06 ± 0.43	4.99 ± 0.22	9.10 / 1.10
L4-P11	Det105	682872-02	1200/60	0.8961	1.99%	5.694	11.0	87.52 ± 0.07^1	4.45 ± 0.17	6.47 / -
L4-P12	Det98	682871-01	1500/40	0.8819	2.18%	5.680	14.0	85.25 ± 0.91	4.99 ± 0.22	8.19 / 0.29
L4-P13	Det113	682873-03	1500/50	0.8593	2.51%	5.708	10.0	89.07 ± 0.48	4.12 ± 0.15	9.34 / 1.10
L4-P14	Det101	682871-05	1100/50	0.7830	2.13%	5.674	11.0	88.73 ± 0.55	4.95 ± 0.22	8.08 / 1.10
L4-P15	Det109	682872-06	1500/60	0.8228	2.88%	5.720	11.0	87.52 ± 0.07^1	4.75 ± 0.20	7.95 / -
L4-P16	Det106	682872-03	1100/50	0.7987	3.22%	5.750	11.0	87.97 ± 0.65	4.74 ± 0.20	9.00 / 1.11
average of layer			2.32%	5.7323	11.3			87.77 ± 0.39	4.54 ± 0.19	8.01 / 1.05

List of Figures

1.1	Fundamental vertex in lowest order QED.	2
1.2	Feynman rules of the QED.	3
1.3	Concept of the Standard Model of particle physics.	4
1.4	Overview of the particle content of the Standard Model.	6
1.5	Illustration of the connection between the Bethe-Weizsäcker mass formula and the droplet model of atomic nuclei.	9
1.6	Illustration of the binding energy per nucleon for a schematic representation of the chart of nuclei.	10
1.7	Feynman diagrams illustrating the three common forms of nuclear β -decay.	12
1.8	Attenuation of γ -rays in CZT based on the NIST database for photon cross sections.	14
1.9	Illustration of the energy loss of electrons and positrons in lead.	16
1.10	Illustration of the muon stopping power in copper as a function of the momentum.	17
2.1	Illustration of the two possible neutrino mass orderings resulting from the three flavor PMNS parametrization.	25
2.2	Interplay of different neutrino mass observables.	34
3.1	Feynman diagrams of double beta transitions with two electrons in the final state.	36
3.2	Expected experimental signatures of the double beta decay modes of ^{116}Cd	37
3.3	Illustration of the mass parabolas according to the Bethe-Weizsäcker mass formula for atomic nuclei with $A = 116$	39
3.4	Illustration of the Schechter-Valle theorem as Feynman diagram.	40
3.5	Comparison of nuclear matrix elements, Q -values and natural isotopic abundance for the most promising $0\nu\beta\beta$ -decay candidates.	42
4.1	Schematic drawing for the three most common CZT detector types.	54
4.2	Working principle of planar electrode CZT detectors.	55
4.3	Working principle of CPG-CZT detectors.	56
4.4	Comparison of underground laboratories around the world.	61
4.5	Schematic map of the LNGS underground complex.	61
4.6	Schematic drawing of the COBRA demonstrator setup at the LNGS.	63
4.7	Schematic side view of a 4×4 CPG-CZT detector holder.	63
4.8	Block scheme of COBRA's DAQ chain.	64

4.9	Working principle of differential signaling.	65
4.10	Illustration of the XDEM shielding components.	67
4.11	Projected half-life sensitivity of a large-scale COBRA experiment.	68
4.12	Design proposal for a potential King-COBRA large-scale experiment.	68
5.1	Schematic electrode layout of the CPG-CZT detectors deployed in the COBRA demonstrator.	70
5.2	Illustration of the projected weighting potentials for the raw signals of the CA and NCA and the corresponding difference signal in the bulk region of a CPG-CZT detector.	71
5.3	Impressions of the weighting factor optimization using laboratory data of a single CPG-CZT detector for a calibration with ^{137}Cs	72
5.4	Block scheme of the signal processing with MAnTiCORE.	74
5.5	Characteristics of the analytic event reconstruction for CPG-CZT detectors.	79
5.6	Visualization of the GDML implementation of the COBRA demonstrator.	83
6.1	Overview of monolithic CPG-CZT detector designs investigated by the COBRA collaboration.	86
6.2	Overview of the CPG-CZT detector concept of the COBRA demonstrator.	87
6.3	Overview of the qCPG-CZT detector concept for the COBRA XDEM upgrade.	88
6.4	Illustration of the working point determination for a CPG-CZT detector using ^{137}Cs	90
6.5	Results of the working point determination measurements for a 6 cm^3 prototype qCPG-CZT detector.	91
6.6	Results of the working point determination measurements for the 6 cm^3 sCPG-CZT detector.	92
6.7	Determination of the absolute full-energy efficiency for homogeneous ^{137}Cs irradiation measurements at different distances.	94
6.8	Exemplary results of the two-dimensional γ -ray scanning of a side wall of a 1 cm^3 CPG-CZT detector.	97
6.9	Localized ^{137}Cs γ -ray scanning of one side of a qCPG-CZT prototype detector.	98
6.10	Distribution of multi-sector FEP events for a localized ^{137}Cs γ -ray scanning of one side of a qCPG-CZT prototype detector.	98
6.11	Quantitative validation of the depth reconstruction for different kinds of CPG-CZT detectors.	99
7.1	Typical pulse-shape of a single-site interaction.	102
7.2	Effect of the data-cleaning steps with respect to the combined energy spectrum for a special trigger run of the COBRA demonstrator at the LNGS.	104
7.3	Crosscheck of the data-cleaning cuts based on the combination of several calibration runs of the COBRA demonstrator using the radionuclide ^{228}Th	105
7.4	Distribution of the interaction depth above the ^{113}Cd energy region for the total exposure of the COBRA demonstrator.	106
7.5	Distribution of the interaction depth in the ^{113}Cd energy range based on the data of the COBRA demonstrator.	107
7.6	Illustration of the difference signal's weighting potential.	108
7.7	Typical example pulse-shapes for lateral surface events as found in calibration measurements of the COBRA demonstrator.	109
7.8	Typical example pulse-shapes for single-site and multi-site interactions as found in calibration measurements of the COBRA demonstrator.	110

7.9	Example of the derivative definition applied in the PSA method to identify multi-site interactions.	112
7.10	Illustration of the kinematics involving pair production via γ -ray interactions inside CZT	114
7.11	Laboratory measurement of the energy spectrum of a natural ^{232}Th sample by a CPG-CZT detector.	116
7.12	Results of the sensitivity optimization for the PSA method.	117
7.13	Results of the A/E optimization based on the combined data of a single ^{228}Th calibration measurement of the COBRA demonstrator.	118
7.14	Energy dependency of the MSE fraction based on the optimized PSA approach and a single detector laboratory measurement using a natural ^{232}Th sample.	119
7.15	Distribution of the A/E criterion for a single detector laboratory measurement using a natural ^{232}Th sample.	120
7.16	Application of the inverted PSA method to enhance the intensity of weak γ -lines in a single detector laboratory measurement using a natural ^{232}Th sample.	121
7.17	Illustration of the energy dependence of the A/E parameter based on a single detector laboratory measurement using a natural ^{232}Th sample.	122
7.18	Comparison of the optimized A/E cut values before and after a calibration of the A/E parameter based on DEP events.	123
7.19	Schematic drawing of the Compton scattering setup developed at TUD.	125
7.20	Illustration of the goniometer device developed for the Compton scattering setup at TUD.	126
7.21	Characteristics of the ^{60}Co β -decay via the first excited states of ^{60}Ni and the involved de-excitation γ -rays.	127
7.22	Illustration of the angular dependency of the Compton kinematics and the differential cross section.	128
7.23	Coincident energy spectra for various scattering angles ϑ using the Compton scatter setup with a pre-collimated ^{137}Cs γ -ray source.	129
7.24	Examples of the two-dimensional representation of the coincident energy spectra obtained by the Compton scattering experiment.	131
7.25	Illustration of some examples of the created SSE pulse-shape library based on the Compton coincidence technique.	132
7.26	Feynman diagrams of the production of charged pions π^\pm in deep inelastic proton interactions induced by primary cosmic rays	135
7.27	Feynman diagrams of the weak decay of muons into the lightest charged leptons and the corresponding neutrinos.	136
7.28	Effect of the FADC saturation of the raw CPG detector signals CA and NCA with respect to the reconstruction of the energy and interaction depth.	138
7.29	Illustration of the classification of expected muon-induced interactions for the example of a single CPG-CZT detector as used for the COBRA demonstrator array.	139
7.30	Estimate of the cosmic muon flux using laboratory long-term background measurements with different CZT detector types.	144
7.31	Illustration of the analytic muon reconstruction model for long-term laboratory background measurements using 1 cm^3 CPG-CZT detectors.	145
7.32	Illustration of the analytic muon reconstruction model for long-term laboratory background measurements using two different 6 cm^3 CPG-CZT detectors.	146
7.33	Determination of the hole shift $s(z_\mu)$ for vertically incoming muons using laboratory background measurements with different CZT detector types.	151

8.1	Exemplary results of an energy calibration of the COBRA demonstrator	157
8.2	Examples of energy calibrated single detector spectra.	157
8.3	Exposure accumulation for the COBRA demonstrator at the LNGS.	159
8.4	Illustration of prominent background features identified for the COBRA demonstrator during its operation at the LNGS	161
8.5	Multi-dimensional illustration of the full data set accumulated with the COBRA demonstrator.	163
8.6	Effect of consecutively applied event selections on the combined energy spectrum obtained with the COBRA demonstrator at the LNGS.	164
8.7	Example detector spectra with a clear indication for a localized ^{22}Na contamination of the COBRA demonstrator setup.	168
8.8	Comparison of the inverted $(A/E)_{90\%}$ selection and the MSE flagging algorithm to enhance weak γ -lines in the combined spectrum of the COBRA demonstrator.	168
8.9	Suppression of α -contaminants for the COBRA demonstrator.	171
8.10	Illustration of the analytic muon model with respect to the physics data obtained by the COBRA demonstrator at the LNGS.	172
8.11	Nuclear model predictions for the ^{113}Cd spectrum-shape dependence on the effective value of the axial-vector coupling g_A	176
8.12	Shortcomings and details of the present nuclear model calculations.	177
8.13	Results of the COBRA demonstrator's stability study.	179
8.14	Example of a single detector ^{113}Cd spectrum used in the COBRA demonstrator's stability study.	180
8.15	Comparison of ^{113}Cd spectra based on the shape factors as determined with previous CdW ₀₄ experiments.	180
8.16	Evolution of the average threshold of the four layers of the COBRA demonstrator.	181
8.17	Temperature surveillance of the COBRA demonstrator prior and during the dedicated ^{113}Cd run.	184
8.18	Variation of the individual detector thresholds by the end of the dedicated ^{113}Cd run.	186
8.19	Example of an energy resolution fit to extract $\text{FWHM}(E)$ for one detector.	188
8.20	Results of the low-energy background characterization.	198
8.21	Compilation of spline examples for a constant energy slice of the original set of ^{113}Cd templates.	203
8.22	Threshold dependence of the template normalization exemplarily shown for the ISM.	204
8.23	Simulated detector response matrix for an average-sized CZT detector	206
8.24	Comparison of the simulated detector response function $\varepsilon_{\text{det}}(E)$ and the intrinsic full-energy detection efficiency $\varepsilon_{\text{int}}(E)$	207
8.25	Example of a COBRA single detector spectrum compared to a set of five interpolated ^{113}Cd templates.	210
8.26	Example $\chi^2_{\text{red}}(g_A)$ curves of the spectrum-shape comparison for one COBRA single detector spectrum and the interpolated templates	211
8.27	Distribution of the 45 best match g_A values for the ISM, MQPM and IBFM-2.	214
8.28	Distribution of the minimum χ^2_{red} values of the 45 best match g_A values for the single detector spectrum-shape comparison.	214
8.29	Allowed spectrum range for the ^{113}Cd β -decay according to the spectrum-shape results	216

8.30	Distribution of the 44 best match g_A values for the ISM, MQPM and IBFM-2 under the CVC hypothesis.	221
8.31	Example $\chi^2_{\text{red}}(g_A)$ curves of the spectrum-shape comparison for one COBRA single detector spectrum and the interpolated templates under the CVC hypothesis.	222
8.32	Distribution of the minimum χ^2_{red} values of the best match g_A values for the single detector spectrum-shape comparison under the CVC hypothesis.	223
8.33	Allowed spectrum range for the ^{113}Cd β -decay according to the spectrum-shape results under the CVC hypothesis.	225
8.34	Conversion of the experimental results $\bar{g}_A^{\text{cvc}} \pm \bar{\sigma}_{\text{sys}}^{\text{cvc}}$ into the corresponding half-life range following the SSM prediction under the improved CVC hypothesis.	227
8.35	Comparison of experimentally determined half-lives for the $2\nu\beta\beta$ -decay of ^{116}Cd	231
8.36	Evolution of the observed data rate for the COBRA demonstrator over the lifetime of the experiment.	233
8.37	Combined effect of the data partitioning and the PSD event selection on the z -versus- E display of the physics data of the COBRA demonstrator.	235
8.38	Comparison of the combined COBRA demonstrator data and the MC prediction for the $2\nu\beta\beta$ -decay of ^{116}Cd	237
8.39	Comparison of the combined energy spectrum of the COBRA demonstrator and its four detector layers with respect to the α -decay of ^{190}Pt	242
8.40	Normalized MC spectra of the ^{190}Pt α -decay for different thicknesses of the platinum layer using the COBRA demonstrator geometry.	244
8.41	Effect of a Gaussian energy smearing for two example simulations of the ^{190}Pt α -decay for different platinum thicknesses.	245
8.42	Results of the χ^2 test procedure to determine the best match MC spectra with respect to the average thickness of the CZT detectors' Pt-layer.	247
8.43	Comparison of the combined data of the COBRA demonstrator and the MC spectrum corresponding to the best match of the χ^2 test.	248
8.44	Decay schemes of the double beta transitions of ^{116}Cd and ^{130}Te via potential excited states.	255
8.45	Multiplicity distribution for double beta decay transitions of ^{116}Cd simulated for the COBRA demonstrator.	258
8.46	Multiplicity distribution for double beta decay transitions of ^{130}Te simulated for the COBRA demonstrator.	259
8.47	Examples of the M2 detector pair distribution for simulated double beta transitions of ^{116}Cd with the COBRA demonstrator.	260
8.48	Comparison of the M2 detector pair distribution for the $0\nu\beta\beta$ -decay of ^{116}Cd via the 2_1^+ state of ^{116}Sn	261
8.49	Effect of a Gaussian energy smearing onto the VENOM simulations of several double beta decay processes.	262
8.50	Representation of coincident energy spectra of M2 events for double beta transitions of ^{116}Cd	263
8.51	Representation of coincident energy spectra of M2 events for double beta transitions of ^{130}Te	264
8.52	Comparison of normalized MC spectra for the investigated double beta transitions of ^{116}Cd	265
8.53	Comparison of normalized MC spectra for the investigated double beta transitions of ^{130}Te	267

8.54	Examples for the selection of excited state signatures for $2\nu\beta\beta$ -decays of ^{116}Cd based on the $M2_s$ spectra.	269
8.55	Examples for the selection of excited state signatures for $0\nu\beta\beta$ -decays of ^{116}Cd based on the $M2_s$ and $M2_\Sigma$ spectra.	270
8.56	Effect of the excited states' event selections with respect to the M2 detector pair distribution for two examples of the simulated $2\nu\beta\beta$ -decay transitions of ^{116}Cd	274
8.57	Illustration of the topological detector classifications based on their position in the COBRA demonstrator.	275
8.58	Distribution of the topological M2 detector pairs for the simulated double beta decay transitions of ^{116}Cd with the COBRA demonstrator.	277
8.59	Distribution of the topological M2 detector pairs for the $2\nu\beta\beta$ -decay modes of ^{116}Cd using the ROI restrictions based on the excited states' γ -lines	278
8.60	M2 detector pair distributions for the simulated $2\nu\beta\beta$ -decay modes of ^{116}Cd under the ROI energy restrictions and the optimized detector pair selection no-NN.	279
8.61	Updated analysis examples for the selection of the $2\nu\beta\beta$ -decay excited state signatures of ^{116}Cd	281
8.62	Projected half-life sensitivity of COBRA XDEM for the $0\nu\beta\beta$ -decay of ^{116}Cd	287
A.1	Overview of the COBRA demonstrator setup at the LNGS.	291
A.2	Inner parts of the COBRA demonstrator array.	291
A.3	Evolution of the detector layer concept.	292
A.4	Impressions of the COBRA XDEM installation.	292
A.5	Overview of the detector arrangement and numbering scheme for the COBRA demonstrator and the XDEM layer.	293
B.1	Experimental apparatus for the localized γ -ray irradiation measurements.	294
B.2	Overview of the long-term background measurement setup.	294
B.3	Overview of the Compton scattering experiment's shielding and electronics.	295
B.4	Details of the CPG-CZT detector setup of the Compton scattering experiment.	295
C.1	Example for a central and one-sided confidence interval for a normalized Gaussian distribution.	297
C.2	Example for the application of Bayes' theorem in Bayesian statistics.	298
D.1	Illustration of the definitions of the LSE identification quantities.	299
D.2	Distribution of the LSE identification quantities for γ -ray interactions.	299
D.3	Illustration of the definition of the A/E parameter.	300
D.4	Comparison of different A/E definitions and the influence of the smoothing window size in the construction of the current pulse.	300
D.5	Typical pulse-shape examples of muon-induced events.	301
D.6	Derivatives of the difference pulse for muon-induced events.	301
D.7	Results of a detector simulation for a traversing muon with a highly non-vertical incident angle for a 1 cm^3 CPG-CZT detector.	302
D.8	Illustration of the natural decay chains (adapted from [Tan16], originally referring to [Wikd]). The fourth series related to ^{237}Np is already extinct on Earth, which is why it does not play a role in low-background experiments and the search for rare events.	303
D.9	Correlation of the COBRA demonstrator's total count rate and the relative humidity.	303

D.10	Results of the working point measurements for sector 1 of a qCPG-CZT prototype detector.	306
D.11	Results of the working point measurements for sector 2 of a qCPG-CZT prototype detector.	306
D.12	Results of the working point measurements for sector 3 of a qCPG-CZT prototype detector.	307
D.13	Results of the working point measurements for sector 4 of a qCPG-CZT prototype detector.	307
D.14	Example case to illustrate the ability of expressing a model preference based on the run method.	308
D.15	Compilation of the experimental ^{113}Cd spectra measured with (Det3 – Det15) of the COBRA demonstrator.	309
D.16	Compilation of the experimental ^{113}Cd spectra measured with (Det18 – Det26) of the COBRA demonstrator.	310
D.17	Compilation of the experimental ^{113}Cd spectra measured with (Det27– Det40) of the COBRA demonstrator.	310
D.18	Compilation of the experimental ^{113}Cd spectra measured with (Det41 – Det53) of the COBRA demonstrator.	311
D.19	Compilation of the experimental ^{113}Cd spectra measured with (Det54 – Det64) of the COBRA demonstrator.	311
D.20	Compilation of examples for the ^{113}Cd depth distribution.	312
D.21	Analytic models for the low-energy background description of the ^{113}Cd energy range.	313
D.22	Nuclear model predictions for the ^{113}Cd spectrum-shape dependence on g_A under the CVC hypothesis.	314
D.23	M2 detector pair distributions for simulated double beta transitions of ^{116}Cd with the COBRA demonstrator.	315
D.24	M2 detector pair distributions for simulated double beta transitions of ^{130}Te with the COBRA demonstrator.	316
D.25	Comparison of normalized MC spectra for the investigated double beta transitions of ^{116}Cd	317
D.26	Comparison of normalized MC spectra for the investigated double beta transitions of ^{130}Te	318
D.27	Distribution of the topological M2 detector pairs for the simulated double beta decay transitions of ^{130}Te with the COBRA demonstrator.	319

List of Tables

1.1	Summary of the particle content of the SM.	7
1.2	Explanation of the terms contained in the semi-empirical Bethe-Weizsäcker mass formula and their origin in the droplet model of atomic nuclei.	10
1.3	Classification of nuclear β -decays.	12
2.1	Timeline of important experimental milestones with respect to the role of neutrinos within the SM.	22
2.2	Summary of the PMNS parameters as determined in a global analysis of the available neutrino oscillation data.	25
2.3	Comparison of the neutrino mass observables in cosmology, β -decay investigations and the search for the hypothesized $0\nu\beta\beta$ -decay.	34
3.1	Overview of recently applied experimental techniques and their associated advantages and challenges.	46
3.2	Compilation of experimental results of the most recent double beta decay surveys.	48
4.1	Properties of CZT compared to other well known semiconductor materials. . . .	50
4.2	Molar masses of CZT compound elements.	52
4.3	CZT impurities as reported by <i>Redlen Technologies</i> using ICP-MS on material samples from a spent solvent.	52
4.4	List of nuclides contained in CZT that are known for rare nuclear transitions. . .	59
6.1	Summary of the pre-selection results for the entire two-dimensional scanning data recorded in the course of the characterization of the COBRA demonstrator detectors.	96
7.1	Overview of MAnTiCORE's data-cleaning conditions.	103
7.2	Deduced efficiencies of the physical volume selection via different z -cut definitions based on the intrinsic ^{113}Cd β -decay.	108
7.3	Summary of the PSA and the A/E optimization results.	118
7.4	Summary of the data-taking with the Compton scattering experiment at TUD. .	128
7.5	List of the expected energy depositions corresponding to an applied scattering angle ϑ and its angular acceptance of the two-detector-system.	130
7.6	Estimate of the expected mean energy loss of minimum-ionizing muons in CZT based on the Bethe-Bloch formula.	136
7.7	Overview of long-term laboratory background measurements performed with different CPG-CZT detectors to study muon-induced interactions.	142

7.8	Determination of the hole shift $s(z_\mu)$ for vertically incoming muon using laboratory background measurements with different CZT detector types.	151
8.1	Short description of LNGS calibration parameters.	156
8.2	Summary of the physics data-taking with the COBRA demonstrator at the LNGS.	160
8.3	Overview of identified or expected γ -lines for the combined spectrum of the COBRA demonstrator and each of its detector layers.	167
8.4	Overview of identified α -decays as background for the COBRA demonstrator.	169
8.5	Compilation of previous studies on ^{113}Cd	177
8.6	List of γ -lines used for the energy calibration of the COBRA demonstrator in the ^{113}Cd run.	186
8.7	Summary of the detector pool selection for the ^{113}Cd spectrum-shape analysis	192
8.8	List of material impurities considered for the low-energy background modeling.	194
8.9	Conversion factors from ppb to mBq/kg.	196
8.10	List of simulated material impurities from inner- to outermost.	199
8.11	List of systematic uncertainties considered in the ^{113}Cd spectrum-shape analysis.	217
8.12	List of systematic uncertainties considered in the preliminary ^{113}Cd spectrum-shape analysis based on the CVC update.	224
8.13	Overview of previous experiments to determine the $2\nu\beta\beta$ -decay half-life of ^{116}Cd	230
8.14	Effect of the data partitioning on the exposure accumulated with the COBRA demonstrator.	236
8.15	Impact of the data partitioning and the PSD cuts on the ^{116}Cd background index achieved with the COBRA demonstrator.	236
8.16	Summary of the quantitative sensitivity study regarding the observation of the $2\nu\beta\beta$ -decay of ^{116}Cd with the COBRA demonstrator.	238
8.17	Isotopic composition and atomic masses of natural platinum.	244
8.18	Overview of the systematic uncertainties of the half-life determination of the ^{190}Pt α -decay with the COBRA demonstrator.	250
8.19	Overview of experimental results involving excited state transitions in $2\nu\beta\beta$ -decays.	253
8.20	Experimental results and half-life predictions for excited state transitions in ^{116}Cd and ^{130}Te	256
8.21	Relative multiplicity fractions for the simulated ^{116}Cd double beta decay modes using the COBRA demonstrator.	258
8.22	Relative multiplicity fractions for the simulated ^{130}Te double beta decay modes using the COBRA demonstrator.	259
8.23	Overview of selection criteria to identify excited state transitions for the isotopes ^{116}Cd and ^{130}Te in the M2 channel.	268
8.24	Results of the excited states feasibility study based on MC simulations of potential double beta transitions of ^{116}Cd with the COBRA demonstrator.	272
8.25	Results of the excited states feasibility study based on MC simulations of potential double beta transitions of ^{130}Te with the COBRA demonstrator.	273
8.26	Overview of the detectors that belong to one of the four topological detector classes.	276
8.27	Overview of the topological detector pairs based on the categorization of the detectors according to their position in the demonstrator array.	276
8.28	Updated analysis results for the simulation of the $2\nu\beta\beta$ -decay modes of ^{116}Cd via the first excited states with the COBRA demonstrator array.	280
8.29	Comparison of the intrinsic full-energy detection efficiency ε_{int} for several $\beta^-\beta^-$ -decays and detector geometries investigated by COBRA.	283
8.30	List of additional experimental parameters required for the $0\nu\beta\beta$ -decay half-life sensitivity estimate.	284

8.31	Half-life sensitivity estimate for five neutrinoless $\beta^- \beta^-$ g.s. to g.s. transitions and the full exposure of the COBRA demonstrator after the HRP+MRD partitioning.	285
D.1	Overview of calibrations runs of the COBRA demonstrator at LNGS between 2011–2013.	304
D.2	Overview of calibrations runs of the COBRA demonstrator at LNGS between 2014–2019.	305
E.1	Compilation of the COBRA demonstrator’s L1 detector parameters.	321
E.2	Compilation of the COBRA demonstrator’s L2 detector parameters.	322
E.3	Compilation of the COBRA demonstrator’s L3 detector parameters.	323
E.4	Compilation of the COBRA demonstrator’s L4 detector parameters.	324

List of Acronyms

$0\nu\beta\beta$	Neutrinoless double beta decay	CKM	Cabibbo-Kobayashi-Maskawa
$2\nu\beta\beta$	Two neutrino double beta decay	C.L.	Confidence level
AGATA	Advanced Gamma Tracking Array	CMS	Compact Muon Solenoid
AMoRE	Advanced Molybdenum-based Rare process Experiment	CNGS	CERN Neutrinos to Gran Sasso
AME	Atomic mass evaluation	COBRA	Cadmium Zinc Telluride 0-Neutrino Double Beta Research Apparatus
ASIC	Application-specific integrated circuit	COSINUS	Cryogenic Observatory for Signatures seen in Next-generation Underground Searches
ATLAS	A Toroidal LHC ApparatuS	CP	Charge conjugation parity
BAT	Bayesian Analysis Toolkit	CPG	Coplanar grid
BCS	Bardeen-Cooper-Schrieffer	CRES	Cyclotron radiation emission spectroscopy
BI	Background index	CRESST	Cryogenic Rare Event Search using Superconducting Thermometers
Borexino	Boron solar neutrino experiment-ino	CS	Compton scattering
BV	Bulk voltage	CSDA	Continuous-slowing-down approximation
CA	Collecting anode	CSNSM	Centre de Sciences Nucleaires et de Sciences de la Matiere
CANDLES	CAlcium fluoride for the study of Neutrinos and Dark matters by Low Energy Spectrometer	CUORE	Cryogenic Underground Observatory for Rare Events
CAD	Computer-aided design	CUPID	CUORE Upgrade with Particle Identification
CB	Conductive band	CVC	Conserved vector current
CCE	Charge collection efficiency	CZT	Cadmium zinc telluride
CCT	Compton coincidence technique	DAMA	DArk MATter (experiment)
CERN	Conseil Europeen pour la Recherche Nucleaire		
CJPL	China JinPing underground Laboratory		

DAQ	Data acquisition	GEANT4	GEometry ANd Tracking
DAQCorE	Data-Acquisition and Control Environment	GINGER	Gyrosopes IN GEneral Relativity
Darkside	DarkSide-50	GR	Guard-ring
DCC	Data-cleaning cut	GRETINA	Gamma Ray Tracking In beam Tracking Ar-ray
DEP	Double-escape peak	g.s.	Ground-state
DLB	Dortmund low-background facility	GT	Gamow-Teller
DM	Detector module	GUT	Grand Unified Theories
DMC	Detector module carrier	GWS	Glashow-Weinberg-Salam
DPL	Diagonal path length	HALO	Helium and Lead Observatory
DUNE	Deep Underground Neutrino Experiment	h.c.	Hermitian conjugate
DUSEL	Deep Underground Science and Engineering Laboratory	HdM	Heidelberg-Moscow
EC	Electron capture	HPB	High-pressure Bridgman
ECHo	Electron Capture $^{163}\text{Holmium}$	HPGe	High-purity germanium
EDF	Energy density functional	HRP	High-rate period
EDX	Energy-dispersive X-ray spectroscopy	HRD	High-rate detector
EM	Electromagnetic	HTTP	Hypertext Transfer Protocol
EMG	Exponentially modified Gaussian	HV	High voltage
EMI	Electromagnetic interference	ICARUS	Imaging Cosmic And Rare Underground Signals
ERT	Early rise time	ICP-MS	Inductively coupled plasma - mass spectrometry
ERMES	Environmental Radioactivity Monitoring for Earth Sciences	INFN	Istituto Nazionale di Fisica Nucleare
e.s.	Excited state	IBM	Interacting boson model
ESA	European Space Agency	IBFM-2	Interacting boson-fermion model
EXO	Enriched Xenon Observatory	ISM	Interacting shell model
FADC	Fast analog-to-digital converter	JSON	JavaScript Object Notation
FEE	Full-energy detection efficiency	JUNO	Jiangmen Underground Neutrino Observatory
FEP	Full-energy peak	KamLAND	Kamioka Liquid Scintillator Antineutrino Detector
FPGA	Field programmable gate array	KamLAND-Zen	KamLAND Zero-Neutrino Double-Beta Decay
FROAST	Functional ROOT-oriented Analysis and Settings	KATRIN	Karlsruhe Tritium Neutrino experiment
FWHM	Full-width at half-maximum	KM3NeT	Cubic Kilometre Neutrino Telescope
GB	Grid bias	LA	Linear amplification
GDML	Geometry Description Markup Language	LAr	Liquid Argon
GERDA	Germanium detector array		

LEGEND	Large Enriched Germanium Experiment for Neutrinoless Double Beta Decay	NEMO	Neutrino Ettore Majorana Observatory
LEP	Large Electron-Positron Collider	NEXT	Neutrino Experiment with a Xenon TPC
LHC	Large Hadron Collider	NIM	Nuclear Instrumentation Module
LIBRA	Large sodium Iodide Bulk for RAre processes	NIST	National Institute of Standards and Technology
LNGS	Laboratori Nazionali del Gran Sasso	NME	Nuclear matrix element
LNV	Lepton number violation	OFHC	Oxygen-free high-conductivity
LSE	Lateral surface event	OPERA	Oscillation Project with Emulsion-tracking Apparatus
LSM	Laboratoire Souterrain de Modane	PA	Photoelectric absorption
LUMINEU	Luminescent Underground Molybdenum Investigation for NEUtrino mass and nature	PandaX	Particle and astrophysical Xenon experiment
LUNA	Laboratory for Underground Nuclear Astrophysics	PCB	Printed circuit board
LVD	Large Volume Detector	PH	Pulse-height
M1	Multiplicity $m = 1$	PHFB	Projected Hartree-Fock Bogoliubov
M2	Multiplicity $m = 2$	PINGU	Precision IceCube Next Generation Upgrade
MAC-E	Magnetic adiabatic collimation with an electrostatic	PIPS	Passivated Implanted Planar Silicon
MAnTiCORE	Multiple-Analysis Toolkit for the COBRA Experiment	ppb	Parts per billion
MC	Monte-Carlo	PMNS	Pontecorvo-Maki-Nakagawa-Sakata
MIT	Massachusetts Institute of Technology	PMT	Photomultiplier tube
MOON	Mo/Majorana Observatory Of Neutrinos	POM	Polyoxymethylene
MPI	Max-Planck-Institut	PR	Physics run
MPL	Maximum path length	PSA	Peak-search algorithm
MQPM	Microscopic quasiparticle-phonon model	PSD	Pulse-shape discrimination
MRD	Medium-rate detector	PSF	Phase-space factor
MSE	Multi-site event	QCD	Quantum chromodynamics
MSW	Mikheyev-Smirnov-Wolfenstein	qCPG	Quad coplanar-grid
MWA	Moving window average	QED	Quantum electrodynamics
m.w.e.	Meter of water equivalent	QFD	Quantum flavor dynamics
NaI	Sodium iodide	QFT	Quantum field theory
NCA	Non-collecting anode	QRPA	Quasiparticle random phase approximation
NDF	Number of degrees of freedom	RC	Resistor-capacitor
		R&D	Research and Development
		RMS	Root mean square
		ROI	Region of interest

ROOT	An Object-Oriented Data Analysis Framework, developed at CERN	THM	Traveling heater method
SABRE	Sodium Iodide with Active Background Rejection Experiment	TPC	Time projection chamber
S/B	Signal-to-background ratio	TTL	Transistor-transistor logic
SB	Side-band	TUD	Technische Universität Dresden
sCPG	Sample-CPG	ULA	Ultra low-activity
SE	Single-ended	UPS	Uninterruptible power supply
SEP	Single-escape peak	UUID	Universally unique identifier
SigProCxx	Signal Processing Classes for C++	VB	Valence band
SLAC	Stanford Linear Accelerator Center	VENOM	COBRA GEANT4 simulation toolkit
SM	Standard Model	VIP	VIolation of the Pauli exclusion principle
SNEWS	Supernovae Early Warning System	VME	Versa module Eurocard
SNO	Sudbury Neutrino Observatory	VPL	Vertical path length
SRIM	Stopping and Range of Ions in Matter	XDEM	EXtended DEMonstrator
SSE	Single-site event	XENON1T	XENON1T
SSM	Spectrum-shape method	XML	Extensible markup language
STL	Standard template libraries	XRF	X-ray fluorescence
		ZIH	Center for Information Services and High Performance Computing

List of co-supervised theses

- K. Rohatsch, *Charakterisierung von großvolumigen CdZnTe-Detektoren mit segmentierter CPG-Anodenkonfiguration für das COBRA-Experiment*, Diploma thesis, TU Dresden, 2016. [Roh16]
- A. Hemmetter, *Development of an Arduino-controlled Nitrogen Flushing System of Measurement Boxes for the Characterization of CZT Detectors for the COBRA Experiment*, Bachelor thesis, TU Dresden, 2016. [Hem16]
- L. Dathe, *Analogiebetrachtungen von Neutrinos und Antineutrinos und Koinzidenzanalyse von Computersimulationen des COBRA-Experiments*, Besondere Lernleistung (BeLL), Bernhard-von-Cotta-Gymnasium Brand-Erbisdorf, TU Dresden, 2016. [Dat16]
- R. Kantelberg, *Evaluation of the Event Selection for the Beta Decay Study of Cd-113 with the COBRA Experiment*, Bachelor thesis, TU Dresden, 2017. [Kan17]
- T. Kreße, *Investigation of the temperature behavior of CdZnTe room temperature semiconductor detectors for the COBRA experiment*, Bachelor thesis, TU Dresden, 2017. [Kre17]
- A. Heimbold, *Spectral shape analysis of the fourfold forbidden beta decay of Cd-113 with the COBRA experiment*, Master thesis, TU Dresden, 2018. [Hei18]
- J. Volkmer, *Prospects of the investigation of EC/ β^+ decays with the COBRA experiment*, Master thesis, TU Dresden, 2018. [Vol18]
- J. Küttler, *Investigation of the $2\nu 2\beta$ -spectrum of Cd-116 with the COBRA experiment*, Master thesis, TU Dresden, 2019. [Küt19]

Bibliography

- [AAGI14] S. Awadalla, M. Al-Grafi, and K. Iniewski. *High voltage optimization in CdZnTe detectors*. NIM A, 764:193–197, 2014. doi:10.1016/j.nima.2014.07.026.
- [ABB⁺10] C. Arnaboldi, C. Brofferio, A. Bryant, et al. *Production of high purity TeO₂ single crystals for the study of neutrinoless double beta decay*. Journal of Crystal Growth, 312 (20):2999–3008, 2010. doi:10.1016/j.jcrysGro.2010.06.034.
- [ABC⁺94a] A. Alessandrello, C. Brofferio, D. Camin, et al. *Bolometric measurement of the beta spectrum of ¹¹³Cd*. Nuclear Physics B, 35:394–396, 1994. doi:10.1016/0920-5632(94)90288-7.
- [ABC⁺94b] A. Alessandrello, C. Brofferio, D. Camin, et al. *Large calorimetric devices for double beta decay and dark matter*. NIM A, 344 (1):243–249, 1994. doi:10.1016/0168-9002(94)90678-5.
- [AFF⁺04] P. Antonioli, R. T. Fienberg, F. Fleurot, et al. *SNEWS: the SuperNova Early Warning System*. New Journal of Physics, 6:114–114, 2004. doi:10.1088/1367-2630/6/1/114.
- [AL97] M. S. Amman and P. N. Luke. *Coplanar-grid detector with single-electrode readout*. Proc. SPIE, 3115:205–213, 1997. doi:10.1117/12.277687.
- [ALE89] D. DeCamp, B. Deschizeaux, J.-P. Lees, et al., ALEPH collaboration. *Determination of the number of light neutrino species*. Physics Letters B, 231 (4):519–529, 1989. doi:10.1016/0370-2693(89)90704-1.
- [ALE06] S. Schael, R. Barate, R. Bruneliere, et al., ALEPH collaboration, DELPHI collaboration, L3 collaboration, OPAL collaboration, SLD collaboration, LEP electroweak working group, SLD electroweak and heavy flavour groups. *Precision electroweak measurements on the Z resonance*. Physics Reports, 427 (5–6):257–454, 2006. doi:10.1016/j.physrep.2005.12.006.
- [ALL06] M. Amman, J. Lee, and P. Luke. *Temperature Study of CdZnTe Coplanar-Grid Detectors*. IEEE Transactions on Nuclear Science, 53 (5):3035–3040, 2006. doi:10.1109/TNS.2006.879909.
- [AME17] M. Wang, G. Audi, F. G. Kondev, et al., AME. *The AME2016 atomic mass evaluation (II). Tables, graphs and references*. Chinese Physics C, 41 (3):030003, 2017. doi:10.1088/1674-1137/41/3/030003.

- [AMo19] V. Alenkov, H. W. Bae, J. Beyer, et al., AMoRE collaboration. *First results from the AMoRE-Pilot neutrinoless double beta decay experiment.* The European Physical Journal C, 79 (9):791, 2019. doi:10.1140/epjc/s10052-019-7279-1.
- [Apa20] Apache Software Foundation. *CouchDB*, 2020, <https://couchdb.apache.org/>, date of access: 2020-03-07.
- [Arl16] J.-H. Arling. *Characterization of Coplanar Grid CdZnTe Detectors and Instrumentation of the Guardring for the COBRA Experiment.* Master thesis, TU Dortmund, 2016.
- [AS05] T. Asaka and M. Shaposhnikov. *The ν MSM, dark matter and baryon asymmetry of the universe.* Physics Letters B, 620 (1-2):17–26, 2005. doi: 10.1016/j.physletb.2005.06.020.
- [ATL15] G. Aad, B. Abbott, J. Abdallah, et al., ATLAS collaboration. *Search for type-III Seesaw heavy leptons in pp collisions at $\sqrt{s} = 8$ TeV with the ATLAS Detector.* Physical Review D, 92 (032001), 2015. doi:10.1103/PhysRevD.92.032001.
- [Aur18] A. S. Barabash, P. Belli, R. Bernabei, et al., Aurora collaboration. *Final results of the Aurora experiment to study 2β decay of ^{116}Cd with enriched $^{116}\text{CdWO}_4$ crystal scintillators.* Physical Review D, 98 (9):092007, 2018. doi: 10.1103/PhysRevD.98.092007.
- [Aut20] Autodesk. *official website*, 2020, <https://www.autodesk.de>, date of access: 2020-05-09.
- [Bah64] J. N. Bahcall. *Solar Neutrinos. I. Theoretical.* Physical Review Letters, 12 (11):300–302, 1964. doi:10.1103/PhysRevLett.12.300.
- [Bak88] E. Alexeyev, L. Alexeyeva, I. Krivosheina, et al., Baksan collaboration. *Detection of the neutrino signal from SN 1987A in the LMC using the INR Baksan underground scintillation telescope.* Physics Letters B, 205 (2-3):209–214, 1988. doi:10.1016/0370-2693(88)91651-6.
- [Bar89] R. J. Barlow. *Statistics: A Guide to the Use of Statistical Methods in the Physical Sciences.* John Wiley & Sons, reprint edition, 1989. ISBN 978-0471922957.
- [Bar10] A. S. Barabash. *Precise half-life values for two-neutrino double- β decay.* Physical Review C, 81 (3):035501, 2010. doi:10.1103/PhysRevC.81.035501.
- [Bar17] A. S. Barabash. *Double beta decay to the excited states: Review.* AIP Conference Proceedings, 1894:020002, 2017. doi:10.1063/1.5007627.
- [Bar19a] A. S. Barabash. *Average and recommended half-life values for two-neutrino double beta decay: Upgrade-2019.* AIP Conference Proceedings, 2165:020002, 2019. doi:10.1063/1.5130963.
- [Bar19b] A. S. Barabash. *Possibilities of Future Double Beta Decay Experiments to Investigate Inverted and Normal Ordering Region of Neutrino Mass.* Frontiers in Physics, 6, 2019. doi:10.3389/fphy.2018.00160.

- [BB36] H. A. Bethe and R. F. Bacher. *Stationary States of Nuclei*. Reviews of Modern Physics, 8 (2):82–229, 1936. doi:10.1103/RevModPhys.8.82.
- [BBB⁺07] P. Belli, R. Bernabei, N. Bukilic, et al. *Investigation of β decay of Cd-113*. Physical Review C, 76 (6):64603, 2007. doi:10.1103/PhysRevC.76.064603.
- [BBD⁺19] P. Belli, R. Bernabei, F. A. Danevich, et al. *Experimental searches for rare alpha and beta decays*. The European Physical Journal A, 55 (8):140, 2019. doi:10.1140/epja/i2019-12823-2.
- [BCS57] J. Bardeen, L. N. Cooper, and J. R. Schrieffer. *Microscopic Theory of Superconductivity*. Physical Review, 106 (1):162–164, 1957. doi:10.1103/PhysRev.106.162.
- [BD18] L. Bodenstein-Dresler. *Preparation for the COBRA XDEM phase including design of mechanical parts, tests of electronics and measurement of β -suppression*. Master thesis, TU Dortmund, 2018.
- [Ber13] Y. Bernau. *Untersuchung der elektromagnetischen Abschirmung für das COBRA Experiment*. Bachelor thesis, TU Dortmund, 2013.
- [Bet12] A. Bettini. *The world deep underground laboratories*. The European Physical Journal Plus, 127 (9):114, 2012. doi:10.1140/epjp/i2012-12114-y.
- [Bet14] A. Bettini. *New underground laboratories: Europe, Asia and the Americas*. Physics of the Dark Universe, 2014. doi:10.1016/j.dark.2014.05.006.
- [BGK⁺18] A. Baldini, D. Glenzinski, F. Kapusta, et al. *A submission to the 2020 update of the European Strategy for Particle Physics on behalf of the COMET, MEG, Mu2e and Mu3e collaborations*. arXiv pre-print, 2018, <http://arxiv.org/abs/1812.06540>.
- [BGS⁺17] M. Braun, Y. M. Georgiev, T. Schönherr, et al. *A new precision measurement of the α -decay half-life of ^{190}Pt* . Physics Letters B, 768:317–320, 2017. doi:10.1016/j.physletb.2017.02.052.
- [BHNU09] A. S. Barabash, P. Hubert, A. Nachab, et al. *Investigation of $\beta\beta$ decay in ^{150}Nd and ^{148}Nd to the excited states of daughter nuclei*. Physical Review C, 79 (4):045501, 2009. doi:10.1103/PhysRevC.79.045501.
- [BHS⁺10] M. Berger, J. Hubbell, S. Seltzer, et al. *XCOM: Photon Cross Section Database (version 1.5)*. National Institute of Standards and Technology, 2010. doi: <https://dx.doi.org/10.18434/T48G6X>.
- [BJ69] H. Behrens and J. Janecke. *Numerical Tables for Beta-Decay and Electron Capture*. Springer-Verlag, Berlin/Heidelberg, 1969. ISBN 3-540-04593-7. doi:10.1007/b19939.
- [BKI15] J. Barea, J. Kotila, and F. Iachello. *$0\nu\beta\beta$ and $2\nu\beta\beta$ nuclear matrix elements in the interacting boson model with isospin restoration*. Physical Review C, 91 (3):034304, 2015. doi:10.1103/PhysRevC.91.034304.
- [Bor12] G. Bellini, J. Benziger, D. Bick, et al., Borexino collaboration. *Cosmic-muon flux and annual modulation in Borexino at 3800 m water-equivalent depth*. Journal of Cosmology and Astroparticle Physics, 2012 (05):015–015, 2012. doi:10.1088/1475-7516/2012/05/015.

- [Bor19] M. Agostini, K. Altenmüller, S. Appel, et al., Borexino collaboration. *Simultaneous precision spectroscopy of pp, Be-7, and pep solar neutrinos with Borexino Phase-II*. Physical Review D, 100 (8):082004, 2019. doi:10.1103/PhysRevD.100.082004.
- [BP92] J. N. Bahcall and M. H. Pinsonneault. *Standard solar models, with and without helium diffusion, and the solar neutrino problem*. Reviews of Modern Physics, 64 (4):885–926, 1992. doi:10.1103/RevModPhys.64.885.
- [BR97] R. Brun and F. Rademakers. *ROOT - An object oriented data analysis framework*. NIM A, 389 (1-2):81–86, 1997. doi:10.1016/S0168-9002(97)00048-X.
- [CAI⁺08] H. Chen, S. A. Awadalla, K. Iniewski, et al. *Characterization of large cadmium zinc telluride crystals grown by traveling heater method*. Journal of Applied Physics, 103 (1):014903, 2008. doi:10.1063/1.2828170.
- [CCC⁺97] K. Chattopadhyay, H. Chen, K.-T. Chen, et al. *Gamma Ray Spectrometers Fabricated from Modified Bridgman/Annealed CZT Crystal Material*. MRS Proceedings, 487:123, 1997. doi:10.1557/PROC-487-123.
- [CEG77] M. S. Chanowitz, J. Ellis, and M. K. Gaillard. *The price of natural flavour conservation in neutral weak interactions*. Nuclear Physics B, 128 (3):506–536, 1977. doi:10.1016/0550-3213(77)90057-8.
- [CER17] CERN. *GDML user’s guide (version 2.7)*, 2017, <http://lcgapp.cern.ch/project/simu/framework/GDML/doc/GDMLmanual.pdf>, date of access: 2020-02-23.
- [Cha32] J. Chadwick. *Possible Existence of a Neutron*. Nature, 129 (3252):312–312, 1932. doi:10.1038/129312a0.
- [CHLR18] Y. Cai, T. Han, T. Li, et al. *Lepton Number Violation: Seesaw Models and Their Collider Tests*. Frontiers in Physics, 6, 2018. doi:10.3389/fphy.2018.00040.
- [CKK09] A. Caldwell, D. Kollár, and K. Kröninger. *BAT – The Bayesian analysis toolkit*. Computer Physics Communications, 180 (11):2197–2209, 2009. doi:10.1016/j.cpc.2009.06.026.
- [CKL⁺17] J.-P. Cheng, K.-J. Kang, J.-M. Li, et al. *The China Jinping Underground Laboratory and Its Early Science*. Annual Review of Nuclear and Particle Science, 67 (1):231–251, 2017. doi:10.1146/annurev-nucl-102115-044842.
- [CLP18] J. Cooley, J. C. Loach, and A. W. P. Poon. *The radiopurity.org material database*. AIP Conference Proceedings, 1921:040001, 2018. doi:10.1063/1.5018992.
- [CMPN⁺05] E. Caurier, G. Martínez-Pinedo, F. Nowacki, et al. *The shell model as a unified view of nuclear structure*. Reviews of Modern Physics, 77 (2):427–488, 2005. doi:10.1103/RevModPhys.77.427.
- [CMPS06] R. Chytracek, J. McCormick, W. Pokorski, et al. *Geometry Description Markup Language for Physics Simulation and Analysis Applications*. IEEE Transactions on Nuclear Science, 53 (5):2892–2896, 2006. doi:10.1109/TNS.2006.881062.

- [CMS17] A. M. Sirunyan, A. Tumasyan, W. Adam, et al., CMS collaboration. *Search for Evidence of the Type-III Seesaw Mechanism in Multilepton Final States in Proton-Proton Collisions $\sqrt{s} = 13$ TeV*. Physical Review Letters, 119 (22):221802, 2017. doi:10.1103/PhysRevLett.119.221802.
- [CNR20] CNRS. *Laboratoire Souterrain de Modane (LSM)*, 2020, <http://www-lsm.in2p3.fr>, date of access: 2020-01-24.
- [COB05] C. Goessling, M. Junker, H. Kiel, et al., COBRA collaboration. *Experimental study of ^{113}Cd β decay using CdZnTe detectors*. Physical Review C, 72 (6):064328, 2005. doi:10.1103/PhysRevC.72.064328.
- [COB09a] J. V. Dawson, C. Montag, C. Reeve, et al., COBRA collaboration. *An investigation on cooling of CZT co-planar grid detectors*. NIM A, 599 (2-3):209–214, 2009. doi:10.1016/j.nima.2008.11.013.
- [COB09b] J. V. Dawson, C. Reeve, J. R. Wilson, et al., COBRA collaboration. *An investigation into the ^{113}Cd beta decay spectrum using a CdZnTe array*. Nuclear Physics A, 818 (3-4):264–278, 2009. doi:10.1016/j.nuclphysa.2008.12.010.
- [COB14] M. Fritts, J. Tebrügge, J. Durst, et al., COBRA collaboration. *Pulse-shape discrimination of surface events in CdZnTe detectors for the COBRA experiment*. NIM A, 749:27–34, 2014. doi:10.1016/j.nima.2014.02.038.
- [COB16a] J. Ebert, M. Fritts, D. Gehre, et al., COBRA collaboration. *Results of a search for neutrinoless double- β decay using the COBRA demonstrator*. Physical Review C, 94 (2):024603, 2016. doi:10.1103/PhysRevC.94.024603.
- [COB16b] J. Ebert, M. Fritts, D. Gehre, et al., COBRA collaboration. *The COBRA demonstrator at the LNGS underground laboratory*. NIM A, 807:114–120, 2016. doi:10.1016/j.nima.2015.10.079.
- [COB16c] J. Ebert, D. Gehre, C. Gößling, et al., COBRA collaboration. *Characterization of a large CdZnTe coplanar quad-grid semiconductor detector*. NIM A, 806:159–168, 2016. doi:10.1016/j.nima.2015.09.116.
- [COB16d] J. Ebert, C. Gößling, D. Gehre, et al., COBRA collaboration. *Long-term stability of underground operated CZT detectors based on the analysis of intrinsic ^{113}Cd β^- -decay*. NIM A, 821:109–115, 2016. doi:10.1016/j.nima.2016.03.012.
- [COB17] J.-H. Arling, M. Gerhardt, C. Gößling, et al., COBRA collaboration. *Suppression of alpha-induced lateral surface events in the COBRA experiment using CdZnTe detectors with an instrumented guard-ring electrode*. Journal of Instrumentation, 12 (11):P11025—P11025, 2017. doi:10.1088/1748-0221/12/11/p11025.
- [COB20] L. Bodenstein-Dresler, Y. Chu, D. Gehre, et al., COBRA collaboration. *Quenching of g_A deduced from the β -spectrum shape of ^{113}Cd measured with the COBRA experiment*. Physics Letters B, 800:135092, 2020. doi:10.1016/j.physletb.2019.135092.
- [Com23] A. Compton. *Quantum Theory of the Scattering of X Rays by Light Elements*. Physical Review, 21 (5):483–502, 1923.

- [COM19] COMSOL Inc. *Introduction to COMSOL Multiphysics (version 5.5)*, 2019, https://cdn.comsol.com/doc/5.5/IntroductionToCOMSOLMultiphysics.de_DE.pdf, date of access: 2020-02-23.
- [Cos09] M. C. Carbone, M. Pinto, F. Antonelli, et al., Cosmic Silence collaboration. *The Cosmic Silence experiment: on the putative adaptive role of environmental ionizing radiation*. Radiation and Environmental Biophysics, 48 (2):189–196, 2009. doi:10.1007/s00411-008-0208-6.
- [COS16] G. Angloher, P. Carniti, L. Cassina, et al., COSINUS collaboration. *The COSINUS project: perspectives of a NaI scintillating calorimeter for dark matter search*. The European Physical Journal C, 76 (8):441, 2016. doi:10.1140/epjc/s10052-016-4278-3.
- [CRE19] A. H. Abdelhameed, G. Angloher, P. Bauer, et al., CRESST collaboration. *First results from the CRESST-III low-mass dark matter program*. Physical Review D, 100 (10):102002, 2019. doi:10.1103/PhysRevD.100.102002.
- [CRH⁺56] C. L. Cowan, F. Reines, F. B. Harrison, et al. *Detection of the Free Neutrino: a Confirmation*. Science, 124 (3212):103–104, 1956. doi:10.1126/science.124.3212.103.
- [CUO12] E. Andreotti, C. Arnaboldi, F. T. Avignone, et al., CUORICINO collaboration. *Search for double- β decay of ^{130}Te to the first 0^+ excited state of ^{130}Xe with the CUORICINO experiment bolometer array*. Physical Review C, 85 (4):045503, 2012. doi:10.1103/PhysRevC.85.045503.
- [CUO18] C. Alduino, F. Alessandria, K. Alfonso, et al., CUORE collaboration. *First Results from CUORE: A Search for Lepton Number Violation via $0\nu\beta\beta$ Decay of Te-130*. Physical Review Letters, 120 (13):132501, 2018. doi:10.1103/physrevlett.120.132501.
- [CUO19a] C. Alduino, K. Alfonso, D. R. Artusa, et al., CUORE-0 collaboration. *Double-beta decay of ^{130}Te to the first 0^+ excited state of ^{130}Xe with CUORE-0*. The European Physical Journal C, 79 (9):795, 2019. doi:10.1140/epjc/s10052-019-7275-5.
- [CUO19b] A. Caminata, D. Adams, C. Alduino, et al., CUORE collaboration. *Results from the Cuore Experiment*. Universe, 5 (1):10, 2019. doi:10.3390/universe5010010.
- [CUP15] CUPID Interest Group. *CUPID: CUORE (Cryogenic Underground Observatory for Rare Events) Upgrade with Particle IDentification*. arXiv pre-print, 2015, <http://arxiv.org/abs/1504.03599>.
- [CUP17] D. R. Artusa, F. T. Avignone, J. W. Beeman, et al., CUPID collaboration. *Enriched TeO_2 bolometers with active particle discrimination: Towards the CUPID experiment*. Physics Letters B, 767:321–329, 2017. doi:10.1016/j.physletb.2017.02.011.
- [DAM18] R. Bernabei, P. Belli, A. Bussolotti, et al., DAMA/LIBRA collaboration. *First model independent results from DAMA/LIBRA-phase2*. Nuclear Physics and Atomic Energy, 19 (4):307–325, 2018. doi:10.15407/jnpae2018.04.307.

- [Dar18] P. Agnes, I. F. M. Albuquerque, T. Alexander, et al., DarkSide-50 collaboration. *Low-Mass Dark Matter Search with the DarkSide-50 Experiment*. Physical Review Letters, 121 (8):081307, 2018. doi:10.1103/PhysRevLett.121.081307.
- [Dat16] L. Dathe. *Analogiebetrachtungen von Neutrinos und Antineutrinos und Koinzidenzanalyse von Computersimulationen des COBRA-Experiments*. Besondere Lernleistung (BeLL), Bernhard-von-Cotta-Gymnasium Brand-Erbisdorf, TU Dresden, 2016.
- [Day19] D. Adey, F. P. An, A. B. Balantekin, et al., Daya Bay collaboration. *Improved measurement of the reactor antineutrino flux at Daya Bay*. Physical Review D, 100 (5):052004, 2019. doi:10.1103/PhysRevD.100.052004.
- [DEL89] P. Aarnio, P. Abreu, W. Adam, et al., DELPHI collaboration. *Measurement of the mass and width of the Z^0 -particle from multihadronic final states produced in e^+e^- -annihilations*. Physics Letters B, 231 (4):539–547, 1989. doi:10.1016/0370-2693(89)90706-5.
- [DGG⁺62] G. Danby, J.-M. Gaillard, K. Goulian, et al. *Observation of High-Energy Neutrino Reactions and the Existence of Two Kinds of Neutrinos*. Physical Review Letters, 9 (1):36–44, 1962. doi:10.1103/PhysRevLett.9.36.
- [DGK⁺95] F. Danevich, A. Georgadze, V. Kobychev, et al. *The research of 2β decay of ^{116}Cd with enriched $^{116}\text{CdWO}_4$ crystal scintillators*. Physics Letters B, 344 (1-4):72–78, 1995. doi:10.1016/0370-2693(94)01528-K.
- [DGK⁺96] F. Danevich, A. Georgadze, V. Kobychev, et al. *Beta decay of ^{113}Cd* . Physics of Atomic Nuclei, 59 (1):1–5, 1996, https://inis.iaea.org/search/search.aspx?orig_q=RN:35057135.
- [DGK⁺00] F. A. Danevich, A. S. Georgadze, V. V. Kobychev, et al. *New results of ^{116}Cd double β decay study with $^{116}\text{CdWO}_4$ scintillators*. Physical Review C, 62 (4):045501, 2000. doi:10.1103/PhysRevC.62.045501.
- [DGK⁺03] F. A. Danevich, A. S. Georgadze, V. V. Kobychev, et al. *Search for 2β decay of cadmium and tungsten isotopes: Final results of the Solotvina experiment*. Physical Review C, 68 (3):035501, 2003. doi:10.1103/PhysRevC.68.035501.
- [DHH68] R. Davis, D. S. Harmer, and K. C. Hoffman. *Search for Neutrinos from the Sun*. Physical Review Letters, 20 (21):1205–1209, 1968. doi:10.1103/PhysRevLett.20.1205.
- [Dir28] P. Dirac. *Quantum theory of the electron*. Proceedings of the Royal Society of London. Series A., 117 (778):610–624, 1928.
- [DLM11] M. Duerr, M. Lindner, and A. Merle. *On the quantitative impact of the Schechter-Valle theorem*. Journal of High Energy Physics, 2011 (6):91, 2011. doi:10.1007/JHEP06(2011)091.
- [DMVV16] S. Dell’Oro, S. Marcocci, M. Viel, et al. *Neutrinoless double beta decay: 2015 review*, 2016. doi:10.1155/2016/2162659.

- [DON01] K. Kodama, N. Ushida, C. Andreopoulos, et al., DONUT collaboration. *Observation of tau neutrino interactions*. Physics Letters B, 504 (3):218–224, 2001. doi:10.1016/S0370-2693(01)00307-0.
- [DUN20] B. Abi, R. Acciarri, M. A. Acero, et al., DUNE collaboration. *Deep Underground Neutrino Experiment (DUNE), Far Detector Technical Design Report, Volume I: Introduction to DUNE*. arXiv pre-print, 2020, <http://arxiv.org/abs/2002.02967>.
- [Dur08] J. Durst. *Modellierung und Simulation physikalischer Eigenschaften photonenzählender Röntgenpixeldetektoren für die Bildgebung*. PhD thesis, FAU Erlangen-Nürnberg, 2008.
- [EB64] F. Englert and R. Brout. *Broken Symmetry and the Mass of Gauge Vector Mesons*. Physical Review Letters, 13 (9):321–323, 1964. doi:10.1103/PhysRevLett.13.321.
- [EBB99] J. D. Eskin, H. H. Barrett, and H. B. Barber. *Signals induced in semiconductor gamma-ray imaging detectors*. Journal of Applied Physics, 85 (2):647–659, 1999. doi:10.1063/1.369198.
- [ECH17] L. Gastaldo, K. Blaum, K. Chrysalidis, et al., ECHo collaboration. *The electron capture in ^{163}Ho experiment – ECHo*. The European Physical Journal Special Topics, 226 (8):1623–1694, 2017. doi:10.1140/epjst/e2017-70071-y.
- [ECM17] ECMA International. *The JSON Data Interchange Syntax*, 2017, <http://www.ecma-international.org/publications/files/ECMA-ST/ECMA-404.pdf>, date of access: 2020-03-07.
- [EFH⁺95] H. Ejiri, K.-i. Fushimi, R. Hazama, et al. *Double Beta Decays of ^{116}Cd* . Journal of the Physical Society of Japan, 64 (2):339–343, 1995. doi:10.1143/JPSJ.64.339.
- [EGGHC⁺19] I. Esteban, M. C. Gonzalez-Garcia, A. Hernandez-Cabezudo, et al. *Global analysis of three-flavour neutrino oscillations: synergies and tensions in the determination of Θ_{23} , δ_{CP} , and the mass ordering*. Journal of High Energy Physics, 2019 (1), 2019. doi:10.1007/JHEP01(2019)106.
- [EHM87] S. R. Elliott, A. A. Hahn, and M. K. Moe. *Direct evidence for two-neutrino double-beta decay in Se-82*. Physical Review Letters, 59 (18):2020–2023, 1987. doi:10.1103/PhysRevLett.59.2020.
- [Ein05] A. Einstein. *Über einen die Erzeugung und Verwandlung des Lichtes betreffenden heuristischen Gesichtspunkt*. Annalen der Physik, 322 (6):132–148, 1905. doi:10.1002/andp.19053220607.
- [EM17] J. Engel and J. Menéndez. *Status and future of nuclear matrix elements for neutrinoless double-beta decay: a review*. Reports on Progress in Physics, 80 (4):046301, 2017. doi:10.1088/1361-6633/aa5bc5.
- [ERM13] W. Plastino, M. Laubenstein, S. Nisi, et al., ERMES project. *Uranium, radium and tritium groundwater monitoring at INFN Gran Sasso National Laboratory, Italy*. Journal of Radioanalytical and Nuclear Chemistry, 295 (1):585–592, 2013. doi:10.1007/s10967-012-1818-7.

- [ESZ19] H. Ejiri, J. Suhonen, and K. Zuber. *Neutrino-nuclear responses for astro-neutrinos, single beta decays and double beta decays*. Physics Reports, 797:1–102, 2019. doi:10.1016/j.physrep.2018.12.001.
- [EW27] C. D. Ellis and W. A. Wooster. *The average energy of disintegration of radium E*. Proceedings of the Royal Society of London. Series A., 117 (776):109–123, 1927. doi:10.1098/rspa.1927.0168.
- [EXO14] J. B. Albert, M. Auger, D. J. Auty, et al., EXO-200 collaboration. *An improved measurement of the $2\nu\beta\beta$ half-life of ^{136}Xe with the EXO-200 detector*. Physical Review C, 89 (1), 2014. doi:10.1103/PhysRevC.89.015502.
- [EXO16] J. B. Albert, D. J. Auty, P. S. Barbeau, et al., EXO-200 collaboration. *Search for $2\nu\beta\beta$ decay of ^{136}Xe to the 0_1^+ excited state of ^{136}Ba with the EXO-200 liquid xenon detector*. Physical Review C, 93 (3), 2016. doi:10.1103/PhysRevC.93.035501.
- [EXO18a] J. B. Albert, G. Anton, I. Badhrees, et al., EXO-200 collaboration. *Search for Neutrinoless Double-Beta Decay with the Upgraded EXO-200 Detector*. Physical Review Letters, 120 (7):72701, 2018. doi:10.1103/PhysRevLett.120.072701.
- [EXO18b] S. Delaquis, M. Jewell, I. Ostrovskiy, et al., EXO-200 collaboration. *Deep neural networks for energy and position reconstruction in EXO-200*. Journal of Instrumentation, 13 (08):P08023–P08023, 2018. doi:10.1088/1748-0221/13/08/P08023.
- [FDG⁺13] M. Fritts, J. Durst, T. Göpfert, et al. *Analytical model for event reconstruction in coplanar grid CdZnTe detectors*. NIM A, 708:1–6, 2013. doi:10.1016/j.nima.2013.01.004.
- [Fer34] E. Fermi. *Versuch einer Theorie der β -Strahlen*. Zeitschrift für Physik, 88 (3-4):161–177, 1934. doi:10.1007/BF01351864.
- [Fey85] R. P. Feynman. *QED: The Strange Theory of Light and Matter*. Princeton University Press, 1985. ISBN 9781400847464. doi:10.2307/j.ctt2jc8td.
- [FGM58] R. P. Feynman and M. Gell-Mann. *Theory of the Fermi Interaction*. Physical Review, 109 (1):193–198, 1958. doi:10.1103/PhysRev.109.193.
- [Fur39] W. H. Furry. *On transition probabilities in double beta-disintegration*. Physical Review, 56 (12):1184–1193, 1939. doi:10.1103/PhysRev.56.1184.
- [FY86] M. Fukugita and T. Yanagida. *Baryogenesis without grand unification*. Physics Letters B, 174 (1):45–47, 1986. doi:10.1016/0370-2693(86)91126-3.
- [GAF⁺15] T. Gleixner, G. Anton, M. Filipenko, et al. *Improvement of the energy resolution of pixelated CdTe detectors for applications in $0\nu\beta\beta$ searches*. Journal of Instrumentation, 10 (07):P07010–P07010, 2015. doi:10.1088/1748-0221/10/07/P07010.
- [Gag06] N. D. Gagunashvili. *Comparison of weighted and unweighted histograms*. arXiv pre-print, 2006, <http://arxiv.org/abs/physics/0605123>.

- [Gam30] G. Gamow. *Mass defect curve and nuclear constitution.* Proceedings of the Royal Society of London. Series A., 126 (803):632–644, 1930. doi:10.1098/rspa.1930.0032.
- [Gar73a] F. Hasert, H. Faissner, W. Krenz, et al., Gargamelle Neutrino collaboration. *Search for elastic muon-neutrino electron scattering.* Physics Letters B, 46 (1):121–124, 1973. doi:10.1016/0370-2693(73)90494-2.
- [Gar73b] F. Hasert, S. Kabe, W. Krenz, et al., Gargamelle Neutrino collaboration. *Observation of neutrino-like interactions without muon or electron in the gargamelle neutrino experiment.* Physics Letters B, 46 (1):138–140, 1973. doi:10.1016/0370-2693(73)90499-1.
- [GEA03] S. Agostinelli, J. Allison, K. Amako, et al., GEANT4 collaboration. *Geant4 – a simulation toolkit.* NIM A, 506 (3):250–303, 2003. doi:10.1016/S0168-9002(03)01368-8.
- [GEA16] J. Allison, K. Amako, J. Apostolakis, et al., GEANT4 collaboration. *Recent developments in GEANT4.* NIM A, 835:186–225, 2016. doi:10.1016/j.nima.2016.06.125.
- [Geh17] D. Gehre. *Investigations on CdZnTe-Semiconductor-Detectors for the Search of the Neutrinoless Double Beta Decay.* PhD thesis, TU Dresden, 2017.
- [GER13a] M. Agostini, M. Allardt, E. Andreotti, et al., GERDA collaboration. *Pulse shape discrimination for Gerda Phase I data.* The European Physical Journal C, 73 (10):2583, 2013. doi:10.1140/epjc/s10052-013-2583-7.
- [GER13b] M. Agostini, M. Allardt, E. Andreotti, et al., GERDA collaboration. *Results on neutrinoless double- β decay of Ge-76 from Phase I of the GERDA experiment.* Physical Review Letters, 111 (12):122503, 2013. doi:10.1103/PhysRevLett.111.122503.
- [GER15a] M. Agostini, M. Allardt, A. M. Bakalyarov, et al., GERDA collaboration. *$2\nu\beta\beta$ decay of ^{76}Ge into excited states with GERDA Phase I.* Journal of Physics G, 42 (11), 2015. doi:10.1088/0954-3899/42/11/115201.
- [GER15b] M. Agostini, M. Allardt, A. M. Bakalyarov, et al., GERDA collaboration. *Results on $\beta\beta$ decay with emission of two neutrinos or Majorons in ^{76}Ge from GERDA Phase.* European Physical Journal C, 75 (9), 2015. doi:10.1140/epjc/s10052-015-3627-y.
- [GER17] C. Bauer, E. Bellotti, S. Belogurov, et al., GERDA collaboration. *Background-free search for neutrinoless double- β decay of ^{76}Ge with GERDA.* Nature, 544 (7648):47–52, 2017. doi:10.1038/nature21717.
- [GER18a] M. Agostini, A. M. Bakalyarov, M. Balata, et al., GERDA collaboration. *Improved Limit on Neutrinoless Double- β Decay of Ge-76 from GERDA Phase II.* Physical Review Letters, 120 (13):132503, 2018. doi:10.1103/PhysRevLett.120.132503.
- [GER18b] M. Agostini, A. M. Bakalyarov, M. Balata, et al., GERDA collaboration. *Upgrade for Phase II of the GERDA experiment.* The European Physical Journal C, 78 (5):388, 2018. doi:10.1140/epjc/s10052-018-5812-2.

- [GG74] H. Georgi and S. L. Glashow. *Unity of All Elementary-Particle Forces*. Physical Review Letters, 32 (8):438–441, 1974. doi:10.1103/PhysRevLett.32.438.
- [GGS58] M. Goldhaber, L. Grodzins, and A. W. Sunyar. *Helicity of Neutrinos*. Physical Review, 109 (3):1015–1017, 1958. doi:10.1103/PhysRev.109.1015.
- [GIN17] J. Belfi, N. Beverini, F. Bosi, et al., GINGER collaboration. *Deep underground rotation measurements: GINGERino ring laser gyroscope in Gran Sasso*. Review of Scientific Instruments, 88 (3):034502, 2017. doi:10.1063/1.4977051.
- [Git20a] Git. *official website*, 2020, <https://git-scm.com/>, date of access: 2020-02-15.
- [Git20b] GitHub. *official website*, 2020, <https://github.com/>, date of access: 2020-02-15.
- [Gla61] S. L. Glashow. *Partial-symmetries of weak interactions*. Nuclear Physics, 22 (4):579–588, 1961. doi:10.1016/0029-5582(61)90469-2.
- [Gla80] S. L. Glashow. *The Future of Elementary Particle Physics*. Springer, Boston, MA, 1980. doi:10.1007/978-1-4684-7197-7_15.
- [GLZ18] C. Giganti, S. Lavignac, and M. Zito. *Neutrino oscillations: The rise of the PMNS paradigm*. Progress in Particle and Nuclear Physics, 98:1–54, 2018. doi:10.1016/j.ppnp.2017.10.001.
- [GM35] M. Goeppert-Mayer. *Double Beta-Disintegration*. Physical Review, 48 (6):512–516, 1935. doi:10.1103/PhysRev.48.512.
- [GMRS79] M. Gell-Mann, P. Ramond, and R. Slansky. *Complex Spinors and Unified Theories*. arXiv retro-preprint, 1979, <http://arxiv.org/abs/1306.4669>.
- [GMS01] D. E. Groom, N. V. Mokhov, and S. I. Striganov. *Muon stopping power and range tables 10 MeV–100 TeV*. Atomic Data and Nuclear Data Tables, 78 (2):183–356, 2001. doi:10.1006/adnd.2001.0861.
- [GN11] H. Geiger and J. Nuttall. *The ranges of the α particles from various radioactive substances and a relation between range and period of transformation*. The London, Edinburgh, and Dublin Philosophical Magazine and Journal of Science, 22 (130):613–621, 1911. doi:10.1080/14786441008637156.
- [GW12] D. Gehre and T. Wester. *EDX analysis on CZT*. Internal technical report, TU Dresden, 2012.
- [HAL08] C. A. Duba, F. Duncan, J. Farine, et al., HALO collaboration. *HALO – the helium and lead observatory for supernova neutrinos*. Journal of Physics: Conference Series, 136 (4):042077, 2008. doi:10.1088/1742-6596/136/4/042077.
- [HBB⁺11] M. Haffke, L. Baudis, T. Bruch, et al. *Background measurements in the Gran Sasso Underground Laboratory*. NIM A, 643 (1):36–41, 2011. doi:10.1016/j.nima.2011.04.027.
- [He01] Z. He. *Review of the Shockley-Ramo theorem and its application in semiconductor gamma-ray detectors*. NIM A, 463 (1-2):250–267, 2001. doi:10.1016/S0168-9002(01)00223-6.

- [Hei01] H. Klapdor-Kleingrothaus, A. Dietz, L. Baudis, et al., Heidelberg-Moscow collaboration. *Latest results from the HEIDELBERG-MOSCOW double beta decay experiment*. The European Physical Journal A, 12 (2):147–154, 2001. doi:10.1007/s100500170022.
- [Hei13] F. Heiße. *Investigation of the beta decay spectrum of ^{113}Cd with the COBRA experiment*. Bachelor thesis, TU Dresden, 2013.
- [Hei14] N. Heidrich. *Monte-Carlo-based Development of a Shield and Total Background Estimation for the COBRA Experiment*. PhD thesis, Universität Hamburg, 2014.
- [Hei18] A. Heimbold. *Spectral shape analysis of the fourfold forbidden beta decay of Cd-113 with the COBRA experiment*. Master thesis, TU Dresden, 2018.
- [Hem16] A. Hemmetter. *Development of an Arduino-controlled Nitrogen Flushing System of Measurement Boxes for the Characterization of CZT Detectors for the COBRA Experiment*. Bachelor thesis, TU Dresden, 2016.
- [Her18] C. Herrmann. *Monte-Carlo Based Studies of Potential Background in the XDEM-phase of the COBRA Experiment*. Master thesis, TU Dortmund, 2018.
- [HHM⁺19] P. Holl, L. Hauertmann, B. Majorovits, et al. *Deep learning based pulse shape discrimination for germanium detectors*. The European Physical Journal C, 79 (6):450, 2019. doi:10.1140/epjc/s10052-019-6869-2.
- [Hig64] P. W. Higgs. *Broken Symmetries and the Masses of Gauge Bosons*. Physical Review Letters, 13 (16):508–509, 1964. doi:10.1103/PhysRevLett.13.508.
- [HKS17] M. Haaranen, J. Kotila, and J. Suhonen. *Spectrum-shape method and the next-to-leading-order terms of the β -decay shape factor*. Physical Review C, 95 (2):24327, 2017. doi:10.1103/PhysRevC.95.024327.
- [HKW⁺96] Z. He, G. F. Knoll, D. K. Wehe, et al. *1-D position sensitive single carrier semiconductor detectors*. NIM A, 380 (1-2):228–231, 1996. doi:10.1016/S0168-9002(96)00352-X.
- [HKWM97] Z. He, G. Knoll, D. Wehe, et al. *Position-sensitive single carrier CdZnTe detectors*. NIM A, 388 (1-2):180–185, 1997. doi:10.1016/S0168-9002(97)00318-5.
- [Hom12] M. Homann. *Simulations and Data-Analysis for Background Reduction for the COBRA-Experiment*. Master thesis, TU Dortmund, 2012.
- [Hom13] M. Homann. *Simulation of a Na-22 point source in the COBRA demonstrator setup*. Conference presentation, TU Dortmund, 2013.
- [HR13] J. Heeck and W. Rodejohann. *Neutrinoless quadruple beta decay*. Europhysics Letters, 103 (3):32001, 2013. doi:10.1209/0295-5075/103/32001.
- [HS15] J. Hyvärinen and J. Suhonen. *Nuclear matrix elements for $0\nu\beta\beta$ decays with light or heavy Majorana-neutrino exchange*. Physical Review C, 91 (2):024613, 2015. doi:10.1103/PhysRevC.91.024613.
- [HSS16] M. Haaranen, P. C. Srivastava, and J. Suhonen. *Forbidden nonunique β decays and effective values of weak coupling constants*. Physical Review C, 93 (3):34308, 2016. doi:10.1103/PhysRevC.93.034308.

- [Hyp18] K. Abe, K. Abe, H. Aihara, et al., Hyper-Kamiokande proto-collaboration. *Hyper-Kamiokande Design Report*. arXiv pre-print, 2018, <http://arxiv.org/abs/1805.04163>.
- [ICA15] M. Antonello, P. Aprili, B. Baibussinov, et al., ICARUS collaboration. *Operation and performance of the ICARUS T600 cryogenic plant at Gran Sasso underground Laboratory*. Journal of Instrumentation, 10 (12):P12004–P12004, 2015. doi:10.1088/1748-0221/10/12/P12004.
- [Ice13] M. G. Aartsen, R. Abbasi, Y. Abdou, et al., IceCube collaboration. *First Observation of PeV-Energy Neutrinos with IceCube*. Physical Review Letters, 111 (2):021103, 2013. doi:10.1103/PhysRevLett.111.021103.
- [Ice17] M. G. Aartsen, K. Abraham, M. Ackermann, et al., IceCube-Gen2 Collaboration. *PINGU: a vision for neutrino and particle physics at the South Pole*. Journal of Physics G, 44 (5):054006, 2017. doi:10.1088/1361-6471/44/5/054006.
- [II91] F. Iachello and P. van Isacker. *The Interacting Boson-Fermion Model*. Cambridge University Press, Cambridge, 1991. ISBN 9780511549724. doi: 10.1017/CBO9780511549724.
- [IMB87] R. M. Bionta, G. Blewitt, C. B. Bratton, et al., IMB collaboration. *Observation of a neutrino burst in coincidence with supernova 1987A in the Large Magellanic Cloud*. Physical Review Letters, 58 (14):1494–1496, 1987. doi: 10.1103/PhysRevLett.58.1494.
- [IN220] IN2P3. *History of the Neutrino*, 2020, <https://neutrino-history.in2p3.fr/>, date of access: 2020-05-25.
- [INF20] INFN. *Laboratori Nazionali del Gran Sasso (LNGS)*, 2020, <https://www.lngs.infn.it>, date of access: 2020-01-05.
- [IUP16] J. Meija, T. B. Coplen, M. Berglund, et al., IUPAC. *Isotopic compositions of the elements 2013 (IUPAC Technical Report)*. Pure and Applied Chemistry, 88 (3):293–306, 2016. doi:10.1515/pac-2015-0503.
- [JUN15] T. Adam, F. An, G. An, et al., JUNO collaboration. *JUNO Conceptual Design Report*. arXiv pre-print, 2015, <http://arxiv.org/abs/1508.07166>.
- [Kam87] K. Hirata, T. Kajita, M. Koshiba, et al., Kamiokande collaboration. *Observation of a neutrino burst from the supernova SN1987A*. Physical Review Letters, 58 (14):1490–1493, 1987. doi:10.1103/PhysRevLett.58.1490.
- [Kam16a] K. Asakura, A. Gando, Y. Gando, et al., KamLAND collaboration. *KamLAND sensitivity to neutrinos from pre-supernova stars*. The Astrophysical Journal, 818 (1):91, 2016. doi:10.3847/0004-637X/818/1/91.
- [Kam16b] K. Asakura, A. Gando, Y. Gando, et al., KamLAND-Zen collaboration. *Search for double-beta decay of ^{136}Xe to excited states of ^{136}Ba with the KamLAND-Zen experiment*. Nuclear Physics A, 946 (171–181):171–181, 2016. doi:10.1016/j.nuclphysa.2015.11.011.

- [Kam16c] A. Gando, Y. Gando, T. Hachiya, et al., KamLAND-Zen collaboration. *Search for Majorana Neutrinos Near the Inverted Mass Hierarchy Region with KamLAND-Zen*. Physical Review Letters, 117 (8):82503, 2016. doi:10.1103/PhysRevLett.117.082503.
- [Kan14] F. Kandzia. *Investigation on intrinsic Alpha Particle Events in CdZnTe Detectors*. Diploma thesis, TU Dresden, 2014.
- [Kan17] R. Kantelberg. *Evaluation of the Event Selection for the Beta Decay Study of Cd-113 with the COBRA Experiment*. Bachelor thesis, TU Dresden, 2017.
- [KAT19] M. Aker, K. Altenmüller, M. Arenz, et al., KATRIN collaboration. *Improved Upper Limit on the Neutrino Mass from a Direct Kinematic Method by KATRIN*. Physical Review Letters, 123 (22):221802, 2019. doi:10.1103/PhysRevLett.123.221802.
- [KEFT14] M. F. Kidd, J. H. Esterline, S. W. Finch, et al. *Two-neutrino double- β decay of ^{150}Nd to excited final states in ^{150}Sm* . Physical Review C, 90 (5):055501, 2014. doi:10.1103/PhysRevC.90.055501.
- [KHS17] J. Kostensalo, M. Haaranen, and J. Suhonen. *Electron spectra in forbidden β decays and the quenching of the weak axial-vector coupling constant g_A* . Physical Review C, 95 (4):44313, 2017. doi:10.1103/PhysRevC.95.044313.
- [KI12] J. Kotila and F. Iachello. *Phase-space factors for double- β decay*. Physical Review C, 85 (3):034316, 2012. doi:10.1103/PhysRevC.85.034316.
- [KKDHK01] H. V. Klapdor-Kleinhrothaus, A. Dietz, H. L. Harney, et al. *Evidence for neutrinoless double beta decay*. Modern Physics Letters A, 16 (37):2409–2420, 2001. doi:10.1142/S0217732301005825.
- [KL19] A. Korichi and T. Lauritsen. *Tracking γ -rays in highly segmented HPGe detectors: A review of AGATA and GRETINA*. The European Physical Journal A, 55 (7):121, 2019. doi:10.1140/epja/i2019-12787-1.
- [Kle16] M. Kleineberg. *Koinzidenzanalyse beim COBRA-Experiment*. Master thesis, TU Dortmund, 2016.
- [KM316] S. Adrián-Martínez, M. Ageron, F. Aharonian, et al., KM3Net collaboration. *Letter of intent for KM3NeT 2.0*. Journal of Physics G, 43 (8):084001, 2016. doi:10.1088/0954-3899/43/8/084001.
- [Köt12] T. Köttig. *Sensitivity Studies of CdZnTe Semiconductor Detectors for the COBRA Experiment*. PhD thesis, TU Dortmund, 2012.
- [Kre17] T. Kreße. *Investigation of the temperature behavior of CdZnTe room temperature semiconductor detectors for the COBRA experiment*. Bachelor thesis, TU Dresden, 2017.
- [Kro20] Kromek. *official website*, 2020, <https://www.kromek.com>, date of access: 2020-01-11.
- [KS17] J. Kostensalo and J. Suhonen. *g_A -driven shapes of electron spectra of forbidden β decays in the nuclear shell model*. Physical Review C, 96 (2):24317, 2017. doi:10.1103/PhysRevC.96.024317.

- [KS18] J. Kostensalo and J. Suhonen. *Mesonic enhancement of the weak axial charge and its effect on the half-lives and spectral shapes of first-forbidden $J^+ \leftrightarrow J^-$ -decays*. Physics Letters B, 781 (1):480–484, 2018. doi:10.1016/j.physletb.2018.02.053.
- [Küt19] J. Küttler. *Investigation of the $2\nu 2\beta$ -spectrum of Cd-116 with the COBRA experiment*. Master thesis, TU Dresden, 2019.
- [LBP⁺15] P. Loaiza, V. Brudanin, F. Piquemal, et al. *Obelix, a new low-background HPGe at Modane Underground Laboratory*. AIP Conference Proceedings, 1672:130002, 2015. doi:10.1063/1.4928012.
- [LCA⁺19] A. Loureiro, A. Cuceu, F. B. Abdalla, et al. *Upper Bound of Neutrino Masses from Combined Cosmological Observations and Particle Physics Experiments*. Physical Review Letters, 123 (8):081301, 2019. doi:10.1103/PhysRevLett.123.081301.
- [LCC⁺16] J. Loach, J. Cooley, G. Cox, et al. *A database for storing the results of material radiopurity measurements*. NIM A, 839:6–11, 2016. doi:10.1016/j.nima.2016.09.036.
- [LCCP20] J. C. Loach, J. Cooley, G. A. Cox, et al. *Public database of material radiopurity measurements*, 2020, <https://www.radiopurity.org>, date of access: 2020-01-24.
- [LE96] P. Luke and E. Eissler. *Performance of CdZnTe coplanar-grid gamma-ray detectors*. IEEE Transactions on Nuclear Science, 43 (3):1481–1486, 1996. doi:10.1109/23.507088.
- [Lee80] S. Lee Glashow. *Toward a Unified Theory: Threads in a Tapestry*. Science, 210 (4476):1319–1323, 1980. doi:10.1126/science.210.4476.1319.
- [LEG17] N. Abgrall, A. Abramov, N. Abrosimov, et al., LEGEND collaboration. *The large enriched germanium experiment for neutrinoless double beta decay (LEGEND)*. AIP Conference Proceedings, 1894:020027, 2017. doi:10.1063/1.5007652.
- [Les10] K. T. Lesko. *Deep Underground Science and Engineering Laboratory (DUSEL) Project Overview*. Presentation, 2010, https://sites.nationalacademies.org/cs/groups/bpasite/documents/webpage/bpa_060038.pdf, date of access: 2020-01-02.
- [LL02] T. J. Loredo and D. Q. Lamb. *Bayesian analysis of neutrinos observed from supernova SN 1987A*. Physical Review D, 65 (6):063002, 2002. doi:10.1103/PhysRevD.65.063002.
- [LMMP13] J. Lesgourgues, G. Mangano, G. Miele, et al. *Neutrino Cosmology*. Cambridge University Press, Cambridge, 2013. ISBN 9781139012874. doi:10.1017/CBO9781139012874.
- [LRB⁺19] L. Lewandowski, P. Reiter, B. Birkenbach, et al. *Pulse-Shape Analysis and position resolution in highly segmented HPGe AGATA detectors*. The European Physical Journal A, 55 (5):81, 2019. doi:10.1140/epja/i2019-12752-0.

- [Luk94] P. N. Luke. *Single-polarity charge sensing in ionization detectors using coplanar electrodes.* Applied Physics Letters, 65 (22):2884–2886, 1994. doi: 10.1063/1.112523.
- [LUM16] E. Armengaud, Q. Arnaud, C. Augier, et al., LUMINEU collaboration. *LUMINEU: a search for neutrinoless double beta decay based on ZnMoO₄ scintillating bolometers.* Journal of Physics: Conference Series, 718:062008, 2016. doi:10.1088/1742-6596/718/6/062008.
- [LUN18] C. Broggini, D. Bemmerer, A. Caciolli, et al., LUNA collaboration. *LUNA: Status and prospects.* Progress in Particle and Nuclear Physics, 98:55–84, 2018. doi:10.1016/j.ppnp.2017.09.002.
- [LVD15] N. Y. Agafonova, M. Aglietta, P. Antonioli, et al., LVD collaboration. *Implication for the core collapse supernova rate from 21 years of data of the Large Volume Detector (LVD).* The Astrophysical Journal, 802 (1):47, 2015. doi:10.1088/0004-637X/802/1/47.
- [LY56] T. D. Lee and C. N. Yang. *Question of Parity Conservation in Weak Interactions.* Physical Review, 104 (1):254–258, 1956. doi:10.1103/PhysRev.104.254.
- [MAB⁺07] R. N. Mohapatra, S. Antusch, K. S. Babu, et al. *Theory of neutrinos: a white paper.* Reports on Progress in Physics, 70 (11):1757–1867, 2007. doi: 10.1088/0034-4885/70/11/R02.
- [Maj37] E. Majorana. *Teoria simmetrica dell'elettrone e del positrone.* Il Nuovo Cimento, 14 (4):171–184, 1937. doi:10.1007/BF02961314.
- [MAJ16] N. Abgrall, I. Arnquist, F. Avignone, et al., MAJORANA collaboration. *The Majorana Demonstrator radioassay program.* NIM A, 828:22–36, 2016. doi: 10.1016/j.nima.2016.04.070.
- [MAJ19] I. S. Guinn, I. J. Arnquist, F. T. Avignone, et al., MAJORANA collaboration. *Results of the MAJORANA DEMONSTRATOR’s Search for Double-Beta Decay of ⁷⁶Ge to Excited States of ⁷⁶Se.* arXiv pre-print, 2019, <http://arxiv.org/abs/1912.05761>.
- [MAS06] M. T. Mustonen, M. Aunola, and J. Suhonen. *Theoretical description of the fourth-forbidden non-unique β decays of Cd-113 and In-115.* Physical Review C, 73 (5):54301, 2006. doi:10.1103/PhysRevC.73.054301.
- [MII⁺18] P. Morciano, R. Iorio, D. Iovino, et al. *Effects of reduced natural background radiation on *Drosophila melanogaster* growth and development as revealed by the FLYINGLOW program.* Journal of Cellular Physiology, 233 (1):23–29, 2018. doi:10.1002/jcp.25889.
- [Min77] P. Minkowski. $\mu \rightarrow e\gamma$ at a rate of one out of 10^9 muon decays? Physics Letters B, 67 (4):421–428, 1977. doi:10.1016/0370-2693(77)90435-X.
- [MNS62] Z. Maki, M. Nakagawa, and S. Sakata. *Remarks on the Unified Model of Elementary Particles.* Progress of Theoretical Physics, 28 (5):870–880, 1962. doi:10.1143/PTP.28.870.
- [Moh15] R. N. Mohapatra. *Supersymmetry and R-parity: an Overview.* arXiv pre-print, 2015, <http://arxiv.org/abs/1503.06478>.

- [MOO10] K. Fushimi, Y. Kameda, K. Harada, et al., MOON collaboration. *MOON for double-beta decays and neutrino nuclear responses*. Journal of Physics: Conference Series, 203:012064, 2010. doi:10.1088/1742-6596/203/1/012064.
- [MPCN09] J. Menéndez, A. Poves, E. Caurier, et al. *Disassembling the nuclear matrix elements of the neutrinoless $\beta\beta$ decay*. Nuclear Physics A, 818 (3-4):139–151, 2009. doi:10.1016/j.nuclphysa.2008.12.005.
- [MPS14] M. Mirea, T. Pahomi, and S. Stoica. *Phase Space Factors for Double Beta Decay: an up-date*. arXiv pre-print, 2014, <http://arxiv.org/abs/1411.5506>.
- [MS80] R. N. Mohapatra and G. Senjanović. *Neutrino Mass and Spontaneous Parity Nonconservation*. Physical Review Letters, 44 (14):912–915, 1980. doi:10.1103/PhysRevLett.44.912.
- [MS86] S. P. Mikheyev and A. Y. Smirnov. *Resonant amplification of ν oscillations in matter and solar-neutrino spectroscopy*. Il Nuovo Cimento C, 9 (1):17–26, 1986. doi:10.1007/BF02508049.
- [MSV12] M. Mitra, G. Senjanović, and F. Vissani. *Neutrinoless double beta decay and heavy sterile neutrinos*. Nuclear Physics B, 856 (1):26–73, 2012. doi:10.1016/j.nuclphysb.2011.10.035.
- [Muh08] C. D. Muhlberger. *Experiment IX: Angular Correlation of Gamma Rays*. public webpage, 2008, <http://pages.physics.cornell.edu/cmuhlberger/documents/phys405-paper.pdf>.
- [Mün07] D. Münstermann. *Construction of a Low Background Facility for the COBRA Experiment and its Performance*. PhD thesis, TU Dortmund, 2007.
- [Nat12] National Research Council. *An Assessment of the Science Proposed for the Deep Underground Science and Engineering Laboratory (DUSEL)*. National Academies Press, Washington, D.C., 2012. ISBN 978-0-309-21723-1. doi:10.17226/13204.
- [NDS20] NDS. *Live Chart of Nuclides*, 2020, <https://www-nds.iaea.org/relnsd/vcharthtml/VChartHTML.html>, date of access: 2020-01-17.
- [NEM96] R. Arnold, C. Augier, A. Barabash, et al., NEMO-2 collaboration. *Double- β decay of ^{116}Cd* . Zeitschrift für Physik C, 72 (2):239–247, 1996. doi:10.1007/s002880050241.
- [NEM04] R. Arnold, C. Augier, J. Baker, et al., NEMO-3 collaboration. *Study of 2β -decay of ^{100}Mo and ^{82}Se using the NEMO3 detector*. Journal of Experimental and Theoretical Physics Letters, 80 (6):377–381, 2004. doi:10.1134/1.1830651.
- [NEM10] J. Argyriades, R. Arnold, C. Augier, et al., NEMO-3 collaboration. *Measurement of the two neutrino double beta decay half-life of Zr-96 with the NEMO-3 detector*. Nuclear Physics A, 847 (3-4):168–179, 2010. doi:10.1016/j.nuclphysa.2010.07.009.
- [NEM14] R. Arnold, C. Augier, A. Barabash, et al., NEMO-3 collaboration. *Investigation of double beta decay of ^{100}Mo to excited states of ^{100}Ru* . Nuclear Physics A, 925:25–36, 2014. doi:10.1016/j.nuclphysa.2014.01.008.

- [NEM15] R. Arnold, C. Augier, J. D. Baker, et al., NEMO-3 collaboration. *Results of the search for neutrinoless double- β decay in Mo-100 with the NEMO-3 experiment.* Physical Review D, 92 (7):72011, 2015. doi:10.1103/PhysRevD.92.072011.
- [NEM16] R. Arnold, C. Augier, J. D. Baker, et al., NEMO-3 collaboration. *Measurement of the $2\nu\beta\beta$ decay half-life of ^{150}Nd and a search for $0\nu\beta\beta$ decay processes with the full exposure from the NEMO-3 detector.* Physical Review D, 94 (7):072003, 2016. doi:10.1103/PhysRevD.94.072003.
- [NEM17a] R. Arnold, C. Augier, J. D. Baker, et al., NEMO-3 collaboration. *Measurement of the $2\nu\beta\beta$ decay half-life and search for the $0\nu\beta\beta$ decay of Cd-116 with the NEMO-3 detector.* Physical Review D, 95 (1):12007, 2017. doi:10.1103/physrevd.95.012007.
- [NEM17b] R. Arnold, C. Augier, A. S. Barabash, et al., NEMO-3 collaboration. *Search for Neutrinoless Quadruple- β Decay of ^{150}Nd with the NEMO-3 Detector.* Physical Review Letters, 119 (4):041801, 2017. doi:10.1103/PhysRevLett.119.041801.
- [NEM19] R. Arnold, C. Augier, A. S. Barabash, et al., NEMO-3 collaboration. *Detailed studies of ^{100}Mo two-neutrino double beta decay in NEMO-3.* The European Physical Journal C, 79 (5):440, 2019. doi:10.1140/epjc/s10052-019-6948-4.
- [NEX16] J. Martín-Albo, J. Muñoz Vidal, P. Ferrario, et al., NEXT collaboration. *Sensitivity of NEXT-100 to neutrinoless double beta decay.* Journal of High Energy Physics, 2016 (5):159, 2016. doi:10.1007/JHEP05(2016)159.
- [nEX18] J. B. Albert, G. Anton, I. J. Arnquist, et al., nEXO collaboration. *Sensitivity and discovery potential of the proposed nEXO experiment to neutrinoless double- β decay.* Physical Review C, 97 (6):065503, 2018. doi:10.1103/PhysRevC.97.065503.
- [NHTV05] E. do Nascimento, O. Helene, C. Takiya, et al. *Doppler broadening of positron annihilation radiation: fitting the coincidence spectrum.* NIM A, 538 (1-3):723–730, 2005. doi:10.1016/j.nima.2004.09.013.
- [NIS17] M. Berger, J. Coursey, M. Zucker, et al., NIST. *Stopping-Power & Range Tables for Electrons, Protons, and Helium Ions.* NIST Standard Reference Database 124, 2017. doi:<https://dx.doi.org/10.18434/T4NC7P>.
- [Nob03] NobelPrize.org. *The Nobel Prize in Physics 1903,* 1903, <https://www.nobelprize.org/prizes/physics/1903/summary/>, date of access: 2020-05-22.
- [Nob65] NobelPrize.org. *The Nobel Prize in Physics 1965,* 1965, <https://www.nobelprize.org/prizes/physics/1965/summary/>, date of access: 2020-05-21.
- [Nob79] NobelPrize.org. *The Nobel Prize in Physics 1979,* 1979, <https://www.nobelprize.org/prizes/physics/1979/summary/>, date of access: 2020-05-21.
- [Nob13] NobelPrize.org. *The Nobel Prize in Physics 2013,* 2013, <https://www.nobelprize.org/prizes/physics/2013/summary/>, date of access: 2020-05-22.
- [Nob15] NobelPrize.org. *The Nobel Prize in Physics 2015,* 2015, <https://www.nobelprize.org/prizes/physics/2015/summary/>, date of access: 2020-05-22.

- [Noe71] E. Noether. *Invariant variation problems*. Transport Theory and Statistical Physics, 1 (3):186–207, 1971. doi:10.1080/00411457108231446.
- [NuF20] NuFit. *NuFIT 4.1 (2019)*, 2020, <http://www.nu-fit.org/>, date of access: 2020-05-25.
- [Old15] C. Oldorf. *Operation of CdZnTe Semiconductor Detectors in Liquid Scintillator for the COBRA Experiment*. PhD thesis, Universität Hamburg, 2015.
- [OO19] L. Oberauer and J. Oberauer. *Neutrinophysik*. Springer, Berlin, Heidelberg, 2019. ISBN 978-3-662-59334-9. doi:10.1007/978-3-662-59335-6.
- [OPA89] M. Akrawy, G. Alexander, J. Allison, et al., OPAL collaboration. *Measurement of the Z^0 mass and width with the OPAL detector at LEP*. Physics Letters B, 231 (4):530–538, 1989. doi:10.1016/0370-2693(89)90705-3.
- [OPE18] N. Agafonova, A. Alexandrov, A. Anokhina, et al., OPERA collaboration. *Final Results of the OPERA Experiment on ν_τ Appearance in the CNGS Neutrino Beam*. Physical Review Letters, 120 (21):211801, 2018. doi:10.1103/PhysRevLett.120.211801.
- [OPE19] N. Agafonova, A. Alexandrov, A. Anokhina, et al., OPERA collaboration. *Measurement of the cosmic ray muon flux seasonal variation with the OPERA detector*. Journal of Cosmology and Astroparticle Physics, 2019 (10):003–003, 2019. doi:10.1088/1475-7516/2019/10/003.
- [PAB⁺75] M. L. Perl, G. S. Abrams, A. M. Boyarski, et al. *Evidence for Anomalous Lepton Production in $e^+ - e^-$ Annihilation*. Physical Review Letters, 35 (22):1489–1492, 1975. doi:10.1103/PhysRevLett.35.1489.
- [Pan17] X. Chen, C. Fu, J. Galan, et al., PandaX-III collaboration. *PandaX-III: Searching for neutrinoless double beta decay with high pressure ^{136}Xe gas time projection chambers*. Science China Physics, Mechanics & Astronomy, 60 (6):061011, 2017. doi:10.1007/s11433-017-9028-0.
- [Pau30] W. Pauli. *Pauli letter collection: letter to Lise Meitner*. Letter, 1930, <http://cds.cern.ch/record/83282>, date of access: 2020-05-26.
- [Pau80] W. Pauli. *General Principles of Quantum Mechanics*. Springer, Berlin, Heidelberg, 1980. ISBN 978-3-540-09842-3. doi:10.1007/978-3-642-61840-6.
- [PDG18] M. Tanabashi, K. Hagiwara, K. Hikasa, et al., PDG (Particle Data Group). *Review of Particle Physics*. Physical Review D, 98 (3):030001, 2018. doi:10.1103/PhysRevD.98.030001.
- [PFA⁺77] M. Perl, G. Feldman, G. Abrams, et al. *Properties of the proposed τ charged lepton*. Physics Letters B, 70 (4):487–490, 1977. doi:10.1016/0370-2693(77)90421-X.
- [Pla19] N. Aghanim, Y. Akrami, M. Ashdown, et al., Planck collaboration. *Planck 2018 results. VI. Cosmological parameters*. arXiv pre-print, 2019, <http://arxiv.org/abs/1807.06209>.
- [Pon58] B. Pontecorvo. *Inverse beta processes and nonconservation of lepton charge*. Sov. Phys. JETP, 7:172–173, 1958, <https://inspirehep.net/literature/42736>.

- [Pon60] B. Pontecorvo. *Electron and Muon Neutrinos*. Sov. Phys. JETP, 10:1236–1240, 1960, <https://inspirehep.net/literature/25384>.
- [Pon68] B. Pontecorvo. *Neutrino Experiments and the Problem of Conservation of Leptonic Charge*. Sov. Phys. JETP, 26:984–988, 1968, <https://inspirehep.net/literature/51319>.
- [PR81] H. Primakoff and S. P. Rosen. *Baryon Number and Lepton Number Conservation Laws*. Annual Review of Nuclear and Particle Science, 31 (1):145–192, 1981. doi:10.1146/annurev.ns.31.120181.001045.
- [Pro17] A. A. Esfahani, D. M. Asner, S. Böser, et al., Project 8 collaboration. *Determining the neutrino mass with cyclotron radiation emission spectroscopy – Project 8*. Journal of Physics G, 44 (5):054004, 2017. doi:10.1088/1361-6471/aa5b4f.
- [PRSZ97] B. Povh, K. Rith, C. Scholz, et al. *Teilchen und Kerne*. Springer, Berlin, Heidelberg, 1997. ISBN 978-3-540-61737-2. doi:10.1007/978-3-662-10281-7.
- [PRTV10] G. Pagliaroli, F. Rossi-Torres, and F. Vissani. *Neutrino mass bound in the standard scenario for supernova electronic antineutrino emission*. Astroparticle Physics, 33 (5-6):287–291, 2010. doi:10.1016/j.astropartphys.2010.02.007.
- [PS15] P. Pirinen and J. Suhonen. *Systematic approach to β and $2\nu\beta\beta$ decays of mass $A = 100 - 136$ nuclei*. Physical Review C, 91 (5):054309, 2015. doi:10.1103/PhysRevC.91.054309.
- [PTZ00] O. A. Ponkratenko, V. I. Tretyak, and Y. G. Zdesenko. *Event generator DECAY4 for simulating double-beta processes and decays of radioactive nuclei*. Physics of Atomic Nuclei, 63 (7):1282–1287, 2000. doi:10.1134/1.855784.
- [Raj10] S. Rajek. *How to build and contact a complete 4x4-CPG-layer*. Internal technical report, TU Dortmund, 2010.
- [Raj12] S. Rajek. *Investigation of CZT with Fischerscope X-Ray XDV-SDD*. Internal technical report, TU Dortmund, 2012.
- [Raj13] S. Rajek. *Design of two COBRA Large Scale CPG Setups*. Internal technical report, TU Dortmund, 2013.
- [Ram39] S. Ramo. *Currents induced by electron motion*. Proceedings of the IRE, 27 (9):584–585, 1939. doi:10.1109/JRPROC.1939.228757.
- [RCC⁺13] P. K. Rath, R. Chandra, K. Chaturvedi, et al. *Neutrinoless $\beta\beta$ decay transition matrix elements within mechanisms involving light Majorana neutrinos, classical Majorons, and sterile neutrinos*. Physical Review C, 88 (6):064322, 2013. doi:10.1103/PhysRevC.88.064322.
- [Reb15] H. Rebber. *Discrimination of Alpha Particles in CdZnTe Detectors with Coplanar Grid*. Master thesis, Universität Hamburg, 2015.
- [Red20] Redlen Technologies. *official website*, 2020, <https://redlen.com>, date of access: 2020-01-24.

- [REE⁺11] S. Rahaman, V.-V. Elomaa, T. Eronen, et al. *Double-beta decay Q values of ^{116}Cd and ^{130}Te* . Physics Letters B, 703 (4):412–416, 2011. doi:10.1016/j.physletb.2011.07.078.
- [RMP10] T. R. Rodríguez and G. Martínez-Pinedo. *Energy Density Functional Study of Nuclear Matrix Elements for Neutrinoless $\beta\beta$ Decay*. Physical Review Letters, 105 (25):252503, 2010. doi:10.1103/PhysRevLett.105.252503.
- [Roh94] J. W. Rohlf. *Modern Physics from α to Z^0* . Wiley, New York, 1st edition, 1994. ISBN 0471572705. doi:<https://www.wiley.com/en-us/Modern+Physics+from+alpha+to+Z0-p-9780471572701>.
- [Roh16] K. Rohatsch. *Charakterisierung von großvolumigen CdZnTe-Detektoren mit segmentierter CPG-Anodenkonfiguration für das COBRA-Experiment*. Diploma thesis, TU Dresden, 2016.
- [RPH⁺09] K. Roemer, G. Pausch, C. M. Herbach, et al. *A technique for measuring the energy resolution of low-Z scintillators*. IEEE Nuclear Science Symposium Conference Record, pages 6–11, 2009. doi:10.1109/NSSMIC.2009.5401909.
- [SAB19] M. Antonello, E. Barberio, T. Baroncelli, et al., SABRE collaboration. *Monte Carlo simulation of the SABRE PoP background*. Astroparticle Physics, 106:1–9, 2019. doi:10.1016/j.astropartphys.2018.10.005.
- [Sak91] A. D. Sakharov. *Violation of CP invariance, C asymmetry, and baryon asymmetry of the universe*. Soviet Physics Uspekhi, 34 (5):392–393, 1991. doi:10.1070/PU1991v034n05ABEH002497.
- [Sal68] A. Salam. *Weak and electromagnetic interactions*. Conference Proceedings C, 680519:367–377, 1968. doi:10.1142/9789812795915_0034.
- [SB16] B. Sahu and S. Bhoi. *Viola-Seaborg relation for α -decay half-lives: Update and microscopic determination of parameters*. Physical Review C, 93 (4):044301, 2016. doi:10.1103/PhysRevC.93.044301.
- [SBB⁺12] C. Smorra, T. Beyer, K. Blaum, et al. *Direct mass measurements of cadmium and palladium isotopes and their double- β transition Q values*. Physical Review C, 85 (2):027601, 2012. doi:10.1103/PhysRevC.85.027601.
- [Sch97] N. Schmitz. *Neutrinophysik*. Vieweg+Teubner Verlag, Wiesbaden, 1997. ISBN 978-3-519-03236-6. doi:10.1007/978-3-322-80114-2.
- [Sch11] O. Schulz. *Exploration of new Data Acquisition and Background Reduction Techniques for the COBRA Experiment*. PhD thesis, TU Dortmund, 2011.
- [Sch12] L. Schröder. *Untersuchungen zur Temperaturabhängigkeit der Energieauflösung von CdZnTe-Detektoren für das COBRA-Experiment*. Bachelor thesis, TU Dresden, 2012.
- [Sch14] B. Schoene. *U-Th-Pb Geochronology*. Treatise on Geochemistry, 4:341–378, 2014. doi:10.1016/B978-0-08-095975-7.00310-7.
- [SCS⁺04] C. Szeles, S. E. Cameron, S. A. Soldner, et al. *Development of the high-pressure electro-dynamic gradient crystal-growth technology for semi-insulating CdZnTe growth for radiation detector applications*. Journal of Electronic Materials, 33 (6):742–751, 2004. doi:10.1007/s11664-004-0076-z.

- [SCS⁺09] N. D. Scielzo, S. Caldwell, G. Savard, et al. *Double- β Decay Q-values of Te-130, Te-128, and Te-120*. Physical Review C, 80 (2):025501, 2009. doi:10.1103/PhysRevC.80.025501.
- [SGM⁺18] P. F. de Salas, S. Gariazzo, O. Mena, et al. *Neutrino Mass Ordering from Oscillations and Beyond: 2018 Status and Future Prospects*. Frontiers in Astronomy and Space Sciences, 5, 2018. doi:10.3389/fspas.2018.00036.
- [Sho38] W. Shockley. *Currents to Conductors Induced by a Moving Point Charge*. Journal of Applied Physics, 9 (10):635–636, 1938. doi:10.1063/1.1710367.
- [Sil16] Silvia Pascoli. *A portal to new physics*. CERN Courier, 2016, <https://cerncourier.com/a/a-portal-to-new-physics/>.
- [SM13] S. Stoica and M. Mirea. *New calculations for phase space factors involved in double- β decay*. Physical Review C, 88 (3):037303, 2013. doi:10.1103/PhysRevC.88.037303.
- [SM19] S. Stoica and M. Mirea. *Phase Space Factors for Double-Beta Decays*. Frontiers in Physics, 7, 2019. doi:10.3389/fphy.2019.00012.
- [SNO01] Q. R. Ahmad, R. C. Allen, T. C. Andersen, et al., SNO collaboration. *Measurement of the rate of $nue + d \rightarrow p + p + e^-$ interactions produced by 8B solar neutrinos at the Sudbury Neutrino Observatory*. Physical Review Letters, 87 (7):071301, 2001. doi:10.1103/PhysRevLett.87.071301.
- [SNO15] S. Andringa, E. Arushanova, S. Asahi, et al., SNO+ collaboration. *Current Status and Future Prospects of the SNO+ Experiment*. Advances in High Energy Physics, 2016, 2015. doi:10.1155/2016/6194250.
- [Sör11] A. Sörensen. *Ortsaufgelöste Effizienzbestimmung von CdZnTe Halbleiterdetektoren mit kollimierter Gammastrahlung für das C0BRA-Experiment*. Diploma thesis, TU Dresden, 2011.
- [ŠRFV13] F. Šimkovic, V. Rodin, A. Faessler, et al. *$0\nu\beta\beta$ and $2\nu\beta\beta$ nuclear matrix elements, quasiparticle random-phase approximation, and isospin symmetry restoration*. Physical Review C, 87 (4):045501, 2013. doi:10.1103/PhysRevC.87.045501.
- [Sto19] S. Stoica. *Computation of products of phase space factors and nuclear matrix elements for double beta decay*. Chinese Physics C, 43 (6):064108, 2019. doi:10.1088/1674-1137/43/6/064108.
- [Stu86] R. H. Stuewer. *Gamow's Theory of Alpha-Decay*. In *The Kaleidoscope of Science*, pages 147–186. Springer, 1986. doi:10.1007/978-94-009-5496-0_14.
- [STY⁺01] T. Schlesinger, J. Toney, H. Yoon, et al. *Cadmium zinc telluride and its use as a nuclear radiation detector material*. Materials Science and Engineering R, 32 (4-5):103–189, 2001. doi:10.1016/S0927-796X(01)00027-4.
- [Suh17] J. T. Suhonen. *Value of the Axial-Vector Coupling Strength in β and $\beta\beta$ Decays: A Review*. Frontiers in Physics, 5 (5), 2017. doi:10.3389/fphy.2017.00055.

- [Suh19] J. Suhonen. *Neutrino-Nuclear Responses and the Effective Value of Weak Axial Coupling*. Presentation, 2019, <https://indico.utef.cvut.cz/indico/event/15/session/2/contribution/45/material/slides/0.pdf>, date of access: 2020-02-09.
- [Sup98] Y. Fukuda, T. Hayakawa, E. Ichihara, et al., Super-Kamiokande collaboration. *Evidence for Oscillation of Atmospheric Neutrinos*. Physical Review Letters, 81 (8):1562–1567, 1998. doi:10.1103/PhysRevLett.81.1562.
- [Sup10] R. Arnold, C. Augier, J. Baker, et al., SuperNEMO collaboration. *Probing new physics models of neutrinoless double beta decay with SuperNEMO*. The European Physical Journal C, 70 (4):927–943, 2010. doi:10.1140/epjc/s10052-010-1481-5.
- [Sup20] M. Tanaka, K. Abe, C. Bronner, et al., Super-Kamiokande collaboration. *Search for proton decay into three charged leptons in 0.37 megaton-years exposure of the Super-Kamiokande*. Physical Review D, 101 (5):052011, 2020. doi:10.1103/PhysRevD.101.052011.
- [SV82] J. Schechter and J. W. Valle. *Neutrinoless double-decay in $SU(2) \times U(1)$ theories*. Physical Review D, 25 (11):2951–2954, 1982. doi:10.1103/PhysRevD.25.2951.
- [Tak84] E. Takasugi. *Can the neutrinoless double beta decay take place in the case of Dirac neutrinos?* Physics Letters B, 149 (4-5):372–376, 1984. doi:10.1016/0370-2693(84)90426-X.
- [Tan16] C. Tan. *Big Gaps and Short Bridges: A Model for Solving the Discontinuity Problem*. Answers Research Journal, 9:142–162, 2016, <https://assets.answersingenesis.org/doc/articles/pdf-versions/arj/v9/discontinuity-problem.pdf>.
- [TD35] G. Temple and P. A. M. Dirac. *The Principles of Quantum Mechanics*. The Mathematical Gazette, 19 (235):301, 1935. doi:10.2307/3606137.
- [Teb11] J. Tebrügge. *New read-out electronics and pulse shape analysis for the COBRA experiment*. Diploma thesis, TU Dortmund, 2011.
- [Teb16] J. Tebrügge. *Commissioning of the COBRA demonstrator and investigation of surface events as its main background*. PhD thesis, TU Dortmund, 2016.
- [Tem17] R. Temminghoff. *Investigation of the Depth Reconstruction and Search for Local Performance Variations With a Large Coplanar-Quad-Grid CdZnTe Detector*. IEEE Transactions on Nuclear Science, 64 (7):1934–1941, 2017. doi:10.1109/TNS.2017.2711922.
- [Tem19] R. Temminghoff. *The COBRA Extended Demonstrator – Conception, Characterization, Commissioning*. PhD thesis, TU Dortmund, 2019.
- [Thu20] J. Thurn. *High-precision measurement of the beta spectrum of Bi-210 using PIPS detectors*. PhD thesis in preparation, TU Dresden, 2020.
- [Tim15] J. Timm. *Studien seltener neutroneninduzierter Prozesse und Koinzidenzanalysen zur Bestimmung und Reduktion von Untergrundbeiträgen im COBRA-Experiment*. PhD thesis, Universität Hamburg, 2015.

- [Tre15] V. Tretyak. *DECAY0 event generator for initial kinematics of particles in α , β and 2β decays.* Presentation, 2015, https://agenda.infn.it/event/9358/attachments/57515/67844/Tretyak_2015.pdf, date of access: 2020-02-16.
- [TS98] J. Toivanen and J. Suhonen. *Microscopic quasiparticle-phonon description of odd-mass $^{127-133}\text{Xe}$ isotopes and their β decay.* Physical Review C, 57 (3):1237–1245, 1998. doi:10.1103/physrevc.57.1237.
- [TTM06] O. Tavares, M. Terranova, and E. Medeiros. *New evaluation of alpha decay half-life of ^{190}Pt isotope for the Pt-Os dating system.* NIM B, 243 (1):256–260, 2006. doi:10.1016/j.nimb.2005.08.122.
- [TZ95] V. Tretyak and Y. Zdesenko. *Tables of double beta decay data.* Atomic Data and Nuclear Data Tables, 61 (1):43–90, 1995. doi:10.1016/S0092-640X(95)90011-X.
- [TZ02] V. I. Tretyak and Y. G. Zdesenko. *Tables of Double Beta Decay Data - an Update.* Atomic Data and Nuclear Data Tables, 80 (1):83–116, 2002. doi:10.1006/adnd.2001.0873.
- [UCN10] J. Liu, M. P. Mendenhall, A. T. Holley, et al., UCNA collaboration. *Determination of the Axial-Vector Weak Coupling Constant with Ultracold Neutrons.* Physical Review Letters, 105 (21):219903, 2010. doi:10.1103/physrevlett.105.219903.
- [Var16] Various CouchApp Contributors. *CouchApp: Web Application Hosted in Apache CouchDB*, 2016, <https://couchapp.readthedocs.io/en/latest/>, date of access: 2020-03-07.
- [VIP17] J. Marton, S. Bartalucci, A. Bassi, et al., VIP collaboration. *VIP-2 at LNGS: An experiment on the validity of the Pauli Exclusion Principle for electrons.* Journal of Physics: Conference Series, 873:012018, 2017. doi:10.1088/1742-6596/873/1/012018.
- [Vol18] J. Volkmer. *Prospects of the investigation of EC/ β^+ decays with the COBRA experiment.* Master thesis, TU Dresden, 2018.
- [VRM75] V. Viola, C. Roche, and M. Minor. *Alpha decay of natural ^{186}Os .* Journal of Inorganic and Nuclear Chemistry, 37 (1):11–13, 1975. doi:10.1016/0022-1902(75)80115-1.
- [Wei35] C. F. v. Weizsäcker. *Zur Theorie der Kernmassen.* Zeitschrift für Physik, 96 (7-8):431–458, 1935. doi:10.1007/BF01337700.
- [Wei67] S. Weinberg. *A Model of Leptons.* Physical Review Letters, 19 (21):1264–1266, 1967. doi:10.1103/PhysRevLett.19.1264.
- [Wei79] S. Weinberg. *Baryon- and Lepton-Nonconserving Processes.* Physical Review Letters, 43 (21):1566–1570, 1979. doi:10.1103/PhysRevLett.43.1566.
- [Wes12] T. Wester. *Characterization of CdZnTe Coplanar Grid Detectors and Pulse Shape Analysis for the COBRA Experiment.* Diploma thesis, TU Dresden, 2012.

- [Wes19] T. Wester. *Characterisation of Coincidence Data of the Gerda Experiment to Search for Double Beta Decays to Excited States*. PhD thesis, TU Dresden, 2019.
- [WikA] Wikimedia. *Particle content of the Standard Model*, https://commons.wikimedia.org/wiki/File:Standard_Model_of_Elementary_Particles.svg, date of access: 2020-05-20.
- [WikB] Wikimedia. *Schematic of Bayes' theorem*, https://commons.wikimedia.org/wiki/File:Prior,_Likelihood,_Posterior_schematic.svg, date of access: 2020-03-19.
- [WikC] Wikimedia. *Semi-empirical mass formula*, https://commons.wikimedia.org/wiki/File:Semi-empirical_mass_formula.png, date of access: 2019-12-28.
- [WikD] Wikipedia. *Decay chain*, https://en.wikipedia.org/wiki/Decay_chain, date of access: 2020-02-25.
- [Wil68] F. L. Wilson. *Fermi's Theory of Beta Decay*. American Journal of Physics, 36 (12):1150–1160, 1968. doi:10.1119/1.1974382.
- [Wil20] H. Wilsenach. *Long-lived alpha decay*. PhD thesis in preparation, TU Dresden, 2020.
- [WMB⁺97] R. J. Walker, J. W. Morgan, E. S. Beary, et al. *Applications of the ¹⁹⁰Pt-¹⁸⁶Os isotope system to geochemistry and cosmochemistry*. Geochimica et Cosmochimica Acta, 61 (22):4799–4807, 1997. doi:10.1016/S0016-7037(97)00270-6.
- [Wol78] L. Wolfenstein. *Neutrino oscillations in matter*. Physical Review D, 17 (9):2369–2374, 1978. doi:10.1103/PhysRevD.17.2369.
- [WZ05] M. Wójcik and G. Zuzel. *Low-²²²Rn nitrogen gas generator for ultra-low background counting systems*. NIM A, 539 (1-2):427–432, 2005. doi:10.1016/j.nima.2004.10.023.
- [XEN19a] E. Aprile, J. Aalbers, F. Agostini, et al., XENON1T collaboration. *Light Dark Matter Search with Ionization Signals in XENON1T*. Physical Review Letters, 123 (25):251801, 2019. doi:10.1103/PhysRevLett.123.251801.
- [XEN19b] E. Aprile, J. Aalbers, F. Agostini, et al., XENON1T collaboration. *Observation of two-neutrino double electron capture in ¹²⁴Xe with XENON1T*. Nature, 568 (7753):532–535, 2019. doi:10.1038/s41586-019-1124-4.
- [Yan80] T. Yanagida. *Horizontal Symmetry and Masses of Neutrinos*. Progress of Theoretical Physics, 64 (3):1103–1105, 1980. doi:10.1143/PTP.64.1103.
- [Zat14] S. Zatschler. *Identification of Multi-Site Events in Coplanar-Grid CdZnTe-Detectors for the COBRA-Experiment*. Diploma thesis, TU Dresden, 2014.
- [Zat15] S. Zatschler. *The COBRA experiment – status and prospects on the search of neutrinoless double beta-decay*. AIP Conference Proceedings, 1686 (1):20027, 2015. doi:10.1063/1.4934916.

- [Zat17a] S. Zatschler. *Discrimination of single-site and multi-site events in CZT-CPG detectors for the COBRA experiment*. In *IEEE Nuclear Science Symposium Conference Record*. 2017. doi:10.1109/NSSMIC.2016.8069958.
- [Zat17b] S. Zatschler. *Pulse-shape discrimination techniques for the COBRA double beta-decay experiment at LNGS*. *Journal of Physics: Conference Series*, 888:12076, 2017. doi:10.1088/1742-6596/888/1/012076.
- [Zub01] K. Zuber. *COBRA - Double beta decay searches using CdTe detectors*. *Physics Letters B*, 519 (1-2):1–7, 2001. doi:10.1016/S0370-2693(01)01056-5.
- [Zub11] K. Zuber. *Neutrino Physics (Series in High Energy Physics, Cosmology and Gravitation)*. CRC Press, 2nd edition, 2011. ISBN 1420064711.

Acknowledgments

First of all, I would like to thank Prof. Kai Zuber for his constant trust and support during my time as a PhD student in his group and for being the primary reviewer of my thesis. I am especially grateful for the opportunity to work in such an international research group with connections to various interesting projects all over the world. Moreover, I thank Prof. Kevin Kröninger for being the second reviewer of the present work and helpful discussions.

I also like to thank the organizers of the *Graduiertenkolleg GRK 1504* and the German Research Foundation DFG for financial support and the opportunity to attend international conferences, summer schools and the block courses of the graduate school.

Furthermore, I would like to thank all members of the *Institute of Nuclear and Particle Physics (IKTP)* for the inspiring working atmosphere and especially the *Netzwerk Teilchenwelt* and its predecessor initiative for strengthen my interest in particles physics by starting the *International Masterclass* program during my high school time. This initiative and the opportunity to prepare a high school thesis at the IKTP greatly encouraged me to enroll for the study of physics at the TU Dresden. Particular thanks deserves the IKTP administration staff (in order of appearance): Gisela Schöler, Birgit Becker, Kristin Walter, Susanne Busch, and Nicole Beyer. Especially Nicole was a constant source of support and acted as the good spirit of the institute over the past years. Moreover, I thank the current and past IT administration team – Wolfgang Mader, Thomas Göpfert, Robert Mantey, Robert Ross and Rainer Hentges – as well as Andreas Glatte from the electronic laboratory for their constant support and advice in all kind of matters. The same applies to the members of the former radiation group of Jürgen Henniger and the TU Dresden physics workshop led by Martin Siegel.

I really enjoyed being part of the neutrino physics groups of Kai Zuber and I am especially grateful for the extensive discussions, constructive criticism and mutual interest in the present variety of research projects brought in by the group members. I hope that all of you keep their ambitions high and their open minded attitudes.

As a member of the COBRA collaboration, I would like to thank all fellows for the enjoyable collaboration meetings, their regular feedback and comments, and the constant trust in the proceeding of the project against sometimes harsh external conditions. I would like to thank in particular my fellow COBRA shifters (in order of appearance) – Daniel Gehre, Jan Tebrügge, Henning Rebber, Robert Temminghoff, Lucas Bodenstein-Dresler, Juliane Volkmer, Yingjie Chu and Julia Köttler. You have made each trip to the LNGS a memorable experience from dealing with seemingly never ending, on first sight unsolvable problems, over the accidental triggering of an alarm on a Sunday night, to literally tons of antipasti, pizza and arrosticini at the *Giampy* or the legendary *Trattoria Fore le Mura da Franchino*. Thank you for experiencing commonly the *joy of sorbetto* at Franchino’s, the philosophical discussion on how vegetarians can become/get fed and the forays into *downtown Assergi* and

the surrounding country sides. For past and current on-site support at the LNGS, I have to thank our local supervisors Nicola Rossi, Vincenzo Caracciolo and Marco Balata and our former TU Dresden colleagues Bjoern Lehnert, Axel Boeltzig and Jan Thurn.

A big thanks belongs to the three persons that *volunteered* to participate in the proof-reading of my thesis: Thomas Wester, Katja Voigt and Birgit Zatschler. I really appreciated your commitment, effort to think things through and the valuable input you provided.

My whole family deserves my deep gratitude for being an incredible moral and financial support during my study time, as well as for being the animating spirit to indulge myself in holidays and short resting times from the daily struggles as a PhD student. Thank you all for being patient and understanding, and for keeping up my spirit in difficult times. Speaking to all of you encouraged me to value what I have achieved and experienced in life so far, even though from your point of view it might have been almost incomprehensible to understand the fascination behind the hunt for answers to the fundamental nature of neutrinos and the universe we are all in. A special thanks goes to my mother for bringing the joy of reading and the spirit of natural sciences into my life at a very early stage.

I would also like to thank Prof. Miriam Diamond for offering me a postdoctoral fellowship at the University of Toronto in the SuperCDMS project. I am really looking forward to switching from rare nuclear decay searches to the dark matter community and to team-up with some of my former supervisors and colleagues – namely Matthew Fritts and Belina von Krosigk, who are both substantially responsible for me pursuing a PhD in the first place.

Finally, and by no means least, I am deeply grateful to my wife Biggi for being the person that completes my daily life and shares my passion for science. Thank you for your constant trust, support and all the exciting and sometimes troublesome adventures we went through the past years. Thank you for completing what I call home, despite from where we are.

All decisions, good or poor, led me to where I am today. Thanks to all of you for being part of this journey and I hope to see many of you along the road towards upcoming – scientific and real life – adventures that will come to pass in the future.

Thank you all very much!

Versicherung

Hiermit versichere ich, dass ich die vorliegende Arbeit ohne unzulässige Hilfe Dritter und ohne Benutzung anderer als der angegebenen Hilfsmittel angefertigt habe; die aus fremden Quellen direkt oder indirekt übernommenen Gedanken sind als solche kenntlich gemacht. Die Arbeit wurde bisher weder im Inland noch im Ausland in gleicher oder ähnlicher Form einer anderen Prüfungsbehörde vorgelegt.

Die Promotion wurde an der Technischen Universität Dresden, am Institut für Kern- und Teilchenphysik unter der wissenschaftlichen Betreuung von Prof. Dr. Kai Zuber durchgeführt.

Ich erkenne die Promotionsordnung des Bereichs Mathematik und Naturwissenschaften der TU Dresden vom 23.02.2011 an.

Stefan Zatschler
Dresden, 29. Juni 2020